Detection and characterization of exoplanets in high contrast images by the inverse problem approach

Faustine Cantalloube

Communauté
UNIVERSITÉ Grenoble Alpes

ONERA
THE FRENCH AEROSPACE LAB

THÈSE

Pour obtenir le grade de

DOCTEUR DE LA COMMUNAUTE UNIVERSITE GRENOBLE ALPES

préparée dans le cadre d'une cotutelle *entre la Communauté Université Grenoble Alpes et l'Onera*

Spécialité : **Astrophysique et Milieux Dilués**

Arrêté ministériel : le 6 janvier 2005 - 7 août 2006

Présentée par

Faustine CANTALLOUBE

Thèse dirigée par **David MOUILLET** et **Laurent MUGNIER**

préparée au sein de **l'IPAG** et de **l'Onera**

dans **l'École Doctorale de Physique de Grenoble**

Détection et caractérisation d'exoplanètes dans des images à grand contraste, par la résolution de problème inverse.

Thèse soutenue publiquement le **30 Septembre 2016,**
devant le jury composé de :

Mr Thierry FORVEILLE
Astronome, IPAG, Président
Mr Wolfgang BRANDNER
Senior Scientist, MPIA , Rapporteur
Mr Laurent PUEYO
Senior Scientist, STScI, Rapporteur
Mr Arthur VIGAN
Chargé de Recherche, LAM, Membre
Mr Sasha HINKLEY
Senior Lecturer, University of Exeter, Invité
Mr David MOUILLET
Chargé de Recherche, IPAG, Directeur de thèse
Mr Laurent MUGNIER
Maître de Recherche, Onera, Co-Directeur de thèse

Abstract

Direct imaging of exoplanets provides valuable information about their nature, their interactions with their host star environment and their atmospherical composition through the light they emit. In order to image such objects, advanced data processing tools adapted to the instrument are needed. In particular, the presence of quasi-static speckles in the images, due to optical aberrations distorting the light from the observed star, prevents planetary signals from being distinguished. In this thesis, I present two innovative image processing methods, both based on an inverse problem approach, enabling the disentanglement of the quasi-static speckles from the planetary signals. My work consisted of improving these two algorithms in order to be able to process on-sky images.

The first one, called ANDROMEDA, is an algorithm dedicated to point source detection and characterization via a maximum likelihood approach. ANDROMEDA makes use of the temporal diversity provided by the image field rotation during the observation, to recognize the deterministic signature of a rotating companion over the stellar halo. From application of the original version on real data, I have proposed and qualified improvements in order to deal with the non-stable large scale structures due to the adaptative optics residuals and with the remaining level of correlated noise in the data. Once ANDROMEDA became operational on real data, I analyzed its performance and its sensitivity to the user-parameters proving the robustness of the algorithm. I also conducted a detailed comparison to the other algorithms widely used by the exoplanet imaging community today showing that ANDROMEDA is a competitive method with practical advantages. In particular, it is the only method that allows a fully unsupervised detection. By the numerous tests performed on different data set, ANDROMEDA proved its reliability and efficiency to extract companions in a rapid and systematic way (with only one user parameter to be tuned). From these applications, I identified several perspectives whose implementation could still significantly improve the performance of the pipeline.

The second algorithm, called MEDUSAE, consists in jointly estimating the aberrations (responsible for the speckle field) and the circumstellar objects by relying on a coronagraphic image formation model. MEDUSAE exploits the spectral diversity provided by multispectral data. In order to refine the inversion strategy and probe the most critical parameters, I applied MEDUSAE on a simulated data set generated with the model used in the inversion. To investigate further the impact of the discrepancy between the image model used and the real images, I applied the method on realistic simulated images. At last, I applied MEDUSAE on real data and from the preliminary results obtained, I identified the important input required by the method and proposed leads that could be followed to make this algorithm operational to process on-sky data.

Résumé

L'imagerie d'exoplanètes permet d'obtenir de nombreuses informations sur la lumière qu'elles émettent, l'interaction avec leur environnement et sur leur nature. Afin d'extraire l'information des images, il est indispensable d'appliquer des méthodes de traitement d'images adaptées aux instruments. En particulier, il faut séparer les signaux planétaires des tavelures présentes dans les images qui sont dues aux aberrations instrumentales quasi-statiques. Dans mon travail de thèse je me suis intéressée à deux méthodes innovantes de traitement d'images qui sont fondées sur la résolution de problèmes inverses.

La première méthode, ANDROMEDA, est un algorithme dédié à la détection et à la caractérisation de point sources dans des images haut contraste via une approche statistique basée sur une estimation par maximum de vraisemblance. ANDROMEDA exploite la diversité temporelle apportée par la rotation de champ de l'image (où se trouvent les objets astrophysiques) alors que la pupille (où les aberrations prennent naissance) est gardée fixe. A partir de l'application sur données réelles de l'algorithme dans sa version originale, j'ai proposé, évalué et validé des améliorations afin de prendre en compte les résidus non modélisés par la méthode tels que des structures de bas ordres variant lentement et le niveau résiduel de bruit correlé dans les données. Une fois l'algorithme ANDROMEDA opérationnel, j'ai analysé ses performances et sa sensibilité aux paramètres utilisateurs, montrant la robustesse de la méthode. Une comparaison détaillée avec les algorithmes les plus utilisés dans la communauté a prouvé que cet algorithme est compétitif avec des performances très intéressantes dans le contexte actuel. En particulier, il s'agit de la seule méthode qui permet une détection entièrement non-supervisée. De plus, l'application à de nombreuses données prises sur ciel venant d'instruments différents a prouvé la fiabilité de la méthode et l'efficacité à extraire rapidement et systématiquement (avec un seul paramètre utilisateur à ajuster) les informations contenues dans les images. Ces applications ont aussi permis d'ouvrir des perspectives pour adapter cet outil aux grands enjeux actuels de l'imagerie d'exoplanètes.

La seconde méthode, MEDUSAE, consiste à estimer conjointement les aberrations et les objets d'intérêt scientifique, en s'appuyant sur un modèle de formation d'images coronographiques. MEDUSAE exploite la redondance d'informations apportée par des images multi-spectrales. Afin de raffiner la stratégie d'inversion de la méthode et d'identifier les paramètres les plus critiques, j'ai appliqué l'algorithme sur des données générées avec le modèle utilisé dans l'inversion. J'ai ensuite appliqué cette méthode à des données simulées plus réalistes afin d'étudier l'impact de la différence entre le modèle utilisé dans l'inversion et les données réelles. Enfin, j'ai appliqué la méthode à des données réelles et les résultats préliminaires que j'ai obtenus ont permis d'identifier les informations importantes dont la méthode a besoin et ainsi de proposer plusieurs pistes de travail qui permettront de rendre cet algorithme opérationnel sur données réelles.

Aux supernovae, nos mamans à tous

Remerciements

My first warm thanks go to W. Brandner and L. Pueyo who both kindly and bravely accepted to review this thesis whereas Wolfgang was commissioning the GRAVITY adaptive optics system (CIAO being the name) and Laurent commissioning his brand new daughter (Aveline being the name). I also owe a great thank to the full jury, including Sasha and Arthur to have made it to Grenoble (and Thierry of course but the journey was somewhat easier): I really had an awesome time during the defense (despite the whooping cough!). Thanks also to have read the whole manuscript until page "one thousand eighty something" (sorry Sasha you couldn't see more of Grenoble the day before).

Évidemment un grand merci à Laurent et David d'avoir tous les deux acceptés de me prendre en thèse il y a de ça trois ans ! Haha si j'avais su ! Bah, j'aurais sûrement fait la même bêtise en fait !

Laurent, je te promets solennellenent de quantifier tous mes résultats à partir de ce jour et de fournir un dictionnaire Faustine-Français à toute personne susceptible d'intervenir dans ma vie de scientifique. En tout cas, c'était vraiment pas mal du tout[1] ;-)

David, merci de t'être donné à fond pour me soutenir, particulièrement pendant ma dernière année (et d'avoir assumé qu'il s'agissait de 86% de psychologie et non d'astrophysique) et pour tes mails encourageants à coup de 4G [2] !

Un grand merci à la VORTEX team, menée brillamment par Olivier Absil, pour m'avoir prise sous son aile. J'espère vraiment que je vais continuer à travailler avec l'équipe à l'avenir. Et merci aussi à tous mes collaborateurs qui ont gentillement accepté de me donner de la pitance scientifique durant ces trois années et avec qui j'espère également continuer à travailler.

Un dernier remerciement top spécial pour mes deux cobureaux de rêve : Jeff côté Onera et Sibylle côté IPAG. Vous êtes tous les deux les plus chouettes cobureaux de la Terre, mais pourquoi a-t-il fallu que vous ne soyez là que 10% du temps !? C'est vraiment trop inzuste ! Un immense merci pour votre amitié et la distribution imprévisible d'épaules pour chouiner dessus. Et surtout Sibylle pour tes essentiels encouragements via ta propre expérience dans la recherche.

Au cours de ces 3 années de thèse, j'ai eu la chance inouïe de rencontrer tout un tas de "ptits chous"[3] incroyablement "cools" ! Et comme un ptit dessin vaut parfois mieux qu'un long discours : merci à tous [4] !

[1] Voir traduction p. 3 du dictionnaire : correspond à un EQM de 70% ±10.

[2] Private joke : Go Go Go Go !

[3] Dur dur de ne pas plus profiter de l'occasion unique des remerciements de thèse, désolée d'avance pour ceux que j'ai oublié.

[4] Avec un spécial big-up pour tout ceux qui se sont bougés le popotinou jusqu'à Grenoble - parfois de très loin (record de 12 500km) - afin de combler la salle Forestini de tout votre kiffe en ce 30 septembre 2016 - date de l'écrabouillement de Rosetta sur Chury' - et de mon carambolage dans le monde des docteurs.

"Love et paillettes sur vos têtes, parce que la thèse c'est chouette"©.

Contents

General introduction **10**

1 Exoplanet imaging with high contrast instruments **12**
1.1 Studying exoplanets . . . 13
1.1.1 Indirect methods of detecting and studying exoplanets . . . 14
1.1.2 Direct imaging for exoplanet study . . . 19
1.2 High contrast imaging with ground-based telescopes . . . 25
1.2.1 Adaptive optics systems . . . 26
1.2.2 High contrast for exoplanet imaging: Coronagraphy . . . 30
1.2.3 The speckle noise limitation . . . 34
1.2.4 Dedicated instruments to high contrast exoplanet imaging . . . 34
1.3 Image processing for exoplanet observation . . . 39
1.3.1 Image restoration: inverse problems . . . 39
1.3.2 Current image processing for exoplanet imaging . . . 43

Summary in French of the introduction chapter **50**

I ANDROMEDA: Exploitation of the temporal diversity in the images. **54**

2 The ANDROMEDA approach and initial status **56**
2.1 ANDROMEDA's principle . . . 57
2.1.1 Theoretical concept . . . 57
2.1.2 Practical solutions . . . 59
2.1.3 Inversion method . . . 63
2.2 Previous work on the ANDROMEDA method . . . 67
2.2.1 Description of the simulated data used to test the method . . . 67
2.2.2 Theoretical study of the potential sources of errors . . . 68
2.2.3 Optimal set of user-parameters derived from simulated data application . . . 69
2.3 Application of ANDROMEDA on real data as it is . . . 73
2.3.1 Description of the real data used to apply ANDROMEDA . . . 73
2.3.2 Output provided by ANDROMEDA . . . 74
2.3.3 Detected problems affecting ANDROMEDA's capabilities on real data . . . 76
2.3.4 Conclusion on ANDROMEDA's original capabilities . . . 77

3 ANDROMEDA: making it operational to process real data **79**
3.1 Stages required to make ANDROMEDA operational . . . 80
3.1.1 Removing the low spatial frequencies in the reduced images . . . 80
3.1.2 Correcting for the radial dependency of the SNR statistics . . . 87
3.1.3 Conclusion on ANDROMEDA in its operational state . . . 97
3.2 Exploring variations on building the differential images . . . 97
3.2.1 Description of the data to illustrate this part . . . 98
3.2.2 Interpretation of the scaling factor γ after pre-filtering the images . . . 98

3.2.3 Refining the ADI process included in ANDROMEDA . . . 102
3.2.4 Test of the robust affine fit in real differential images . . . 104
3.2.5 Adapting the model of the planetary signature in the differential images . . . 109
3.3 Automatic companion extraction, properties and reliability criteria . . . 112
3.3.1 Detection and astrometry . . . 112
3.3.2 Photometry . . . 114
3.3.3 Sorting out artifacts from probable true detections . . . 115
3.3.4 Estimation of the detection limit . . . 116
3.3.5 Ergonomics of the detection module . . . 116

4 Sensitivity to user-defined parameters and final contrast performance 119
4.1 Test case: VLT/NaCo data in H-band . . . 119
4.1.1 Target star: data set TYC-8979-1683-1 . . . 120
4.1.2 Reference case: user-parameters setting . . . 120
4.1.3 Reference case: Results with ANDROMEDA . . . 121
4.2 Sensitivity to the user-defined parameters . . . 121
4.2.1 Pre-filtering of the reduced images . . . 122
4.2.2 Building the differential images via ADI . . . 124
4.2.3 Building the model of the differential images . . . 130
4.2.4 Post-normalization of the SNR map . . . 134
4.3 Discussion on the threshold set for the detection . . . 137
4.4 Performance of the ANDROMEDA method . . . 138

5 ANDROMEDA: Comparison with other methods 143
5.1 Dataset: The SPHERE-IRDIS blind test . . . 144
5.1.1 Description of the provided dataset . . . 144
5.1.2 Synthetic companions injected . . . 144
5.1.3 Description of the provided images . . . 145
5.2 Short description of the other algorithms used . . . 145
5.2.1 Radial ADI, r-ADI . . . 146
5.2.2 Upgraded T-LOCI . . . 148
5.2.3 Classical PCA, c-PCA . . . 149
5.2.4 ANDROMEDA . . . 150
5.3 Comparison criteria . . . 151
5.3.1 Detection capabilities . . . 152
5.3.2 Characterization capabilities . . . 153
5.3.3 Practical aspects . . . 155
5.3.4 Ranking metric used for this study . . . 155
5.4 Results obtained and comparison . . . 155
5.4.1 Final images obtained by the pipelines . . . 156
5.4.2 Detected planetary companions . . . 157
5.4.3 Results of the characterization by the pipelines . . . 157
5.4.4 Processing time for each pipeline . . . 160
5.4.5 Practical aspects . . . 161
5.4.6 Conclusion on the different pipelines performance . . . 162

6 ANDROMEDA: Applications on various experimental data 164
6.1 Response of ANDROMEDA to the different narrow band filters offered by SPHERE-IRDIS . . . 166
6.1.1 The planetary companion GJ504 b . . . 166
6.1.2 Properties of the GJ504 IRDIS images . . . 167
6.1.3 User-parameters to run ANDROMEDA on the GJ504 IRDIS images . . . 167
6.1.4 Results from ANDROMEDA applied to the GJ504 SPHERE-IRDIS images . . . 168

6.2 Response of ANDROMEDA to different observing conditions . . . 169
6.2.1 Observation conditions of the star GJ504 at different epochs . . . 170
6.2.2 User-parameters set to process the images of GJ504 at different epochs . . . 170
6.2.3 Results from the application of ANDROMEDA on the GJ504 images at different epochs . . . 170
6.3 Investigating for a difficult source: the case of 51Eri b in H-band . . . 173
6.3.1 The planetary companion 51Eri b . . . 173
6.3.2 Observation conditions of the star 51Eri by SPHERE-IRDIS in H-band . . . 174
6.3.3 ANDROMEDA user-parameters to process the SPHERE-IRDIS 51Eri data . . . 174
6.3.4 Results of ANDROMEDA applied to the SPHERE-IRDIS images of 51Eri . . . 174
6.4 SDI+ADI process of SPHERE-IRDIS data in DBI mode, by ANDROMEDA . . . 175
6.4.1 The case of a companion showing an absorption band: 51Eri images in H2H3 bands . . . 176
6.4.2 The case of the planetary system HR8799 in H2H3 bands . . . 177
6.5 Processing SPHERE-IFS data with ANDROMEDA . . . 182
6.5.1 Multispectral cubes properties and user-parameters set for ANDROMEDA . . . 182
6.5.2 Collapsing the images to obtain the detection . . . 182
6.5.3 Multi-channel detection and channelwise spectrum estimation . . . 184
6.5.4 Using SADI to increase the detectability and sensitivity . . . 188
6.5.5 Preliminary spectra retrieved by ANDROMEDA . . . 191

Summary in French of the first part **198**

II MEDUSAE: Exploitation of the spectral diversity in the images. **203**

7 The MEDUSAE approach and initial status **205**
7.1 The MEDUSAE approach: image model and inversion . . . 206
7.1.1 Model of the multispectral images . . . 206
7.1.2 Inversion criterion . . . 210
7.1.3 Methods to estimate the three unknowns . . . 210
7.1.4 Minimization algorithm used for the phase retrieval in MEDUSAE . . . 212
7.1.5 Inversion scheme to run MEDUSAE . . . 212
7.2 Main hypothesis used in MEDUSAE . . . 213
7.3 Previous work on the MEDUSAE method . . . 214
7.3.1 Simulated data to validate the MEDUSAE concept . . . 214
7.3.2 Tests and conclusion from the inverse crime MEDUSAE application . . . 215

8 Refining the MEDUSAE strategy on inverse crime **219**
8.1 Simulated data and analysis criteria . . . 219
8.1.1 Simulated data used for tests . . . 219
8.1.2 Analysis criteria . . . 221
8.2 Inversion scheme: revisiting the strategy . . . 222
8.2.1 Multispectral phase retrieval for a known object . . . 223
8.2.2 Initialization procedure . . . 224
8.2.3 MEDUSAE core . . . 228
8.3 Corruption due to intense planetary signals . . . 230
8.4 Sensitivity to the inputs required by MEDUSAE . . . 231
8.4.1 Error on the downstream aberration map δ_{down} . . . 231
8.4.2 Error on the residual phase structure function $D_{\phi_{res}}$ . . . 234

9 Towards application on real data: tests on realistic simulated data 237
9.1 Simulation of realistic multispectral high contrast images . . . 238
9.1.1 Short exposure realistic coronagraphic PSF . . . 238
9.1.2 SPHERE-IFS data characteristics . . . 239
9.1.3 Chosen characteristics of the images . . . 240
9.1.4 Generation of a representative $D_{\phi_{res}}$ . . . 241
9.1.5 Resulting realistic simulated images . . . 242
9.2 Application of MEDUSAE on the realistic simulated data . . . 244
9.2.1 First application: Reference case . . . 244
9.2.2 Estimating the speckle field only . . . 247
9.2.3 Estimating the object map with MEDUSAE . . . 252
9.3 Perspectives for the MEDUSAE methods . . . 255

Summary in French of the second part 258

General conclusion 262

General conclusion in French 264

Appendix 265

A Publication on the ANDROMEDA pipeline applied on VLT/NaCo data 265

B User Manual for the ANDROMEDA pipeline 285

C Analytical models of long exposure coronographic PSF 304
C.1 Notations and hypothesis: . . . 304
C.1.1 Notations for the coronagraph setup: . . . 304
C.1.2 Definition of the residual turbulence phase structure function: . . . 305
C.1.3 Definition of convolution, inter-correlation and auto-correlation: . . . 305
C.2 Ideal coronagraph (Sauvage et al., 2010) . . . 305
C.2.1 Difference between the two models . . . 305
C.3 Almost perfect coronagraph (Ygouf, 2012) . . . 305
C.4 The Fourier coronagraph (Hercovisci et al., 2016) . . . 306
C.4.1 Special case of Eq. C.20: without coronagraph . . . 308
C.4.2 Special case of Eq. C.20: without turbulence . . . 308

D Preliminary results: Application of MEDUSAE on in-lab data 309
D.1 Description of the in-lab data . . . 309
D.2 Results from MEDUSAE applied on in-lab data . . . 309
D.2.1 Different couples of ϕ_{down} and $D_{\phi_{res}}$ input . . . 309
D.2.2 Results of further tests for the MEDUSAE application on the in-lab data . . . 312
D.2.3 Conclusions on preliminary tests on the in-lab data . . . 315

E List of communications 317

Bibliographic references 319

General introduction

Exoplanet imaging is a major field of astrophysics which, complementary to other indirect techniques, provides valuable information on exoplanetary systems. In particular, direct imaging presents three major areas of intensive research:

1. The detection of massive giant planets at large orbits (more than 5-10 AU): By studying the derived parameters (e.g. the range of their masses, their distance to the host star and the age or type of the host star), we can, on the one hand, better understand the nature of these objects, and on the other, constrain their orbital parameters to get clues about the formation and migration process of giant planets.
2. The deep analysis of planetary emission spectra: This allows the study of their atmospheric composition (such as chemical compounds, dust amount, cloud layers or weather) and investigate the presence of biomarkers.
3. In case of the presence of a circumstellar disk (either protoplanetary for young systems or debris for more mature ones): The study of the disk to planet connection brings further constraints on the current models of planetary formation and evolution.

For the proper determination of these astrophysical quantities we need to optimize the current image processing tools and to develop specific innovative algorithms adapted to the instrument, so as to minimize the systematic uncertainties. During the past few years, major evolutions in both instrumentation, sensors and computer capabilities enabling the use of advanced signal processing techniques, resulted in scientific breakthroughs such as the discovery of 51 Eri b unveiled with GPI (Macintosh et al., 2015), the detailed features and the enigmatic rapidly moving ripples revealed by a deep imaging of the AU Mic disk with SPHERE (Boccaletti et al., 2015) or the retrieved spectrum of the HR8799 e companion at short wavelength (Bonnefoy et al., 2016; Zurlo et al., 2016). The discovery of the giant exoplanet Beta-Pictoris b (Lagrange et al., 2010) from 2003 NaCo images or the rediscovery of HR8799 b, c and d in archival HST NICMOS data (Soummer et al., 2011) and the ALICE project (Choquet et al., 2015) show that applying innovative detection tools on older data can lead to essential discoveries or objects follow-up, which are both essential to strengthen the constraints on the planetary formation models.

There are still pending questions about the optimization of current signal processing algorithms used by the community and new methods to be developed specifically for the instrument used and the type of object sought. For instance, up to now, no method enabled to detect planetary companions in an unsupervised way. Also no dedicated method fully exploits the information provided by multispectral coronagraphic images. This manuscript presents the work I have done during the three years of my PhD on two algorithms which address these problematics. The originality of these two algorithms is that they are both based on an inverse problem approach: an image model is used to directly estimate the most probable unknowns of the problem, such as the position and the flux of a potential planetary companion.

In the first chapter, I describe the motivations of exoplanet imaging and why image processing methods are essential to optimally exploit the infrared high contrast instruments used for this purpose.

In the first part of the thesis, I present my work on the ANDROMEDA algorithm, which exploits the temporal diversity of the images provided by the current high contrast instruments. The principle

of this algorithm has been developed by Mugnier et al. (2009) but was not yet operational on real data. My approach was to implement means of compensating the discrepancy between the model used in the algorithm and the real images properties. Once this ANDROMEDA algorithm was able to process on-sky data, I refined the method, conducted a thorough analysis of its performance and compared it to the three major image processing methods currently used by the exoplanet imaging community. In a last chapter, I present various applications of this algorithm to on-sky data, revealing new detections and fine characterizations of stellar companions.

In the second part of this thesis, I present my work on the MEDUSAE algorithm, which exploits the spectral diversity provided by integral field spectrographs. The basis of this algorithm has been established by Ygouf et al. (2013) but this algorithm had not been applied on real data yet. My approach was to revisit the algorithm strategy and conduct sensitivity tests on ideal simulated data. I then present applications of this algorithm on realistic simulated data, following the properties of the SPHERE-IFS instrument. I also present preliminary application of MEDUSAE on real in-lab data, which raise several perspectives to make this algorithm operational on on-sky data in the future.

Chapter 1

Exoplanet imaging with high contrast instruments

Contents

1.1 Studying exoplanets 13
1.1.1 Indirect methods of detecting and studying exoplanets 14
1.1.2 Direct imaging for exoplanet study 19
1.2 High contrast imaging with ground-based telescopes 25
1.2.1 Adaptive optics systems 26
1.2.2 High contrast for exoplanet imaging: Coronagraphy 30
1.2.3 The speckle noise limitation 34
1.2.4 Dedicated instruments to high contrast exoplanet imaging 34
1.3 Image processing for exoplanet observation 39
1.3.1 Image restoration: inverse problems 39
1.3.2 Current image processing for exoplanet imaging 43

This chapter introduces the context of the research I conducted during the three years of my PhD.

Unlike experimental sciences, the only information astrophysicists have comes from observations. Simulations or in-lab experiments try to reproduce what is observed in the distant universe but it is impossible to access the system under study and to tune the parameters to better understand it. Moreover the physics laws apply in extremely different conditions which usually cannot be reproduced in laboratory. By the different scales of distance, size and time of the event as well as the physical conditions (such as pressure and temperature) in which the studied objects evolve, astrophysics is a particularly challenging science and related to many fields of physics. Planet formation is a very good example: it cannot be reproduced in laboratory, and only observations of our own, already formed solar system are available while observations of younger extra-solar systems are very challenging and provide scarce but very valuable information.

My PhD work is in the field of exoplanets which is a very young field of research as the first exoplanet discovery was announced in the 90's. The orbital time scales are from days to tens of years and the size of the objects under study are of the order of magnitude of the planets constituting our solar system. Today about 3500 exoplanets have been discovered[1] among the close stars of our Galaxy (less than 10kpc from the Sun). Among these detections, various configurations and objects that were not expected have been discovered. There is no strict definition for an exoplanet[2]. For now it can be defined as:

[1] Source: http://exoplanet.eu/ as on July 2016.

[2] Two official definitions are established by the International Astronomical Union (IAU), one concerning the small planets of size comparable to those of our solar system, and the other concerning the giant exoplanets which is still controversial. The definitions can be found in http://w.astro.berkeley.edu/~basri/defineplanet/IAU-WGExSP.htm

1. an object whose mass is below the limit of deuterium fusion (i.e. $< 13 M_{jup}$);
2. an object which revolves around a star (or a compact object);
3. an object which is massive enough so that its overall spherical shape is dominated by its gravitation (and not by its electrostatics forces) and so that it is the dominating body on its orbit (unlike dwarf planets or a population of asteroids occupying a common orbit);

However this definition does not take into account potential free-floating planets (considered as *sub-brown dwarfs*) yet unveiled by gravitational microlensing (Sumi et al., 2011) or by direct imaging (Delorme et al., 2012). A physical definition should certainly include the fact that planets are formed within the gas and dust disk surrounding young stars during their first million years. This definition directly motivates a better understanding of the formation processes of planets, and how they impact the observational properties of planetary-mass companions detected possibly billions of years later. For now, two main scenarios of planetary formations are considered:

(1) the *Core Accretion* scenario (Pollack et al., 1996) favors a model in which planetesimals, formed from the dust grains constituting the protoplanetary disk (essentially made of silicate and metals in its inner part and ice in its outer part), coagulate in massive rocky cores by using all the available material until its mass stabilizes. If the disk is massive enough, these cores can reach the necessary mass to accrete gas, then becoming giant gaseous planets. Because the disk disperses its gaseous disk in some million years (by photoevaporation, accretion onto the star and photodesorption mainly), this stage is assumed to be fast enough (less than a million years). Also this stage is favored by the presence of ice, so formation of giant planets is facilitated at larger distance from the star, beyond the ice line (further than a few AUs depending on the stellar mass), but close enough to keep enough disk mass (below 10-15 AUs).

(2) the *Gravitational Instability* scenario (Boss, 2002) states that local instabilities induce the fragmentation of the protoplanetary disk into objects of several Jupiter masses whose collapse forms giant planets. The latter is a faster process which could explain the presence of giant planets at large separation from young stars that have been detected by direct imaging.

However, these two models do not explain the huge variety of exoplanets observed for twenty years. Other processes such as migration and interaction with the planetary environment (disks or other planets) must be taken into account to better understand the variety of these observations.

My subject of study focuses on the direct imaging of such objects in infrared, that is necessary to complete our understanding of exoplanets. In Sect. 1.1, I expose the various exoplanet detection techniques along with their limitation and biases, which motivate exoplanet imaging in spite of the observational difficulties. More specifically, my work is in the field of image post-processing that is necessary to detect and characterize exoplanets within high-contrast images. The post-processing methods I present in this thesis are based on the instrument knowledge and cannot be disentangled from the instrument features. In Sect. 1.2 I describe the instrumental solutions used to address the technical challenges imposed by exoplanet direct imaging. The fundamental limits of these instrumental solutions are the main stake motivating my work on image post-processing techniques. In Sect. 1.3 I specifically describe what are the main characteristics that can be used to develop image processing techniques for exoplanet detection, knowing the properties and fundamental limits of the instrument.

1.1 Studying exoplanets

In this section, I focus on why direct imaging is an important field of exoplanetary science by the kind of information and objects it has access to. Exoplanet study has several purposes that can be summarized in four interrelated questions:

1. How do giant planets and telluric planets form (in close relation to how do stars form)?
2. What are the typical architectures of planetary systems and how do they evolve?

3. What are the physical properties of exoplanets (structure and atmosphere) and how do they evolve?

4. Are there biomarkers on planets outside of the solar system? And particularly for telluric planets in the so-called *habitable zone*.

In order to address the first question, it is needed to study the interactions between the star forming region and the planetary companions. Only direct imaging can study simultaneously the disk-planet interactions (either in submillimeter or visible/infrared wavelengths and using either classical imaging or interferometry). Also, it is needed to study the occurrence of exoplanets around different types of star (age, metallicity, spectral type), for which imaging is complementary to other techniques.

In order to address the second and third questions, it is needed to detect as many different planets as possible, that is to say, with different ages, masses, sizes and distances to their host star. Among the five techniques I expose in this section, direct imaging is the only one which specifically probes companions that are younger, more massive and further from their host star compared to planets detected with indirect methods. In this prospect, the combination of different observation techniques is crucial to probe planetary companions in various situations.

In order to address the fourth question, it is required to obtain a spectrum of the observed exoplanet. Access to the photons from the planets through direct imaging is a key point here.

In this section, I describe the five well established methods used to detect exoplanets nowadays and give some of their specificity that help addressing these questions. I chose to present these methods by chronology of first detections since it indicates if the method is technically accessible and easy to set-up. I also sort these methods by the physical concept on which they rely and not by the physical parameter which is used (such as time or photometry). Note that I only go through the classical main methods although different flavors of each of them can be found, because only a few detections have been found with these specific flavors.

1.1.1 Indirect methods of detecting and studying exoplanets

1.1.1.1 Pulsar timing

The very first detection of an exoplanet has been made thanks to *pulsar timing*.

A pulsar (for pulsating radio star) is a neutron star remaining from an intermediary mass star (between 10 and 30 solar masses) which ended its life in a supernovae. During the parent star collapse, the remaining core (of about 10 kilometers diameter) preserved almost all the angular momentum and magnetic field making this object spinning very fast around its axis and creating two radio-beams from its magnetic poles (frequencies between 150 kHZ and 3 GHz). If one of the two beams is visible from Earth, the source is called a pulsar and emits brief and periodic signals[3]. Milliseconds pulsars (rotating with a period of the order of milliseconds, as discovered by Backer et al., 1982) have a highly regular rotation period on short time scales. This regularity is used as precise clocks or to probe the interstellar medium (along the line of sight of the beam), to study gravitational waves (by indirect observation, see the first discovery by Hulse and Taylor, 1975 who obtained a Nobel prize in 1993) or to study the pulsars' environment.

That is how the first two exoplanets have been detected by Wolszczan and Frail (1992) who noticed anomalies in the pulsating period of $PSR1257+12$. These anomalies where analyzed as being due to two or more Earth-sized bodies located at close distance to the host pulsar. This discovery was unexpected since it is not understood how such an object could survive a supernovae explosion or form after such an explosion.

Today, 23 planets have been unveiled thanks to this technique (belonging to 18 different planetary systems). The first so-called *super-earth* has been discovered thanks to this technique (Wolszczan and Frail, 1992).

[3]Nowadays, more than 2000 pulsars have been found in our Milky Way, since their discovery by Hewish et al. (1968).

Accessible astrophysical parameters This technique gives access to the mass of the companion and most of its orbital properties (semi-major axis, eccentricity and sometimes inclination) and thus orbital period.

Fundamental limitations and biases This technique only probes planets revolving around pulsars and thus marginally addresses the questions (1) and (3). Moreover, as pulsars are compact objects (very massive for their sizes), the planetary companions discovered thanks to this technique are usually very close to their host body (less than 10 AU).

Many questions remain from these discoveries, such as where do these planets come from (was it still part of the system, are they wandering bodies that have been gravitationally captured by the system or have they been formed from the material left over by the supernovae). This technique thus permits to marginally explore questions (1) and (2) and does not allow one to address question (4).

1.1.1.2 Radial velocity

For the scale of exoplanets, a two-body system revolves around the common center of mass whose location depends on the relative mass of the two objects. For instance, the center of mass of the Jupiter-Sun system is located at about 700,000 km from the center of the Sun (close to its surface). If a substellar companion is massive enough compared to the mass of its host star, their center of mass is significantly shifted from the more massive body towards the second body (see Fig. 1.1). From the Earth, it is possible to observe the star revolving around this gravity center by radial velocity (which observes the radial motion of the star) or astrometry (which observes the tangential motion of the star). The idea of the radial velocity (RV) method is to observe the periodic radial motion of the star (due to its rotation around the center of mass) by Doppler spectroscopy: the spectrum of the observed star is periodically shifted (from reference spectral lines) due to the presence of planetary companions.

The first discovery of a planetary companion by radial velocity triggered the exoplanet hunt since it is considered as the first exoplanet discovery. An object of a few jupiter masses, revolving around its host star 51Peg in 4.2 days at a distance of 0.052AU has been discovered by Mayor and Queloz (1995) thanks to the ELODIE spectrograph installed at the Observatoire de Haute-Provence (France). This discovery was quite puzzling as such a massive companion was not expected that close to its host star. Indeed, the only example we had at the time, were the eight planets of the solar system. This is the first discovery of the so-called *hot jupiters*.

In July 2015, 670 planets within 508 stellar systems have been discovered thanks to this technique.

Note that instead of looking at the Doppler shifted star light, a precise astrometry follow-up of the star can also show the rotation of the star around a different mass center due to the presence of planetary companions. In this case, the stellar system must be as perpendicular to the line of sight as possible to enable the identification of the star orbital motion. This technique, called *astrometry*, resulted in one confirmed detection (Muterspaugh et al., 2010).

Astrophysical parameters accessible with this method This technique enables one to retrieve the minimum mass of the detected companion but not the true mass since it depends on the inclination of the system which cannot be known by this technique alone. Astrometric measurements must be combined to the RV measures or imagery, in order to obtain the inclination, to derive the mass and potentially the spectrum when combined with imagery. Note that the astrometric method, even if the physical concept is the same, concerns different instruments (such as GAIA), different observation strategies (observation of crowded fields) and different objects (it is less sensitive to the stellar activity). The latter technique, combined with RV or imagery, will probably provide a harvest of results in the ten next years. All the orbital properties are also derived from this technique but the inclination of the system. The GAIA space observatory, operating since early 2014, should measure the orbits and

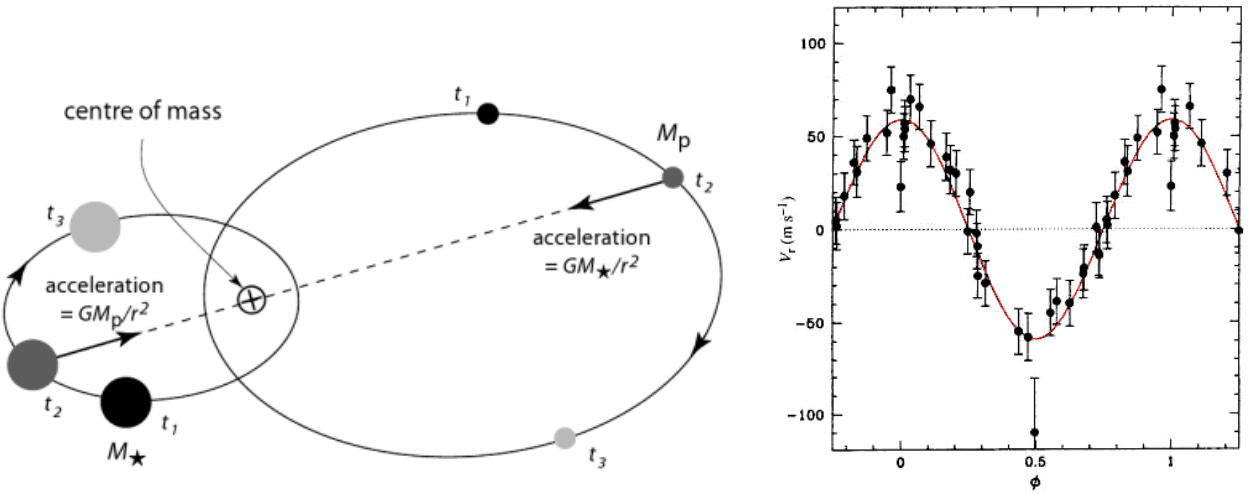

Figure 1.1 – Principle of the astrometry exoplanet detection method. Left: Schematic view of the common center of mass for a planet-star system (Figure from Perryman, 2011). Right: Radial velocity of the star 51 Peg observed by ELODIE, the red solid line showing the fitted solution to derive the system parameters (Figure from Mayor and Queloz, 1995).

inclinations of thousands[4] of extrasolar planets (Lattanzi and Sozzetti, 2010; Perryman et al., 2014), determining their true mass by astrometric measurements.

Fundamental limitations and main detection biases Detections through this technique are easier at short separations and also naturally for massive planets (such as hot Jupiters). Also, it is easier to find companions around low-mass star (M-type stars of 0.3 to $0.5 M_\odot$). By principle, it is easier to detect planetary systems that are edge-on (inclination of 90°) whereas it is impossible for a pole-on system (null inclination).

False alarms For very stable instruments and high signal to noise measurements, the detection capability of this method is ultimately limited by the perturbations of the RV caused by the star itself ("stellar jitter"). Stellar pulsations and stellar photospheric activity (i.e. surface spots and plages, Borgniet et al., 2015) induce RV noise at different period and amplitude scales, thus either mimicking or masking a small-mass planet RV signal.

Technical challenges The most critical instrumental challenge is related to the difficulty in calibrating the spectrograph in wavelength, in centering the fibers and stabilizing the temperature and pressure of the system so as to reach the accuracy and stability required for such detections. Currently, an accuracy better than 1.0 m/s is achieved by the HARPS spectrograph (La Silla observatory, Chile), which probes companions of mass down to super-Earth (1 to $5 M_\oplus$) at short separation. To give an order of magnitude, Jupiter induces a semi-amplitude of about 13 m/s over a period of 12 years whereas the Earth shows a semi-amplitude of 9 cm/s over one year.

Main instruments dedicated to RV Many ground-based instruments and large scale observational surveys are dedicated to exoplanet detection using the RV method although it must be used with other methods to derive the full companions' orbital parameters. As this technique is efficient and well established, it is still one of the favored method, hence the numerous projects to investigate nearby stars. Among the instruments in operation, there are SOPHIE (Observatoire de Haute-Provence, France), CORALIE (La Silla observatory, Chile), HARPS (La Silla observatory, Chile) and

[4] Perryman et al. (2014) states that about 21 000 new detections by astrometry are expected during the five years of its mission. These detections are for high-mass (from 1 to $15 M_{jup}$) and long period planets, revolving around stars located at about 500 pc from Earth).

its northern counterpart HARPS-N (Roque de los Muchachos Observatory, La Palma, Spain), UCLES (Anglo-Australian Observatory, Australia), APF (Lick observatory, USA) and EAPSNet, a project which gathers the three facilities BOAO (Korea), Xinglong (China), and OAO (Japan). One of the major projects for RV exoplanet search is ESPRESSO (P.I.: F. Pepe), currently being installed at Paranal observatory (Chile), whose first light is planned in 2017 and whose goal is to observe semi-amplitude variations of down to 5 m/s (depending on the instrument configuration).

In summary, this method mostly gives hints about the nature of exoplanets (addressing questions (1), (2) and (3)) and, via models, gives access to both the internal and atmospherical composition of the companions (question (4)).

1.1.1.3 Planetary transit

When a planet passes in front of its host star, it can be visible from Earth as the star brightness dims by an amount which depends on the relative sizes of the star and the planet (see Fig. 1.2). This technique was first imagined by O. Struve in 1952 (Struve, 1952), but the first transit observation of a known object was made by Charbonneau et al. (2000), while the first discovered exoplanet thanks to the transit technique was made by Konacki et al. (2003).

Today, about 2630 planets have been detected by this method, belonging to 1955 different systems, but most of these detections have to be further confirmed by other techniques, given the important number of false positives.

Note that the same kind of experiment can unveil planetary companions by detecting a specific signature due to a secondary eclipse (the brightness of the observed star decreases when the companion passes behind the star since the actual observed light was the addition of the two bodies light).

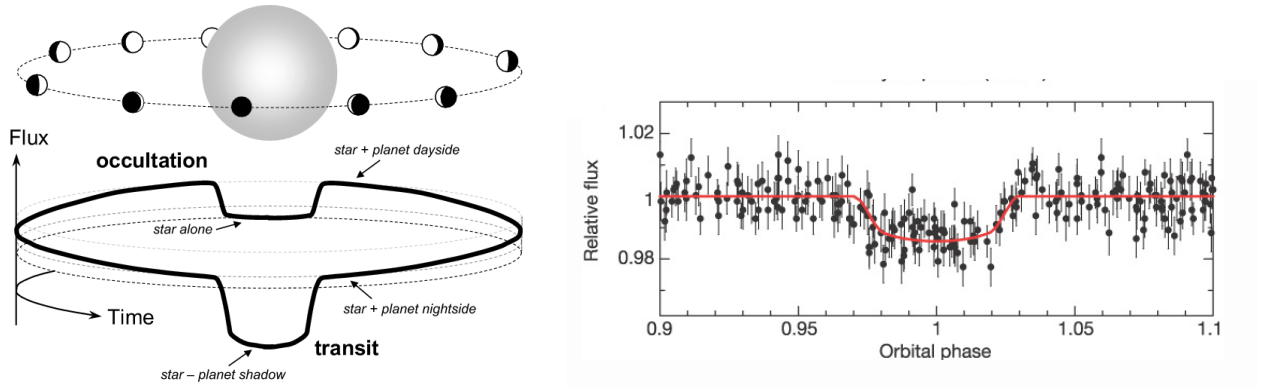

Figure 1.2 – Principle of the transit exoplanet detection method. Left: Schematic view of the primary and secondary transits (Figure from Perryman, 2011). Right: Light curve of the star OGLE-TR-56, the red solid line showing the fitted solution to derive the system parameters (Figure from Konacki et al., 2003).

Accessible astrophysical parameters This technique directly gives access to the radius of the planetary companion (the brightness decrease is proportional to the star-planet surface ratio), as well as its orbital period. In order to obtain the mass or eccentricity, it has to be combined with RV observations which provides the minimum mass (and the density) and most orbital parameters or variations in the timing of the transit has to be observed (transit-timing variation technique, TTV). Also, it is possible to probe the planetary atmosphere by high resolution spectroscopy (the starlight goes through the atmosphere of the planet and specific absorption lines can be observed). Secondary eclipses can also help disentangling contributions from the star atmosphere and from the planetary companion atmosphere. The latter technique is really challenging. It has been applied on a dozen of favorable cases (massive and hot companions) observed in infrared (where the contrast remains moderate during many transits) with space-based observations (stable conditions). Future observations from space, on either large scale general-use instruments (such as the JWST) or dedicated

missions (such as the ARIEL project), should considerably extend such spectral measurements. Note that the secondary eclipses and the transmission transits are usually called *semi-direct* techniques since they access the trace of the emitted photons.

Fundamental limitations and main detection biases In order to observe planetary companions with this technique, the stellar system inclination must exactly match the line of sight. There is a probability of about 10% to obtain such a configuration for a planetary companion located at 0.05 AU from its host star whose radius is 1 solar radius. This configuration is more likely to happen for companions at close separation to their host star. Moreover, this method mostly probes companions whose relative radii with the star is great enough to detect the star dim: for instance, the Sun-Jupiter system would provoke a light decrease of about 1%. It is possible to observe such transits around further stars (up to 3000pc whereas RV probes stars located at up to 300pc from Earth). Up to now, the most productive missions, designed to probe many transits (such as the spatial observatories CoRoT then KEPLER), targeted dense and thus distant stellar fields, providing then very few systems around bright enough stars (appropriate for very detailed characterization). The mission of the space observatory PLATO, planned for 2024, is to search for Earth-like planets around up to one million stars of various types, including the bright and nearby ones, by using this technique.

False alarms This detection method is riddled with many biases since a transit signature can be produced by many other effects such as diluted eclipsing binary, brown dwarf eclipse, background eclipse or stellar spot. For instance Santerne et al. (2012) showed thanks to a RV follow-up using SOPHIE, that a false positive rate of about 40% was to be expected for most companions already discovered by this method using the KEPLER instrument. A similar study by Morton et al. (2016) shows that among 7056 potential companions discovered by KEPLER, 428 are actually false alarms, 1284 are to be confirmed and 1935 have a high probability of being true detections. In order to confirm the discoveries it is required to add observations with other techniques such as RV (as proposed by Bouchy et al., 2009) or to perform extensive studies of the object by using transit-time variation technique (as proposed by Holman et al., 2010).

Main instruments dedicated to transit This technique can be relatively easy and cheap to install when looking for giant planets close to their host star, but when looking for super-Earths and their spectra, it requires the use of space telescopes equipped with advanced technologies. Many ground-based and space-based instruments are dedicated to exoplanet detection by transit. Among the two major space missions, CoRoT and KEPLER discovered thousands of new planetary candidates. CHEOPS, PLATO and TESS are the next missions planned to detect planetary transits and retrieving their atmosphere spectra.

This technique, if combined with other techniques, can bring important information about the nature of exoplanets in spite of its observational biases. One important aspect of this method which will lead future experiments is the possibility of retrieving exoplanet atmospheric spectra and thus address questions (2), (3) and (4).

1.1.1.4 Gravitational micro-lensing

The Shapiro effect states that light is curved when passing close to a massive object, such as a star, due to its gravitational potential. Thus in a configuration when the line of sight of an observed background star crosses a stellar system, this stellar system acts as a so-called gravitational lens (hence the name of this method, see Paczynski, 1986). If a stellar companion is present around the lensing star, a specific signature will appear in the observed light curve from the background star (see Fig. 1.3). This method has an increased sensitivity for low mass companions at large separation, typically between 0.5 and 10 AU. This technique can also probe free-floating companions, as unveiled in Sumi et al. (2011) and around black holes. The planetary systems probed by this technique are located at 1 to 8 kpc from the sun (further than for most indirect techniques).

The first exoplanet unveiled thanks to this technique has been published by Bond et al. (2001).

Today, 47 planets have been detected among 45 different planetary systems. A review of these discoveries can be found in Cassan et al. (2012).

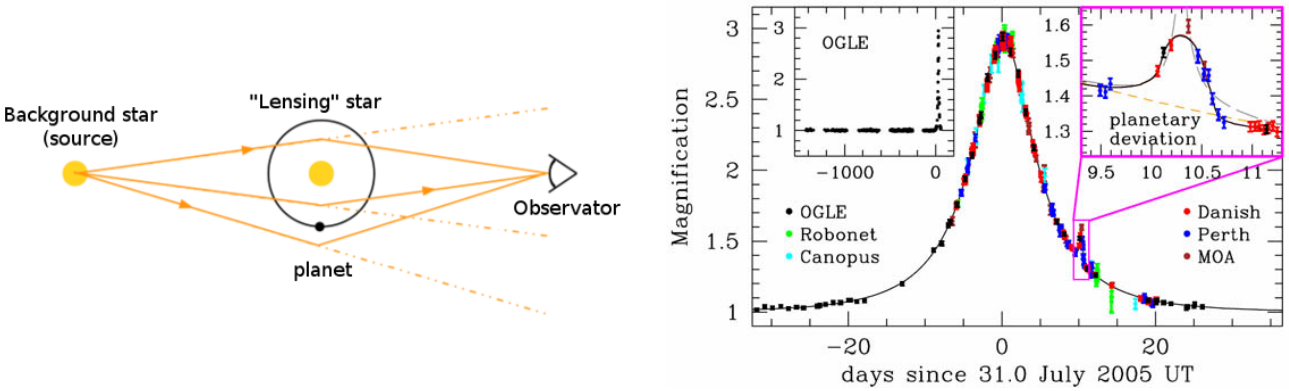

Figure 1.3 – Principle of the gravitational microlensing detection method. Left: Schematic view of a microlensing phenomenon: The "lensing" star is passing in front of the observed source star. Right: Light curve of the star OGLE-2005-BLG-390 showing an exoplanetary signal (Source: *David Bennet*, `www.iap.fr`).

Accessible astrophysical parameters From this method, it is possible to derive the mass of the companion relative to the star (from which we can make statistical guesses of its absolute mass), its period and its semi-major axis. Also, it is sensitive to faint free-floating planets that are not targeted by any other technique, and can therefore give an insight into the population of such objects for which little information is known.

Fundamental limitations and main observational biases The main disadvantage of this method is that it is a non-reproducible method: once the peak is observed, there is an extremely low probability that another background star may pass close enough to the microlensing star system. As in general, the lensing probability is very low, very large samples of stars must be continuously monitored. In order to have as many background sources as possible, the observed background stars are usually located in the Milky-Way plane. For instance, the OGLE project aims at continuously observing the galactic plane to spot such events.

This technique enables one to learn more about the statistics of exoplanets down to terrestrial masses at large separation but it is very limited since non-reproducible and it must be combined with other techniques such as direct imaging (as in Ranc et al., 2015) or interferometry (as in Cassan and Ranc, 2016) to have more information about the detection and address question (2).

1.1.1.5 Summary of the indirect observational methods for exoplanets

To summarize, these four indirect methods give access to specific parameters and to specific stellar systems whose properties are gathered in Tab. 1.1 and Tab. 1.2 respectively.

Note that 209 planets found thanks to the transit method are yet to be confirmed.

Thus the four indirect techniques enable the discovery of exoplanets which are mostly close to their host star. On the contrary, direct imaging can probe larger stellar systems and give access to different parameters to complete the overview of exoplanets. The next section focuses on what complementary information can be revealed by exoplanet direct imaging.

1.1.2 Direct imaging for exoplanet study

In this section, I focus on the direct imaging (DI) technique which motivates the topic of my PhD.

Detection method	Accessible parameters	First detection	Number of detections
Pulsar timing	M, a	Wolszczan and Frail (1992)	23
Radial velocities	M_{min}, P, a, e, ω, Ω	Mayor and Queloz (1995)	671
Transit	R, P, a, e, i	Konacki et al. (2003)	2628
Gravitational lensing	M, P, a	Bond et al. (2001)	47

Table 1.1 – Summary of the parameters accessible by the four indirect techniques described in this section and number of planetary detections as of July the 5th 2016. M is the mass of the companion, R its radius, P is its rotation period, a its semi-major axis, e its eccentricity, i the inclination of the system, ω the argument of peristar and Ω the right ascension of the ascending node.

Detection method	Distance range $[AU]$	Mass range $[M_{jup}]$	Age of the host star $[Gyrs]$
Pulsar timing	5.10^{-3} - 25	1.10^{-4} - 10	-
Radial velocities	2.10^{-2} - 10	1.10^{-2} - 1.10^{+2}	0.5-14
Transit	1.10^{-2} - 5	1.10^{-3} - 1.10^{+2}	0.01-15
Gravitational lensing	2.10^{-1} - 10	2.10^{-3} - 1.10^{+2}	any

Table 1.2 – Summary of the range of planetary companion mass, semi major axis and host star age accessible by the four indirect techniques described in this section, as on July 2016.

1.1.2.1 Astrophysical context enabling direct imaging

The planet mostly reflects visible light from its host star, depending on its albedo (that is to say its surface and/or atmospheric composition) and emits infrared or shorter wavelength light, depending on its temperature (itself mostly dependent on its mass and age). Direct imaging aims at detecting the photons emitted or reflected by the planetary companions. In this section I will focus on the detection of the light emitted by such bodies in the near-infrared (NIR). In such a configuration, the contrast between the host star and the light emitted by the internal heat of the planet is lower than at shorter wavelengths where the stellar blackbody emission is usually higher compared to its reflected light by the planet.

To detect the photons emitted by the planetary companions, it must have an angular distance wide enough to separate its signal from the star signal and must be bright enough to be visible. Within these considerations, only giant planets at wide separation can be imaged today. Finding a planet of given mass and age is easier around a low-mass star because it offers a more favorable contrast. On the other hand, massive planets are possibly also more likely around massive stars which also drove target selection for young massive stars and provided interesting detections.

The choice of the target stars is driven by the following considerations: they must be young enough to provide a rather good contrast between the planet and the star ($\leq$ 500Myrs) and close enough to provide a relatively good resolution ($\leq$ 100 pc). In total, less than 1000 candidates can be observed under these conditions, considering the current work of young, nearby stars identification in the Sun vicinity.

More details about the technical challenges required for direct imaging are discussed in next section.

First detection of an exoplanet by direct imaging Due to the technical challenge required to image an exoplanet, the first detection of a planetary mass companion was made in 2004 by Chauvin et al. who detected a giant planet around a brown dwarf. This *2MASSWJ 1207334-393254* brown dwarf belongs to the TW Hydrae association, whose age is estimated of $\sim$ 8 Myrs. This brown dwarf is located at 70 pc from the Earth and its estimated mass is $25M_{Jup}$. The coldness of this object made it possible to reach the necessary contrast to image the giant planet revolving at a projected distance of 55 AU. Several models have been used to estimate its mass to $5 \pm 2M_{Jup}$ and its

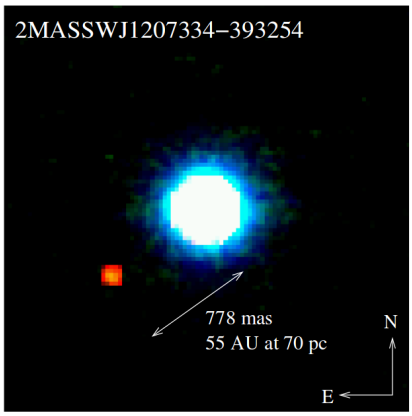

Figure 1.4 – First exoplanet detected around a brown dwarf, using the VLT/NaCo instrument (Figure from Chauvin et al., 2004).

effective temperature of 1250 ± 200 K. Note that this companion may be a brown dwarf and not a giant planet, depending on the formation mechanism and definition chosen. The moderate mass ratio between the primary brown dwarf and this planetary mass companion excludes the possibility for a planetary formation within the circumstellar disk.

Companions detected by direct imaging today Today, a few tens of exoplanets and bounded brown dwarfs have been unveiled by direct imaging. These companions lie in a range of projected distances to their host-star between $\sim$ 10 and $\sim$ 7000 AU, for estimated masses between $\sim$ 3 and $\sim 62 M_{Jup}$.

1.1.2.2 Derived astrophysical parameters

From the images, the characterization of the detected companions gives access to the planet-star contrast and the projected planet-star position of the substellar companion. During my PhD, I worked on image post-processing techniques whose goal is to detect companions and provide the most accurate position and contrast estimation of the detected companions. Post-processing methods also provide the detection limit, that is to say the faintest detectable signal as a function of the distance to the star. During my PhD, I did not work on the conversion of these values into astrophysical parameters such as the mass and the orbital parameters of the companions. The main properties of the planetary companions are derived from this characterization thanks to models.

Obtaining information about the orbital properties of the stellar system Direct imaging gives access to the projected separation to the star. In order to confirm the presence of a planetary companion, it is usually observed twice in order to check if it is co-moving with the target star (and that it is not a background star). The seven planetary orbital parameters can be derived from these data points (the eccentricity being a very important parameter in the framework of the planet interaction with its environment such as other planets or disks). For instance, two main ways of fitting the orbital parameters, that are currently massively used by the community, are the following: a MCMC estimation (which takes guess values in input then explores the different parameter combinations) and a LSMC estimation (which is a generalization of the MCMC estimation but which uniformly explores the seven orbital parameters). These two methods need the separation, the position angles as well as the corresponding uncertainties on these parameters. Thus when developing image processing tools, these parameters must be delivered with specific attention, mostly for the uncertainties which are not trivial.

If the companion is revolving fast enough around its host star, from at least three observations at three different epochs, it is possible to constrain the dynamic of the stellar system (via direct observation and models). In particular, the stability of the system is investigated for multiple planetary systems or planets detected within bright disks.

Note that in the case of companions at short separations, it is also possible to combine the astrometric data points with RV (or astrometric in the future) detections and use dedicated codes, as described on the Beta Pictoris planetary system in Bonnefoy et al. (2014), to better constrain the orbital parameters. The potential of such a combination can be found in Crepp and Johnson (2010).

Once the orbital parameters are estimated, it is possible to study the dynamical stability of the system: when the planet has formed, where in the stellar environment, did it migrate etc.

Obtaining the mass of the detected companion Direct imaging gives access to the relative luminosity of the planetary companion to its host star. Knowing the age of the host star, it is possible to determine the mass of the planetary companion from its estimated contrast via evolutionary models (giving the mass-luminosity relation). Such models should in particular predict the evolution of the total luminosity with age (such as Baraffe et al., 2003 and Saumon and Marley, 2008). The conditions of formation (and amount of gravitational energy effectively kept or radiated in this young age) may

have an important impact on such predictions (Marley et al., 2007). In short, there are two main models, referred to as the hot start and cold start models. The hot start model assumes that all the gravitational energy from the gaseous cloud, which collapses to form the planet, is incorporated into the planet in the form of thermal energy: the planets is bright during its formation and cools away with time. The cold start model assumes that the gravitational energy is radiated away through a shock wave and that the planets ends up much fainter at young age. Intermediate cases between those 2 models have also been developed. For a given total metallicity, the flux detected as a function of wavelength is also a strong function of the physics of the atmosphere: composition, stratification, and also possible cloud content.

Note that in the current landscape of knowledge, there is an important uncertainty, of about two orders of magnitude, on the luminosity of giant exoplanets. The combination of RV and imagery could potentially increase the exploration of the mass-luminosity diagram, and to decrease this uncertainty.

Constraining the estimations by probing different wavelengths Multispectral observations increase the constrain on the estimated temperature. Also, the thermal emission of young planets is much higher at longer infrared wavelengths ($> 3\mu$m). The larger the wavelength the easier it is to constrain the estimated temperature of the planetary companion. However, at larger wavelengths, the resolution decreases and the thermal background noise increases which will intrinsically limit the performance of the system. There is thus a compromise to make between shorter wavelength to obtain images of high resolution and larger wavelengths for a better contrast and a better estimation of the planets properties. Observations at several wavelengths are complementary and with the current instruments, observing in the H-band (around 1.6μm) is a good compromise. Moreover, the H-band proximity with the methane absorption band makes it an interesting indicator for the temperature. The L' band (around 3.8μm) is also complementary for the interpretation since it shows a more favorable flux for lukewarm companions and moderate observational difficulties making it better in terms of mass limit.

Deriving exoplanet atmospheric spectra From multispectral data, it is possible to derive spectra which are compared to atmospheric models or known objects, given the flux emitted by the surface of the object. Several models have been developed, parametrized by the effective temperature, the metallicity and the surface gravity of the companion and taking into account clouds (through their optical thickness) and dust (through the size of the grains). For instance, the recent model Exo-REM established by Baudino et al. (2015), derives the effective temperature, the surface gravity and the planetary radius from spectral data points of an exoplanetary companion. From the spectra obtained, the chemical composition can be extracted, with the presence of molecules such as methane, water, ammoniac etc.

Obtaining constrains on the presence of exoplanets The provided detection limit constrains the presence of other planetary companions on the stellar system thanks to evolutionary models (depending on the age of the host star, some solutions are excluded). Further codes exclude planetary companions with precise orbital parameters, such as MESS-2 (Bonavita et al., 2012 and Lannier et al. 2016, subm.). Thus, it is very important to provide a correct detection limit in order to not bias the results of large surveys that eliminate the possibility of detecting companions with specific properties. As the resulting conclusion is used to eliminate planet formation scenario, it is critical to provide consistent detection limits.

1.1.2.3 Major results obtained thanks to DI

As imaged exoplanets are massive and young (because they are brighter and thus easier to detect than their older counterparts), their atmospheres show low surface gravity properties probably responsible for the deduced presence of thick clouds, as well as the non-equilibrium chemistry processes observed. Several questions are still not solved: what are the boundaries between brown dwarf and exoplanets,

do giant gaseous planets form like the smaller rocky planets (likely it is a different processus) and which kind of scenario is the best suited to explain the observations.

The simplistic picture of planets forming in smooth, rotationally symmetric disks is more and more challenged by the detection of gaps, substructures and spiral arm patterns in proto-planetary disks (Benisty et al., 2015). These observations raised more than a question about the formation process of stellar systems.

Fig. 1.5 and Fig. 1.6 show examples of outstanding discoveries directly demonstrating the interest of direct imaging, which makes it possible to study the close interaction between the planet its environment, to probe planetary companions at large separations and to derive spectra from their emitted light. Among the numerous discoveries, we can point out for instance:

- The discovery of 2MASSWJ-1207334-393254 by Chauvin et al. (2004), showing an infrared excess that were not expected from the models, which triggered new research on L-type atmospheres (see Fig. 1.4).

- The discovery of the multiple system HR8799 by Marois et al. (2010b) constituted of four planets with an inner and outer ring, which gave information about the stellar systems architectures (see Fig. 1.6).

- The Beta Pictoris b companion have been found responsible for the inner warp in the disk surrounding Beta Pictoris (Lagrange et al., 2012), showing the interest of direct imaging to study the disk-planet interactions (see Fig. 1.5).

- The observation of young T-dwarf planets, such as Eri51 b (Macintosh et al., 2015), which is critical to constrain the atmospheric models of young exoplanets.

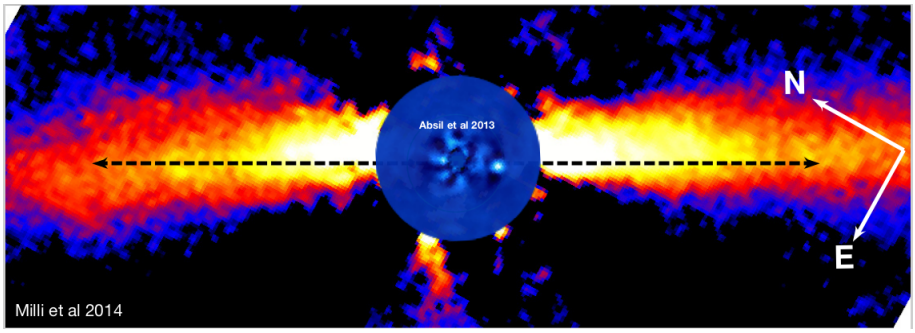

Figure 1.5 – Interaction between the debris disk and the planetary companion: the example of the star Beta Pictoris surrounded by a debris disk whose structure witnessed the potential presence of a companion (Mouillet et al., 1997), later unveiled by Lagrange et al. (2010). Figures obtained in L' band using VLT/NaCo (Absil et al., 2013 for the planet and Milli et al., 2014 for the disk).

1.1.2.4 False positives in direct imaging

Three different types of noise can corrupt the exoplanet detection: the observational noise (due to the observed scene), the instrumental noise (due to the imperfect set up to obtain the data) and the "post-processing" noise (due to how the data are handled to perform the detection).

Observational noise One detected substellar companion can be due to a background star. It is needed to re-observe the target star to check if the detected companion is indeed comoving with the target star.

Instrumental noise Most instrumental biases are due to the remaining instrumental aberrations, which are apparent under the shape of speckles that mimic planetary signals. In spite of advanced data processing, some speckles might remain and be regarded as detections.

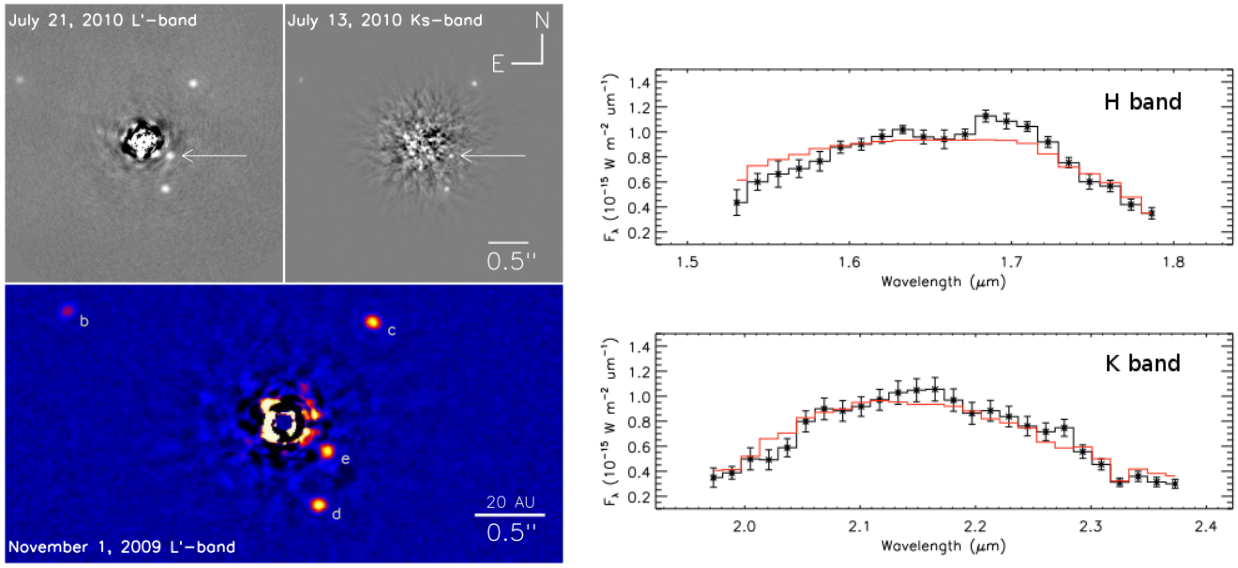

Figure 1.6 – The four planet system around HR8799. Left: Discovery of four giant planetary companions around the star HR8799 using Keck/NIRC2 (Figure from Marois et al., 2010b). Right: First extracted spectra of the furthest companion HR8799b in H band ($\sim 1.6\mu$m) and K band ($\sim 2.1\mu$m) (Figure from Barman et al., 2011).

Processing and human noise In spite of the advanced post-processing techniques used, the companion is usually visually detected in the subtracted image. In practice, several post-processing techniques are used to check the truthfulness of a detection. If the detection seems nevertheless present, it is re-observed at a different epoch to confirm that it is not a background star or a spurious speckle. However, some companions might be missed because of this visual inspection. My PhD topic is to make operational methods that avoid such false alarms.

Conclusions on the direct imaging capabilities for exoplanet study

Direct imaging currently gives access to giant planet companions revolving at more than 10 AU from their host stars, for stars located at 100 pc or beyond from the Sun. This is complementary to the other techniques which only have access to the internal part of stellar systems. Direct imaging is thus essential to complete the view of stellar systems architecture.

Moreover direct imaging probes planetary companions around young stars (preferentially in the few 1 to 100 Myrs) whereas other techniques probe the close environment of older stars (from 0.1 to 15 Gyrs). Direct imaging is thus essential to probe the formation and evolution process of exoplanets, in synergy with the other indirect techniques. This complementarity is visible on Fig. 1.7 showing the exoplanet detected as a function of the method used for the various distances to the host star and estimated mass of the companions.

As a conclusion, direct imaging is a powerful technique, complementary to the four other indirect techniques, from which it is possible to:

- Characterize the physical properties of an exoplanet by directly studying its emitted light;
- Follow the planet orbital motion in order to derive its orbital parameters;
- Study the interactions between the planet and its environment (other planets or circumstellar disks);
- Analyze the statistical properties and occurrences of giant planets at wide orbits.

From these results, further constraints on the planet properties as well as their formation and evolution processes and the presence of potential biomarkers are obtained. Direct imaging is thus essential in order to address the four main questions motivating the exoplanet field of research.

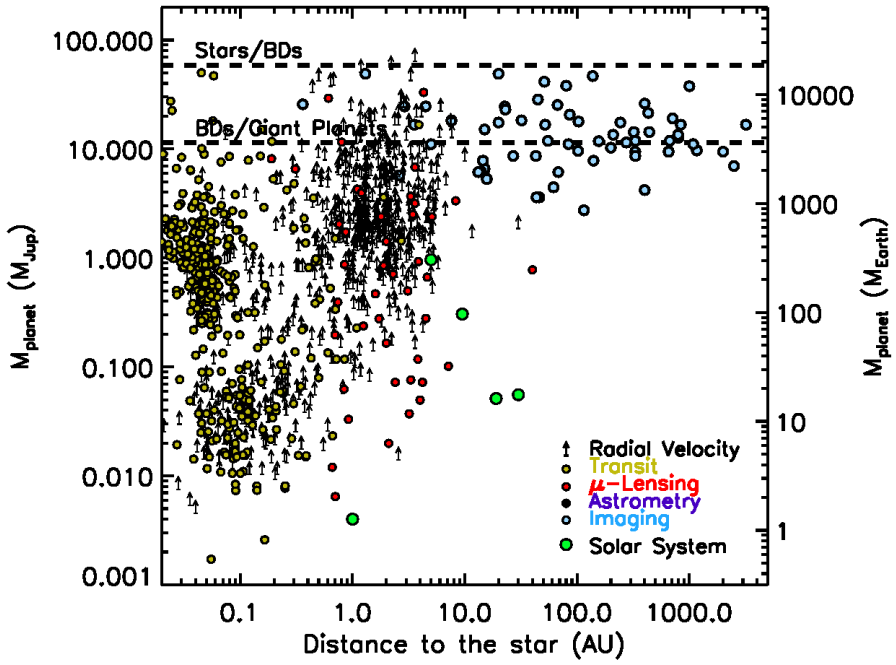

Figure 1.7 – Detected exoplanets masses as in May 2016 as a function of their distances to the host star, considering the five different planet hunting techniques. Courtesy of G. Chauvin (from exoplanet.eu).

1.2 High contrast imaging with ground-based telescopes

Imaging extrasolar planets and circumstellar disks requires dedicated instruments and strategies to bypass the two main obstacles:

1. The projected angular separation between the star and its companion is very small: it is typically $0.5''$ for a planet orbiting at 10 AU around a star located at 20 pc from the Sun (and it is of course even closer for shorter separations and/or stars further away). To give an order of magnitude, the theoretical (diffraction limited) angular resolution of the VLT (8-meter telescope) in H-band (1.6μm) is 40 mas. For ground-based telescopes, the main aberrations that prevent from reaching the theoretical limit are due to the atmospheric turbulence, decreasing the resolution down to over $1''$.

2. The contrast between the star and its companion is very high: from 10^{-4} for young giant planets (by emission, in the infrared) to 10^{-10} for Earth-like planets (by reflection, in visible light).

To reach such a high dynamical range, it is needed to use advanced instrumental solutions. For ground-based telescopes, adaptive optics (AO) in association with coronagraphic devices are one of the established instrumental solutions necessary to recover both a resolution close to the theoretical diffraction limit and a high contrast. Other solutions such as speckle imaging (Labeyrie, 1970), sparse aperture masking (Baldwin et al., 1986), lucky imaging (Law et al., 2006) or interferometry (Le Bouquin and Absil, 2012) are also considered but they do not provide both the high resolution and high contrast required for exoplanet and disks imaging. In this chapter, I present the high-contrast imaging solution provided by instruments equipped with adaptive optics systems and coronagraphs.

In order to understand the main problematic of image reconstruction for high contrast imaging, I describe in this section adaptive optics systems (Sect. 1.2.1) and coronagraphic devices (Sect. 1.2.2) that together reach both the required resolutions and the required contrast for exoplanet and circumstellar disks imaging. The major limitation of the resulting high-contrast images comes from the presence of quasi-static speckles in the field of view (Sect. 1.2.3). In the last section, I present the main instruments equipped with such technologies and with which we can perform direct imaging

(Sect. 1.2.4). These instruments are the ones on which it is possible to apply the image processing techniques I developed during my PhD.

1.2.1 Adaptive optics systems

Due to the bad thermal conductivity of the terrestrial atmosphere, there are strong inhomogeneities of temperature. These inhomogeneities, of sizes from millimeters to several meters, deviate the incoming light (since the refractive index is dependent upon the temperature[5]). Thus when observing an astrophysical object with a ground-based telescope, the incoming light undergoes a phase shift at each location of the entrance pupil, that varies temporally. This results in an important loss of resolution, directly linked with the wind direction and speed in the atmosphere along the line of sight. It is necessary to use an adaptive optics system to compensate for these induced aberrations.

In this section, I introduce the notions that I am using later in the manuscript.

1.2.1.1 Characterizing the turbulence strength

Seeing and Fried parameter Without AO correction, the angular resolution of the telescope is limited by the atmospheric turbulence (and not by the diffraction of its aperture). The corresponding angular resolution limit is given by the seeing defined as $s = \frac{\lambda}{r_0}$ (it is the FWHM of the resolution element in arcsec). r_0 is the Fried parameter, representing the equivalent diameter of the entrance pupil in the presence of atmospheric turbulence (scaling as $\lambda^{6/5}$). The seeing is thus the typical size of the pattern on the non-corrected image in Fig. 1.8-Middle.

Cn^2 profile A more thorough description of the astronomical seeing at an observatory is given by producing a profile of the turbulence strength as a function of the altitude, called a C_n^2 profile. This profile can be measured at the observatory location by profiling techniques such as MASS (Tokovinin and Kornilov, 2007, Multi Aperture Scintillation System), SCIDAR (Vernin and Roddier, 1973, SCIntillation Detection And Ranging) or SLODAR (Wilson, 2002, SLOpe Detection And Ranging) and upgraded versions of these principles. This point is critical in the framework of wide field corrections but for the on-axis corrections dealt with in this thesis, only its integral really matters (well represented by the seeing).

Coherence time To evaluate the level of turbulence, the correlation time, also known as the Greenwood time delay, is also a relevant parameter. It is defined as $\tau_0 = 0.314\frac{r_0}{\mathbf{v}}$, where $\mathbf{v}$ is the mean wind speed weighted by the turbulence profile along the line of sight (Roddier, 1981). This parameter is also proportional to $\lambda^{6/5}$, therefore correcting in the near-infrared is easier than in the visible where the turbulence evolves faster.

1.2.1.2 Adaptive optics system

Adaptive optics consists in analyzing the incoming wavefront by using a *wavefront sensor* (WFS) and correcting this wavefront thanks to a *deformable mirror* (DM) located generally in a pupil plane to which the command is sent from a *real time computer* (RTC). This whole set-up works in closed loop to ensure a continuous correction. The first idea of such a system has been published by Babcock (1953) and the first astronomical on-sky demonstration has been made with the COME-On system (Rousset et al., 1990). Fig. 1.8 shows a seeing limited image and the corresponding AO corrected image (SPHERE instrument).

Wavefront sensing A wavefront sensor is a device which measures the wavefront distortion. A review on the wavefront sensor capabilities for adaptive optics can be found in Guyon (2005). The

[5]The refractive index is also dependent upon the pressure via the Gladstone-Dale law.

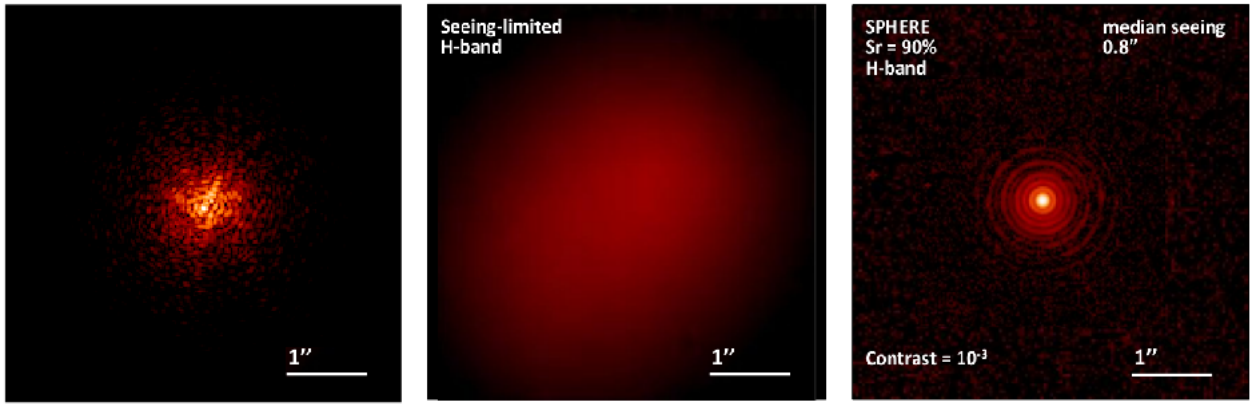

Figure 1.8 – Adaptive optic correction, example of a point source image in H-band ($\lambda = 1.6\mu$m) for the VLT (of diameter $D = 8$ m). Left: Short exposure image, without AO correction; the typical size of the speckle is λ/D and they spread over a $(\lambda/r_0)^2$ area. Middle: Long exposure image of a star without AO correction; the typical size of the pattern is λ/r_0 (seeing). Right: Long exposure AO-corrected image (using the SAXO adaptive optics of SPHERE).

most commonly used WFS for adaptive optics are pupil plane wavefront sensors, which are sampling the wavefront in a conjugated telescope pupil plane, such as:

1. The Shack-Hartmann wavefront sensor (Shack and Platt, 1971, SH-WFS), installed on most AO systems and in particular on VLT/SPHERE, Gemini-S/GPI and Palomar/P3K;
2. The pyramid wavefront sensor (Ragazzoni and Farinato, 1999, Py-WFS), installed at the LBT/FLAO, GMT/MagAO and Subaru/SCExAO;
3. The curvature wavefront sensor (Roddier, 1988, C-WFS), installed at the Subaru Telescope.

The SH-WFS samples the incoming wavefront via a lenslet array which focuses the light on a camera. The position of the image given by one lenslet is directly proportional to the slope of the incident wavefront. With this wavefront sensor, each actuator of the DM is conjugated with the four corners of each adjacent sub-pupil. The Py-WFS consists of a pyramid element whose top is placed at the focal point. The pyramid top acts as a Foucault knife but in both directions (x and y) and the wavefront error is computed from the four resulting pupil images. The C-WFS measures the intensity of the spots on either side of an extra-pupillary plane (whose location with respect to the focal and pupil planes is linked with spatial frequency range that are being analyzed) from which the curvature of the wavefront in the pupil plane is derived. In practice, a detector is located in the pupil plane and a vibrating mirror at the focal plane whose curvature is modified in a direction then in the opposite direction to provide two conjugated extra-pupillary images. The distance to the pupil (defining the sensitivity of the WFS) is set via the curvature of the vibrating mirror.

Alternatively, focal plane wavefront sensors estimate the phase directly from the images, by phase diversity (Gonsalves, 1982) and derived methods such as LIFT (Meimon et al., 2010). In the MEDUSAE method I present in this PhD thesis, phase diversity is used to estimate the residual aberrations from the post-adaptive optics and post-coronagraphic images.

Extreme AO Extreme adaptive optics (XAO) concerns high density DM and fast RTC. If the WFS is a SH-WFS, it is associated with a spatial filter, placed at its focal plane, to avoid aliasing by removing high spatial frequencies (a pinhole whose size is varied as a function of the seeing).

Main limitations of the AO concept In spite of the AO correction, all the instrumental aberrations that are *after* the WFS are not corrected (after the beam splitter sending part of the light to the WFS). These aberrations are the *non-common path aberrations* (NCPA) that must be calibrated or corrected with other means (such as COFFEE by Paul et al., 2014; Sauvage et al., 2012 or ZELDA N'Diaye et al., 2013, 2016). As most NCPAs are low order aberrations, they can also be corrected

continuously, with dedicated WFS. For instance, the instruments P1640 and GPI use a modified Mach-Zehnder interferometer combining the light reflected off the coronagraph spot with a reference wavefront, compared to the image from the science camera to measure the quasi-static components of the complex electric field in the pupil plane following the coronagraphic stop (Cady et al., 2013). The LLOWFS system (Singh et al., 2014) used in SCExAO uses a reflective Lyot stop to send part of the starlight in a dedicated focal plane wavefront sensor.

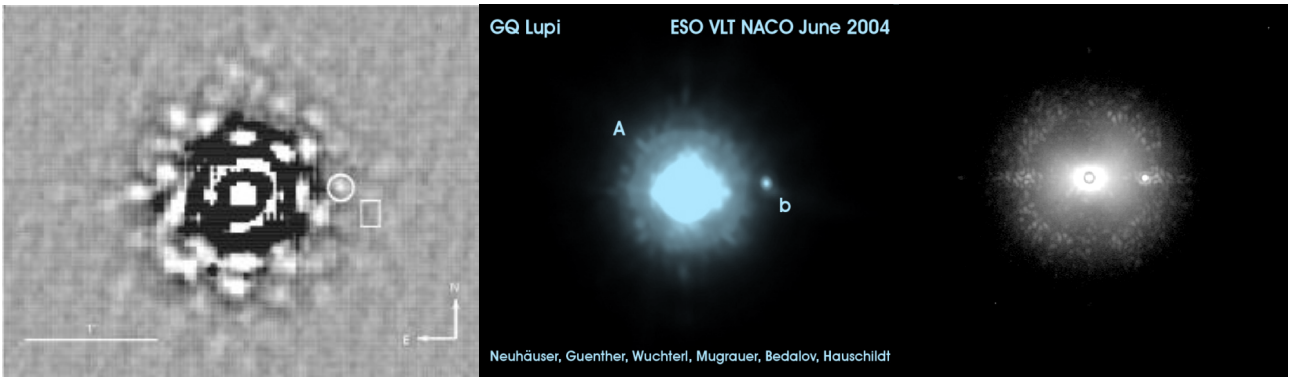

Figure 1.9 – Illustration of the AO correction evolution over the past 20 years on the same target, GQ-Lupi. Left: Image from one of the first AO system for astronomy in 1994 (COME-ON+) installed on a 3.6m telescope, which uses a SH-WFS and a 62 actuators DM (SR $<$ 10%). Middle: Image from VLT/NaCo in 2005, using a SH-WFS associated with a 185 actuators DM (SR ∼40-50%). Right: Image from VLT/SPHERE in 2015, using a SH-WFS associated with a 1200 actuators DM (SR ∼80-90%)

1.2.1.3 Characterizing the post-AO images

Residual phase variance The phase variance after the AO correction (also called residual phase), ϕ_{res}, is one of the most common criterion to quantify the AO performance since it is directly linked with the variable on which the AO system acts (the phase). As the AO system provides a real time correction to obtain long-exposures, the AO performances are usually characterized by the temporal mean variance that can be defined as:

$$\sigma^2_{\phi_{res}} = \frac{1}{T}\int_0^T \left[\frac{1}{S}\int (\phi_{res}(\mathbf{r},t))^2\, d\mathbf{r} - \left(\frac{1}{S}\int (\phi_{res}(\mathbf{r},t)\right)^2\right] dt \tag{1.1}$$

Where T is the time of the long exposure and S the size of the pupil over which the phase is defined. This variance characterizes the temporal mean, over one long-exposure, of the energy present in the residual phase (for a perfect correction the phase is null, as well as its variance). Also, the residual phase variance is chromatic: $\sigma^2_{\phi_{res}}(\lambda_2) = \sigma^2_{\phi_{res}}(\lambda_1) \times (\frac{\lambda_1}{\lambda_2})^2$.

Strehl ratio The Strehl ratio (SR) is defined as the ratio between the on-axis intensity of the corrected PSF to the theoretical aberration-free diffraction limited PSF of the telescope given by the Airy function:

$$SR = \frac{FEP(\alpha = 0)}{Airy(\alpha = 0)} \tag{1.2}$$

This is equivalent to the ratio of the integrals of the corresponding optical transfer functions[6] which makes it possible to compute this parameter directly from the images. This parameter expresses the amount of energy that is found in the central core of the corrected PSF. However this parameter does not provide information on the energy distribution in the areas surrounding the central peak and particularly on the high frequencies present in the images. In the small phase regime, this parameter can be expressed as: $SR \simeq e^{-\sigma^2_\phi}$, where σ^2_ϕ is the variance of the residual phase (post-correction).

[6]The optical transfer function is defined as the Fourier transform of the PSF and represents the spatial frequency content of the image.

Extreme AO systems are systems able to achieve Strehl ratios above 90%, while standard previous generation of AO systems typically reach 40 to 60% at 1.6μm (corresponding to a wavefront error of 50 nm rms in the first case and 200 nm rms in the second case). Fig. 1.9 shows the evolution of the post-AO images according to different correction quality.

Power spectral density The power spectral density of the residual phase gives access to the spatial frequency energy distribution of the residual phase:

$$PSD_{\phi_{res}}(\mathbf{f}) = \langle |FT[\phi_{res}(\mathbf{r})]|^2 \rangle \tag{1.3}$$

Where $\langle . \rangle$ is the spatial mean that can be replaced by a temporal mean in practice (by ergodicity). FT is the Fourier transform operator (2D here), defined here as:

$$FT[f(\mathbf{r})](\mathbf{f}) = \tilde{f}(\mathbf{f}) = \iint_{-\infty}^{\infty} f(\mathbf{r})\, e^{-2\pi i\, \mathbf{f}.\mathbf{r}}\, d\mathbf{r}, \tag{1.4}$$

where i is the imaginary unit defined as $i^2 = -1$. In this manuscript, I choose the convention such that the inverse Fourier transform is used to propagate the light from the pupil to the focal plane. Moreover, we have the relation between the PSD and the variance: $\int \int_{-\infty}^{\infty} PSD_{\phi_{res}(\mathbf{r})}(\mathbf{f}) d\mathbf{f} = \sigma^2_{\phi_{res}(\mathbf{r})}$. The latter is useful to characterize the errors due to an imperfect AO correction.

Residual phase structure function In order to study the spatial structure of the residual turbulent phase Φ_{res}, we can define the residual turbulent phase structure function[7]:

$$D_\Phi(\rho, r) = \langle |\Phi(\rho) - \Phi(\rho - r)|^2 \rangle \tag{1.5}$$

Under the assumption that the phase is ergodic, this mean can be either a spatial or a temporal mean. For a long-exposure, the AO-corrected PSF of the system can be expressed as: $h = h_{static} * |TF^{-1}(e^{-\frac{D\phi_{res}}{2}})|^2$, where h_{static} is the PSF of the system with only the static aberrations (Roddier formula in Roddier, 1981).

1.2.1.4 Limitations of an AO system

For a classical AO system and for point source observation, the main contributors to the residual phase variance σ^2_ϕ are the following (Conan, 1994; Gendron, 1995):

$$\sigma^2_\phi = \sigma^2_{\text{fitting}} + \sigma^2_{\text{aliasing}} + \sigma^2_{\text{servolag}} + \sigma^2_{\text{noise}} + \sigma^2_{\text{NCPA}} + \sigma^2_{\text{calibrations}} + \sigma^2_{\text{exogenous}} \tag{1.6}$$

- $\sigma^2_{\text{fitting}}$ is the error due to the finite number of actuators which prevents from correcting all the spatial frequencies. We have $\sigma^2_{\text{fitting}} \propto N_{\text{act}}^{-5/6} \left(\frac{D}{r_0}\right)^{5/3}$ hence the importance of a large number of actuators N_{act} and good seeing conditions. This is the major source of error. The cutoff frequency due to the DM is defined as $f_c = \frac{N\lambda}{2D}$ where N is the number of actuators of the DM on the side and D the pupil diameter. For SPHERE, this cutoff frequency is at $20\lambda/D$ and is visible on Fig. 1.9-Right.
- $\sigma^2_{\text{aliasing}}$ is the error due to the finite number of wavefront sampling elements in the WFS (the number of microlens for a SH-WFS), which prevents from analyzing the high spatial frequencies which are then folded in the low frequencies (hence the spatial filter on SPHERE). As a general rule, $\sigma^2_{\text{aliasing}} \approx \sigma^2_{\text{fitting}}/3$ (without spatial filter).
- $\sigma^2_{\text{servolag}}$ is the error due to the time delay between the wavefront analysis and the conversion into commands for the DM, compared to the evolution of the turbulent wavefront defined by τ_0. The temporal sampling of the wavefront, f_t, is an important parameter that reduces this error (for SPHERE, the sampling frequency is 1.2kHz). We have $\sigma^2_{\text{servolag}} \propto (f_t \tau_0)^{-5/3}$.

[7] The structure function of a random variable A is defined by: $D_A(\rho, r) = \langle |A(\rho) - A(\rho - r)|^2 \rangle$, $\langle . \rangle$ being the mean. This describes the statistics of the random fluctuations of the physical quantity A.

- σ^2_{noise} is the error on the WFS measurements. For a SH-WFS it is linked to the photon and detector noises at each lenslet focal plane. This is thus directly linked with the magnitude of the target star in the analysis wavelength and with the sensor spectral bandpass.
- σ^2_{NCPA} is the error due to the NCPAs mentioned above.
- $\sigma^2_{\text{calibrations}}$ is the error due to mis-calibrations of the system. In particular the calibration of the interaction matrix linking the command sent to the DM and the actual wavefront deformation can induce errors. For a SH-WFS, the reference slopes must be carefully calibrated to avoid sending an inadequate command to the DM. The influence function of the DM (the response of the DM when pushing one actuator) must also be well calibrated to send the correct command to the DM.
- $\sigma^2_{\text{exogenous}}$ are the errors due to the AO environment that disturb the adaptive optics correction (such as mechanical vibrations).

In this error budget the chromatic errors that are due to the propagation and diffraction of the light through the atmosphere are neglected since they are not major.

In Sect. 9.1.4, I use this type of contributor analysis and the notions evoked to characterize the AO system in order to estimate the residual phase structure function $D_{\phi_{res}}$.

1.2.2 High contrast for exoplanet imaging: Coronagraphy

Once a good resolution is achieved (so that most of the light is confined in the central PSF core) and a small residual phase regime reached (so that the core PSF position is highly stable), one has to deal with the high contrast obstacle[8]. This means (i) getting rid of the diffracted starlight within the zone of interest and (ii) getting rid of the star core light to prevent the detector saturation. In order to reach a high contrast for exoplanet imaging, additional constraints must be satisfied that can be sorted in five main metrics to be regarded:

1. **Contrast:** The ratio of the peak of the stellar PSF to the starlight residuals at the planet location (see Eq. 1.8);
2. **Throughput:** The amount of energy from the planetary signal which is preserved (similar to the transmission of the coronagraph, it depends on the position in the field of view);
3. **Inner Working Angle (IWA):** The smallest angle on the sky at which the needed contrast is achieved and where the planet signal intensity is reduced by no more than 50% (arbitrary throughput chosen for the sake of the definition);
4. **Bandwidth:** The spectral bandwidth over which the coronagraph can achieve the needed contrast (this is particularly important when using broad-band filters or IFUs);
5. **Sensitivity:** The degree to which contrast is degraded in the presence of aberrations.

To reach good performance, these five aspects must be maximized, so as to detect exoplanet signals within high-resolution images (that is to say reaching a high enough SNR for the science case presented at Sect. 1.1, knowing that the final SNR depends on these five aspects).

In the case of a diffraction limited image with an entrance aperture defined by $\mathcal{P}$ whose incoming wavefront has a phase Φ, in the Fraunhofer diffraction approximation (the observed point source is at an infinite distance from the actual diffracting element, which is the telescope aperture defining the pupil plane; the PSF being located in the corresponding image plane), the point spread function h of the system writes (at a given time):

$$h(x,y) = |FT^{-1}[\mathcal{P}(u,v).e^{j\Phi(u,v)}]|^2(x,y) \tag{1.7}$$

Where (x,y) and (u,v) are respectively the coordinates in the focal plane and in the pupil plane. The contrast to be maximized can be defined, at a specific location (x,y), as:

$$C(x,y) = \frac{\mathcal{I}(x,y)}{h(0,0)} \tag{1.8}$$

[8]The notion of resolution can be difficult to define in high-contrast imaging, since it is a combination of AO and coronagraphy. In any case, the use of coronagraph requires a high enough Strehl ratio.

Where $h(0,0)$ is the on-axis non-coronagraphic PSF and $\mathcal{I}(x,y)$ the location of the coronagraphic image where the contrast is estimated. In order to remove this light, the principle of coronagraphy is to perform an energy transfer (absolute, if the energy is preserved, or relative, if part of the energy is lost during the transfer) in either the focal plane or pupil plane.

Fig. 1.10 shows a schematic view of a coronagraphic set-up where the input beam enters through the so-called *upstream* pupil, $\mathcal{P}_{up}$, with an incoming wavefront defined by the upstream phase ϕ_{up}. Before the detector plane and after the coronagraph, the light goes through a *downstream* intermediate pupil plane, $\mathcal{P}_{do}$, and undergoes a downstream phase ϕ_{do}. Thus, if one wants to remove the starlight, several levers can be investigated: (1) directly in the focal plane and acting on the amplitude, (2) directly in the focal plane and acting on the phase, (3) directly in the pupil plane and acting on the amplitude and (4) directly in the pupil plane and acting on the phase. The Eq. 1.9 defines the

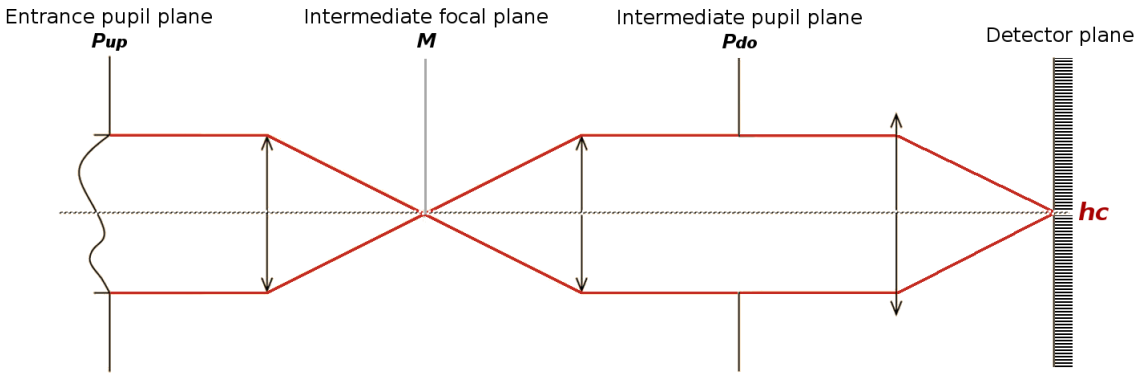

Figure 1.10 – Optical scheme of a coronagraphic set-up.

corresponding coronagraphic PSF in the detector plane, h_c, including the four levers which can be tuned:

$$h_c = |FT^{-1}[FT[FT^{-1}[\mathcal{P}_{up} \times \mathcal{P}_c \, e^{i\,\phi_{up}+\psi_c}] \, \eta_c \, e^{i\,\delta_c}] \, \mathcal{P}_{do} \, e^{i\,\phi_{do}}]|^2 \tag{1.9}$$

As visible on this generic formula, (1) can be made by tuning η_c in the intermediate focal plane, (2) by tuning δ_c, (3) by tuning $\mathcal{P}_c$ and (4) by tuning ψ_c.

A coronagraph cannot remove the speckles due to turbulent or quasi-statics wavefront errors: only the coherent part of the beam can be removed. Coronagraphs are thus useful to get rid of the photon noise due to the diffracting elements and the coherent amplification between the speckles and the diffraction pattern, to avoid the saturation of the detectors and to limit scattering and parasitic reflections in the optical train, downstream of the coronagraph. In other words, current coronagraphs are designed to locally attenuate the static diffraction pattern (usually due only to the telescope and the instrument), without addressing the dynamic phase and/or amplitude errors. These dynamic errors are dealt with thanks to advanced image processing techniques, as the ones presented in this manuscript.

All the current coronagraphic concepts developed so far are trying to play on these four levers (either one or several of them) while trying to maximize the five metrics evoked above. In the following I describe the main coronagraphic designs that are currently used. As one of the two image processing methods I dealt with during my PhD relies on an imaging model taking into account this coronagraphic device, it is important to be aware of the existing technologies to, on the one hand understand the main limitations between the imaging model I use and the real images, and, on the other hand, having ideas of how to modify this model so that it corresponds better to reality.

1.2.2.1 Focal plane mask coronagraphs (FPM)

The classical Lyot coronagraph The Lyot coronagraph (Lyot, 1939) consists of an occulting mask placed at the focal plane in order to hide the central core of the PSF. By doing so, some starlight is

diffracted by the edges of this mask. To reduce this effect, a Lyot stop is placed in the following pupil plane before focusing the light on the detector plane (see Fig. 1.11). This coronagraph proved efficient in practice and has been installed on many high-contrast instruments. Its main limitation is that its physical size and resulting diffraction effects prevent from reaching a very small IWA[9] and reduce the throughput. Also, the presence of the Lyot stop reduces the angular resolution. Note that the size of the FPM is optimized for one wavelength (if the wavelength of observation is larger leakages may appear and if it is smaller, the IWA is affected) but it is not the main limitation.

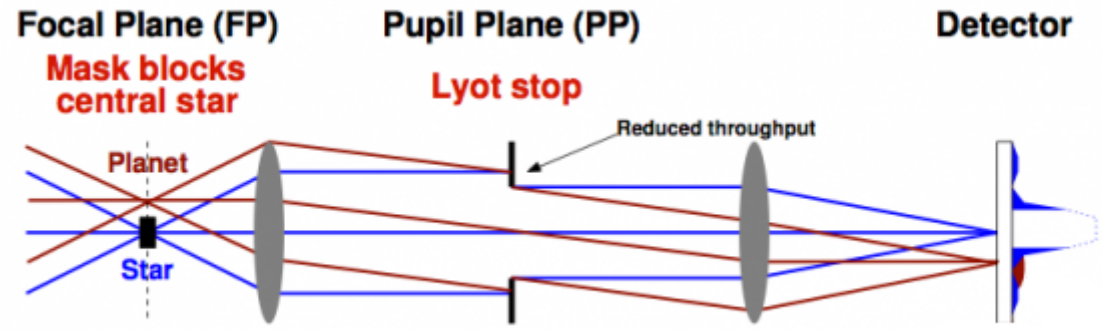

Figure 1.11 – Sketch of the optical layout of a classic Lyot coronagraph. Source: M. Kenworthy (Leiden University).

Phase focal mask coronagraphs Instead of an amplitude focal plane mask, one can use a phase focal plane mask in order to introduce a phase shift to the on-axis light which will destructively self-interfere. Several concepts have been developed based upon this idea, among which the Roddier & Roddier phase mask (Roddier and Roddier, 1997), the four quadrant phase mask (4QPM Rouan et al., 2000) and the vector vortex coronagraphs such as the annular groove phase mask (AGPM Mawet et al., 2005). These examples have been successfully installed on-sky. The main limitation of this kind of coronagraph is that they are highly chromatic since it is based on a phase-shift. These coronagraphs show a better IWA but a greater sensitivity to tilt errors and therefore, they must be precisely centered to be efficient. Phase mask coronagraphs can ideally achieve a 1-2λ/D IWA with infinite contrast, and 100% throughput.

1.2.2.2 Pupil apodizers

Amplitude apodization In order to avoid pointing errors, another way of removing the stellar central core is to use pupil apodizers[10] that can be either binary mask (Kasdin et al., 2003; Spergel and Kasdin, 2001) or graded transmission pupil mask (Nisenson and Papaliolios, 2001). The general term for this kind of coronagraph is shaped pupil (SP).

Phase apodization The amplitude apodizers reduce the resolution of the image by definition. An alternative to such coronagraphs is to use transmitting or reflecting optics acting on the phase at the pupil plane (beam remapping). One of the most commonly used of these coronagraph is the apodizing phase plate design (APP Kenworthy et al., 2007), as shown on Fig. 1.12 (it is a static deformed surface, as opposed to the surface of a deformable mirror). The main limitations of the APP is that it suppresses the stellar PSF for only half the field of view in a D-shaped pattern which is related to the total energy transmission and IWA. The phase-induced amplification apodization (PIAA Guyon,

[9]The physics of the Lyot coronagraph is such that there is a contrast vs IWA trade-off which is not compatible with exoplanet direct imaging (high enough contrast can be achieved only for large IWA, low IWA gives too low contrast).

[10]Note that 19th century astronomers routinely used simple binary masks to get a better resolution by reducing the aberrations level (i.e., getting closer to the Gauss conditions).

2003) uses aspheric optics in order to shape the pupil to create the phase aberration that reduces the intensity of the PSF wings.

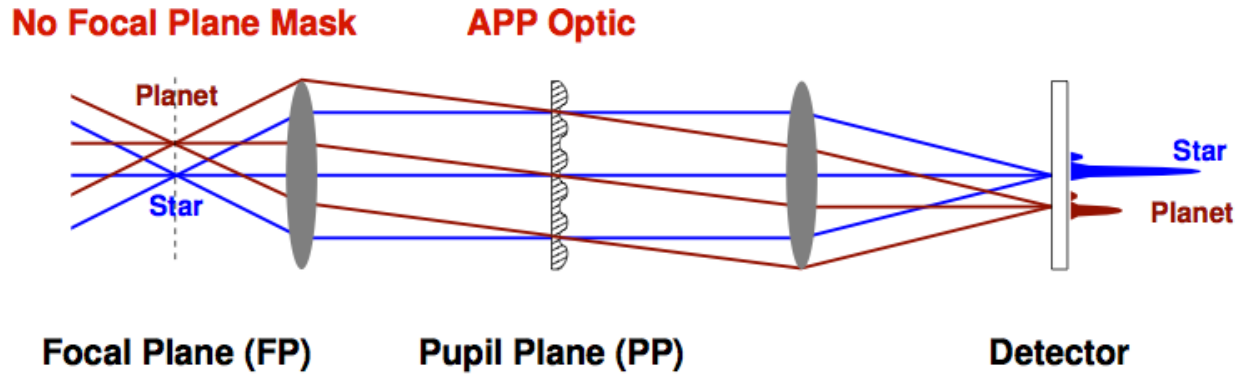

Figure 1.12 – Sketch of the optical layout of the apodizing phase plate (APP) coronagraph. Source: M. Kenworthy (Leiden University).

1.2.2.3 Hybrid coronagraph

From these different concepts, hybrid coronagraph designs have been developed that combine these concepts. The most common hybrid coronagraph used on sky is the apodized pupil Lyot coronagraph (APLC Soummer et al., 2011) which combines an adapted apodized upstream pupil with a classic Lyot coronagraph. The dual zone phase mask (DZPM Soummer et al., 2003) is a polychromatic generalization of the Roddier&Roddier coronagraph which uses a complex apodization of the entrance pupil and a dual phase zone focal plane mask.

A review of all these technologies can be found in Guyon et al. (2006) and Mawet et al. (2012). Today, we can distinguish between two kinds of coronagraphs: direct apodization (such as SP or APP) for moderate contrast and IWA, and hybrid coronagraphs for higher contrast and small IWA (constituted of pupil apodizer, focal plane mask and Lyot stop). On current instruments, the APLC is the most common, which proved efficient in practice while being well known. The vector vortex coronagraph (VC) is becoming more and more common and several installations are foreseen for the next years, as on SPHERE. Other technologies such as the PIAA and the apodized vortex are already used in labs and being considered for near-future space missions, or ELTs ground-based instruments.

1.2.2.4 Measuring and correcting for low-order aberrations to center the coronagraph

Several solutions have been implemented to center the coronagraphic focal plane mask. As mentioned in Sect. 1.2.1, the centering issue is linked with the presence of low order aberrations, and particularly the tip-tilt errors. On SPHERE, the differential tip-tilt sensor (DTTS Baudoz et al., 2010) uses an image of a fraction of the light before the coronagraph and centers the source via a closed loop. The ZELDA sensor (ZELDA Dohlen et al., 2013; N'Diaye et al., 2013), currently installed on SPHERE, will be likely used in the future to perform low to mid-order calibrations in real time (which is crucial to reach small IWA as required for Earth-like observations). On SCExAO, a low order wavefront sensor uses the light back reflected by the FPM and/or by the Lyot stop to analyze the low order aberrations, and specifically the tip/tilt, and correct them via a closed loop (LLOWFS Guyon et al., 2009 and CLOWFS Singh et al., 2014).

1.2.2.5 Current limitations and future designs of coronagraph

The main limitations of the current technologies is that the inner working angle is limited by the presence of residual instrumental aberrations inducing starlight leakages from the coronagraph. In order to alleviate this problem, both the wavefront control and the precision of the coronagraph

centering must be increased (which are linked as the low order aberrations are the tip/tilt aberrations, responsible for the de-centering of the source). Due to these residual errors, current coronagraphs are designed for IWA of about 3-4λ/D that are more robust to low order errors. If the low order errors are small, some concepts, thus requiring a fine control of the pointing, can reach 1-2λ/D.

Another strong limitation is due to the bandwidth since, for the commonly used coronagraph, they are optimized for one wavelength, which is problematic for broadband images and multispectral images as the ones I am working with in this manuscript. Many coronagraphs are now designed for 5-20% bandwidths (this is also the case for the vortex and other phase coronagraphs).

Future technologies are to investigate the beam remapping technique (as in Guyon et al., 2005; Pueyo and Norman, 2013), to bring optimized exotic pupil apodizers (as in Carlotti et al., 2012; Kasdin et al., 2003) or to specifically work on small IWA coronagraph concepts (as in Baudoz et al., 2008)... and to do all of the above at the same time.

1.2.3 The speckle noise limitation

Among the instrumental aberrations some are time dependent and give rise to the presence of quasi-static speckles in the images. These speckles cannot be calibrated and they are not varying fast enough to be averaged in a smooth halo. The temporal variations arise from potential imperfections of the rotative optical devices (such as ADC or derotator), from mechanical stress evolution (during the observation or the instrument lifetime), unfiltered vibrations or thermal variations that occur in the instrument. In the previous section, we saw that in AO-corrected images, there are still aberrations remaining due to either the limitations of the AO system or the NCPAs which can be quasi-static.

The main limitation in the post-AO long exposure images are due to these quasi-static speckles which prevent from detecting faint companions. It is expected that such speckle noise will also limit future high-contrast imaging instruments for both ground- and space-based telescopes. The theoretical formalism laid to describe the speckle noise is presented in Goodman (1975) in the framework of laser interferometry. This formalism has been adapted to post-AO images by Cagigal and Canales (2000) and experimentally demonstrated by Fitzgerald and Graham (2006). It has also been adapted to post-AO coronagraphic images in Aime and Soummer (2004) and numerically demonstrated in Soummer et al. (2007a).

The speckle intensity probability density function (PDF) for one location in the image plane and random temporal phase errors can be shown to be a modified Rician function (MR). At a specific location, this PDF can be written:

$$p_{MR}(I) = \frac{1}{I_s}\exp\left(-\frac{I+I_c}{I_s}\right) I_0\left(\frac{2\sqrt{I\times I_c}}{I_s}\right) \tag{1.10}$$

where I is the total PSF intensity that can be separated into two terms: I_c the local time-averaged static PSF (deterministic part) and I_s the mean intensity of the speckle noise (inhomogeneous random part), such as $I = I_c + I_s$. $I_0(x)$ is the zero-order modified Bessel function of the first kind. If $I_c >> I_s$ then this PDF is similar to a Gaussian function showing a bright positive tail. If $I_c << I_s$, then this PDF is an exponential function.

This PDF is valid for a specific location. It is showed in Marois et al. (2008a) that for the case of high-contrast images for exoplanet detection, the PDF is constant over annuli surrounding the star.

The PDF of Eq. 1.10 is also valid for a specific time. A detailed description of the temporal evolution of the speckle noise in high contrast images can be found in Hinkley et al. (2007) who showed that the quasi-static speckles have a typical evolution time from minutes to hours.

1.2.4 Dedicated instruments to high contrast exoplanet imaging

1.2.4.1 Current instrument

In this section, I will introduce the instruments used in this part of the manuscript. These instruments are dedicated to high-angular resolution and high-contrast imaging in small field of view which makes them suitable for exoplanet imaging (see Sect.1.2).

1.2.4.2 Previous generation of high contrast instruments: the example of VLT/NaCo

The NaCo instrument was installed at the Nasmyth focus of VLT/UT4 (Cerro Paranal observatory, Chile) in October 2001 and is now still in operation on UT1. This instrument is the contraction of NAOS, an adaptive optics facility and Conica, an IR camera.

Figure 1.13 – NaCo instrument at the Nasmyth focus of the VLT-UT4 (before 2014). The NAOS system is within the light blue box and the Conica camera within the red box. Credit: ESO.

The adaptive optics module NAOS NAOS, *Nasmyth Adaptive Optics System*, is the adaptive optics module which is equipped with a Shack-Hartmann wavefront sensor constituted of 14×14 micro-lenses (working either in IR, 0.8-2.5μm, or visible, 0.45-1μm), associated with a 15×15 actuators deformable mirror, enabling to reach a $SR > 30\%$ in H-band (depending on the brightness of the observed star) (Rousset et al., 2003).

The infrared camera CONICA CONICA, *COudé Near Infrared CAmera*, is an infrared camera and spectrometer equipped with an Aladdin3 1024×1024 pixels InSb array detector, ranging from 0.8-5.5μm (working in 5 different modes according to the wavelength of observation) (Lenzen et al., 2003).

Observation modes available The features of this instrument still evolve after its on-sky installation. Many of these features were motivated by high-contrast imaging: pupil tracking mode (PT), with or without coronagraphic mode (focal plane masks and/or apodized phase plate in the pupil plane), using Sparse Aperture Interferometric Masks (SAM), spectroscopy mode, polarimetric mode and simultaneous differential imaging mode at two different wavelengths (this mode is not efficient enough for exoplanet detection). In the first part of the thesis, I use observations made with this instrument in PT mode and with or without the L' band AGPM coronagraph commissioned in 2013 (Mawet et al., 2013).

Spectral bands available for exoplanet imaging The classical imaging mode can be used using one of the five bands of the instrument, centered on the J (1.265μm), H (1.66μm), K_s (2.18μm), L' (3.80μm) and M' (4.78μm) bands. The typical resolution of each band is $\Delta\lambda/\lambda \lesssim 10\%$ (but in H, it is 15%).

Coronagraphic masks available Concerning the coronagraphic modes, several focal plane coronagraphic masks can be used, among which two classical Lyot coronagraphs (mask size of 0.7″and 0.14″), one semi transparent mask attenuating the central PSF core (central mask size of 0.7″), two 4QPMs (optimized in H and K bands) and one AGPM (optimized for 4μm). However, only the AGPM and the APP are used today since the other coronagraph are not efficient enough to remove the star diffraction residuals left after the AO correction. Thus, before the arrival of the AGPM on-sky in 2013 (Absil et al., 2013), in order to investigate the close environment of the target star, another method is to use saturated exposures of the star, which I used during my PhD.

In this configuration, this instrument enabled scientific breakthroughs such as the first detection of a planetary mass companion by direct imaging and spectroscopy (Chauvin et al., 2004; Fig. 1.4), the unveiling of the β Pictoris b companion (Lagrange et al., 2010; Fig. 1.5) or the discovery of the exoplanetary companion HD95086 b (Rameau et al., 2013).

I mention here similar instruments whose images could be exploited exactly the same way as the NaCo images since they all offer a pupil tracking mode, an AO correction and sometimes coronagraphs. The image processing applied can thus be of the same kind. The ANDROMEDA image processing method I present in the first part of the thesis can be applied to process images from these instruments:

- The Gemini South telescope (Cerro Pachon, Chile) with the NiCi instrument (Artigau et al., 2008);
- The W. M. Keck telescope (Mauna Kea, Hawaii) with its NGS-AO system (Wizinowich et al., 2000) combined with the NIRC2 camera (McLean and Chaffee, 2000);
- The Gemini North telescope (Mauna Kea, Hawaii) with the ALTAIR AO system (Herriot et al., 2000) combined with the NIRI instrument (Hodapp et al., 2003);
- The Subaru telescope (Mauna Kea, Hawaii) with the AO system AO188 (Hayano et al., 2008) equipped with the HiCIAO camera (Suzuki et al., 2010); (Hinkley et al., 2011).

1.2.4.3 Recent generation of high-contrast instruments: the example of VLT/SPHERE

The SPHERE instrument (Beuzit et al., 2008) was installed at the Nasmyth focus of VLT/UT3 (Cerro Paranal, Chile) in May 2014. Contrary to NaCo, this instrument is specifically dedicated to the exploration of the nearby environment of stars to detect and characterize protoplanetary disks, debris disks and exoplanets. In order to address this challenge this instrument is constituted of a common path infrastructure (CPI) containing the fore-optics (such as ADC and derotator) and high-contrast devices (AO system and coronagraph) that have been designed separately but in co-design with the science cameras. Then there are three imaging instruments (called sub-systems): IRDIS the infrared dual band spectro-imager (Dohlen et al., 2008), IFS the integral field spectrograph (Antichi et al., 2008) and ZIMPOL the visible polarimetric imager (Roelfsema et al., 2010). All these instruments are installed on a fix shelf, unlike NaCo, which allows a good temporal stability. The SPHERE instrument has been integrated at IPAG in 2012-2013 before its transport to the Paranal observatory.

In the following, I will point out the major differences in the design of SPHERE which provides images quality to probe planetary companions with a contrast of down to 10^{-6}.

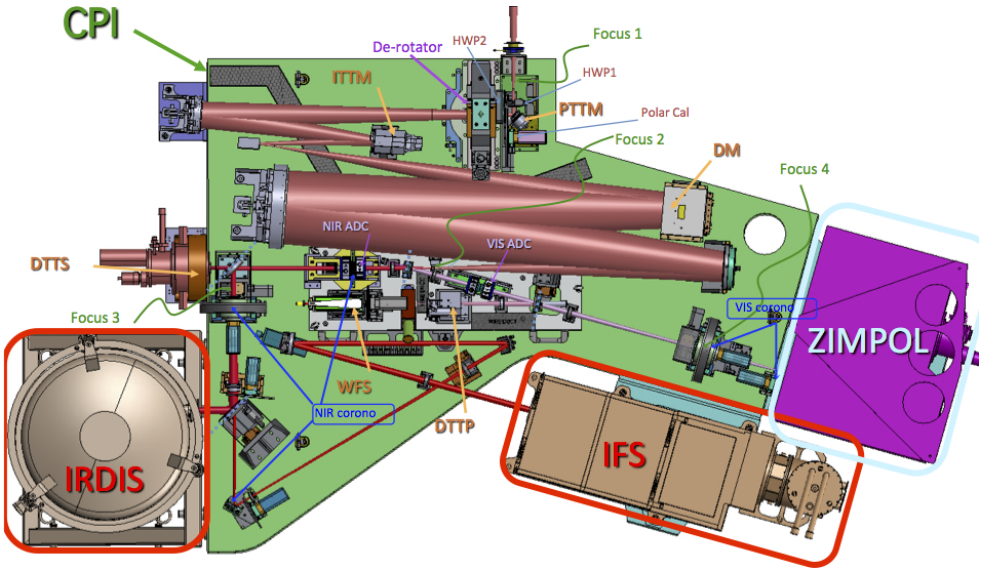

Figure 1.14 – Layout of the SPHERE-CPI. The two infrared instruments are framed in red (IRDIS and IFS) and the visible instrument in blue (ZIMPOL).

SAXO: the extreme adaptive optics module The design of the SPHERE extrem adaptive optics system, called SAXO for *SPHERE AO for eXoplanet Observation*, has been made by the Onera team (Fusco et al., 2016, 2006; Petit et al., 2008). SAXO is part of the Common Path and infrastructure (CPI) of SPHERE (see Fig. 1.14). It is constituted of a 40×40 lenslet SH-WFS, conjugated to a 41×41 actuator piezoelectric DM. The frame rate of the AO loop is 1.2 kHz and is going with a tailored control law (Petit et al., 2014) included in the RTC, called SPARTA for *Standard Platform for Adaptive optics Real Time Applications*. As mentioned above, the SH-WFS is equipped with a spatial filter that is automatically adjusted on the turbulence level (Poyneer and Macintosh, 2004).

An EMCCD detector for the SH-WFS allows a powerful noise reduction (sub-electron) to cover all star magnitudes up to 16. Results on on-sky integration of the SAXO module can be found in Fusco et al. (2014). This XAO system achieved more than 90% of SR in H band and a 3 mas residual jitter.

Coronagraphic masks and pupil apodization The coronagraphic focal plane masks and the pupil apodizers are also part of the CPI. The differential tip-tilt sensor (DTTS Baudoz et al., 2010), insures the centering of the beam on the FPM. For now, SPHERE is equipped with a classic Lyot coronagraph, an APLC and a 4QPM. The most frequently used coronagraph is the APLC.

IRDIS: the different observing modes The different modes have been designed by Dohlen et al. (2008). This instrument has several observing modes: *Dual band imaging* (DBI Vigan et al., 2010), *long slit spectroscopy* (LSS Vigan et al., 2008), *dual-polarization imaging* (DPI Langlois et al., 2010) and a classic imaging mode, either using narrow-band filters (NB) or broad-band filters (BB). In my thesis, I will use images obtained in DBI and BB modes: Fig. 1.16 shows the transmission of the filters in these two modes. The DBI mode filters combination have been carefully chosen to be close enough while the signal of the planet is expected to be null in one of the two band (as expected from models of giant gaseous planet atmosphere). The spectral resolution is about 50 in narrow band and about 350 in broad band. The detector is a Hawaii II 2048×1024 pixels array, offering a 11×11 ″field of view. The pixel scale is of 12.25 mas/pixel and it is Nyquist sampled at 950μ m (shortest wavelength).
Final on-sky performance can be found in Vigan et al. (2014).

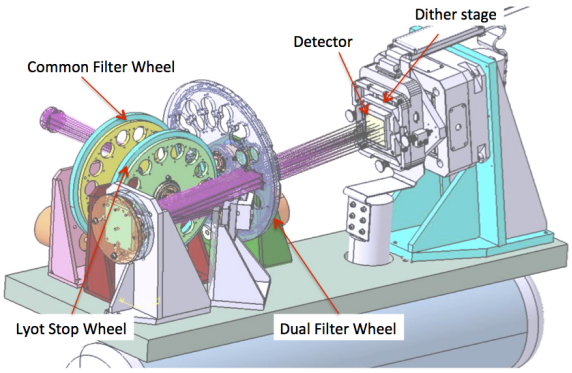

Figure 1.15 – Layout of SPHERE-IRDIS.

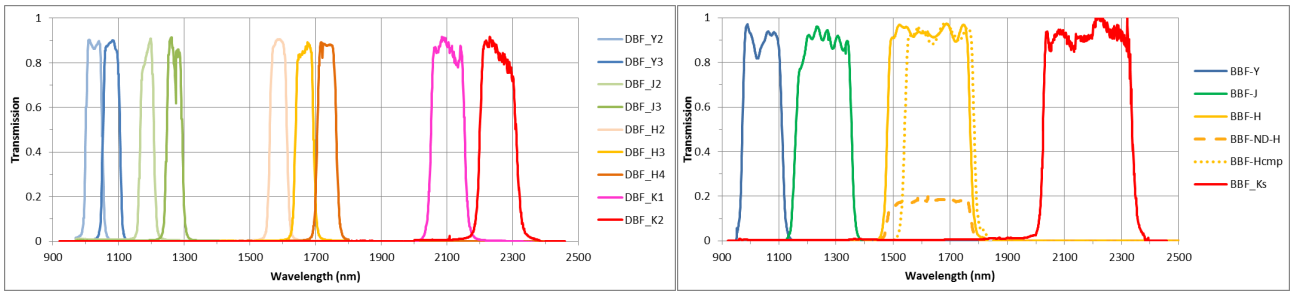

Figure 1.16 – Observation wavelengths of the IRDIS modes I use in this manuscript. Left: Filter doublets available for the DBI modes. Right: Broad band filters available.

IFS: the different observing modes The instrument design is described in Antichi et al. (2008) and general instrument description can be found in Claudi et al. (2008). This IFU is based on the BIGRE concept (Antichi et al., 2009): the image is sampled by a double lenslet array focusing (Fig. 1.18-Left) on the spectrograph, here constituted of two Amici prisms, dispersing the light on the final image. The resulting sub-spectra, are registered onto a hexagonal lattice configuration (Fig. 1.18-Middle-Left), whose detection area is called *spaxel*. This design is made to minimize

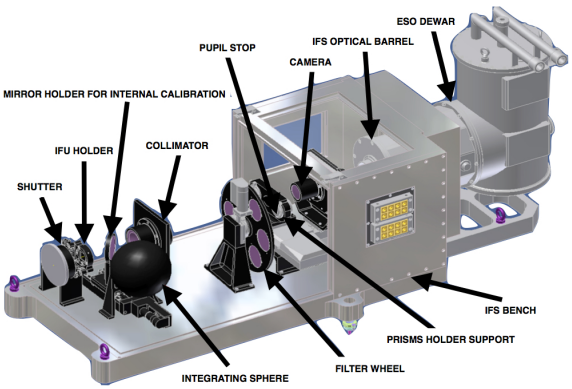

Figure 1.17 – Layout of SPHERE-IFS.

the cross-talk between adjacent spectra while maximizing the final contrast level. The image provided by the spectrograph is thus constituted of small spectra, as shown on Fig. 1.18-Middle-Right. The detector is a Hawaii II 2048 × 2048 pixel array and provides a $1.73 \times 1.73''$ field of view, Nyquist sampled at 950μm (the shortest wavelength). This image is then re-sampled into a multispectral cube of 39 narrow band images of resolution 7.46 mas/pix, as on Fig. 1.18-Right. Two wavelengths ranges are proposed by the SPHERE-IFS instrument: the YH band mode, from 0.97μm to 1.66μm with a spectral resolution of about 30 and the YJ band mode, from 0.96μm to 1.34μm, with a spectral resolution of about 50. The main limitation of this design is the cross-talk. Calibration must be carefully performed in order to avoid light leakages from one wavelength to another.
Final performance can be found in Mesa et al. (2015). Usually, the IFS and IRDIS mode are working in parallel (called IRDIFS mode).

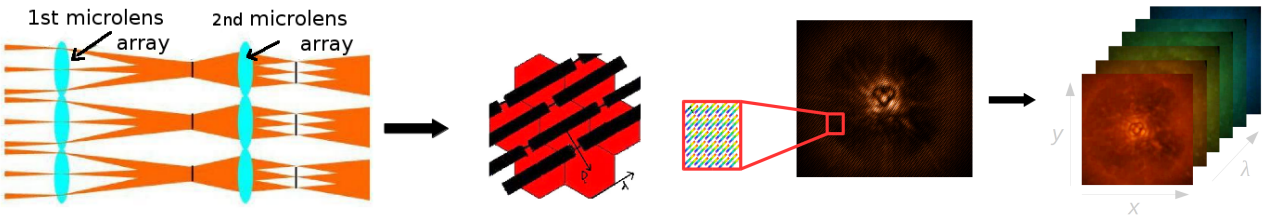

Figure 1.18 – Coronagraphic images from SPHERE-IFS. Right: BIGRE dual lenslet design to sample the images (Figure from Claudi et al., 2008). Middle-Right: Spaxel array (Figure from Antichi et al., 2008). Middle-Left: Raw image at the detector and schematic view of the spaxel. Right: Reduced multispectral cube (39 images with SPHERE-IFS).

Major results obtained with SPHERE This instrument notably helped refining the characterization of the system HR8799 and observe the closest companion HR8799e in J band for the first time (Bonnefoy et al., 2016; Zurlo et al., 2016). SPHERE also unveiled new intriguing features in debris disks such as concentric broken rings of HD 141569A (Perrot et al., 2016) and revealed the presence of enigmatic fast radial moving ripples in the AU Mic debris disks (Boccaletti et al., 2015).

I mention here similar instruments whose images could be exploited exactly the same way as the SPHERE images since they all offer an XAO correction and advanced coronagraphic devices along with pupil apodizer designs. The image processing applied are thus of the same kind and the ANDROMEDA image processing method presented in the first part of the thesis (Part. I) can be applied to process images from these instruments:

- The Magellan Clay telescope (Las Campanas Observatory, Chile) with the AO system MagAO (Close et al., 2012; Morzinski et al., 2014) associated with either the Clio camera (NIR) (Kopon et al., 2010) or VisAO (visible) (Sivanandam et al., 2006);
- The Large Binocular Telescope Interferometer (Mount Graham, Arizona) with its FLAO system (Esposito et al., 2010) combined with LMIRCam (Garden, 1994; Skrutskie et al., 2010).

More specifically, the instruments equipped with IFUs and on which the MEDUSAE image processing method presented in the second part of the thesis (Part. II) can be applied are the following:

- The Gemini South telescope (Cerro Pachon, Chile) with the GPI instrument (Macintosh et al., 2008) installed in November 2014;
- The Subaru telescope (Mauna Kea, Hawaii) with the AO system AO188 (Hayano et al., 2008) followed by the SCExAO extrem adaptive optics module (Guyon et al., 2010; Jovanovic et al., 2015) and by the integral field spectrograph CHARIS (Peters-Limbach et al., 2013) which will be commissioned in fall 2016;
- The Hale telescope (Palomar Observatory, California) with the PALM-3000 AO system (Dekany et al., 2013) combined with the P1640 integral field spectrograph.

Note that ANDROMEDA cannot be applied to images from the Hale/P1640 instrument since it does not provide a pupil tracking mode, which is essential for ANDROMEDA.

High contrast for exoplanet imaging: conclusion

With the arrival of new dedicated instruments on-sky it is currently the golden age for high contrast imaging. These technologies are essential to detect faint objects at very close separations to the star. However, even when using such advanced technologies, there are still residual instrumental aberrations provoking leakages of the starlight, resulting in the presence of speckles in the image field. By their nature, these speckles are of the typical size of a resolution element (as for the planetary signals) and are often brighter than the planetary signals. In the obtained image, the typical raw contrast is of 10^{-4} at 0.2-1″making it difficult to detect planetary companions. Moreover, below the turbulent speckles, quasi-static speckles lie at a level of several 10^{-5} with a typical evolution time from seconds to several hours: they are evolving too slow to be averaged in a smooth halo during the exposure and too fast to be calibrated and removed. Thus one of the most important parameters in exoplanet imaging is the temporal coherence time of the speckles which directly affects the quality of the images. The typical temporal variation depends on the source of the aberrations, from the rotative elements in the set-up (such as ADC or derotator) to the mechanical deformation of the optical elements and changes in temperature or pressure. To optimally exploit the current high contrast instruments, the image processing techniques must be developed in synergy with the instrumental design. This is an excellent context for my PhD.

The next section introduces the different concepts on which the image processing methods currently used by the imaging exoplanet community rely in order to detect the faint circumstellar objects within such images. As the image processing methods I am using in this manuscript are based on inverse problems, I start this section by introducing the notions of image reconstruction via inverse problems that I use along the manuscript.

1.3 Image processing for exoplanet observation

A real image is a bi-dimensional continuous signal (analogical). When recording an image, this signal is sampled (temporally and spatially) by a detector then digitized to be stored. The numerical image is of finite dimension and has discrete values (given for each pixel). Image processing techniques are meant to exploit the content of the images by highlighting the information included in the image but hidden.

In this section, I introduce the notions of image processing for exoplanet imaging that are used throughout this manuscript. During my PhD, the methods on which I worked are based on specific solutions to inverse problems. In a first section, I introduce the general concept of inverse problems and provide notions of image processing methods using an inverse problem approach that I use in the manuscript (Sect. 1.3.1). In a second section, I describe the main image processing methods currently used to detect and characterize planetary companions within high contrast images (Sect. 1.3.2).

1.3.1 Image restoration: inverse problems

An inverse problem consists in finding the parameters from a set of observations that depend on them. Inverse problems deal with the parameters that are not directly observed. Many fields of experimental science use inverse problems. In exoplanet imaging, the main goal is to find the objects within the images corrupted by the speckle noise. A thorough introduction to inverse problems for astronomical data can be found in Mugnier and Le Besnerais (2001) and Mugnier (2012).

Forward problem A forward problem models the data using the laws of physics and assuming that the parameters of interest are known. When an image of an object is made, some information of interest get mixed up: the data provided by the observation do not correspond directly to the physical values of interest. However, these physical values are linked with the observation by known laws.

Forward modeling consists in mathematically writing the link between the object and the data. For instance, for a linear model of image, it is possible to write the image i (the measurement) obtained from an object o (the unknown) as $i = Ho + n$ where n is the noise due to the image acquisition and H being an operator called *observation operator* which represents the governing equations that relate the model parameters to the observed data. The computation of i knowing the object is a forward problem.

Inverse problem An inverse problem starts with the data and infers the parameters of interest. For instance, estimating the object from the image is the corresponding inverse problem which requires a model of image formation to be inverted. The inversion can make good use of the knowledge on the statistical behavior of the measurement uncertainties (the noise). If the observation operator H is linear, then it is a linear inverse problem.

Ill-posed problem Another important notion is the notion of *well-posed* and *ill-posed* problem. Most inverse problems are ill-posed because of the noise, the measures' uncertainties and/or the measures' sampling etc. One definition of a well-posed problem, proposed by Hadamard, states that the inversion of a model of physical phenomenon is well-posed if it has the three following properties:

1. A solution exists;
2. The solution is unique;
3. The solution is stable wrt the noise (the solution continuously depends on the data): a small variation of the noise induces only a small variation of the solution.

Data processing in physics, and especially in astronomy, essentially consists in solving an inverse problem, often ill-posed, and in practice after a pre-processing or reduction of the data. In exoplanet imaging, this data reduction consists in applying dark and flat calibrations, removing the bad pixels and re-centering the frames. In the manuscript, I call *reduced data* the images that have been cosmetically processed and *raw data* those obtained directly on the detector.

Inversion process Because of the inevitable noise or modeling errors, it is impossible to directly derive the object corresponding to the true object within the images. A basic and general idea is for instance to minimize the difference between the mathematical model of the data formation and the data (the image). The estimated object, $\hat{o}$, corresponds to the object which minimizes a criterion representing the difference between the data and the model of the data. The next section explains how to find the correct estimator to solve such a problem in the framework of image formation.

1.3.1.1 Deterministic approach

Without an explicit model of the noise, it is possible to minimize a least-square distance between the data and our model of these data. For images, the criterion J_{LS} to be minimized wrt the unknown object o is defined by $J_{LS} =\| i - H\hat{o} \|^2$. In that case, the existence and uniqueness is guaranteed in practice (i.e., infinite dimension). In this approach, the prior information about the noise are not taken into account.

1.3.1.2 Stochastic approach

The Stochastic approach consists in specifically taking into account the information on the statistics of the different types of noise present in the image in order to define the norm (the criterion to be minimized). The maximum likelihood is a solution to inverse problem with this stochastic approach: instead of minimizing the quadratic distance between the data and the model (as in the deterministic approach), we maximize the probability of observing the data knowing the model. In image reconstruction, the likelihood represents the probability of measuring the image i, knowing the object o. This probability can be written: $p(i|o) = p_n(i - Ho)$, where p_n is the probability density function of

the noise n. The maximum likelihood solution is given by the maximum of this term. Thus, we obtain: $\hat{o}_{MV} = \arg\max(p(i|o))$ ($\arg\max(x)$ being the value of the variable that maximizes the quantity x). If the noise is white and stationary, the maximum likelihood solution is equal to the least-square solution. This solution is the one used in the ANDROMEDA method that I present and apply on on-sky data in the first part of this manuscript (Part. I).

1.3.1.3 Regularization

In both cases, even with a statistic model of noise, the problem is ill-posed since it is too sensitive to the noise (the stability is not guaranteed). Amplification of the noise present in the image is observed. In order to guarantee the stability regarding the noise and the uniqueness, it is possible to regularize the problem. Regularization consists in introducing additional information (prior knowledge) about the parameters of interest in order to solve an ill-posed problem and to prevent over-fitting (i.e., fitting the noise). Two types of regularization can be used:

(1) parametric regularization acts directly on the unknown parameters: its shape, its intensity etc.

(2) non-parametric regularization consists in adding a term to the criterion to be minimized (called *penalization term*).

The regularization is usually weighted by a hyper-parameter (1D or 2D) that can control the strength of the regularization.

With such a regularization, the stochastic approach is no longer the maximum likelihood *ML* but the maximum a posteriori *MAP* which consists in looking for the most probable object knowing the data by maximizing $p(o|i)$. In the Bayesian framework, we have $p(o|i) = \frac{p(i|o)\times p(o)}{p(i)}$ and considering $p(i)$ as constant, the two terms in the numerator are to be maximized: $\hat{o}_{MAP} = \arg\max p(o|i) = \arg\max p(i|o) \times p(o)$. The MAP approach thus consists in stating that the estimated object $\hat{o}$ is the object that minimizes the criterion $J(o)$ given by $J(o) = J_i(o) + J_o(o) = -\ln(p(i|o)) - \ln(p(o)) - C$ which is the sum of the ML term and the regularization term (fidelity to prior), to a constant C.

1.3.1.4 Model of noise

In signal processing, the noise is a general term for unwanted (and in general unknown) modifications that a signal may suffer during capture, storage, transmission, processing, or conversion. Noise is also the word used to describe the random signals that carry no useful information but which hinders the information retrieval.

The noise is usually classified by its statistical distribution. For instance, the detector noise is a random process that approximatively follows a normal law: it is a Gaussian noise. In image processing, the photon noise is another example of noise (also called Shot noise) which is a random process following a Poisson law. Both noises are also white noises (they have a constant power spectral density). The detector noise is additive (it is added to the image) since its origin is decorrelated from the signal whereas the photon noise depends on the flux level in the image. From their respective origins, the detector noise is a stationary process while the photon noise is not (it depends on the brightness of the source).

1.3.1.5 Example of image deconvolution with MAP

Deconvolution is a typical example of an ill-posed inverse problem and it is part of the MEDUSAE method described and tested in Part. II. In this section, I present its basic ingredients.

When the PSF h of the system is known, it is the case of *classical deconvolution*. In that case the estimated object by MAP writes:

$$\hat{o}_{MAP} = \arg\min_{o}[J_b(o(\mathbf{r})) + J_o(o(\mathbf{r}))] \tag{1.11}$$

For classical astronomical images, the dominant noise in the images is due to the photon noise and detector noise. For high flux observed sources, the photon noise can be well approximated by a

Gaussian noise (Mugnier et al., 2004). Hence the first term (likelihood term) follows a non-uniform Gaussian law and writes:

$$J_b(o(\mathbf{r})) \simeq \frac{1}{2\sigma^2(\mathbf{r})} \sum_{\mathbf{r}} [(h * o)(\mathbf{r}) - i(\mathbf{r})]^2 \tag{1.12}$$

where $\sigma^2 = \sigma^2_{phot} + \sigma^2_{det}$ and $\mathbf{r}$ is the image coordinates. In this case, we consider the detector noise to be dominant wrt the photon noise whose variance can be estimated as: $\sigma^2_{phot} = \max(i(\mathbf{r}), 0)$. Examples of common regularizations on the object that I will use in this manuscript are given below.

Positivity constraint As the image is defined by the intensity, the object is obviously positive. There are several ways to include this prior in the criterion: (i) by re-parametrization of the estimated object (e.g: estimating $a^2(\mathbf{r}) = o(\mathbf{r})$ which is by definition positive, Thiébaut and Conan, 1995); (ii) by forcing the minimization to remain in the positive parameter space (Nakamura et al., 1988); or (iii) by adding an entropy term in the criterion that infinitely penalizes the presence of negative points (Narayan and Nityananda, 1986).

L2 spatial regularization on the object For an object following a Gaussian statistics, the penalization term, under the L2 regularization, can be written (Conan et al., 1998):

$$J_o(\tilde{o}(\mathbf{f})) = \frac{1}{2} \sum_{\mathbf{f}} \frac{|\tilde{o}(\mathbf{f}) - \tilde{o}_m(\mathbf{f})|^2}{PSD_o(\mathbf{f})} \tag{1.13}$$

where $\tilde{x}(\mathbf{r}) = FT(x)(\mathbf{f})$, o_m is the mean of the object and PSD_o the power spectral density of the object. The latter can be estimated via models. However, if the object is presenting sharp edges, this type of regularization induces oscillations on the edges in the restored image (due to the Gibbs effect).

L1L2 spatial regularization on the object A way of alleviating this oscillation problem for objects presenting sharp edges is to use a L1L2 regularization. The goal of such a regularization is to penalize a lot when there is small intensity gradient between pixels while restoring the high intensity gradients of the image. Mathematically, this can be written (Mugnier et al., 2001):

$$J_o(o(\mathbf{r})) = \mu \sum_r [\frac{\nabla_o(\mathbf{r})}{\delta} - \ln(1 + \frac{\nabla_o(\mathbf{r})}{\delta}] \tag{1.14}$$

where $\nabla_o = \sqrt{(\nabla_x o(\mathbf{r})^2 + \nabla_y o(\mathbf{r})^2)}$, with $\nabla_x o$ the gradient of the object along the x direction. When the gradient is low (∇_o small), it tends toward a L2 regularization (the term $\ln(1 + |x|)$ dominates) which smooths the noise and penalizes the edges. When the gradient is important (∇_o high), it tends toward a L1 regularization (the term $|x|$ dominates) which is a sparse regularization, independent of the gradient. The hyperparameter δ thus controls the transition between the linear regularization and the quadratic regularization. The hyperparameter μ controls the global weight of this L1L2 regularization.

Another way to define the hyperparameters is to write this regularization as:

$$J_o(o(\mathbf{r})) = d^2 \sum_r [\frac{\nabla_o(\mathbf{r})}{s \times d} - \ln(1 + \frac{\nabla_o(\mathbf{r})}{s \times d}] \tag{1.15}$$

Where d and s are intricated hyperparameters that must be tuned together: when $d \to \infty$ then $J_o \sim \sum_{\mathbf{r}} \frac{|\nabla_o(\mathbf{r})|^2}{2 \times s^2}$. In this manuscript, I use the latter notation.

L^p spatial regularization on the object As a general rule, it is possible to use a L^p regularization (Mugnier et al., 1998), which consists in writing the penalization term as:

$$J_o(o(\mathbf{r})) = \mu \sum_r \nabla_o(\mathbf{r})^p \tag{1.16}$$

According to the value of p, this regularization favors either the sharp edges ($p \sim 1$) or smooth background (~ 2).

Note that when the PSF of the system h is not fully known, we talk about *myopic deconvolution*. If the PSF is completely unknown, we talk about *blind deconvolution*. For exoplanet imaging with high-contrast instruments, the PSF of the system is not fully known and most image processing techniques developed so far aim at reconstructing the PSF of the system by using the redundant information present in the images. The next section summarizes the principles of the current image processing methods used for exoplanet imaging.

1.3.2 Current image processing for exoplanet imaging

Within high contrast images for exoplanets and disk imaging around bright stars, the dominant noise is due to the quasi-static speckles. In order to disentangle the speckles from planetary companions, one must find a diversity, that is to say a parameter for which the speckles have a different behavior from the circumstellar objects. The speckles originate from the residual instrumental aberrations deviating the starlight which is an on-axis intense point source. The circumstellar objects are faint off-axis sources. During my PhD, I focused on the detection of planetary companions, that are off-axis point sources.

Most image processings today are based on *differential imaging*: the goal is to build a *model PSF*, here being the image of the star only, as seen by the camera at the specific moment of the observation, and to subtract this model PSF to the science image so as to recover the circumstellar objects. Such a model PSF is not easy to obtain since it needs to be very accurate to reach high contrast. That is why the diversity is exploited to create a model PSF as close as possible to the real speckle field shown in the science image. This operation can be repeated for several science frames in order to increase the signal to noise ratio by smartly combining the subtracted images.

Today, most of the established methods are building empirically the model PSF, directly from the set of images to be processed. The main drawback of such image processing is that part of the planetary signal is removed during the subtraction. Some techniques provoke non-negligible self-subtraction if the empirical PSF model still contains part of the planetary companion's signal. Intensive post-processing are then applied to characterize the detections by assessing this self-subtraction rate.

In the following, I describe the main diversities that are currently used to build the model PSF and perform differential imaging.

1.3.2.1 Exploitation of the temporal diversity: ADI

ADI is the most commonly used method. At first order the optics diffracting the star light are assumed to be in the pupil plane whereas the planetary signals are part of the image plane. When using a telescope with an alt-azimuthal mount, the pupil plane and the image plane are rotating during the observation at different deterministic velocities. One can choose to fix the pupil (by using a pupil derotator) to temporally stabilize the aberrations in the images while the observed field rotates with an angle analytically computable at each instant. The relative angle position of the field with respect to a fixed direction on the detector is given by the *parallactic angle* which depends on the declination and hour angle of the observed object and on the latitude of the observatory.

In this so-called *pupil tracking mode*, several exposures of the target are recorded and their corresponding parallactic angles are computed during the data reduction (prior to data processing). Fig. 1.19 shows such an apparent rotation of the field of view while the speckle field is approximatively fixed.

The basic principle of ADI is to compute the PSF model as the median of the temporal cube. This PSF model is then subtracted to each individual frame of the temporal cube. Each subtracted frame is then rotated to align with the true North then co-added to form the final image. This ADI concept has been first proposed by Marois et al. (2006) who demonstrated that this method is efficient if the

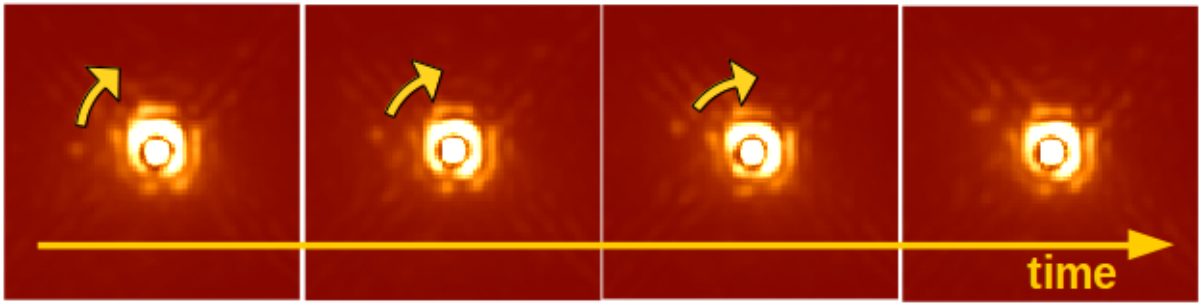

Figure 1.19 – Field rotation as a function of time. Images of the star Beta Pictoris with SPHERE: the planet is seen moving clockwise in these images.

companion has rotated of at least two FWHM in the temporal cube. However, if the coherence time of the speckles is short compared to the observation duration, the PSF model is not representative enough of the frame to frame speckle field. From this basic idea, different techniques have been developed in order to optimize the subtraction by building the most accurate PSF model possible.

In the following, I present the main methods that are commonly used by the imaging exoplanet community today. There are several ways of sorting and presenting these methods and I choose to present them from a user point of view. I thus separate these methods in three concepts: classical ADI, LOCI and PCA whereas they are all linked by their principle. These three concepts have different flavors that I will not describe in detail but mention the reference. An interesting review of these methods concept can be found in Savransky (2015).

Classical ADI From the simple ADI concept, evolved ways of building the PSF model have been established. I provide here a list of the most commonly used methods based on ADI:

1. Smart ADI (s-ADI Marois et al., 2006): consists in building one PSF model for each frame by using the frames before and after the regarded frame, that have rotated of at least $1\lambda/D$ compared to the regarded frame;

2. Radial ADI (r-ADI Marois et al., 2006): as the field rotation depends on the distance to the centered star, the latter rotation limit is set for each annulus surrounding the star (the thickness of each annulus is a user-defined parameter);

3. Image rotation and subtraction (IRS Ren et al., 2012): makes use of the centro-symmetry of the speckles in the field to rotate the images by 180° in order to form the PSF model.

For these classical ADI methods, all the images of the cube have the same weight whereas the speckle field might not show the same correlation from one image to another. The following methods try to optimally combine the images in order to build a model PSF that is more similar to the true speckle field, by giving a different weight to each image of the temporal cube.

Locally optimized combination of images, LOCI This method, published by Lafrenière et al. (2007) consists in building the model PSF by making a linear combination of the images in the temporal cube and computes each linear coefficient so as to minimize the residuals (in the least-square sense). The linear coefficients are computed within specific zones called *optimization zones* which differ from the actual *subtraction zones* in order to avoid the planet self-subtraction. The subtracted images are then combined into the final image in which the detection is visually performed. Several flavors of this concept aims at optimizing the SNR of the detected companions. I mention here some of these methods dedicated to pupil tracking monochromatic images:

1. Damped LOCI (D-LOCI Pueyo et al., 2012): this method first modifies the cost function that determines the linear coefficients used to construct the model PSF (so that the subtraction zone allows high signals whereas the residuals are minimized over the optimization zone) and it forces these coefficients to be positive (this method does not require priors on the planetary spectrum);

2. Template LOCI (T-LOCI Marois et al., 2014): this technique uses an input spectrum and reference PSFs (non-coronagraphic or unsaturated exposures) to optimize the computation of the linear coefficients of the model PSF while minimizing the planet self-subtraction. In order to maximize the speckle subtraction, the frame to frame correlation matrix is conditioned.

3. Adaptive LOCI (A-LOCI Currie et al., 2012a): filters the images by their degree of speckle correlation and determines the combination of algorithm parameters that maximizes the SNR of point source.

4. Matched LOCI (M-LOCI Wahhaj et al., 2015): consists in injecting synthetic sources in the field of view and finding the linear combination that maximizes the SNR of the synthetic sources in the final image.

5. Optimized Image rotation and subtraction (OIRS Dou et al., 2015): as for IRS, it makes use of the centro-symmetry of the speckles in the field to form the PSF model while optimally combining the frames as in LOCI.

Instead of fully using each image of the cube with a specific weight to build the model PSF, another idea is to use part of the information contained in the whole image cube by, for instance, decomposing it into its statics vs variable components. The following method decomposes the image cube in its most temporally correlated features to then combine them to form the model PSF.

Principal component analysis, PCA In the standard PCA method, the whole cube is decomposed into its eigen-modes (obtained by projecting the images on an orthogonal basis by performing a singular value decomposition of the images): higher order modes show the most temporally correlated features in the cube whereas lower order modes show the higly variable features (that is to say the noise for very low orders). For each science frame, the eigen-modes are then linearly combined so as to minimize the distance between the eigen-modes combination and each regarded image (thus building the model PSF). It is thus needed to truncate the number of eigen-modes (or principal modes) used in the projection: an infinite number of modes would perfectly remove the residual noise but would also subtract the companions' signals. To choose the correct amount of low order modes kept, a trade off has to be made between the amount of residuals and the self-subtraction of the signal. In other words, the images are projected on a subspace made of the first K eigen-modes, where K is the number of actual modes removed. By subtracting these projected frames to the regarded science frame, most of the static pattern (common to all frames) is removed and only the content of the image that is different in most frames (such as the astrophysical signal) remains. This method has been proposed by Amara and Quanz (2012) and Soummer et al. (2012). From this concept, evolved ways of building the PSF model have been established, such as:

1. Smart PCA , s-PCA: instead of using all the images before and after the considered science frame, s-PCA consists in using only the frames that have rotated of more than about one FWHM (the number of FWHM is a user-defined parameter). As the rotation degree depends on the distance to the central star, s-PCA sets such a limit for each annuli surrounding the star (the thickness of each annulus is a user-defined parameter).

2. Low-rank plus sparse decomposition (LLGS Gomez Gonzalez et al., 2016a): the image is decomposed into three components: the *low rank* (the speckle field), the *sparse* (the peaky planet signals) and the Gaussian noise component (residuals). This decomposition removes the speckle noise more efficiently, resulting in an improved SNR of the companion in the final image.

Note that the PCA approach is very similar to the LOCI approach (see Savransky, 2015) and in any case it is an inverse problem solved by using a deterministic approach: the distance between the image and the model PSF is minimized in the least-square sense. The two methods I am dealing with in this manuscript use a stochastic approach to inverse problems which takes into account a model of the noise statistics in the images.

Most discoveries made to date in exoplanet imaging have been obtained thanks to these different techniques. In practice, different algorithms are used to check whether the companion is still detected when using another image processing method along with various user-parameters. The main limitation of these methods is that part of the companion flux is removed during the process. An intensive post-processing is therefore performed to estimate the relative photometry of the planetary companion (Pueyo, 2016). The detection limit of the images must also be computed separatly. Moreover, for all of these methods, the companions are detected by visual inspection of the final image as there is no systematic detection procedure. The two algorithms I studied during my PhD aim to address these three main limitations.

1.3.2.2 Exploitation of the spectral diversity: SDI and SSDI

If two or more images are taken simultaneously at different wavelengths (under the same turbulence conditions), one can exploit the spectral diversity present in such images. In the general case, the position, size and amplitude of the speckles vary with the wavelength: at first order, the speckles spread radially in the image field while their size broadens when the wavelength increases (because they originate from the on-axis centered starlight). However the planetary signal remains fix in the field of view from one wavelength to another (because it is a faint off-axis point source so only the size of its core is increasing with the wavelength). Fig. 1.20 shows the radial spread of the speckle field when the wavelength of observation increases while the position of the planetary companion does not vary.

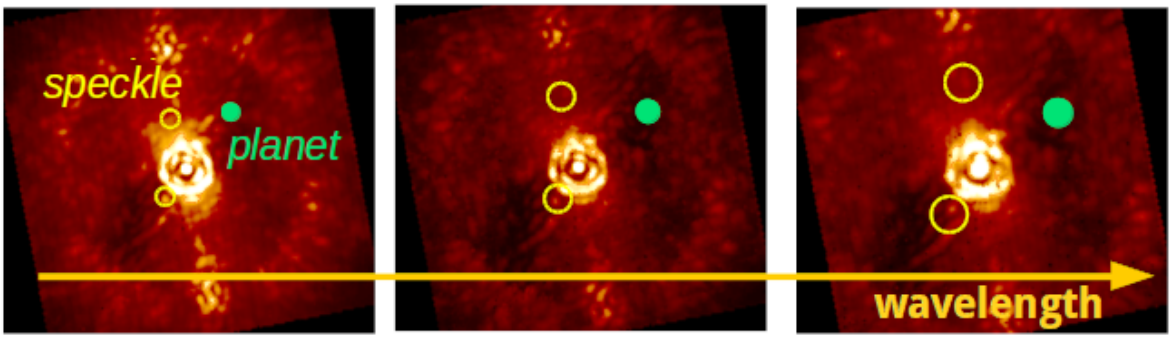

Figure 1.20 – Speckle field spreading with the wavelength while the planetary companion is fixed. Images of the star Beta Pictoris with SPHERE.

The basic principle of spectral differential imaging is to assume that, at first order, the radial motion of the speckle is deterministic. It is thus possible to rescale one image to another to obtain the model PSF of the second image (Sparks and Ford, 2002). This basic SDI concept has been first introduced in Racine et al. (1999) and Marois et al. (2005b) and concerns the case of two images observed simultaneously. In order to avoid self-canceling the planetary signal during the subtraction the planet must be significantly fainter (ideally absent) in one of the image than in the other or the planet must be far enough from the star so that its fixed position is nicely discriminated from a radially shifted speckle. Using spectrum models of planets permits to choose carefully the two spectral channels used. For instance, the methane absorption line is commonly used (Borysow et al., 2003; Lenzen et al., 2004; Marois et al., 2005a, 2000) and a list of compounds ratio can be found in Madhusudhan et al. (2013).

Assuming that the aberrations are achromatic and that the small phase approximation is valid, the PSF at wavelength λ_2, denoted by $h^{\lambda_2}(\mathbf{r})$, can be rescaled at λ_1 following (Cornia et al., 2010; Pueyo and Kasdin, 2007):

$$h^{\lambda_2}\left(\frac{\lambda_2}{\lambda_1}\,\mathbf{r}\right) = \left(\frac{\lambda_1}{\lambda_2}\right)^2 . h^{\lambda_1}(\mathbf{r}) \tag{1.17}$$

The latter equation assumes that only the star PSF resides in the field so the rescaling operation should better be performed on the image which does not contain the planetary signals. The image at

λ_2 rescaled at λ_1, $i_{t,res}^{\lambda_2}$, is then computed as:

$$i_{t,res}^{\lambda_2}(\mathbf{r}) = \left(\frac{\lambda_2}{\lambda_1}\right)^2 . i_t^{\lambda_2}\left(\frac{\lambda_2}{\lambda_1}\mathbf{r}\right) \tag{1.18}$$

Since the model used to rescale the PSF in wavelength is only of the first order, it is better to choose the two wavelengths λ_1 and λ_2 as close as possible to minimize errors that could arise from this rescaling operation. However there are two main limitations when using the classical SDI algorithms: (1) the bias in the estimated contrast is significant and (2) the estimated contrast depends on the real spectrum of the companion (Rameau et al., 2015).

To go further, the same kind of concept can be applied to multispectral images (SSDI). In this case, the diversity is increased by the number of spectral channels:

1. Any adaptations of ADI and/or SDI on each channel separately are commonly considered. For instance, multispectral PCA is adapted to process several wavelengths, T-LOCI takes into account the spectrum of the star given in input to optimize the companion extraction. A version of the KLIP algorithm accompanied with forward modeling (KLIP-FM Pueyo, 2016), based on perturbation theory, constrains the estimated spectrum of the planetary companion to avoid over/self-subtraction of the companion signal.

2. The spectral deconvolution (SD Sparks and Ford, 2002; Thatte et al., 2007): after rescaling each image of the multispectral cube, a polynomial fit is performed along the wavelength direction for each pixel of the rescaled datacube. The resulting fit is then subtracted from the rescaled datacube to reduce the speckle noise. Each frame is then rescaled to its original dimension so that the planetary signal is at the same position in every frame while the speckle noise is significantly reduced. However, once again, part of the signal is subtracted. This method is also very sensitive to wavelength calibration.

3. The spectral diversity Burke and Devaney (2010): uses a multispectral phase retrieval (also called *wavelength diversity*) which consists in estimating the model PSF by minimizing the distance between the image and the PSF model along a stochastic approach (maximum likelihood) for all the wavelengths. In order to decrease the number of unknowns, the multispectral phases are parametrized by the optical path difference, assumed achromatic. However this method is designed for non-coronagraphic systems and thus does not take into account the model of coronagraphic image.

In the second part of this manuscript, I present the MEDUSAE method which uses the same information as spectral diversity but taking into account the coronagraph and priors on the instrument in order to fully exploit the multispectral images, while avoiding the planetary signal self-subtraction.

1.3.2.3 Other information exploited

Instead of using the spectral or temporal diversity as in this manuscript, I mention in the following several techniques that make use of various diversities combined with differential imaging.

Polarimetric differential imaging, PDI The light reflected by planetary companions in the visible or the light scattered by the circumstellar dust is polarized in a specific direction. By observing the two linear polarizations simultaneously, one can subtract one frame to the other to unveil the circumstellar objects. In practice, this method introduced by Kuhn et al. (2001) is efficient for disk imaging and motivated the design of the SPHERE polarimetric imaging modes in the visible (ZIMPOL, Roelfsema et al., 2010) and in the near-IR (IRDIS-DPI, Langlois et al., 2010).

Reference differential imaging, RDI Another idea, is to obtain the model PSF by observing another reference star, close to the actual observed star, which has almost the same brightness (Mawet et al., 2005; Rameau et al., 2012). This approach was used on NaCo even before the pupil tracking

was implemented and the first detection of Beta Pictoris b was obtained this way (Lagrange et al., 2010). An evolution of this idea is to create a library of PSF and to look for the most correlated frames with the PSF library, similarly to PCA. The paper Milli et al. (2016) investigates the temporal correlations between images in order to choose for the better frames.

Coherence differential imaging, CDI Another technique is to use the fact that the speckles originate from the same source (the star light) and thus, that they are coherent. An idea, proposed by Guyon (2004), is to exploits the coherence of the speckles to make them interfere destructively with the central core of the PSF. This method, called synchronous interferometric speckle suppression, can remove speckles regardless of their evolution time. A similar idea published by Baudoz et al. (2005) is to divide in amplitude the incident field into two different images for which the speckles destructively interfere. This set up, called hybrid interfero-coronagraph, is suitable to detect faint sources at very close angular separation.

Binary differential imaging, BDI In the case of a binary star (which is the case of many objects observed in exoplanet detection), an idea published by Rodigas et al. (2015) is to use the information provided by the presence of the secondary star to obtain an estimate of the PSF model to be subtracted to the primary star. This method is being exploited for the current MagAO survey.

Note that ADI and SDI methods are by definition fundamentally limited close to the star while these different methods have access to shorter separation.

Conclusion of this chapter

Along this chapter I demonstrated the interest of exoplanet imaging as well as the technological difficulties to overcome in order to detect faint companions. I presented the main hardware and software solutions that are implemented in the high-contrast instruments currently in operation. Among the main ingredients for high contrast imaging, one can find adaptive optics systems, coronagraphic devices and advanced image processing methods. The association of these ingredients allows the astronomers to reach a contrast of about 10^{-6} in infrared images.

Fig. 1.21 is a block diagram illustrating the whole assembly line for exoplanet imaging, from the astrophysical scene to its estimated properties. My PhD focuses on image processing (yellow box): it starts with the so-called *reduced images* (*raw images* from the telescope, that have been cleaned thanks to the calibration files, centered and often selected and/or temporally binned) and consists in delivering the *processed images* in which it is possible to detect the planetary companions and to characterize them. The characterization is to estimate their projected position, relative contrast to the star as well as the detection limit of the data-set. From these characterizations, astronomers are using models to derive some physical properties of the exoplanet that are compared to simulations in order to understand the nature of exoplanets as well as their formation and evolution processes.

The principle on which the current image processing methods are based is differential imaging. This technique resulted in numerous scientific breakthroughs in the exoplanets field. However, it is still limited and some specific limitations must be alleviated if one wants to, on the one hand, correctly process and interpret the results from large surveys and, on the other hand, search and confirm the presence of faint and close companions. My PhD work is within this context and directly addresses this topic.

Outline of this manuscript

In the first part of this thesis, I present the work I have done on the ANDROMEDA algorithm which exploits the temporal diversity provided by the rotating image field. I first present the concept of ANDROMEDA and the status of the algorithm when I started my PhD. After presenting the solutions implemented to the original algorithm to make it operational, I present a neat analysis of its

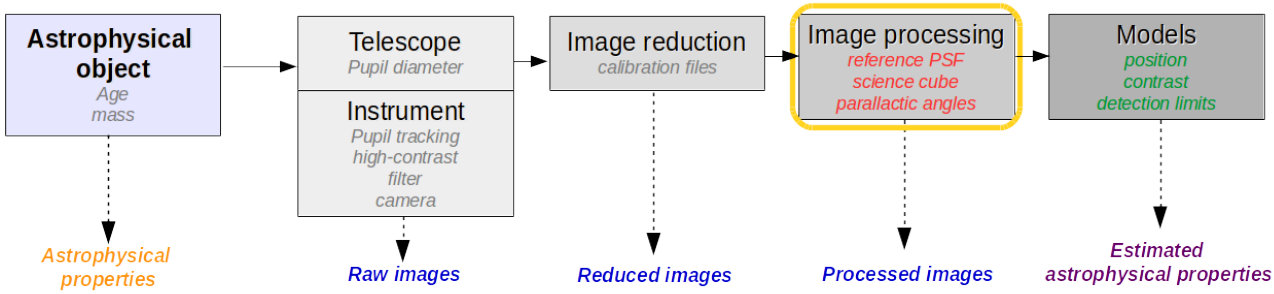

Figure 1.21 – Diagram illustrating the main steps with the main information used from the astrophysical object with unknown properties (in orange) to its estimated properties (in purple). The intermediate images are written in blue. My work focuses on delivering the information from which the astrophysical propertied (green) are estimated from the reduced data (red).

performance and a thorough comparison to the other main algorithms used. I finally present various on-sky results demonstrating the response brought by the ANDROMEDA solution to the limitations of the current algorithms commonly used and which lead to various perspective for this method.

In the second part, I present the work I have done on the MEDUSAE algorithm which exploits the spectral diversity provided by multispectral data. I first present the concept of MEDUSAE and the status of the algorithm when I started my PhD. This is followed by results of tests performed on data simulated using the same model as the one used in the inversion. Following these preliminary tests, I adapted MEDUSAE and applied it, in its original state, on real data. Results showed the importance of simulating realistic data to analyze the algorithm capabilities in a first step. I simulated realistic SPHERE-like data and applied MEDUSAE in its original state. The results from these preliminary tests open perspectives that are necessary to investigate in order to make MEDUSAE operational on on-sky data.

Résumé en français du chapitre d'introduction : l'imagerie d'exoplanètes avec des instruments de haut contraste

Dans le chapitre d'introduction qui précède, je détaille le contexte dans lequel j'ai réalisé mes travaux de thèse de doctorat : il s'agit de l'imagerie d'exoplanètes avec des instruments à haut contraste. Plus spécifiquement, mon sujet de thèse se focalise sur la partie traitement d'images afin de détecter et caractériser des exoplanètes dans de telles images. Pour ce faire, j'utilise des méthodes basées sur la résolution de problèmes inverses.

Ainsi, dans une première partie, j'introduis le contexte astrophysique : comment peut-on définir une exoplanète, quelles sont les informations que l'on cherche à obtenir grâce à leur étude, et comment peut-on les détecter et les étudier (1.1)? Dans une seconde partie, je décris les solutions technologiques mises en jeu afin d'obtenir des images à haute dynamique, nécessaires pour l'étude de ces objets faibles et proches de leur étoile hôte (1.2). Enfin, dans une troisième partie, je décris l'état de l'art des différentes méthodes de traitement d'images qui permettent de détecter et caractériser des exoplanètes ou disques circumstellaires dans les images obtenues (1.3). Dans la suite, je résume les motivations principales menant à mon sujet de thèse en suivant le plan utilisé dans le manuscrit.

Intérêt de l'imagerie des exoplanètes

Une exoplanète n'a pas de définition stricte. Bien qu'il existe des planètes flottantes, qui ont été détectées, la définition courante est qu'il s'agit d'un objet gravitant autour d'une étoile (ou d'un résidu d'étoile type objet compact), et qui soit suffisamment massif pour que les forces de cohésion soient dominées par la gravitation et pour qu'il ait nettoyé son orbite, mais pas trop massif pour que la fusion du deutérium ne soit pas démarrée (auquel cas, l'appellation naine brune est préférée, à partir de 14 masses de Jupiter).

Ces objets circumstellaires et leur environnement sont un sujet d'étude essentiel si l'on veut comprendre les processus de formation d'exoplanètes (liés à la formation stellaire), l'évolution de ces objets (lié à l'environnement de ces objets, disques circumstellaires ou autres planètes) et étudier leur composition atmosphérique (sondant ainsi la présence de marqueurs biologiques) et ainsi trouver une définition adéquate. Ces problématiques étant évidemment connectées les unes aux autres.

Dans ce cadre, l'imagerie des exoplanètes est essentielle puisqu'elle permet de compléter les connaissances que nous avons sur ces objets. Aujourd'hui, il existe cinq techniques majeures qui permettent d'étudier les exoplanètes. Chacune de ces méthodes, de par son principe, a accès à un type d'objets particuliers, à des paramètres physiques spécifiques sur ces objets et à des limites fondamentales propres (résumées à la section 1.1[11].). L'imagerie d'exoplanètes est particulièrement complémentaire aux

[11] Pour chaque méthode, j'évoque aussi les grandes découvertes, le nombre de détections effectuées à ce jour et les projets instrumentaux en cours ou à venir afin d'exploiter au mieux ces méthodes.

autres techniques, dites indirectes, puisqu'elle permet de sonder la présence de compagnons à plus large séparation de leur étoile hôte (quelques unités astronomiques) et est restreinte à des objets plus massifs (de l'ordre de la dizaine de masses de Jupiter, afin de détecter leur lumière émise). Trois points majeurs peuvent être notés concernant l'imagerie :

Détection par imagerie directe Les détections sont cependant rares (seulement une trentaine de détections à ce jour) car les résidus de la lumière de l'étoile sont très difficiles à gérer : chaque détection est donc critique pour remplir l'espace des paramètres explorés afin de mieux comprendre la nature même de ces objets par des études statistiques. Quand il n'y a pas de détection, il est tout aussi important d'obtenir des limites de détection fiables puisque l'absence de compagnon est directement liée au scenario de formation et d'évolution planétaires.

Spectro-photométrie par imagerie directe D'autre part, l'imagerie permet d'avoir directement accès aux photons et donc de caractériser le flux du compagnon afin d'en étudier l'atmosphère ainsi que de contraindre ses propriétés physiques, selon les modèles d'évolution choisis. Étant donné que ces modèles concurrents sont très similaires, il est essentiel d'obtenir autant de points que possible (une bonne couverture en longueur d'onde) et d'avoir des incertitudes très petites sur ces derniers afin de discriminer ces modèles d'atmosphère, et de formation et d'évolution des planètes.

Astrométrie par imagerie directe Un suivi astrométrique d'un compagnon dans le temps permet de contraindre l'orbite de l'objet en interaction avec son environnement (autres planètes et/ou disque circumstellaire) et donc d'évaluer les scenarii de formation et d'évolution des planètes (en particulier les processus de migration planétaire).

Ces trois aspects motivent directement la construction d'instruments dédiés afin d'être plus sensible aux compagnons de faible masse (quelques masses de Jupiter) à grande séparation (quelques dizaines d'unités astronomiques) et affiner les points de données astrométriques et photométriques sur les détections obtenues.

L'imagerie à haut-contraste pour l'étude des exoplanètes

Afin de pouvoir détecter des exoplanètes, il faut typiquement atteindre des résolution de 0.5 $''$ pour un contraste de 10^{-6} en infrarouge pour des planètes jeunes de type géantes gazeuses. Les observations sont réalisées en infrarouge car le contraste entre la lumière émise par l'étoile hôte et celle émise par la planète est le plus favorable dans cette gamme de longueurs d'onde.

Pour atteindre la sensibilité nécessaire, il faut utiliser de grands télescopes, essentiellement installés au sol. Cependant, la présence de l'atmosphère terrestre induit une perte de résolution non négligeable qui empêche l'exploitation des images obtenues. Un système d'optique adaptative permet de corriger en temps réel les aberrations introduites par la turbulence atmosphérique et d'atteindre ainsi un contraste typique de 10^{-3} à 500mas en bande H ($1.6\mu m$). Afin d'éliminer la lumière diffractée par l'étoile, l'utilisation d'un coronographe s'avère nécessaire pour atteindre un contraste de 10^{-4} à 500mas. C'est à ce stade qu'il est aussi nécessaire d'utiliser des méthodes de traitement d'images adaptées afin d'atteindre un contraste de 10^{-5}-10^{-6} à 500mas. En effet, le coronographe enlève la partie cohérente de la lumière stellaire. Ce qui reste dans les images, après le coronographe, est lié aux aberrations résiduelles dues à la turbulence atmosphérique et aux aberrations résiduelles de l'instrument.

Dans le manuscrit, je décris les éléments principaux d'une optique adaptative (1.2.1) et les différents type de coronographes qui existent (1.2.2) ainsi que les limitations fondamentales de ces composants optiques, motivant directement le développement de méthodes de traitement d'images adaptées (1.2.3). J'y introduis aussi les notions nécessaires à la compréhension de mon travail. À la suite de ces parties, je décris les différents instruments dédiés au haut contraste pour lesquels il est possible d'appliquer les méthodes de traitement d'images développées pendant mon travail de thèse (1.2.4). En particulier,

j'ai travaillé avec des images obtenues avec les instruments VLT/NaCo et VLT/SPHERE que je décris dans ces parties.

Traitement d'images pour la détection d'exoplanètes

Dans les images obtenues, il y a des tavelures (*speckles* en anglais) qui sont l'expression plan focal de la lumière de l'étoile déviée par les aberrations résiduelles. Une partie de ces tavelures évolue de façon quasi-statique et il est impossible de les étalonner pour les retirer ou de les moyenner en un halo lisse dans l'image (qui peut être rejeté a posteriori). De plus ces tavelures, de par leur nature, ont typiquement la taille d'un élément de résolution, tout comme les signaux planétaires attendus (sources non-résolues). L'intensité des tavelures est donc directement liée au flux de l'étoile et au niveau des aberrations résiduelles ce qui les rend souvent plus brillantes que le signal attendu sur les compagnons planétaires.

Afin de discriminer les objets d'intérêt astrophysique parmi ce bruit de tavelures, il faut utiliser une diversité, c'est à dire une différence de comportement pour ces deux composantes. Durant mon travail de thèse, j'ai exploité deux diversités:

Diversité temporelle grâce au suivi de pupille Puisque les tavelures ont pour origine la présence d'aberrations instrumentales, qui, au premier ordre, appartiennent au plan pupille, il est possible de fixer spatialement les tavelures en utilisant un derotateur de champ placé en suivi de pupille (*pupil tracking*). Dans le cas d'un télescope à monture alt-az, le champ image tourne alors à une vitesse déterministe donnée par les angles parallactiques (dépendant de la position de la source et de la localisation de l'observatoire). Ainsi, dans une séquence temporelle d'images, les objets hors-axe tournent à une vitesse connue alors que les tavelures restent fixes dans le champ.

Diversité spectrale grâce à l'imagerie multispectrale Puisque les tavelures sont l'image de l'étoile à travers l'instrument, ils se déplacent radialement vers l'extérieur de l'image (l'image de l'étoile étant centrée) quand la longueur d'onde d'observation augmente. Cependant, les objets d'intérêt (qui sont moins brillants) restent immobiles. Ainsi, un instrument capable de faire simultanément plusieurs images à différentes longueurs d'ondes (cas des spectrographes à intégrale de champ, IFS), permet d'exploiter cette redondance d'information.

À ce jour, les différentes méthodes de traitement d'images utilisées par la communauté des chercheurs en imagerie d'exoplanètes, et qui exploitent ces diversités, consistent à créer un modèle empirique de l'image de l'étoile seule et à la soustraire aux images (il s'agit donc d'imagerie différentielle). Malgré les nombreux résultats obtenus grâce à de telles méthodes ces dernières années, elles sont limitées essentiellement par trois aspects : (1) une partie du flux du compagnon est soustraite et il faut calculer a posteriori cette fraction de flux afin de retrouver le vrai contraste du compagnon; (2) de la même manière, la limite de détection est calculée a posteriori par des calculs intensifs; (3) il n'existe pas de procédure de détection systématique et les compagnons sont visuellement détectés dans les images. Dans tous les cas, les informations sur la formation d'image (telles que le comportement non-linéaire des tavelures ou encore les motifs apparaissant après soustraction d'images) ne sont pas prises en compte.

La motivation principale de mon travail de thèse est de répondre à ces limitations en explorant d'autres pistes pour exploiter les images. Au cours de ma thèse, j'ai exploité ces diversités dans le cadre de la résolution de problèmes inverses. Il s'agit de définir un modèle de données dépendant des paramètres d'intérêt à estimer (tels que la position et le flux du compagnon), puis d'exploiter l'ensemble des données ainsi que toutes les informations a priori qui sont disponibles afin d'estimer les paramêtres les plus probables qui expliquent les données.

Plan du manuscrit de thèse

La première partie de ce manuscrit est consacrée à mon travail sur l'algorithme ANDROMEDA qui exploite la diversité temporelle des images. La seconde partie de ce manuscrit est consacrée à mon travail sur la méthode MEDUSAE qui exploite la diversité spectrale des images. Un résumé en français se trouve à la fin de de chaque partie. Une conclusion générale en français se trouve à la fin du manuscrit.

Part I

ANDROMEDA: Exploitation of the temporal diversity in the images.

The goal of this part of the thesis is to present the work I have done during my PhD on the ANDROMEDA algorithm, which is a method dedicated to the detection and characterization of point sources within images taken in pupil tracking mode.

In the introduction chapter, I presented the main algorithms widely used today in exoplanet imaging that can be sorted in three main concepts: c-ADI (Marois et al., 2006), LOCI (Lafrenière et al., 2007) and PCA (Amara and Quanz, 2012; Soummer et al., 2012). The major limitations of these algorithms are the following:

1. The companions are visually detected in the final image: it depends on the observer acuteness;
2. Part of the planetary signal is subtracted: extensive post-analysis are required to estimate the flux of the planetary signal.

The ANDROMEDA algorithm that I present in this first part of the manuscript intents to address these limitations. ANDROMEDA is an ADI-based algorithm which solves the inverse problem in a stochastic approach, that is to say by taking into account a model of the noise distribution in the images.

Chapter 2

The ANDROMEDA approach and initial status

Contents

2.1 ANDROMEDA's principle 57
2.1.1 Theoretical concept 57
2.1.2 Practical solutions 59
2.1.3 Inversion method 63
2.2 Previous work on the ANDROMEDA method 67
2.2.1 Description of the simulated data used to test the method 67
2.2.2 Theoretical study of the potential sources of errors 68
2.2.3 Optimal set of user-parameters derived from simulated data application 69
2.3 Application of ANDROMEDA on real data as it is 73
2.3.1 Description of the real data used to apply ANDROMEDA 73
2.3.2 Output provided by ANDROMEDA 74
2.3.3 Detected problems affecting ANDROMEDA's capabilities on real data 76
2.3.4 Conclusion on ANDROMEDA's original capabilities 77

In order to address the issues mentioned above, an original idea published by Mugnier et al. (2009), is to develop an image processing method dedicated to point source extraction in images taken in pupil tracking mode, based on inverse problem solving (similarly to Thiébaut and Mugnier, 2006). This method, called ANDROMEDA for *ANgular DiffeRential OptiMal Exoplanet Detection Algorithm* is the subject of this part of the thesis.

ANDROMEDA is an ADI-based method whose first step is to build the so-called *differential images* obtained by subtracting two images for which, if a planetary companion is present, it has moved in a deterministic manner whereas the stellar halo has remained mostly fixed. The key point of the ANDROMEDA method consists in building a model of the differential images and in minimizing the distance between this model and the actual scientific images, given the statistical distribution of the errors on the model. Thus, the idea of ANDROMEDA is to use the ADI technique, not only to minimize the impact of the speckles in the resulting image, but as a mean to (i) make the residual noise as white as possible to enable the use of a statistical approach to discriminate planetary signals from the speckles and (ii) make arise a specific and known signature when a companion is present that can be easily disentangled from residual speckles by inverse problem solving.

This chapter describes the status of ANDROMEDA before I started working on this algorithm to adapt it to the real data properties. I will first describe the ANDROMEDA method in its theoretical principle (Sect. 2.1), that is to say in the case of ideal images, following the work of Mugnier et al. (2009). This theoretical concept has been validated on simulated data, and I will present the conclusions drawn out from this work (Sect. 2.2). My work consisted in making this method operational on real data, starting from this first version of the method. In Sect. 2.3, I will apply ANDROMEDA in

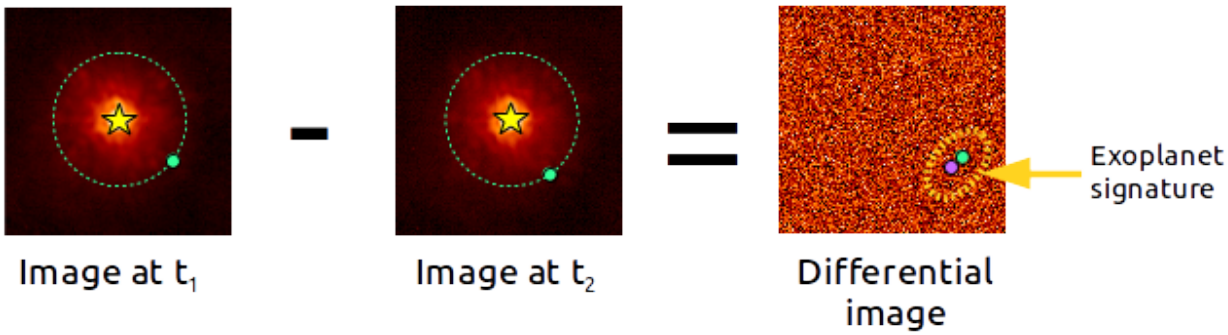

Figure 2.1 – Schematic principle of ANDROMEDA: the exoplanet signature is tracked in the differential image via inverse problem solving, under the assumption that most of the starlight has been removed by the ADI.

its original configuration on real data, in order to bring out the issues (expected or not) leading to all the stakes on which my work on this algorithm is based.

2.1 ANDROMEDA's principle

The ANDROMEDA method is based on inverse problem solving by using a maximum likelihood estimation of the sought parameters. This section describes the approach followed by the algorithm from its very theoretical aspect to its practical implementation.

2.1.1 Theoretical concept

The ANDROMEDA concept relies on differential imaging in order to, on the one hand, remove as much starlight as possible and consequently whiten the noise, and on the other, reveal a deterministic signature when a planetary companion is present. Indeed the star image evolves in a non-deterministic way which makes it complex to model and estimate via inverse problem (see next part for discussion about modeling the speckle field). Using ADI helps builing a consistent model of the resulting so-called *differential images* to be inverted via a maximum likelihood. As the likelihood relies on the statistical distribution of the noise in the data, whitening the noise is useful to compute this likelihood in an analytical way. The specific planet signature is useful to better disentangle planetary companions from remaining bright speckles and build the corresponding model.

2.1.1.1 Differential images: Accommodating the noise distribution and appearance of a planet signature

Assuming that we find a couple of images i_1 and i_2 for which:
-The planetary companion is moving in a *deterministic* way in the field of view;
-The stellar halo is as stable as possible;
Then we can subtract one of these two images to the other, resulting in a differential image Δ:

$$\Delta(\mathbf{r}) = i_1(\mathbf{r}) - i_2(\mathbf{r}) \tag{2.1}$$

In this differential image, most of the starlight has been removed (the error comes from the limited star PSF stability in between the two frames) and a specific shape appears at the location of the planetary companion in the two frames.

If no companion is present in the field of view (hypothesis H_0), then only the residual noise n_Δ remains in the differential image:

$$\Delta(\mathbf{r})|_{H_0} = n_\Delta(\mathbf{r}) \tag{2.2}$$

As most of the starlight has been removed, we can assume that the starlight residuals are now decorrelated and that this remaining noise is mainly made of photon and detector noise.

If a companion is present in the field of view (hypothesis H_1), then a so-called *planet signature* appears in the field of view. This planet signature is a function of the planetary signal p which is itself defined by its intensity a and its position in the first image i_1, $\mathbf{r_1}$. The differential image can thus be written:

$$\Delta(\mathbf{r})|_{H_1} = m(a, \mathbf{r_1}) + n_\Delta(\mathbf{r}) \tag{2.3}$$

Where $m(a, \mathbf{r_1})$ is the model of the planet signature, dependent upon the two unknown parameters (the position of the planetary companion $\mathbf{r_1}$ and its flux a) and $n_\Delta(\mathbf{r})$ the so-called *modeling error* between the data Δ and its model m, which includes the noise and the model approximation.

In the first image i_1, the planetary signal of flux a and at position $\mathbf{r_1}$, can be written $p(a, \mathbf{r_1}) = a.(\delta(\mathbf{r_1}) * h(\mathbf{r}))$, where $\delta(\mathbf{r_1})$ is the Dirac function at the position $\mathbf{r_1} = (r_1, \theta_1)$, and $h(\mathbf{r})$ is the PSF of the system. Thus, in the resulting differential image $\Delta(\mathbf{r})$ defined by Eq. 2.1, the planetary signature model $m(a, \mathbf{r_1})$ can be written:

$$m(a, \mathbf{r_1}) = a.[\delta(r_1, \theta_1) * h(\mathbf{r})] - a.[\delta(r_2, \theta_2) * h(\mathbf{r})] \tag{2.4}$$

The following part describes how to estimate the two unknown parameters a and $\mathbf{r_1}$ thanks to a maximum likelihood estimation.

2.1.1.2 Maximum likelihood estimation (MLE) of the planetary signals' parameters

In order to determine the unknown parameters of our statistical model given the data, the original and fundamental idea of the ANDROMEDA method is to use a maximum likelihood estimation. The estimated parameters are then the one which reproduce the best the observed data. This estimator is commonly used to estimate the parameters from noisy data, which is the case here, by maximizing the agreement between the model and the observed data.

The likelihood is defined as the probability of observing the data (here the differential images $\Delta(\mathbf{r}, k)$, where k encodes for the chosen diversity[1]) knowing its parameters (a and $\mathbf{r_0}$, given through the model $m(a, \mathbf{r_0})$). In our problem the likelihood[2] thus writes:

$$\mathscr{L}(m(a, \mathbf{r_0})|\Delta(\mathbf{r}, k)) = Pr(\Delta(\mathbf{r}, k)|m(a, \mathbf{r_0})) \tag{2.5}$$

This is the probability of observing the data Δ given that the model m is true. The latter term is the probability density function of the distance between the model m and the data Δ. As we have $\Delta(\mathbf{r}, k) = m(a, \mathbf{r_0})(\mathbf{r}, k) + n_\Delta(\mathbf{r}, k)$, the likelihood is the probability density function of the residual noise $n_\Delta(\mathbf{r}, k)$.

The residual noise distribution in the differential images is non-stationary for one differential image to another and it can be considered as Gaussian (in time and space) with a good approximation[3]. Indeed, before the subtraction, the noise was constituted of detector noise, photon noise and quasi-static speckle noise. After the subtraction, only the part of the quasi-static speckle noise which is decorrelated remains[4], as well as the linear combination of the photon and detector noise of the two images subtraction. Considering that this normal distribution is centered (it has a null spatio-temporal mean $\mu_\Delta(\mathbf{r}, k)$) and has a variance $\sigma^2_\Delta(\mathbf{r}, k)$, the noise probability density function for a given $\mathbf{r}$ and a given k, denoted x, can be expressed as:

$$p_{n_\Delta}(x) = \frac{1}{\sqrt{(2\pi\sigma^2_\Delta(x))}}.\exp\left(-\frac{1}{2}\frac{|n_\Delta(x)|^2}{\sigma^2_\Delta(x)}\right) \tag{2.6}$$

[1] Though ANDROMEDA has been developed specifically to process ADI data, I chose here to use a generic k, index of the couple of the two subtracted images, which could encode any variation, such as temporal or spectral. See perspectives at the end of this part for more details.

[2] Based on the Bayesian formula, by assuming that there is no prior on the sought parameters and to within a constant, the likelihood can directly be written as such.

[3] Attempts to prove this point can be found in Marois et al. (2008a) or Absil et al. (2013) by performing normality tests. I will further discuss this point in the next chapter at Sect. 3.1.2.

[4] In other words, the contribution of the speckle noise which is static in between the two images has been removed.

Moreover, if the Gaussian noise is decorrelated, as it is approximatively the case in the differential images, the noise probability density function of the residual noise in all the differential images becomes, for all the $\mathbf{r}$ and k:

$$p_{n_\Delta}(\mathbf{r},k) = \frac{1}{\prod_{\mathbf{r},k}\sqrt{(2\pi\sigma_\Delta^2(\mathbf{r},k))}}.\exp\left(-\frac{1}{2}\sum_{\mathbf{r},k}\frac{|n_\Delta^2(\mathbf{r},k)|}{\sigma_\Delta^2(\mathbf{r},k)}\right) \tag{2.7}$$

Note that the variance of the residual noise in the differential image still depends on the spatial (through $\mathbf{r}$) and chosen diversity (through k) variables. One can wonder why the variance term σ_Δ^2 cannot be moved outside the sum over the spatial and temporal variable. First, the quasi-static speckles distribution varies radially which means that the variance of their residuals is not spatially constant. Second, the chosen couples lead to different decorrelation levels (given that their correlation degree before subtraction is different for each couple). A more detailed discussion about this variance term is presented at Sect. 2.1.2.4.

At last, via the Eq. 2.3 which describes the relation between the data and the model, we can finally write:

$$\mathscr{L}(m(a,\mathbf{r_0})|\Delta(\mathbf{r},k)) \propto \exp\left(-\sum_{\mathbf{r},k}\frac{|\Delta(\mathbf{r},k)-m[a,\mathbf{r_0}](\mathbf{r},k)|^2}{2\,\sigma_\Delta^2(\mathbf{r},k)}\right) \tag{2.8}$$

2.1.2 Practical solutions

In practice, for this maximum likelihood solution, three inputs are needed: (i) a method to whiten the residual noise in the differential images, (ii) a model of the differential images and (iii) the variance of the error distribution.

2.1.2.1 Differential images: image couple selection

As explained in introduction for images taken in pupil tracking mode, the quasi-static speckle field is spatially stabilized in the field of view, while the astrophysical object rotates around the star during the observation. The idea is thus to use this angular motion of the field of view to find the most correlated frames to be subtracted one to another. In the resulting differential images, the noise has been partially whitened since the static (temporally correlated) part of the starlight has been removed. To do so, a couple of images to be subtracted has to be chosen within the following constraints[5]:

(1) The speckle field is as similar as possible in the two chosen frames;

(2) The companion position in the two frames must be different enough to avoid its self-subtraction.

As on real data the dominant error is due to the temporal variation of the quasi-static speckles (see 1.2.3), ANDROMEDA assumes that the most correlated frames are the frames that are the closest in time[6]. Thus in the ANDROMEDA development, it has been chosen to consider a simple solution to whiten the noise in the images by using a basic temporal ADI (note that more sophisticated ways of whitening the noise could be investigated, as mentioned in the perspectives of this part). In this case, the two constraints naturally become constraints on the time delay between the two frames to be subtracted:

(1) It must be short enough so that the speckle field did not have the time to evolve too much;

[5]Note that instead of performing a basic angular subtraction, Smith et al. (2009) have proposed to avoid the subtraction by directly estimating the moving source within the quasi-static speckle field, which enables the exploitation of every single frame. However their hypothesis is very strong since the star is assumed to be fixed during the whole observation sequence.

[6]Note that if the dominant error was due to another optical device we could have chosen another more adapted constraint on the image couples. For instance, if the ADC or derotator mis-pointing was the dominant error, then the frames that are symmetric wrt the meridian would be the most correlated ones and thus the most likely to be subtracted. In his PhD thesis, A. Cornia showed that using this strategy was not efficient enough to have a residual noise distribution as Gaussian as possible in the differential images (Cornia, 2010, Sect. 3.2)

(2) It must be long enough so that the angular position of the companion has sufficiently rotated to not subtract its own signal[7].
The latter constraint depends on the distance of the companion to the star (located at the center of the frames): for a given parallactic angle rotation, the closer the companion, the less apparent motion. The parameter responsible for this constraint is δ_{min}, the minimum azimuthal distance of the planetary companion in the two considered frames. As this parameter depends on the distance to the star (see Fig. 2.2), it has been chosen in ANDROMEDA to constraint the angular subtraction for each separation to the star via annuli surrounding the star. The width of the annuli is thus another user-defined parameter d_r which can be set either constant with the distance to the star or increasing with the distance to the star (since it becomes less critical at larger separation as the time delay between two frames separated of δ_{min} is shorter).

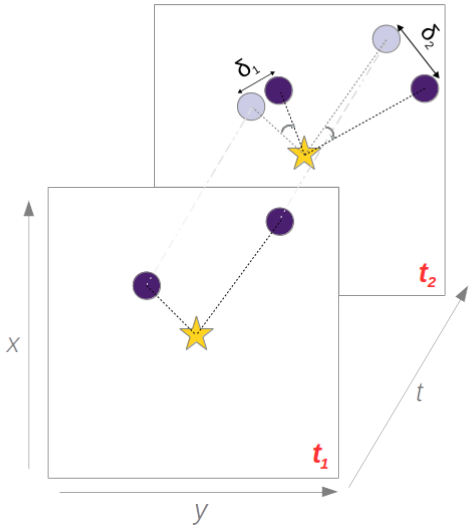

Figure 2.2 – Schematic view of the distance δ to be constrained via the parameter δ_{min} between off-axis objects at two different times in the field of view, as a function of the distance to the star.

To summarize the ADI process established in ANDROMEDA, two images of a couple indexed k respecting the two conditions (1) and (2) mentioned above, are subtracted one to another. The resulting differential image can be written:

$$\Delta(\mathbf{r}, k_{annulus(r)}) = i_{k_{annulus(r)}}(\mathbf{r}, t_1) - i_{k_{annulus(r)}}(\mathbf{r}, t_2) \tag{2.9}$$

where $\mathbf{r}$ stands for the whole field of view and $k_{annulus(r)}$ is the index of the couple chosen for a specific annulus at a certain separation to the star r. $i_k(\mathbf{r}, t_1)$ is the image of the science cube at t_1 and $i_k(\mathbf{r}, t_2)$ the image at t_2. These two images must respect the two conditions mentioned above:
(1) $\Delta t = |t_2 - t_1|$ is as small as possible;
(2) For a specific separation to the star, $|\mathbf{r}_{t_1} - \mathbf{r}_{t_2}| \geq \delta_{min}$.

For more readability, I will express by a generic index k (encoding the time variation) the $k_{annulus(r)}$, but one has to keep in mind that this index is chosen for a specific distance to the star. In total, there are as many index k as analyzed annuli and, for each of these annuli, as many couples meeting the two conditions above as possible. For a regarded distance to the star, the maximum number of image couples is thus the number of images in the cube, as in the ideal case *every* image of the cube is used. If no couple is found, it means that there is not enough field rotation at this distance and that the δ_{min} constraint should be decreased.

[7] In his PhD thesis, A. Cornia assessed the energy loss amount as a function of the chosen δ_{min} , in the case of noiseless Airy patterns (Cornia, 2010, Sect. 3.2). However this does not affect the flux estimated by ANDROMEDA since this energy loss, due to the signal self-subtraction, is taken into account in the planetary signature model defined at Eq. 2.4.

2.1.2.2 Differential images: image couple flux scaling

Given the constraint (1) and (2), the average intensity distribution might have evolved significantly between the two images, thus showing a non-negligible intensity offset in the resulting differential image. These intensity variations from one frame to another are usually due to variations of the adaptive optics correction quality and/or sudden changes of seeing conditions (see 1.2.1). To accommodate this flux difference, one of the image must be adjusted with respect to the other via a scaling factor γ so as to compute the differential image as:

$$\Delta(\mathbf{r}, k) = i_k(\mathbf{r}, t_1) - \gamma_k(\mathbf{r})\ i_k(\mathbf{r}, t_2)\ , \tag{2.10}$$

The scaling factor is empirically calculated for each image couple k found for each distance to the star r. One method to calculate this scaling factor is by doing a so-called *total ratio* which minimizes the total intensity by solving $\sum_{\mathbf{r_{sub}}} i_k(\mathbf{r}, t_1) - \gamma_{TR}\ \sum_{\mathbf{r_{sub}}} i_k(\mathbf{r}, t_2) = 0$ (Cornia et al., 2010), where $\mathbf{r_{sub}}$ is the pixels contained in the regarded annulus of thickness d_r and on which the constraint δ_{min} is applied, also called *subtraction zone*. By solving this, the corresponding scaling factor γ_{TR} is:

$$\gamma_{TR} = \frac{\sum_{\mathbf{r_{sub}}} i_k(\mathbf{r}, t_1)}{\sum_{\mathbf{r_{sub}}} i_k(\mathbf{r}, t_2)} \tag{2.11}$$

However this method might create artifacts if the sum of the pixels within the regarded annulus, $\sum_{\mathbf{r_{sub}}} i_k(\mathbf{r}, t_2)$, is close to zero. Thus, another method is to minimize the total intensity of the differential image in the least-square sense, that is to say by minimizing $\|\sum_{\mathbf{r_{sub}}} i_k(\mathbf{r}, t_1) - \gamma_{LS}\ \sum_{\mathbf{r_{sub}}} i_k(\mathbf{r}, t_2)\|^2$ (Cornia et al., 2010). By solving this, the corresponding scaling factor γ_{LS} is:

$$\gamma_{LS} = \frac{\sum_{\mathbf{r_{sub}}} i_k(\mathbf{r}, t_1)\ i_k(\mathbf{r}, t_2)}{\sum_{\mathbf{r_{sub}}} i_k(\mathbf{r}, t_2)^2} \tag{2.12}$$

Experiences on simulated data showed that optimizing the ADI in such a way usually makes come out discontinuities in the resulting SNR map between adjacent annuli. Indeed, the mean of the scaling factor for every couple k at a certain distance to the star could have a very different value from one annulus to its neighbor (due to the radial dependence of the intensity distribution in the images and to the fact that different pairs k of images are chosen from one annulus to the other, mostly close to the star). As a consequence, to avoid these edge effects, the scaling factor γ_k is calculated over a so-called *optimization area* that shares the same inner radius as the actual subtraction area but generally has a larger outer radius (that is to say $\geq d_r$), as shown on Fig. 2.3. The ratio optimization to subtraction area, R_A, is a user-defined parameters, set constant for all the annuli.

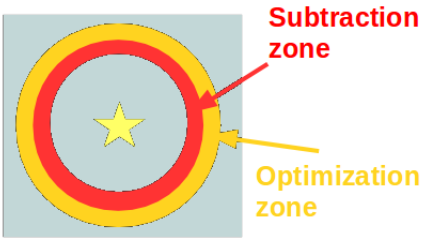

Figure 2.3 – Description of the subtraction zone (red annulus of width defined by d_r) and of the optimization zone (red plus orange annuli).

2.1.2.3 Building the model of a potential companion signature

For one differential image indexed k, the model of the planet signature can be written following Eq. 2.4 adapted to the temporal diversity exploited here via the ADI:

$$m_k(a, \mathbf{r_0}) = a.[\delta(r, \theta_{t_0}) * h(\mathbf{r}) - \delta(r, \theta_{t_1}) * h(\mathbf{r})] \tag{2.13}$$

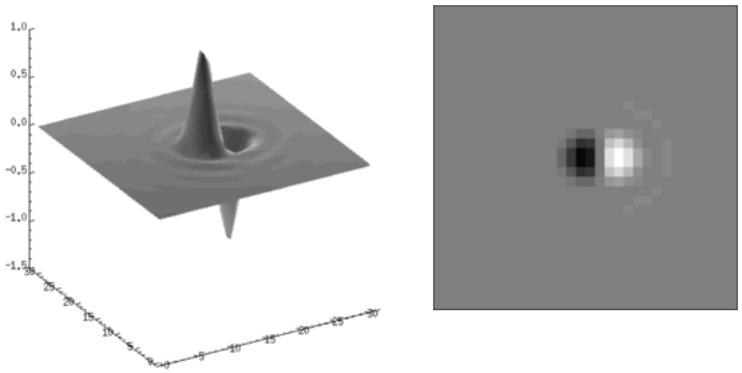

Figure 2.4 – Typical planet signature obtained by shifting the reference PSF of δ_{min} (here only the distance δ_{min} is not angular but along the x-axis; $\delta_{min} = 1\lambda/D$). This illustration is made thanks to an Airy pattern sampled with an oversampling rate of 1.6. This noiseless ideal reference PSF has been normalized to its maximum.

The angular distance between $\mathbf{r_{t_0}}$ and $\mathbf{r_{t_1}}$ being determined thanks to the parallactic angles at t_0 and t_1.

In order to build this model, we need an estimate of the imaging system PSF h. One solution would be to jointly estimate this reference PSF as proposed in Smith et al. (2009) or Ygouf et al. (2013). However here, it has been chosen to approximate this PSF by the image of the star (being unresolved), hereafter referred to as the *reference PSF*. Depending on the system, there are two solutions to obtain such an image:

-If no coronagraph is present, the images to be processed are saturated exposures; the reference PSF can be obtained by making an unsaturated exposure (by using a neutral density to avoid the saturation of the detector).

-If a coronagraph is used, the reference PSF can be obtained either by removing the coronagraph (when possible) and making an image of the star, or by making an off-axis exposure of the star (still by using a neutral density to avoid the saturation of the detector).

For this model to be included in the likelihood, this reference PSF must be normalized (by its total intensity) in order to estimate the contrast of the potential planetary companions by maximizing the likelihood. Also, any optics which impacts the flux of the reference PSF (such as neutral density transmission factors or throughput of the coronagraph) must be taken into account to derive the final estimated contrast of the detected point sources wrt to its host star.

This solution is rather efficient but has three main underlying assumptions:

1. It does not take into account the temporal variability of the star PSF during the observation. Consequently, the estimated flux will have greater error-bars. A solution would be to have a follow-up of the PSF quality (through its SR for instance) and to include this quality factor in our model for each couple of image (see perspectives in 6.5.5).

2. It assumes that there is no smearing of the objects in the field of view during the exposure. Consequently, this can decrease the SNR of the detected planetary signal and thus increase the flux error-bars. One solution would be to take into account the smearing by implementing a way of building the smeared PSF according to the distance to the star.

3. It assumes that the reference PSF is the same throughout the field of view, that is to say, that there is no distortion or off-axis aberration which would affect the planetary signal response wrt this reference PSF.

However tests and results suggested that these issues were of second order since the main error between our model and our data is due to the estimation of the residual noise distribution in the differential images.

2.1.2.4 Estimation of the noise variance to compute the likelihood

In order to compute the likelihood we need the variance of the residual noise distribution in the differential images. There is three ways of empirically computing this variance from the images according to the noise distribution in the data cube:

1. **3D-variance** The noise variance is estimated on each image of the regarded couple indexed k and then the residual noise distribution in the differential image is calculated as follow:

$$\sigma^2_\Delta(\mathbf{r}, k) = \sigma^2(i_k(\mathbf{r}, t_1)) + \sigma^2(i_k(\mathbf{r}, t_2)) \tag{2.14}$$

   According to the dominant noise in the images this variance can be approximated to be easily calculated. Under the assumption that the photon and the detector noise are dominant, the variance in the image can be calculated as: $\sigma^2_i(\mathbf{r}, t) = max\{i(\mathbf{r}, t); 0\} + \sigma^2_{det}$, (Cornia et al., 2010). However this method is not suited if other sources of noise, such as residual speckles, are present in the differential image.
   This variance is called *3D-variance* in the following.

2. **2D-variance** The variance is estimated from the full set of differential images obtained following:

$$\sigma^2_\Delta(\mathbf{r}) = \langle[\Delta(\mathbf{r}, k)]^2\rangle_k - [\langle\Delta(\mathbf{r}, k)\rangle_k]^2 \tag{2.15}$$

   This method assumes a temporally homogeneous variance. Thus, the same 2D map of variance is used for every differential image and without taking into account its temporal variability.
   This variance is called *2D-variance* in the following.

3. **1D-variance** The variance is estimated for each differential image obtained following:

$$\sigma^2_\Delta(k) = \langle[\Delta(\mathbf{r}, k)]^2\rangle_\mathbf{r} - [\langle\Delta(\mathbf{r}, k)\rangle_\mathbf{r}]^2 \tag{2.16}$$

   This method assumes a spatially homogeneous variance. Thus one scalar value is computed for each differential image and the spatial variability is not taken into account. This variance is called *1D-variance* in the following.

A very last option would be to use one scalar value computed following the 1D-variance and use this same value for all the differential images.

Note that in any of these cases, if the ADI is optimized by using a scaling factor γ, the latter must be taken into account in the computation of σ^2_Δ.

The ANDROMEDA strategy in practice

To summarize, the strategy adopted by ANDROMEDA to fulfill in practice its conceptual approach is (i) to use angular differential imaging in order to both whiten the residual noise in the resulting differential images and reveal a specific planetary signature, (ii) to use one reference PSF by imaging the star itself to build the model and (iii) to estimate the variance in an empirical way, directly from either the images or the differential images.

Note that the knowledge on the star PSF and on the noise variance can be regarded as a prior knowledge to be added to constrain the resolution of the inverse problem. In other words, the precision on these two parameters is not essential but could significantly increase the precision on the flux estimation and lead to a better SNR of the point sources detected in the field of view.

2.1.3 Inversion method

The ANDROMEDA method, under the assumptions leading to Eq 2.8, has an analytically computable solution which is extremely easy to implement numerically. This section describes the inversion method and the output delivered by the ANDROMEDA method. It is the core of ANDROMEDA under the scheme explained in details above.

2.1.3.1 Maximizing the likelihood

At this point, for each differential image, originating from a couple indexed k (temporal index), one differential image can be expressed following Eq. 2.9.

As the natural log of a function achieves its maximum value at the same point of the function itself, we can use the log-likelihood which is more convenient when an exponentiation is involved in the likelihood. The log-likelihood J to be minimized writes:

$$J(\mathbf{r}_0, a) \doteq \ln L(\mathbf{r}_0, a) \propto -\sum_{\mathbf{r},k} \frac{|\Delta(\mathbf{r},k) - a \cdot m(\mathbf{r},k;\mathbf{r}_0)|^2}{2\sigma_\Delta^2(\mathbf{r})} \tag{2.17}$$

For each annular zone at a certain distance from the star, this log-likelihood is computed for each differential image (sum over index k, from 1 couple to all the N_k couples found for this particular distance from the star), and over the whole field of view (sum over all the pixels in the image field, $\mathbf{r}$).

Within a constant additive C, the likelihood criterion can also be expressed as:

$$J(\mathbf{r_0}, a) = -\frac{a^2}{2}\sum_{k,\mathbf{r}} \frac{m^2(\mathbf{r},k;\mathbf{r_o})}{\sigma_\Delta^2(\mathbf{r},k)} + a\sum_{k,\mathbf{r}} \frac{m(\mathbf{r},k;\mathbf{r_o})\,\Delta(\mathbf{r},k)}{\sigma_\Delta^2(\mathbf{r},k)} + C \tag{2.18}$$

This form is easier to derivate so as to find its minimum values, which is the best estimator taking into account the noise statistics. Maximizing the log-likelihood is equivalent to minimizing the sum of squared residuals between the data (differential images) and the model, weighted by the variance of the residual noise.

2.1.3.2 Estimating the flux a of the companion

To estimate the optimal flux value $\hat{a}$ for each possible initial position of the planet, we assume that the initial position $\mathbf{r_0}$ is fixed and we analytically calculate the minimum of the log-likelihood wrt a by solving $\left.\frac{\partial J(\mathbf{r_o},a)}{\partial a}\right|_{\mathbf{r_o}} = 0$. We thus obtain the fundamental expression of the estimated flux:

$$\hat{a}(\mathbf{r}_0) = \frac{\sum_k \sum_{\mathbf{r}} m(\mathbf{r},k;\mathbf{r}_0)\Delta(\mathbf{r},k)/\sigma_\Delta^2(\mathbf{r})}{\sum_k \sum_{\mathbf{r}} m^2(\mathbf{r},k;\mathbf{r}_0)/\sigma_\Delta^2(\mathbf{r})} \tag{2.19}$$

This equation shows that the estimated flux can be regarded as a cross-correlation between the model of the planet signature and the differential image, weighted by the noise variance; the whole being averaged on every differential image. The denominator is a normalization constant.

In the ANDROMEDA code, after computing this estimated flux for each distance to the star, the results are combined in a single 2D map called **flux map**, in units of flux relative to the input reference PSF (i.e., A companion with the same flux as the star would be identified with a unity flux). On this flux map, each pixel gives *the flux of the point source, if the point source has this pixel position.*

2.1.3.3 Estimating the uncertainty $\sigma(a)$ on the flux map

In order to compute the uncertainty on the estimated flux, one way to proceed is to compute, for each possible initial position, the variance of the estimated flux, $\sigma^2[\hat{a}(\mathbf{r}_0)]$, given by:

$$\sigma^2[\hat{a}(\mathbf{r}_0)] = \left[\sum_k \sum_{\mathbf{r}} m^2(\mathbf{r},k;\mathbf{r}_0)/\sigma_\Delta^2(\mathbf{r})\right]^{-1} \tag{2.20}$$

ANDROMEDA thus provides a 2D-map called **map of the standard deviation of the flux**, in units of flux relative to the input reference PSF (as for the flux map), which describes how the noise propagates from the differential image toward the flux map. It thus gives the *detection limit*, that is to say the faintest detectable companion flux as a function of the separation from the star with a 1σ signal to noise ratio. In other words each pixel of this map gives the 1σ uncertainty on the estimated flux $\hat{a}$.

2.1.3.4 Estimating the initial position r_0 of the companion

Once the flux a has been estimated, we re-inject this estimated value on the likelihood criterion J to obtain another likelihood criterion J', which therefore only depends on the initial position $\mathbf{r_0}$:

$$J'(\mathbf{r_o}) \doteq J(\mathbf{r_o}, \hat{a}(\mathbf{r_o})) = \frac{[\sum_{k,\mathbf{r}} m(\mathbf{r},k;\mathbf{r_o})\,\Delta(\mathbf{r},k)\,/\,\sigma^2_\Delta(\mathbf{r},k)]^2}{\sum_{k,\mathbf{r}} m^2(\mathbf{r},k;\mathbf{r_o})\,/\,\sigma^2_\Delta(\mathbf{r},k)} + C \tag{2.21}$$

C being a constant. The criterion $J'(\mathbf{r}_0)$ is a measure of the likelihood that there is a point source at position $\mathbf{r}_0$ on the first image of the sequence. This formula is easily interpretable by saying that the planet has a high probability of being found at the position where the correlation between the model and the differential image is the closest to one.

In practice $J'(\mathbf{r}_0)$ is computed for each possible initial position of the planet on a grid chosen as the original pixel grid of the images. The results are combined in a single 2D-map called **likelihood map**. On this likelihood map, *higher values are at positions where the presence of a companion is more probable.*

2.1.3.5 Link between the likelihood and the SNR

Notably, we can highlight that the log-likelihood is simply the square of the signal-to-noise ratio (SNR) defined as $SNR = a/\sigma(a)$:

$$J'(\mathbf{r_o}) = \left(\frac{\hat{a}(\mathbf{r_0})}{\sigma[\hat{a}(\mathbf{r_0})]}\right)^2 \doteq SNR^2 \tag{2.22}$$

This means that maximizing the likelihood map is equivalent to maximizing the SNR map to find the most-likely position of a potential companion. Also, thresholding the SNR to zero is equivalent to computing $\hat{a}(\mathbf{r_0})$ under the positivity constraint. The latter equation shows that the log-likelihood directly incorporates this positivity constraint.

In summary, the likelihood and the SNR maps contain the same information, but we choose to use the SNR map to perform the detection since it directly yields the statistical significance of each detection. Indeed, in the Gaussian framework, the SNR is linked with a probability of false alarm (PFA) which assesses whether a signal is a true planetary signal. Thus, the SNR naturally writes:

$$\mathrm{SNR}(\mathbf{r}_0) = \frac{\hat{a}(\mathbf{r}_0)}{\sigma[\hat{a}(\mathbf{r}_0)]} = \frac{\sum_k \sum_{\mathbf{r}} m(\mathbf{r},k;\mathbf{r}_0)\Delta(\mathbf{r},k)/\sigma^2_\Delta(\mathbf{r})}{\sqrt{\sum_k \sum_{\mathbf{r}} m^2(\mathbf{r},k;\mathbf{r}_0)/\sigma^2_\Delta(\mathbf{r})}} \tag{2.23}$$

This is a 2D-map in sigma-units, in which there is a direct connection between PFA and threshold: *thresholding the SNR map automatically yields to every potential planetary signals corresponding to the given confidence level.* In the case the SNR has a normal distribution of null mean and unit variance $\mathcal{N}(\mu = 0, \sigma = 1)$ (the normal distribution is centered and standardized), then when no planetary companion is present (hypothesis H_0) the PFA as a function of the threshold τ writes:

$$PFA(\tau) = 0.5 \times [1 - erf(\frac{\tau}{\sqrt{2}})] \tag{2.24}$$

Where erf is the Gauss error function defined as $erf(x) = \frac{2}{\sqrt{\pi}} \int_0^x \exp^{-t^2} dt$. Thus, a threshold $\tau = 5\sigma$ will reveal only point source signals having a probability of presence of more than 99.9968% (corresponding to a $PFA = 2.98e^{-7}$).

2.1.3.6 Positivity constraint on the estimated flux

We note here that it is possible to improve the estimator $J'(\mathbf{r}_0)$ by constraining the estimated flux to be positive. This optional positivity constraint arises from the fact that the value of $\hat{a}(\mathbf{r}_0)$ obtained from Eq. 2.19 is not necessarily positive, whereas astrophysical fluxes are. Since $\hat{a}(\mathbf{r}_0)$ is a one-dimensional

optimization, the optimal flux subject to the positivity constraint is simply $\hat{a}_{\rm pos}(\mathbf{r}_0) = \max\{\hat{a}(\mathbf{r}_0), 0\}$. Under the positivity constraint, the criterion $J'(\mathbf{r}_0)$ becomes:

$$J''(\mathbf{r}_0) \triangleq J[\mathbf{r}_0, \hat{a}_{\rm pos}(\mathbf{r}_0)] = \begin{cases} J'(\mathbf{r}_0) & \text{if } \hat{a}(\mathbf{r}_0) > 0 \\ 0 & \text{if } \hat{a}(\mathbf{r}_0) \leq 0 \end{cases}, \tag{2.25}$$

where $\hat{a}(\mathbf{r}_0)$ is given by Eq. 2.19 and $J'(\mathbf{r}_0)$ by Eq. 2.21. In other words, applying the positivity constraint is equivalent to thresholding the SNR map to the positive values (at 1σ) and thus it decreases the number of false detections.

Fig. 2.5 shows the expected shape of a planetary signal in the resulting flux and SNR maps, either with or without the positivity constraint. The typical shape of this planetary pattern is oval, having its major axis along the radial direction (whose size is linked with the δ_{min} constraint chosen) and having its perpendicular minor-axis of typical length one element resolution ($1\lambda/D$). When the positivity constraint is not set, this pattern is surrounded by two negative lobes in the azimuthal direction of typically half the height of the main positive peak, due to the ADI process (the negative part of the planet signature in the differential images, see Fig. 2.4).

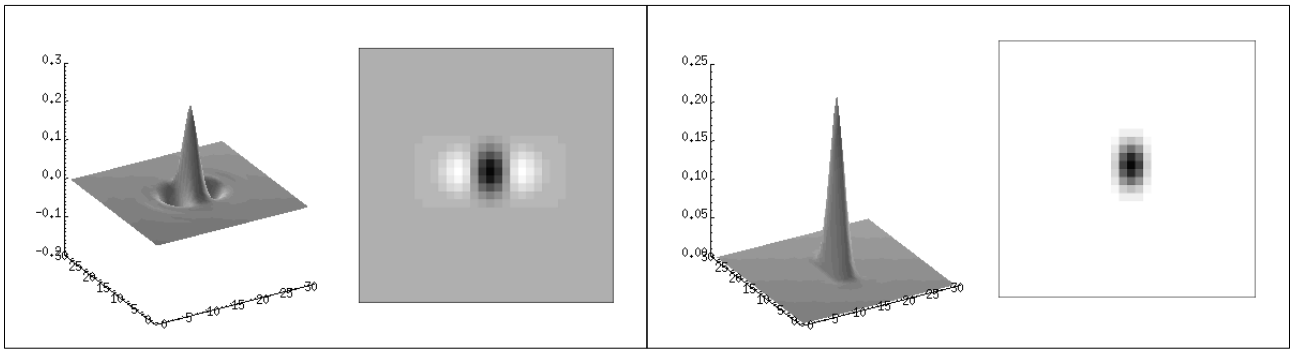

Figure 2.5 – Typical planetary pattern expected either in the flux map and in the SNR map, without (left) or with (right) the positivity constraint. These figures have been obtained by cross-correlating the planetary signature at Fig. 2.4 where δ_{min} is set to $1\lambda/D$ along the x-axis. Colors have been inverted: Black is high values and white is low values. The resulting planetary pattern is indeed oval, having its major axis perpendicular to the PSF shift axis (here the x-axis).

2.1.3.7 Conclusion on ANDROMEDA's principle

At the beginning of my PhD, practical solutions had been brought to make the ANDROMEDA concept feasible and to numerically implement this method. The output provided by ANDROMEDA are four 2D images: a SNR map, a flux map, a likelihood map and a standard deviation of the flux map.

In the ideal case were the model perfectly matches the data and that the theoretical concept works, the ANDROMEDA method aims to:

- Provide a SNR map having a statistical significance that is to say in which each value is directly linked with a probability of false alarm;
- Enable the use of a systematic and objective detection criterion based on this false alarm probability;
- Estimate the flux directly, without intensive post-process of the output images;
- Estimate the position of the companion (where the probability of presence is higher);
- Estimate the detection limit along with the flux estimation.

2.2 Previous work on the ANDROMEDA method

The basis of ANDROMEDA have been implemented in the IDL computer programming language (Exelis Visual Information Solutions, Boulder, Colorado). Most of the work achieved to numerically implement ANDROMEDA has been laid out by A. Cornia during his PhD at Onera, whose defense took place in 2010 at the Paris 7 university (see his PhD thesis: Cornia, 2010).

In particular, during his PhD thesis, A. Cornia studied the effect of the main foreseen sources of error on the ANDROMEDA capabilities. He also run ANDROMEDA on simulated data to obtain the best user-parameter set under which ANDROMEDA provides the best performance. These data have been simulated to be the most alike to the one expected from SPHERE at the time. My work on ANDROMEDA starts from the conclusions he obtained from his work and I did not do such a parametric study since my work focused on real data application and adaptation. This section describes the SPHERE-like simulated data (Sect. 2.2.1), the conclusions drawn out from his study of the main sources of errors (Sect. 2.2.2) and his study of the user-defined parameters (Sect. 2.2.3). Note that in this section, I will only evoke the work done in ADI-mode although A. Cornia looked into the case of SDI combined with ADI mode, hereafter denoted *SADI*.

2.2.1 Description of the simulated data used to test the method

These data have been simulated for the purpose of testing image processing methods on SPHERE-like data, before the instrument was commissioned at the VLT. These simulated data were used by A. Cornia to refine the first versions of ANDROMEDA (Cornia, 2010).

These simulations made use of the Code for Adaptive Optics System (CAOS, Carbillet et al., 2008), under conditions from the SPHERE technical report: it includes variations of the AO system correction, variations of the seeing, variations of the wind speed and direction, and variations of the quasi-static aberrations position during the observation (by simulating the rotation and motion of the main contributors to the non-common path aberrations of the instrument). The simulated coronagraph is an APLC.

In the end, the simulated data cube is constituted of 144 images having the properties gathered in Tab. 2.1.

Property	**Value**
Instrument	SPHERE
ESO program ID	Simulations using CAOS
Observation date	-
Atmospheric conditions	Good (seeing 0.85 ± 0.15)
Pupil tracking	ON
High contrast	APLC optimized in H-band
Wavelength of observation	H2-band: $1.587 \mu m$
Sensor pixel scale	12.25 mas/px
Star magnitude	G0 at 10pc
Image size	536×536 pixels
Number of images	144
Total field rotation	$120°$; $(-60.0° \rightarrow 60.0°)$
Offset angle wrt true North	104.84°
DIT image	100 sec
Total integration time	4 h

Table 2.1 – Table summarizing the characteristics of the simulated SPHERE-like data, used to test ANDROMEDA.

Twelve synthetic planets have been injected in this data set, at three different separations from the star (0.2″, 0.5″and 1″), at four different azimuthal positions (90° from one row to another) and

having a star-planet contrast of 10^{-6} (see Fig. 2.6). The effect of the smearing of the companions in each frame is ignored here.

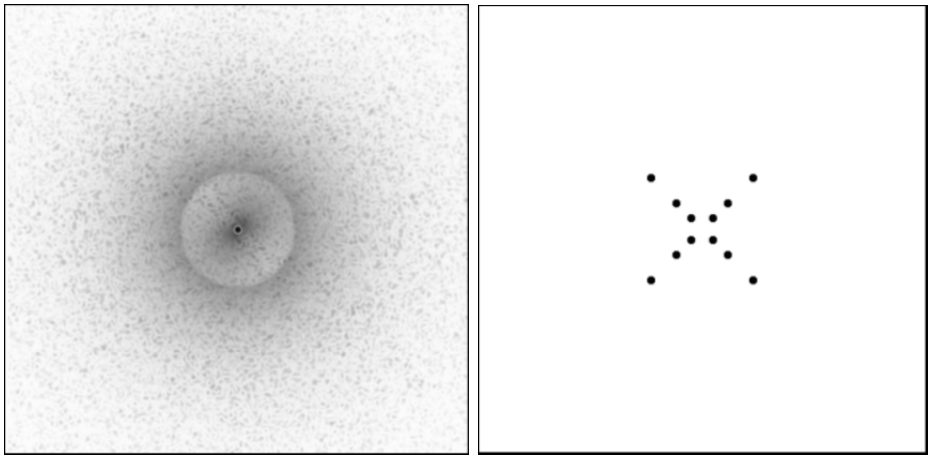

Figure 2.6 – Simulated data used to test ANDROMEDA, similar to the one expected from SPHERE. *Left*: One reduced image of the temporal cube. *Right*: Location of the twelve synthetic planets injected. Colors are inverted.

2.2.2 Theoretical study of the potential sources of errors

Four kinds of sources of error have been thoroughly analyzed thanks to the simulated data. These sources of errors are not dependent upon the user-defined parameters but only on the data properties. I quickly review these different sources A. Cornia has studied and give the main conclusions from his study. Only the effects on the estimated flux are considered in his study. For more details, please refer to his PhD manuscript: Cornia (2010).

Errors due to a bad centering of the images The first aspect is to assess the effect of a bad centering of the images. As expected, the more the frames are bad-centered, the greater the error. For instance, if the center deviated from the true one of half a pixel, the error on the flux estimation is of 2.7%. Note that this effect is constant whatever the distance to the star.

Errors due the smearing of the companion An other aspect studied is if some smearing appears for the companions, due to the non-instantaneous exposure time. As expected since the model does not take into account the smearing of the companion, the more smearing, the greater the error on the flux estimation. Obviously, this effect depends on the distance of the planetary companion to the star: the further, the more the planetary signal is smeared. This error also depends on the speed of the field rotation during the exposure: the closer to the meridian, the more smearing and thus the greater the error. For instance, for a typical exposure time of 20sec for a star at a declination of 45°, the error on the flux estimation is of less than 0.5% for a companion at 1.5″(averaged on the whole image cube).

Errors due to the level of photon noise in the images As expected, the fainter the signal the greater the error and the brighter the star, the greater the error. Since the star is centered in the frames, this error also depends on the distance of the companion to the star. In the case of a star flux of $2.25e^4$ $phot/s/m^2$ and a star-planet contrast of 10^5, the photon noise level implies an error of about 5% on the flux estimation of a companion at a separation of 1.25″from the star (assuming there is only photon noise in the images) for the given DIT (100 sec here).

Errors due to the level of speckle noise residuals For the error due to the speckle noise, since the speckle noise level varies as a function of the distance to the star (as it follows a MR distribution,

see Sect. 1.2.3), it depends on the planet separation. Also, as expected, the fainter the signal the greater the error. In the previous case (contrast of 10^5), the speckle noise level implies an error on the flux estimation from 8% at large separation ($1''$), to 40% at short separation ($0.2''$).

As a conclusion, the main source of error in the images is given by the speckle noise which remains in the differential images. In work I led during my PhD, this will be indeed of main importance.

2.2.3 Optimal set of user-parameters derived from simulated data application

On the original version of ANDROMEDA, seven user-parameters can be defined. I quickly review these user-parameters along with their dependence and their impact on the ANDROMEDA output. I then summarize the optimal set of user-parameters A. Cornia retrieved from his studies, which aimed at optimizing the flux estimation accuracy.

Size of the reference PSF window N_{PSF} To choose the size of the reference PSF window, one has to make a trade off between the computing time (which decreases with a smaller window) and the flux estimation accuracy (which increases for a larger window since the more information about the flux, the better the estimated contrast). The size of the PSF window is given in pixel whereas the total energy in the window depends on the wavelength of observation. In the case of the simulated data, in H-band, a good compromise is to use a 32×32 pixels window within which most of the reference PSF flux is enclosed.

Minimum separation constraint for the ADI δ_{min} As expected, the smaller, the better the speckle subtraction, and the most accurate the MLE. A δ_{min} of $0.5\lambda/D$ seems appropriate for each variation of the other user-defined parameters. This parameter is critical since it is the one responsible for how much of the star PSF is removed in the differential images, that is to say of how much decorrelated residuals remain from the speckle noise.

Thickness of the annuli in which the minimum separation constraint applies d_r This parameter has to be set as a trade off between the computing time (which decreases with a greater thickness) vs estimated flux accuracy (which increases for thinner annuli). However this is not a critical parameter and a thickness of one resolution element, $d_r = 1\lambda/D$, proved efficient enough while not too long to be computed.

Optimization method used for the ADI subtraction Either optimization methods to compute the scaling factor (by total ratio or least-square fit) provide similar results. However, it is better to use the least-square value of the scaling factor in case the sum of the residuals in the differential images is close to zero. The latter case mostly happens if an SDI process is performed before the ADI, as it was foreseen for ANDROMEDA in order to apply it on DBI data obtained with SPHERE-IRDIS.

Optimization to subtraction area ratio R_A The results are hardly affected by this parameter. However, on simulated data, choosing $R_A = 1$ seems to be the best option, which yields to both lower artifacts and higher true signals.

Type of variance for the likelihood computation On simulated data, the 3D-variance (or spatially inhomogeneous variance) provides better results in terms of flux estimation and less residuals are found in the final output map (as in Mugnier et al., 2009). However, in real images, the quasi-static speckles are expected to be the dominant noise and the use of this 3D-variance might be inadequate.

Precision of the subpixel shift to build the planet signature model In order to reach a higher SNR and a good flux estimation of the potential planetary companions, the model of the planet signature must correspond to the true angular distance. To do so, the reference PSF is shifted by a fraction of a pixel, given by PSF_{shift}. This angular distance is directly computed from the parallactic angles given in input to ANDROMEDA. The precision by which the reference PSF is shifted is a user-defined parameter. Experiences on simulated data showed that a shift of 1/50 is enough to have an error smaller than 0.001% on the estimated flux which is negligible compared to the other sources of error. Note that the companion is searched on a grid of one pixel pitch (see Eq. 2.5 of the MLE). This PSF_{shift} parameter is only used to build the model.

Positivity constraint As expected theoretically, adding the positivity constraint to compute the flux increases the detectability and the flux estimation accuracy.

Conclusion & summary To conclude, the most influential of these seven parameters are the δ_{min} constraint and the size of the reference PSF window N_{psf}. Tab. 2.2 summarizes the user-defined parameters, which optimize the flux estimation accuracy wrt the injected flux, set as default to run ANDROMEDA.

Parameter	Definition	Units	Value	Impact
N_{psf}	Size of the reference PSF window	pixels	32×32	high
PSF_{shift}	Subpixel shift precision for the planet signature model	pixels	1/50	low
ADI method	Optimization method used for ADI	#	LS	low
$\delta_{\min}$	Minimum separation to build the differential images	λ/D	0.5	high
dr	Width of annuli on which ADI is performed	λ/D	1	low
R_A	Ratio optimization to subtraction areas	-	2	low
σ_Δ	Type of residuals variance used	-	3D	low
Positivity	Positivity constraint on the log-likelihood	-	ON	high

Table 2.2 – Summary of the user-defined parameters set as default in ANDROMEDA and their respective significance, after studying their impact on simulated data. Results are from A. Cornia PhD thesis, Cornia (2010).

I also mention here that the typical area where point sources are looked for in the images are defined between the IWA which has to be given as an input and the OWA which depends on the chosen size of the reference PSF, N_{PSF} and on the thickness of the annuli d_r following: $OWA = N_{img}/2 - N_{PSF}/2 - (d_r \times 2 \times oversampling)$ in pixels, where N_{img} is the size of the images.

The choices made about both the practical and implementation solutions that are summarized above, are the results of thorough work achieved during the PhD of Dr. A. Cornia. The corresponding justifications, including a tolerance analysis to the choices made, can be found in his PhD thesis, submitted in 2010 - Chap 4. As a result, ANDROMEDA could detect on realistic SPHERE-like simulated data a companion of 10^5 *contrast to the star, at a separation of 0.5″. For these data, the use of a 3D-variance maps and of the positivity constraint were critical to obtain such a result.*

During my PhD, I reviewed each of these user-defined parameters in the framework of the application of ANDROMEDA on real data, as it is detailed in the Chap. 4. However some parameters should not change on real data, such as the precision of the subpixel shift to build the planet signature model. I thus assumed in the following that the precision of the subpixel shift to build the planet signature model is set to $PSF_{shift} = 1/50$ pixel.

Summary of the original version of ANDROMEDA

As mentioned above, my work starts with the version of ANDROMEDA described in this chapter. Fig. 2.7 is a schematic view of the different steps performed by the ANDROMEDA method as it was originally implemented, from the required input to the useful output it provides.

In the next section, I will apply the ANDROMEDA code as it is on real data from the NaCo instrument and list the unexpected obstacles which arose. This will give hints on the strategy chosen to make ANDROMEDA operational on real data in a systematic way.

I also mention here that the final chapter of A. Cornia's PhD thesis (Cornia, 2010, Chap. 5) present preliminary results of ANDROMEDA applied on real data. As this work was very preliminary, in the next section, I will start to work using the original version of the software as described above. Note that two conclusions arose from his preliminary real data application: (i) the 2D-variance map should be used when bad pixels remain in the reduced images, and (ii) a least-square ADI optimization seems more robust in case many point sources are present in the field of view.

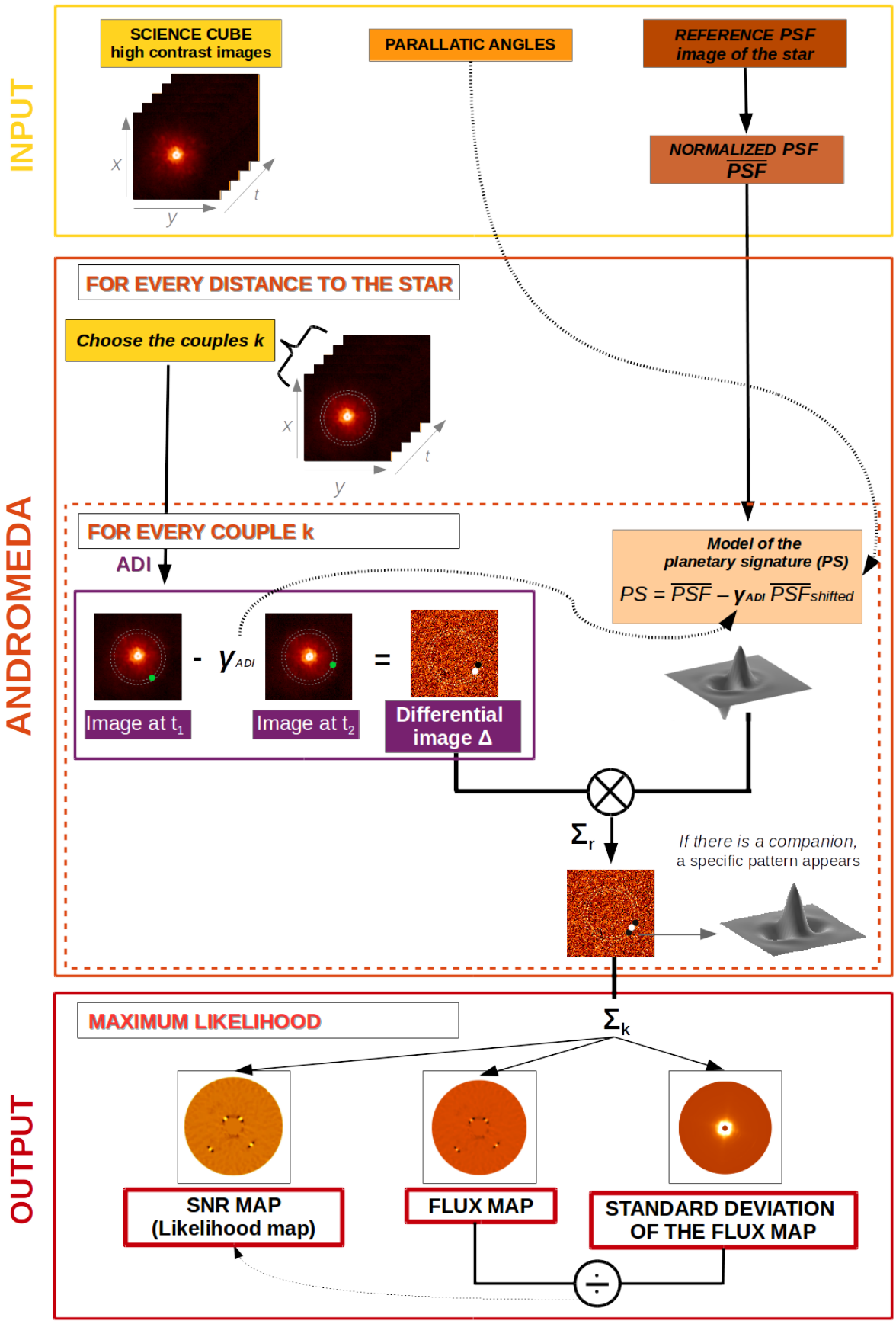

Figure 2.7 – Diagram describing the ANDROMEDA's principle from the input to its useful output.

2.3 Application of ANDROMEDA on real data as it is

From these theoretical basis, the goal is to make ANDROMEDA operational on real data. In this section I present the application of ANDROMEDA as it is described in the previous sections, on real data taken with the VLT/NaCo instrument. The main expected problem is that the model of noise chosen in the post-ADI data (white, Gaussian and non-stationary) might not be completely realistic which would prevent ANDROMEDA to bring up point source signals in the final output.

2.3.1 Description of the real data used to apply ANDROMEDA

The real data used to test ANDROMEDA are constituted of a bright star surrounded by numerous background stars that are natural point sources to be detected by the algorithm. Synthetic companions were added inside the images in order to better quantify the ability of ANDROMEDA to accurately detect and characterize the point sources in the images.

These data have been collected as part of the NaCo Large Program survey (NaCo-LP, PI: J.-L. Beuzit), whose goal was to analyze the occurrence of giant planets and brown dwarf companions at wide orbits (10-2000 AU) around 110 young, solar-type stars (Chauvin et al., 2015). This particular data cube was used as a test case in the framework of the NaCo-LP program, since it presents a nice crowded field and the saturated images were of good quality.

Target star properties The data collected are sequences of saturated exposures (there is no coronagraph in that setup) taken in pupil tracking mode. The chosen star is TYC-8979-1683-1 (also called CD-62-657), observed in 2011 on May the 5^{th} within the ESO program 184.C-0567(D). This star is a G7 star of 17 Myr ($V = 9.36$, $H = 7.47$) located at 75.6 pc from the Sun. The observation was made in H-band (filter centered around $1.66\mu m$) and stored in a 1024×1024 pixel frame (S13 camera inside the CONICA imager having a field of view of $13.6'' \times 13.6''$), the pixel scale being 13.22 mas/pixel.

Observation conditions The star was observed during a total integration time of 36 min (giving 11 cubes of 29 frames each with an exposure time of 6.8 sec) and for a total field rotation of 18.5°. Seeing conditions were good but variable (seeing of $0.57''$to $1.15''$; coherence time of 4-9 ms; Strehl ratio of the reference PSFs: 21% and 26%). The empirical PSF core FWHM is estimated to be of 4.75 ± 0.05 pixels. The target star was observed close to meridian crossing, the PSF core is saturated inside a radius of 10-15 pixels ($0.13''$-$0.20''$), and integration times are set short enough so that the angular smear of potential companions is small, especially in the outer part of the field.

Data reduction: science frames The data reduction of saturated exposures included sky subtraction (sky frame constructed from the median combination of exposures obtained at the five different jitter positions: on minute timescales, the image center is moved by ±3 arcsec in x or y on the detector field), flat fielding, bad pixels correction, and rejection of poor-quality exposures. The location of the star center on each frame is determined by fitting the unsaturated portion of the saturated PSF with a 2D Moffat function. Individual frames are then shifted and registered to a common image center in between four pixels. The first reduced image constituting the final data cube is shown in Fig. 2.8.

Data reduction: reference PSF A short series of exposures with the unsaturated star was taken before and after the main saturated sequence in order to build the reference PSF required as an input for ANDROMEDA. These unsaturated sequences were acquired with an exposure time of 1.7927 seconds, using a neutral density filter of $1.19 \pm 0.05\%$ transmission factor.

Data reduction: parallactic angles The parallactic angle associated with each frame of saturated images is computed from the observing time (converted from UTC to LST), assuming that individual exposures are recorded at constant time intervals within each data cube (time information is available only for the beginning and end of each data cube).

Summary of the data-set properties All the input needed by ANDROMEDA are included in this data set: reduced images, reference PSF, parallactic angles and wavelength of observation. For better readability, Tab. 2.3 below summarizes the main properties of the dataset to be processed using ANDROMEDA.

Property	Value
Instrument	VLT/NaCo - S13
ESO ID program	184.C-0567(D)
Observation date	2011/05/05
Atmospheric conditions	Average (seeing: 0.57 ″to 1.15 ″)
Pupil tracking	ON
High contrast	Saturated exposure
Wavelength of observation	H-band: $1.66\mu m$
Sensor pixel scale	13.22 mas/px
Resolution	$1\lambda/D = 4.75 \pm 0.05$ pixels
Star magnitude	7.47 (H)
Image size	$600 \times 600 pixels$
Number of images	296
Total field rotation	18.52°; $(-22.2470 \rightarrow -3.72198°)$
Offset angle wrt true North	90.4°
DIT image	6.8 sec
Total integration time	36 min
Neutral density transmission for the reference PSF	$1.19 \pm 0.05\%$
DIT reference PSF	1.7927 sec

Table 2.3 – Table summarizing the characteristics of the observation of the star TYC-8979-1683-1 with NaCo-S13, used to test ANDROMEDA.

Introduction of synthetic companions To better quantify and optimize the detection performance of ANDROMEDA using NaCo data, 20 additional synthetic substellar companions have been injected in the image cube. The signal of each synthetic companion was modeled using the unsaturated PSF image and inserted in the individual reduced frames, taking into account the field rotation that occurred between the exposures (as in Chauvin et al., 2012). In other words, the reference PSF is normalized then multiplied by the desired contrast and finally injected in each science frames, knowing the parallactic angles variation between them.

The twenty synthetic companions were introduced along five radial directions of respective position angles of 299.6°, 329.6°, 359.6°, 29.6° and 59.6° on the first image and at five angular separations of 0.26″, 0.53″, 1.06″, and 2.12″. The synthetic companions of the same position angle are of equal flux, each with peak intensities corresponding to magnitude differences of respectively 12.85, 12.10, 11.35, 10.60, and 9.85 for the five position angles in increasing order. The location of these 20 introduced synthetic companions is shown on Fig. 2.8.

2.3.2 Output provided by ANDROMEDA

In order to run ANDROMEDA, several user-defined parameters have to be carefully chosen. Tab. 2.4 summarizes the values chosen for this specific case, along with the previous section considerations (from ANDROMEDA application on simulated data and preliminary real NaCo data application).

The resulting four 2D-maps provided by the method are shown at Fig. 2.10. First, the likelihood map and the SNR map are the same but the detected signals are more visible in the SNR map as foreseen by its definition (in the following I will not show the likelihood map anymore since it contains the same information). Also the flux map is very similar to the SNR map provided, as expected since

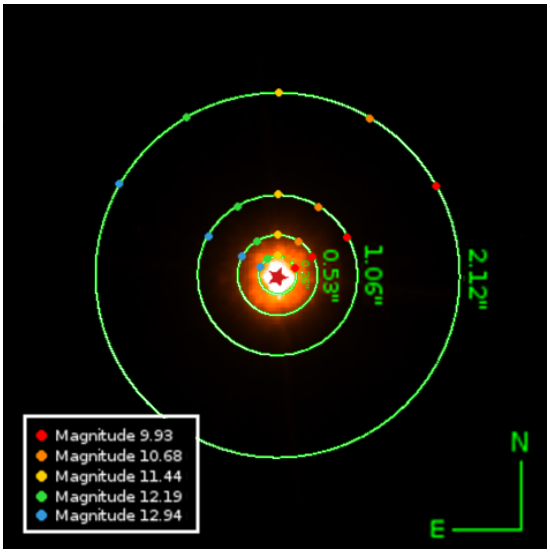

Figure 2.8 – One cosmetically reduced image of the data cube of the star TYC-8979-1683-1 obtained with NaCo (600×600 pixels, linear scale). The position of the injected synthetic planets is indicated with colored dots on the green circles.

User-defined parameter	**Used value**
Minimum distance for the ADI, δ_{min}	0.5 λ/D
Width of the annuli for the ADI, dr	1.0 λ/D
Optimization method for the ADI	No optimization
Size of the reference PSF window, N_{psf}	32×32 pixels
Precision of the reference PSF shift, PSF_{shift}	1/50 pixel
Variance of the residual noise, σ_Δ	3D-variance
Positivity constraint	ON

Table 2.4 – User-defined parameter values chosen to run ANDROMEDA on the TYC-8979-1683-1 VLT/NaCo data.

they are linked via Eq. 2.23. From now on only the SNR map will be used for the detection and position retrieval and the flux map for the photometry retrieval.

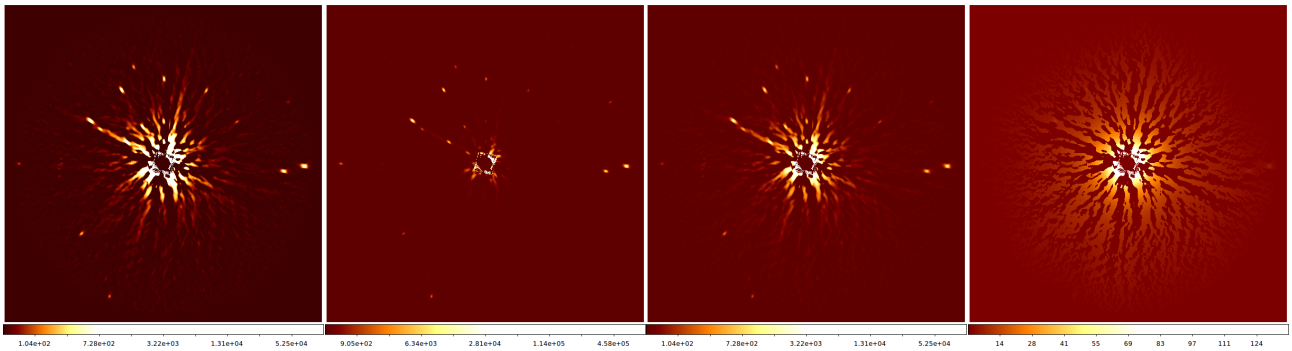

Figure 2.9 – Output provided by ANDROMEDA, using the parameters at Tab. 2.4. From left to right: SNR map, likelihood map, flux map and map of the standard deviation of the flux (the scales are logarithmic, except for the map of the standard deviation of the flux, which is linear; all the units are arbitrary except the SNR map which is in sigma unit).

Some patterns, having the expected oval shape along the radial direction (see Fig. 2.5) are indeed present in the SNR map and easily visible. These results are promising but close to the star (below $1''$), it is impossible to detect companions due to the high level of residuals.

2.3.3 Detected problems affecting ANDROMEDA's capabilities on real data

The Fig. 2.10 shows the SNR map obtained in the same conditions as the one gathered at Tab. 2.4 but with different ADI optimization and using either the 3D or 2D-variance map.

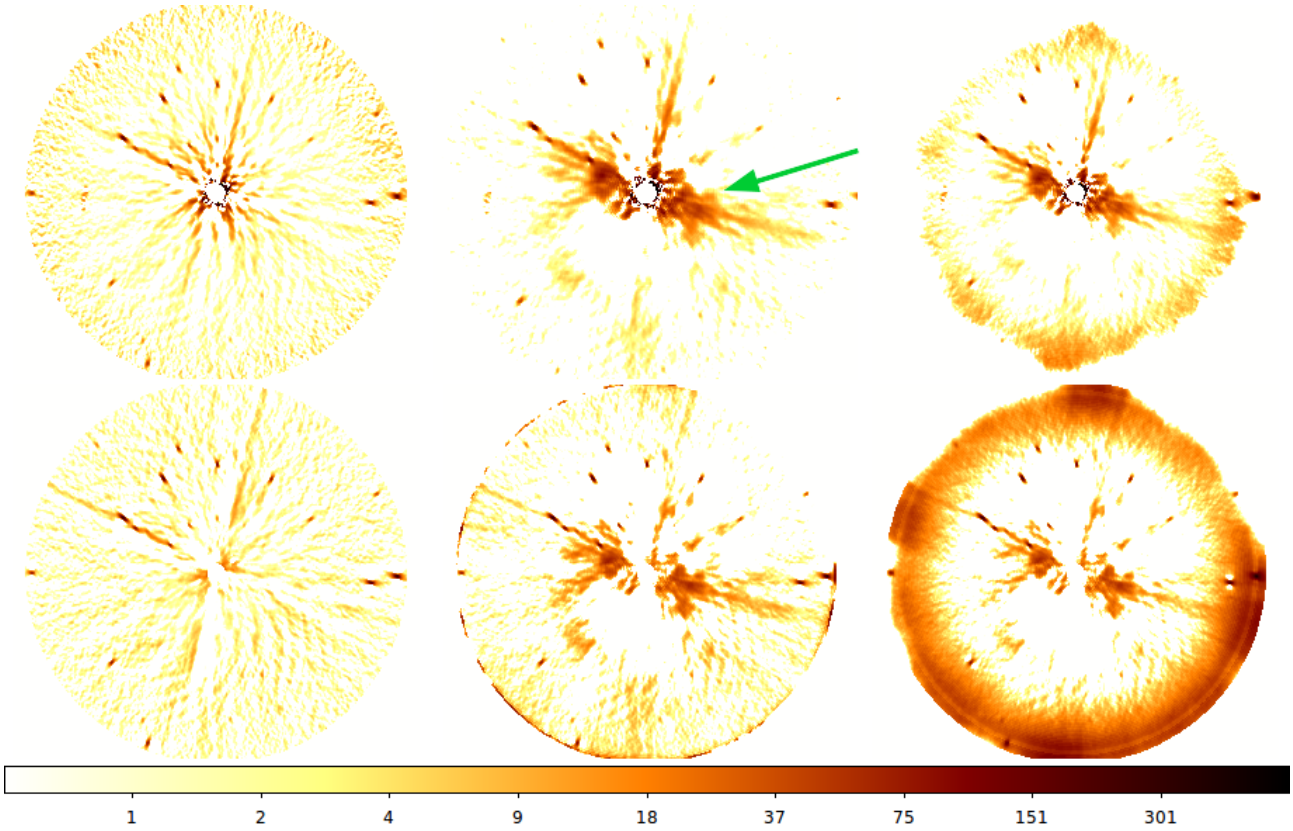

Figure 2.10 – SNR maps provided by ANDROMEDA using the parameters gathered in Tab. 2.4. From left to right: Without ADI optimization, with the total ration (TR) optimization, with the least-square (LS) optimization. Top: using the 3D-variance map. Bottom: using the 2D-variance map. The scale is logarithmic (in sigma units).

The visible detections in the 2D-variance maps have a twice higher SNR than the 3D-variance. Moreover, more residual structures are visible close to the star (at less than 0.5″) whereas this is a region of strong interest. With these data, assuming that the noise in the images is mainly made of photon and detector noise is an inadequate hypothesis.

Using the optimization of the ADI leads to less residuals in the region between 0.5″to 1″but higher residuals closer to the star. The diffuse structure close to the star, indicated by a green arrow on Fig. 2.10, is along the wind direction (as visible on the raw images) and has the typical shape that the wind induces in the images[8]. This means that the ADI optimization is efficient since this wind effect is preserved in the resulting map and is not being averaged as for the non-optimized subtraction. The optimization procedure (either using a total ratio or a least-square fit to compute the scaling factor γ) is essential to scrutinize regions closer to the star.

The main difference between the total ratio and least-square optimization is at large separation where the least-square induces intense smooth structures in the SNR map (from about 3″). Indeed, in this region, the noise is made of photon and detector noise so the pixel value reach close-to-zero values. Thus the scaling factor computed by total-ratio diverges at large separation (as shown on Fig. 2.11-Left). For the same reason, the scaling factor computed by least-square slowly decreases because the denominator of Eq. 2.12 increases when the detector noise dominates (see Fig. 2.11-Right). A scaling factor smaller than one in this region will induce a flux offset in the differential image, which remains

[8]This typical shape is for instance visible on raw SPHERE data as shown in Chap. 6 and on SPHERE-like simulated data, as shown in Chap. 9.1 which reproduces this wind effect on simulation

in the resulting SNR map.

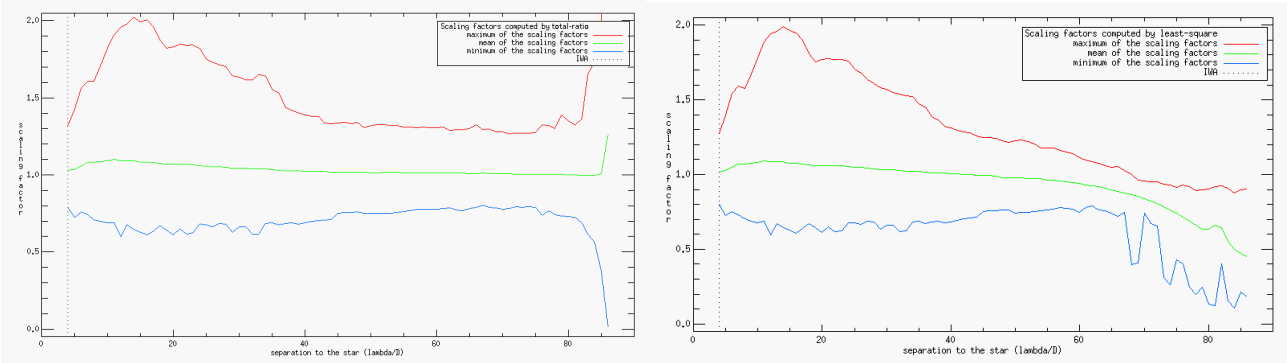

Figure 2.11 – Mean value of the scaling factor as a function of the distance to the star. Left: Using the total ratio computation of the scaling factor. Right: Using the least-square computation of the gamma.

In any case, the performance is extremely limited by the starlight residuals preventing from detecting companions at close separation. This is even more visible when thresholding the SNR map by a constant 5σ threshold: The three maps shown at Fig. 2.12 are the thresholded SNR maps obtained using the 2D-variance map and the three different ADI optimization.

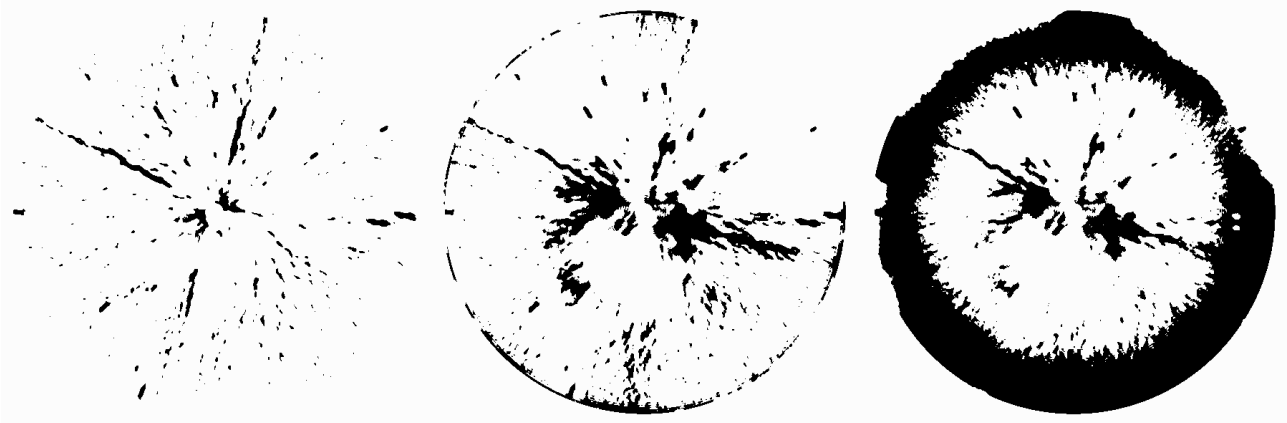

Figure 2.12 – SNR maps thresholded at 5σ, provided by ANDROMEDA using the parameters gathered in Tab. 2.4, using a empirical 2D-variance map. From left to right: without ADI optimization, with a total ratio optimization of the ADI and with a least-square optimization. Colors are inverted: white corresponds to zero and black to one.

On Fig. 2.12, the residuals are higher below $1''$, where the quasi-static speckles are dominant, and from about $3''$, where the photon and detector noise are dominant. However, in between these two regions a low amount of artifact remains above the 5σ threshold but it is still not enough to perform a proper detection.

2.3.4 Conclusion on ANDROMEDA's original capabilities

In spite of a rigorous and careful implementation, the advantages ANDROMEDA should have brought by its principle are not carried out when applying the method on real data. The major problem being that the model of residual noise (which is equivalent to the error made on the model) does not take into account the presence of artifacts in the real data, which is a common issue in inverse problem solving. As a consequence we lose the main features of ANDROMEDA:

- It it impossible to perform an automatic detection: in the SNR map, too many spurious peaks appear above threshold whereas most of them are false alarms;

- It is impossible to detect companions close to the star (less than 1″);
- It is impossible to detect faint companions (less than 11 mag of contrast);

In particular, the inhomogeneities preventing from thresholding the SNR map are under the shape of low spatial frequencies in the images and are function of the separation to the star.

The next chapter describes the steps added to the original software described in this chapter to bypass these obstacles and make ANDROMEDA operational on real data according to the specific properties of the method itemized at Sect. 2.1.3.7.

I mention here that preliminary applications on real data have also been conducted by A. Eggenberger, whose work was published in a poster at the *In the Spirit of Lyot, 2010* conference (Eggenberger et al., 2010). In her work, limits had been identified and first tracks evoked at the beginning of my PhD. However, a careful implementation as well as an in-depth study remained to be done.

Chapter 3

ANDROMEDA: making it operational to process real data

Contents

3.1 Stages required to make ANDROMEDA operational 80
3.1.1 Removing the low spatial frequencies in the reduced images 80
3.1.2 Correcting for the radial dependency of the SNR statistics 87
3.1.3 Conclusion on ANDROMEDA in its operational state 97
3.2 Exploring variations on building the differential images 97
3.2.1 Description of the data to illustrate this part 98
3.2.2 Interpretation of the scaling factor γ after pre-filtering the images 98
3.2.3 Refining the ADI process included in ANDROMEDA 102
3.2.4 Test of the robust affine fit in real differential images 104
3.2.5 Adapting the model of the planetary signature in the differential images 109
3.3 Automatic companion extraction, properties and reliability criteria . . . 112
3.3.1 Detection and astrometry 112
3.3.2 Photometry 114
3.3.3 Sorting out artifacts from probable true detections 115
3.3.4 Estimation of the detection limit 116
3.3.5 Ergonomics of the detection module 116

In this chapter I describe the adaptations made to the ANDROMEDA method in order to make it an operational pipeline able to process on-sky data.

In the following, I first describe the pre-processing and post-processing stages implemented in ANDROMEDA which enable the method to offer the promised features described in the previous chapter (Sect. 3.1). I then revisit each step of the algorithm in order to make sure that they are fully adapted to the real data characteristics (Sect. 3.2). Once ANDROMEDA provides exploitable outputs, I developed a procedure to make use of these outputs, in line with the core of the algorithm (Sect. 3.3). This detection module performs an extraction of the point sources present in the field of view and provides additional reliability criteria. These three steps made the ANDROMEDA method a fully operational pipeline which, from the reduced data cube, provides valuable astrophysical information.

The improvements I brought to the ANDROMEDA method are summarized in the publication Cantalloube et al. (2015) which can be found in the appendix, App. A. In this chapter I present these improvements in details by describing the tests performed and the interpretation of the results.

3.1 Stages required to make ANDROMEDA operational

As shown at the previous chapter, applying ANDROMEDA as it was at the beginning of my PhD on real data does not provide the outputs expected from its theoretical development. The first step was to understand the origins of these differences in order to find adapted solutions to bypass these obstacles. Here, the two main goals are (1) to enable the detection of companions at close separation to the star and (2) to enable the use of a constant threshold throughout the whole SNR map to perform an automatic detection. Once these goals are reached and ANDROMEDA is operational, I will go through fine tuning of the whole algorithm in the next section.

To illustrate this section, I will use the TYC-8979-1683-1 data from VLT/NaCo (described in Sect. 2.3.1).

3.1.1 Removing the low spatial frequencies in the reduced images

The SNR map provided by ANDROMEDA shows large scale inhomogeneities which prevent to detect companions, mostly at close separation.

These inhomogeneities originate from slowly varying low frequencies in the images that are not subtracted during the ADI process since they have significantly evolved between the two frames constituting the couple k to be subtracted. This effect is particularly problematic close to the star since, in order to respect the condition imposed by δ_{min}, the time delay between the two images to be subtracted is higher. Consequently the difference between the two frames will show higher inhomogeneities, making the detection particularly difficult at close separation, as observed in the SNR map.

These low frequencies may arise from post-adaptive optics residual turbulence: temporal variation of the strength of the wind and/or of its direction. The typical structures revealed in the SNR map on NaCo data (see Fig. 2.10-Right) indeed correspond to structures due to the wind direction and speed, as shown in both simulation of high contrast images (see Chap. 9.1) and in the SPHERE images (see Chap. 6).

Because these low frequencies are not included in the model and not removed through ADI, they must be eliminated beforehand. A pre-processing step has thus been added to the ANDROMEDA method in order to get rid of these disturbing structures.

3.1.1.1 Implementation of a high-pass Fourier filtering

The goal is to remove as much as possible these low spatial frequency artifacts while preserving as much as possible the scientific signal. As a point source has a large spectrum, a simple spatial filtering is efficient to isolate these two contributions.

The proposed solution is to perform a Fourier high-pass filtering of the reduced images: a window of zero value at low frequency and of unit value at high frequency is thus multiplied to the Fourier transform of each reduced image. The window chosen to perform this filtering is built from a Hann profile, for three major reasons:

- It is linear;
- Its slope is quite steep so there are not much residuals of lower frequency than the chosen cutoff;
- It is continuous so as to avoid the Gibbs phenomenon (or ringing artifacts, due to discontinuous edges provoking oscillations in the image when going from real to Fourier space, back to real space)[1].

The profile of this Hann window follows the equation:

$$Filter_{highpass}(f) = 0.5 - 0.5\ \cos(\pi \frac{f}{f_{cutoff}}) \tag{3.1}$$

[1]Note that another kind of window, such as Planck-taper window with a rather low tapering parameter, could have been chosen, as long as it respects the three conditions above. However the exact shape of the window is not critical and the usual Hann window used here as a classical solution to these three conditions.

Where $f_{cutoff} = F.f_{Nyquist}$ is the chosen cutoff frequency (see Fig. 3.3). F is the *filtering fraction*, that is to say the amount of low spatial frequencies removed wrt to the total spatial frequencies constituting the images, defined by $f_{Nyquist}$, the frequency at Nyquist.

Due to the optical cutoff, the astronomical signal stops at the maximum frequency D/λ (with D the diameter of the entrance pupil and λ the wavelength of observation), which is defined by the oversampling factor ovs along $D/\lambda \doteq f_{Nyquist} \times 1/ovs$. In order not to remove all the astronomical signal, the filtering fraction must be such that $F < 1/ovs$.

A filtering fraction of 1 will not fully removed all the frequencies in the images due to the Hann window shape (see Fig. 3.4, above dash-dotted blue line): remaining frequencies are left since the slope is not perfectly vertical (see its profile at Fig. 3.3).

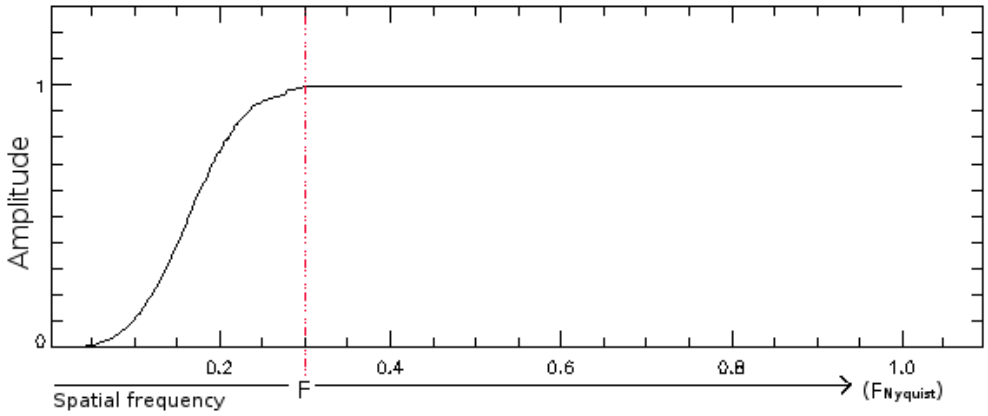

Figure 3.1 – 1-D profile of the Hann window used for the Fourier high-pass filtering. The filtering fraction has been set to $F = 1/3$ in this example.

3.1.1.2 High-pass filtered images

The Fig. 3.2a shows one reduced image of the NaCo TYC-8979-1683-1 science cube, with or without a spatial high-pass filtering. As expected, the filtering, even with a low filtering fraction, removes the smooth stellar halo surrounding the star and reveals the obvious bright point sources in the image. Obviously, removing more low spatial frequencies makes the filtered image smoother, revealing more and more high frequency signals. Fig. 3.2b shows the corresponding Power Spectral density whose central part is removed / reduced by the 2D-Hann window.

For more readability, the Fig. 3.3 shows the mean radial profile of the PSD as a function of the distance to the star, according to different filtering fraction. The zero frequency (the mean in the images) is removed while other low frequencies are significantly reduced.

3.1.1.3 Energy loss of the companion signal induced by the pre-filtering

The filtering fraction F has to be chosen carefully in order to remove efficiently the low frequencies while preserving the signal in the images. For a point source, such as a planetary companion, the energy loss due to the filtering can be quantified by filtering an Airy pattern:

$$E_{loss} = 1 - \frac{\int (airy_{filtered})^2}{\int (airy_{non-filtered})^2} \tag{3.2}$$

The Fig. 3.4 shows the energy loss as a function of the filtering fraction, for an Airy pattern sampled at a typical oversampling factor of 1.6 (corresponding to the oversampling of NaCo in H-band, used for the TYC-8979-1683-1 data), defined on a 64×64 pixels window. A filtering of one fourth of the low spatial frequencies thus leads to a loss of 36%.

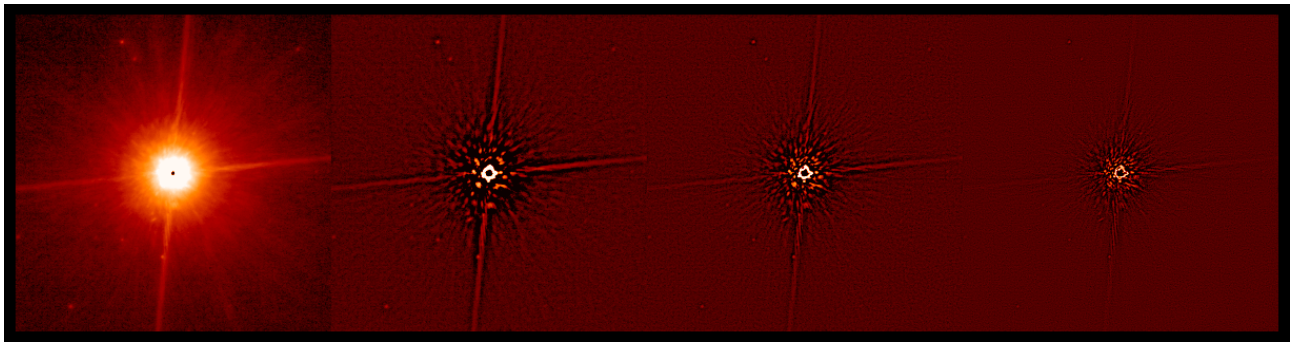

(a) : First reduced image of the star TYC-8979-1683-1 by Naco. From left to right: Without filtering, with filtering $F = 1/8$, with filtering $F = 1/4$ and with filtering $F = 1/2$.

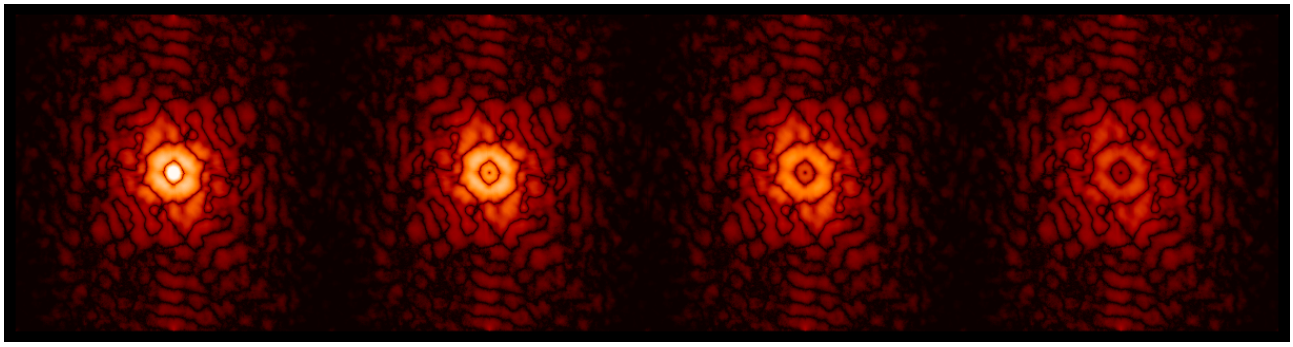

(b) : Power spectral density (PSD) of the first reduced image of the star TYC-8979-1683-1 by Naco. From left to right: Without filtering, with filtering $F = 1/8$, $F = 1/4$ and $F = 1/2$. The color scale is logarithmic.

Figure 3.2 – Images and corresponding power spectral density (PSD) of the first reduced image of the star TYC-8979-1683-1 data cube, with different filtering fraction values.

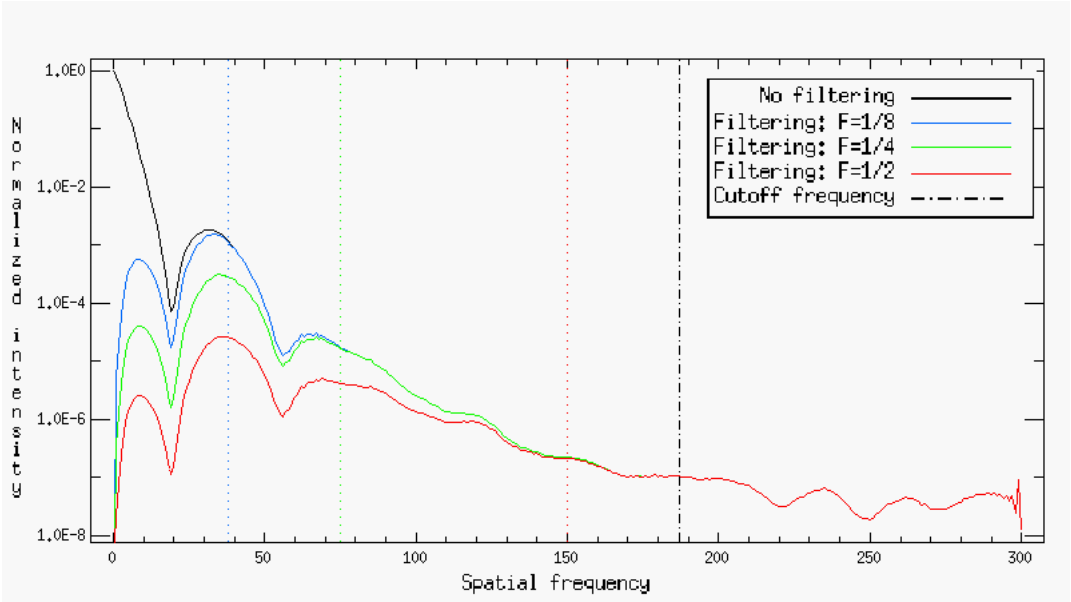

Figure 3.3 – Radial profiles of the power spectral density (PSD) of the first reduced image of the cube, with or without high-pass filtering. On the x-axis, the sampling Nyquist frequency is at 300 (half the size of the image used to produce this graph). Using an oversampling factor of 1.6, the signal cutoff frequency ($f_{Nyquist}/ovs$) is indicated by the black dashed line. Above this frequency, the PSD reveals the level of white noise. Various filtering at frequencies $F \times f_{Nyquist}$ are indicated by the colored dotted lines.

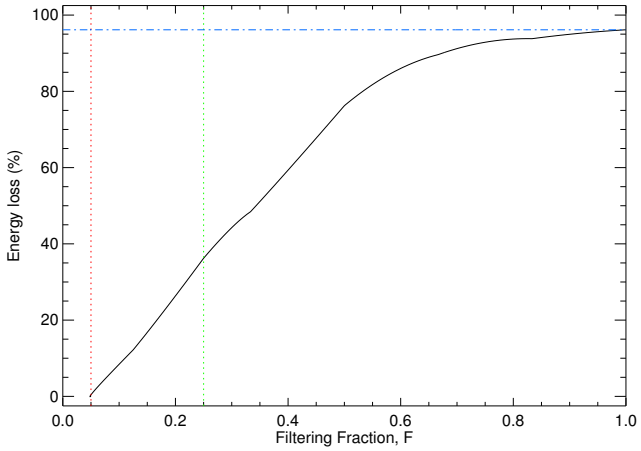

Figure 3.4 – Energy loss of a planetary signal as a function of the filtering fraction, when filtering an Airy pattern sampled at a typical oversampling factor of 1.6 and defined on a 64×64 pixels grid. The red dotted line shows the lowest filtering fraction possible in this specific case ($F_{min} = 1/20$). The green dotted line shows a typical filtering fraction $F = 1/4$, leading to an energy loss of about 36% in this case. Above the blue dotted-dashed line, the remaining frequencies that cannot be removed due to the Hann filter profile (about 4% of the energy remains).

3.1.1.4 Consequences on ANDROMEDA's principle

A consequence of this filtering is that the differential images are no longer described by Eq. 2.13 but by:

$$\mathscr{F}(\Delta(\mathbf{r},\mathbf{k});\mathbf{F}) = \mathscr{F}(\mathbf{i_k}(\mathbf{r},\mathbf{t_1});\mathbf{F}) - \gamma_\mathbf{k}\,\mathscr{F}(\mathbf{i_k}(\mathbf{r},\mathbf{t_2});\mathbf{F}) \tag{3.3}$$

where $\mathscr{F}(x;F)$ is the filtering function at a filtering fraction F.

Thus its model, defined at Eq. 2.3, must be modified in line with this filtering process:

$$\mathscr{F}(\Delta(\mathbf{r});F) = a.\mathscr{F}(m(\mathbf{r},k;\mathbf{r_0});\mathbf{F}) + \mathscr{F}(\mathbf{n_\Delta}(\mathbf{r});\mathbf{F}) \tag{3.4}$$

Under the hypothesis H_0 (no companion is present in the field), there are only residuals in the differential images constituted of low frequency artifacts and noise. The low frequency artifacts are different from the noise and they introduce:

-A non-null mean,

-Non-Gaussian residuals,

-A pixel-to-pixel dependence.

Thus, removing the low frequency artifacts helps improving these three aspects. The high-pass filtering proposed in this section decreases the pixel to pixel correlation within the images, making the pixels more independent and randomly distributed with a mean of 0 (as the null spatial frequency is removed). As a consequence, *the filtering helps our model of noise to be more consistent with the real residuals distribution* and thus leads to a more correct inversion.

In other words, without the pre-filtering, in each differential annulus, there is a flux offset due to the low frequency artifacts. Thus, within each of these annuli, the pixel distribution is approximately Gaussian but not centered around the same value. When computing the MLE via Eq. 2.5, the sum of the images will not be centered on zero and the Gaussian distribution greatly affected by this effect. *For ANDROMEDA to work, it is needed to make the residuals in the differential images independent and centered on zero.*. The Fig. 3.5 shows the histogram of the residual noise in the differential image from the simulated data, at different distances from the star, either with or without high-pass filtering of the image (using $F = 1/4$). Once filtered, the values are indeed centered around zero.

Under the hypothesis H_1 (a companion is present in the field), the model of the planetary signal $m(\mathbf{r},k;\mathbf{r_0})$ must be filtered the same way the images are. Through Eq. 3.4, it means that the reference PSF used to build the model must be filtered the same way. Thus, the model remains consistent

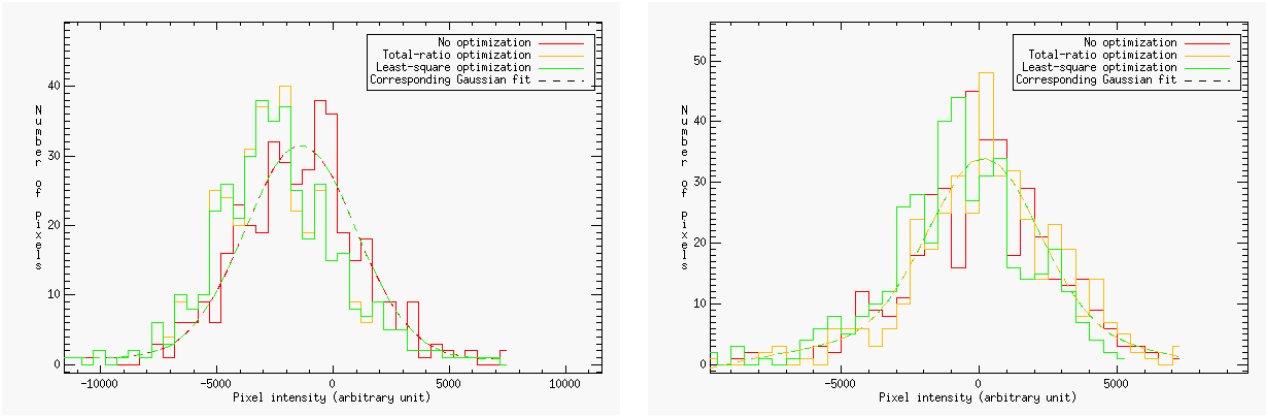

(a) : Without Filtering.

(b) : With Filtering ($F = 1/4$).

Figure 3.5 – Histograms of the residuals in one of the differential images $i_k(t_1, \mathbf{r_{sub}}) - \gamma i_k(t_2, \mathbf{r_{sub}})$, at $7\lambda/D$ from the star, on simulated SPHERE-like data (Sect. 2.2.1). The data are those within an annulus of $1\lambda/D$ width whose inner radius is at $7\lambda/D$ from the star ($\simeq$ 287mas), as for Fig. 3.19. The binning factor to plot the histograms is set to 1000.

with the data as long as the reference PSF is filtered as the reduced images are. Consequently, *the estimated flux is not biased by the pre-filtering procedure* and in practice, there is no need for any a posteriori correction.

3.1.1.5 Consequences on the computation of the scaling factor γ

In practice, when applying a high-pass filter on the images, the mean of the images of the cube is set to zero since the null frequency is removed. As a consequence, it is not possible to use the total ratio optimization proposed in a first version of ANDROMEDA. Indeed, through Eq. 2.11, the denominator may have zero values making the calculation of the γ_{TR} diverge. Thus one must use the least-square optimization to compute the γ scaling factor.

3.1.1.6 Consequences on ANDROMEDA's output

This pre-filtering of the images has several consequences, in particular, on the shape of the planetary pattern, on the optimization method used to perform the ADI and, obviously, on the SNR map output by ANDROMEDA.

Shape of the planetary pattern in the SNR map As the reference PSF must be filtered the same way, it affects the model of the planet signature and consequently the planetary pattern in the SNR map. To have an idea of this effect, consider a perfect noiseless Airy pattern as the reference PSF. High-pass filtering an Airy pattern induces to dig negative wings around the central core. These negative wings become a positive crescent in the planetary signature (since it is the difference of two Airy patterns, one being shifted of a few pixels). If, for the sake of this example, we assume that the model perfectly matches the data and that the data is noiseless, Eq. 2.23 is equivalent to performing the autocorrelation of this planetary signature. The autocorrelation of the planetary signature preserves this peculiar crescent feature which appears on both sides of the planetary pattern. The Fig. 3.6 shows the reference PSF, the planetary signature (using $\delta_{min} = 1\lambda/D$) and the corresponding pattern, either filtered or non-filtered, following this example.

In the SNR map this effect must be taken into account for the detection: if a signal has a very high SNR, these so-called *tertiary lobe* artifacts could have a SNR above the threshold set, and thus be regarded as detections. The Sect. 3.3, describing the procedure to exploit the ANDROMEDA output, deals with this problem and details the implemented solutions to avoid detecting these artifacts.

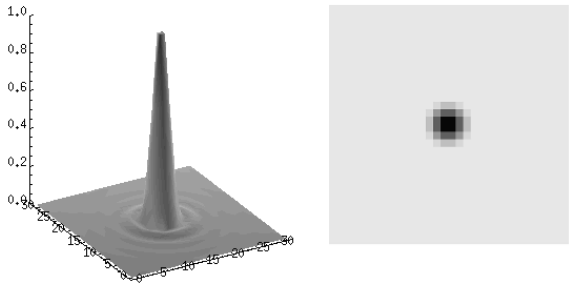

(a) : Reference PSF (here a noiseless Airy pattern defined on a 64×64 pixels frame, with an oversampling of 1.66) - Without filtering.

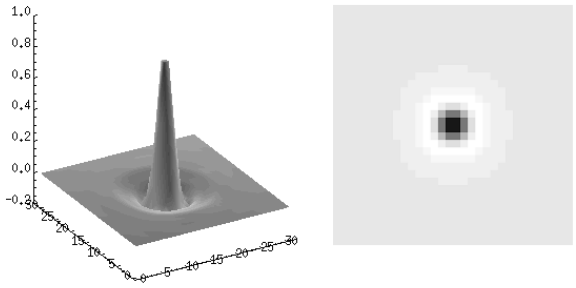

(b) : Reference PSF (here a noiseless Airy pattern defined on a 64×64 pixels frame, with an oversampling of 1.66) - With filtering ($F = 1/4$).

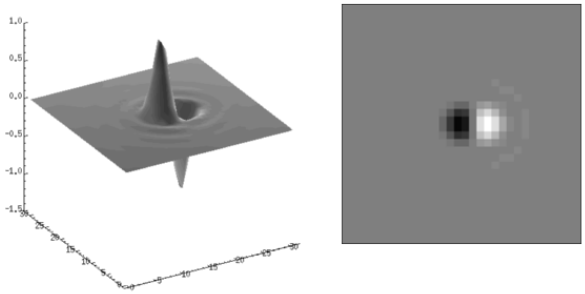

(c) : Resulting planet signature after the ADI (using $\delta_{min} = 1\lambda/D$) - Without filtering.

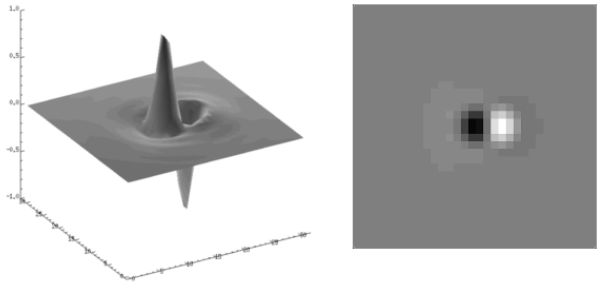

(d) : Resulting planet signature after the ADI (using $\delta_{min} = 1\lambda/D$) - With filtering ($F = 1/4$).

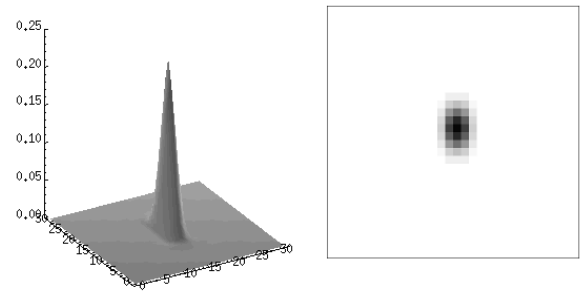

(e) : Resulting pattern after the MLE (using the positivity constraint) - Without filtering.

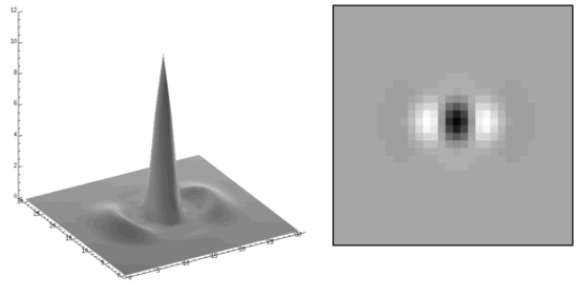

(f) : Resulting pattern after the MLE (using the positivity constraint) - With filtering ($F = 1/4$).

Figure 3.6 – Simulated input reference PSF (Airy pattern), post-ADI planetary signature ($\delta_{min} = 1\lambda/D$), and final pattern obtained in the ANDROMEDA output map (with positivity), obtained with or without filtering. Fig. 3.6f shows the apparition of two spurious bulges surrounding the main peak in the PSF shift direction (x-axis here), due to the filtering process.

Consequences on the SNR map The Fig. 3.7 shows the SNR map obtained with ANDROMEDA according to different filtering fraction and different ADI optimization methods, obtained by processing the TYC-8979-1683-1 NaCo data. As expected, the pre-filtering increases the visibility of the companions, in particular at close separation, that were hidden in the surrounding noise, as on Fig. 2.10. The more these images are filtered, the sharper the planetary signals are.

Another information enhanced by the pre-filtering is the presence of the diffraction pattern due to the spiders of the telescope which are not properly removed by the ADI, mainly visible in Fig. 3.7. This is probably due to either a bad stabilization of the pupil field, inducing a bad estimation of the parallactic angles, or to the varying luminosity of this diffraction pattern from one exposure to the other, inducing light remaining after the ADI, even though the ADI is optimized per annuli, to have the best starlight flux subtraction on average. This observational artifact must be kept in mind to

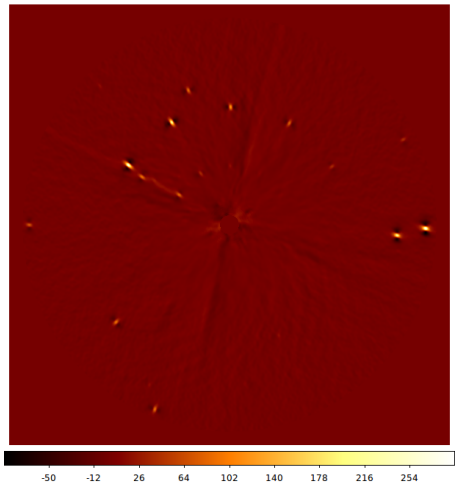

(a) : SNR map obtained by using no ADI optimization - Without filtering.

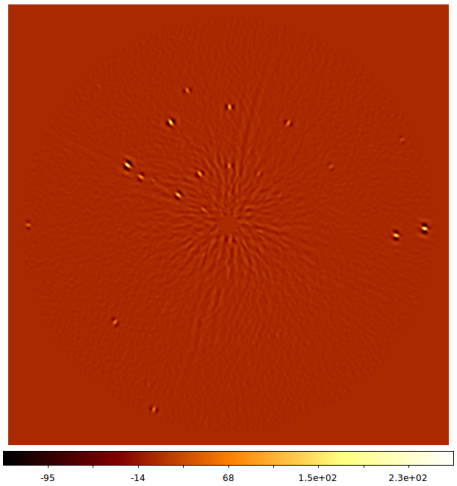

(b) : SNR map obtained by using no ADI optimization - With filtering.

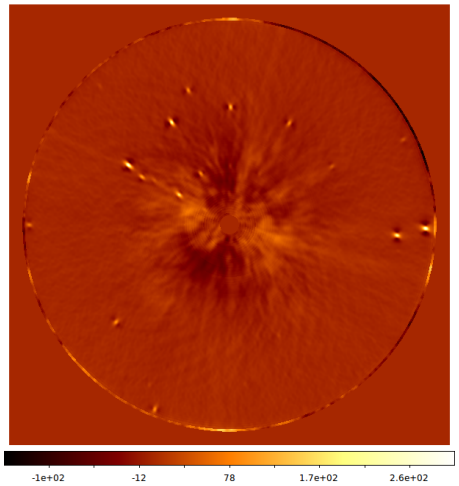

(c) : SNR map obtained by using a total-ration ADI optimization - Without filtering.

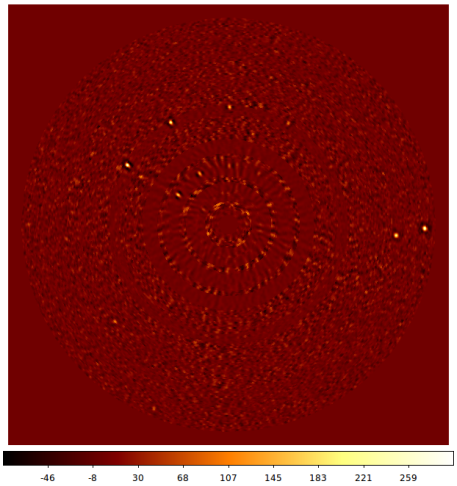

(d) : SNR map obtained by using a total-ration ADI optimization - With filtering.

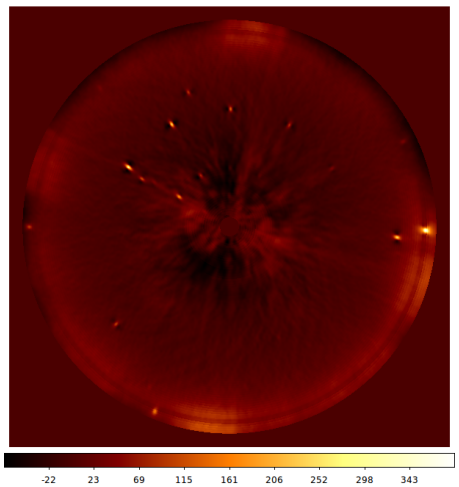

(e) : SNR map obtained by using a least-square ADI optimization - Without filtering.

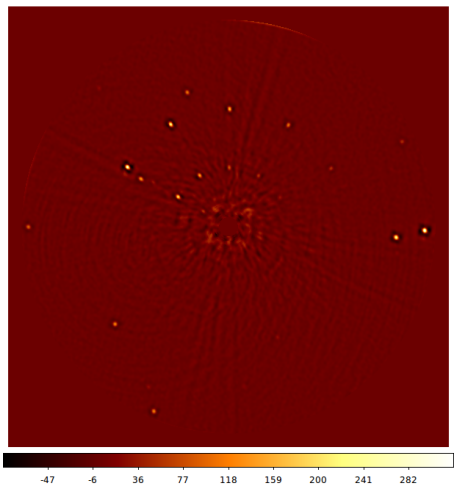

(f) : SNR map obtained by using a least-square ADI optimization - With filtering.

Figure 3.7 – SNR map output by ANDROMEDA from the TYC-8979-1683-1 NaCo data with or without the pre-filtering (using $F = 1/4$) of the images and for different pre-ADI optimization.

better exploit the SNR map for the detection, as it is detailed in Sect. 3.3.

Conclusion on ANDROMEDA's pre-processing

This pre-processing step added to the original version of ANDROMEDA leads to a better SNR map since it makes the data more consistent with the model used in ANDROMEDA. This solution is reliable and efficient on different data set. Thanks to the formalism used in ANDROMEDA, this solution does not affect the flux estimation which remains unbiased.

The filtering fraction F is a user-defined parameter to be tuned at the user's convenience. Experience showed that a typical value of filtering fraction $F = 1/4$ is usually enough to get rid of the low frequencies artifacts and obtain an exploitable SNR map in terms of detection and astrometry retrieval capabilities. This value is the same to process SPHERE images since the filtering fraction to be set mostly depends on the temporal variation of the wind strength and/or direction which significantly affects the SPHERE images.

However, when thresholding the obtained SNR map, there are still many false alarms remaining above threshold. This effect is due to the discrepancy between the model of noise used in the algorithm and the real noise distribution in the differential images. Next section describes this discrepancy and the solution implemented in ANDROMEDA to take it into account.

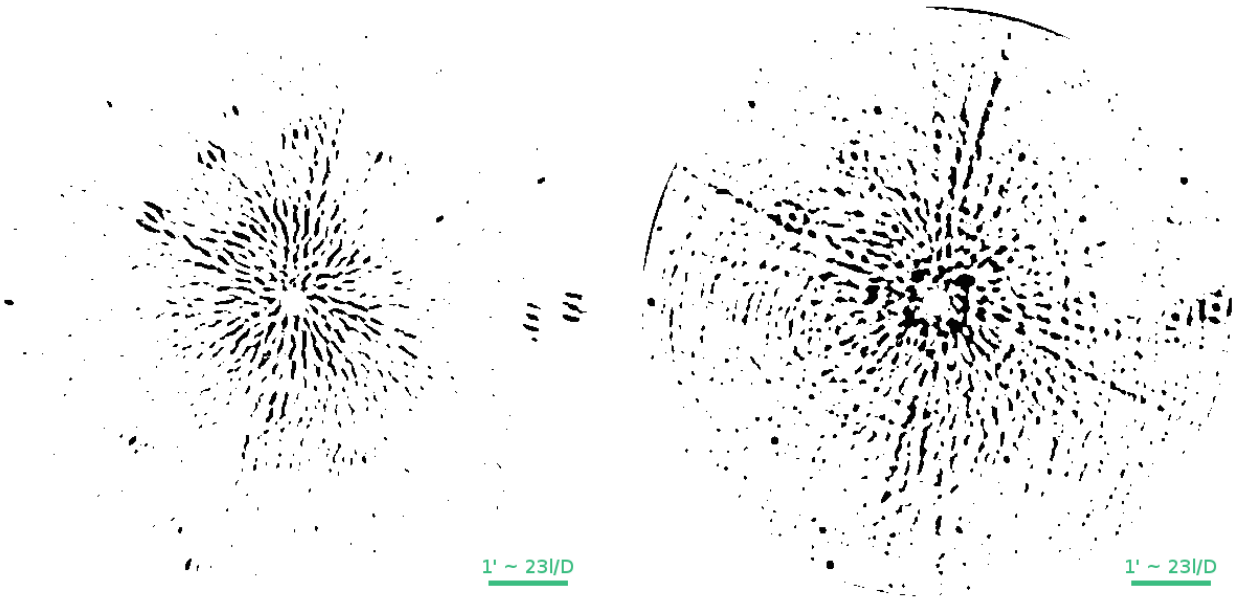

Figure 3.8 – Thresholded SNR maps to 5σ obtained with ANDROMEDA including the pre-filtering procedure. Left: Without ADI optimization. Right: With ADI optimization (least-square). Colors are inverted (black means 1 and white means 0).

Moreover, we can note that this pre-filtering method might be interesting to be implemented in other image processing pipelines. Indeed, as explained in this section, high-pass filtering makes the residuals centered and more independent. Providing that most image processing techniques described at Sect. 1.3.2 are combining the images, the residuals should be less correlated and more Gaussian in the final processed image when removing these low frequencies. However if one is looking for faint extended sources, one must be really careful of the filtering fraction applied to not remove the signal of interest.

3.1.2 Correcting for the radial dependency of the SNR statistics

On the obtained SNR map, too many false alarms appear above threshold. This false alarm amount shows a radial trend, being higher close to the star. This effect was expected since the model of noise

used in ANDROMEDA is, in spite of the pre-filtering and the ADI, not fully verified, that is to say not fully white and Gaussian. If this noise model was consistent with the real one, a uniform threshold could be applied all over the field and yield directly the False Alarm Probability.

In this section, I will first discuss qualitatively the origins of this discrepancy and check that this discrepancy indeed takes place in the real data. I will then detail the solution used for ANDROMEDA to take into account this model discrepancy. A last part is a discussion about how this discrepancy affects the detection limits derived by ANDROMEDA.

3.1.2.1 Inconsistency between the model of noise and the real noise distribution in the differential images

The model of noise adopted in ANDROMEDA does not completely correspond to the real noise distribution in the differential images. This was expected since the model of noise being white and Gaussian is simplistic whereas, the real noise distribution is partially correlated and non-Gaussian.

Qualitative explanations on the origins of the noise model discrepancy This discrepancy arises from two effects. First, on a temporal aspect, the quasi-static speckles vary too fast to be completely removed thanks to the ADI (along with the chosen ADI strategy, which is here to use the closest frames in time as long as they are separated of at least δ_{min}) thus leaving correlated features in the differential images. This effect is stronger at close separation since the time delay between the two subtracted images is longer due to the δ_{min} constraint. Second, on a spatial aspect, the quasi-static speckles in the reduced images follow a MR distribution (see Eq. 1.10) which shows a higher intensity close to the star. Thus the residual speckles in the differential images have their intensity varying with the distance to the star (but their intensity distribution is constant within annuli surrounding the star).

These two effects combined affect the residual noise distribution in the differential images: close to the star the noise is dominated by bright correlated speckle residuals. As a consequence, the model deviation is higher at short separation. This trend is clearly visible on the thresholded SNR map shown at Fig. 3.8, where more false alarms are present close to the star. This trend prevents from thresholding the SNR map by a single value throughout the field of view since it corrupts the connection between the PFA and the threshold: compared to the ideal threshold, the threshold to be set on real data should be higher (having greater values at short separation) in order to reproduce the theoretical PFA given by a 5σ threshold.

From a certain separation to the star, the ADI efficiently removes the speckles in the differential images and the noise model is more consistent with the residual noise distribution[2]. As a consequence the SNR values from this distance is more linked to the true corresponding confidence level of the detections. On the SNR map obtained at Fig. 3.8, this happens from a distance of about $\sim 60\lambda/D$. This distance depends on the quality of the data, in particular, from which separation the speckle level is negligible and/or the stellar halo is smooth.

Note that the discrepancy between the model of noise and the real noise distribution does not affect the flux estimation in itself, but it does affect the error on the flux estimation.

Whiteness of the noise in the differential images In order to visualize how much of the residual noise in the differential images deviates from the model, we can plot the autocorrelations of the residuals in the differential images. The autocorrelation of a signal describes the correlation between values of a random process at different time, as a function of the delay. This is a useful tool to probe information about repeated events in the signal or any similarities between signals as a function of the delay. Thus, if the signal is a purely white noise, its autocorrelation is a Dirac peak at the origin and zero elsewhere (ie: the signal is only similar to itself - that is to say for a delay of zero - but is completely decorrelated through time).

[2]The residuals come from photon, readout and dark current noises, all being independently and randomly distributed. This property is preserved by the ADI.

Fig. 3.9 shows the autocorrelation of the residuals left in the differential images (using $\delta_{min} = 0.5\lambda/D$), at two different distances to the star, averaged on every differential image found at this distance, for NaCo or SPHERE data. These autocorrelations indeed present an intense peak centered on zero surrounded by variations around zero. Close to the star, the central peak is broader and less intense than at larger separation and the standard deviation of the autocorrelation at non-null delays is higher than the one at larger separation[3]. Moreover the SPHERE images of the star HR-7581 (obtained during the SPHERE commissioning (May 2014) and kindly provided by Dr. A. Vigan) are taken under very good conditions (good adaptive optics correction and stable atmospheric conditions) which has an non negligible impact on the noise whitening via ADI which is way better than for the NaCo images (taken under fair conditions and obviously less good adaptive optics correction). Note that the two filters, the cameras, the DITs used and the observation conditions are quite different from the NaCo to the SPHERE data so a rigorous comparison is not possible but these graphs still provide a fair idea of the images quality.

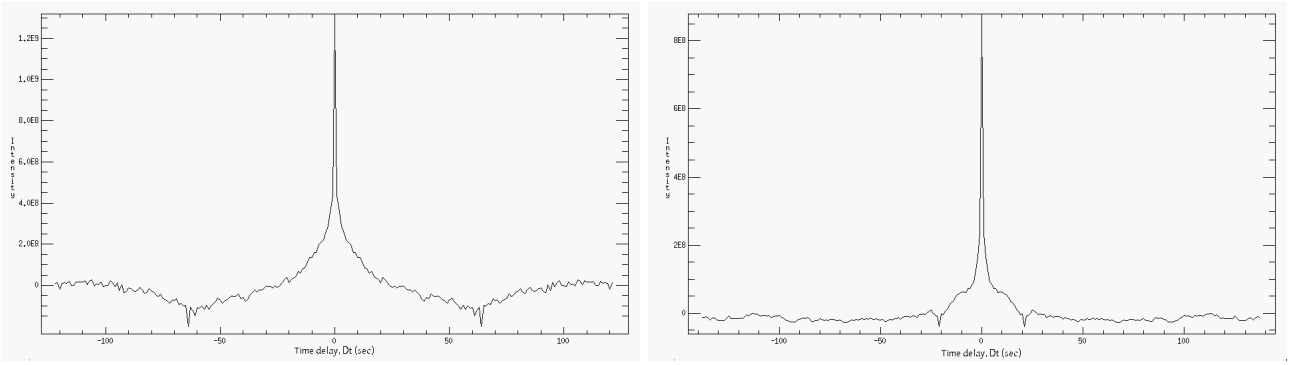

(a) : images of the star TYC-8979-1683-1 by the NaCo instrument in H-band. *Left:* At an angular separation of 50 pixels from the star ($\sim 17\lambda/D$); at this distance, 244 couples have been subtracted. *Right:* At an angular separation of 150 pixels from the star ($\sim 51\lambda/D$); at this distance, 276 couples have been subtracted.

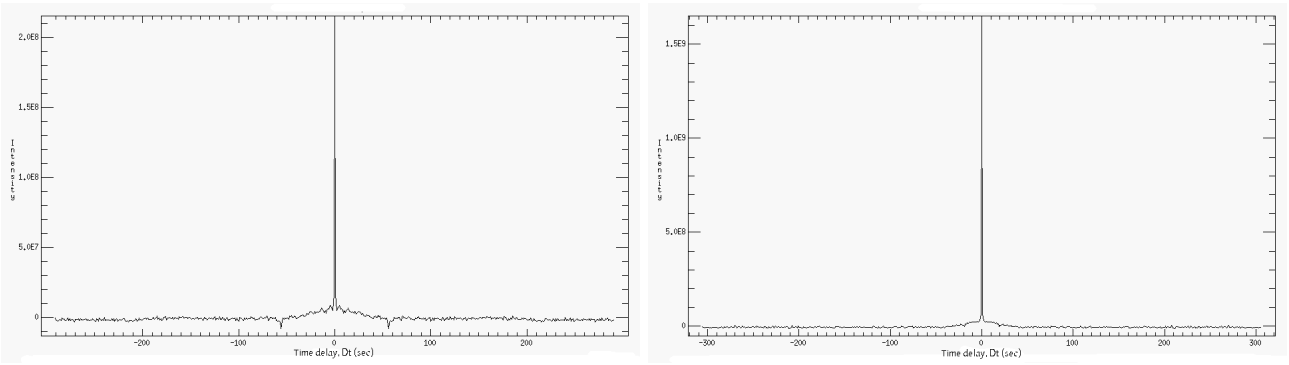

(b) : images of the star HR-7581 by the SPHERE-IRDIS instrument in H2-band. *Left:* At an angular separation of 50 pixels from the star ($\sim 15\lambda/D$); at this distance, 582 couples have been subtracted. *Right:* At an angular separation of 150 pixels from the star ($\sim 46\lambda/D$); at this distance, 612 couples have been subtracted.

Figure 3.9 – Autocorrelation of the residuals in the post-ADI images, within an annulus of $1\lambda/D$ width, using a pre-filtering of $F = 1/4$, for NaCo (3.9a) and SPHERE data (3.9b). The discrepancy between the real noise and its model as chosen in ANDROMEDA depends on the distance to the star and on the quality of the images.

From these figures, we can conclude that the residual noise in the differential images is indeed structured and not perfectly white. Moreover, the deviation of this residual noise distribution from a purely white noise is higher at close separation and depends on the quality of the images (observation conditions, wavefront corrections and pupil tracking).

[3]The two small anti-correlation peaks present on either side of the central peak are linked with the chosen δ_{min} : one specific frame $i_1(t_1)$ is subtracted to an other at $i2(t_2)$ (resulting in $\Delta = i_1(t_1) - i_2(t_2)$); but the frame at t_1 can be used to be subtracted from an other frame at t_3 (resulting in $\Delta = i_3(t_3) - i_1(t_1)$), resulting in a repeating pattern visible here. As the delay between the frame imposed by δ_{min} is dependent upon the distance to the star, these anti-correlation peaks do not have the same delay position wrt to the chosen distance (left and right panels of Fig. 3.9).

Consequences on the SNR map output by ANDROMEDA When applying ANDROMEDA on real data, this discrepancy between the noise model used and the real one affects the SNR map through Eq. 2.23 which shows its dependence upon σ_Δ. The residuals in the output SNR map from ANDROMEDA have the same distribution as the residual noise in the differential images (as it is preserved via the Eq. 2.23), when, of course, excluding the pixels containing the signal of a planetary companion. Under the assumption that the noise is white and Gaussian, the residuals in the SNR map should have a Gaussian distribution with mean of zero and a standard deviation of one. Thus by thresholding the SNR map by a constant value, only signals with a probability of presence set by the chosen threshold should show up.

However, in the SNR map obtained on real data, the standard deviation of the noise is higher than one at short separation which corrupt the connection between the PFA and the threshold. Moreover, the standard deviation of the noise is greater close to the star and decreases up to one at larger separation which prevents from applying a unique threshold over the whole field of view.

Consequently, if one wants to enable an automatic detection, as theoretically predicted by ANDROMEDA, there is a need in accommodating this trend.

Solutions to account for the noise model discrepancy A first idea is to modify the model of noise used to compute the likelihood, which would correspond to the real noise statistics in the differential images. Several studies aimed at deriving a complete statistical model for the residuals speckle distribution in post-ADI images (e.g., Marois et al., 2008a). However this is not mature enough since such a distribution would be very dependent upon the observation conditions which results in adding parameters in the image processing method and thus potential sources of error. Moreover, one interesting feature of ANDROMEDA is its simplicity since the maximum likelihood under the chosen hypothesis has an analytical solution which is therefore easy to implement numerically.

Another solution could be to compute the equivalent threshold at each distance to the star, which would account for this discrepancy, following, for instance, the reasoning in Mawet et al. (2014) (who used a frequentist approach to compute an equivalent threshold in the framework of the small sample statistics) or numerical simulations as in Marois et al. (2008a) (who showed that the presence of quasi-static speckle noise, leads to a detection threshold up to 3 times higher to obtain a confidence level equivalent to that at 5σ for a purely Gaussian noise). However no systematic solution has been developed so far which could permit to compute the real threshold (which would be fully linked with the true PFA) to be applied as a function of the separation to the star.

In the case of ANDROMEDA, for the sake of simplicity, we chose to perform a post-processing of the obtained SNR map. This a posteriori correction makes it possible to modify only the SNR map output by ANDROMEDA instead of modifying either the model of noise (here white and Gaussian) or the definition of the threshold (here set constant throughout the field).

3.1.2.2 Implementation of a normalization procedure for the SNR map

Knowing that we would like to obtain a SNR map that has a zero mean and a standard deviation of one throughout the whole field of view, a simple solution, chosen here, consists in normalizing the SNR map by its own radial standard deviation.

Normalizing the SNR map by its own radial standard deviation profile Normalizing the SNR map is an empirical solution which is easy to implement by computing the standard deviation in each annulus of one pixel width, centered around the star.

In order to not take into account spurious peaks due to either planetary companions or bright speckles, which would alter the statistics, the *robust standard deviation* is computed (following Hoaglin et al. (1983) and Beers et al. (1990) method which consists in calculating the median absolute deviation divided by a normalization factor enabling a robust estimate of the standard deviation[4]). The resulting profile of the robust standard deviation from the TYC-8979-1683-1 SNR map is shown on Fig. 3.10.

[4]The factor is chosen so that the regular standard deviation and the robust value are identical in the case of a Gaussian distribution (which is true with a good approximation here): $\sigma = median(abs(x - median(x)))/0.6745$.

The obtained 1D profile is often quite jagged, mostly close to the star, since at this distance, the standard deviation varies a lot from one annulus to the other, for the reasons explained above. Thus, in order to only obtain the global trend of the radial profile obtained (decreasing from close to large separation to the star), this profile must be smoothed.

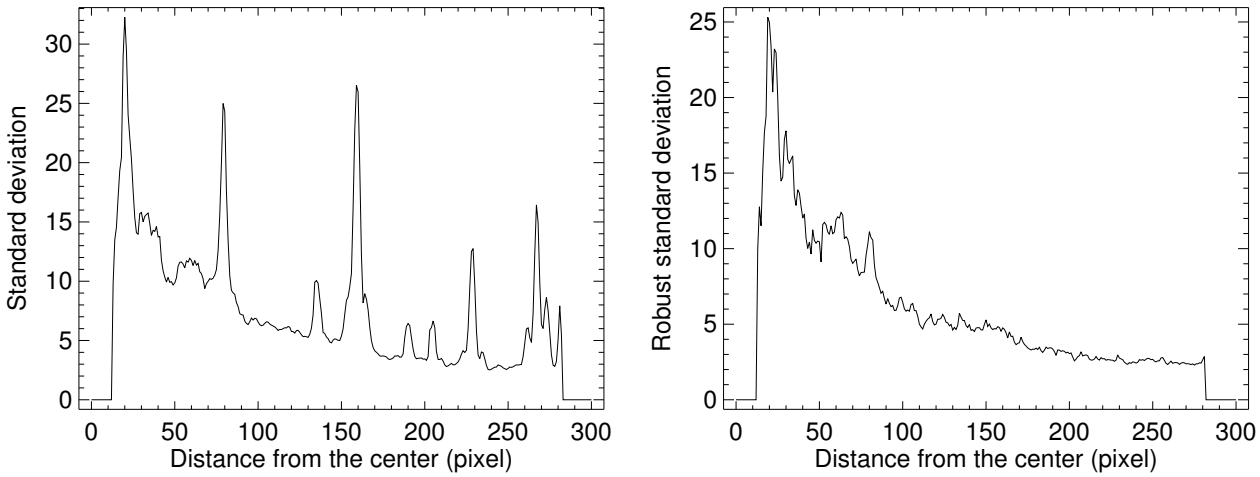

Figure 3.10 – Azimuthal mean standard deviation of the SNR map as a function of the distance to the star TYC-8979-1683-1. *Left:* Regular radial profile of the SNR standard deviation. We can visualize the high peaks indicating the presence of companions at certain separations (where the synthetic companions are located). *Right:* Radial profile of the SNR robust standard deviation. The highest peaks have disappeared but the profile is still jagged. (Figure from Cantalloube et al. (2015))

The raw SNR map output by ANDROMEDA is divided by this smoothed profile for each azimuthal position.

Smoothing the normalization profile To obtain a typical profile which encodes the global trend without taking into account the small variations of the azimuthal standard deviatio ren and/or the potentially strong impact of the presence of planetary companions, the profile must be smoothed.

Looking at the obtained profile shown on Fig. 3.10-*Right*, one can think of a first process would be to fit this profile by a polynomial of the fourth order. However the obtained fit is too smooth and in particular, it does not show the peculiar two regimes profiles, close and far from the star, as visible on the Fig. 3.11-*Left*. As a consequence the close companions are not detected, as shown on Fig. 3.11-*Right*.

Another simple idea would be to smooth one given pixel over values on *either* sides of the regarded pixel, the number of pixels on which the profile is smoothed being a user-parameter. The obtained profile, shown on Fig. 3.12-*Left*, now shows the two regimes (before and after ~ 100 pixel on Fig. 3.10) and seems to match better the raw profile. However the normalized SNR map obtained, does not allow one to detect close companions, as shown on Fig. 3.12-*Right*.

A solution is to artificially increase the SNR of the planetary signals located at short separation by under-normalizing the regions close to the star. In practice, it consists in smoothing one pixel according to its neighboring pixels but only by the ones at larger separation, as shown on Fig. 3.13. Due to the global trend of the robust profile, this method over-smooths close to the star while the smoothing does not affect the normalization level far from the star.

This way of doing the normalization increases the detectability by slightly reducing the normalization. But this method has *no* impact at large separation. It is really helpful at close separation since the radial trend decreases very fast, as we can see on the profiles. When applying the normalization procedure to the SNR map, we can check that from now on, if the SNR map is thresholded to the usual value of 5σ, only very probable companions are visible, as shown on Fig. 3.14. In particular, the 11 furthest and brightest injected synthetic companions out of the 15 are clearly found above this

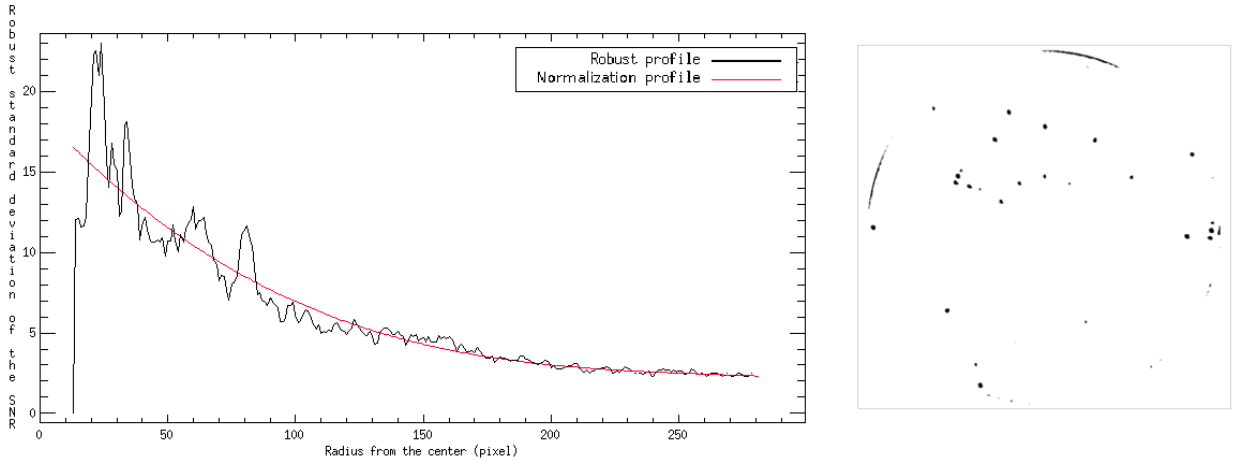

Figure 3.11 – Smoothing the normalization profile. Left: Normalization profile (red solid line) obtained by a 4th order fit of the radial robust standard deviation of the SNR map (black solid line). Right: SNR map normalized by this profile, thresholded to 5σ. The close companions are missing though visible on the non-thresholded SNR map.

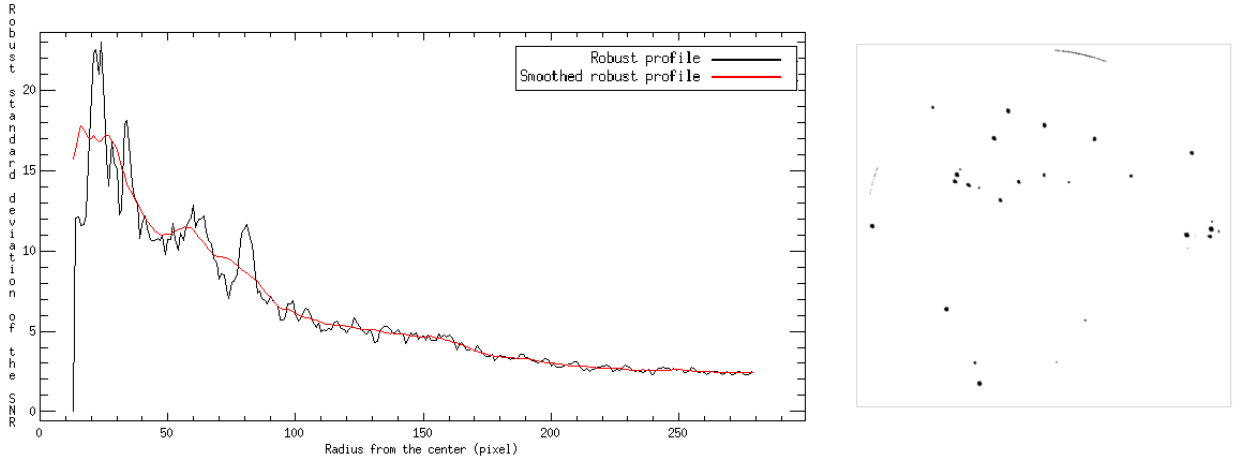

Figure 3.12 – Smoothing the normalization profile. Left: Normalization profile (red solid line) obtained by smoothing symmetrically over 18 pixels the radial robust standard deviation of the SNR map (black solid line). Right: SNR map normalized by this profile, thresholded to 5σ. The close companions are missing though visible on the non-thresholded SNR map.

threshold. The brightest companion at a separation of $0.53''$this time appears above threshold whereas it was not the case with the two other smoothing methods.

This chosen strategy to normalize the SNR map does not impact the flux estimation. Indeed, $\hat{a}$ is fixed and since $SNR = \hat{a}/\sigma(\hat{a})$, only the estimated flux error-bars are affected.

Effect of the smoothing amount on the normalized SNR map The number of pixels on which the profile is smoothed is a user-parameter which is dependent upon the images quality: if the speckle field is temporally stable, this profile will already be quite smooth and will not require an important smoothing; however if the speckle field is not stable, the residuals level might be quite different from one annulus to the other, thus showing a jagged profile, which therefore must be much smoothed.

If the profile is too smoothed, it will tend toward a flat profile which is equivalent to no normalization: the radial trend must be preserved and must be realistic, as shown on Fig. 3.15-Right. In this case, more artifacts will remain at close separation. However we will see at Sect. 3.3 which is dedicated to the exploitation of ANDROMEDA output, that it is possible to efficiently reject such

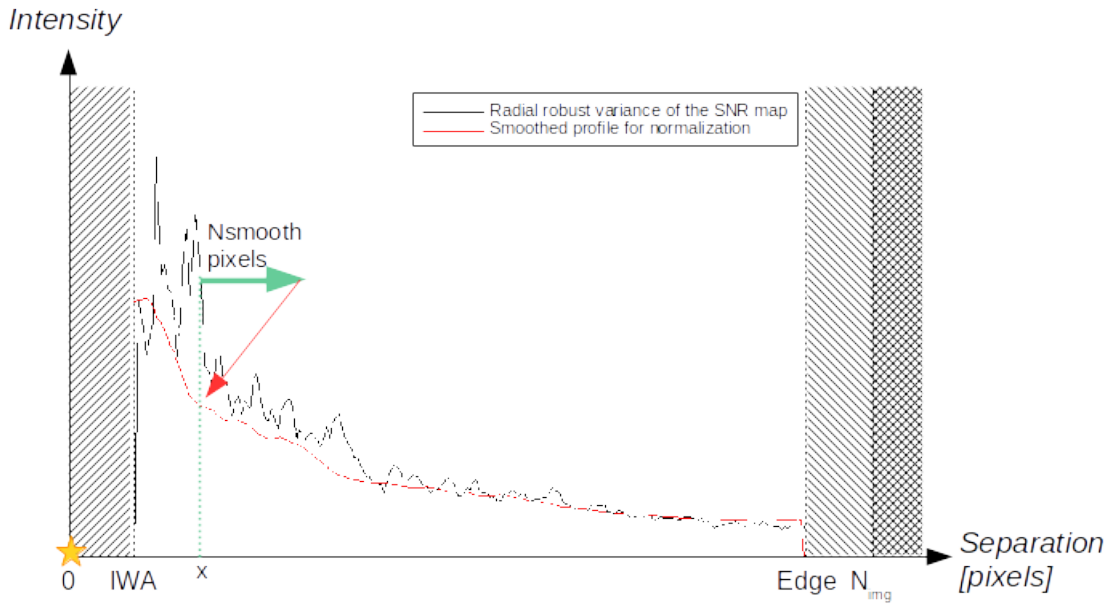

Figure 3.13 – Schematic drawing of the method used to smooth the radial robust SNR standard deviation profile (black solid line). The red solid curve is the obtained normalization profile.

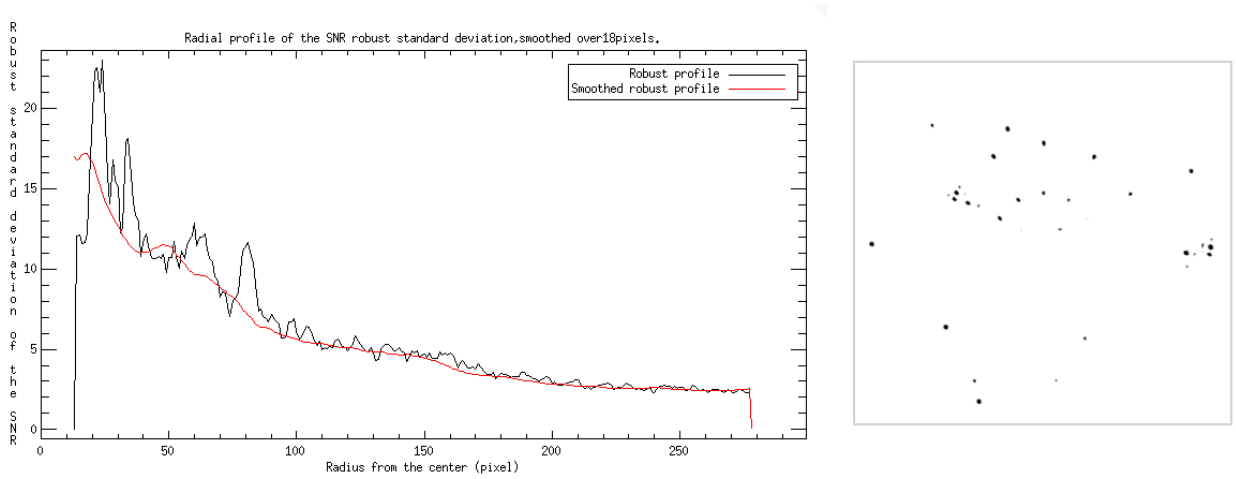

Figure 3.14 – Smoothing the normalization profile. Left: Normalization profile (red solid line) obtained by smoothing over 18 pixels towards larger separation the radial robust standard deviation of the SNR map (black solid line). Right: SNR map normalized by this profile, thresholded to 5σ. This time, the close companions are above the 5σ threshold.

signals a posteriori.

If on the contrary the profile is not smoothed enough, spurious peaks may remain above threshold and regarded as detections, as shown on Fig. 3.15-Left. This effect is particularly pronounced at short separation since this is the area where the profile has a steep slope (see Fig. 3.10-Right).

The sensitivity to the user-defined parameter N_{smooth}depends on the separation to the star: close to the star it is very sensitive whereas further it is not sensitive. This is explained by the steepness of the profile which is deep at short separation (and thus very sensitive to the smoothing) and flat from a particular distance where the speckle noise is no longer dominant (and thus not sensitive to the smoothing). Generally speaking, this N_{smooth}user-defined parameter depends on the quality of the observation condition (that is to say whether the stellar halo is very spread in the image) which will determine the steepness of the slop and the location from where it becomes rather flat.

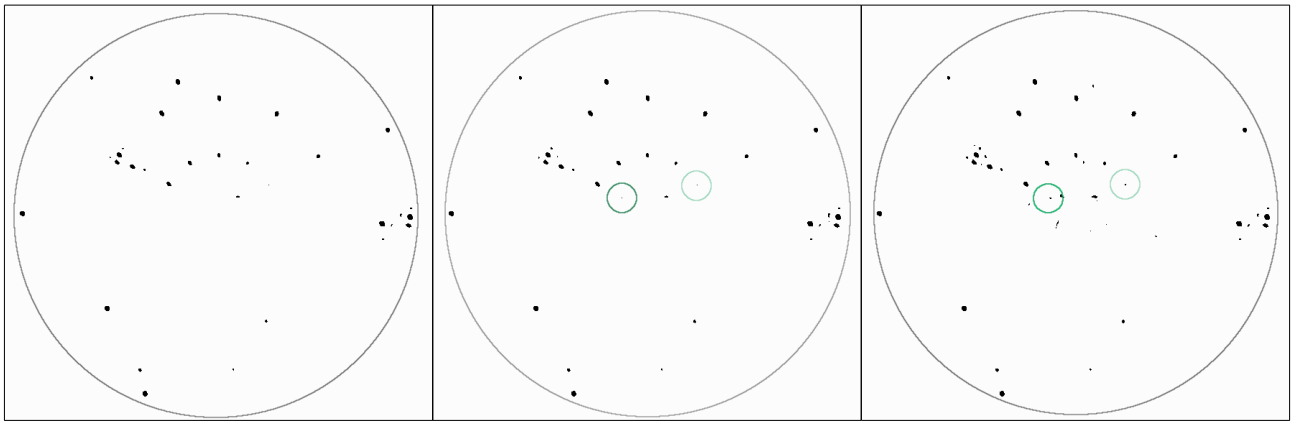

Figure 3.15 – Normalized SNR map thresholded to 5σ for different smoothing value N_{smooth}. From left to right: N_{smooth}= 12 pixels, N_{smooth}= 18 pixels, N_{smooth}= 50 pixels. From N_{smooth}= 14 pixels, the two close and faint synthetic companions visible on the SNR are detected above threshold. For $N_{smooth}\geq$ 14 pixels, no more close synthetic companions are detected but more and more artifacts arose above threshold.

In practice a good compromise is to visually check the smoothed profile with respect to the robust profile and check that the trend is satisfactory within these two regimes.

From tests performed on several data set, it appeared that typical values of N_{smooth}mainly depend on the instrument under use. For NaCo data, this $N_{smooth}$is rather wide, with a typical value of N_{smooth}= 18 pixels in H-band and smaller at larger wavelength. For SPHERE-IRDIS data, a typical value of N_{smooth}= 2 pixels is usually enough, whatever the wavelength, which demonstrates the quality factor gained by this instrument.

To summarize, once a convenient value is found, one has to keep in mind that at very close separation, this normalization procedure only helps detecting companions close to the star. The associated probability of presence must be read with care since it does not correspond to the intrinsic one.

3.1.2.3 Corresponding detection limits estimated with ANDROMEDA

As the normalization procedure is made on the SNR map output from ANDROMEDA, it only affects the SNR map. To remain consistent, the map of the standard deviation of the flux must be multiplied by the same normalization profile since:

$$\overline{SNR} = \frac{\mathrm{SNR}(\mathbf{r})}{Normalization_{SNR}(\mathbf{r})} = \frac{\hat{a}(\mathbf{r}_0)}{(\sigma[\hat{a}(\mathbf{r}_0)] \times Normalization_{SNR}(\mathbf{r}))} \tag{3.5}$$

The normalized map of the standard deviation of the flux thus gives the corresponding 1σ error bar on the flux estimation. This map can also be used to compute the detection limit consistent with the detection capabilities given by the SNR map. The detection limit shows the level of flux from which no companion can be detected in the images, as a function of the separation to the star and for a given confidence level expressed through the threshold τ (in units of sigma). At a chosen threshold τ this detection limit is simply given by $\tau \times \sigma[\hat{a}(\mathbf{r}_0)]$.

Implementing the small sample statistics In order to account for the bias at small separation, induced by the ADI process, I implemented in ANDROMEDA the small sample statistics correction, as defined in Mawet et al. (2014). One of the reasons why the PFA is underestimated at close separation is that there is only a small number of pixels contained in the processed annulus, added to the fact that few couples are found due to the constraint imposed by δ_{min} . These two points reduce the number of degrees of freedom which are, in ANDROMEDA, the number of points inside the annulus, $\mathbf{r}$, plus the number of ADI couples found at this distance, k. This effect corrupts the statistics: we are in a so-called *small sample statistics* regime.

In practice, it consists in computing the equivalent threshold that should be applied to obtain the same PFA a Gaussian statistics would give at the actual chosen threshold. Close to the star, the noise statistics no longer follows a MR distribution, but a robust Student's t-distribution (Mawet et al., 2014), valid for an independent and identically distributed samples, as it tends to be the case when performing differential imaging (Marois et al., 2008a).

Discussion on the notion of detection limit However, one has to keep in mind that computing an objective detection limit for a given threshold, mostly at short separation, is extremely difficult and the derived detection limits must be interpreted with great care. ANDROMEDA provides a systematic detection limit which is however slightly biased at small separation because of the normalization procedure described above which is an empirical solution. For now, there is no proper method to define an unbiased detection limit, independent of the image processing used on the data, which could inform on the real reachable objects range. This knowledge is however critical when interpreting results from large observational surveys.

To illustrate this difficulty, we computed several detection limits on a particular test case, using three different so-called *classical methods*, after processing the data with the same method (here a PCA-KLIP). These classical methods, are the one currently used by the astronomers. It consists in injecting synthetic companions at different separation to the star and with different position angle, and estimating their flux wrt to the injected one. The first method, called *square aperture*, (green lines in Fig. 3.16), consists in evaluating the noise in square boxes of size $3\lambda/D$. The second method, *azimuthal profile* (purple lines in Fig. 3.16), consists in evaluating the noise in annuli of 1 pixel width surrounding the star. The third method, *circular aperture* (blue lines in Fig. 3.16), consists in evaluating the total rms flux within a circular aperture of diameter $1\lambda/D$. The Fig. 3.16 on which the detection limits obtained following these three different ways are over-plotted, show that the profiles do not fully overlap.

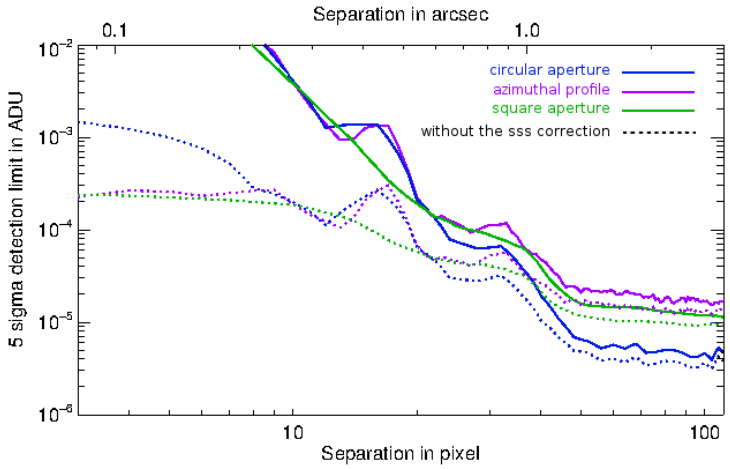

Figure 3.16 – Detection limit at 5σ derived from the same image data set β Pictoris described in Sect. 3.2.1 but processed using a PCA method. Three different methods are used to derive these curves (see text). Image provided by J. Milli (ESO).

For ANDROMEDA, since the detection limit is directly provided without needing synthetic companion injection, such an arbitrary choice does not exist. However choosing if we are providing the 2D map (which keeps the tracks of bright companions), or providing a 1D-profile, either giving a range (a thick curve) or giving a minimum limit or an average limit is something worth thinking of. In the following, I chose to show the averaged detection limit, that is to say the azimuthal median of the map of the standard deviation of the flux (to not take into account the presence of planetary companions), and to over-plot the minimum value of each annulus of this map. Indeed, although the first curve provides a fair idea of the detection limit with such a data set (green solid curve in Fig. 3.17), one might found a detection below the curve. However it is impossible to find a companion, with the con-

fidence level given by the chosen threshold, below the minimum curve (red dashed curve in Fig. 3.17). Moreover this output is homogeneous to the one provided with other image processing methods such as the ones in Fig. 3.16.

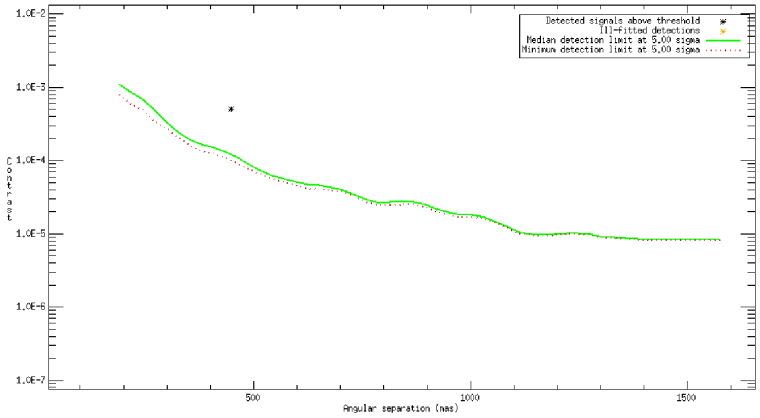

Figure 3.17 – Detection limit at 5σ derived from the same image data set β Pictoris described in Sect. 3.2.1, processed using the ANDROMEDA method. Two different curves are presented: the azimuthal median of the map of the standard deviation of the flux (green solid line) and the azimuthal minimum of the map (red dashed line).

3.1.2.4 Distribution of the residuals in the normalized SNR map

This normalization procedure makes the residuals in the SNR map having a standard deviation of one (which would have been the case if the residual noise in the differential images were white). It is visible in the histograms shown at Fig. 3.18, where the Gaussian distribution is centered ($\mu_{SNR} = 0$) and its FWHM is one ($\sigma_{SNR} = 1$). However this empirical solution is still limited as we can notice that the further from the star, the better the distribution is fitted by a Gaussian (not only because there are more pixels). This procedure must be made along with the pre-filtering, otherwise, the distribution is not well approximated by a Gaussian and the normalization does not help in shifting the mean and alleviating the variance (see Fig. 3.18-*Left* and *Middle*).

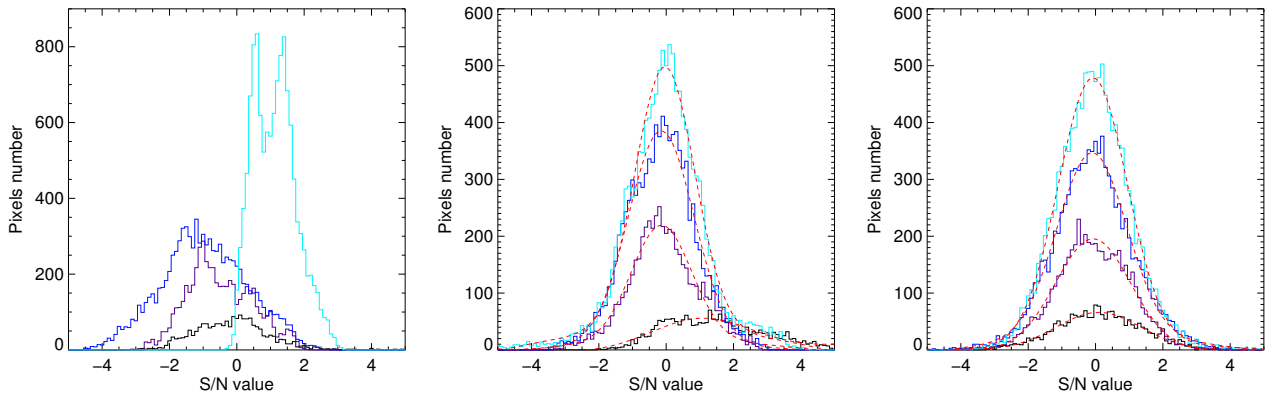

Figure 3.18 – Histograms of the residuals in the normalized SNR map computed from the TYC-8979-1683-1 data, inside four different annuli centered on the star: black solid lines are for an inner radius of 15 pixels ($\sim 5\lambda/D$), purple solid lines for 50 pixels ($\sim 17\lambda/D$), dark blue solid lines for 95 pixels ($\sim 32\lambda/D$), and light blue solid lines for 247 pixels ($\sim 90\lambda/D$). Each annulus has a width of 15 pixels except for the largest, which only has a width of 8 pixels. No obvious planetary-like signal can be found inside these annuli. *Left:* without filtering. *Middle:* with a pre-filtering, using $F = 1/16$. *Right:* with a pre-filtering, using $F = 1/4$. Gaussian fits of the histograms are over-plotted in red dashed lines. (Figure from Cantalloube et al. (2015))

3.1.2.5 Conclusion on ANDROMEDA's post-processing

As a conclusion, the combination of the pre-processing of the images (spatial high-pass filtering) and the post-processing of the SNR map (normalization of the SNR map by its azimuthal standard deviation) both decrease the natural discrepancy which exists between the model of residual noise made and its real distribution.

From experience on real data, empirically normalizing the SNR map is a reproducible method, independent of the data-set as it is shown along the numerous examples given in Chap. 6. Only the user-parameter N_{smooth}must be tuned with care but visualization of the profile permits to easily determine this factor. Also, for the last generation of high-contrast instruments such as SPHERE, the adaptive optics correction stabilizes the trend and thus usually a systematic mild smoothing can be used.

The implemented post-processing method is thus efficient and reliable. Using this normalized SNR map permit to automatically detect point sources in the field of view. Moreover, apart of very close separation regions, the retrieved SNR is now much better linked with the probability of presence of the companion. This method also derives a detection limit corresponding to the ability of the pipeline to extract point source companions in the images. I added a stage to fix the bias at close separation by implementing the small sample statistics inside ANDROMEDA. Thus the detection limit provided by ANDROMEDA is consistent with the retrieved flux and the noise distribution in the data. This information is fundamental to correctly interpret results from observational surveys, as mentioned in Sect. 1.1.2. Indeed the provided limit reached are crucial in Monte Carlo simulations used to derive exoplanet occurrences orbiting various type of stars. The derived frequency is essential to favor one or the other planet formation scenario. Moreover, this bias on the results can also corrupt the strategy chosen for the future surveys.

3.1.3 Conclusion on ANDROMEDA in its operational state

The spatial high-pass filtering applied to the reduced image before running ANDROMEDA *together with* the normalization of the SNR map by its azimuthal standard deviation trend provide three exploitable outputs:

1. A SNR map, which has a statistical significance and thus can be used to perform the detection and astrometry estimation in an objective way;
2. A flux map, used to read the contrast of the detections;
3. A standard deviation of the flux map, providing the error-bars on the estimated flux and from which the detection limit can be derived.

From now on, ANDROMEDA is an operational tool which complies its intended theoretical advantages, such as an objective detection criterion, a non-biased estimation of the flux and a corresponding detection limit.

In order to make this algorithm fully adapted to the real data properties, the next section revisits the full ANDROMEDA algorithm, along with the pre-processing and post-processing described in this section. This study allows one to improve the different steps performed by the algorithm, to detect the crucial steps of the method and to discuss the limitations of each step.

3.2 Exploring variations on building the differential images

Now that ANDROMEDA is fully operational and provides exploitable output, I will go through the two main steps performed by the algorithm to discuss and choose the best strategy with a view to apply ANDROMEDA on real data. In the following, I will not discuss the two added stages of pre and post-processing, extensively dealt with above. However these stages are assumed included in the pipeline for the discussions.

3.2.1 Description of the data to illustrate this part

To test ANDROMEDA, we also applied it to the emblematic and well-known case of β Pictoris . This star is surrounded by a debris disk inside which only one planet, β Pictoris b, has been detected by imaging. This close companion is located at $\sim$ 9 AU from its host star and was first detected by Lagrange et al. (2009). Detecting this planet is challenging because it stands at very short separation ($< 0.5''$).

The β Pictoris data on which ANDROMEDA has been applied ANDROMEDA are described in Absil et al. (2013), including all the information concerning the reducing steps applied (basic cosmetic treatment, re-centering, frame selection, etc.). A summary of this data set properties can be found in Tab. 3.1.

Notably, the observations are made with the NaCo instrument using the L' filter which provides images of relatively good quality in terms of contrast. This set-up is particularly interesting to probe short separations. At larger separation, the background noise is non-negligible.

Property	**Value**
Instrument - camera	NaCo - L27
ESO program ID	60.A-9800
Observation date	2013/01/31
Atmospheric conditions	Good (seeing $\simeq 1''$; SR$\simeq 70-75\%$)
High contrast	L'-band AGPM vector vortex coronagraph
Wavelength of observation	L$\prime$-band: $3.8\mu m$
Sensor pixel scale	27.15 mas/px
Resolution	$1\lambda/D \simeq 4\pm$ pixels
Star magnitude	3.51 (H)
Image size	$150 \times 150 pixels$
Number of images	102 (temporally binned)
Total field rotation	$82.56°$; $(-14.73 \rightarrow 67.83°)$
Offset angle wrt true North	$104.84°$
DIT image	0.2 sec
Total integration time	3.5 h
Neutral density transmission for the reference PSF	None: off-axis exposure
DIT PSF	0.02 sec

Table 3.1 – Table summarizing the characteristics of the observation of the star β Pictoris with NaCo, used to test ANDROMEDA.

Within this data set, Absil et al. (2013) have retrieved the companion β Pictoris b at a separation of 452 ± 9.6 and a contrast of 8.01 ± 0.16 using a PCA-KLIP flavor described in their publication. A detailed comparison of the results obtained with their pipeline with the results obtained using ANDROMEDA on these data are published in Cantalloube et al. (2015).

3.2.2 Interpretation of the scaling factor γ after pre-filtering the images

Without filtering, the computed scaling factor weights for the average intensity difference in the two images $i_k(t_1)$ and $i_k(t_2)$ inside the regarded annulus of thickness d_r (as explained at Sect. 2.2). However, when filtering the low spatial frequencies, the smooth stellar halo is removed (as it is visible on Fig. 3.7). As a consequence, after this filtering, the scaling factor weights for the average pixel to pixel correlation between the images $i_k(t_1)$ and $i_k(t_2)$ inside the regarded annulus of thickness d_r. These two different interpretations of the scaling factor are fundamental and have a non-negligible impact on the choice of the method used to optimize the ADI according to the data set (see Sect. 3.2.3 for further discussion on this aspect).

To visualize the difference between these two interpretations, Fig. 3.19 shows the pixels' intensity in the image $i_k(t_1, \mathbf{r_{sub}})$ as a function of the pixels' intensity in $i_k(t_2, \mathbf{r_{sub}})$, where $\mathbf{r_{sub}}$ is the subtraction

area, that is to say the annulus of width d_r centered on the star in which δ_{min} applies (here, $\delta_{min} = 0.5\lambda/D$). This figure is made on simulated data (those presented at Sect. 2.2.1), where no planetary signal can be found. Note that if there were planetary signals, it would make no difference since it would shift some data points symmetrically on either sides of the bisector. Indeed, at first order, the planetary companion has the same intensity in the two images (More details about these aspects can be found in Sect. 3.2.3). For these plots, I chose typical conditions for which the speckle field has varied enough but is not completely decorrelated ($\delta_{min} = 0.5\lambda/D$, $d_r = 1\lambda/D$ for an inner radius of $7\lambda/D \simeq 287$ mas).

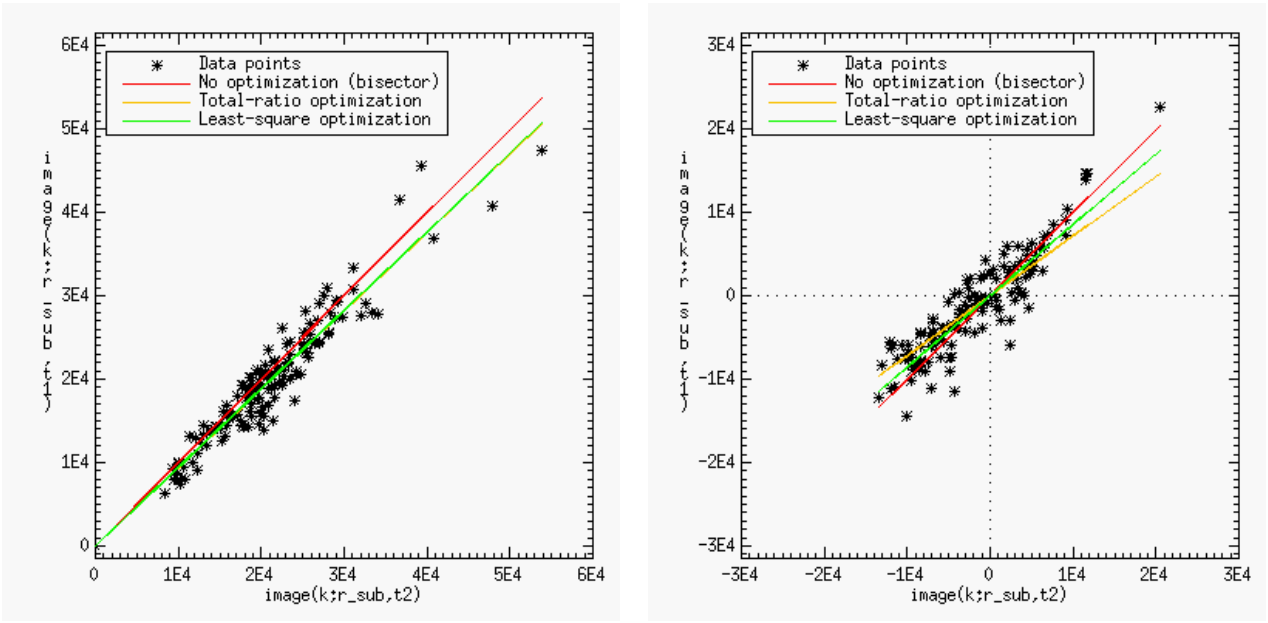

(a) : Without Filtering.

(b) : With Filtering ($F = 1/4$).

Figure 3.19 – Intensity of the pixels contained in $i_k(t_1, \mathbf{r_{sub}})$ as a function of those contained in $i_k(t_2, \mathbf{r_{sub}})$ on simulated SPHERE-like data (Sect. 2.2.1). The data are those within an annulus of $1\lambda/D$ width whose inner radius is at $7\lambda/D$ from the star ($\simeq$ 287mas).

On these graphs, the data points are distributed along an elongated shape on which the major-axis thickness codes for the typical intensity dispersion within the two annuli and the minor-axis codes for the pixel to pixel intensity degree of correlation (contribution of the noise). In agreement with this explanation, we observe that the minor-axis indeed becomes wider under bad conditions and thinner under good conditions (in terms of temporal stability). A schematic view of how to interpret such a graph is presented at Fig. 3.20.

On Fig. 3.19, we indeed observe that the filtering modifies the shape of the data point distribution, making it more oval and centered on zero. When the filtering is applied, the data points lie within a typical Gaussian envelop: there is less decorrelation at high intensity than in the case without filtering, which means that the brightest pixels belong to low frequency structures. At low intensities, the distribution is slightly more dispersed when filtering. As a consequence, the scaling factor γ, which should provide the slope of the major-axis of this Gaussian envelop, indeed probes the pixel to pixel decorrelation degree between the two annuli. On the contrary, without filtering, the scaling factor γ probes for the average flux ratio between the two annuli.

Note that in both cases (with or without filtering), the least-square fits better the data points (green solid line on Fig. 3.19) than the bisector (red solid line on Fig. 3.19). Also, the total ratio fit (orange solid line on Fig. 3.19) is very close to the least-square fit when filtering and quite different without filtering. For this particular couple of images, without filtering, $\gamma_{TR} = 0.9413$ and $\gamma_{LS} = 0.9423$ whereas with filtering, $\gamma_{TR} = 0.7176$ and $\gamma_{LS} = 0.8552$.

The Fig. 3.21 shows the evolution of this least-square scaling factor, γ_{LS}, as a function of the distance to the star, either with or without filtering. The expected behavior is that $\gamma_{LS} \simeq 1$, mostly

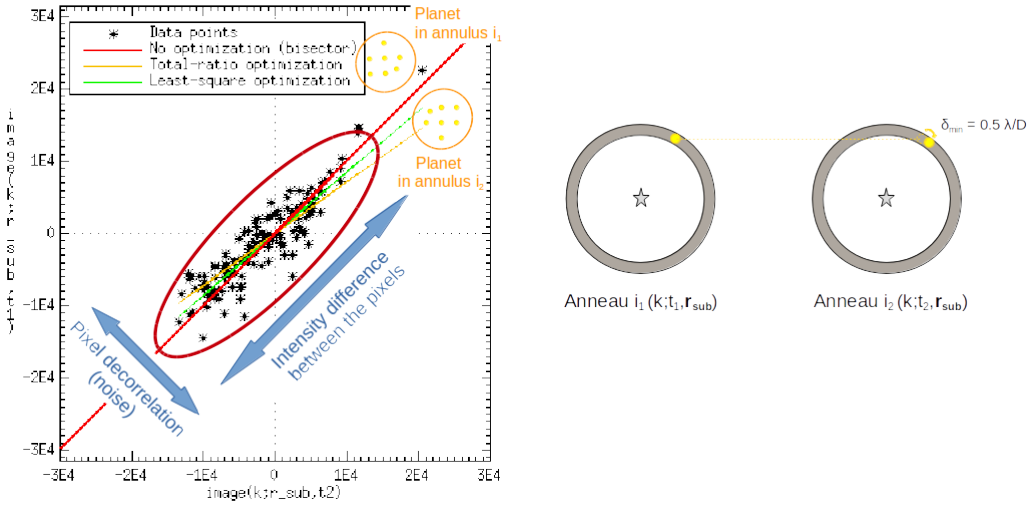

Figure 3.20 – Schematic explanation on how to interpret the graphs shown at Fig. 3.19.

at large separation since the δ_{min} constraint implies a smaller time delay between the two images at large distance (and thus a better similarity between the two frames to be subtracted).

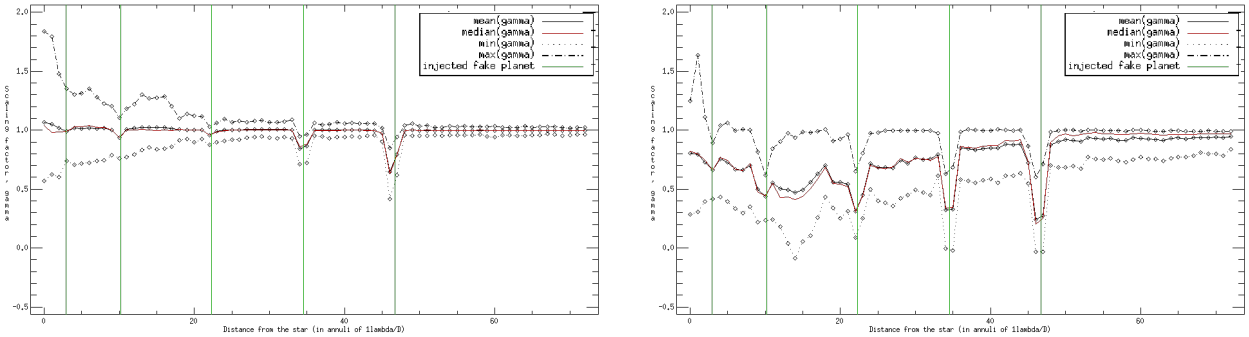

(a) : Without Filtering.

(b) : With Filtering ($F = 1/4$).

Figure 3.21 – Evolution of the minimum, maximum and mean value of the computed scaling factor γ_{LS} as a function of the distance to the star (for annuli of $1\lambda/D$ width, the IWA inducing an offset of $4\lambda/D$), either with or without pre-filtering of the SPHERE-like simulated images (Sect. 2.2.1).

Indeed, without filtering, $\gamma_{LS} \simeq 1$, with smaller dispersion between the couples when going further from the star (that is to say, whatever the couple of images, γ_{LS} remains close to 1). However, with filtering, the scaling factor is lower than one and slowly tends toward one (from about $40\lambda/D$), which means that, as expected, the pixels to pixel correlation is greater at large separation. This effect is worst on real data (see Fig. 3.22): the scaling factor is about 1 without filtering whereas it goes from about 0.8 to 0.2 when filtering. This is due to the fact that the scaling factor accounts for the pixel to pixel decorrelation in the filtered image and further from the star, the noise is mainly constituted of photon and detector noise so it is highly decorrelated from one image to the other.

Another effect worth pointing out, is that the presence of the planets (whose location is indicated by the green solid lines on Fig. 3.21) corrupts the least-square fit. Either with or without filtering, the further from the star, the higher the scaling factor deviates from its mean value: at large separation more noisy pixels are present wrt the number of pixels containing the signal of the planet (which is constant whatever the distance to the star in these simulated data).

Thanks to this new interpretation of the scaling factor, when filtering the images, we can probe the correlation degree between the first frame of the cube and the following ones. Fig. 3.23 shows

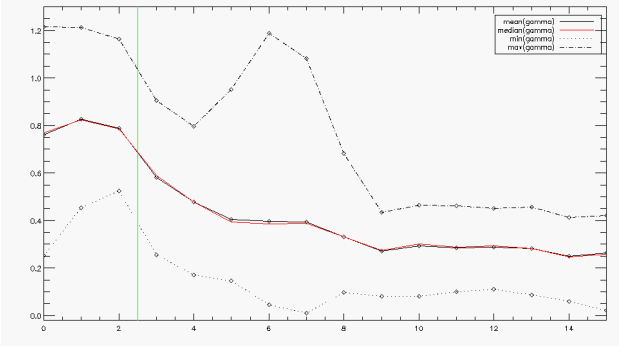

(a) : Images from the NaCo instrument in L' band (3.8μm). (Star: β Pictoris , see Sect. 3.2.1).

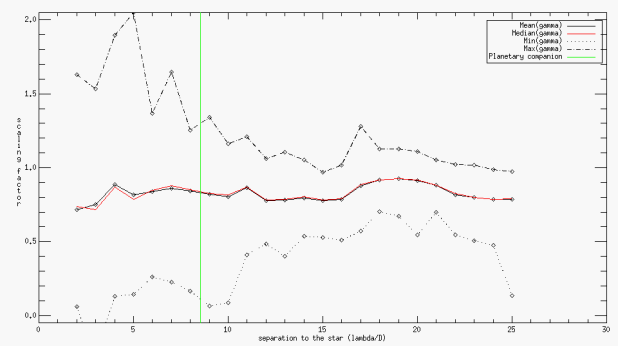

(b) : Images from the SPHERE insstrument in $K1$ band (2.11μm). (Star: Eridani 51, see Sect. 6.3.1).

Figure 3.22 – Evolution of the minimum, maximum and mean value of the computed scaling factor γ_{LS} as a function of the distance to the star (for annuli of $1\lambda/D$ width, the IWA inducing an offset of $2\lambda/D$), of the images from the NaCo instrument or of the SPHERE-IRDIS instrument, both with a pre-filtering $F = 1/4$.

the scaling factor γ_{LS}, calculated between one annulus in the first frame and the same annulus in the following frames constituting the image cube, for different distances to the star and either with or without filtering of these frames.

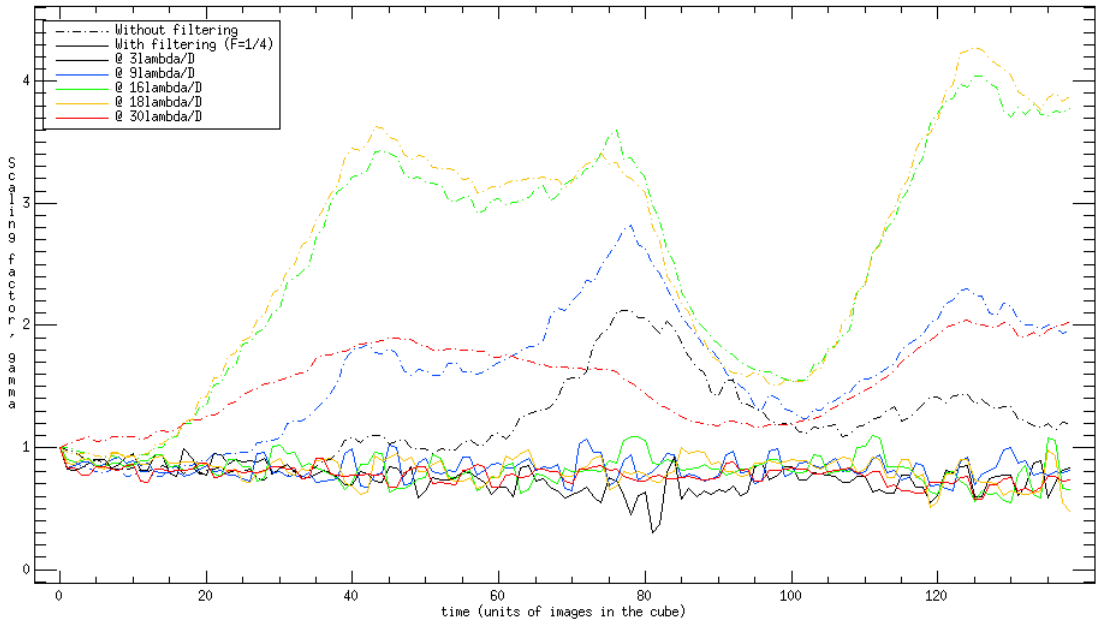

Figure 3.23 – Scaling factor γ_{LS} calculated between the first image of the cube and the i^{th} following image (x-axis, where there are 144 images in total), either without filtering (dashed line) or with filtering using $F = 1/4$ (solid lines). The scaling factor is computed within annuli of $1\lambda/D$ width, for various distances to the star (different colors), using the SPHERE-like simulated data (Sect. 2.2.1).

Without filtering (dashed lines), the trend matches exactly the total flux of the images through time[5] (see Fig.3.4 in Cornia, 2010).

With filtering (solid lines), the correlation decreases slowly between the first frame and the following.

The latter graph confirms that depending whether the images are high-pass filtered, the scaling factor should not be interpreted the same way. With filtering, it probes the pixel to pixel correlation whereas without filtering it probes for the mean intensity difference. The next section, Sect. 3.2.3,

[5]From the 100^{th} frame, the same trend appears, which is due to the way the data have been simulated: a period of 1000 sec has been used to compute the quasi-static speckles.

discusses a different way of optimizing the scaling factor computation in line with the real data properties and the applied high-pass filtering.

3.2.3 Refining the ADI process included in ANDROMEDA

The type of ADI applied in ANDROMEDA to build the differential images is optimized in order to cope with the intensity distribution difference between the two images (as presented in Chap. 2 and discussed at Sect. 3.1.1). In the original version of ANDROMEDA two kinds of optimizations had been implemented: the *total ratio* optimization, which cannot be used anymore due to the pre-filtering (and that I will ignore in the following), and the *least-square* optimization which proved better on both simulated and real data Cornia (2010). Both methods consist in making a linear combination of the two images to be subtracted. The corresponding coefficient (called scaling factor) is computed for each couple of images (defined by the δ_{min} constraint), within an annular area including the actual subtraction zone (of size defined by $d_r \times R_A$).

Robust optimization However, the least-square optimization, is by definition very sensitive to outliers. As this optimization is made inside an annular zone, this effect can affect the least-square fit in two cases: (i) If a bright speckle appears in one of the two images (or more generally has a different brightness in one of the two images), or (ii) a planetary signal has a stronger intensity in one of the two images. Indeed, on the graph shown at Fig. 3.20, we can see that as soon as a signal creates an asymmetry of the data points distribution wrt the bisector, the least-square fit is biased toward this data point. If the fit is biased, it will result in a flux offset in the resulting differential image. Also this bias might smooth the planetary signal (if the computed γ_{LS} is very small), inducing a decrease of its SNR, making it more difficult to detect. One solution to avoid such a bias is to perform a robust fit which would be insensitive to outliers[6]. For instance this would consist in minimizing $\|\sum_{\mathbf{r}} i_k(\mathbf{r}, t_1) - \gamma_k \ \sum_{\mathbf{r}} i_k(\mathbf{r}, t_2)\|$ using the L_1 norm instead of the L_2 norm, as implemented in the original version of ANDROMEDA. In other words, when using the L1-norm, the weight given by an outlier is lower than when using the L2-norm (since it is the absolute distance and not the squared distance to the fit which is taken into account). In particular, when using this L1-norm, the same number of data points are below and above the L1-fit in a graph such as the one presented on Fig. 3.20.

Non-linear subtraction Another point is that the star PSF shape does not vary linearly in the images, as shown on the sketch Fig. 3.24. If there is a sudden evolution in the turbulence strength, the image couple points can be better fitted by an affine law.

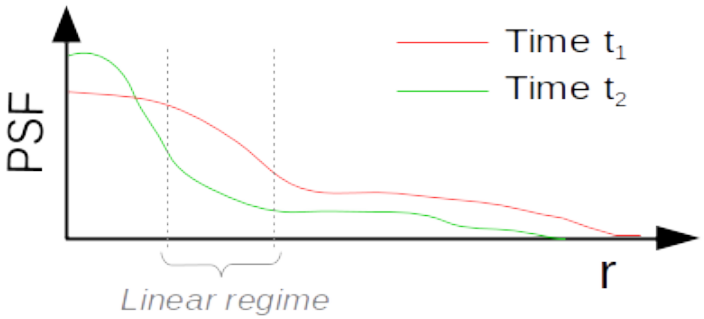

Figure 3.24 – Schematic profile of the star PSF shape at two different times. At t_1 (red line), the post-AO turbulence strength is higher than at t_2 which thus makes its energy less concentrated in the core. A linear regime can be assumed in between the two vertical gray dashed-lines. However, at close separation, where the subtraction is critical, this non-linear behavior may cause some errors.

[6] In this context, outliers are noteworthy departures from the idealized assumption for which the estimator is optimized - here a Gaussian distribution. In this study, the problematic points are the ones deviating from the others of a noteworthy amount.

Proposed solution From these two considerations, the differential images can be computed via:

$$\Delta(\mathbf{r},k) = i_k(\mathbf{r},t_1) - \gamma_k(\mathbf{r})\ i_k(\mathbf{r},t_2)\ - \gamma\prime_k(\mathbf{r}) \tag{3.6}$$

The scaling factor γ_k and the affine term $\gamma\prime_k$ are computed by minimizing: $\|i_k(\mathbf{r}) - \gamma_k \,.\, i_k(\mathbf{r}) - \gamma'_k\|_{L_1}$. This differential image approach is called *L1-affine optimization*.

3.2.3.1 Algorithm to perform a robust affine fit

Minimizing an affine function under the L1-norm can be solved by using the Least Absolute Deviation (LAD) which is resistant to outliers. The L1-norm has a probabilistic interpretation since it is a heavy tailed *pdf* corresponding to an exponential distribution in $e^{-|x|}$ (which decreases more slowly than e^{-x^2} when performing a least-square fit), that is to say the outliers are less likely. The goal is to minimize the following figure of merit:

$$L(y : f(x)) = J(a,b) = |y - f(x)| \equiv \sum_{i=1}^{N} |y_i - b - a\ x_i| \tag{3.7}$$

On which we can identify $y \equiv i_k(\mathbf{r},t_1)$ and $f(x) = \gamma_k(\mathbf{r})\ i_k(\mathbf{r},t_2)\ + \gamma\prime_k(\mathbf{r})$, with $x \equiv i_k(\mathbf{r},t_2)$. The two unknown parameters to be estimated by minimizing J are the linear factor $a \equiv \gamma$ and the affine term $b \equiv \gamma\prime$.

There is no analytical solution to this problem. In particular it is possible that the solution is not unique and/or not stable (which is instinctively understandable since it depends on the weight given to the outliers). It is necessary to find an algorithm which permits to reach the best solution. Among the methods solving this problem, the chosen one is a simplex method found in Press et al. (2007).

This estimator has two specific cases: (1) it passes through, at least, two of the data points and (2) from a given slope (the scaling factor a), we can deduce the affine factor b (the intercept). Indeed the robust solution providing b as a function of a is simply the median of $y_i - a\ x_i$ (which is by definition the norm-L1 in this case).

Then the minimization of a with a known b writes (see Press et al., 2007 for details about this development):

$$\phi \doteq\ -\frac{\partial J}{\partial a} = \sum_{i=0}^{N-1} x_i\ sign(y_i - b - a\ x_i) \tag{3.8}$$

It is therefore possible to develop an iterative algorithm to calculate a and b, starting from a first guess.

One difficulty is to find a good starting point to begin the descent (which can be found in a non-robust way). In our case, it is clear that this first guess can be the least square solution which is not that different from the robust solution at first order. In fact, in our case, where the model is an affine line, it is much simpler to implement. The following describes a method to fit an affine straight line in a robust way.

3.2.3.2 Practical implementation of the robust affine fit in ANDROMEDA

In order to iterate towards the minimum, three major steps are performed:

1. First-guess: the first step consists in performing a basic least-square fit to find the starting point of the iteration. These starting points are a_{LS} and b_{LS}, with which the function ϕ_{LS} is calculated.

2. Bracketing: from the previously retrieved parameters, the χ^2 is computed to provide an estimation of the iteration step to be used (via its standard deviation). A first guess of the bracketing is found at 3 sigma from the a_{LS} value in the downhill direction of ϕ_{LS}. From this new value of a, a new ϕ is calculated via Eq. 3.8. By comparing ϕ to ϕ_{LS}, we check if the zero is indeed included in between these two functions. This process is repeated downhill, until the two last values of ϕ have a different sign.

3. Bissection: Once the range of values found, the parameter a is reduced by half of the interval given by the bracketing, until the function ϕ is close enough to zero (according to the convergence criterion defined above). To do so, we check at each iteration that the last ϕ calculated thanks to the retrieved a is closer to zero; else the descent direction is changed.

4. During this process, each time the function ϕ is calculated, the affine factor b is calculated from the scaling factor a and the data following: $b = MEDIAN(y - a * x)$. Then ϕ is computed with these two last values of a and b in order to check if it is still above the convergence criterion defined by the user (here it is set to 10^{-6}).

3.2.4 Test of the robust affine fit in real differential images

The gain provided by any of the optimization methods depends on several parameters: if there is a pre-filtering applied to the images, if there is a planetary companion, the conditions under which the images are taken and the separation to the star. However, as ANDROMEDA is only operational with the filtering, I will not discuss further this difference (see Sect.3.1.1).

In the following, I thus chose to investigate the performance of the L1-affine fit when the images have been filtered (using $F = 1/4$) and at separations where planetary companions are actively searched (about 500mas). At the chosen distance and for a chosen couple k, I injected a planetary companion (with the same contrast) in order to probe the difference of the fit characteristics, with or without a planetary companion.

The Fig. 3.25, is a plot of the pixels' intensity contained in the first annulus as a function of the pixels' intensity in the second annulus. As the planetary signal is not correlated from one image to the other (since its position changes in the annulus), its signal (blue boxes in Fig. 3.25) will be concentrated on both sides of the bisector (orange solid line in Fig. 3.25). Added to that, the planetary signal has the same flux in the two images so the corresponding data points are gathered symmetrically to the bisector, as we can visualize on Fig. 3.25). At this stage, the planetary signal does not bias the least-square fit since its data points are located symmetrically around the bisector. However, if the planet intensity varies from one image to the other, the least-square fit (green line) will be shifted towards the highest intensity direction.

Following the same reasoning, the speckle intensity (black points on Fig. 3.25) variability in between $i_k(t_1, \mathbf{r_{sub}}$ and in $i_k(t_2, \mathbf{r_{sub}}$ is responsible for the scatter along the the minor axis direction (which represents the noise dispersion, whereas the major axis represents the intensity dispersion of the pixels within the annuli - see Sect. 3.1.1). If one data point represents a speckle present in both images at the same location, but with a lower flux in $i_k(t_1, \mathbf{r_{sub}}$ than in $i_k(t_2, \mathbf{r_{sub}}$, it creates an asymmetry from the bisector. This asymmetry corrupts the least-square fit (green curve) whereas the L1-affine fit is less sensitive to these outliers and fits better the global shape of the scattered data points.

In order to visualize the effect of the subtraction in the differential images, the Fig. 3.26 shows the azimuthal profile of each images, $i_k(t_1, \mathbf{r_{sub}})$ and $i_k(t_2, \mathbf{r_{sub}})$, and their subtraction, according to the three different subtraction scheme. On this graph, one can see that the L1-affine optimization (red solid line on Fig. 3.26) leads to a similar, yet slightly better, speckle subtraction than the least-square optimization (green solid line on Fig. 3.26), as its mean is closer to zero and its variance slightly lower. Another important aspect that it is worth pointing out here, is that the robust fit preserves better the planetary signal when subtracting (ie: the negative bump is deeper because the scaling factor γ is higher) compared to the least-square fit. These aspects have been intensively checked on both simulated SPHERE-like data and on real data which led to the same conclusions.

The latter aspect can be verified by plotting the evolution of the computed scaling factor as a function of the separation, as in Fig. 3.27, either for a least-square or a L1-affine optimization. We can first notice that the scaling factor (left side on Fig. 3.27) is slightly lower for the L1-affine fit than for the least-square fit. However this is mostly the case at close separation (below $5\lambda/D$) since the L1-affine and the least-square fit then provides relatively the same scaling factor from this distance. Also the affine factor (right side on Fig. 3.27) has a very high dispersion at close separation, which decreases significantly from 2-3λ/D and is closer and closer to 0 from $5\lambda/D$. These two aspects indeed

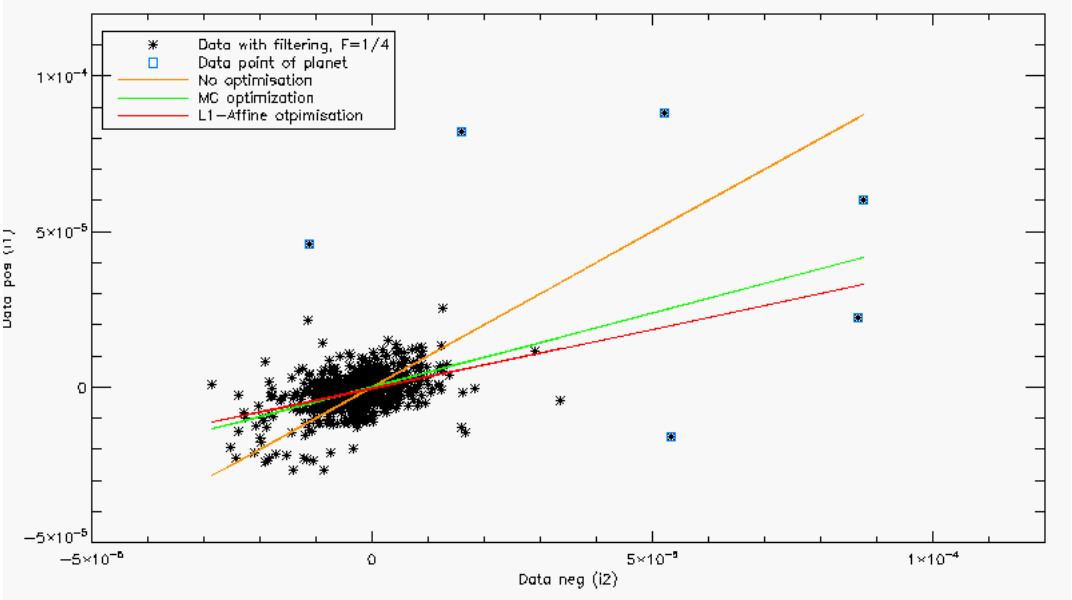

Figure 3.25 – Data points $i_k(t_1, \mathbf{r_{sub}})$, as a function of the data points $i_k(t_2, \mathbf{r_{sub}})$. The subtraction area $\mathbf{r_{sub}}$ is located at a distance of $6\lambda/D$ and has a width of $1\lambda/D$. The images have been pre-filtered using $F = 1/4$ and couples found using $\delta_{min} = 1\lambda/D$. The optimization are made within the regarded annuli (that is to say $R_A = 1.0$).

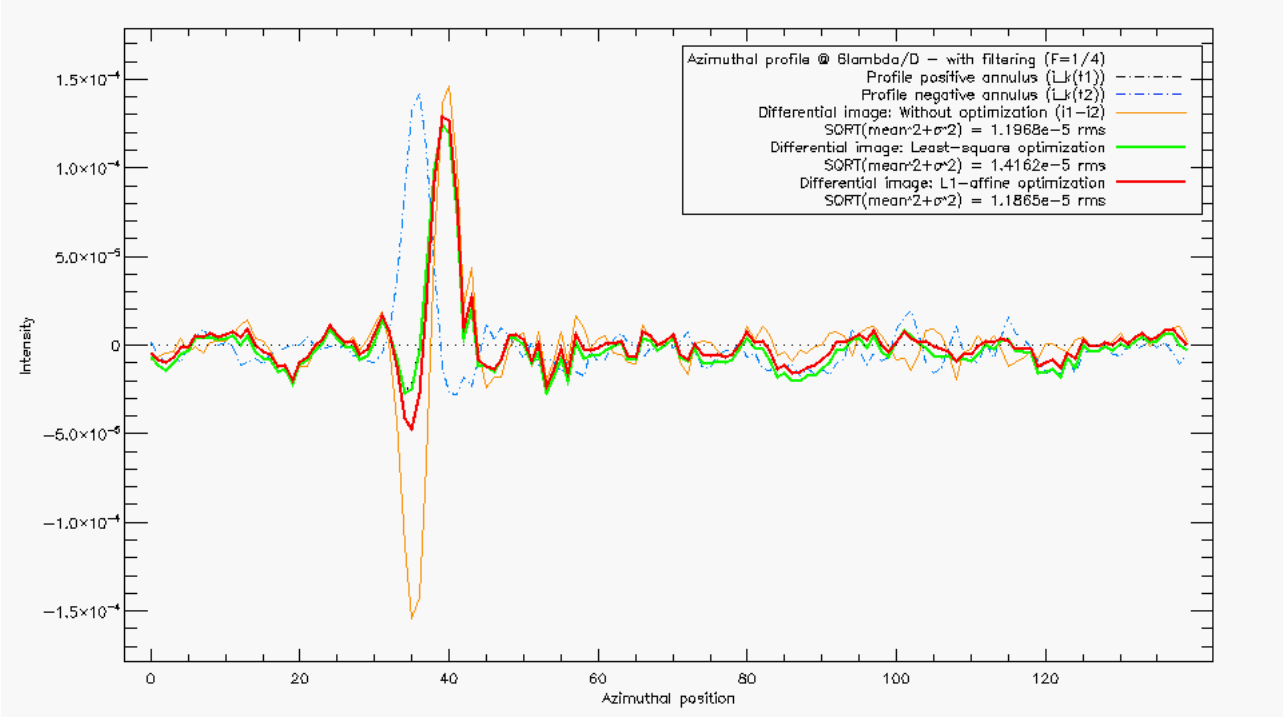

Figure 3.26 – Azimuthal profile (over a one pixel's wide annulus) of the differential images obtained by subtracting the annuli used at Fig. 3.25, according to the optimization method used. In order to compare the three methods, the rms value of the profile deprived of the planetary signal is indicated in the legend. The profile of $i_k(t_1, \mathbf{r_{sub}})$ and $i_k(t_2, \mathbf{r_{sub}})$ are over-plotted in dashed-line (respectively black and blue lines).

confirm that the least-square fit and the L1-affine fit are very similar at separation larger than $5\lambda/D$.

As a conclusion of this section, the three following points are to be kept in mind:

- The important parameter for the robust fit to be effective is whether it exists a non-negligible intensity variation of either a bright speckle or a planetary signal in the two images to be subtracted (Fig. 3.25).

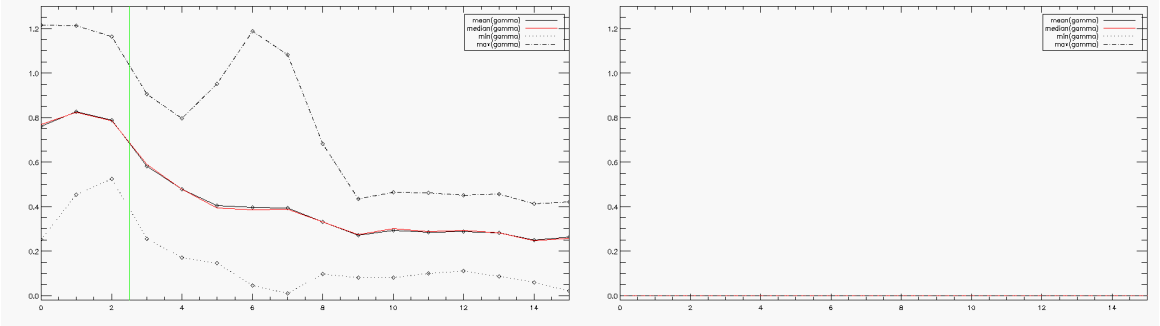

(a) : Evolution of the scaling factor γ (left) and the affine factor γ' (right) for a least-square optimization.

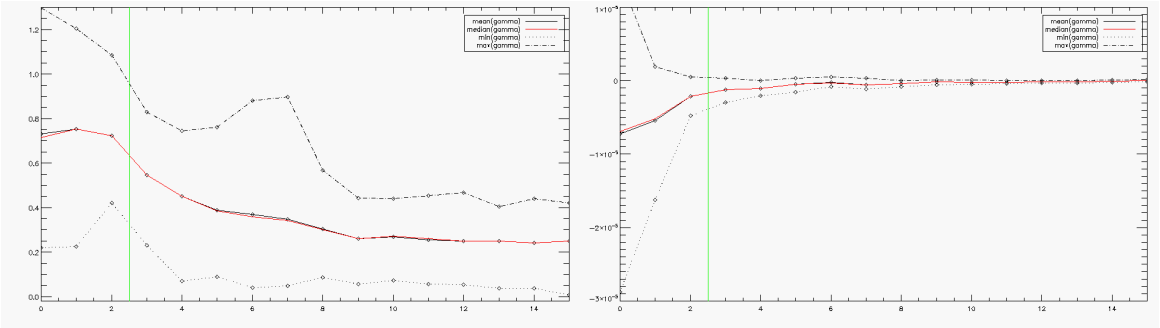

(b) : Evolution of the scaling factor γ (left) and the affine factor γ' (right) for a L1-affine optimization.

Figure 3.27 – Evolution of the minimum, maximum and mean value of the computed scaling (left) and affine (right) factors as a function of the distance to the star (for annuli of $1\lambda/D$ width, the IWA inducing an offset of $2\lambda/D$), either with the least square computations of the factor or the L1-affine, for the NaCo images of β Pictoris (Sect. 3.2.1). The green solid line is located at the separation where the planet β Pictoris b is present.

- At close separation ($\leq 5\lambda/D$) the L1-affine fit proves better at subtracting the speckle and it preserves the planetary signature shape (Fig. 3.26).
- At larger separation ($> 5\lambda/D$), the L1-affine fit is equivalent to the least-square fit (Fig. 3.27).

In the next section, I will check these conclusions on the SNR maps provided by ANDROMEDA.

3.2.4.1 Impact of the robust affine fit on the SNR map

The results presented in this section are obtained by running ANDROMEDA on the β Pictoris data from NaCo with the user-parameters set gathered in the Tab. 3.2.

User-defined parameter	**Used value**
Filtering fraction, F	1/4
Minimum distance for the ADI, δ_{min}	1.0 λ/D
Width of the annuli for the ADI, dr	1.0 λ/D
Ratio optimization to subtraction areas for the ADI, R_A	1
Size of the reference PSF window, N_{psf}	16×16 pixels
Inner working angle, IWA	2 λ/D
Smoothing of the SNR robust standard deviation profile, N_{smooth}	2 pixels

Table 3.2 – User-defined parameter values chosen to run ANDROMEDA on the β Pictoris VLT/NaCo data.

Fig. 3.28 shows the corresponding different SNR maps. The SNR map obtained with an optimization method for the ADI (Fig. 3.28-Middle and Right) shows residuals distributed within annuli of typical width d_r, that are not present in the SNR map without optimization (Fig. 3.28-Left). Also the SNR maps obtained with a least-square optimized ADI or a L1-affine optimized ADI look very

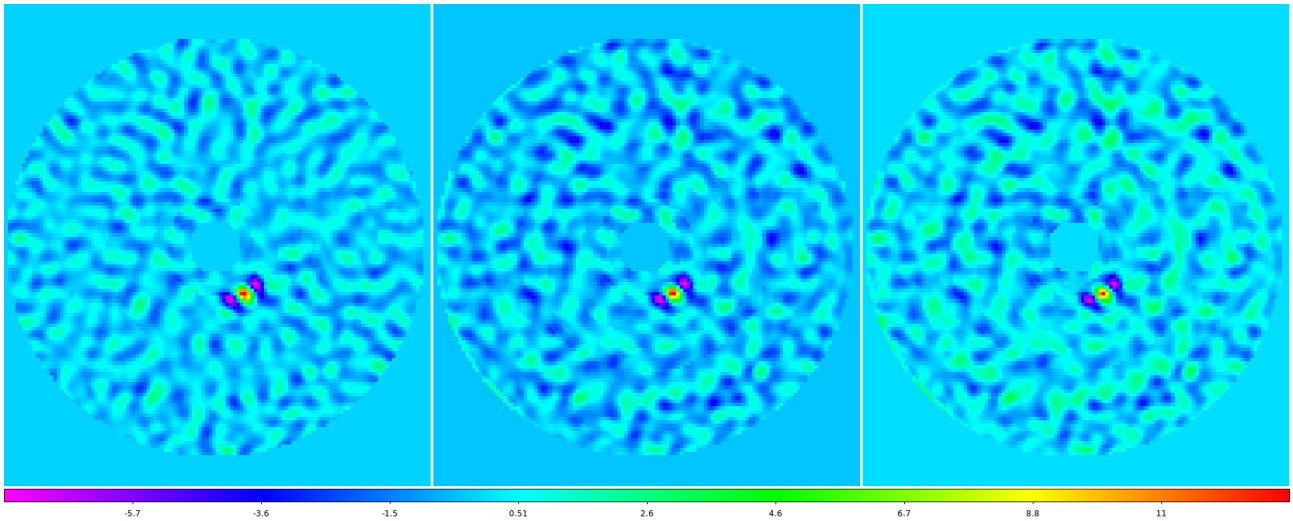

Figure 3.28 – SNR maps obtained by running ANDROMEDA on the data set presented at Sect. 3.2.1, using the parameters gathered in Tab. 3.2. From left to right: SNR map obtained without optimization of the ADI, SNR map obtained with a least-square optimization of the ADI and SNR map obtained with a L1-affine optimization of the ADI. In each of these maps, the companion β Pictoris b is the only signal found above the 5σ threshold, with a SNR of respectively 16.24σ, 14.8σ and 14.08σ.

similar. By looking closer at these maps, it appears that the residuals level is slightly lower at close separation when using a L1-affine optimized ADI (see Fig. 3.30).

Note that the normalization profile obtained without the optimization shows clearly the two regimes, showing a steep slope close to the star and a lower slope from a certain separation, here from about 15-20 pixels (about 500mas), as shown on Fig. 3.29-Left. On the contrary, the normalization profile obtained with the L1-affine optimization has a constant slope all over the field, as shown on Fig. 3.29-Right.

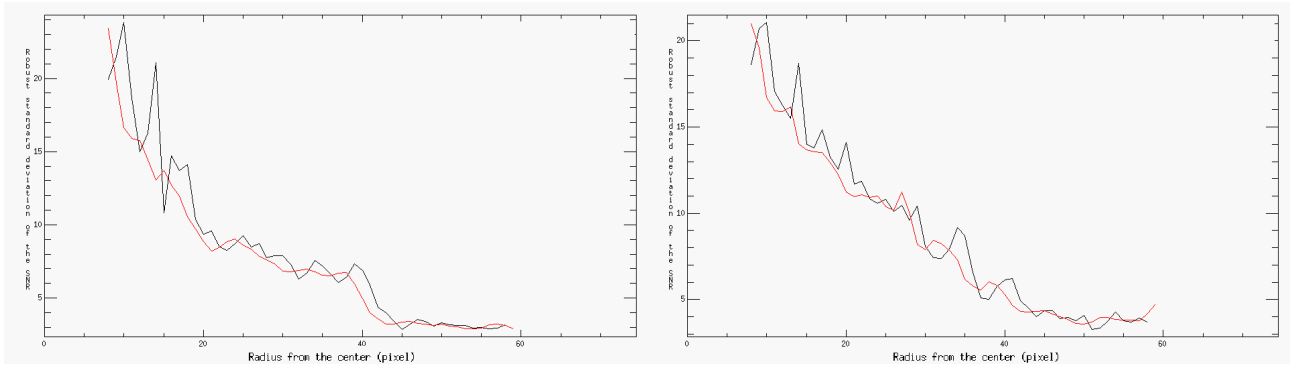

Figure 3.29 – Normalization profiles of the SNR maps of the β Pictoris data (red solid line) obtained by smoothing the radial standard deviation profile of the SNR (black solid line) by three pixels, following the method explained at Sect. 3.1.2. Left: without ADI optimization. Right: with the L1-affine optimization of the ADI.

The planetary signal patterns in the SNR map are affected by the kind of differential image optimization used. Without optimization the planetary signature is symmetrical (see Fig. 3.26) thus the resulting planetary pattern is regular and similar to the theoretical shape (as in Fig. 2.5). However, the optimization induces a slight distortion of the pattern but the difference on the position estimation is below a tenth of a pixel for this planet (order of magnitude, since it depends on the scaling factor). This distortion is due to the signal subtraction when the positive and negative peaks of the planetary signal overlap. The scaling factor shrinks the negative peak (as it is usually smaller than one) which affects the signature when the subtraction is made (which explains why the red and green positive peaks of the planet signature are lower than the orange positive peak on Fig. 3.26).

To visualize better the effect of the L1-affine optimization at close separation, the Fig. 3.30 shows the robust standard deviation profile of the SNR maps, according to the different ADI optimization procedures. Compared to the other methods, the L1-affine optimization indeed permits to reach a lower residuals dispersion around zero and lower residuals, in particular at close separation. At larger separation (from about 1″), the L1 affine profile and the LS profiles are the same. Note that the presence of the β Pictoris companion seems to indeed disturb the least-square fit which shows higher residuals at this separation (green line on Fig. 3.30).

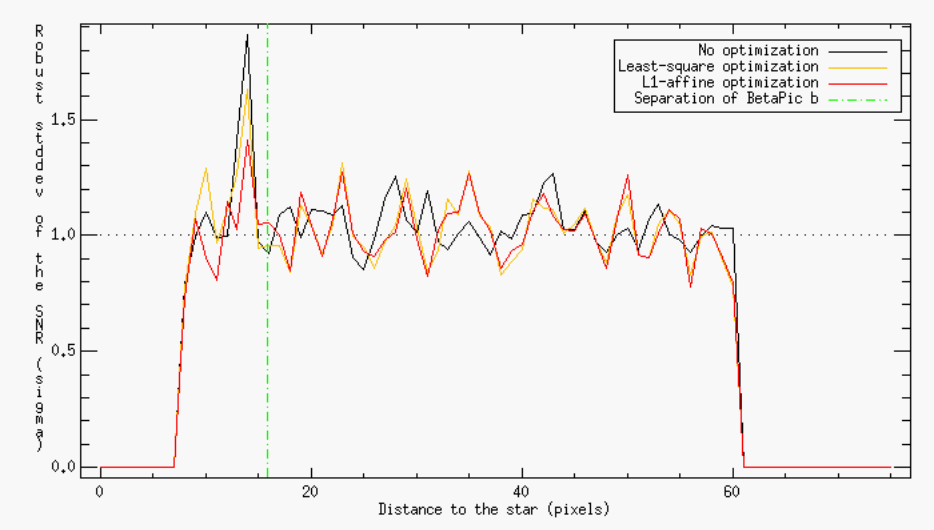

Figure 3.30 – Radial profiles of the robust standard deviation of the SNR map, according to the different methods of ADI optimization. Note that the peaks around 12 pixels are not due to the planetary companion whose position is shown in green, but to bright speckles.

However, as written in the caption of Fig. 3.28, the SNR of the companion decreases when using the optimization. As a consequence, even if the residuals level is indeed reduced at short separation, the corresponding detection limit has to be compared to take into account the SNR difference. Fig. 3.31 shows the detection limits computed by ANDROMEDA under the conditions gathered in Tab. 3.2, for the different ADI optimization methods. From this figure, it appears that the detection limit is

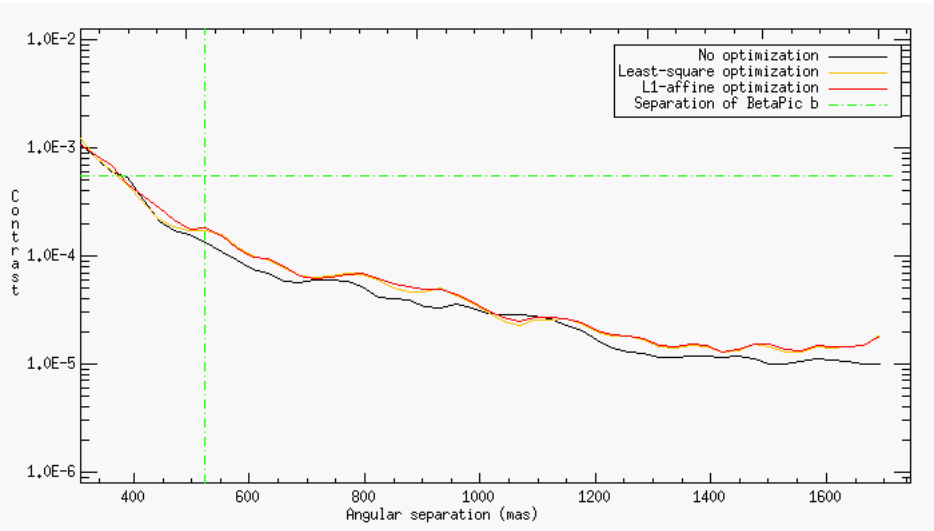

Figure 3.31 – Detection limit computed by ANDROMEDA, according to the different methods of ADI optimization.

globally lower for the method without optimization (black solid line on Fig. 3.31). Also, the detection curves obtained using the least-square optimization and with the L1-affine optimization are very similar

(note that at the separation of the companion β Pictoris b, the least-square is slightly lower than the L1-affine which is in line with the fact the planetary companion has a higher SNR in the latter case).

Note that if there are no speckles (or if they are perfectly fixed), it is better to perform the image difference without optimization. Indeed, on the one hand, it is easier to search for a symmetrical planetary signature via the MLE and on the second, the scatter plot of the points in the first annulus as a function of the points in the second annulus (as in Fig. 3.20) will be symmetrical wrt the bisector.

As a conclusion, the L1-affine optimization does reduce the residuals level but it does not reach a better detection limit. Also, the L1-affine fit is equivalent to the least-square fit at larger distance (from typically $1''$).

3.2.4.2 Conclusion: which differential imaging optimization for which case

As a conclusion, there are three main cases to be considered:

1. If the dominant noise in the images originates from the photon and detector noise, a simple ADI without optimization provides more accurate results;

2. If the dominant noise in the images originates from the flux difference between the two frames, the least-square fit is equivalent to the robust affine fit (when filtering);

3. If the dominant noise in the images originates from the quasi-static speckle noise, the robust-affine fit is the most adapted solution.

The robust-affine fit has been implemented and its application on real data has proven equally or more efficient at reducing the speckle noise on both simulated and real data, while preserving the planetary signal, if any. This L1-Affine optimization is particularly good at very close separation where the intensity of the numerous speckles varies a lot from one image of the couple to the other due to the poor rotation field velocity.

Provided that the image subtraction is performed with an adapted optimization, we saw that the planetary signature is clearly affected by the scaling factor. Thus, a natural question which arose from this work is: do we have to take into account the scaling factor when building the model of the planetary signature ? In the next section, this question is discussed in details.

3.2.5 Adapting the model of the planetary signature in the differential images

From the latter considerations, the question arose of whether one must take into account the scaling factor when building the model of the planetary signal to be inverted. This model must correspond as much as possible to the resulting planetary signature appearing in the differential image obtained following:

$$\Delta(k, \mathbf{r}) = i_k(t_1, \mathbf{r_{sub}}) - \gamma_k \, i_k(t_2, \mathbf{r_{sub}}) - \gamma'_k \tag{3.9}$$

Where γ_k and γ'_k are computed either with a least-square fit (Eq. 2.12) or a robust-affine fit (Eq. 3.6), over the subtraction area $\mathbf{r_{sub}}$.

Taking into account the scaling factor in the planetary signature model In this first case, the model is thus written:

$$m_k(a, \mathbf{r_0}) = p_k(\mathbf{r_{t_1}}) - \gamma_k \, p_k(\mathbf{r_{t_2}}) \tag{3.10}$$

This model is appropriate under the assumption that the planetary signal has exactly the same shape and intensity in the two frames, that is to say it does not vary along with the stellar halo. In practice, this can be the case when the dominant factor, responsible for the temporal variations of the image quality, affects only the on-axis PSF (i.e., the jitter temporal variation is dominant), that is to say when the speckles decorrelate from t_1 to t_2 but the planetary signal remains the same. For instance, an increased wind speed might significantly increase the AO temporal residuals and thus the level of stellar halo in the corrected area, whereas the Strehl ratio (and companion PSF core) is hardly modified. Thus when tuning the second image, $i_k(t_2, \mathbf{r})$, via the scaling factor, the negative pattern

is scaled and to take into account this scaling, the scaling factor γ must be taken into account in the model (which is the original way implemented in ANDROMEDA). This also means the planetary signature model is non-symmetrical, the negative bump will be greater than -1 since, when filtering, γ_{LS} is still less than 1.0 (see typical planetary signature on Fig. 3.32-Right).

Without taking into account the scaling factor in the planetary signature model In this second case, the model writes:

$$m_k(a, \mathbf{r_0}) = p_k(\mathbf{r_{t_1}}) - p_k(\mathbf{r_{t_2}}) \tag{3.11}$$

This model is appropriate under the assumption that the planetary signal varies in the same way as the stellar halo. In practice, this can be the case when the dominant factor, responsible for the temporal variations of the image quality, affects the whole field of view the same way (for instance, clouds passing in front of the telescope pupil). Thus, optimizing the ADI (scaling $i_k(t_2, \mathbf{r_{sub}})$ wrt $i_k(t_1, \mathbf{r_{sub}})$) is equivalent to making the planet signature symmetrical in the resulting differential image (see typical planetary signature on Fig. 3.32-Left), hence the scaling factor γ must not be taken into account in the model.

Impact on the ANDROMEDA performance on real data Choosing either one or the other model thus depends on the observing conditions (and it might turn out to be a mix of these two cases). For instance, on the TYC-8979-1683-1 data, the scaling factor must be taken into account to spot the synthetic planetary companions since they have been injected without taking into account any flux variation (only the field rotation is taken into account during the injection). However, in NaCo $L\prime$ data and on SPHERE data, it is better to not take into account the scaling factor, as shown on Fig. 3.33, which shows the SNR map obtained either with or without the scaling factor in the model (after using a least-square optimized scaling factor during the ADI process).

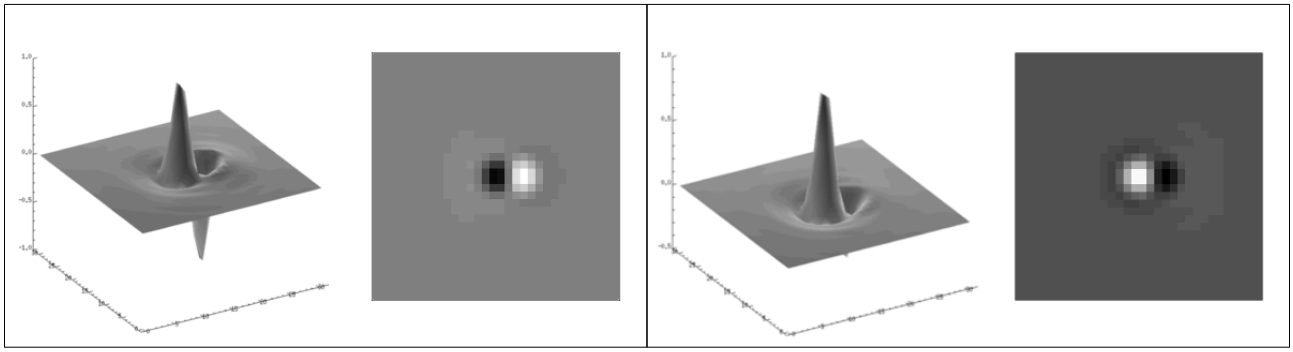

Figure 3.32 – Model of the planet signature (with pre-filtering, $F = 1/4$), without (left) or with (right) the scaling factor taken into account ($\gamma_{LS} = 0.4$ in this example). As in Fig. 2.4, this planet signature is obtained by shifting the reference PSF of δ_{min} (here only the distance δ_{min} is not angular but along the x-axis; $\delta_{min} = 1\lambda/D$). This illustration is made thanks to an Airy pattern sampled with an oversampling rate of 1.6 and normalized to its maximum.

Another more practical interpretation of this result is that when using a non-symmetrical shape, mostly when γ_{LS} is lower than 0.5 which happens often on real data (see Fig. 3.27), the signature is mainly made of the positive bump (as on Fig. 3.32) which will correlate better with speckle residuals. On the contrary, there is lower chance to correlate with residual speckles when the planetary signature model is symmetrical which is a shape very specific to a point source. The latter interpretation can be verified by running ANDROMEDA in the same conditions, either with or without the scaling factor in the model, as in next section.

Impact on the ANDROMEDA SNR maps Fig. 3.28 shows the different SNR maps obtained by running ANDROMEDA on the β Pictoris data from NaCo (Sect. 3.2.1) using the parameters gather in Tab. 3.2 for the two ADI optimization and the two different models. The SNR maps obtained with

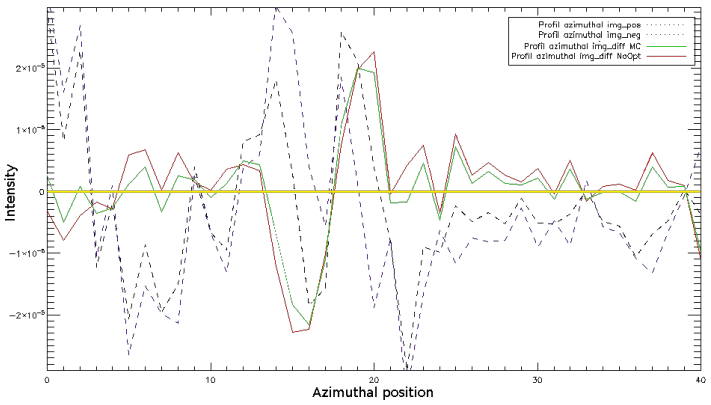

(a) : Azimuthal profile of the differential image for the annulus of 1 pixel width containing the planetary companion β Pictoris b, with or without the optimization.

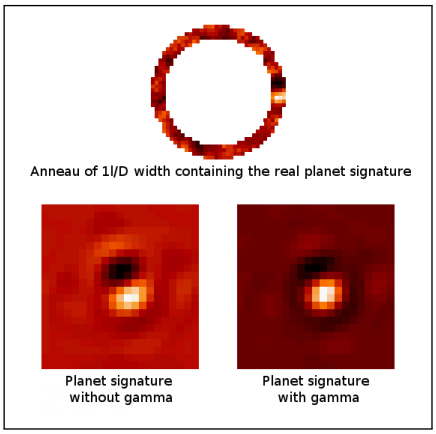

(b) : One differential annulus of width $d_r = 1\lambda/D$ containing the signal of β Pictoris b and corresponding planet signature.

Figure 3.33 – Shape of the planetary signature due to the companion β Pictoris b in the NaCo images, located at about 455mas, using $\delta_{min} = 0.5\lambda/D$.

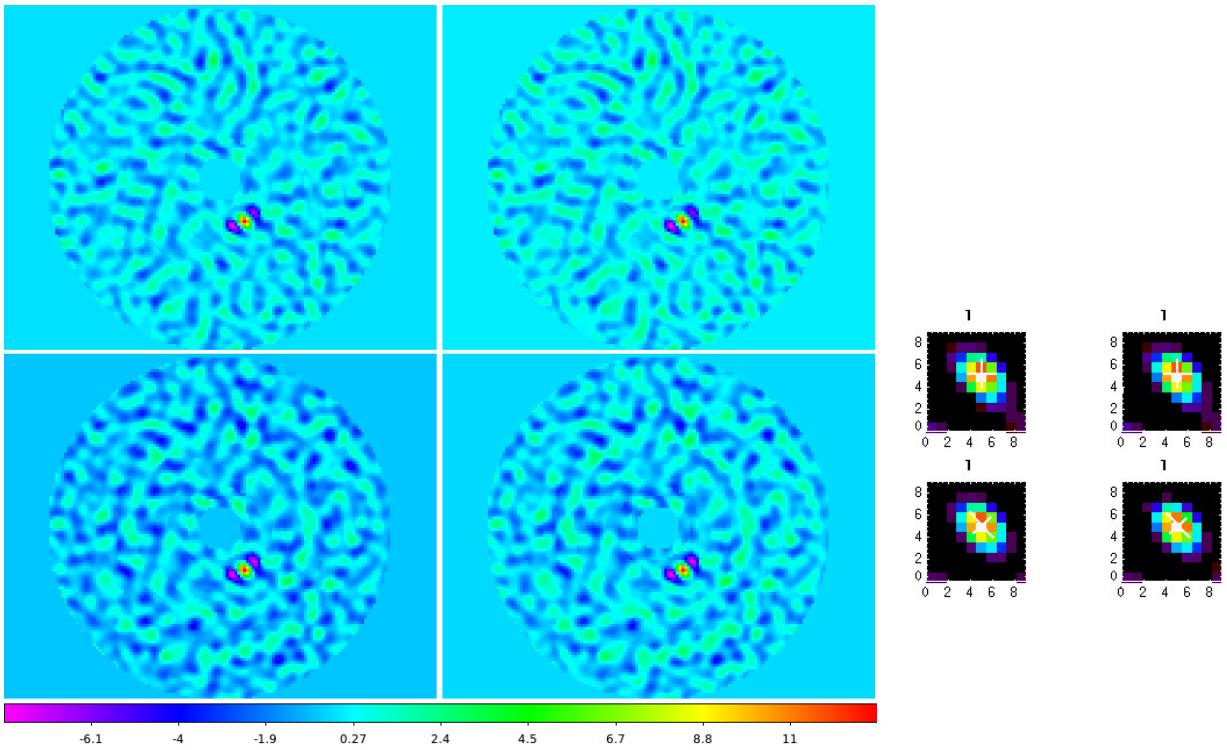

Figure 3.34 – SNR maps (left) and corresponding subimages (right) obtained by running ANDROMEDA on the data set presented at Sect. 3.2.1, using the parameters gathered in Tab. 3.2. From left to right: SNR map obtained with a least-square optimization and SNR map obtained with a L1-affine optimization. From top to bottom: SNR map obtained by using a model without the scaling factor and SNR map obtained by using a model with the scaling factor. In each of these maps, the companion β Pictoris b is the only signal found above the 5σ threshold, with a SNR of (from left to right, top to bottom): 14.80σ, 14.08σ, 14.47σ and 14.03σ.

the scaling factor taken into account in the model shows higher residuals into annular areas which could arise above the threshold set. For this specific data set, the scaling factor should better not be taken into account.

As a consequence, for this data set, the corresponding detection limit curves, presented on Fig. 3.35 are lower in the case where the scaling factor is not taken into account in the model of the planetary signature model.

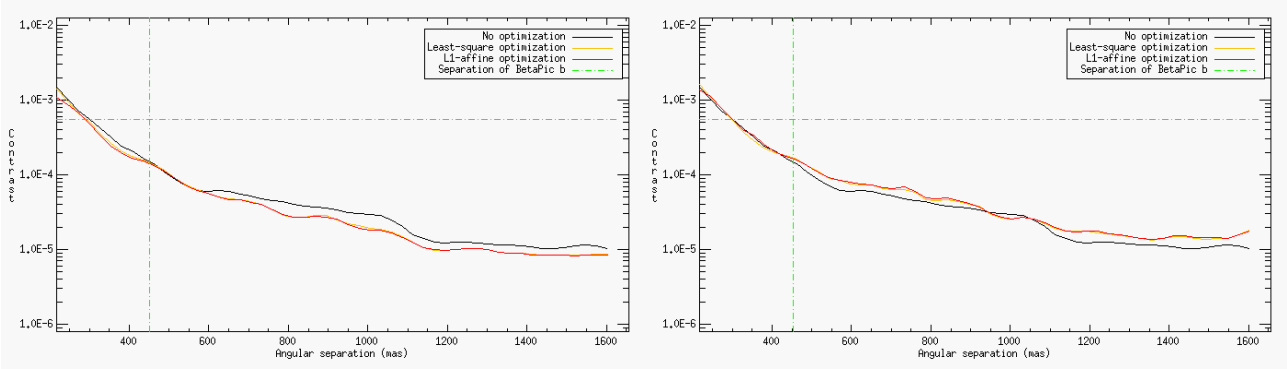

Figure 3.35 – Detection limits corresponding to the SNR map presented on Fig. 3.34. From left to right: Without the scaling factor and with the scaling factor.

As a conclusion, if some detections are suspicious and could be artifacts, one way to check if they are true detection is to run ANDROMEDA twice, once with and once without the scaling factor, in order to check if the detection remain in both SNR maps with a significant SNR.

Note that in any case, the affine factor $\gamma\prime$ must not be taken into account since it is only used to obtain a better speckle subtraction during the ADI process. It is an offset used only for the subtraction and it does not affect the planetary companion signal since its value only introduces an extremely low offset (see Fig. 3.27b-Right).

At last, choosing either model only affects the SNR of the companion and the SNR map residuals since the flux is estimated wrt the positive bump $p_k(\mathbf{r_{t_1}})$ which is normalized and not scaled by any factor.

3.3 Automatic companion extraction, properties and reliability criteria

This section describes the detection module that I have implemented in ANDROMEDA, along with the ANDROMEDA approach. This module extracts the information recorded in the three maps output by ANDROMEDA: the SNR map, the flux map and the map of the standard deviation of the flux. This detection module automatically provides the list of the *detections* (here referring to any signal found above the threshold set), and sort them out into so-called *firm detections* and *probable artifacts* (Sect. 3.3.3). Once this sorting is completed, the signals are thoroughly analyzed to obtain their sub-pixel position (Sect. 3.3.1) and contrast wrt the central star (Sect. 3.3.2), along with the corresponding error bars. Then the 1D detection limit curve is computed by the module (Sect. 3.3.4). One specificity of this module is that it allows the used to visualize and to store the results in a user-friendly way (Sect. 3.3.5).

Note that this toolbox can be used in line with other image processing methods, as long as point source signals are searched in a 2D-map for a given threshold. It is easy to adapt this module in order to analyze such output from various image processing methods.

3.3.1 Detection and astrometry

For the detection and position estimation, the SNR map is used.

Automatic detection The automatic detection consists in finding every signal above the chosen threshold. To do so the highest signal is looked for and it is checked whether it is above the threshold set. If it is the case, the signal is regarded as a *detection*. It is then analyzed before being removed from the SNR map by erasing all the surrounding pixels belonging to this detected signal which stand above the threshold. Then, the next highest signal is looked for, until one is found to be below the

threshold. The detections are thus gathered from the highest SNR signal to the lowest following this clean-like scheme.

Subpixel position estimation To analyze the signal, a subwindow is extracted from the SNR map. This square subwindow must fully enclose the planetary-like pattern. Knowing the expected shape of this pattern (see Sect. 3.1.1 for instance), the typical size of the subwindow is of $3\lambda/D \times 3\lambda/D$. Thus, it only depends on the pixel scale of the images and on the wavelength of observation.

Within this window, a 2D-Gaussian fit of the pattern is performed. Rigorously this SNR pattern would be better fitted by the exact shape of the expected pattern (as in Fig. 2.5) than by a Gaussian function. However the important aspect in the analysis of the pattern is the computed FWHM and the position of the maximum, and the discrepancy of the pattern to a Gaussian shape pattern is mainly on the edges of the pattern. Thus a more corresponding fit would not bring more information than a Gaussian fit, and for simplicity, a Gaussian fit has been implemented. In IDL this fit is performed by using the `MPFIT2DPEAK` procedures by Markwardt (2009).

From this 2D-Gaussian fit, the position of the maximum of the signal is retrieved, as sketched on Fig. 3.36. The final estimated position is the position of the maximum of the 2D-Gaussian fit of the analyzed SNR pattern. Thus, this procedure provides a subpixel precision on the estimated position.

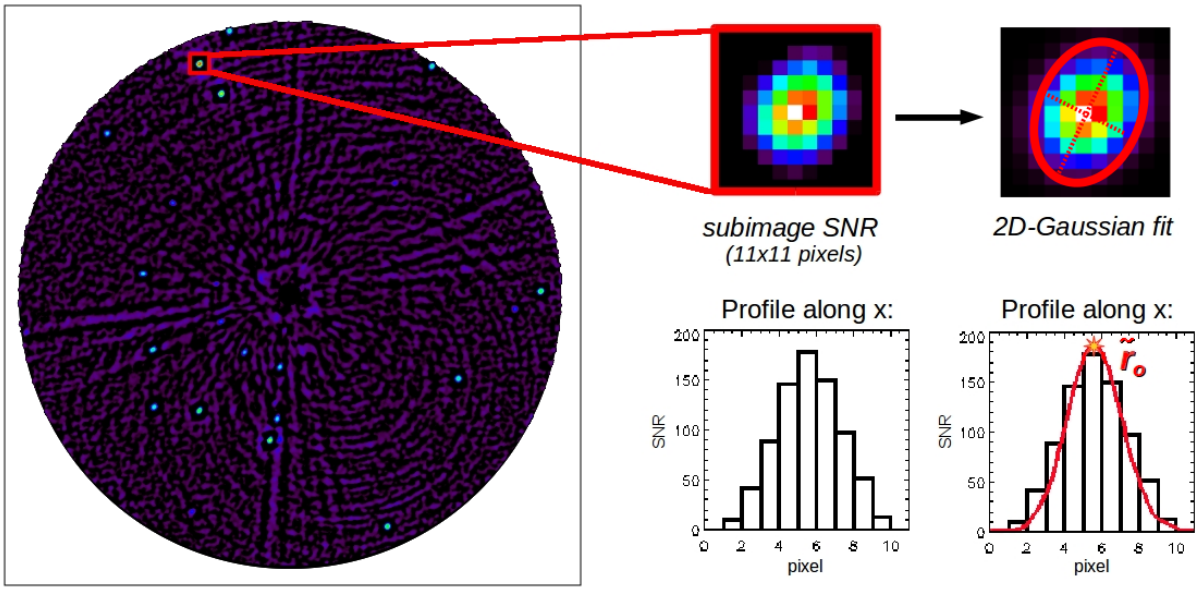

Figure 3.36 – Sketch of the determining of the signal position by a 2D-Gaussian fit.

Note that the normalization procedure might bias the position estimation in the radial direction, depending on the slope of the normalization profile where the detection is localized. If the slope is very steep, it affects the position of the planetary signal of less than three pixels (backwards if the slope is negative). It is thus better to have a quite smoothed normalization profile to remove the jagged parts whose slopes are very steep, in case a planetary companion could be present at this separation.

Estimation of the detection SNR The SNR of the detected signal is given by the maximum of the 2D-Gaussian fit (which is the value of the signal at the estimated position).

Estimation of the 3-σ error on the position estimation This module computes and provides the 3σ error on the 2D-Gaussian uncertainty, following three considerations:

1- The `MPFIT2DPEAK` procedure provides the measured 1σ uncertainties on the fit parameters (fitting error). To compute this uncertainty, I set a weight map which values 1 for any pixel within

the subimage which is above threshold, else 0.

2- The `MPFIT2DPEAK` procedure assumes that the chi-square is equal to one (that is to say that pure noise is surounding the pattern). In order to take the real noise distribution into account, the latter error is scaled by the true reduced chi-square value: if the reduced chi-square is greater than one, it is multiplied to the previous error.

3- The latter error assumes that the surrounding noise has a variance of 1. Thus, I computed the azimuthal robust standard deviation of the SNR inside the annuli where the analyzed detection lies (of width the size of the subimage). If this value is greater than one (which should not be the case thanks to the normalization), it is also multiplied to the previous error.

Eventually the final error is multiplied by 3 to obtain the 3σ error bar on the estimated position. This error bar only account for the subpixel position estimation once the SNR map is computed. This error bar does not provide the errors due to the algorithm robustness in itself (due to the sensitivity of the algorithm to its user-defined parameters). These errors are discussed in the next chapter in which I make vary each of the user-defined parameters to evaluate the deviation of the astrometric estimations wrt to the retrieved value (Chap 4).

3.3.2 Photometry

For the contrast estimation, the flux map is used. The exact same subimage is extracted but in the flux map. A 2D-Gaussian fit is also performed on the planetary pattern (which should have the same shape in both the SNR and flux maps). The estimated flux is the flux read on the 2D Gaussian fit at the sub-pixel position retrieved earlier: $\hat{a}(\hat{\mathbf{r_0}})$.

Contrast estimation The read flux is given wrt to the input reference PSF. The first step is to convert this input reference PSF according to the science images. This conversion is made from the knowledge about the observation conditions used to image the reference PSF: its integration time, the transmission of the neutral density (if one used), the throughput of the coronagraph (if one used) or any other parameter which would affect the integrated flux of the reference PSF wrt the integrated flux in the science images. Note that usually, the reduced reference PSF is normalized to all these parameters. The second step is to convert the estimated intensity into contrast. Provided that ANDROMEDA estimates the flux wrt the total flux included in the input reference PSF[7] (which is given within a subwindow of size N_{PSF}), the contrast is obtained by simply dividing the estimated signal intensity by the total converted flux within the reference PSF window[8].

Note that this approach is fully consistent during the whole ANDROMEDA process: any pre-processing applied to the data is also applied to the reference PSF (such as the pre-filtering and optimized subtraction for instance). As a consequence the estimated flux is not biased by such process, and contrary to other approaches such as PCA or LOCI, there is no companion flux loss.

Estimation of the 3-σ error on the contrast estimation The 1σ error on the flux estimation is directly read on the flux standard deviation map, at the estimated position: $err_{\hat{a}} = \sigma(\hat{a}(\hat{\mathbf{r_0}})$. The detection module converts the retrieved value in terms of contrast, following the same procedure as for the contrast estimation, and finally provides the corresponding 3σ error bar.

Note that this error does not take into account the fact that the observation conditions (and thus the reference PSF) may have varied during the integration time (see Chap. 6.5.5 for perspectives on this aspect).

[7] By doing so, the potential time variations of the PSF are not taken into account since, for now, we do not have any information regarding its temporal variation.

[8] Indeed, the planetary signature model is built from the input PSF and the flux is estimated via the sum on every position $\mathbf{r}$ in Eq. 2.19.

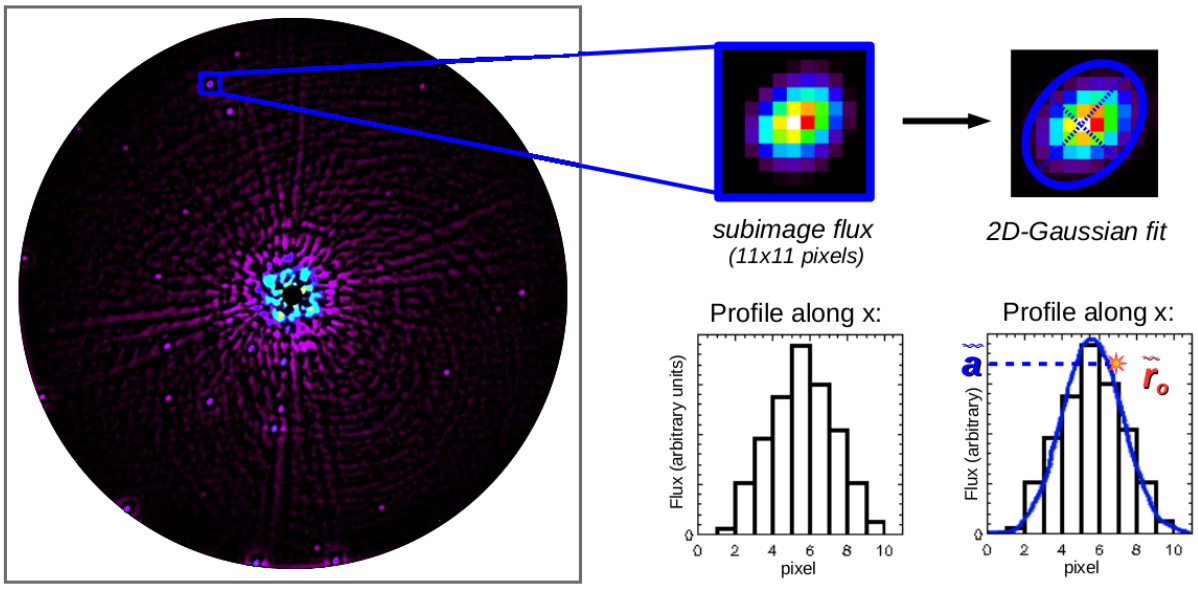

Figure 3.37 – Sketch of the determining of the point source signal flux by a 2D-Gaussian fit, at the estimated position $\hat{r_0}$.

3.3.3 Sorting out artifacts from probable true detections

Some false alarms might remain above the threshold whereas they are actually not true point sources. The detection module has been developed to sort out such artifacts. The whole sorting method is based on the morphological aspect of the patterns. Theoretically, the pattern should be oval with its major axis in the radial direction and the minor axis length linked with the δ_{min} set. As an example the signal arises from an intense residual speckle which therefore correlated with the planetary signature model, the resulting pattern should be distorted compared to the theoretical expected shape.

By scrutinizing the obtained SNR map, four pathologic cases have been encountered:

1. If the signal pattern is broader than the theoretical expected one, it means that this signal is certainly a residual speckle;
2. Signals arising from residual diffraction patterns due to the spider of the telescope which are not efficiently subtracted: they are significantly elongated in the radial direction;
3. Signals due to the bulges caused by the spatial filtering of the reference PSF (called *tertiary lobes* hereafter): they have a very specific sickle-shape and are found at a deterministic distance from a high SNR signal (see Sect. 3.1.1);
4. Signals too close to the edge which cannot be investigated.

All these artifacts have a specific signature in the SNR map. To disentangle them from potentially true detections, I chose to constrain the 2D-Gaussian fit as follow:

-The fit must converge, else it means that the signal has a very distorted shape;

-The center of the Gaussian fit should not deviate for more than $0.25\lambda/D$ from the highest pixel position in the subimage (about 0.75 pixel in H-band using NaCo);

-The HWHM (Gaussian sigma) semi-major axis of the Gaussian must be less or equal than $0.85\lambda/D$ (about 2.8 pixels in H-band using NaCo);

-The HWHM (Gaussian sigma) semi-minor axis of the Gaussian must be greater or equal than $0.2\lambda/D$ (about 0.66 pixel in H-band using NaCo);

We added a weight map to take into account in the analysis, mostly the pixels above the threshold set.

Note that constraining the direction of the semi-major axis of the ellipse does not bring more information and might be too constraining when using the least-square optimization for the ADI (since the patterns appear more symmetrical).

These artifact are called *ill-fitted* detections in the following and are a posteriori rejected by the pipeline.

The Fig. 3.38 shows these four typical signals rejected upon morphological aspects. Notably, the lower the detection, the more the detections are rejected (as shown by a white asterisk in Fig. 3.38-Right, from the detection #37 there are only artifacts). This confirms that the a posteriori rejection uses a good criterion to sort out true detections from potential artifacts.

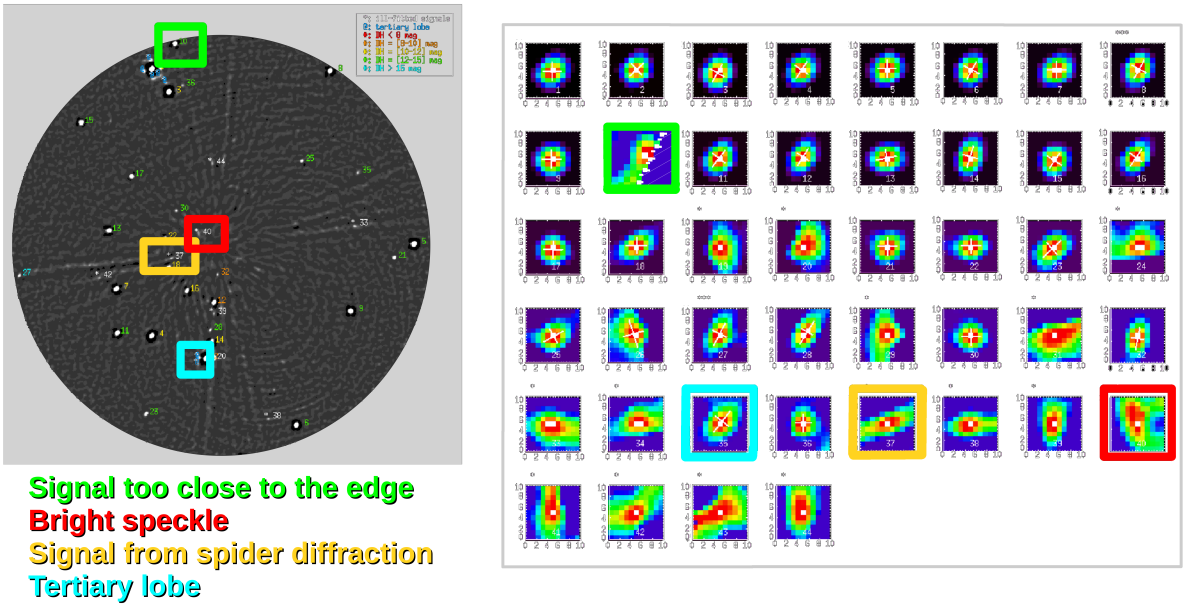

Figure 3.38 – Typical artifact a posteriori rejected by constraining the 2D-Gaussian fit of the signals. Left: Detection map with four typical case. Right: Corresponding subimages.

3.3.4 Estimation of the detection limit

For the detection limit estimation, the map of the standard deviation of the flux is used. In order to give a fair idea of the detection limit, I chose to calculate the azimuthal median profile of the latter map. However, one can chose to calculate the minimum azimuthal value (below which no companion can be found using ANDROMEDA), the detection limit according to different thresholds set (in order to have an idea of the dependence to the threshold) and/or correct the detection limit for the small sample separation as explained earlier.

3.3.5 Ergonomics of the detection module

To make the ANDROMEDA pipeline user-friendly, some images and files are displayed and created when running the detection module. I quickly mention here what kind of files are created. The following chapter will make use of these output to review the ANDROMEDA performance.

Detection map When running the detection module, a so-called detection map is created, displayed and recorded. This is the SNR map on which each detection is indicated by an index (the lower index the higher its SNR) whose color correspond to a contrast range. Moreover, if the signal has been a posteriori rejected, it is also indicated: An asterisk means it is either a residual speckle or a spider diffraction artifact; a sign means it is a tertiary lobe artifact; three asterisks means that the signal is too close to the edge and cannot be correctly analyzed. See Fig. 3.38-Left for examples.

Subimages of the detections An image showing all the subimages enclosing the detected signals is displayed and recorded. These subimages are shown from the highest to the lowest SNR (from the lowest to the higher index). On each of the subimages, if the 2D Gaussian fit has converged, a cross showing the FWHM of the 2D Gaussian fit is over-plotted on the signal. If the fit could not converge, an asterisk is shown above the subimage. If the signal is too close to the edge and cannot be correctly analyzed, three asterisks are shown above the subimage. See Fig. 3.38-Right for examples.

Detection limit The detection limit is plotted and the detections are placed on the same graph. The median as well as the minimum detection limit are plotted on the graph.

Results file In the results file, all the needed information about the detections are gathered (index of the detection, SNR, position, flux, flags about the Gaussian fit etc.). This file permits to a posteriori check the detections parameters, even the one rejected to better judge for the truthfulness of the detected point source.

In order to take the ANDROMEDA pipeline in hand, a user manual describes in details the output given by the detection module and how to interpret them. This user manual can be found in the appendix, App. B. Please refer to this document for more technical details.

Summary: ANDROMEDA in its operational state

The ANDROMEDA approach has been implemented into a pipeline which is now able to detect and characterize point sources present in the field of view. The pipeline is fully operational and, from the scientific images, the reference PSF and the parallactic angles, delivers the position, the SNR and the contrast of each detected point sources, along with the complete detection limit. This image processing tool has interesting features, new to other image processing pipelines used so far in the exoplanet imaging community, among which, an automatic detection process, a bias-less contrast estimate and a detection module providing direct estimates and valuable information to assess the detection quality. Also, the whole pipeline runs quite fast (about 20 minutes for $512 \times 512 \times 128$ images) which is another advantage compared to, for instance, the LOCI-based pipelines.

Fig. 3.39 shows a diagram of the fully operational ANDROMEDA pipeline.

In order to look deeper into its performance and probe the principal limitations of the method, the next chapter analyzes the sensitivity of ANDROMEDA to its user-parameters to investigate potential optimal set of parameters, and which ones are the most critical. A fine analysis of its performance in terms of detection and characterization capacity is also conducted.

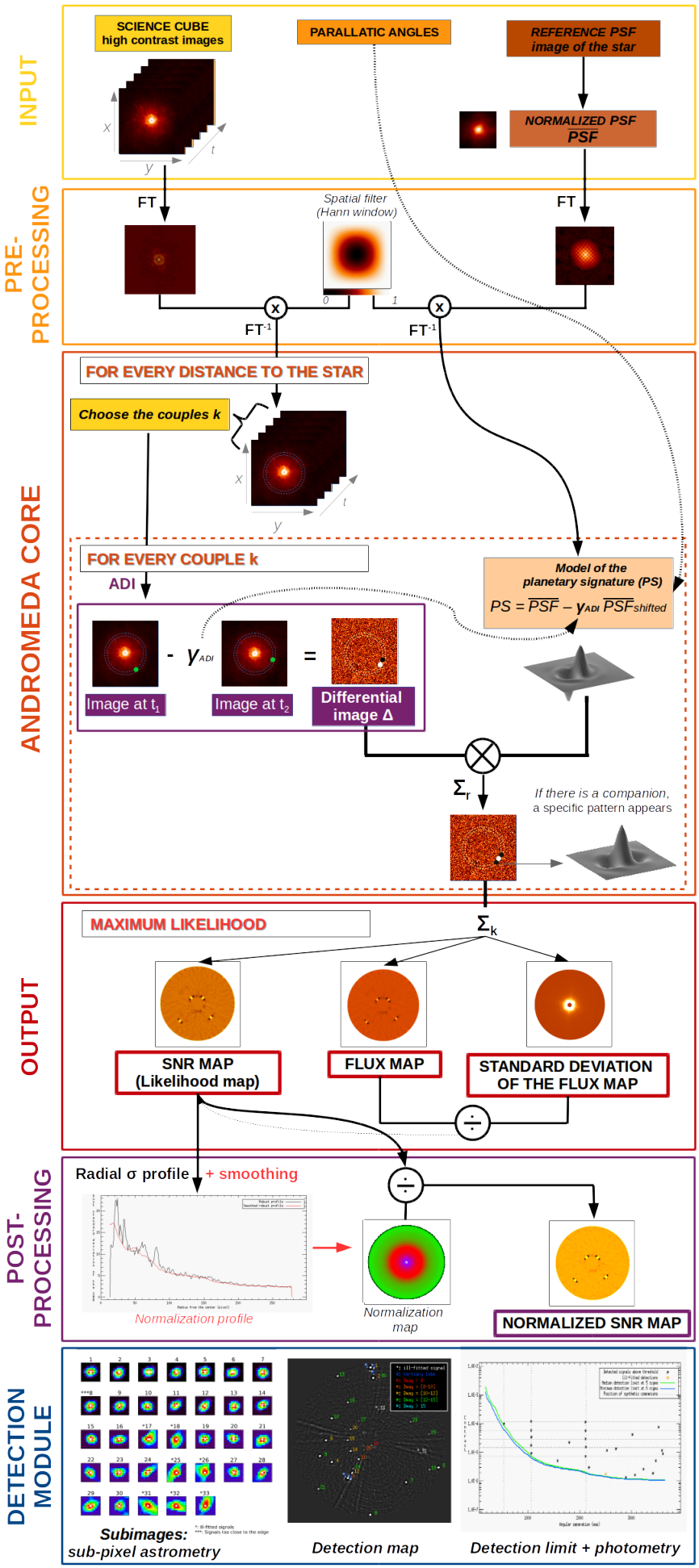

Figure 3.39 – Diagram describing the operational ANDROMEDA pipeline from the input to its delivered output.

Chapter 4

Sensitivity to user-defined parameters and final contrast performance

Contents

4.1 Test case: VLT/NaCo data in H-band 119
4.1.1 Target star: data set TYC-8979-1683-1 120
4.1.2 Reference case: user-parameters setting 120
4.1.3 Reference case: Results with ANDROMEDA 121
4.2 Sensitivity to the user-defined parameters 121
4.2.1 Pre-filtering of the reduced images 122
4.2.2 Building the differential images via ADI 124
4.2.3 Building the model of the differential images 130
4.2.4 Post-normalization of the SNR map 134
4.3 Discussion on the threshold set for the detection 137
4.4 Performance of the ANDROMEDA method 138

Now that the ANDROMEDA pipeline is fully operational on real data and provides the necessary information to correctly interpret its results, there is a need in characterizing its performance in details.

In the framework of the ANDROMEDA pipeline development, one goal is to enable a systematic use of the algorithm so that it is less dependent upon the user. To do so, it is needed to be aware of the impact of each of its user-parameters in order to obtain the fewest number of these parameters to be tuned and to choose the default values of these parameters.

The goal of this chapter is to look deeper into the performance of ANDROMEDA, in terms of sensitivity to the user-parameters (Sect. 4.2), in terms of extraction capabilities according to the threshold set (Sect. 4.3) and in terms of its characterization capabilities (Sect. 4.4). To discuss these three points, I will use the TYC-8979-1683-1 NaCo data in H-band described in Sect. 2.3.1, under the conditions that I will describe in Sect. 4.1.

4.1 Test case: VLT/NaCo data in H-band

To look into details on the ability of ANDROMEDA to extract the companions information, the sensitivity tests will be conducted on NaCo data taken in H-band. Such a data set is quite constraining, as it is less stable than SPHERE-IRDIS data and more challenging than $L\prime$-band observations for instance. Working on NaCo H-band data thus provides general statements whose conclusions can be applied on other instruments or setup of better quality (e.g., see Chap. 6 for numerous applications of ANDROMEDA on SPHERE data).

4.1.1 Target star: data set TYC-8979-1683-1

The target star, the observation conditions and the reduced images properties are described in details at Sect. 2.3.1.

4.1.2 Reference case: user-parameters setting

In order to evaluate the response of ANDROMEDA to a variation of its user-defined parameters, we need a reference case to be compared with the results obtained. The following Tab. 4.1 summarizes the values of this reference test-case which has been previously used to develop the detection module at Sect. 3.3. The chosen values for this reference case are based upon previous work on simulated data, as well as my preliminary work on real data, which proved that this set of user-parameters should be the most appropriate to begin with.

Parameter	Definition	Units	Reference value
F	Filtering fraction	-	1/4
δ_{min}	Minimum separation to build the differential images	λ/D	0.5
dr	Width of annuli on which the ADI is performed	λ/D	1.0
R_A	Ratio optimization to subtraction areas for the ADI	-	2
N_{psf}	Size of the reference PSF frame	pixel	32×32
PSF_{shift}	PSF shift precision to build the planet signature model	pixels	1/50
N_{smooth}	Smoothing of the SNR robust standard deviation profile	pixels	18

Table 4.1 – Reference parameters that are used to compare the ANDROMEDA capabilities when tuning only one parameter of this reference parameter-set.

Four more remarks must be taken into account:

1. As seen previously, the variance of the residuals in the differential images is empirically computed following the 2D-variance scheme (see Eq. 2.15).

2. As the reduced images are high-pass filtered, the scaling factor cannot be computed using the total ratio method (see Eq. 2.11). As on these NaCo data the L1-affine optimization method does not really provide better results (see Sect. 3.2.3), it is chosen here to use the scaling factor computed with a least-square optimization (see Eq. 2.12).

3. As the performance will be assessed on the synthetic companions injected with a constant flux, the scaling factor γ must be taken into account in the model of the planetary signature (see Sect.3.2.5).

4. As the normalization of the SNR map is performed, the positivity constraint cannot be set (see Sect. 3.1.2).

Also, I chose an inner working angle, from which the companion search is started, at $4\lambda/D$ (about 171 mas or 13 pixels). The outer working angle is initially set by the size of the images ($N_{img} =$ 600pixels $\sim 185\lambda/D$). It is then slightly reduced by the reference PSF window size ($N_{PSF} = 32$pixels $\sim 10\lambda/D$) and the size of the working annuli ($d_r = 1\lambda/D \sim 3.2$pixels), thus leading to a SNR and flux maps having an outer working angle of $179\lambda/D$ (about 44 mas or 580 pixels).

In order to perform the detection, I chose a threshold $\tau = 5\sigma$: any signal of the SNR map above this threshold is regarded as a detection.

For this test case, we recall that to run the detection module which sorts and analyzes the detections (see Sect.3.3), the size of the subwindow in which the signals are analyzed is set to 11 pixels ($\sim 3\lambda/D$) to fully enclose the planetary signals obtained in this reference case. The typical distance to a tertiary lobe is set to 16 pixels ($\sim 5\lambda/D$): any detection found close to another signal from less than this distance is carefully checked. The SNR ratio between these two neighbor detections is inbuilt in the code and its value is set as a function of the input filtering fraction. The size of the subwindow and the distance to a tertiary lobe are not user-defined, since they mainly depend on the wavelength

of observation and are defined in λ/D units. However, it can be tuned if needed since some of the user-defined parameters gathered in Tab. 4.1 might influence the typical size of the pattern.

4.1.3 Reference case: Results with ANDROMEDA

Fig. 4.1 shows the detection map and the detection limit obtained by running ANDROMEDA on the TYC-8979-1683-1 data described at Sect. 2.3.1 and using the parameters gathered in Tab. 4.1.

In order to give an idea of the quality of the characterization made by ANDROMEDA, the horizontal and vertical lines in the detection limit plot cross where a synthetic companion stands (we should detect a planetary signal at each crossing).

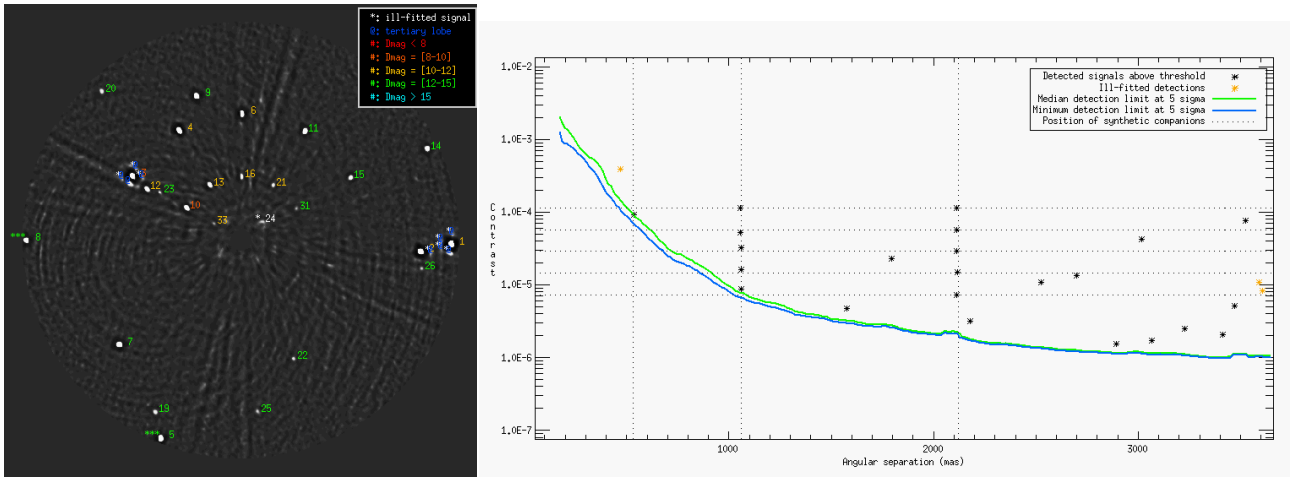

Figure 4.1 – Final detection map (left) and detection limit curve (right) output by the ANDROMEDA pipeline, using the reference set of user-parameters described in Sect. 4.1.2. The synthetic companions have been injected at *each intersection* of the dotted lines. The asterisks show what have been succesfully detected by the ANDROMEDA method (including background sources and synthetic companions).

In the following, we assume that all the detections found within this reference parameter set are the true ones and any other signal found above this 5σ threshold will be regarded as a false alarm. Thus the following comparison assumes a total of 37 detections above threshold, including 23 firm detections that are not rejected by the detection module (based on morphological aspects, see Sect. 3.3). We note here that the highest signal (#1 on Fig. 4.1) has a SNR of 154σ.

For this data cube constituted of $600 \times 600 \times 296$ images, the whole ANDROMEDA algorithm runs in 42 minutes (from the pre-processing to the output obtained by the detection module) when using the reference set of user-parameters of Tab. 4.1.

4.2 Sensitivity to the user-defined parameters

This section aims to assess the global sensitivity of the ANDROMEDA pipeline to variations of the user-defined parameters. The user-defined parameters of ANDROMEDA are rather independent so in this section, I chose to compare the reference case with the results obtained by varying the user-parameters one by one.

The goal is to give an idea of the influence of each of these parameters in terms of extraction capabilities in order to know which parameters must be carefully tuned by the user and which can be definitely set at their default values. At the same time, this study makes find the correct default values to be set and assess if these default values are only for *this* peculiar data set or can be applied to any type of data. Note that in this section, I will not look deeper into the fine performance of the algorithm which will be dealt with in details in Sect. 4.4.

For each test performed, I will qualitatively describe what is theoretically expected before showing the actual results. Then, I will display the output detection maps and the detection limits retrieved, as on Fig. 4.1. I will further discuss the following points:

(1) How the shape of the planetary signals in the SNR map (the planetary pattern) is affected by the parameter;

(2) The number of true detections extracted wrt the number of artifacts rejected;

(3) How the SNR of the signals are affected;

(4) How the estimated positions and contrast are affected by the parameter (based on the estimations obtained with the reference case and on the knowledge of the 15 synthetic companions injected);

(5) How the detection limit curves are impacted by the parameter;

(6) Whether the computing time is increased.

I will finally conclude on the default value chosen for the parameter in question, as well as if the final results are sensitive to a slight variation from this default value and if this default value is dependent upon the instrument used.

Though all these information are inter-related, it is interesting to look into details the consequences of a variation of parameter on all these aspects one by one. This study is mainly qualitative and aims at proposing explanations why such results are obtained.

I chose to present this parameter sensitivity study from the first to the last parameter, in the order they are used inside the algorithm (from the pre-filtering to the post-normalization).

4.2.1 Pre-filtering of the reduced images

The only user parameter related to this pre-processing step is the filtering fraction F. As explained at Sect. 3.1.1, this filtering fraction is a number without unit, which stands between 0 (no filtering) and 1 (all the frequencies are removed). At Sect. 3.1.1, it has been shown that $F = 1/4$ was a good value to start with, hence the choice as a reference.

Expected results: If the filtering fraction is too low, some low frequencies will remain in the differential images, resulting in more false alarms in the final SNR map. Moreover, the planetary patterns in the SNR map will be broader and might be regarded as artifacts. The overall performance depends on the SNR regime in the reduced images since the filtering procedure contribution depends on the trade off between the halo subtraction (noise level) and the energy loss of the planetary signal. Thus, the filtering might increase the error bars on the estimated flux.

Obtained results: As expected, the results obtained with ANDROMEDA are quite sensitive to this filtering fraction parameter, F.

(1) The more the images are filtered (F increases), the sharper the planetary patterns (see Fig. 4.3). Note that although one could modify the size of the subwindow analysis, having broad patterns is not to be favored since (i) the signals could be a posteriori rejected and (ii) they could hide a close companion signal (like detections #9 and #20 in Fig. 4.3-Right, which are not disentangled in Fig. 4.3-Left).

(2) For a low amount of frequencies removed, the faint and close companions are missing (#33 and #31 on Fig. 4.1-Left) and more artifacts stand above threshold, particularly on the residual diffraction patterns of the spiders and, close to the star where the four waffle artifacts are revealed (such as signals #21 #25 #31 on Fig. 4.3-Middle, for $F = 1/8$). At high filtering fraction ($F = 1/2$ for instance, as on Fig. 4.3-Right), some signals are detected whereas they are likely to be artifacts (such as #29 or #33 on Fig. 4.3-Right which are certainly due to, respectively, spider diffraction pattern and speckle). However these detections are a posteriori rejected so the most important consideration is if some companions are missed ($F > 1/8$). This is due to the fact that (i) the patterns are sharper when filtering to much (see remark (1) above) which makes the residual speckles look more similar to planetary signals and (ii) the SNR increases when the filtering fraction increases (see remark (3) below). We should therefore avoid filtering too much the data ($F \geq 1/2$).

(3) Depending on the flux of the companion and its separation (or more generally the speckle noise level surrounding the signal), the filtering fraction decreases or increases the SNR of the detections. Tab. 4.2 shows the SNR variation of the brightest detection (#1 on Fig. 4.3, which lies at 3.5″from the star): it increases with the filtering fraction. However for a fainter and closer companion this

trend is inverted from a specific filtering fraction.This explains why faint and close companions are not detected at low filtering fractions, as visible on Fig. 4.3 (See Sect. 3.1.1 for explanation of how higher filtering fraction F can improve the detectability).

(4) Except at very high filtering fraction ($F \geq 1/2$), the estimated positions and contrasts are hardly modified by the filtering procedure (mostly compared to the intrinsic error bar on these estimations), as it were expected. At low filtering fraction ($F \leq 1/16$), only some detections are underestimated and it is because the pattern is too broad (see point (1)) and cannot be correctly fit by a 2D-Gaussian (as shown on Fig. 4.3-Left, with the asterisks showing the non-convergence of the fit).

(5) The detection limits are lower when the filtering fraction increases (Fig. 4.4). The detection limit curve obtained is smoother when the filtering increases since the mean azimuthal intensity level is more homogeneous.

(6) The chosen filtering fraction does not impact the computing time which, for this step, depends only on the number of images in the cube.

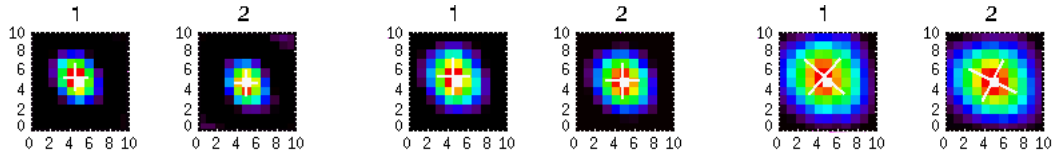

Figure 4.2 – Subimages of the first two detections according to the filtering fraction. From left to right: $F = 1/2$, $F = 1/4$ (default) and $F = 1/8$.

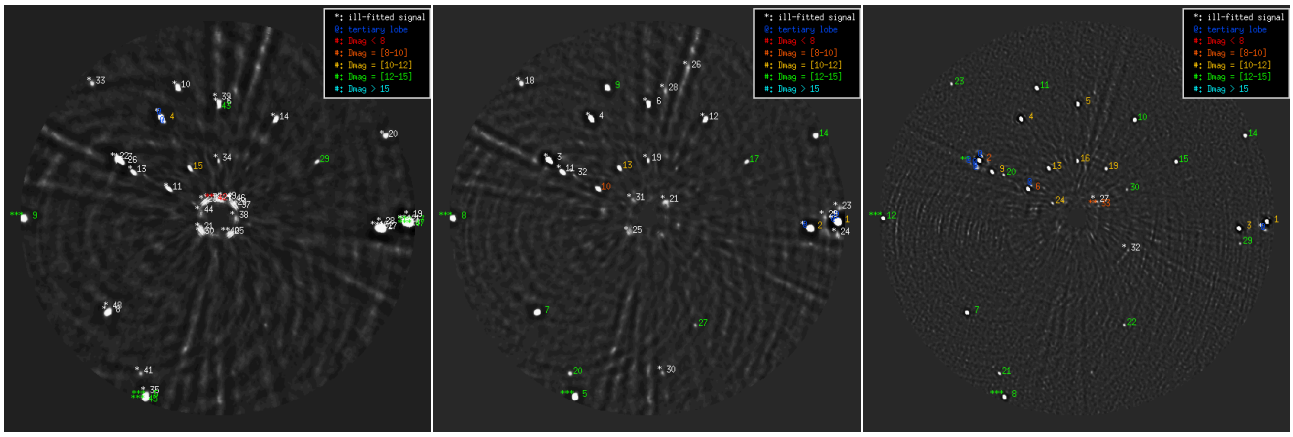

Figure 4.3 – Final detection maps output by the ANDROMEDA pipeline, by making the filtering fraction F vary from its reference value. From left to right: $F = 1/16$, $F = 1/8$ and $F = 1/2$ (The reference value at Fig. 4.1 is $F = 1/4$).

Filtering fraction F	**SNR #1 (σ)**	**SNR #31 (σ)**
1/1.5	215	5.74
1/2	200	6.26
1/4	154	5.82
1/8	102	2.82
1/16	70	2.19

Table 4.2 – SNR of the brightest companion (#1 on Fig. 4.3) and faint close companion (#31 on Fig. 4.3), as a function of the filtering fraction F.

Conclusion: For this data set, the default value should be set at $F = 1/4$, so that the low spatial frequencies are efficiently removed to sharpen the patterns and increase their SNR while not inducing

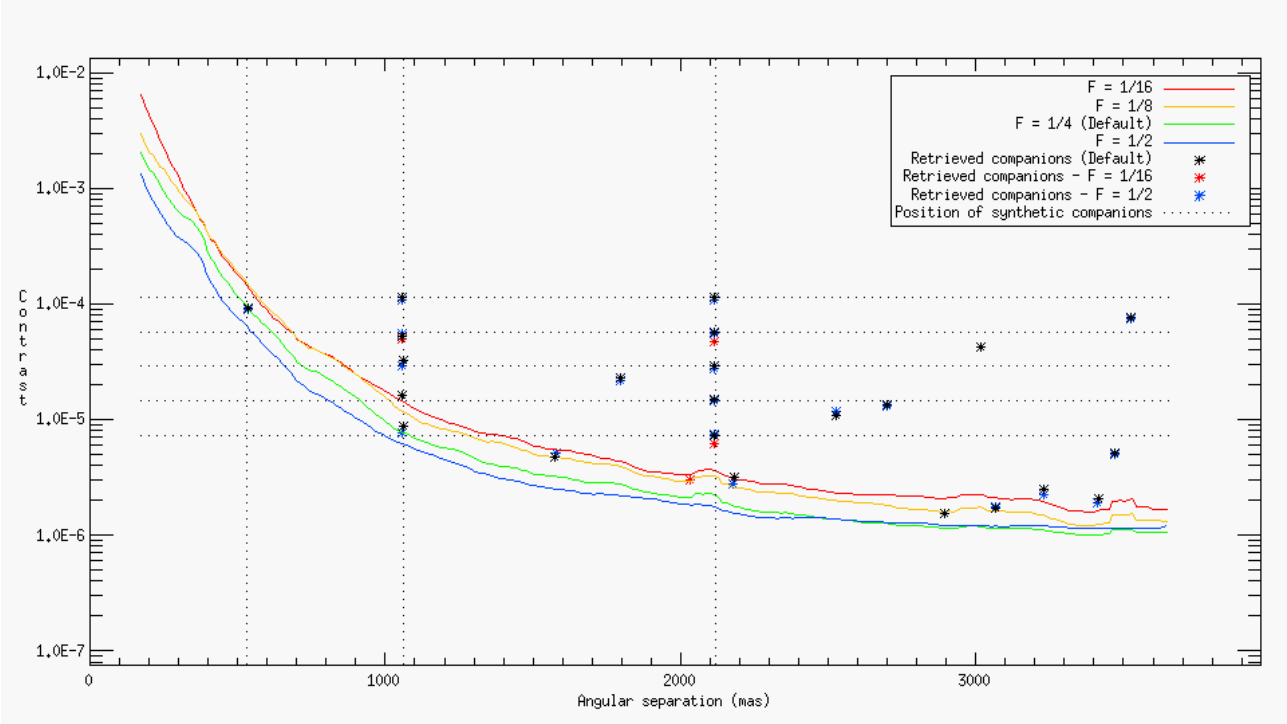

Figure 4.4 – Detection limits retrieved as a function of the filtering fraction set, F, that is to say the amount of low spatial frequencies removed from the reduced images feeding ANDROMEDA.

fake detections by the same effect or overestimating the contrast. Generally speaking, depending on the observation conditions (strength of the wind), and on the instrument use, F should be typically around this default value (see Chap. 6 for examples on SPHERE data).

4.2.2 Building the differential images via ADI

In order to build the differential images (in which the specific planetary signatures appear and in which the noise has been partially whitened), ANDROMEDA uses ADI (see Chap. 2). For the ADI procedure implemented in ANDROMEDA, there are three user-defined parameters (knowing that the least-square fit is used to optimize the angular subtraction): the minimum angular separation between the two frames to be subtracted, δ_{min} ; the thickness of the annuli within which the δ_{min} constraint apply, d_r; the optimization to subtraction area ratio, R_A, that is the ratio between the area where the optimal (in the least-square sense) scaling factor γ is computed and the actual subtraction area defined by d_r (see Sect. 3.2.3 for details).

4.2.2.1 Minimum angular separation, δ_{min}

This parameter is the minimum angular rotation allowed to perform the subtraction. As a reminder, this angular distance must be (i) as small as possible so that the time delay between the two images to be subtracted is short, and thus the noise is as decorrelated as possible in the resulting differential image[1] and, (ii) large enough so that the planetary companion does not self-subtract in the resulting differential image. Results on simulated data showed that a good compromise for this δ_{min} parameter was to set it to $0.5\lambda/D$, hence the reference value chosen.

Expected results: The results depend on the temporal stability of the speckle fields in the image cube.

For a given data-set, it is expected that, if δ_{min} is too low (less than $0.5\lambda/D$), the planet signature will be extremely affected and have a lower signal which will make it difficult to be found among

[1] Under the assumptions that the most correlated frames are the closest in time.

the surrounding noise; even though the surrounding noise is reduced, the search for companions by ML might be affected by the low planetary signature signal. Thus, a decrease of their SNR should be observed. Moreover, as shown on Fig. 4.5, the lower the δ_{min} , the more the planetary signature resembles a remaining speckle. Consequently, many false alarms should appear (since residuals speckles will be regarded as detections by their similarity with the model) but might be a posteriori rejected owing to their morphological aspect.

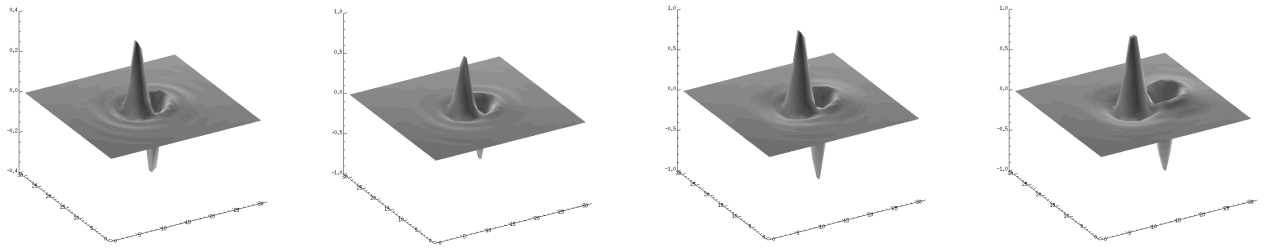

Figure 4.5 – Theoretical planet signatures (noiseless Airy patterns) for different values of δ_{min} (using a filtering fraction $F = 1/4$). From left to right: $\delta_{min} = 0.25\lambda/D$ $\delta_{min} = 0.5\lambda/D$, $\delta_{min} = 1\lambda/D$ and $\delta_{min} = 2\lambda/D$.

On the contrary, if δ_{min} is wide enough (greater than $1\lambda/D$), the particularity of the planet signature shape makes it easier to be disentangled from the residual speckles (although these residuals will be higher) via their correlation with the corresponding planet signature model. Thus, larger δ_{min} values can be worth to apply if the speckle field is stable as in SPHERE images.

Note that δ_{min} cannot be too large since some couples have to be found. Thus, when there is a low amount of field rotation, a trade of must be made between the wanted IWA and the chosen δ_{min} .

Obtained results: The δ_{min} parameter must be chosen with care to obtain good performance with ANDROMEDA.

(1) Given the shape of the planet signature as a function of δ_{min} , the resulting pattern is less elongated in its azimuthal direction as δ_{min} decreases.

(2) The detection maps at Fig. 4.6 show that for a low δ_{min} (for instance $\delta_{min} = 0.25\lambda/D$ as on Fig. 4.6-Left), more artifacts are present close to the star and in general more speckle residuals are visible whereas it was expected to better subtract the speckle with a low δ_{min} . This is due to the fact the main feature of ANDROMEDA is to perform a maximum likelihood search from a planetary signature model. For a low δ_{min} , Fig. 4.5 shows that the signature is very small and more alike to a residual speckle whereas higher δ_{min} (from $0.5\lambda/D$) show a very specific pattern which is easily disentangled from speckles residuals. For $\delta_{min} = 1\lambda/D$, the results are very similar to the reference $\delta_{min} = 0.5\lambda/D$ except that in the latter the rejected companion #24 which arises from the waffle is not detected but a spider diffraction residual is detected (#24 on Fig. 4.6-Middle at $\delta_{min} = 1\lambda/D$). These two artifacts are nevertheless rejected by the sorting module. For high values of δ_{min} ($\delta_{min} \geq 2\lambda/D$), the two faint and close companions are missed (#31 and #33 on the reference detection map). Moreover, more artifacts due to the diffraction of the spider are visible. Two more companions (#27 and #29 on Fig. 4.6-Right at $\delta_{min} = 2\lambda/D$) are found above threshold as in the map obtained with $\delta_{min} = 0.25\lambda/D$ (#25 and #27 on Fig. 4.6-Left). There is no proper way to reject these two detections, however these two extreme values of δ_{min} do not have the expected behavior which favor the cases of $\delta_{min} = 1\lambda/D$ or $\delta_{min} = 0.5\lambda/D$.

Also, it is worth pointing out that the level of the residuals in the SNR map are higher for low values ($\delta_{min} \leq 0.25\lambda/D$) and high values ($\delta_{min} \geq 2\lambda/D$) compared to the reference. At low δ_{min} value, this effect is due to higher correlation rate between some residual speckles and the model of the planetary signature. A high δ_{min} value, this effect is due to a bad subtraction of the speckles since, in this case, they had time to evolve significantly between the two subtracted frames.

(3) The SNR of the detections are quite affected by the δ_{min} parameter: the Tab. 4.3 gathers the different SNR for two different companions (#1 on the reference case on Fig. 4.1 at $3.5''$and #21 at

1″) as a function of the δ_{min} set. Notably, at closer separation, the SNR is higher for a δ_{min} of $1.0\lambda/D$, which favors the later value for this test case (the closest companion, #28 on Fig. 4.6-Middle, has a SNR of 6σ when $\delta_{min} = 1.0\lambda/D$ and of 5.7σ when $\delta_{min} = 1.0\lambda/D$) .

(4) When δ_{min} is smaller than $0.5\lambda/D$, the contrast is slightly underestimated, probably due to the self subtraction of the planetary signal which is not perfectly modeled in the planet signature. From $\delta_{min} \geq 0.5\lambda/D$, the estimated contrasts are stable. The estimation of the position is not affected by a variation of δ_{min} .

(5) The detection limit curve is lower when δ_{min} increases as shown on Fig. 4.7. When δ_{min} is wide enough, the SNR map is filtered of the residual tiny structures (see Eq. 2.3) which, in the end, leads to smoother detection limit curves. On the contrary, when δ_{min} is very small the model correlates better with the residuals (post-ADI), resulting in more small structures left in the SNR map and thus in a higher and more jagged detection limit curve. This explanation is supported by the fact the trend is inverted from $2200mas$ on Fig. 4.7. Indeed, from this separation, the noise in the images is mainly made of photon and detector noise, which, in any case, does not correlate well with the model.

(6) The computing time is slightly affected by this parameter: the lower the more frames can be exploited, leading to more ADI couples and thus more ML calculations. From $\delta_{min} = 0.1\lambda/D$ to $\delta_{min} = 0.5\lambda/D$ This increases the computing time of about 2% (about one minute here).

Note that in order to process these data using $\delta_{min} = 2\lambda/D$, the inner working angle must be increased to $8\lambda/D$, else no couples respecting the δ_{min} condition can be found.

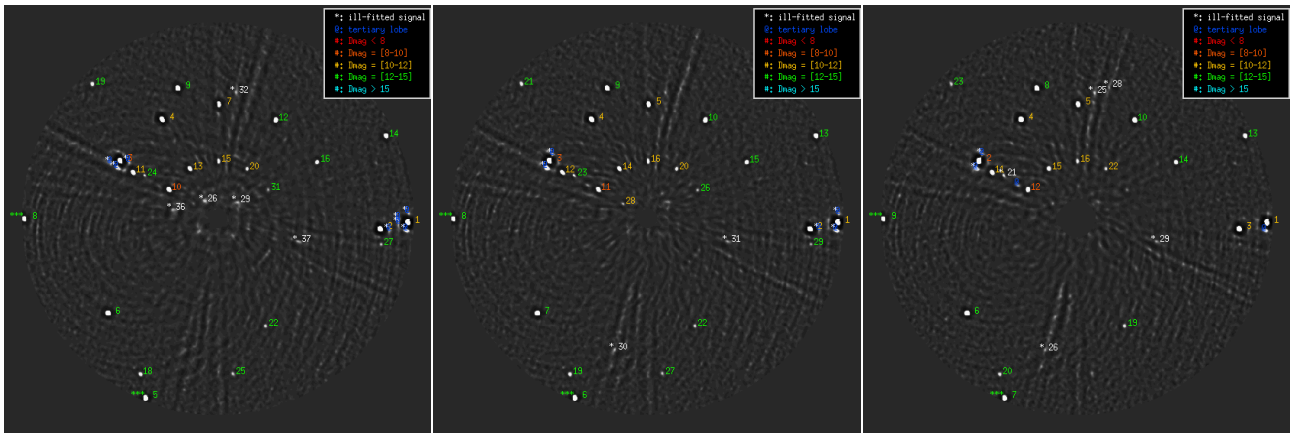

Figure 4.6 – Final detection maps output by the ANDROMEDA pipeline by making the minimum separation δ_{min} varies from its reference value. From left to right: $\delta_{min} = 0.25\lambda/D$, $\delta_{min} = 1.0\lambda/D$ and $\delta_{min} = 2.0\lambda/D$, (reference value is $\delta_{min} = 0.5\lambda/D$).

Value of d_r set	**SNR #1 (σ)**	**SNR #21 (σ)**
$0.25\lambda/D$	154	9.62
$0.5\lambda/D$	154	9.88
$1\lambda/D$	151	10.31
$2\lambda/D$	120	7.82

Table 4.3 – SNR of the companion #1 (at a separation of 3.5″) and of #21 (at a separation of 1″), as a function of the minimum angular separation for the ADI, δ_{min} .

Conclusion: The default value should be set at $\delta_{min} = 1.0\lambda/D$ for this NaCo data. In general, this parameter should lie between $0.5\lambda/D$ and $1.0\lambda/D$, according to the temporal stability of the noise in the images and the brightness of the companion. If the speckle field is very stable, it is better to favor $1\lambda/D$ since the planetary signature is easily disentangled from the residual speckles thanks to the ML approach. This is unique for the ANDROMEDA method since other image processing methods

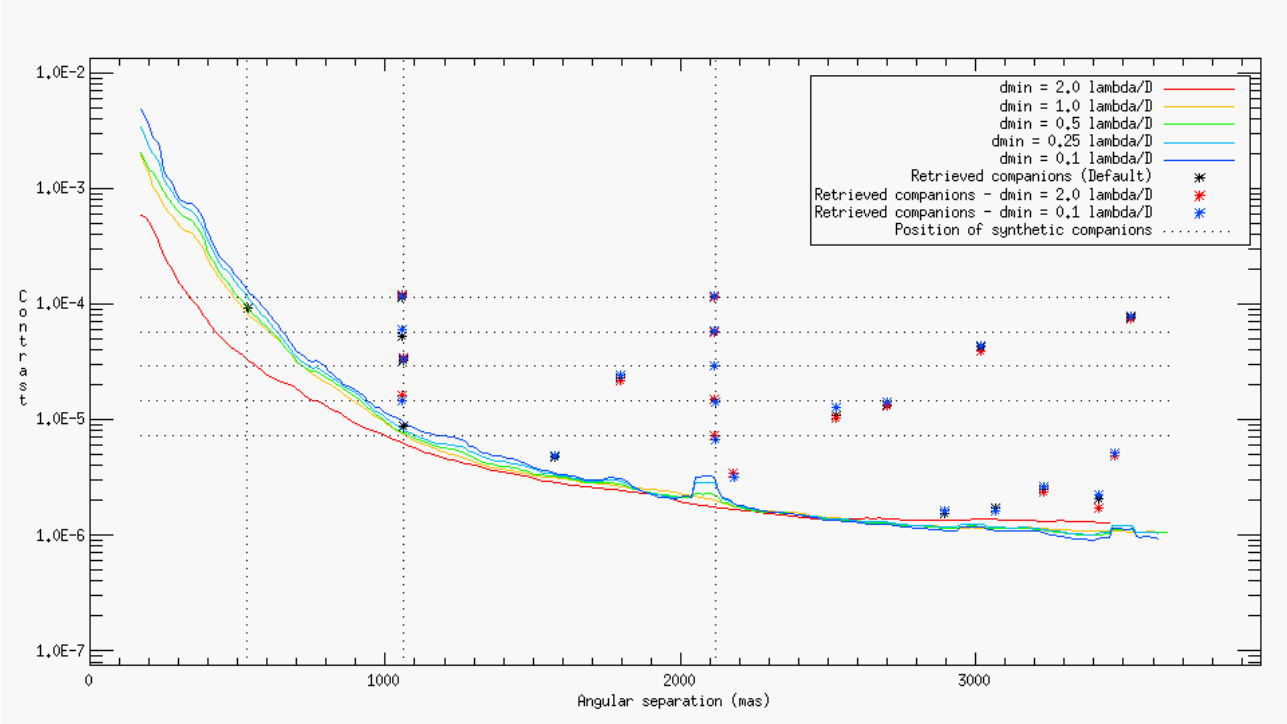

Figure 4.7 – Detection limits retrieved as a function of the minimum separation set, δ_{min} , that is to say the lowest angular separation allowed to perform the ADI in ANDROMEDA.

mainly aim at reducing the speckle noise, reduction which is favored by a low δ_{min} . For instance, Marois et al. (2008a) have shown that a good compromise to is to set $\delta_{min} = 0.5\lambda/D$.

4.2.2.2 Annuli width, d_r

As the angular motion, constrained by δ_{min} , depends on the distance to the star, ANDROMEDA specifies a δ_{min} within each annulus surrounding the star. These annuli have a constant width defined by d_r[2]. The computing time increases when d_r decreases since more annuli must be processed. A trade off must be made to account the computing time vs the detection capabilities.

Expected results: If this parameter is too high, the δ_{min} constraint will be too strong for small separations thus some frames might not be exploited, resulting in a decrease of the SNR.

Obtained results: The results obtained with ANDROMEDA are not very sensitive to the annuli thickness set d_r.

(1) The patterns are not affected by this parameter since the search for companions is made over the whole map (see Eq. 2.23). The annuli thickness is only used to decide which couples are chosen (according to δ_{min}) and the area in which the scaling factor γ is computed (within the annular area $R_A \times \sum_r d_r$). However, if there is a sudden change in the γ value, the edge of the annulus can be visible, as it is the case close to the star (see Fig. 4.8).

(2) When d_r is very small (1 pixel width), the waffle[3] artifacts are regarded as detection (see Fig. 4.8-Left). This is probably due to the same effect as (1) since the waffle signal is not smoothed by the scaling factor. However these detections are a posteriori rejected. Otherwise, the same detections are revealed for each value.

(3) The SNR of the detections does not show any significant trend as a function of dr.

[2]In the original version of ANDROMEDA, this thickness could vary but I chose to set it constant to better exploit every frame

[3]The waffles in the NaCo images are the four symmetrical spots surrounding the star, visible at about 300 mas on these images.

(4) The estimations are unchanged except for the companions close to the detection limit which are overestimated at low d_r (of about 1 pixel) and underestimated at larger d_r (greater than $2\lambda/D$).

(5) The retrieved detection limits are the same. The reasoning followed above is supported by the fact that at separation where many companions can be found, the detection limit for low d_r values show a bump which means the other companions have an influence on its performance.

(6) The computing time is slightly affected by this parameter: the thinner the annuli the more frames are exploited, leading to more ADI couples and thus more ML calculations. From $d_r = 0.3\lambda/D$ to $d_r = 1\lambda/D$, the computing time is increased of about 50% (20 minutes here).

Another point, is that the smaller d_r, the smaller the OWA of the SNR map since it is equal to $\frac{N_{img}}{2} - \frac{N_{PSF}}{2} - d_r$. This effect is visible on the detection maps shown on Fig. 4.8.

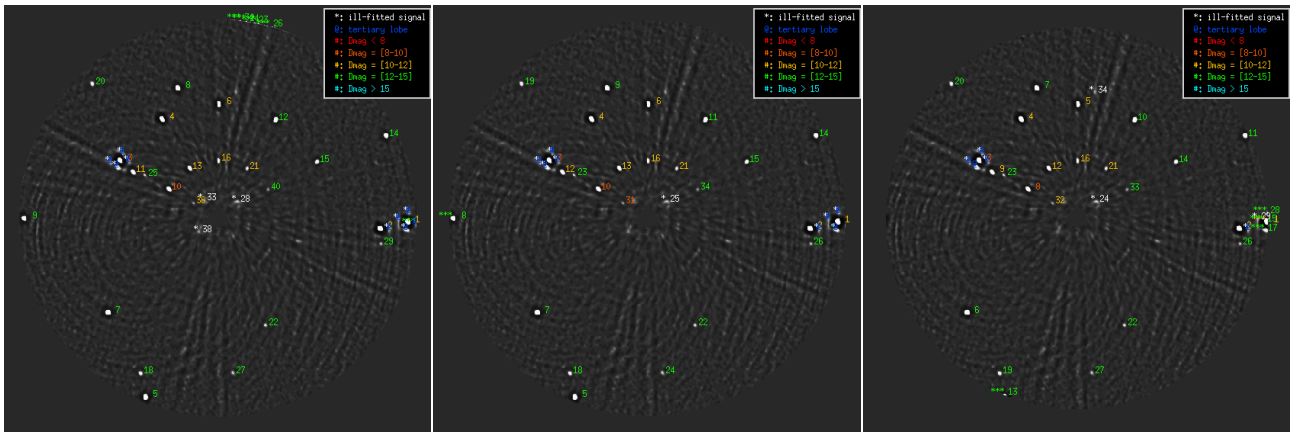

Figure 4.8 – Final detection maps output by the ANDROMEDA pipeline by making the annuli thickness d_r varies from its reference value. From left to right: $d_r = 0.3\lambda/D$, $d_r = 0.5\lambda/D$ and $d_r = 2\lambda/D$ (reference value is $d_r = 1\lambda/D$).

Value of d_r set	SNR #1 (σ)	SNR #21 (σ)	SNR #33 (σ)
$0.3\lambda/D$	145	9.75	5.63
$0.5\lambda/D$	151	9.86	5.77
$1\lambda/D$	154	9.88	5.76
$2\lambda/D$	181	9.83	5.85
$3\lambda/D$	-	9.83	6.3

Table 4.4 – SNR of the companion #1 (at a separation of 3.5″), #21 (at a separation of 1″) and #33 (at a separation of 0.5″), as a function of the thickness of the annuli for which the ADI is performed, d_r.

Conclusion: Considering the different aspects mentioned above, the default value is set to $d_r = 1\lambda/D$. A d_r of $2\lambda/D$ would have been correct but this parameter is absolutely not critical and its effect on the results is actually caused by the parameter R_A. It is thus better to directly tune the latter parameter.

4.2.2.3 Optimization to subtraction areas ratio, R_A

Since the scaling factor γ is calculated for each couple of images k and for each annulus surrounding the star, some discontinuities may appear in the final SNR map between annuli (arising from a sudden change of γ). To avoid these discontinuities, the scaling factor is computed inside an area larger or equal than the actual subtraction area (see Fig. 2.3). The ratio between the subtraction and optimization area is given by the user-parameter R_A, greater or equal to 1.

Expected results: The discontinuities might make arise false alarms. One can expect that the larger R_A the less false alarms. However a large R_A will disrupt the least-square fit by taking into

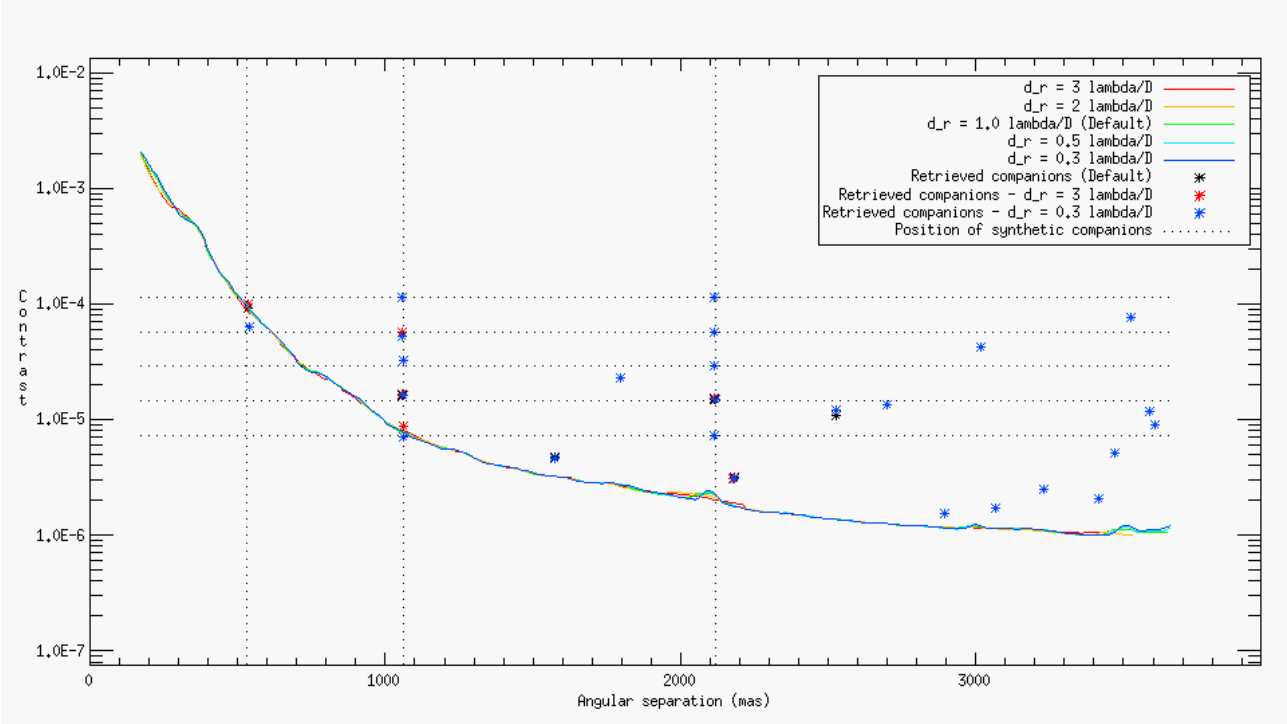

Figure 4.9 – Detection limits retrieved as a function of the minimum separation set, δ_{min} , that is to say the lowest angular separation allowed to perform the ADI in ANDROMEDA.

account areas whose flux distribution are quite different from the one in the subtraction area. Thus large areas should provide more false alarms in the resulting SNR map.

Obtained results: The results obtained with ANDROMEDA are not sensitive to the optimization to subtraction area ratio R_A.

(1) The patterns are azimuthally wider when R_A increases, as shown on Fig. 4.10. Since the optimization zone shares the inner radius of the subtraction area (see Fig. 2.3), increasing R_A implies taking into account areas with lower speckle noise. The resulting scaling factor might be lower which induces an asymmetry of the planetary signature (see discussion about Fig. 3.26 for instance) that is not perfectly modeled.

(2) The detections are strictly the same. The residuals in the SNR map seem slightly smoother when R_A increases, as shown on Fig. 4.11.

(3) The SNR varies the same way as for the d_r parameter. See explanations at the previous section (see Tab. 4.5).

(4) The estimated position and flux do not vary with this parameter R_A (see Fig. 4.12).

(5) The computed detection limit does not vary with this parameter R_A (see Fig. 4.12).

(6) The computing time is not affected by this parameter R_A.

Note that this R_A parameter was more important without filtering the images. With the new interpretation of the scaling factor when pre-filtering the images, this parameter becomes almost obsolete and the smaller the better (since the optimization is consistent with the actual subtracted annulus).

Conclusion: Considering these different aspects, the default value should be set at $R_A = 1$ since this is the ideal case while it does not changes the ANDROMEDA extraction capabilities. Indeed, we want R_A to be the closest to one as possible in order to avoid biasing the computation of the scaling factor γ.

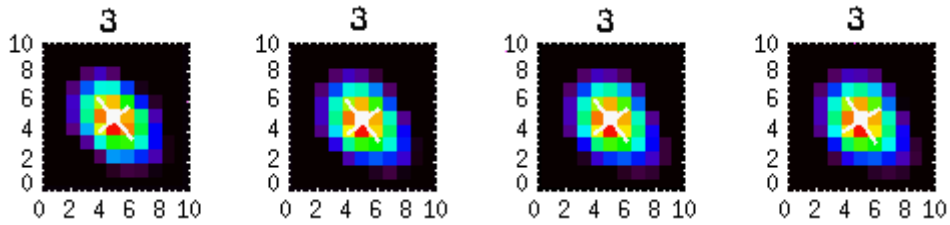

Figure 4.10 – Subimages of the third detection #3, according to the chosen R_A. From left to right: $R_A = 1$, $R_A = 2$ (default), $R_A = 3$ and $R_A = 4$.

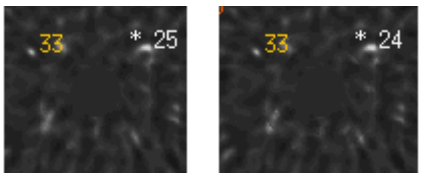

Figure 4.11 – Zoom of the SNR map on the region close to the star. From left to right: $R_A = 1$ and $R_A = 4$

Value of R_A set	SNR #1 (σ)	SNR #21 (σ)
1	154	10.89
2	154	9.88
3	160	9.85
4	151	9.78

Table 4.5 – SNR of the companion #1 (at a separation of 3.5″) and of #21 (at a separation of 1″), as a function of the optimization to subtraction area ratio, R_A.

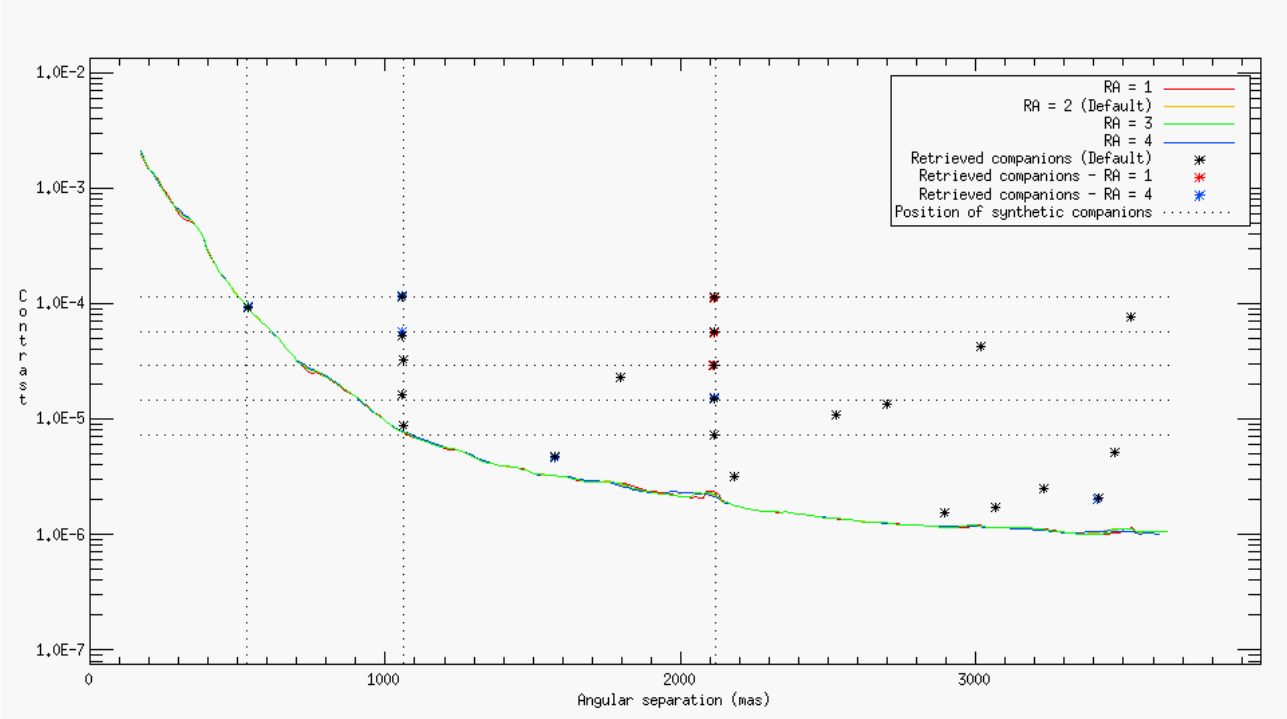

Figure 4.12 – Detection limits retrieved as a function of the optimization to subtraction area set, R_A.

4.2.3 Building the model of the differential images

In order to build the models corresponding to each post-ADI images and from which the maximum likelihood is computed, a reference PSF is needed. The size of the input PSF, N_{PSF} is a user-defined parameter, as well as the subpixel precision by which this PSF is shifted to build the model, PSF_{shift}.

I recall that the final contrast is estimated from the cropped reference PSF.

4.2.3.1 Size of the input reference PSF, N_{PSF}

The size of the input PSF is the major parameter at stake in terms of computing time, as already investigated in previous work by A. Cornia (Cornia, 2010).

Expected results: The size of the PSF is given in pixels but is dependent upon the wavelength of observation (and should rather be given in λ/D, as it is set as default in the provided ANDROMEDA batch which is in the package). In ANDROMEDA, the contrast is estimated wrt the integral of the flux inside the reference PSF frame and not to the maximum of the reference PSF. As a consequence, the bigger the size of the PSF, the most information it contains and the better the flux estimation. However, at some point the information brought is negligible (from the third Airy ring for instance). In addition, the computing time increases a lot with larger window. On the contrary, if the size of the PSF is too small, some information could be lost (see Fig. 4.13), resulting in a bad contrast estimation.

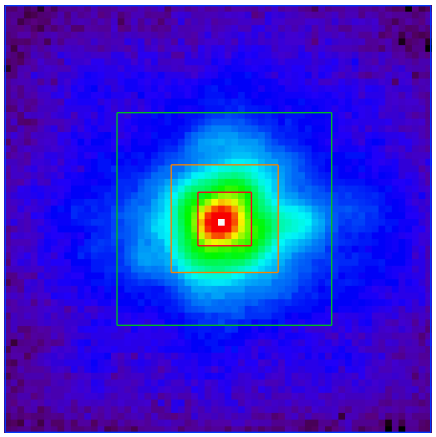

Figure 4.13 – Reference PSF with different window size: $N_{PSF} = 8 \times 8$ pixels (red), $N_{PSF} = 16 \times 16$ pixels (orange), $N_{PSF} = 32 \times 32$ pixels (green - Default value) and $N_{PSF} = 64 \times 64$ pixels (blue - full image). Note that in H-band and with such an instrument, $1\lambda/D \simeq 3.23$ pixels.

Obtained results: There is a minimum size below which the estimated flux is strongly impacted. Above this size, the results are not sensitive to the given size (but the computation time increases).

(1) The size of the PSF subwindow slightly affect the size of the patterns when the core of the reference PSF is not fully enclosed in the frame. Indeed, the resulting planetary signature will be cropped, and the resulting pattern will be smaller (see Fig. 4.15).

(2) The detections are strictly the same, including the same artifacts that are a posteriori rejected.

(3) The SNR of the companions are strongly affected by the size of the PSF window only when the latter is too small and does not enclose enough information (which is here for $N_{PSF} < 16$ pixels. For instance, the companion #1 has a SNR of 94σ when $N_{PSF} = 8$ whereas for $N_{PSF} \geq 16$ it has a SNR of 154σ.

(4) Following the same reasoning (since the SNR and estimated flux are linked), when the window is too small, the amount of starlight taken into account is not enough to compute the true contrast. It thus leads to an underestimation of the final contrasts (by the same amount for every detection). On the contrary, when the window is too large, some noise is taken into account but does not belong to the star which leads to a slight overestimation of the contrast (still by the same amount), as shown with the symbols on Fig. 4.16.

(5) Once the window fully encloses enough intensity from the star, the detection limits are exactly the same since the normalization is correct. However for $N_{PSF} = 8$, the detection limit is biased by the incorrect contrast estimation evoked earlier.

(6) The computing time is highly affected by the chosen size of the reference PSF given as an input. The Tab. 4.6 gives the computing time for four different window sizes.

Another point worth noting here, is that the smaller N_{PSF}, the larger the OWA of the SNR map (as explained in Sect. 4.2.3.1) since it is equal to $\frac{N_{img}}{2} - \frac{N_{PSF}}{2} - d_r$. This effect is visible on the detection maps shown on Fig. 4.14. Also, as the size of the reference PSF is smaller, the residual structure in the SNR map is thinner, as it is also visible on Fig. 4.14-Left. However, once the information contained in the core of the reference PSF is fully enclosed in the window, the residual structure in the SNR map keeps the same scale (determined by the typical size of the PSF core).

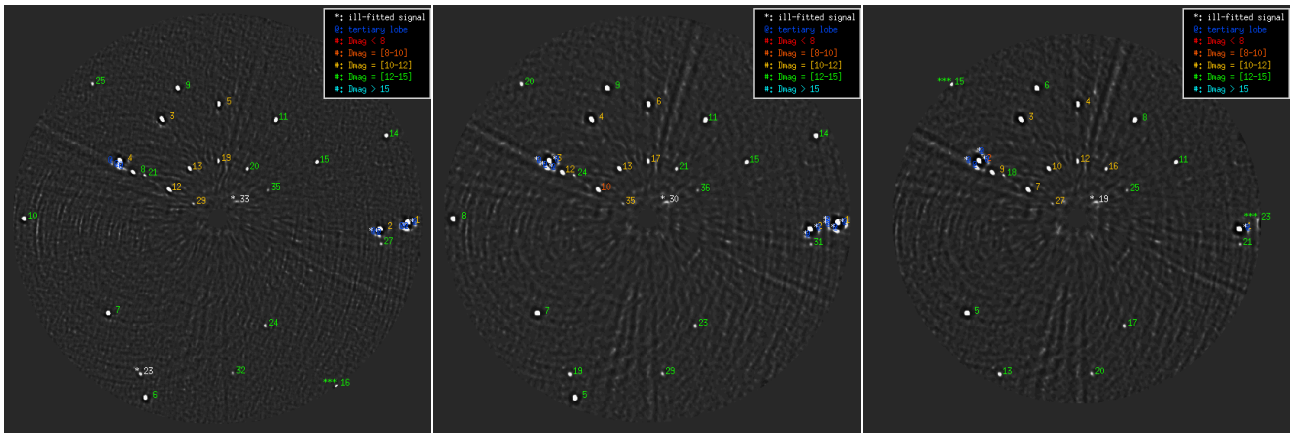

Figure 4.14 – Final detection maps output by the ANDROMEDA pipeline by making N_{PSF} varies from its reference value. From left to right: $N_{PSF} = 8 \times 8$ pixels, $N_{PSF} = 16 \times 16$ pixels and $N_{PSF} = 64 \times 64$ pixels (reference value is $N_{PSF} = 32 \times 32$.

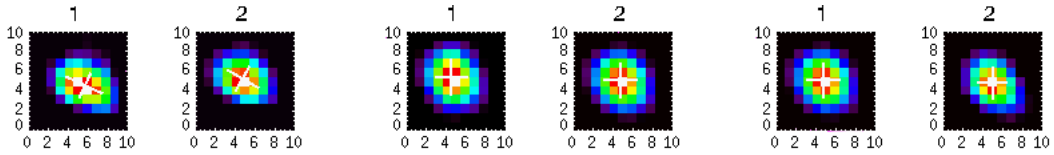

Figure 4.15 – Subimages of the first two detections according to the size of the reference PSF window set. From left to right: $N_{PSF} = 8 \times 8$ pixels, $N_{PSF} = 16 \times 16$ pixels and $N_{PSF} = 64 \times 64$ pixels

Size N_{PSF}	**Computing time (min)**
8×8	19.26
16×16	24.82
32×32	41.46
64×64	106.44

Table 4.6 – Computing time as a function of the reference PSF window size. The computing time increases as the square root of the window size (which here has still a ratio of 0.707 from one line to the other).

Conclusion: The two most important parameters are (i) the amount of star intensity information contained in the window and (ii) the computing time. A good compromise, is to set N_{PSF} such that it fully encloses the secondary rings of the reference PSF while not using negligible information from outer rings. In other words, the default value is set to N_{PSF} corresponding to $10\lambda/D$.

4.2.3.2 Precision of the PSF subpixel shift, PSF_{shift}

The precision on the estimated companion position angle depends on this parameter. The exact needed shift is determined by the parallactic angles provided.

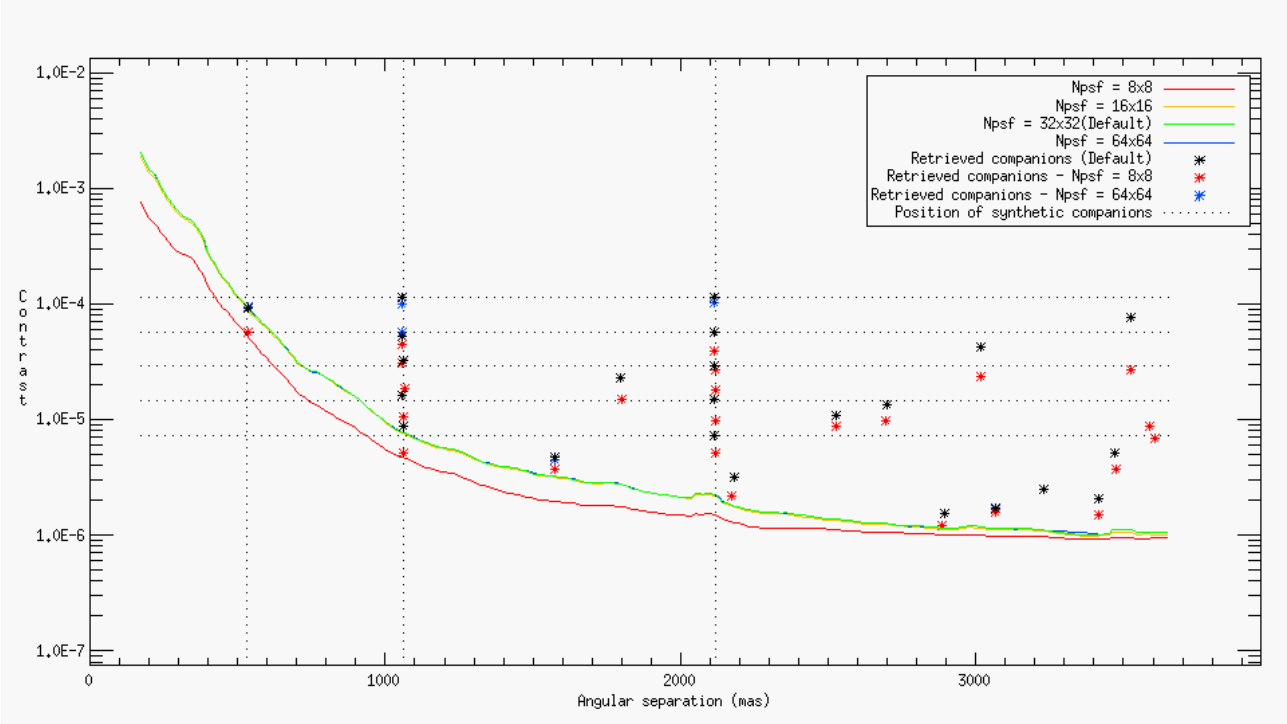

Figure 4.16 – Detection limits retrieved as a function of the size of the reference PSF window, N_{PSF}, used to build the model of the planet signature in the post-ADI images.

Expected results: The finer the grid on which the reference PSF is given, the better the planet signature and its model match, which should increase the planetary signal SNR. However, choosing a grid too fine (as from PSF_{shift} smaller than 1/100) would not bring much more information. Moreover, the platescale error is completely dominant. It is thus needed to find the value which provides an intrinsic error on the astrometry fully negligible wrt the other sources of error.

Obtained results: The effect on the results provided by ANDROMEDA from a variation of this PSF_{shift} parameter are extremely faint.

(1) As expected, the patterns are not affected by a change of PSF_{shift}.

(2) The detection maps are exactly the same, whatever the chosen PSF_{shift} precision.

(3) The SNR is slightly lower when the precision of the subpixel shift is of less than a half pixels (for the brightest companions it goes from 156.7σ to 157.8σ for respectively $PSF_{shift} = 1/2$ and $PSF_{shift} = 1/100$).

(4) The astrometric and photometric estimations are not affected by this parameter. Only when the subpixel shift is of less than a half pixels the contrast is slightly overestimated (mainly for the close and faint companions) but this is a very fine effect, way below the error bars. The same effect appears for the astrometry, but it is once again below the error bars.

(5) The detection limit provided by ANDROMEDA are strictly the same, whatever the chosen PSF_{shift} precision (see Fig. 4.17).

(6) The shifted reference PSF are pre-computed before the core of the algorithm runs. Then for each couple of images, the model is computed from these shifted PSF (rounded up to the closest value allowed by PSF_{shift} precision). Thus the computing time is not affected by this parameter. It takes less than a second to pre-compute the shifted PSF, whatever the chosen precision.

Conclusion: We chose to set the default value at $PSF_{shift} = 1/50$, since, for any data this shift should be fine enough in comparison with the instrumental precisions. Indeed, the computation of the shifted PSF with such a precision does not cost a lot and is not critical. It is thus safer to set it to a fine precision and never modify its value anymore (even though $PSF_{shift} = 1/10$ would be enough).

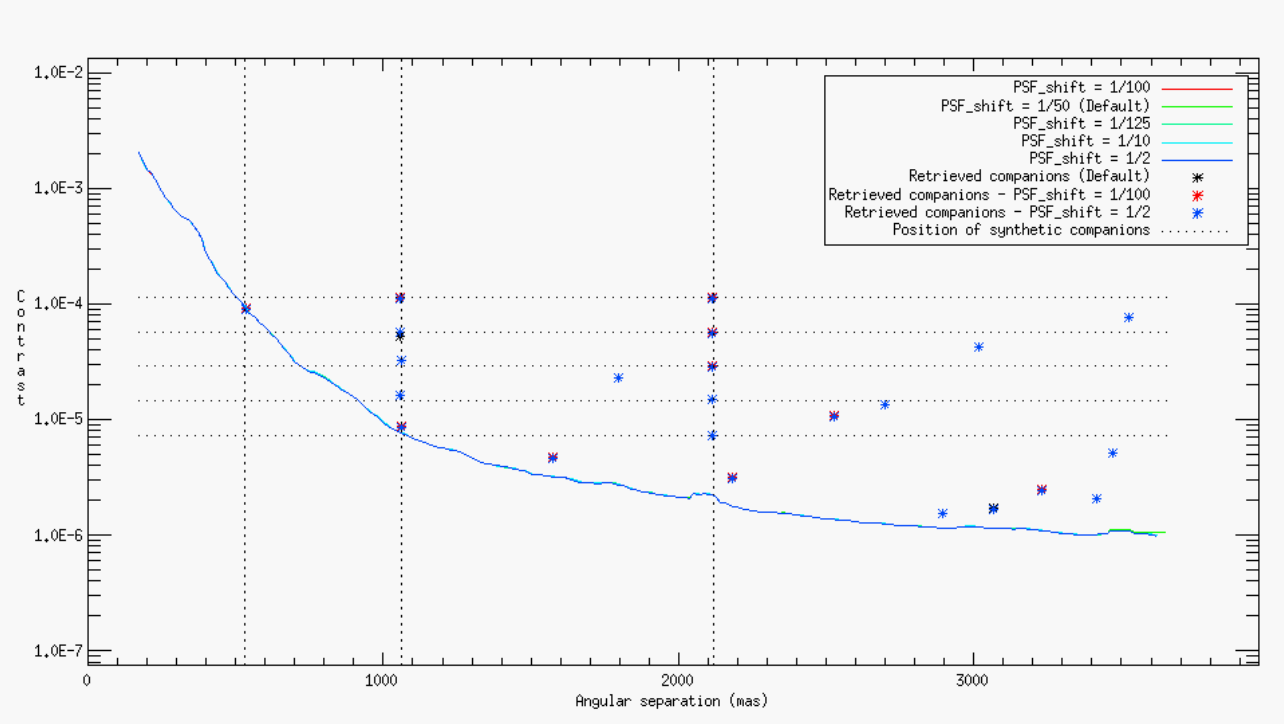

Figure 4.17 – Detection limits retrieved as a function of the size of the reference PSF subpixel shift, PSF_{shift}, used to build the model of the planet signature in the post-ADI images.

4.2.4 Post-normalization of the SNR map

The only user-defined parameter used for the normalization of the SNR map is the number of pixels on which the radial profile of the SNR standard deviation is smoothed, as explained in Sect. 3.1.2. As explained in the corresponding section, the detection capabilities of ANDROMEDA are strongly dependent upon this parameter. And this parameter strongly depends on the quality of the data set processed by ANDROMEDA. The best procedure is to visualize the profile and the smoothed profile to assess by eyes if this smoothed profile shows a correct trend. However, ANDROMEDA is developed in the idea of being as independent as possible of the users' judgment. This short analysis aims to find any clue to decrease the range of N_{smooth}values providing the same results.

Expected results: As explained at Sect. 3.1.2, a large N_{smooth}increases the number of false alarms while for small N_{smooth}, some signals are missing. The normalization profiles obtained for various N_{smooth}values are shown on Fig. 4.18.

Obtained results: ANDROMEDA capabilities are very dependent upon the chosen smoothing value N_{smooth}.

(1) the planetary pattern shapes are not affected by the normalization procedure, as expected, (see tests performed in Sect. 3.1.2).

(2) Generally speaking, the number of detections increases with N_{smooth}. From N_{smooth}= 2 to N_{smooth}< 14, the faint and close companions are missing (#31 and #33, as on Fig. 4.19). The optimal value -for this data set and given the present companions - lies between N_{smooth}= 14 to N_{smooth}= 20 (which is a rather short range). From N_{smooth}> 22 more and more artifacts appear above threshold (they are clearly either due to the residual diffraction pattern of the spiders, such as #36 or due to residual speckles, such as #24, as on Fig. 4.19). However these artifacts are systematically rejected by the sorting procedure which again proves the usefulness of such an approach. As a conclusion, the detection capabilities are not degraded for large N_{smooth}provided that $N_{smooth}$is large enough to avoid missing any companion (here $N_{smooth} \geq 14$).

(3) The SNR of the easiest detection (companion #1) decreases from N_{smooth}= 2 to N_{smooth}= 14 pixels, from 167σ to 154σ and then is stable at this value, whatever the N_{smooth}value chose. For these two reasons, I chose to set the default N_{smooth}value, for this data set, to 18 pixels.

(4) The astrometric and photometric estimations are not affected by the normalization procedure, as expected (see tests in Sect. 3.1.2).

(5) Since the normalization procedure affects the standard deviation of the flux map, the detection limit is lowered as N_{smooth}increases, as shown on Fig. 4.20. Also, as the standard deviation of the flux map from which the detection limit is calculated, is multiplied by the smoothed profile, the more the normalization profile is smoothed, the more the detection limit curve is smoothed. The default value chosen, green solid line at Fig. 4.20, shows a global trend in agreement with all the curves obtained. Note that, as expected, the normalization procedure affects mainly the detection limit close to the star, whereas at large separation, the curves get mixed.

(6) As the normalization procedure is a post-processing, this single step does not affect the computing time.

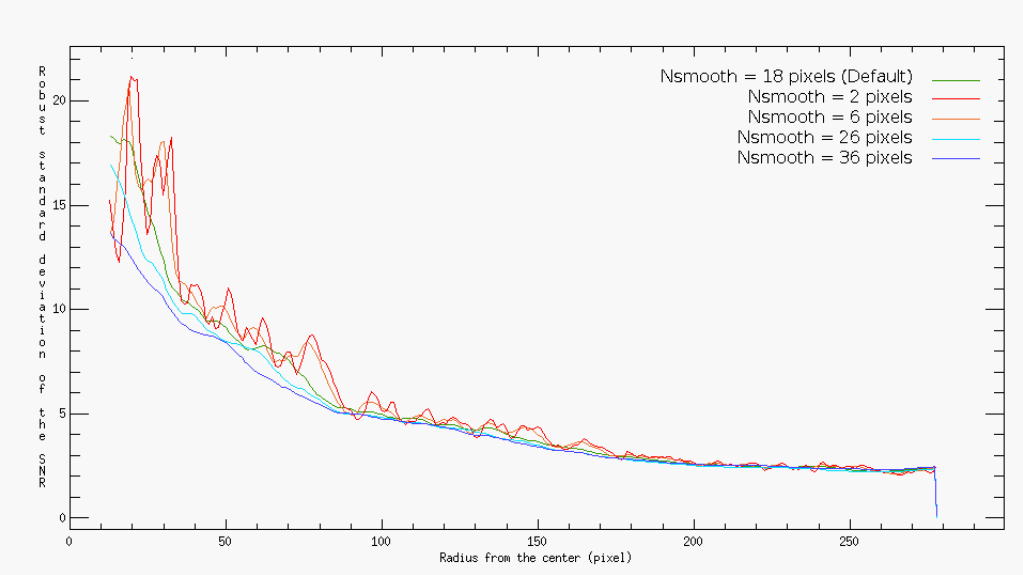

Figure 4.18 – Normalization profiles obtained for various N_{smooth}values.

Conclusion: The default value is set at N_{smooth}= 18 pixels but this value is highly dependent on the data quality[4] (in terms of Strehl ratio) and stability (if the speckle field is temporally stable during the observation). Setting a too low N_{smooth}value can result in missing true companions so this step should be performed with care. The ANDROMEDA pipeline is not affected by a too large N_{smooth}value

Summary of the user-parameters default values

The following Tab. 4.7 summarizes the values of all the user-defined parameters used in ANDROMEDA, as well as their importance in terms on impact on the final detection capabilities. Most parameters should be kept as default value. Only three parameters (δ_{min} , the way of optimizing the ADI procedure and N_{smooth}) could be modified at the users' convenience, according to the quality of the data set at hands (mostly its stability and its dominant noise characteristics).

This study resulted in the setting of these default values included in the ANDROMEDA software. The package containing the IDL functions and procedure as well as examples to run on either NaCo or SPHERE data, is accompanied by a User Manual which can be found in Appendix B. The default values are gathered in this document, as well as hints to tune the different user-parameters.

[4]This default value is different for data from SPHERE, as we will see in Chap. 6, for which most of the time a low N_{smooth}value is enough to normalize the SNR map in a correct way.

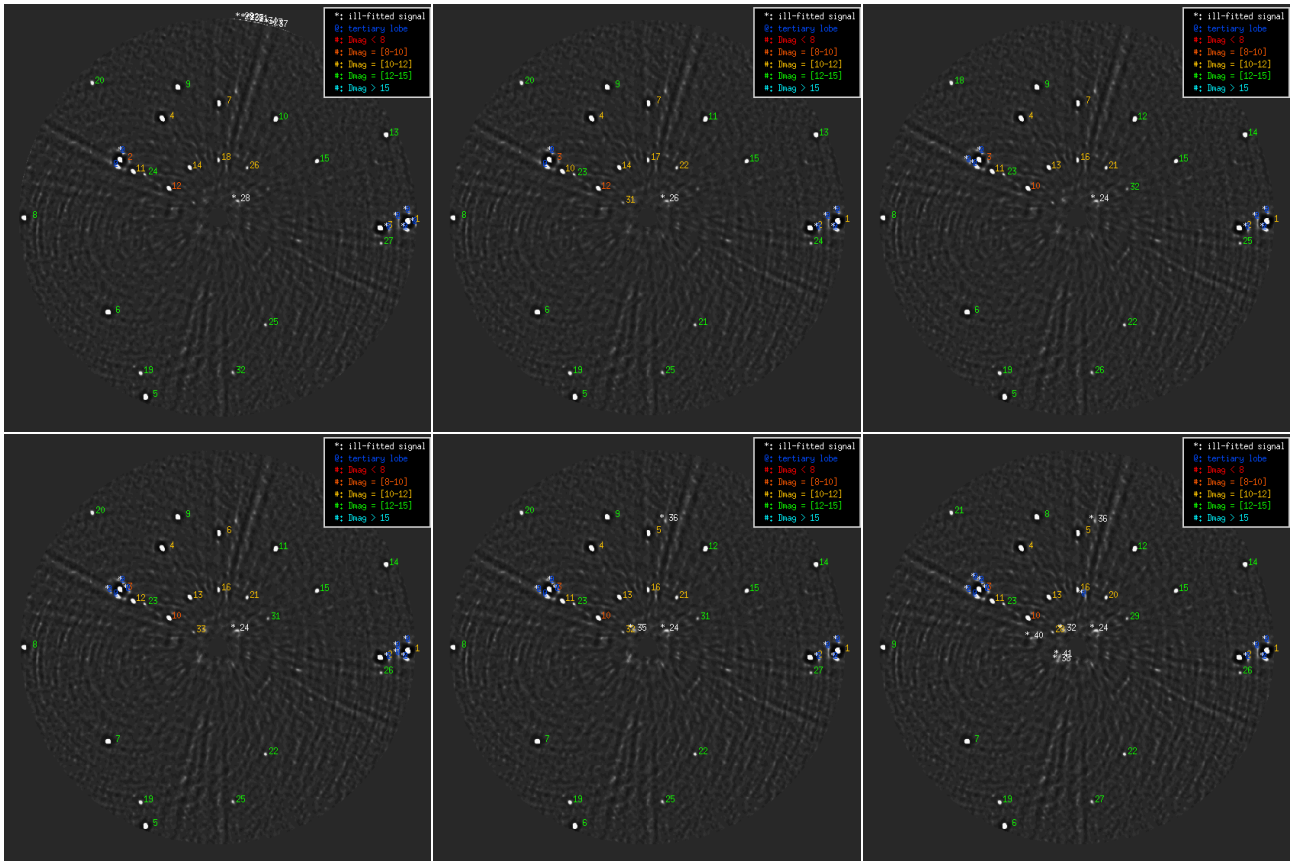

Figure 4.19 – Final detection maps output by the ANDROMEDA pipeline by making N_{smooth}varies from its reference value. From left to right and top to bottom: N_{smooth}= 2, N_{smooth}= 6, N_{smooth}= 12, N_{smooth}18 (Default), N_{smooth}= 26 and N_{smooth}= 36.

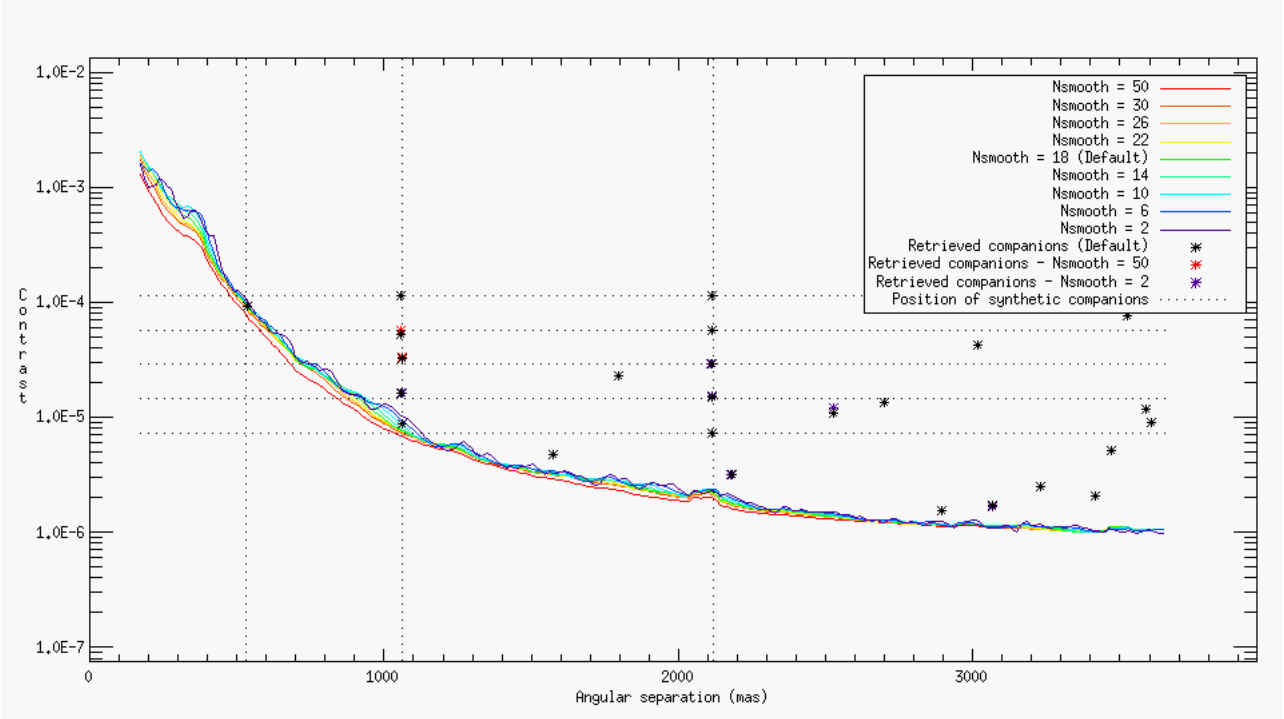

Figure 4.20 – Detection limits retrieved as a function of the smoothing value N_{smooth}set to perform the normalization of the SNR map.

Parameter	Definition	Units	Default value	Impact
F	Filtering fraction	-	1/4	low
ADI method	Method to optimize the ADI	-	LS	high
δ_{min}	Minimum separation to build the differential images	λ/D	1.0	high
dr	Width of annuli in which the ADI is performed	λ/D	1.0	low
R_A	Ratio optimization to subtraction areas for the ADI	-	1	low
N_{psf}	Size of the reference PSF frame	λ/D	10	low
PSF_{shift}	PSF shift precision to build the planet signature model	pixels	1/50	low
positivity	Positivity constraint to compute the likelihood	-	OFF	low
σ^2_Δ	Variance of the residuals in the differential images	-	2D	low
N_{smooth}	Smoothing of the SNR robust standard deviation profile	pixels	18	high

Table 4.7 – User-defined parameters set as defaults in the ANDROMEDA pipeline and their respective significance. The right column shows the impact of the user-defined parameters over the whole process: If *low*, the value can remain fixed and if *high*, it should be tuned according to the data set.

Moreover, in practice, the critical parameter is N_{smooth}since a δ_{min} of $1\lambda/D$ or $0.5\lambda/D$ are both acceptable and no optimization of the ADI process is a good starting point providing correct results. Tuning the other parameters only result in fine gains. I thus advice to use the default parameters set and no normalization as a first step and do the normalization afterwards to check several cases and choose the one the most suited to the data (so that the normalization profile is smooth enough while consistent with the real one).

4.3 Discussion on the threshold set for the detection

This section discusses the optimal threshold range that would reveal as many true companions as possible, while not missing any. In particular, it is tested whether a constant detection threshold is efficient all over the field of view.

This discussion relies upon a study of the behavior of the number of detections as a function of the threshold. Discussing missed detections and false positives requires assumptions on the actual number of companions present in the field. The series of fake companions is a firm basis. The number of astronomical background stars produces additional test cases to check the detection capability homogeneity. We assume in the following that the exact number of detectable point sources for this data set is 25. The graph in Fig. 4.21 was obtained by running ANDROMEDA under the same conditions as before (Tab. 2.4), and represents the number of detections as a function of the threshold, which varies from 3σ to 6σ. On this graph, both the total number of detections and the number of so-called reliable detections are indicated.

This graph shows the existence of a short optimal threshold range, between 4.7σ and 5.1σ, for which the number of detections is exactly the one suspected of being the true one. This test proves that choosing a 5σ threshold is indeed a good value bringing out significant signals.

When increasing the threshold above this range, the faintest signals (like #39) and/or the ones very close to the star (like #33) are the first to be missed by the automatic detection process (these two signals are part of the injected synthetic companions so it is certain that they are true detections).

When decreasing the threshold, the number of detections exponentially increases. Some detections that are actually not true signals are detected and still pass the test that is supposed to sort out artifacts from potential real signals. These detections are usually faint signals ($\Delta H \sim$ 14-16), located far from the star where the algorithm should show better performance.

This plot is similar to a ROC curve (Receiver Operating Characteristic) which is the plot of the true positive rate (TPR) as a function of the false positive rate (FPR) for various threshold settings. In the ideal case, we want to find the threshold for which the TPR is 100% while the FPR is 0%[5]. On Fig. 4.21, it happens in the green area, where false detections have been efficiently rejected by the a posteriori sorting. As a general rule, one wants to maximize the area below the ROC curve

[5]Of course, such a threshold does not exist but in the ideal case, that is what would be perfect to obtain.

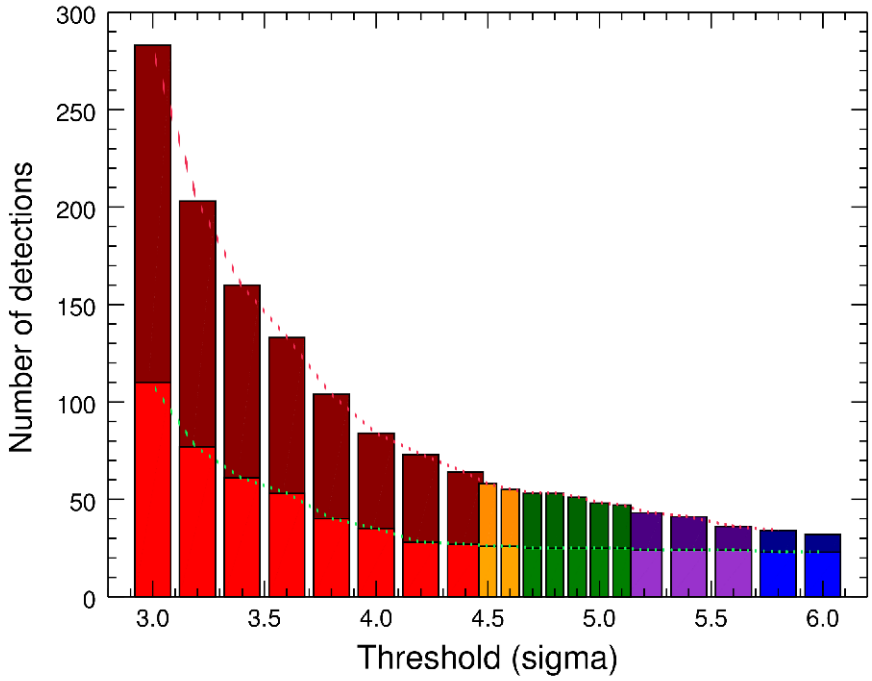

Figure 4.21 – Number of total detections (dark colors) and of confirmed detections (light color) as a function of the threshold set for the TYC-8979-1683-1 NaCo images. The optimal zone (where all 25 companions are detected) is shown in green. A false alarm zone is shown in red (more than one false detection) and orange (one false detection) and a loss zone in blue (more than one true companion is not detected) and purple (one true companion is not detected). Figure from Cantalloube et al. (2015).

(which means the TPR is higher than the FPR). The Fig. 4.21 shows the gain brought by the a posteriori sorting of the detection since the red dotted curve never crosses the green curves (so the optimal range is never reached). Moreover, the red dotted curve decreases way faster than the green one (in the ideal case, the green line should be constant on the total number of true companions, or at least its derivative to be as close to zero as possible). Also, the number of ill-fitted detections becomes significantly higher than the number of true detections, whereas above the threshold this ratio remains quite constant. For a very high threshold (greater than 6σ), it is expected that the green and red dotted curves finally meet.

Note that in exoplanet detection, the problem is a binary problem (either the planet is detected or not). A thorough analysis could be done by injecting a much larger number of companions at different separation and position angle from the star and for different flux. It would be more rigorous but valid only for this specific data set. As it is also very long to compute the ROC curve, I chose to only base the discussion on the point sources present in the field of view. Here, this study is valid only for this data set, which has the advantage of containing many point sources, so it still gives a fair idea of the behavior of the algorithm as a function of the threshold.

4.4 Performance of the ANDROMEDA method

Once the optimal set of parameters for this data case is found and that the chosen threshold is consistent, it is needed to precisely quantify for the performance of the method in terms of estimating their positions and contrast. To do so, we use the knowledge we have about the 20 injected synthetic planets (described at Sect. 2.3.1): knowing their exact position and contrast, it is possible to compare them with the values retrieved by the algorithm. The table Tab. 4.8 gathers the injected vs estimated values for each of these 20 synthetic companions, as well as their SNR.

On the second hand, it is also important to check that all the planetary companions detected

I_{sep} [mas]	I_{PA} [°]	$I_{contrast}$ [mag]	Index	SNR	E_{sep} [mas]	E_{PA} [°]	$E_{contrast}$ [mag]
260	299.6	12.85	-	-	-	-	-
260	329.6	12.10	-	-	-	-	-
260	359.6	11.35	-	-	-	-	-
260	29.6	10.60	-	-	-	-	-
260	59.6	9.85	-	-	-	-	-
530	299.6	12.85	-	-	-	-	-
530	329.6	12.10	-	-	-	-	-
530	359.6	11.35	-	-	-	-	-
530	29.6	10.60	-	-	-	-	-
530	59.6	9.85	#29	6.02	534.16 ±2.99	59.66 ±0.93	10.02 ±0.87
1060	299.6	12.85	#26	6.36	1060.62 ±8.68	299.49±0.14	12.58 ±0.73
1060	329.6	12.10	#20	10.37	1058.39 ±5.60	329.76 ±0.04	11.92 ±0.38
1060	359.6	11.35	#16	14.20	1061.53 ±3.68	359.50 ±0.12	11.17 ±0.26
1060	29.6	10.60	#14	22.53	1056.22 ±0.87	29.75 ±0.13	10.60 ±0.16
1060	59.6	9.85	#11	31.94	1057.06 ±0.47	59.79 ±0.13	9.81 ±0.10
2120	299.6	12.85	#15	18.52	2114.17 ±2.64	299.57 ±0.02	12.84 ±0.20
2120	329.6	12.10	#10	34.67	2115.15 ±1.47	329.59 ±0.01	12.06 ±0.10
2120	359.6	11.35	#5	50.23	2112.73 ±1.29	359.60 ±0.03	11.34 ±0.07
2120	29.6	10.60	#4	72.97	2113.79 ±0.39	29.64 ±0.03	10.62 ±0.05
2120	59.6	9.85	#3	94.38	2113.87 ±0.3	59.66 ±0.04	9.86 ±0.04

Table 4.8 – Injected sources characteristics and their estimated value by ANDROMEDA for each of the 20 synthetic point sources.

are indeed above the detection limit derived from this data set. Figure 4.22 shows the contrast in terms of magnitude of the detected point sources as a function of the angular separation between the detected signal and the central star. On this graph, five horizontal lines represent the true contrast of the synthetic companions and four vertical lines are placed at their true separation from the star. Consequently, we know that signals from the synthetic planets ought to be found at every crossing between the horizontal and vertical lines. The detection limit is over-plotted on the graph (solid line) and the error bars in terms of 3σ error on the contrast estimation are added to the graph. Three types of errors are taken into account in the following discussion: (1) the error given by the estimations (for the specific user-parameter set), (2) the intrinsic error due to the sensitivity of the algorithm to the user-defined parameters and (3) the extrinsic errors due to the instrumental calibrations. In the previous section, the sensitivity study proved that the source (1) and (2) are the same since the intrinsic error bars (2) are included in the errors on the estimation (1).

The following conclusions are drawn out for the given 5σ threshold which has proven to be consistent in terms of detection probability (see Sect. 4.3).

Detection capabilities All the detected signals are indeed above the detection limit. Notably, the artifacts (detections that were a posteriori rejected on morphological criteria) are close to the detection limit (since they are usually the low SNR signals). Concerning the synthetic companions, only the brightest companion is detected at $0.5''$. None of the 5 injected synthetic companions at $0.26''$are detected. The detection limit provided by ANDROMEDA is consistent with these considerations. Note that even with a very low threshold, it is impossible to detect these faint and close signals. As any other image processing based on ADI, detecting faint companions ($\sim 10^{-5}$) at small separation ($< 0.5''$) is very challenging even though ANDROMEDA has a very innovative way of exploiting these post-ADI data. This limitation is due to (i) the limited field rotation, (ii) the δ_{min} limit which prevents from decorrelating the quasi-static speckles close to the star and (iii) the intense residuals that arose due to the intensity of the quasi-static speckle at close separation.

Separation estimation The estimated separation of the detected synthetic planets match the injected values, even very close to the star. The error bars in position due to the Gaussian fit uncertainty

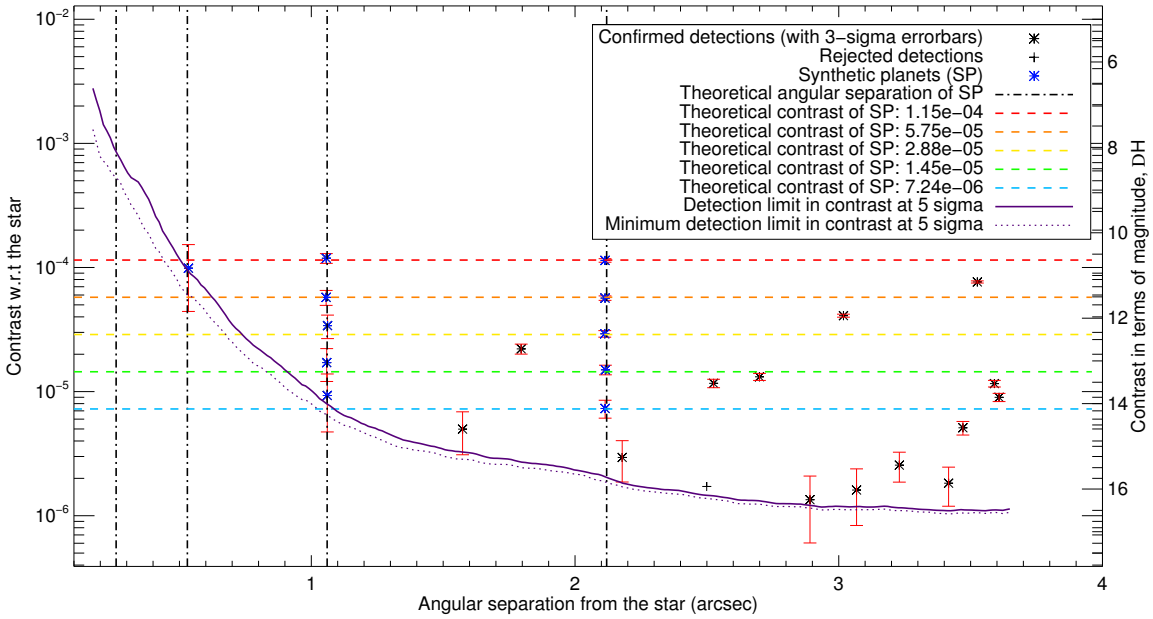

Figure 4.22 – Contrast of the detections as a function of their distance to the star TYC-8979-1683-1. The theoretical contrasts and distances of the 20 injected synthetic planets are shown as vertical and horizontal lines: we should have found a planetary signal at every crossing. The detection limit at 5σ is over-plotted (solid line). This detection limit curve is corrected for the underestimation due to the small sample statistics at close separation from the star. For information, the minimum value of the flux standard deviation map at 5σ for each separation is over-plotted (dotted line). The detected signals assessed to be tertiary lobes are not shown on the graph, but a posteriori rejected detections are shown in orange.

at 3σ are specified in Tab. 4.8. These errors on the estimated separation are not shown in Fig. 4.22 since they are smaller than the symbol size. To that, the instrumental errors must be added. The three main contributors to the astrometric error are: the error on the astrometric calibration (plate scale error, for these TYC-8979-1683-1 data it has been assessed to be of 3 to 7 mas, depending on the separation), the error on the centering of the frames (about 0.5pixels = 6.61mas) and the error on the position of the source (fitting error, about 0.01 pixel = 0.13mas). As these sources of error are independent, they can be quadratically added, giving a total of about 9.7mas (in the worst case). For the astrometry, the so-called instrumental errors are dominant (here, particularly because of the determination of the frames center).

Position angle estimation The estimated position angle of the detected synthetic planets match the injected values, even very close to the star. The error bars in position angle due to the Gaussian fit uncertainty at 3σ are specified in Tab. 4.8. The extrinsic instrumental error are due to two main contributors: the true North error (about 0.1°) and the derotator offset (about 0.01°). Here, the dominant error is the intrinsic error due to the algorithm. As these sources of error are independent, they can be quadratically added, giving a total of about 0.32° in the worst case.

Contrast estimation As expected, the flux is better estimated when the companion is bright and far from the star. A good agreement is still observed between the theoretical contrast and the estimated value and the true value is still included within the estimated error bars, knowing that the error bars shown in Fig. 4.22 are only the ones given by the map of the flux standard deviation but without taking into account the instrumental errors or the algorithm's intrinsic errors. Therefore, on this graph we observe that the closer the signal is to the detection limit, the bigger its error bars on the flux. To that, the instrumental errors must be added. The three main contributors to the

photometric error are: the variation of the PSF flux during the observation (usually about 0.3mag), the estimation of the source flux (can be up to $\sim$ 0.7mag, in particular when Considering possible star variation) and the neutral density error (here it has been estimated at 0.1mag). As these sources of error are independent, they can be quadratically added, giving a total of about 0.93mag (in the worst case). For the photometry, the so-called dominant errors are the intrinsic errors and the error on the variation of the PSF. In the perspectives, Chap. 6.5.5, solutions to minimize these sources of errors are proposed.

Estimation of the detection limit The trend of the computed detection limit is rather smooth and is in line with the detected signals and their contrasts. Notably, the closest detected companion (the synthetic companion at 0.53″) is really close to the detection limit but nevertheless detected. This example shows that the detection limit provided by ANDROMEDA really makes sense and does describe the detection limits according to this specific algorithm, and to this specific data set.

As a conclusion, when taking into account most sources of error, the real position and flux of the injected companions are within the estimated values by ANDROMEDA. Moreover, ANDROMEDA provides a detection limit consistent with these performance. Thus ANDROMEDA proved its success in both detection and characterization capabilities.

Conclusion on ANDROMEDA's performance and sensitivity

The performance of ANDROMEDA in terms of detection are very good but still limited at close separation by the low field rotation and by the high level of quasi-static speckle noise. This limitation applies to all ADI-based methods and here, even the original ANDROMEDA approach does not allow one to investigate very close separations to the star (below 0.5″).

The astrometry estimations are very accurate, added to the fact that ANDROMEDA provides a sub-pixel estimation of the companions position. The photometry estimations are also really good and the error on the flux estimation is usually below the instrumental error bars and well predicted by the estimated flux uncertainties. On this aspect, the main strength of the ANDROMEDA algorithm is that this flux estimation is direct and is not obtained by extensive post-processing, including massive synthetic companions injection.

Also the detection limit provided by ANDROMEDA seems really consistent with the actual detected companions. Once again, this detection limit curve is obtained without needing an extensive post-processing. However, one question remains about the use of this detection limit as it is (a 1D curve). The 2D map provided by ANDROMEDA and directly translated in terms of contrast would be another good information, taking into account the azimuthal variations in the data (which exists, as shown by the spider diffraction residuals for instance). Otherwise a thick detection limit curve, as it is presented here, could bring more information about the extraction capabilities of the algorithm to this data set. Another important useful aspect of ANDROMEDA is that these information can be easily obtained from the computed map of the standard deviation of the flux.

Another conclusion from this chapter is that ANDROMEDA is not very sensitive to most user-parameters it includes. In particular only one user-parameter needs to be carefully fine tuned by the user (the smoothing parameter, N_{smooth}), even if, smoothing too much is not an issue in terms of detection. All the other parameters can be set as their default value to provide good results. If one wants to specifically tune these parameters to extract as much information as possible, this study helps the user to know which parameters are the most sensitive and useful. This study also showed the importance of the detection module which extracts the correct information and rejects artifacts upon morphological criteria, thanks to the knowledge of the functioning of ANDROMEDA.

This whole work led to an independent package, easy to use (with only one user parameter to be fine tuned) and providing systematic and reliable results. This instituted some collaborations to apply this operational and effective tool to real data, as some are presented in Chap.6. From these collaborations, I wrote a user manual of the whole package whose goal is to allow any user to

quickly understand and take over the software. This user-manual is presented in the appendix, App. B.

Now that the specifications of ANDROMEDA are established on the basis of injected synthetic companions, a neat comparison with other state-of-the-art algorithms must be led to check if ANDROMEDA has comparable or better performance than these methods. The next chapter aims to compare the limitations and strengths of ANDROMEDA to three other pipelines that are currently widely used by the exoplanet imaging community.

Chapter 5

ANDROMEDA: Comparison with other methods

Contents

5.1 Dataset: The SPHERE-IRDIS blind test 144
5.1.1 Description of the provided dataset 144
5.1.2 Synthetic companions injected 144
5.1.3 Description of the provided images 145
5.2 Short description of the other algorithms used 145
5.2.1 Radial ADI, r-ADI 146
5.2.2 Upgraded T-LOCI 148
5.2.3 Classical PCA, c-PCA 149
5.2.4 ANDROMEDA 150
5.3 Comparison criteria 151
5.3.1 Detection capabilities 152
5.3.2 Characterization capabilities 153
5.3.3 Practical aspects 155
5.3.4 Ranking metric used for this study 155
5.4 Results obtained and comparison 155
5.4.1 Final images obtained by the pipelines 156
5.4.2 Detected planetary companions 157
5.4.3 Results of the characterization by the pipelines 157
5.4.4 Processing time for each pipeline 160
5.4.5 Practical aspects 161
5.4.6 Conclusion on the different pipelines performance 162

In order to compare the different image processing methods available to the community today, a blind test was organized by the SPHERE consortium. In this chapter, I will use the results obtained with the three main other ADI-based pipelines described in Sect. 1.3.2.1 and compare them to the results obtained from ANDROMEDA. The results of this blind test were published in a report, accessible to the SPHERE consortium members, in November 2015. Another similar blind test was conducted whose results were presented at the conference *In The spirit of Lyot, 2015* on a poster (Galicher et al., 2015). There is no proper and objective recipe to compare the image processing methods. Here I chose to focus on three main aspects that I found relevant for the astronomers using these different tools[1]:

1. The performance in terms of detection capabilities: which algorithm can detect as many true companions as possible with a low number (if any) of false alarms;

[1]Most criteria used by the SPHERE consortium differ from the ones I present here.

2. The performance in terms of astrophysical information retrieval: how close to the true astrometry and photometry the estimated values are;

3. The performance on a very pragmatic and practical aspect: which algorithm is running fast and has systematic/robust results (e.g., without too many user-defined parameters, without too much sensitivity wrt to these user parameters etc.).

In this chapter I will first describe the data set used for the first SPHERE-IRDIS blind test on which the comparisons in this chapter are based (Sect. 5.1). I will then describe the four different algorithms that I will compare to each other: r-ADI, T-LOCI, PCA and ANDROMEDA (Sect. 5.2). In order to properly compare these different pipelines, I will define comparison criteria for this specific study, based on the massive use of these methods to process large surveys data (Sect. 5.3). At last I will present the results provided by each pipeline and compare them according to these specific criteria (Sect. 5.4).

5.1 Dataset: The SPHERE-IRDIS blind test

To illustrate this chapter, I will analyze the data used for the SPHERE blind test of the IRDIS instrument described at Sect. 1.2.4.3. The goal of this blind test (November 2015) was to make a comparison of the different image processing pipelines which are operational for the SPHERE consortium[2] in order to find the most appropriate algorithm to be used to process data from SPHERE: the selected pipeline should be reliable enough to process massive data from the SPHERE survey, SHINE (about 200 nights), and as fast as possible to quickly know if the target has to be re-observed.

5.1.1 Description of the provided dataset

The dataset is made of real SPHERE-IRDIS images, taken during the third commissioning, Com3 (13th of August 2014), in IRDIFS mode, using the APLC coronagraph. The target star was observed using the $K1K2$ narrow band filters of IRDIS (centered on respectively 2.02μm and 2.30μm). Since in this chapter I mean to focus on the radial ADI mode of the different pipelines considered, in the following, I will only deal with the K1 band image cube.

The dataset provided to the blind test participants has been previously reduced (cosmetically cleaned of bad pixels, centered etc.). The data set was thus constituted of the *science cube* (reduced coronagraphic images taken in pupil tracking mode), the corresponding parallactic angles, reference PSF and the wavelength of observation. Notably, the cubes were centered on the central pixel and the reference PSF was normalized in flux to take into account the fact it was recorded with a different exposure time from the coronagraphic images and using a neutral density.

5.1.2 Synthetic companions injected

The coordinator of the blind test has randomly injected synthetic companions (SC) whose shapes were simulated using real unsaturated data recorded the same night (the calibrated reference PSF, also used to estimate the contrast). Eight synthetic companions have been injected in the data using a procedure which takes into account the field of view rotation during the observation (note that for such exposure time, within the observation conditions, the smearing is negligible), as described in Chauvin et al. (2012). The participants did not know how many SC had been injected in the data.

Apart from these synthetic companions, it is assumed that there is no other point source present in the field of view (like true planetary companions or background stars which could mimic a planetary signal).

Fig. 5.1 shows the location of the eight companions injected as in the first frame of the science cube. Tab. 5.1 gives the characteristics of these eight injected SC (the letter index correspond to the

[2]The results of the blind test were internally published in the SPHERE consortium. The report can be find on the SPHERE Twiki pages, accessible to members of the SPHERE consortium. This report uses different criteria that inspired this chapter.

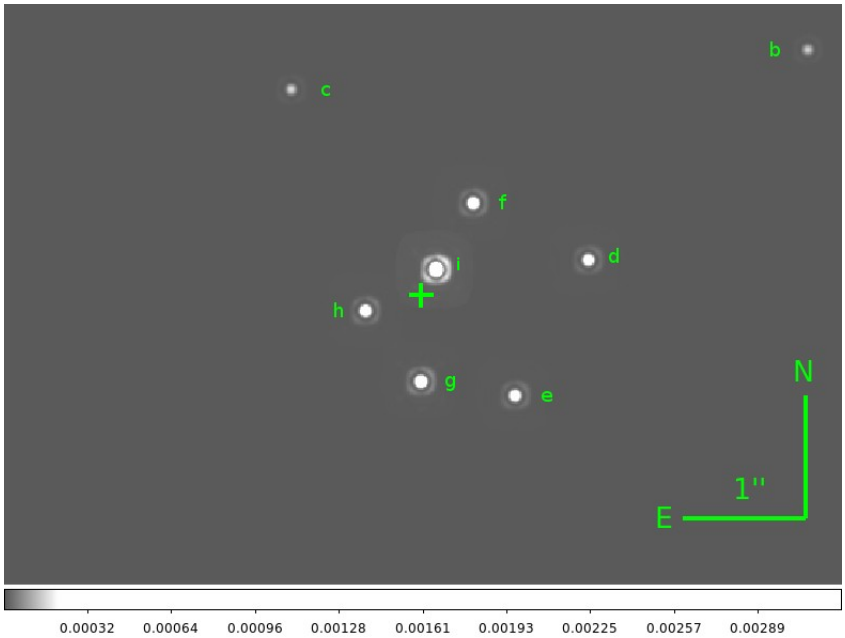

Figure 5.1 – Image showing the location and the contrast of the eight injected synthetic companions inside the SPHERE-IRDIS data. The green cross shows the location of the target star, centered on the central pixel of the frame .

ones in the Fig. 5.1).

Index	Separation (mas)	Position angle (degree)	Contrast (mag)
b	3630.5874	302.52015	16.6195
c	1945.2191	32.778587	16.4626
d	1341.9656	281.91558	15.1024
e	1084.8070	222.34339	15.0443
f	831.10229	331.54469	14.7752
g	690.55261	178.27046	14.4432
h	478.28461	105.46122	14.8770
i	224.79639	333.43495	13.2418

Table 5.1 – Injected positions and contrasts of the eight SC wrt to the target star.

5.1.3 Description of the provided images

The data cube consists of 64 images having a total parallactic angle variation of 87.65° which is a favorable condition to perform ADI. The Tab. 5.2 below recalls the main characteristics of the image cube. The Fig. 5.2 shows one image of the science cube and of the reference PSF. Notably, the frames have not been correctly cleaned of the bad pixels, hot pixels and sensor response (flat field)[3]. Along the images of the cube, remaining artifacts are clearly visible by the dithering between the frames. It is something that users had to deal with to avoid artifacts since, due to the dithering effect, these residuals are moving in the field of view with time and thus, the ADI does not remove them.

5.2 Short description of the other algorithms used

This section describes the different pipelines that have been used to process the blind test images. The description is made from a practical application point of view; for the theoretical description of

[3]Since then, the SPHERE pipeline to reduce the images from raw to exploitable images has been notably improved.

Image parameter	Value
Number of images in the two cubes	64
Size of science frames in the cube	1250×1250 pixels
Size of the reference PSF frame	50×50 pixels
Parallactic angles rotation	From 10.8595° to 98.5090°
Offset angle from true North	none
Filters used	2.02μm ($K1$ band)
Oversampling factors	2.12579
Observation conditions	good

Table 5.2 – Description of the image cubes provided to the SPHERE-IRDIS blind test participants.

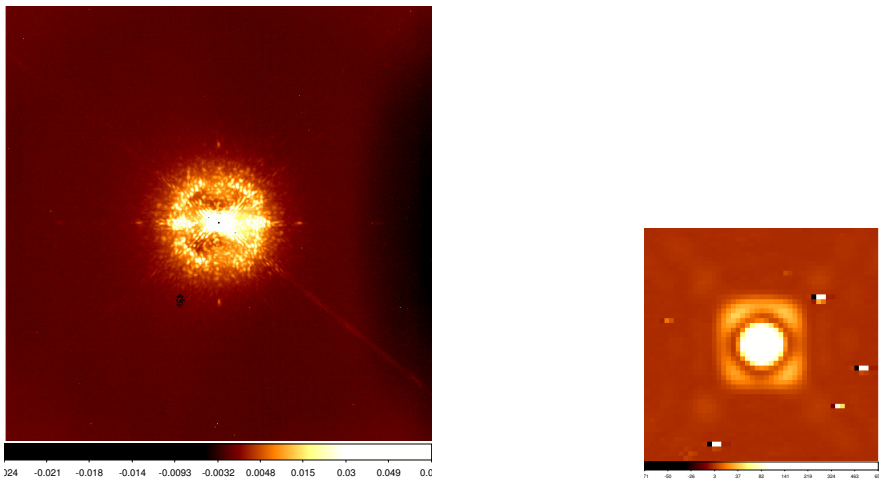

(a) : One reduced image of the science cube provided for the blind test.

(b) : Reduced reference PSF provided for the blind test.

Figure 5.2 – First reduced image of the provided science cube (5.2a) and of the provided reference PSF (5.2b), both in K1 band (asinh scale).

these algorithms, refer to Sect. 1.3.2.1. Four methods are dealt with in this chapter, all based on quite different principles but using ADI: radial ADI, LOCI, PCA and ANDROMEDA. For each image processing pipeline, I will describe the method to first obtain the processed image(s) and second to analyze it in order to perform the detection and characterization (in characterization, I mean the astrometry and photometry of each detection with the associated 3σ uncertainties, as well as the detection limits of the data set). In order to fairly compare the ability of each algorithm to minimize the quasi-static speckle impact in the images under identical conditions, none of these methods are performing either frame selection or binning before processing the images.

5.2.1 Radial ADI, r-ADI

This pipeline comes from the IPAG pipeline which is described in Chauvin et al. (2012) and has been used for surveys led by IPAG, such as the NaCo Large Program (NaCo-LP, probing exoplanets and brown dwarfs at wide orbits from young solar-type stars, Chauvin et al., 2015).

This image processing method has been applied by Dr. G. Chauvin from IPAG, France

Procedure The reduced images are first spatially filtered by a Fourier filter (similar to the one used by ANDROMEDA). Here one fourth of the low spatial frequencies are removed. In each science frame, the following process is made for each annulus centered on the star, of 10 pixels width (about $2\lambda/D$ here). The median of the other science frames, excluding the frames for which the companion at this distance would have rotated of less than $0.75\lambda/D$ and more than $2\lambda/D$ (user-defined), is calculated. The regarded annulus is subtracted of the obtained median (which can be regarded as a PSF model).

It is then rotated to align the North direction with the y-axis. The N_{img} subtracted and rotated images are then co-added (using a mean) to create the final processed image.

Detection The detection is made by computing a SNR map and looking for companions above a 3-sigma threshold. To build this SNR map, the residual noise (in the final image) throughout the field is estimated by calculating its standard deviation in a sliding box of 15 by 15 pixels. The SNR map is then obtained by dividing this noise standard deviation map to the final image.

Characterization A first guess of the detected companion position and flux level is estimated visually. A negative synthetic companion is then injected[4] inside the reduced data, at this first guess position and having this first guess contrast. The r-ADI pipeline, described above, is ran over this new data cube. In this new final image obtained, the residuals are assessed within an aperture defined as a piece of annulus, of dimension $1.5\lambda/D$ radially and $2\lambda/D$ azimuthally, centered on the first guess position (the aperture thus contains the whole typical ADI signature). The flux and positions are estimated by chi-square minimization of the residuals. To do so, the injected negative synthetic companions are adjusted so as to minimize the residuals within this aperture.

This technique, called NEGFC for *NEGative Fake Companion*, to retrieve the flux of the potential planetary companions has been introduced by Marois et al. (2010a) describing the SOSIE pipeline and in (Lagrange et al., 2010) announcing the discovery of the planetary companion β Pictoris b.

Errorbar estimation The error in position is given by the error on the chi-square minimization at the characterization step previously described.

The error on the estimated flux is assessed by injecting 10 positive synthetic companions of known flux, located at the detected planet estimated separation, but at different azimuthal position to probe the speckle influence in the whole annulus. Their flux is retrieved following the method described above and the error made on this flux estimation wrt to the injected flux is recorded. The final error bar is the mean of the flux error retrieved for each of these 10 synthetic companions. Note that the error on the chi-square minimization[5] at the characterization step is also taken into account but is not the dominant one.

Detection limit retrieval The 5σ detection limit is derived by calculating the azimuthal standard deviation in the images (within annuli of 1 pixel width), corrected for the throughput (the flux error due to the PSF reconstruction and subtraction used by the method). This throughput is estimated at each separation, by injecting three synthetic companions every 20 pixel from the star, having three different azimuthal positions (usually at 120° from each other) and of constant SNR. The retrieved flux is compared to the injected flux to estimate the throughput.

This method does not take into account the underlying statistics of the noise, the potential variation of the point source signals through time and the spatial extension of the signal (since the annuli are of 1 pixel width).

Similarities with ANDROMEDA The pre-filtering performed before launching this algorithm is the same as the one performed by ANDROMEDA. It provides a better speckle subtraction for each annular zone which helps detecting the companions visually. The flux loss due to this pre-filtering is

[4]Note that in the following, when I refer to synthetic companions injection, the procedure is the same as the one used to inject the companions in the blind test science frames. This procedure uses the reference PSF provided with the science frames in order to build the synthetic companions to be injected in the reduced data. This procedure only takes into account the rotation of the field of view during the observation (using the parallactic angles provided in the data set).

[5]The measured reduced chi squared follows a χ^2 probability distribution with N degrees of freedom where N is the number of measurements minus the number of free parameters. One can therefore relate the measured reduced chi squared to a probability of getting this value, which can in turn be converted in an error given in sigma, assuming that the parameter is normally distributed.

taken into account by injecting SC using the reference PSF previously filtered of the same amount (as ANDROMEDA does).

The approach to work by annuli to better constrain the angular motion at a specific distance so as to avoid self subtraction while having the speckles as stable as possible in between the two frames is the same as the one chosen for ANDROMEDA.

At last the detection is made thanks to the derivation of a SNR map, as ANDROMEDA does. However this SNR map has no probabilistic significance but it does help to increase the visibility of potential planetary signals. The major criteria to decide whether a detection is present in the field of view is thus visual (hence the help brought by the pre-filtering).

5.2.2 Upgraded T-LOCI

This pipeline is an upgrade of T-LOCI, as presented in Marois et al. (2014) but ran in ADI mode only (without exploiting the potential multispectral information).

This image processing method has been applied by Dr. R. Galicher from LESIA, France

Procedure For each science frame, the 80 most correlated frames are selected under the constraint that the angular rotation between the regarded science frame and the selected correlated frames is great enough so as to keep at least 70% of the companion flux in the resulting image, at all separation, when subtracting the selected frame to the science frame. As this constraint depends on the distance to the star, this is made for each annulus of $1\lambda/D$ width centered on the star (the selection may be different for each considered annulus). The best linear combination of these 80 selected frames is found by minimizing the square of the distance between the science frame and the combined selected frames, within a specific area: the minimization is performed within the external part of the considered truncated annulus whereas the actual subtraction is performed in the inner part of this truncated annulus (see Fig. 5.3). The ensemble of subtracted zones (zone 1 in Fig. 5.3) built that way are gathered to form the PSF model that is subtracted to the reduced image. Once the subtraction is done in every location of the field of view, the subtracted science frame is rotated to align the North direction with the y-axis. The N_{img} subtracted and rotated images obtained this way are then combined, by making the median, to create the final processed image.

Figure 5.3 – Zone used to obtain the final image for TLOCI: The TLOCI coefficients are calculated for the zone in red (zone 2), whereas the subtraction is made in the blue zone (zone 1).

Detection The planetary companions are visually detected in the final processed image.

Characterization A first guess of the detected companion position is estimated visually, then a first fit from this rough position estimates a finer position. The starting flux level is automatically estimated by the pipeline as being the maximum flux of the detection. A so-called *model image* is created by injecting synthetic companions at the detected position (in the first frame), having the first guess flux in an empty cube and then running the T-LOCI algorithm, as described above, using exactly the same parameters (the exact same selected frames linearly combined using the exact same coefficients for each annular zone and each science frame). The model image is then subtracted of the final image and the residual level is assessed within a circular aperture of $3\lambda/D$ diameter centered on the first guess position.

In order to retrieve the position and contrast of the detected companions, the latter procedure is repeated for different subpixel positions around the first guess position and for different flux, until the residuals level is at its minimum within a 50×50 pixels subimage centered on the detection.

Errorbar estimation The error in position is obtained by slowly moving away the synthetic companion in the model image from its estimated position. This shifting is increased until the residuals in the difference between the final image and this model image, within the $3\lambda/D$ diameter circular aperture centered on estimated position, are increased by a factor $\sqrt{2}$ (this factor was empirically determined in Galicher and Marois, 2011).

The same procedure is applied to obtain the uncertainties on the photometry, by slowly varying the flux of the companion in the model image away from its estimated flux.

Detection limit retrieval It is the standard deviation of the final processed image, corrected for the flux throughput, within every annulus of width $0.5\lambda/D$ surrounding the star.

Similarities with ANDROMEDA The constraint on the angular motion to avoid self-subtraction when selecting the frames, and consequently the processing per annuli centered around the star, are also included in the strategy chosen by ANDROMEDA. The optimization within an area larger than the actual subtraction area is similar to the R_A parameter in ANDROMEDA. However in this pipeline, it is deprived of the subtraction zone where the signal could be whereas ANDROMEDA optimizes the subtraction in both zones.

5.2.3 Classical PCA, c-PCA

This pipeline comes from the LAM pipeline which is an update of the pipeline developed in the context of the International Deep Planet Survey (IDPS, probing massive exoplanets at wide orbit around A-stars, Vigan et al., 2012) and the NaCo large program survey (NaCo-LP, probing exoplanets and brown dwarfs at wide orbit around young solar-type stars, Chauvin et al., 2015).

This pipeline requires the frames to be centered in between four pixels. The subpixel shift has been made using a Fourier transform based method. In order to avoid Gibbs effects due to remaining bad pixels in the reduced frames, the given data are previously cleaned[6]

This image processing method has been applied by Dr. A. Vigan from LAM, France

Procedure For each science frame of the cube, a simple PCA analysis is performed including all the other science frames to build a PSF model of the regarded science frame by combining the first twenty principal modes. The science frame is then subtracted of this PSF model. The subtracted science frame is then rotated to align the North direction with the y-axis. The N_{img} subtracted and rotated images obtained this way are then combined, by making the mean, to create the final processed image.

The N_{img} PSF models used for each frame subtraction are recorded to be used later.

Detection The planetary companions are visually detected in the final processed image.

Characterization A first guess of the detected companion astrometry is derived by performing a 2D-Gaussian fit of this detected signal. The fit is performed within a circular aperture of $2\lambda/D$ diameter. The first guess of the companion position is given by the maximum of the Gaussian fit and the first guess of its contrast is given by the flux value at its maximum (wrt to the star intensity).

Then, a negative synthetic companion is injected inside the reduced data, at this first guess position and having this first guess contrast. The PCA pipeline, described above, is ran over this new data cube, using exactly the same parameters (the exact same PSF models are used for each corresponding science frame). In this new final image obtained, the residuals are assessed within a circular aperture of $2\lambda/D$ diameter centered on the first guess position.

Similarly to the r-ADI or T-LOCI pipelines, in order to retrieve the position and contrast of the detected companion, the latter procedure is repeated for different subpixel positions and for different

[6]The cleaning is directly made from the given science frames by detecting the remaining bad pixels in some frames, via a sigma-clipping technique. The detected bad pixels are then replaced by the median of the surrounding pixels. Note that we used the same method before running ANDROMEDA for the same reason.

flux, until the residuals level within this aperture is at its minimum. This procedure is usually repeated 30 to 40 times, depending on how fast the convergence is reached. As the principal components used must be the same as the ones used to obtain the final image, this procedure is made over the whole field of view.

In order to obtain the companion photometry, the flux loss due to the PCA processing must be assessed. This flux loss is obtained by injecting synthetic companions at different azimuthal positions, at the companion separation (with a rather good SNR of about 15 sigma) and retrieving their photometry at the injected position. This flux loss is then taken into account to compute the final companion contrast estimation.

Errorbar estimation The error in position is estimated by injecting negative synthetic companions at different position along the x and y-axis on an area surrounding the true estimated position from a half pixel, until the variance of the reduced chi-square[7] of the detection signal, within the considered aperture reaches a level equivalent to 1 sigma.

The error in flux is estimated by computing the standard deviation of the residuals in the final image over an annulus of $1\lambda/D$ width centered around the star, at the separation of the companion and deprived of the companion signal.

Detection limit retrieval The 5σ detection limit is derived by calculating the azimuthal standard deviation in the images, corrected for the throughput (the flux error due to the PSF reconstruction and subtraction used by the method). This throughput is estimated at each separation, by injecting several synthetic companions at a given separation from the star, having different azimuthal positions.

Similarities with ANDROMEDA The estimation of the uncertainties on position wrt the Gaussian fit is different though ANDROMEDA also performs a 2D Gaussian fit of the planetary pattern. One idea would be to check if this empirical method to retrieve the error bar in position is consistent with the one established in ANDROMEDA, which is directly computed from the 2D-Gaussian fit performed in the sub-image. However, the error on the flux estimation is also defined by the standard deviation of the flux, as for ANDROMEDA.

5.2.4 ANDROMEDA

The procedure to process the reduced images and to detect and characterize companions in the final processed image is described in Chap. 3. To run the operational version of ANDROMEDA the science frames and the reference PSF frame had to be re-centered in between four pixels, as required by the algorithm.

Moreover, we noticed some remaining artifacts (dead pixels and hot pixels) because the SPHERE reduction pipeline was not yet optimized at the time of the blind test. Here, an insufficient flat correction caused the presence of these artifacts. Though it is not critical, these artifacts might have small effects on the algorithms' performance since they are not removed via the ADI part of the algorithm (due to the dithering). We have therefore decided to clean the frames of these artifacts: if a pixel has a very high value (hot pixel) or a /NaN or zero value (dead pixels) then they are replaced by the median within a box of 3 by 3 pixels surrounding the bad pixel detected (which means clusters of dead pixels are smoother but remain in the science frames).

The user defined parameters to run ANDROMEDA are gathered in Tab. 5.3.

The reference PSF is cropped within a 20 by 20 window which contains essentially the central core and the secondary ring.

Due to the observation conditions (rather good but not ideal), remaining low frequency artifacts had to be removed by using $F \geq 1/4$ and the normalization profile is quite jagged (see black solid line in Fig. 5.4-Left) hence the use of $N_{smooth} = 10$ pixels.

[7] Normalized chi-square on the degrees of freedom: the estimation is correct when close to one.

User-defined parameter	Value
Size of the science frames	768×768 pixels
Size of the reference PSF frame	20×20 pixels
Inner Working Angle, IWA	$3\lambda/D$
Filtering fraction, F	$1/4$
Size of annuli, d_r	$1.0\lambda/D$
Minimum separation for ADI, δ_{min}	$1.0\lambda/D$
Optimization method for ADI	No Optimization
Smoothing of the normalization profile N_{smooth}	10 pixels

Table 5.3 – User parameters set to run ANDROMEDA on the IRDIS blind test data.

The results of the ANDROMEDA application as such are shown on Fig. 5.4 and Fig. 5.5. Six companions are automatically detected, without visual inspection, above a 5σ threshold.

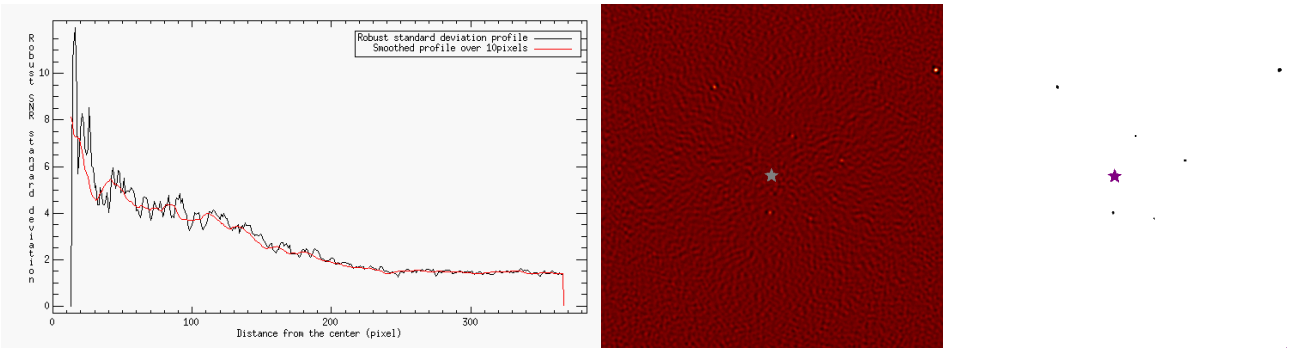

Figure 5.4 – Normalization profile used (Left), SNR map output by ANDROMEDA (Middle) and SNR map thresholded to 5σ (Right). On the latter, 6 companions are detected. In this configuration, the OWA is of 369 pixels, the images have been cropped to 520×520 pixels for more readability.

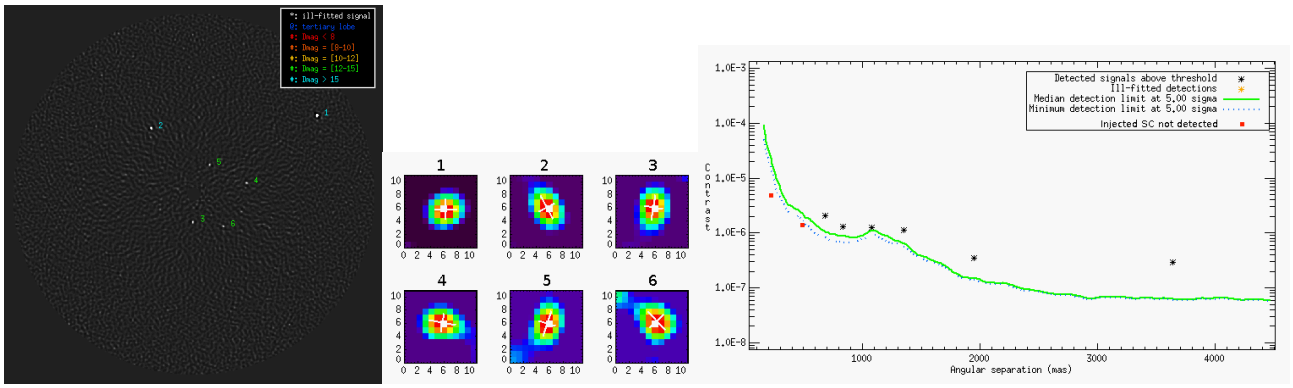

Figure 5.5 – Images output by the detection module of ANDROMEDA (see Sect. 3.3.5). From left to right: Detection map, subimages of each detection and corresponding detection limit at 5σ. For information, I a posteriori added the two non-detected synthetic companions (red squares).

5.3 Comparison criteria

In order to properly compare the four algorithms dealt with in this chapter, there is a need in deriving common comparison criteria. Three aspects can be considered: (i) the detection capabilities, (ii) the characterization capabilities, and (iii) the subjective practical properties of the pipeline.

5.3.1 Detection capabilities

In order to assess the detection capabilities of a pipeline, a first attempt would be to count the number of detected companions wrt the true number of injected companions. However, it is easier to detect companion on the one hand, far from the star and on the other hand, with a high flux. An objective metric should thus take into account these two aspects.

One idea is to use a weighting function f which measures the difficulty in detecting a companion of contrast a and located at a separation r. This function must be strictly independent of the pipeline used. This function $f(r, a)$ can be chosen between 0 (when the detection is easy) and 1 (when the detection is difficult). In a first approach, I chose to separate the two contributions and to define two different functions, $\mathscr{S}(r)$ and $\mathscr{C}(a)$, respectively accounting for the separation and the contrast difficulty. In order to have an indicator, I chose to use the ratio of these two functions, knowing that in a rigorous way, this ratio must be constant for a constant difficulty: $f(r, a) = \mathscr{C}(a)/\mathscr{S}(r)$.

Contrast weighting function $\mathscr{C}(a)$: For the dependence upon the flux, it is enough to normalize the injected flux as a function of a specific value. The natural normalization is wrt to the flux of the star. I thus define a function of the contrast a of the companion, $\mathscr{C}(a)$, which is between 0 and 1 and has greater values when the detection is more difficult (that is to say the contrast is high). In practice, just for this example, I chose to use the injected contrast (relative to the star), multiplied by a factor 10^5 to obtain values closer to one.

Separation weighting function $\mathscr{S}(r)$: For the dependence upon the separation, it depends on the noise level due to the starlight residuals in the images. I thus define a function of the separation to the star r, $\mathscr{S}(r)$, which is between 0 and 1 and has greater values when the detection is easier (that is to say far from the star). In order to obtain this $\mathscr{S}$ function, three major leads can be explored:

-Analytically by deriving the noise distribution (e.g., Modified Rician statistics) as a function of the average Strehl ratio of the observation sequence;

-Empirically, by assuming that the other sources of noise in the images are constant wrt the separation. In that case it can be computed directly from the images, via the azimuthal robust standard deviation for each distance to the star[8]. This profile can then be normalized to obtain the function $\mathscr{S}(r)$ between 0 and 1, as shown at Fig. 5.6-Left.

-A very basic model of dependence can be built as a decreasing linear slope starting from the center of the image and followed by a plateau at the separation where the quasi-static speckles are no longer dominant (only photon and detector noise are present) as shown at Fig. 5.6-Right. From this distance, a given signal at a given contrast has the same difficulty of being detected, whatever its location in this zone. Closer to the star (speckle dominant regime), there is less and less chance to detect a signal at a given contrast.

Note that this may seem similar to the information given by the detection limit curve. However the detection limit curve are derived from the final images and not directly from the images as proposed here. Moreover, the detection limit is dependent upon the chosen pipeline used to derive it whereas the goal of this section is to objectively count the number of detection against the difficulty of retrieving them.

The chosen metric to evaluate the detection capabilities is thus the weighted sum of the detections $d(\hat{\mathbf{r}}, \hat{a})$ by the difficulty due to the separation and contrast of its signal:

$$\mathscr{M}_{detection} = \frac{\sum_{d(\hat{r},\hat{a})} f(r, a)}{\sum_{i(r,a)} f(r, a)} \tag{5.1}$$

[8]Note that if the intensity spatial distribution in the images is stable enough in time, instead of calculating the spatial azimuthal standard deviation, it is better to compute the standard deviation through time, at a particular spatial position. Indeed this method can take into account any non-centrosymmetric feature in the image (such as the diffraction pattern due to the spiders of the telescope) that we loose by azimuthally averaging the information. However, for ADI-based algorithms, these features are not critical (which is not the case for SDI for instance, since the simplistic model used to spatially rescale one of the image to the other's wavelength, is dependent upon the aberration level. Thus more errors should arise from these asymmetric features).

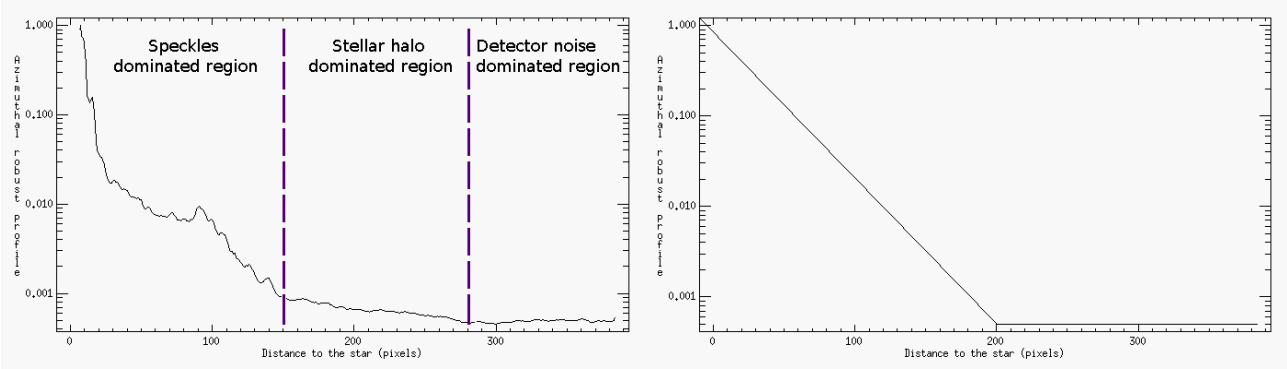

Figure 5.6 – Models of the function $\mathscr{S}(r)$ which accounts for the increasing difficulty in detecting companions closer to the star. Left: Temporal mean of the robust azimuthal profiles of each image of the blind test cube. On the latter we can find the three typical regimes: close to the star the slope is rapidly decreasing, it is then slowly decreasing between ~ 150 to ~ 280 pixels and from $\sim 280 pixels$, it is rather flat. Right: The corresponding simplistic model having a linear slope from the center to the typical distance where the quasi-static speckles are no longer dominant (here typically 200 pixels).

Where $i(r, a)$ is the injected planetary companions, r being the corresponding injected separation to the star and a its injected contrast. Similarly, $d(\hat{\mathbf{r}}, \hat{a})$ is the detected planetary companions by the pipeline.

Thus, this parameter $\mathscr{M}_{detection}$ is between 0 (poor detection capabilities) and 1 (high detection capabilities). For a given number of detections, this parameter rates the most difficult situation as the best one. For a given difficulty, this parameter rates the method which detects more companions. This parameter thus balances between the number of detected companions and the difficulty to detect these companions. Note that this is independent on the method used but it is dependent upon the number of companions detected by the method.

If the detections were automatically provided whatever the pipeline, we could add to this metric the contribution of the false alarms detections, following the same reasoning (it is worse to detect a false alarm far from the star than close to the star).

5.3.2 Characterization capabilities

Another important aspect is to assess the fidelity of the estimated flux and position of the detected companions.

Astrometry: A first very simple criterion is to compute the disparity between the retrieved value $\hat{x}$ (e.g., the separation $\hat{r}$ or the position angle $\hat{\theta}$), and the true value x:

$$\mathscr{M}_x = |\hat{x} - x| \tag{5.2}$$

In the case of ANDROMEDA, the obtained results for the highest signal #1 give: $\mathscr{M}_{separation} = 7.00$ and $\mathscr{M}_{angle} = 0.02$.

Photometry: A very simple criterion is to compute the relative disparity between the retrieved contrast $\hat{a}$ of the detected companion and its true value a:

$$\mathscr{M}_{photometry} = |\hat{a} - a|/a \tag{5.3}$$

In the case of ANDROMEDA, the estimated flux for the highest signal #1 gives: $\mathscr{M}_{photometry} = 1.74\%$.

Astrometry and photometry including uncertainties However the previous metric does not take into account the uncertainties. To take into account the given uncertainties $\Delta_{err}(\hat{x})$ (which are the 3σ uncertainties in this analysis), at least three objectives must be followed:

(1)- To take into account the reliability of the estimation: As for the previous metric, we want the estimated value $\hat{x}$ to be the closest as possible to the injected value x. In geometrical terms, we want to have the smallest distance between x and $\hat{x}$.

(2)- To take into account the reliability of the estimated value in comparison to the estimated uncertainty: we want the true value x to be within the error bars $\hat{x} \pm \Delta_{err}(\hat{x})$. In geometrical terms we want that $(\hat{x} - \Delta_{err}(\hat{x})) < x$ and $(\hat{x} + \Delta_{err}(\hat{x})) > x$. By defining the distance $\ell(x) \doteq \min\{(\hat{x} + \Delta_{err}(\hat{x})) - x; x - (\hat{x} - \Delta_{err}(\hat{x}))\}$, we want $\ell(x) \geq 0$.

(3)- To take into account the length of the error bars, that is to say the distance between the true value x and the uncertainty: we want the distance between the uncertainty and the injected value to be smaller than the distance between the estimated value and the injected value (so that the size of the error bars are taken into account). In geometrical terms we want to have the smallest distance ℓ wrt the distance $|\hat{x} - x|$.

The remarks (2) and (3) together make that we want the global error bar $\Delta_{err}(\hat{x})$ to be the smallest, while still surrounding the true value x. Fig. 5.7 shows a schematic view of these values.

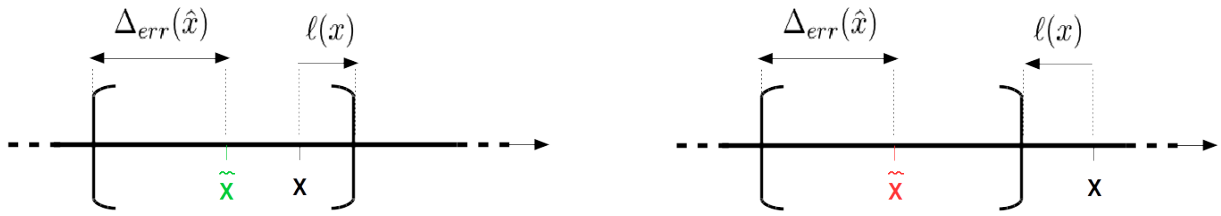

Figure 5.7 – Schematic view of the values used in the rating $\mathscr{M}_{x-error}$. Left: the case $\ell(x) > 0$. Right: the case $\ell(x) < 0$.

Following these considerations, one possible rating $\mathscr{M}_{x-error}$ can be given by:

$$\mathscr{M}_{x-error} = \begin{cases} e^{\ell(x)} \times |\hat{x} - x| & \text{if } \ell(x) \geq 0 \\ (e^{\ell(x)} \times |\hat{x} - x|) - 1 & \text{if } \ell(x) < 0 \end{cases} \tag{5.4}$$

Thus, if $\ell(x) < 0$, this rating provides a negative value, which means the estimation is incorrect. Moreover, the lower the rating, the more the true value deviates from the estimated range. If $\ell(x) \geq 0$, this rating gives a value between 0 (perfect match between the estimated and the true value) and $|\hat{x}-x|$. Moreover, this rating has three special cases (SP):

SP1: When $\hat{x} = x$, the estimation is perfect, $\mathscr{M}_{x-error} = 0.0$. However, if $\hat{x} \simeq x$ then $\mathscr{M}_{x-error} \propto e^{\Delta_{err}(\hat{x})}$ which means it is very close to zero but it increases when the error bars increase.

SP2: When $\ell = 0$, that is to say the true value is *exactly* on the limit given by the uncertainties, then $\mathscr{M}_{x-error} = \Delta_{err}$.

SP3: When $\Delta_{err}(\hat{x}) \to \infty$, then $\mathscr{M}_{x-error} \to \infty$.

This metric should show the relation between the SNR and the estimated uncertainty of a companion. It is thus expected that the general behavior of the $\mathscr{M}_{x-error}$ value is to be positive and closer to zero for furthest and/or brightest companions whereas it can be relatively small (even negative) for close and faint companions.

In the case of ANDROMEDA, the obtained results for the highest signal #1 give:
$\mathscr{M}_{astrometry-error} = 185.99$ which means that the estimation is within the error bars but not excellent;
$\mathscr{M}_{photometry-error} = -1.753$ which means that the injected contrast is not included within the error bars of the retrieved contrast.

These results are to be compared with the previous metric for which less information were included.

5.3.3 Practical aspects

Apart of these concrete numerical criteria, several practical aspects could also be taken into account to assess the ability of a pipeline to detect and characterize companions within a given data set. Among the parameters that add a non-negligible advantage in the use of the image processing pipeline applied, we can think on:

- The objectiveness of the detection procedure;
- The objectiveness of the characterization procedure (first guess, final bias, etc.);
- The time taken for each step (building the final image, detection, characterization including uncertainties and derivation of the detection limit);
- How many steps must be performed by the user from the reduced images to the detection properties;
- How many user-parameters need to be tuned;
- How much the algorithm is sensitive to these user-parameters;
- The number of false alarms and if there exist a way to reject them efficiently;
- The consistency between the detection limit and the flux estimates;
- ...

Here, in the framework of processing numerous data set from big surveys, I will mainly discuss the objectiveness of the detection and characterization procedures and the time to obtain the characterization from the reduced data.

5.3.4 Ranking metric used for this study

Depending on what is primarily expected from these algorithms, there are multiple ways of combining these metrics to assess of the quality of a pipeline. For instance, a simple ranking model given by a linear combination of the different metrics described above could be used to obtain a figure of merit. Depending on the tested abilities of the pipelines, the linear coefficients can be tuned at the user's convenience.

I mention here that such a reasoning could be adapted to different kinds of pipelines (such as the ones with spectral information), to other astrophysical objects (such as extended sources) or to other instruments. In particular, this ranking can prove useful to establish observation strategy for future instruments. Indeed, the next generation instruments, will require advanced image processing methods that will turn crucial to extensively exploit the images. Such a ranking could help disentangling different processing pipelines, along with their reduction pipeline, in order to choose the best strategy in terms of observing time, cost, instrument design complexity.

For the specific study presented here, one of the major issue is to have a quick-look to know, as soon as possible if there is a high probability that a new object is found and consequently whether the target should be re-observed with a high priority. Instead of giving one single figure for the four pipelines, I will provide the results into tables to better visualize each criterion and compare in details the different pipelines' abilities.

5.4 Results obtained and comparison

In this section, I present the results provided by each of the four pipelines dealt with in this chapter. First of all, I discuss the final images in which the detection is performed (Sect. 5.4.1). I then present the detections (Sect. 5.4.2) and characterizations (Sect. 5.4.3) retrieved by each pipeline before deriving the ranking values presented at the previous section (Sect. 5.4.3.1 and Sect. 5.4.3.2). I then compare the detection limits derived along each method and for each algorithm (Sect. 5.4.3.3). I also discuss the computing time of each pipeline (Sect. 5.4.4) and finish with a discussion on the practical aspects brought by each of these pipelines (Sect. 5.4.5). This detailed study highlights the main advantages and drawbacks of ANDROMEDA wrt the current landscape of algorithms used by the exoplanet imaging community.

5.4.1 Final images obtained by the pipelines

The final images are usually given in terms of flux wrt to the host stars (with or without correction of the throughput). Fig. 5.8 shows the final images obtained with each pipeline presented at Sect. 5.2. We recall here that for the PCA and T-LOCI pipelines, the detection is performed visually from these final images. The equivalent map produced by ANDROMEDA is the flux map. The SNR map used to perform the detection with ANDROMEDA is shown at Fig. 5.4-Middle and the images output by the automatic detection module are shown at Fig. 5.5. Even though the detection is not directly performed on this flux map, it is worth to compare it with the other pipelines.

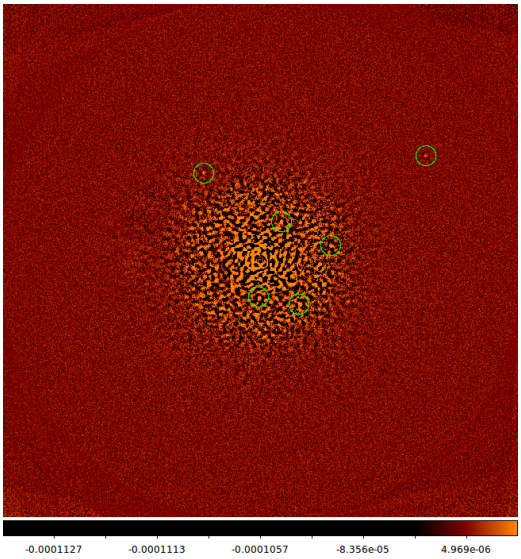

(a) : r-ADI pipeline.

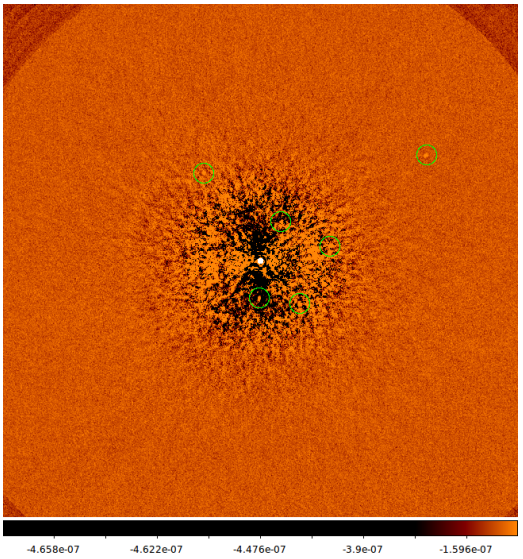

(b) : TLOCI pipeline.

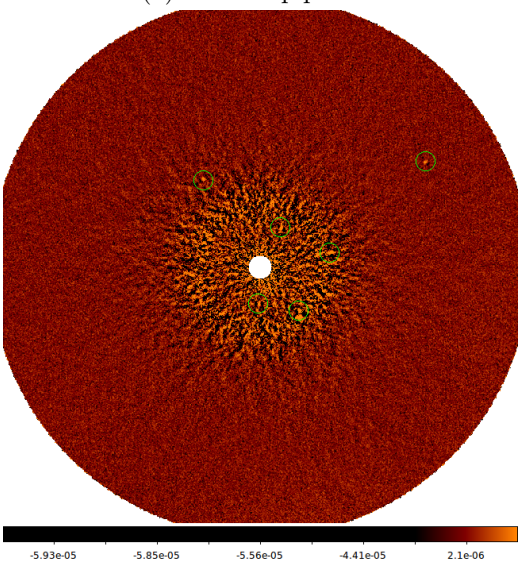

(c) : PCA pipeline.

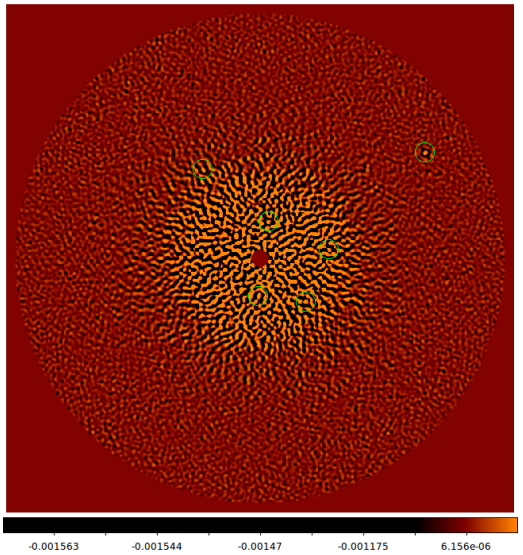

(d) : ANDROMEDA pipeline (flux map).

Figure 5.8 – Final images obtained for each pipeline. The images are given in logarithmic colors. For T-LOCI and PCA, these maps are used to perform the detection by visual inspection. For r-ADI and ANDROMEDA, the detection is made via the SNR map, respectively by visual inspection and by thresholding.

Globally the four maps have the same global flux distribution which shows the intrinsic limitation of such methods which are all based on ADI. For every image, the difficult part of detection is below $1 \sim 1.5''$. The PCA method seems to reach a better speckle subtraction at close separation than the r-ADI method. At large separation (above $2''$) the residuals in each image are quite small (visually similar to salt and pepper noise) except for the flux map given by ANDROMEDA within which the residuals have a typical size of $1\lambda/D$.

5.4.2 Detected planetary companions

All of these four methods detect the furthest six injected companions. Whatever the method applied, they all bring the same detection performance and no false alarms are raised.

5.4.3 Results of the characterization by the pipelines

The tables in Fig. 5.9 gather the results provided by each of the four pipelines on the characterization of the 6 planetary signals detected.

Pipeline	R-ADI					
Companion index	*b*	*c*	*d*	*e*	*f*	*g*
Separation [mas]	3627.90	1944.20	1341.90	1085.03	823.71	694.35
Δerr(Separation) [mas]	1.82	8.29	3.08	5.65	1.64	3.86
PA [deg]	302.55	32.76	281.91	222.50	331.66	178.18
Δerr(PA) [deg]	0.13	0.05	0.20	0.01	0.38	0.34
Contrast [mag]	16.6	16.2	15	14.6	15	14.3
Δerr(Contrast) [mag]	0.2	0.2	0.3	0.3	0.3	0.3

(a) : Results of the characterization obtained using the r-ADI pipeline.

Pipeline	T-LOCI					
Companion index	*b*	*c*	*d*	*e*	*f*	*g*
Separation [mas]	3631.51	1940.84	1345.25	1088.66	826.50	696.32
Δerr(Separation) [mas]	2.72	12.44	8.42	14.13	5.39	15.31
PA [deg]	302.55	32.82	281.97	222.39	331.45	178.27
Δerr(PA) [deg]	0.20	0.08	0.56	0.03	1.21	1.39
Contrast [mag]	16.78	16.57	14.99	14.48	15.14	14.76
Δerr(Contrast) [mag]	0.17	0.17	0.17	0.17	0.24	0.29

(b) : Results of the characterization obtained using the T-LOCI pipeline.

Pipeline	PCA					
Companion index	*b*	*c*	*d*	*e*	*f*	*g*
Separation [mas]	3625.98	1940.54	1340.51	1091.16	825.55	684.26
Δerr(Separation) [mas]	2.73	11.90	9.30	16.95	5.53	7.87
PA [deg]	302.53	32.86	281.84	221.99	331.57	178.41
Δerr(PA) [deg]	0.20	0.05	0.39	0.05	0.75	0.36
Contrast [mag]	16.64	16.30	14.80	14.76	14.72	14.44
Δerr(Contrast) [mag]	0.05	0.11	0.12	0.14	0.12	0.13

(c) : Results of the characterization obtained using the PCA pipeline.

Pipeline	ANDROMEDA					
Companion index	*b*	*c*	*d*	*e*	*f*	*g*
Separation [mas]	3637.59	1948.11	1349.83	1082.20	836.58	685.06
Δerr(Separation) [mas]	10.28	3.01	11.71	0.70	14.16	10.11
PA [deg]	302.54	32.49	282.09	222.97	331.45	178.69
Δerr(PA) [deg]	0.04	0.35	0.29	0.82	0.22	0.71
Contrast [mag]	16.339	16.134	14.862	14.738	14.728	14.207
Δerr(Contrast) [mag]	0.154	0.317	0.459	0.792	0.591	0.402

(d) : Results of the characterization obtained using the ANDROMEDA pipeline.

Figure 5.9 – Retrieved astrometry and photometry by each of the four pipelines, for the 6 companions detected. The true values injected are gathered in Tab. 5.1. $\Delta_{err}(x)$ is the uncertainty on the estimation of the parameter x.

5.4.3.1 Astrometry retrieved with the pipelines

In order to compare in detail the positions estimated by each pipeline, I chose to separate the radial estimation (separation to the star, in mas) from the azimuthal estimation (position angle, in degrees) since the separation estimation is usually the most difficult and most critical estimation.

In this section I present the results given by the rating $\mathscr{M}_x$ (which does not take into account the uncertainties but only the distance between the estimated and the true value) and $\mathscr{M}_{x-error}$ (which additionally incorporates the estimated errorbar and its distance to the true value) for each pipeline (see Sect. 5.3).

Given that all the presented pipelines detect the same companions, when using the first rating method, $\mathscr{M}_x$ defined at Eq. 5.3, it is possible to compare the results by making the sum of the calculated values. A best way is to calculate a sum weighted by the difficulty in extracting a companion as a function of the distance to the star, as discussed in Sect. 5.3.1. The weighting factor can for instance be given by $\mathscr{S}(r)/\mathscr{C}(a)$. The following tables using this first ranking present both the sum and the weighted sum, using the radial robust profile of the reduced images to compute $\mathscr{S}(r)$ and the contrast of the detection (multiplied by 10^5 to obtain smaller values, easier to compare) to compute $\mathscr{C}(a)$.

As the second rating method, $\mathscr{M}_{x-error}$ defined at Eq. 5.4, is not linear when the values are negative, I cannot compare the different estimations by making a sum of these values. Instead, I chose to count which one are incorrect (indicated in red in the corresponding tables), which ones are the easiest to be characterized (far and bright companions) which ones are the closest to 0 (perfect estimation).

Separation to the star: The Tab. 5.4 shows that in terms of estimation of the separation, the four pipelines provide good results, close to zero. The weighted sum shows the same result since every pipeline has lower performance at close separation and for faint objects, which is in line with the increasing difficulty for these conditions.
For this specific case we therefore can say that $rADI > TLOCI > PCA > ANDROMEDA$, where $>$ means "has better performance than".

Pipeline:	b	c	d	e	f	g	Total	Weighted total
r-ADI	2.69	1.02	0.06	0.22	7.39	3.80	15.17	5.78
T-LOCI	0.92	4.38	3.28	3.85	4.60	5.76	22.80	6.65
c-PCA	4.61	4.68	1.45	6.35	5.56	6.29	28.93	7.66
ANDROMEDA	7.00	2.89	7.86	2.61	5.48	5.50	31.34	7.73

Table 5.4 – $\mathscr{M}_{separation}$ (see Eq. 5.3) computed for each detection obtained by each pipeline. A good estimation is when the value is close to zero, which means the estimated value is very close to the injected value (this metric does not take into account the uncertainties). In green, the pipeline of the four which leads to the best results and in red, to the worst.

Taking into account the provided uncertainties does not show the same results. The Tab. 5.5 presents the results using the rating method given by Eq. 5.4. Indeed, T-LOCI is the only method which provides estimations for which the true value is always included in the error bars. However the values are quite high which means that the uncertainties $\Delta_{err}(r)$ are quite large. The r-ADI and PCA pipelines both do not succeed in estimating the separation of the brightest and furthest companion though it should be the easiest detection to characterize.
For this specific case, this rating shows that $TLOCI > ANDROMEDA > PCA > rADI$. Taking into account the uncertainties highlights the fact that rADI is no longer the best algorithm to retrieve the separation and that, on the contrary, it misses two detections. The latter results are due to the fact that the error bars provided by the rADI pipeline are rather optimistic (low) whereas the T-LOCI pipeline provides rather pessimistic error bars (large).

Position angle: The Tab. 5.6 shows that in terms of estimation of the position angle, the four pipelines provide very good results with values very close to zero. It is indeed easier to estimate a

Pipeline:	b	c	d	e	f	g
r-ADI	-0.87	1469.94	1.32	50.71	-1.98	4.04
T-LOCI	5.58	13934.25	555.96	111986.36	10.14	80692.51
c-PCA	-1.30	6428.46	3710.29	254293.10	3.43	30.65
ANDROMEDA	185.99	3.27	367.17	-1.61	32143.87	554.75

Table 5.5 – $\mathscr{M}_{separation-error}$ (see Eq. 5.4) computed for each detection obtained by each pipeline. In red, the pipelines that fail at retrieving a correct estimation. A good estimation is made when the result is positive and close to zero.

good value since, by their principles, the pipelines use the very specific azimuthal shape negative-positive-negative of a detection to estimate its azimuthal position. As for the separation, the weighted sum shows the same result since every pipeline has lower performance at close separation and for faint objects, which is in line with the increasing difficulty for these conditions.
For this specific case we therefore can say that $TLOCI > rADI > PCA > ANDROMEDA$.

Pipeline:	b	c	d	e	f	g	Total	Weighted total
r-ADI	0.03°	0.02°	0.00°	0.15°	0.12°	0.09°	0.41°	0.13°
T-LOCI	0.03°	0.04°	0.05°	0.05°	0.09°	0.00°	0.28°	0.07°
c-PCA	0.01°	0.08°	0.08°	0.35°	0.03°	0.14°	0.69°	0.15°
ANDROMEDA	0.02°	0.29°	0.18°	0.62°	0.10°	0.42°	1.62°	0.40°

Table 5.6 – $\mathscr{M}_{position\_angle}$ (see Eq. 5.3) computed for each detection obtained by each pipeline. A good estimation is when the value is close to zero, which means the estimated value is very close to the injected value (this metric does not take into account the uncertainties). In green, the pipeline of the four which leads to the best results and in red, to the worst.

Taking into account the provided uncertainties does not show the same results. The Tab. 5.7 presents the results using the rating method given by Eq. 5.4. Within this rating method, PCA is the only method which does not succeed in retrieving one correct position angle. Otherwise the other algorithms have comparable results. ANDROMEDA provides larger error bars which makes it having greater values. TLOCI estimates the position angle of the fainter and closer companion (g) with an extremely good accuracy (which might be not realistic).
For this specific case, this rating shows that $TLOCI > rADI > ANDROMEDA > PCA$.

Pipeline:	b	c	d	e	f	g
r-ADI	0.036	0.021	0.003	0.182	0.191	0.111
T-LOCI	0.040	0.049	0.100	0.055	0.289	0.005
c-PCA	0.016	0.097	0.106	-1.740	0.060	0.227
ANDROMEDA	0.024	0.308	0.280	2.619	0.111	1.284

Table 5.7 – $\mathscr{M}_{position\_angle-error}$ (see Eq. 5.4) computed for each detection obtained by each pipeline. In red, the pipelines that fail at retrieving a correct estimation. A good estimation is made when the result is positive and close to zero.

5.4.3.2 Photometry retrieved with the pipelines

The Tab. 5.8 below shows that in terms of contrast estimation, the four pipelines provide good results with values close to zero. The weighted sum shows the same results though the performance does not seem to be linked with the position and contrast of the detections. ANDROMEDA provides rather constant performance and no specific trend are followed by the other methods.
For this specific case we therefore can say that $PCA > ANDROMEDA > rADI > TLOCI$.

Taking into account the provided uncertainties really changes these results. First, the Tab. 5.9 presenting the results using the rating method given by Eq. 5.4, shows that estimating the contrasts of the companion is the most difficult task. None of the method succeed in estimating the true value

Pipeline:	b	c	d	e	f	g	Total	Weighted total
r-ADI	0.00117	0.01595	0.00678	0.02953	0.01521	0.00991	0.07857	0.01981
T-LOCI	0.00966	0.00652	0.00744	0.03751	0.02469	0.02193	0.10776	0.03067
c-PCA	0.00123	0.00988	0.02002	0.01890	0.00374	0.00022	0.05399	0.00958
ANDROMEDA	0.01688	0.01996	0.01592	0.02036	0.00319	0.01635	0.09266	0.01806

Table 5.8 – $\mathscr{M}_{photometry}$ computed for each detection obtained by each pipeline (see Eq. 5.3). A good estimation is when the value is close to zero, which means the estimated value is very close to the injected value (this metric does not take into account the uncertainties). In green, the pipeline of the four which leads to the best results and in red, to the worst.

for all the six companions. T-LOCI misses the furthest and faintest sources but they are the most difficult. On the contrary, ANDROMEDA misses the two brightest and furthest estimation which should be the easiest. With the first metric, PCA was the "best" algorithm of the four, whereas at high SNR, the provided uncertainty is under-estimated.
For this specific case, this rating method shows that $rADI > ANDROMEDA > TLOCI > PCA$.

Pipeline:	b	c	d	e	f	g
r-ADI	0.023	-1.753	0.125	-1.615	0.242	0.168
T-LOCI	0.162	0.114	0.119	-1.619	-1.678	-1.692
c-PCA	0.021	-1.846	-1.748	-1.754	0.059	0.004
ANDROMEDA	-1.753	-1.675	0.299	0.498	0.081	0.279

Table 5.9 – $\mathscr{M}_{photometry-error}$ computed for each detection obtained by each pipeline (see Eq. 5.4). In red, the negative values, that is to say when the injected value is not within the estimated error bars. A good estimation is made when the result is positive and close to zero.

5.4.3.3 Detection limits provided by each pipeline

The Fig. 5.10 shows the 1σ detection limits provided by each pipeline, following the methods described in Sect. 5.2 (without the small sample statistics taken into account at small separation).

The four algorithms provide similar detection limit curves, showing the adaptive optics cutoff at $1.05''$which induces a small rise at this location. For r-ADI, PCA and T-LOCI, the detection limits have a similar level, T-LOCI being slightly higher and r-ADI slightly lower but not significantly. However the curve provided by ANDROMEDA is significantly lower at large separation (from $1.4''$), after the AO cutoff. One interpretation of this effect is that, contrary to other algorithms that are subtracting the speckle floor and are thus limited by the electronic noise in this specific region, ANDROMEDA makes a correlation of the model of the expected planet signature and the residual noise in the differential images which, for this type of residuals, could increase the detection capabilities in this region. At small separation the four curves are merged and begin to differ from $0.4''$. In the AO corrected zone, the detection limit provided by ANDROMEDA is lower than the other ones. This result has to be taken with care and should be confirmed on various data sets.

Also, one has to keep in mind that the detection limits provided really depend on the method used to calculate them, as discussed in Sect.3.1.2.3. Only ANDROMEDA provides a systematic detection limit, directly derived from the map of the standard deviation of the flux (even though one has to choose between the mean, the median, or the minimum azimuthal value of the map). We also demonstrated in Chap. 4 that the detection limit provided by ANDROMEDA is consistent with the actual detection capabilities of the algorithm. For these reasons the one provided by ANDROMEDA could be used as a reference in order to obtain an idea of the detection capabilities for different algorithms.

5.4.4 Processing time for each pipeline

In the ideal case for which the set of user-parameter is fixed and do not require fine tuning, the Tab. 5.10 below gives the computing time taken by the four different pipelines to perform each of

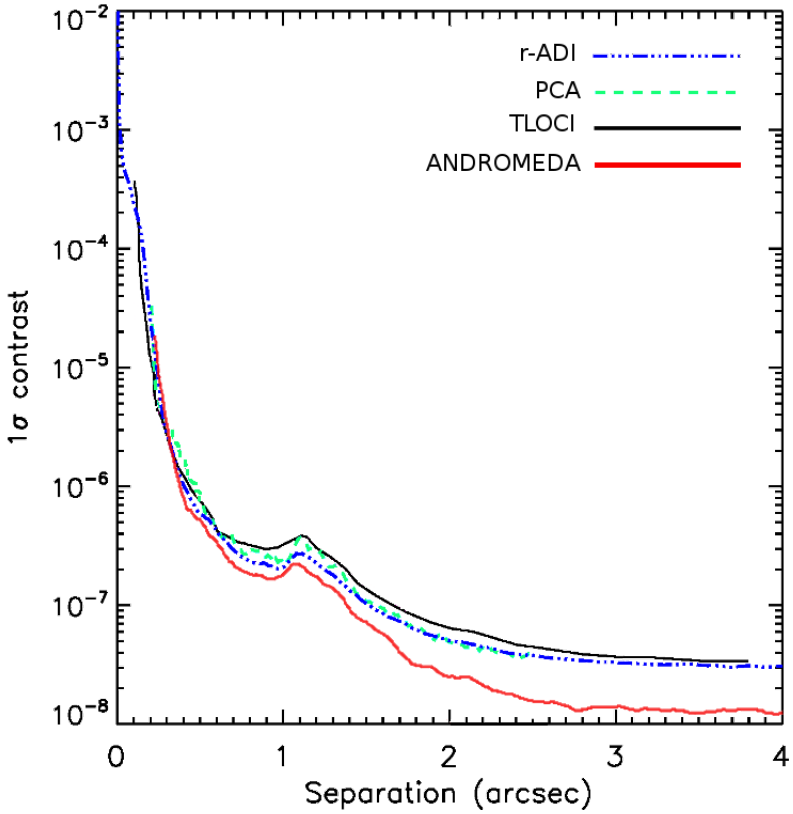

Figure 5.10 – Detection limit at 1σ obtained for the different pipelines.

the main steps, from the reduced images to the complete characterization of the detected planetary signals.

Pipeline:	Final image [s]	Detection [s]	Characterization [s]	Detection limit [s]	Total [min]
r-ADI	300	60	18000	300	310
T-LOCI	40,000	visual inspection	1800	30	700
c-PCA	15	visual inspection	1500	300	30
ANDROMEDA	600	< 1	< 1	< 1	10

Table 5.10 – Time taken by each pipeline to perform the different steps from the reduced image processing to the characterization of the detected signals (order of magnitude since the exact computing time depends on the computer used). Only ANDROMEDA provides the detection without visual inspection which is not included in the total time.

As a conclusion, it takes longer for ANDROMEDA to produce the final image, but once this image is created, all the other steps are performed at once by the detection module (described at Sect. 3.3.5). Moreover regardless of this last remark, the total computation time of ANDROMEDA is way below the other pipelines presented in this part (from the information I could get, it is 3 to 30 times faster). Within these considerations, in terms of computing time, we have: $ANDROMEDA >> PCA > rADI > TLOCI$.

I mention here that recent developments propose pipelines, such as the Vortex Image Processing pipeline (VIP Gomez Gonzalez et al., 2016b), which run faster than the values gathered in the Tab. 5.10 by using the same PCA and r-ADI algorithms, thanks to a module that has been implemented to make the characterization faster than the one presented here.

5.4.5 Practical aspects

Several practical aspects are dealt with in this section, as mentioned at Sect. 5.3.3.

Objectiveness of the detections ANDROMEDA is the only method which does not rely on the user acuteness to perform the detection. The other methods can provide SNR maps but in which the PFA is not linked with a threshold. Thus, even when using the derived SNR maps, one must verify the detections by eye.

Number of user-defined parameters to obtain the final image Apart from PCA, the zone in which the subtraction is optimized increase the number of user-defined parameters: In r-ADI it is only the size of the annuli, in ANDROMEDA it is the size of the annuli and the R_A parameter (subtraction to optimization zone ratio) and in T-LOCI it is the two zones shown at Fig. 5.3. However, for each pipeline, it easy to find the default values for these subtraction zone (in λ/D units). Thus, the main parameters are: (a) For T-LOCI and r-ADI, the δ_{min} parameter must be carefully chosen since this parameter is the basis of a correct speckle subtraction via ADI (as explained at Chap. 4, as the core of ANDROMEDA is not only to subtract the speckle but mainly to perform a MLE in the differential images, this parameter is less critical and can be set to $1\lambda/D$). (b) For the PCA, the number of principal components must be carefully chosen (this parameter is analog to the δ_{min}). (c) For ANDROMEDA, only the N_{smooth}parameter has to be tuned and it can be tested *after* the main ANDROMEDA process so it does not take too long to try 2-3 values before visually choosing one.

Number of steps to obtain the different characterization information r-ADI first computes the final image, then must run the characterization procedure for each detection found and, eventually, compute the detection limit using another different procedure (in total, there are $2+N_{det}$ independent steps). T-LOCI also first computes the final image and runs several characterization procedure to obtain, on the one hand the estimations and on the other the uncertainties on these estimations (from the given estimation made at the previous step) for each detection, added to that, the computation of the detection limit is made using another different procedure (in total, there are $2 + 2.N_{det}$ independent steps). PCA computes the final images and repeats the process several times to perform the characterization (regardless of the number of detections) while the uncertainties and detection limit estimations are calculated directly from the final images (in total, there are 4 independent steps). ANDROMEDA performs only two steps: one to run the actual algorithm and obtain the final images, the other one to run the detection module which exploits the output.

5.4.6 Conclusion on the different pipelines performance

As a conclusion, the four algorithms lead to comparable results in terms of estimation of the position and flux. The main advantages and drawbacks of each of the four methods are the following:

- The T-LOCI is very long and has several user-parameters to be thoroughly set. It has good performances in terms of position and contrast estimations.
- The r-ADI pipeline is quite long but has the advantage of being simple, with a few parameters to be set, while providing good overall results in terms of contrast and position estimation. However, the given uncertainties in terms of position are too optimistic, which can lead to mistakes if the range of value is required for the astrophysical interpretation of the detection.
- The PCA pipeline is less time consuming but one has to be careful of the number of principal modes chosen to obtain the final image. Its performance are quite good, mostly in terms of contrast estimation, for which unfortunately the corresponding uncertainties are too optimistic which can lead to mistakes if the range of value is required for the astrophysical interpretation of the detection.
- The ANDROMEDA pipeline is the fastest and requires only two steps with only one user-parameters to be fine tuned (N_{smooth}, which can be adjusted after the ANDROMEDA process since it is a post-processing). In terms of detection, it is the only algorithm providing an objective detection via the SNR map. In terms of characterization capabilities, its results are comparable

to the other pipelines with no specific qualities nor major problems. However, the detection limit provided by ANDROMEDA is lower at large separation than the one provided with the other pipelines. Added to that, the ergonomics of the ANDROMEDA pipeline makes it particularly easy to use. Also, the uncertainty provided is consistent with the SNR of the detection and does not include a systematic as for other pipelines.

Note that the comparison presented in this chapter is strictly valid only for this specific data-set, which includes only synthetic companions (so no smearing nor flux variation is taken into account), and concerns only these four methods. The general ideas resulting from this chapter are indicators but are not strict conclusions on the algorithms performance.

Conclusion: ANDROMEDA's advantages and drawbacks

As said above, even though ANDROMEDA does not bring breakthrough in terms of position and contrast estimation, it has several non-negligible advantages in terms of practical use. ANDROMEDA runs very fast, with only one user-parameters, N_{smooth}, to be fine tuned, which can be made after the main process delivering the images. Another important feature of ANDROMEDA is its ability to perform the detection in an unsupervised way. Moreover the toolbox within the pipeline permits to quickly visualize the results and provides, within one step, the characterization and the detection limit. The estimated flux does not need to be corrected a posteriori using forward modeling. Moreover, by its principle the detection limit provided by ANDROMEDA is objective and, as seen at the previous chapter, is consistent with the actual detection capabilities. The latter could be used as a reference to compare the detection limits obtained for the various algorithms used by the exoplanet imaging community.

A similar comparison has been carried out on the β Pictoris NaCo data described in Sect. 3.2.1, between the performance obtained from ANDROMEDA and those from PCA (from a first version of the VIP pipeline by Gomez Gonzalez et al. (2016b), in collaboration with the Liège University). The results have been published in Cantalloube et al. (2015) which describes the performance of ANDROMEDA on VLT/NaCo and can be found in appendix (App. A).

This chapter confirms that ANDROMEDA successfully addresses the main stake motivating this PhD work: in the current landscape of the state-of-the-art algorithms used by the exoplanet imaging community today, ANDROMEDA is an adjustable tool which, by its innovative approach, being conceptually different from these other methods, its ease of use, its rapidity and most of all its objectivity (in terms of detection, flux retrieval and detection limit computation) makes it competitive. The skills of ANDROMEDA are particularly beneficial in the context of the massive data from large surveys.

In the next chapter, in the objective of applying massively ANDROMEDA to on-sky data, I processed several data types from the SPHERE instruments. This work allows one to anticipate the potential limitations of the method, to improve the detection module along with the needs of the astronomers and to check that ANDROMEDA is robust to various applications. This work also gives hints on possible extensions to make ANDROMEDA more suited at processing the images delivered specifically by the second generation of high-contrast instruments.

I would like to thank collaborators who processed the data from the blind test using the different pipelines and who helped me with the description of each pipeline and fruitful discussion about data processing: A. Vigan (c-PCA pipeline, LAM, France), G. Chauvin (r-ADI pipeline, IPAG, France) and R. Galicher (T-LOCI pipeline, LESIA, France) and M. Bonnefoy (T-LOCI pipeline, IPAG, France).

Chapter 6

ANDROMEDA: Applications on various experimental data

Contents

6.1 Response of ANDROMEDA to the different narrow band filters offered by SPHERE-IRDIS 166

6.1.1 The planetary companion GJ504 b 166

6.1.2 Properties of the GJ504 IRDIS images 167

6.1.3 User-parameters to run ANDROMEDA on the GJ504 IRDIS images 167

6.1.4 Results from ANDROMEDA applied to the GJ504 SPHERE-IRDIS images . . 168

6.2 Response of ANDROMEDA to different observing conditions 169

6.2.1 Observation conditions of the star GJ504 at different epochs 170

6.2.2 User-parameters set to process the images of GJ504 at different epochs 170

6.2.3 Results from the application of ANDROMEDA on the GJ504 images at different epochs 170

6.3 Investigating for a difficult source: the case of 51Eri b in H-band 173

6.3.1 The planetary companion 51Eri b 173

6.3.2 Observation conditions of the star 51Eri by SPHERE-IRDIS in H-band 174

6.3.3 ANDROMEDA user-parameters to process the SPHERE-IRDIS 51Eri data . . 174

6.3.4 Results of ANDROMEDA applied to the SPHERE-IRDIS images of 51Eri . . . 174

6.4 SDI+ADI process of SPHERE-IRDIS data in DBI mode, by ANDROMEDA 175

6.4.1 The case of a companion showing an absorption band: 51Eri images in H2H3 bands 176

6.4.2 The case of the planetary system HR8799 in H2H3 bands 177

6.5 Processing SPHERE-IFS data with ANDROMEDA 182

6.5.1 Multispectral cubes properties and user-parameters set for ANDROMEDA . . 182

6.5.2 Collapsing the images to obtain the detection 182

6.5.3 Multi-channel detection and channelwise spectrum estimation 184

6.5.4 Using SADI to increase the detectability and sensitivity 188

6.5.5 Preliminary spectra retrieved by ANDROMEDA 191

Since May 2014, the SPHERE instrument has been delivering a large number of data after its installation at the Nasmyth focus of the VLT-UT3. It is interesting to apply ANDROMEDA to images from this instrument in order to potentially push the contrast lower than traditional image processing techniques. ANDROMEDA is particularly suited to process images from IRDIS and IFS offering high-contrast imagery in infrared. These SPHERE instrument subsystems and their various observing modes are described in Sect. 1.2.4.3.

The images delivered by the recent generation of instruments dedicated to high contrast, such as GPI or SPHERE, are substantially different from the images provided by the previous generation (such as NICI or NaCo). The AO system of SPHERE is constituted of a DM with 40×40 actuators (compared to 14×14 in NAOS) which makes the correction zone bigger, with cutoff at $20\lambda/D$ from the star (compared to $7\lambda/D$ with NaCo) and makes reach a SR of about 90% with SPHERE (compared to about 40% with NaCo). Also, the coronagraph in SPHERE is optimized and adapted to the AO performance with a centering follow-up which makes it extremely efficient in removing the coherent part of the starlight. As a result, the dominant features in the SPHERE images are the diffraction residuals whereas the quasi-static speckles arising from residual turbulence are dominant in the NaCo images (despite the use of coronagraphs whose alignment was not optimal, making the star halo very similar to a saturated image), as shown on Fig. 6.1.

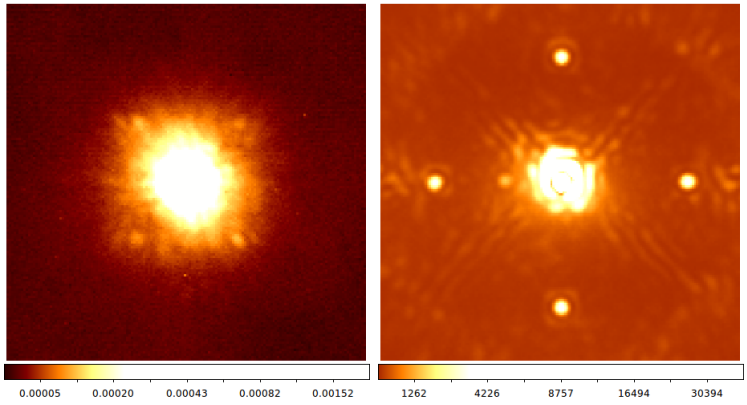

Figure 6.1 – Images from the NaCo instrument (left) in L' band (3.8μm) and from the SPHERE instrument (right) in $K1$ band (2.05μm) of the same target star, β Pictoris (see Sect. 3.2.1). The images size are of $41 \times 41\lambda/D$. The SPHERE images have been taken after applying a waffle pattern to the DM, creating four satellite spots (star images) located at $14\lambda/D$ from the centered star. The four satellite spots present in the NaCo image are the residual from uncontrolled modes of the DM and are located at $7\lambda/D$.

In the context of an image processing method such as ANDROMEDA, these different aspects play an essential role. Extensive tests have shown that the optimal values for some of the user parameters differ between these two different generation instruments. For instance, for SPHERE images, the pre-filtering is still necessary to remove the two smooth symmetrical halo surrounding the centered star that are due to the wind and that are often visible in the reduced images. Moreover the SPHERE coronagraphic images are better exploited without optimization of the ADI step (robust-affine or least-square fit of the image couples, see Sect. 2.1.2.2 and Sect. 3.2.3). If one uses an ADI optimization, the model without the scaling factor is to be favored (see discussion at Sect. 3.2.5). Due to the high stability of the data, a δ_{min} factor of $1\lambda/D$ is favorable in the context of ANDROMEDA to obtain a better SNR of the substellar companions.

In this chapter I present some examples of results obtained by processing SPHERE data with ANDROMEDA. My goal is to show the robustness of ANDROMEDA to process several types of data and to present interesting results in terms of image processing, confirming the whole consistency of the method. My involvement in processing on-sky data from SPHERE allowed me to work in close collaboration with astronomers to, on the one hand, adapt the pipeline to the format of the images (in terms of input), and on the other, improve the pipeline to the users' needs (in terms of output). The numerous discussions arising from the ANDROMEDA applications on SPHERE data raised many ideas guiding the perspectives of such an algorithm in the current landscape of high-contrast instruments and advanced image processing techniques. In particular the various observation modes of the SPHERE instrument can be exploited in different ways by ANDROMEDA.

In the first section, I will use data of the same object, taken with three different narrow-band filters offered by SPHERE-IRDIS and check if the results are consistent with what is expected in high-contrast imaging (Sect. 6.1). I will then process images of the same object but taken under different observing conditions to verify the robustness of ANDROMEDA to these variations (Sect. 6.2). Once

this is set, I focus on the case of a particularly challenging target (Sect. 6.3). From the results, I discuss the SDI+ADI mode of ANDROMEDA and propose solutions to properly exploit DBI data (Sect. 6.4). From this study, I naturally took an interest in processing images from SPHERE-IFS using ANDROMEDA. I propose and apply several simple solutions to retrieve spectra in the case of a challenging source and propose tracks to be followed to extend the ANDROMEDA concept to process multispectral data (Sect. 6.5).

6.1 Response of ANDROMEDA to the different narrow band filters offered by SPHERE-IRDIS

The goal of this section is to probe the response of ANDROMEDA to different filters to check if the results provided by ANDROMEDA are systematic and consistent with what is expected. First, when the wavelength increases, the angular resolution decreases. Second, for a given wavefront error, the image quality is improved at larger wavelength. Third, as the observations are in the infrared, the sky background can be dominant from about 2μm (in K-band), which, depending on the star magnitude, might affect the performance of the image processing method used. Also, the coronagraph is optimized for a specific wavelength and if one observes at a different wavelength, some artifacts (such as the diffraction pattern due to the spiders of the telescope) may be disturbing. As a result, based on its way of working, ANDROMEDA should show different performance wrt the wavelength of observation.

For this section, I chose a stellar system for which the companion is quite far from its host star in order to probe the SNR residuals all over the field, even at close separation, without having spurious effects due to a planetary companion. The chosen target companion, hosted by the star GJ504, is described in Sect. 6.1.1. The observing conditions to obtain the data at the different filters are described at Sect. 6.1.2. The user-parameters chosen to run ANDROMEDA in the framework of this study are described in Sect. 6.1.3. The results presented and discussed at Sect. 6.1.4, are the obtained SNR maps and their corresponding detection limits.

6.1.1 The planetary companion GJ504 b

The companion GJ504 b has been discovered in 2013 within the SEEDS[1] survey (Kuzuhara et al., 2013). This companion is a Jovian exoplanet of mass estimated between [3-10] M_{jup} and at a projected distance of 43.5 AU from its host star. GJ504 is a sun-like star (G0 type) of magnitude 4.107 in H-band[2] and whose relative old age is estimated to be greater than 100 Myrs. The presence of this substellar companion challenges the core accretion paradigm by its mass-distance properties.

GJ504 b is particularly interesting to study the physical and chemical processes of giant gas exoplanets atmospheres since its estimated temperature is very low (about 500K). In particular, a deep methane absorption band at 1.6μm has been observed (Janson et al., 2013) thanks to the SDI mode of the HiCIAO camera (Suzuki et al., 2010), which is characteristic of such objects.

This object has been followed-up in L' band within the LEECH survey[3] (Skemer et al., 2016) which revealed another deep methane absorption band at 3.3μm and showed that the companion metallicity

[1]SEEDS (Tamura, 2009), for *Strategic Exploration of Exoplanets and DiskS*, is a survey using the Subaru telescope (NAOJ, Mauna Kea, USA) equipped with the high contrast infrared camera HiCIAO (Suzuki et al., 2010) and the adaptive optics system AO188 (Hayano et al., 2008). The purpose of this survey is to probe Jovian mass exoplanets (from 1 to 13 M_J) around about 500 target stars either solar-type or massive young stars in H-band (for which the AO correction provides a good resolution and reach a relatively good contrast). This survey started in 2009 and general results from this survey can be found in Brandt et al. (2014).

[2]http://simbad.u-strasbg.fr/simbad/sim-basic?Ident=GJ504&submit=SIMBAD+search

[3]LEECH (Skemer et al., 2014), for *LBT Exozodi Exoplanet Common Hunt*, is a survey using the Large Binocular Telescope (LBT, Mount Graham, USA) equipped with the high contrast infrared camera (Leisenring et al., 2012) and the adaptive optics system FLAO (Esposito et al., 2010). Its goal is to image exoplanets around about 500 target stars within a wide range of ages (0.1 to 1 Gyrs) in L'-band (for which the contrast is particularly favorable for these objects), thanks to the AO quality. This survey started in 2013 and general results from this survey can be found in Skemer et al. (2016).

was different from the host star which is more compatible with a planetary formation process (different from a binary fragmentation).

The SPHERE instrument also observed the GJ504 system, using the different narrow-band filters offered by SPHERE-IRDIS to characterize the companion in J, Y and K bands and to refine its characterization in H band. In this section, I show the results provided by ANDROMEDA applied to the GJ504 SPHERE-IRDIS observations. The coordinator of this target, M. Bonnefoy (IPAG, France) kindly provided me the reduced data set. Results obtained from the characterization of GJ504 b with SPHERE-IRDIS, using ANDROMEDA, will be published in Bonnefoy et al. (in prep.).

6.1.2 Properties of the GJ504 IRDIS images

Tab. 6.1 gathers the main properties of the images of the star GJ504 used in this section, for the three couples of narrow-band filters available in the SPHERE-IRDIS instrument: Y2Y3, H2H3 and K1K2 bands (from the shortest to the longest wavelengths). The images have not been temporally binned but the frames have been selected to remove those presenting too much starlight diffraction residuals. The reference PSF in the provided data set, has been normalized (in intensity and DIT). The science frames have already been rotated to correct for the true North offset.

Property	**Value**		
	Y2Y3 bands	H2H3 bands	K1K2 bands
Observation date	2015/06/06	2015/06/03	2015/06/05
Wavelengths	$1.022\mu m$; $1.076\mu m$	$1.593\mu m$; $1.667\mu m$	$2.110\mu m$; $2.251\mu m$
Seeing	$0.7''$	$1.20''$	$1.15''$
Number of images	1254	93	204
Total field rotation	$35.11°$	$30.54°$	$27.82°$

Table 6.1 – Table summarizing the characteristics of the observation of the star GJ504 with SPHERE-IRDIS at several wavelengths, on which ANDROMEDA is applied.

6.1.3 User-parameters to run ANDROMEDA on the GJ504 IRDIS images

Knowing that we want to analyze the residual structures of the SNR map and that the planetary companion is far from the star, the set of user-parameters chosen to run ANDROMEDA for this particular study is given in Tab. 6.2. The size of the reference PSF window is set to 32×32 pixels, whatever the wavelength since it is big enough for the largest wavelengths (K-band) and, as seen in Sect. 4.2.3.1, having a too large reference PSF window does not affect the contrast estimation (only the computing time).

User-defined parameter	**Value**
Size of the images, N_{img}	512×512 pixels
Size of the reference PSF frames, N_{PSF}	32×32 pixels
Inner Working Angle, IWA	$10\lambda/D$
Filtering fraction, F	$1/4$
Size of annuli, d_r	$1.0\lambda/D$
Minimum separation for ADI, δ_{min}	$0.5\lambda/D$
Optimization method for ADI	No Optimization
Smoothing of the normalization profile, N_{smooth}	5 pixels

Table 6.2 – User parameters set to run ANDROMEDA on the SPHERE-IRDIS images of the star GJ504 whose observation conditions are gathered in Tab. 6.1.2.

6.1.4 Results from ANDROMEDA applied to the GJ504 SPHERE-IRDIS images

In order to compare the results obtained with the different wavelengths, I will discuss the SNR map, and particularly its residual level, and the detection limits (since we saw that the detection limit provided by ANDROMEDA was compatible with the detection capabilities and the error bars provided on the contrast estimation).

6.1.4.1 SNR maps of GJ504 for the different wavelengths of observation

The Fig. 6.2 shows the SNR map output by ANDROMEDA for the six different wavelengths. In all of these maps, when there is a detection, the companion GJ504 b is the only detection above a threshold of 5σ. In the wavelength doublets H2H3 and K1K2, the companion GJ504 b is not detected in respectively H3 and K2 bands[4]. For the Y2Y3 couple of wavelengths, the SNR of the GJ504 b companion is high in Y3 band (SNR=13σ) and lower in Y2 band (SNR=6.6σ).

For the non-detection in one of the two bands of the doublet, ANDROMEDA can retrieve the 3σ upper limit by simply reading the map of the standard deviation of the flux at the location of the detection. The results of estimation are gathered in Tab. 6.3.

Estimated value	**Y2**	**Y3**	**H2**	**H3**	**K1**	**K2**
SNR	6.6σ	13σ	18.2σ	-	18σ	-
Separation [mas]	2488.85 ± 6.7	2492.75 ± 3.5	2491.75 ± 2.5	-	2497.06 ± 2.5	-
Position angle [deg]	323.06 ± 0.03	323.12 ± 0.004	322.99 ± 0.002	-	322.9 ± 0.006	-
Contrast [mag]	16.45 ± 0.7	16.02 ± 0.3	15.29 ± 0.2	-	14.9 ± 0.2	-
3-σ upper limit	-	-	-	17.17	-	16.44

Table 6.3 – Results of the detection of the companion GJ504 b performed by ANDROMEDA.

6.1.4.2 Detection limits for the different wavelengths of observation

To give an idea of the images quality and of the gain in contrast obtained by ANDROMEDA, Fig. 6.3a shows the raw contrast limit computed from the average azimuthal mean in the reduced images for each filter. The adaptive optics cutoff is visible as a small rise at $20\lambda/D$ (between 600 and 1300 mas in these cases).

Fig. 6.3b shows the 5σ detection limits computed by ANDROMEDA, for each filter. No specific trend appears from one lambda to the other since it is a trade off between a better angular resolution and a worse image quality at short wavelength.We can also clearly see the impact of the background noise at large separation for the K2 image (red-dotted curve). The dominant parameter which affects the detection limit might be the observation conditions which differ from one data set to the other in the three cases presented here. In any case, one has to keep in mind that the number of images and the total field rotation is different for these four data-sets.

Conclusion: ANDROMEDA application at different wavelengths

From this application, we can say that ANDROMEDA is a robust tool which provides SNR maps whose properties are indeed dependent upon the wavelength of observation: the size and the level of the residuals are determined by the wavelength of observation (and not by the method itself). However, in terms of performance, the most critical parameter is the observation conditions. The next section further explores the ANDROMEDA response to different observation conditions.

[4]It is therefore possible to apply some SDI treatment with these couples of wavelengths (see further discussions on this particular aspect in the framework of ANDROMEDA at Sect. 6.4)

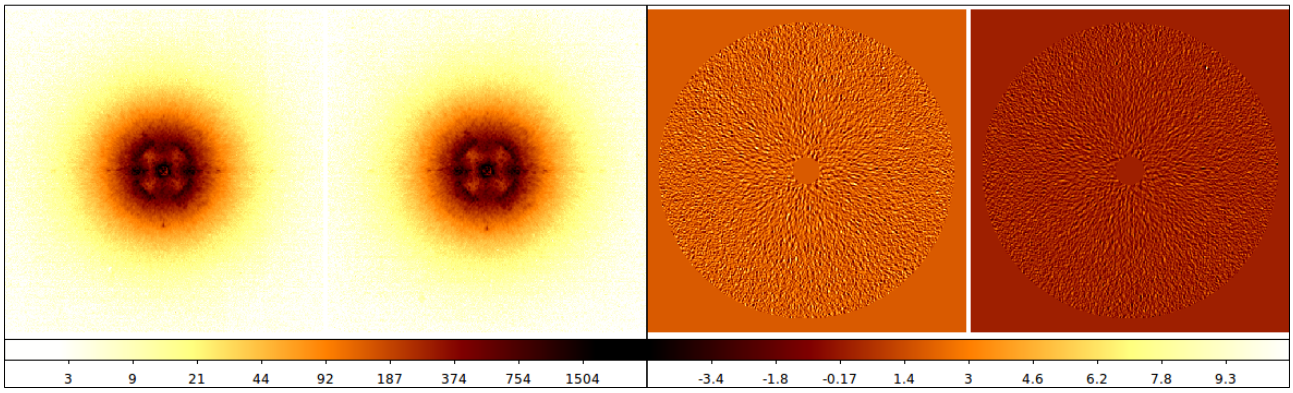

(a) : Reduced images (Left box) and SNR maps (Right box) in Y2Y3 bands. *Left:* Y2 band. *Right:* Y3 band.

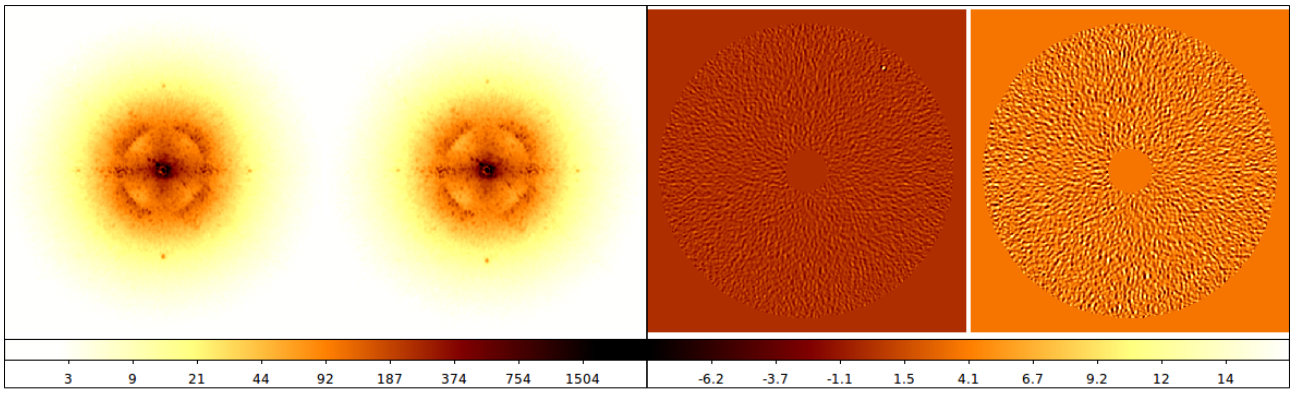

(b) : Reduced images (Left box) and SNR maps (Right box) in H2H3 bands. *Left:* H2 band. *Right:* H3 band.

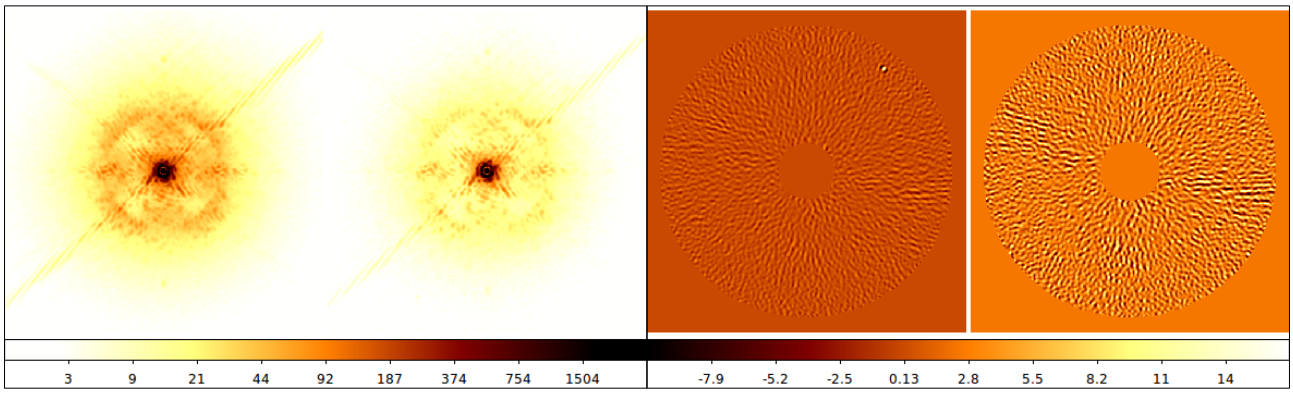

(c) : Reduced images (Left box) and SNR maps (Right box) in K1K2 bands. *Left:* K1 band. *Right:* K2 band.

Figure 6.2 – One reduced image from the cube of the star GJ504 observed under the conditions gathered at Tab. 6.1 (left boxes, logarithmic scale, inverted colors). SNR maps provided by ANDROMEDA when using the user-parameters at Tab. 6.2 (right boxes).

6.2 Response of ANDROMEDA to different observing conditions

As mentioned in the conclusion of Chap. 5, one of the major issue is to select the good frames from the whole observation run. No systematic method has been implemented to perform such a sorting (perspective about this aspect is discussed in Chap. 6.5.5). The goal of this section is to investigate three data sets of the same object taken under different conditions and give a qualitative overview of the ANDROMEDA response as a function of these observation conditions and see if it is robust to the conditions. The number of images and DIT are not identical but the total field rotations are similar for each data set. The images have been previously selected for the best frames. The dominant difference between these images is the atmospheric conditions during the observation run.

To do this study, I chose the GJ504 system (described in Sect. 6.1.1) since it has been observed in

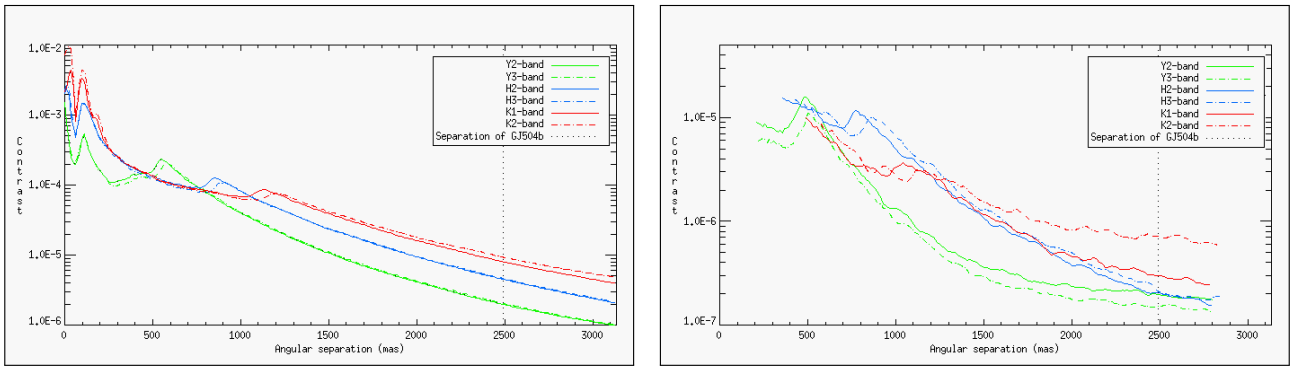

(a) Raw contrast limits.

(b) Detection limits at 5σ.

Figure 6.3 – Raw contrast limits of the images of GJ504 taken with SPHERE-IRDIS and output 5σ detection limit obtained by applying ANDROMEDA on these images (the IWA being set to $5\lambda/D$ for every case).

H2H3 bands, at two different epochs under different observing conditions. As previously, the results presented and discussed at Sect. 6.2.3, are the obtained SNR maps and their corresponding detection limits.

6.2.1 Observation conditions of the star GJ504 at different epochs

The table Tab. 6.4 gathers the main properties of the images of the star GJ504 used in this section, for the two different observation epochs, taken in H2H3 bands. The images have not been temporally binned but the frames have been selected to remove those presenting too much starlight diffraction residuals. The reference PSF in the provided data set, has been normalized (in intensity and DIT). The science frames have already been rotated to correct for the true North offset.

Property	**Value**	
	Epoch#1	Epoch#2
Observation date	2015/05/06	2015/06/03
Seeing	0.72″	1.2″
Number of images	716	128
DIT image	4 sec	16 sec
Total field rotation	29.55°	27.4°

Table 6.4 – Table summarizing the characteristics of the observation of the star GJ504 with SPHERE-IRDIS under the two different observing conditions, on which ANDROMEDA has been applied.

6.2.2 User-parameters set to process the images of GJ504 at different epochs

For this specific study, I used the user-parameter set gathered in Tab. 6.5.

6.2.3 Results from the application of ANDROMEDA on the GJ504 images at different epochs

6.2.3.1 SNR maps of GJ504 for the two different observation conditions

The Fig. 6.4 shows the reduced images and corresponding SNR maps output by ANDROMEDA when using the user-parameters of Tab. 6.5. For the unfavorable epoch, June 2015 (epoch #2), the companion GJ504 b is the only detection above a threshold of 5σ in H2-band (with a SNR of respectively 20σ and 52σ). However, for the favorable epoch, May 2015 (epoch #1), three other signals are detected above the 5σ threshold in H2 band (the SNR of GJ504 b is of 21σ) and two signals are detected above the 5σ threshold in H3 band. These signals are clearly artifacts (see Fig. 6.5) and

User-defined parameter	Value
Size of the images, N_{img}	512×512 pixels
Size of the reference PSF frames, N_{PSF}	32×32 pixels
Inner Working Angle, IWA	$5\lambda/D$
Filtering fraction, F	1/4
Size of annuli, d_r	$1.0\lambda/D$
Minimum separation for ADI, δ_{min}	$1.0\lambda/D$
Optimization method for ADI	No Optimization
Smoothing of the normalization profile, N_{smooth}	10 pixels

Table 6.5 – User parameters set to run ANDROMEDA on the IRDIS images of the star GJ504 whose observation conditions are gathered in Tab. 6.1.2.

they are all automatically rejected by the detection module (see Sect. 3.3.3, here the signals are too elongated). This is due to the fact that the companion GJ504 b is very far from the star (at about $2''$) and is not located in the corrected zone as discussed in the next section.

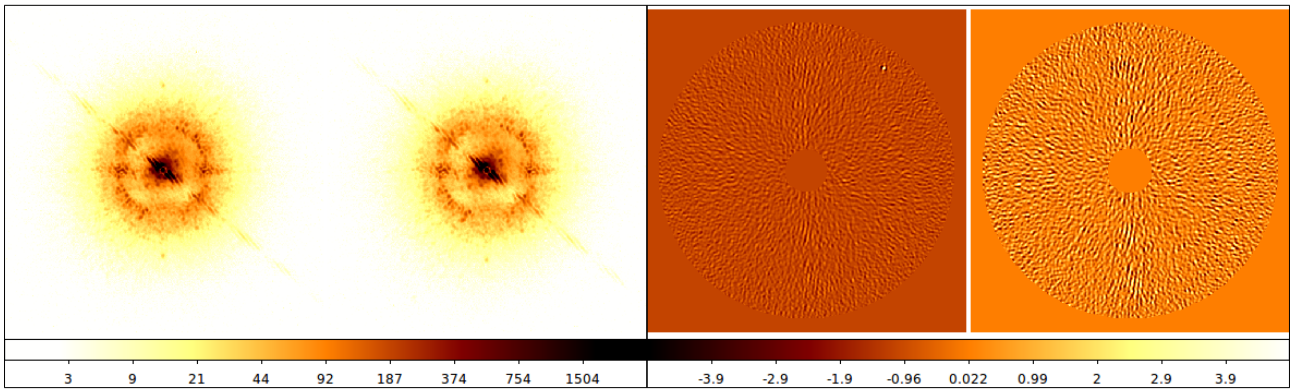

(a) : Reduced images (Left box) and SNR maps (Right box) for the epoch#1 (May 2015).
Left: H2 band. *Right:* H3 band.

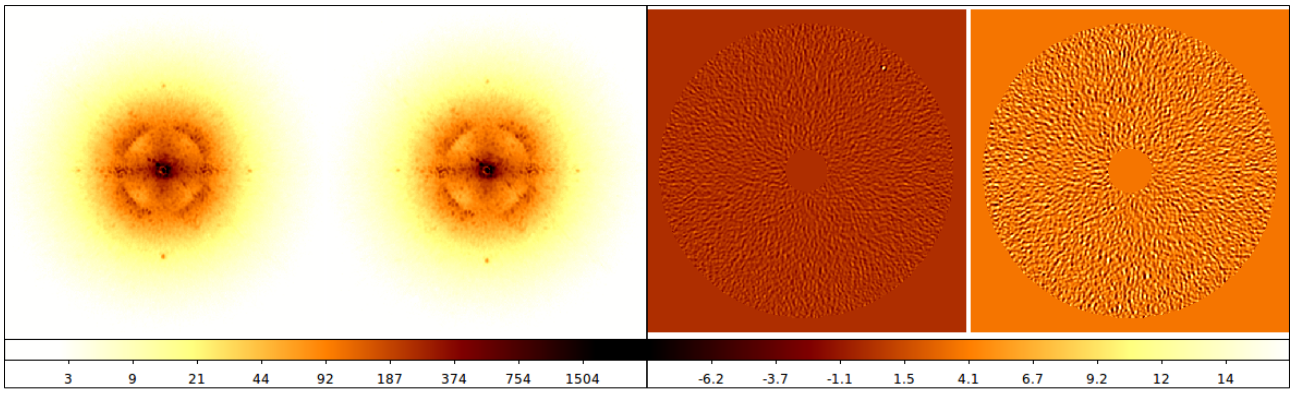

(b) : Reduced images (Left box) and SNR maps (Right box) for the epoch#2 (June 2015).
Left: H2 band. *Right:* H3 band.

Figure 6.4 – One reduced image from the cube of the star GJ504 observed under the conditions gathered at Tab. 6.1 (left boxes, logarithmic scale, inverted colors). SNR maps provided by ANDROMEDA when using the user-parameters at Tab. 6.2 (right boxes).

6.2.3.2 Detection limits of GJ504 for the two different observation conditions

To give an idea of the images quality for the two different epochs, Fig. 6.6a shows the raw contrast limit computed from the temporal average of the reduced images azimuthal means. The impact of a better seeing can be seen as a lower outer uncorrected halo, and also a lower corrected halo. In particular,

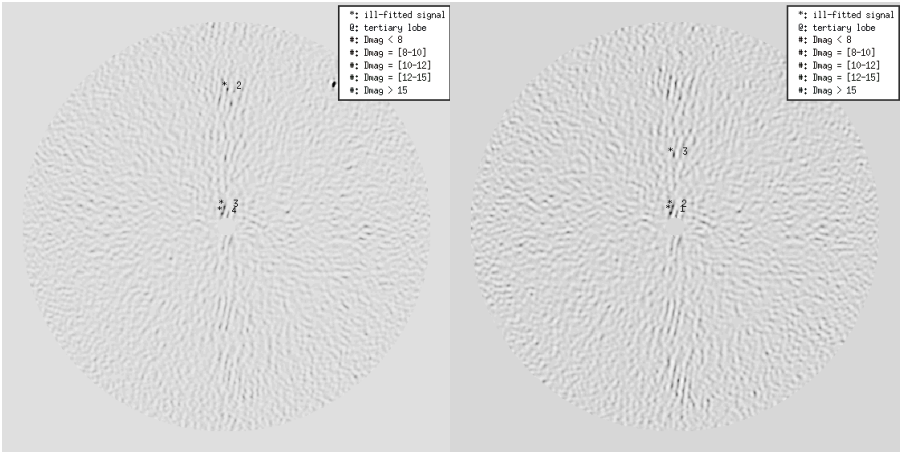

Figure 6.5 – Detection maps provided by the ANDROMEDA detection module after processing the GJ504 images of epoch#1 observations (May 2015). Several rejected artifacts are found above a 5σ threshold in H2 band (left) and H3 band (right). Colors have been inverted (high SNR values are shown in dark).

a narrower AO spatial filter can be used under better seeing conditions (see Sect. 1.2.4.3), which reduces the halo in the 10-20λ/D range. Finally, with low coronagraphic leakage, better seeing also makes possible to choose longer DITs, which is favorable for a lower detector noise at large separation. Such an impact can be seen on the raw contrast profiles: the curve of the favorable epoch#1 (green solid line) is below the one of the unfavorable epoch#2 (red solid line) and is specifically lower in the corrected zone (here below 1″).

Fig. 6.6b shows the 5σ detection limits obtained for the two different epochs. Two regimes are observed:

(i) in the internal part (here below 1.7″), the seeing is better so the images are cleaner and the residuals after processing the images using ANDROMEDA are lower;

(ii) in the external part (here after 1.7″), the images are limited by the detector noises. As the epoch#1 as a lower DIT, this noise has a higher level and is not reduced by ANDROMEDA which explains why the SNR of the companion at the favorable epoch (epoch#1) is lower wrt the SNR of the companion at epoch#2.

The false detections at close separation that are obtained for the favorable epoch (shown on Fig. 6.5) are due to the normalization of the SNR map that is not correctly done (since the two data-sets have the same N_{smooth} parameter though it should be higher in the favorable case). However, one artifact at large separation ($\sim 2''$) still remain after a correct normalization.

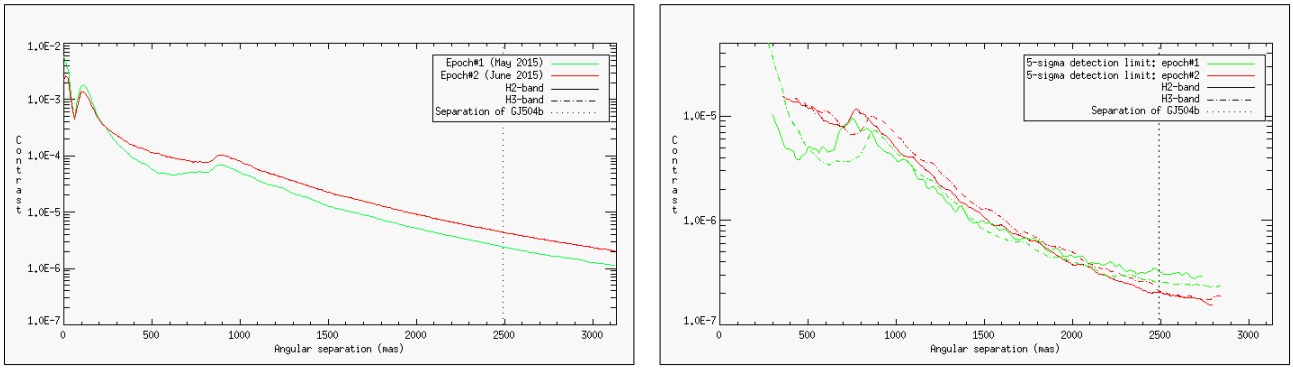

(a) Raw contrast limits.

(b) Detection limits at 5σ.

Figure 6.6 – Raw contrast limits of the images of GJ504 taken with SPHERE-IRDIS in H2H3 band at two different epochs and output 5σ detection limit obtained by applying ANDROMEDA on these images (the IWA being set to $5\lambda/D$ for every case).

Conclusion: ANDROMEDA application under different observation conditions

At large separations, the image quality and the speckle noise have no longer a dominating role contrary to short separations. ANDROMEDA is robust to the different observation conditions and its performance are in line with these conditions, both in the SNR map and in the detection limit provided (and thus in the corresponding error bars). This general agreement between the extrinsic limitations (such as observation conditions or instrumental features) and the results provided by ANDROMEDA are showing, once again, that ANDROMEDA is a rather objective tool and it is fully consistent with the processed data-set quality.

6.3 Investigating for a difficult source: the case of 51Eri b in H-band

Now that we have an idea of the robustness of ANDROMEDA on the two main parameters that could affect its performance (the wavelength of observation and the conditions of observation), I will deal in this section with the specific case of a close and faint companion. To do so, I chose the recently discovered 51Eri b companion, which has been hardly characterized by the past since it can only be observed thanks to a high-Strehl instrument such as second generation of high-contrast instruments dedicated to exoplanet detection. The characteristics of the planetary system host by the star 51Eri is described in Sect. 6.3.1. The observation conditions of the 51Eri data set, using the SPHERE-IRDIS instrument in H2H3 narrow band filters, are described at Sect. 6.3.2. The user-parameters chosen to run ANDROMEDA on this data set are described at Sect. 6.3.3 and the results obtained are shown at Sect. 6.3.4.

6.3.1 The planetary companion 51Eri b

The companion 51Eri b has been unveiled in 2015 within the GPIES[5] survey by Macintosh et al. (2015) and confirmed as a bound companion in De Rosa et al. (2015). This discovery has been made possible thanks to the second generation of high-contrast instrument since it lays at very short separation from its host star (about 450mas) and has a high contrast (about 14.4mag in the H-band). The GPI instrument provided a characterization in H-band (from 1.5 to 1.8μm) and in J-band (from 1.12 to 1.35μm; $R \sim 40$). It has been then observed and characterized in L' band using the Keck/NIRC2 instrument.

The star 51 Eridani is a F0(IV) type star of magnitude 4.77 in H-band[6], located at ~ 29.4 pc. It is part of the β Pictoris star moving group (Zuckerman et al., 2001) and its age is estimated of about ~ 20 Myrs. Its detected companion has been estimated to have a mass between $[2\text{-}12]M_{jup}$ and a projected separation estimated at about 13.2 AU. Its temperature is estimated at $600 - 750$K and its atmosphere is showing strong methane spectral signature and water vapor. By its characteristics, this companion is likely to have been formed by a cold core accretion process.

The SPHERE instrument also observed the 51Eri system, using the different narrow-band filters offered by SPHERE-IRDIS and SPHERE-IFS to characterize the companion in K1K2, H2H3 and obtain its spectrum in YJ (0.95 to 1.35μm; $R \sim 50$) and YH bands (0.95 to 1.65μm; $R \sim 30$). In this section, I show the results provided by ANDROMEDA applied to the 51 Eri SPHERE-IRDIS observations in H2H3 bands for which its detection is very challenging (its detection is straightforward in K1 band and it is absent in K2 band with a 3σ upper limit contrast estimated at 13.89mag with ANDROMEDA). The Sect. 6.5 deals with the ANDROMEDA application to the SPHERE-IFS data. The coordinator of this target, M. Samland (MPIA, Heidelberg) kindly provided me the reduced images. Results obtained from the characterization of 51 Eri b with SPHERE-IRDIS and SPHERE-IFS will be published in Samland et al. (in prep.).

[5]GPIES (Macintosh, 2013), for *Gemini Planet Imager Exoplanet Survey*, is a survey using the Gemini South telescope (Cerro Pachon, Chile) equipped with an high-contrast IR IFS ranging from 0.9 to 2.2μm within five filters (centered in Y, J, H, K1 and K2). Its goal is to explore the close environment of about 600 nearby young stars spanning spectral types from A to M. This survey started in late 2014 and general results from this survey can be found in Marchis et al. (2015).

[6]http://simbad.u-strasbg.fr/simbad/sim-basic?Ident=hip+21547&submit=SIMBAD+search

6.3.2 Observation conditions of the star 51Eri by SPHERE-IRDIS in H-band

The Tab. 6.6 summarizes the main properties of the SPHERE-IRDIS data cube of 51Eri in H2H3 bands on which ANDROMEDA has been applied.

Property	**Value**
Observation date	2015/01/06
Seeing	$1.8''$
Coronagraph	APO1-APLC2
Number of images	256
Total field rotation	$41.76°$; $(-331.910 \rightarrow -290.146°)$
DIT image	16 sec

Table 6.6 – Table summarizing the characteristics of the observation of the star 51Eri with SPHERE-IRDIS, on which ANDROMEDA has been applied.

6.3.3 ANDROMEDA user-parameters to process the SPHERE-IRDIS 51Eri data

The Tab. 6.7 gathers the set of user-parameters applied to run ANDROMEDA on the 51Eri images described in Tab. 6.6.

User-defined parameter	**Value**
Size of the images, N_{img}	130×130 pixels
Size of the reference PSF frames, N_{PSF}	16×16 pixels
Inner Working Angle, IWA	$2\lambda/D$
Filtering fraction, F	1/6
Size of annuli, d_r	$1.0\lambda/D$
Minimum separation for ADI, δ_{min}	$0.5\lambda/D$
Optimization method for ADI	No Optimization
Smoothing of the normalization profile, N_{smooth}	2 pixels

Table 6.7 – User parameters set to run ANDROMEDA on the IRDIS images of the star 51Eri whose observation conditions are gathered in Tab. 6.6.

6.3.4 Results of ANDROMEDA applied to the SPHERE-IRDIS images of 51Eri

The Fig. 6.7 shows the SNR maps output by ANDROMEDA in H2 and H3 bands. In neither of these maps the companion 51Eri is detected above a 5σ threshold. However, when setting the threshold at 3σ, it is detected in the H2-band (with a SNR of 3.7σ), knowing that six artifacts are detected with a higher SNR value. No corresponding signal is found in the H3-band, even at lower threshold. Thanks to the ANDROMEDA capabilities in automatically detecting companions on a threshold basis, it is the first time that Eri51 b is detected and characterized in H2-band directly (without using SDI+ADI procedures for instance) as other methods cannot perform the same.

The Fig. 6.8 shows the detection maps output by the ANDROMEDA detection module in H2 and H3 band, with a threshold set to 3σ. Note that except for the companion #7 in the H2-band map (Fig. 6.8-Left) all the other detections are radially moving outward in the H3-band which proves that they are likely to be speckle artifacts. Hence a combination of these two maps can be used to distinguish likely companions from likely artifact. Solution are proposed in the next section (Sect. 6.4).

Fig. 6.9 shows the corresponding 3σ detection limits provided by ANDROMEDA.

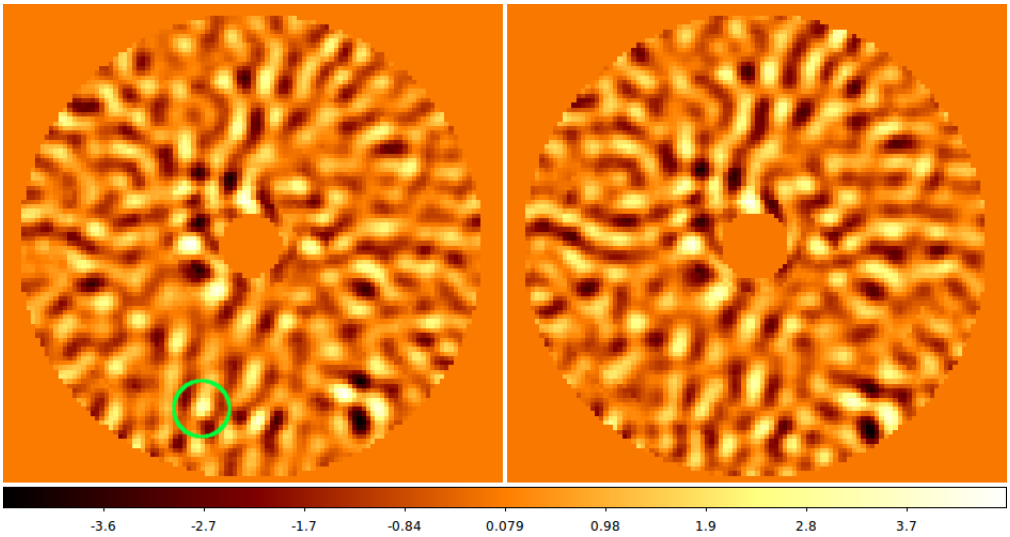

Figure 6.7 – SNR maps obtained by running ANDROMEDA on the 51Eri data, described at Tab. 6.6, using the parameter set at Tab. 6.7, in H2-band (left) and H3-band (right). The companion 51Eri b is visible on the left panel inside the green circle.

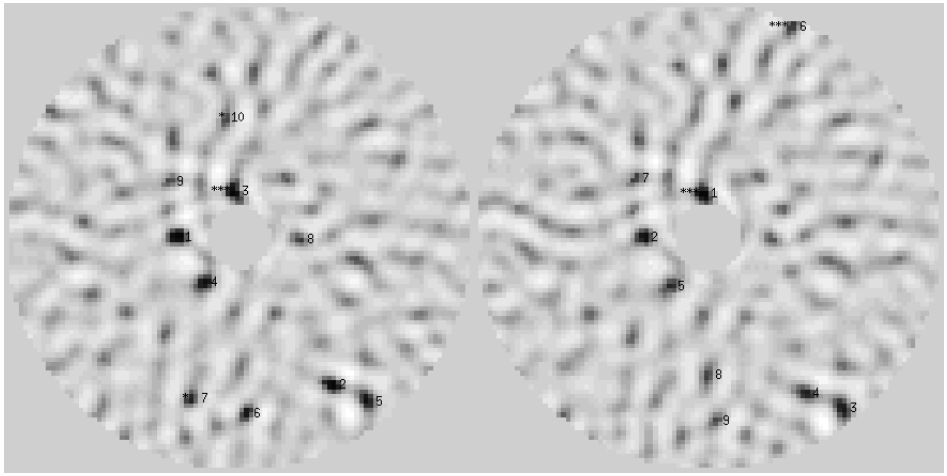

Figure 6.8 – Detection maps obtained by running ANDROMEDA on the 51Eri data, described at Tab. 6.6, using the parameter set at Tab. 6.7. The companion 51Eri b is the signal #7 on the left panel. Colors are inverted: dark color corresponds to high SNR.

As ANDROMEDA does not find any signal corresponding to the 51Eri b companion above a 3σ threshold in the H3-band, it is possible to perform a pre-SDI processing by subtracting the H3 spectrally rescaled image cube to the H2 image cube in order to increase the detectability of the companion in the resulting SNR map. Moreover, the GPI observations found out that the 51Eri companion has a strong absorption line of methane (Macintosh et al., 2015) which means the companion should not be visible in H3 band. The next section discusses the SDI mode implemented in ANDROMEDA, how to use it and how it could be adapted more specifically to process such data.

6.4 SDI+ADI process of SPHERE-IRDIS data in DBI mode, by ANDROMEDA

In the light of the previous section, the dual band imaging (DBI) mode offered by the SPHERE-IRDIS instrument provides additional information that should be exploited by ANDROMEDA to improve its extraction capabilities. This section aims to highlight the interest of a pre-SDI process when using ANDROMEDA and to discuss how to interpret the results provided by ANDROMEDA in this

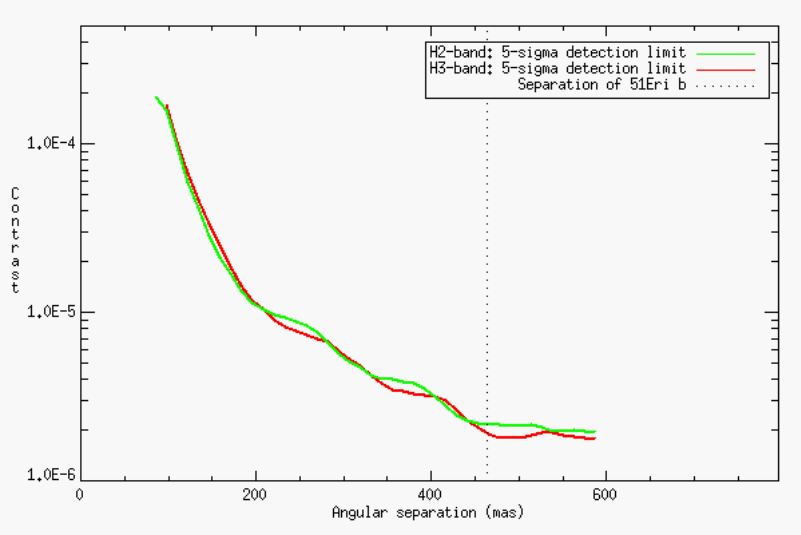

Figure 6.9 – Detection limits at 3σ provided by ANDROMEDA for the H2 and H3 bands independently of the 51Eri SPHERE-IRDIS data.

SDI+ADI mode (hereafter called SADI mode). At last, this leads to evoke what improvements could be implemented in ANDROMEDA to specifically process dual band data.

The SDI concept has been introduced at Sect. 1.3.2.2. We recall here that the spectral subtraction after rescaling one of the two images to the other's wavelength, is fully efficient if there is a way of avoiding the companion self-subtraction. This is possible in two cases: (1) the companion is completely absent in one of the two wavelengths (which is therefore the one for which the images are rescaled) or (2) the distance between the two wavelengths is large enough so that the rescaling induces a radial motion of the companion of more than $1\lambda/D$ in the rescaled frame (the latter also depends on the distance to the star). If none of these cases applies, one must be very careful when interpreting the results.

In this section, I will use two examples to further discuss these cases:

- The case of a close companion which presents a deep absorption in one of the two bands: the 51Eri b companion in the H2H3 bands (Sect. 6.4.1);
- A more general case, without absorption, to discuss the limitations of the SADI and the potential improvements of ANDROMEDA: the HR8799 quadruple planetary system (Sect. 6.4.2).

In ANDROMEDA, the SADI mode (previously implemented before the start of my PhD) performs a wavelength rescaling of one of the two image cubes to the other, then subtract the rescaled cube to the other. Then ANDROMEDA runs in simple ADI-mode on the resulting spectrally subtracted cube.

6.4.1 The case of a companion showing an absorption band: 51Eri images in H2H3 bands

The data are described in Sect. 6.3.2 and the user-parameters set to run ANDROMEDA are described in Sect. 6.3.3. As seen at Sect. 6.3.4, the companion is not visible in the H3 band (at least below a 3σ threshold) and is faint in the H2 band (SNR of 3.7σ). Thus applying a SADI process should increase the detectability of the companion.

The Fig. 6.10 shows the SNR map obtained from the SADI process of ANDROMEDA as well as the detection map to be compared with Fig. 6.7. Only two signals are found above the 5σ threshold, including the companion 51Eri b which has a SNR of 5.8σ (one artifact is found at a higher SNR but it is not well fitted in the flux map). Also, the SNR residuals are lower than the one in the SNR maps presented at Fig. 6.7.

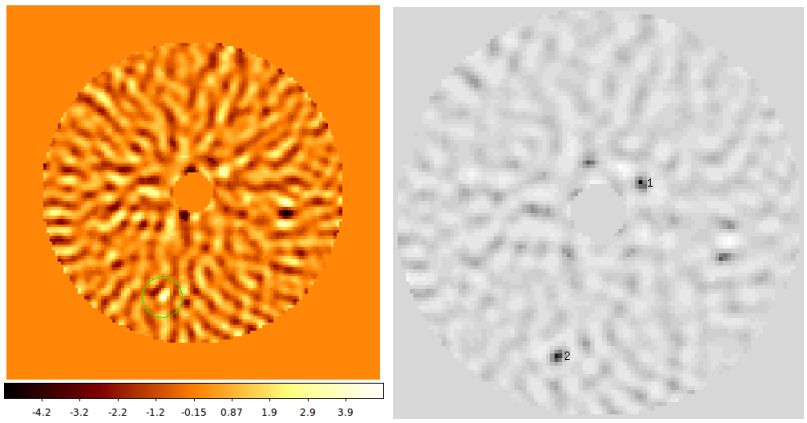

Figure 6.10 – SNR map and detection map at with a 5σ threshold provided by ANDROMEDA ran in SADI mode on the 51Eri images from SPHERE-IRDIS in H2H3 bands. The Eri51 b companion is signal #2 on the right pannel.

The estimated contrast of the 51Eri companion in the H2-band is $\hat{a}_{SADI} = 14.09 \pm 0.8$ in SADI and $\hat{a}_{ADI} = 13.77 \pm 1.8$ in ADI mode. The two values retrieved are consistent with each other and within the given 3σ error bars. As expected, the error bars are smaller in SADI since the signal of the companion is higher.

The estimated separation is 461.54 ± 6.9 in this map whereas in ADI mode, the process estimated a separation of 446.34 ± 14.7 in H2-band. Once again, the error bars given by the SADI process are consistent with the value retrieved in H2-band.

The Fig. 6.11 shows the 5σ detection limit obtained in SADI mode compared to the ones obtained in ADI mode. The detection limit retrieved in SADI mode is indeed way below the ones obtained in ADI mode and this time, the companion 51Eri b (black asterisk on Fig. 6.11) appears above the SADI detection limit curve (red solid line on Fig. 6.11). The small drift inward on the estimated position is also visible in this plot, as well as the potential flux loss (orange point).

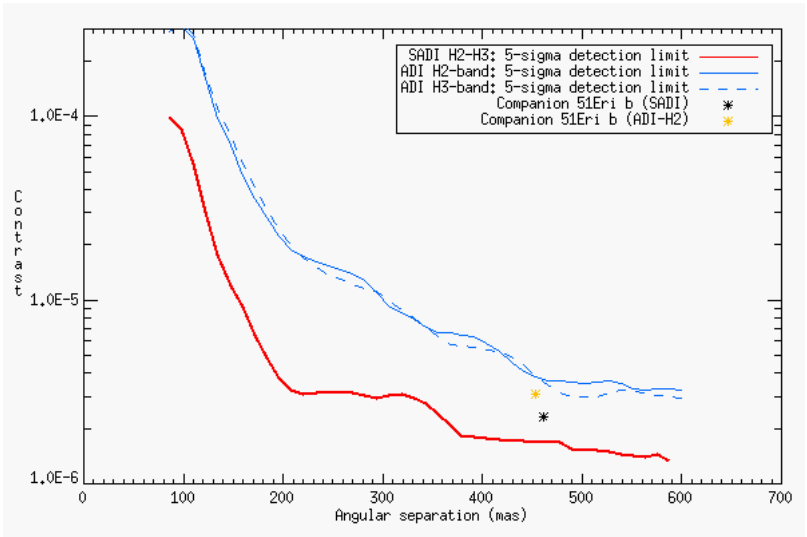

Figure 6.11 – Detection limit at 5σ obtained by running ANDROMEDA on the H2H3 data set of 51Eri in both ADI and SADI mode.

6.4.2 The case of the planetary system HR8799 in H2H3 bands

This section shows a more general case for which the planetary companions do not present an absorption band in one of the two wavelengths of the SPHERE-IRDIS DBI doublets. In the following, I first describe the target used on which the discussion is based. I then describe the SPHERE-IRDIS images

of this target, as well as the user-parameter set to process them with ANDROMEDA. I eventually show the results obtained and discuss potential improvements of the method in this more general case.

6.4.2.1 The planetary system around HR8799

This planetary system was first unveiled by Marois et al. (2008b) with the discovery of three companions orbiting the star HR8799. Advanced image processing permitted to discover later a closer companion HR8799e (Marois et al., 2010b). This planetary system was extensively studied, either to observe its two debris disks (e.g., using SPITZER Su et al., 2009, Herschel Matthews et al., 2014 or recently ALMA Booth et al., 2016) or to characterize the planetary companions at several wavelengths (e.g., LBT in H-band Esposito et al., 2013; Skemer et al., 2012, P1640 Oppenheimer et al., 2013, Subaru/IRCS, VLT/NaCo and MMT/Clio Currie et al., 2011, Keck2/Osiris Bowler et al., 2010; Currie et al., 2012b) and more recently using GPI (Ingraham et al., 2014) and SPHERE (Bonnefoy et al., 2016; Zurlo et al., 2016).

The age of the star hosting the quadruple planetary system is estimated between 20-160 Myrs, and it is located at 39.4pc from the solar system[7]. Its magnitude is 5.28 in the H-band. The planets lie between a projected distance of 15 to 70 AU and are young gaseous giant planets whose masses have been estimated to be about 5 to $7M_{jup}$.

In the atmosphere of the brightest and furthest planetary companion, HR8799b, evidence that water and carbon monoxyde are present (Barman et al., 2015) suggested a non-equilibrium chemistry (dusty atmosphere) including potential heterogeneous thick clouds.

This planetary system is one of the most interesting object to study in the field of exoplanets since it has a unique architecture: it is a the only multi-planetary system discovered in DI and it hosts two debris belts.

6.4.2.2 HR8799 SPHERE-IRDIS data description

The Tab. 6.8 summarizes the main properties of the SPHERE-IRDIS data cube of HR8799 in H2H3 band on which ANDROMEDA has been applied. The data have not been previously selected but they have been temporally binned. These data are the ones used in the paper by Zurlo et al. (2016) (thoroughly described in the latter) which is one of the SPHERE first-light publications.

Property	Value
Observation date	2014/07/13
Atmospheric conditions	variable (seeing from 0.8 to 1″)
Wavelength of observation	H2H3 bands: 1.593μm and 1.667μm
Coronagraph	APO1-ALC2
Number of images	16
DIT image	4 sec × 40 exposures
Total exposure time	43 min
Total field rotation	15.6°; (171.48 → 155.89°)

Table 6.8 – Table summarizing the characteristics of the observation of the star HR8799 with SPHERE-IRDIS, on which ANDROMEDA has been applied.

6.4.2.3 ANDROMEDA user-parameters to process HR8799 SPHERE-IRDIS images

The Tab. 6.9 gathers the set of user-parameters applied to run ANDROMEDA on the HR8799 images described in Tab. 6.8.

[7] http://simbad.u-strasbg.fr/simbad/sim-basic?Ident=HR8799&submit=SIMBAD+search

User-defined parameter	Value
Size of the images, N_{img}	510×510 pixels
Size of the reference PSF frames, N_{PSF}	16×16 pixels
Inner Working Angle, IWA	$5\lambda/D$
Filtering fraction, F	1/4
Size of annuli, d_r	$1.0\lambda/D$
Minimum separation for ADI, δ_{min}	$1.0\lambda/D$
Optimization method for ADI	No Optimization
Smoothing of the normalization profile, N_{smooth}	14 pixels

Table 6.9 – User parameters set to run ANDROMEDA on the IRDIS images of the star HR8799 whose observation conditions are gathered in Tab. 6.8.

6.4.2.4 HR8799 data processed in SADI using ANDROMEDA: results and discussion

In this case, there are no absorption bands and there are companions close to and far from the star (HR8799e and HR8799b respectively), so it is possible to study the impact of the companion self-subtraction in these two generic cases.

The Fig. 6.12 shows the SNR maps obtained in H2, H3 and H2-H3 bands. In each case, the four companions HR8799bcde are the only signals above the 5σ threshold. The corresponding SNR values are gathered in Tab. 6.10: At large separation, the SNR is degraded by the SDI process whereas it is increased for the closest companion. Indeed, there are two cases to be considered to assess the performance of the SADI process:

(i) the companion is close enough so that the speckle noise is better subtracted by the SDI but the companion undergoes more self-subtraction (typically below $1.2''$ here);

(ii) the companion is far enough from the star so that there is no self subtraction but because there is mainly detector noise, the post-SDI noise variance increases as $\sqrt{2}$ which makes the SDI procedure useless (in that case, the ADI-only process is already good enough to subtract speckles at this distance). For this data-set, this corresponds to where the two curves meet (from $1.2''$).

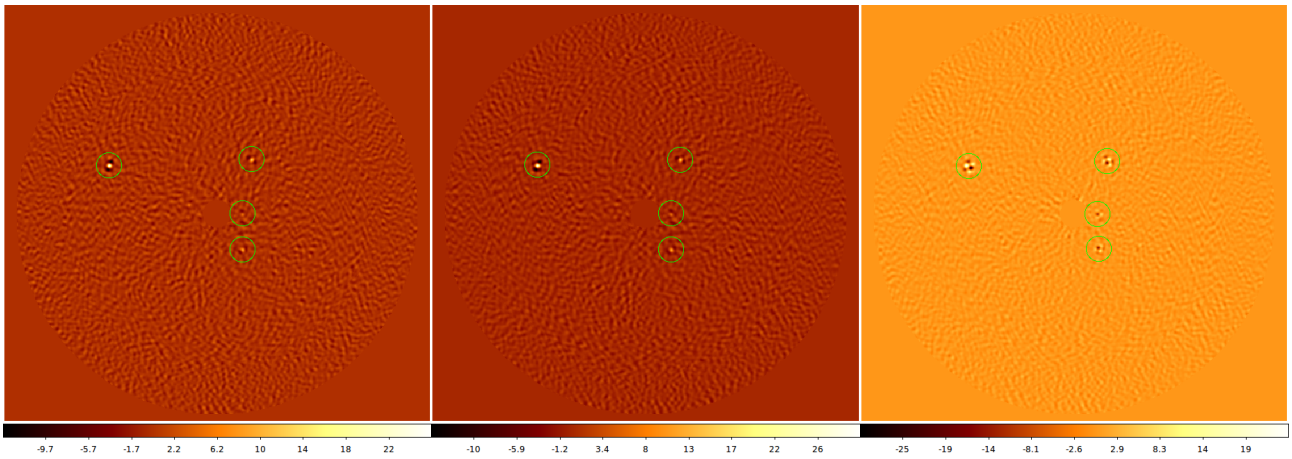

Figure 6.12 – SNR maps provided by ANDROMEDA when processing the HR8799 data described in Tab. 6.8 with the parameters set described at Tab.6.9. From left to right: H2 band, H3 band and SADI mode performing H2-H3 bands.

Companion	SNR in H2 band	SNR in H3 band	SNR in H2-H3 band
HR8799 b	28.6 σ	33.9 σ	26.7 σ
HR8799 e	5.3 σ	6.5 σ	7.7 σ

Table 6.10 – SNR of the furthest (HR8799b) and the closest (HR8799e) companions, in the different maps presented at Fig. 6.12.

The shape of the SNR patterns on Fig. 6.12 shows the self-subtraction effect as a function of the separation: the closest companion is strongly affected whereas the furthest is not. The position estimated from the resulting SNR maps are extracted from the positive bump of the pattern. Thus, the more the signal undergoes self-subtraction, the more its separation is biased. The direction of this bias depends on the wavelength subtracted: If $\lambda_1 > \lambda_2$ then the estimated separation is greater than the real one whereas if $\lambda_1 < \lambda_2$, it is smaller. Tab. 6.11 gathers the estimated separation for the closest and furthest companions: The position and error bars retrieved for the furthest companion make sense but the position retrieved for the closest companion is really affected by the SADI process and is not even within the given error bars in ADI mode.

Companion	Separation in H2 band	Separation in H3 band	Separation in H2-H3 band
HR8799 b	1726.46 ± 3.7 mas	1727.34 ± 3.7 mas	1725.93 ± 3.7 mas
HR8799 e	380.9 ± 11.6 mas	381.65 ± 11.3 mas	409.11 ± 10.8 mas

Table 6.11 – Separation to the star of the furthest (HR8799b) and the closest (HR8799e) companions, in the different maps presented at Fig. 6.12.

The same way, in this version of ANDROMEDA, the contrast is estimated on the positive bump and can thus be strongly affected by the self-subtraction (being over-estimated). Tab. 6.12 gathers the estimated contrast for the closest and furthest companions: The contrast and its uncertainty estimated for the furthest companion make sense (it is close to the contrast retrieved in H2-band) but for the closest companion, the retrieved value is not linked with the value estimated in H2-band.

Companion	Contrast in H2 band	Contrast in H3 band	Contrast in H2-H3 band
HR8799 b	13.31 ± 0.12 mag	12.89 ± 0.1 mag	13.21 ± 0.12 mag
HR8799 e	12.23 ± 0.9 mag	11.94 ± 0.7 mag	13.18 ± 0.5 mag

Table 6.12 – SNR of the furthest (HR8799b) and the closest (HR8799e) companions, in the different maps presented at Fig. 6.12.

In the SADI SNR map shown on Fig. 6.12-Right, the planetary patterns are very specific, due to the spectral rescaling and subtraction. This peculiar shape could help sorting out the detections a posteriori in the SNR map. However, a more rigorous way to account for this specific pattern would be to modify directly the planetary signature model used in ANDROMEDA (see Eq. 2.13), which would avoid the bias on the flux estimation at close separation. One would thus increase the detectability and estimate the flux in the main band (not the one subtracted). To go further, ANDROMEDA could estimate the flux in both bands by adding an unknown parameter to be estimated so that we would have three unknowns: a_{band1}, a_{band2} and $\mathbf{r_0}$ which would be estimated on the positive main peak (so for the band 1 if the SADI is done by subtracting the band 2 to the band 1). Otherwise, if one wants to increase the detectability while not affecting the flux estimation by performing a pre-SDI process, the two SNR maps output from an ADI-only process can be used to disentangle the remaining speckles above threshold: these remaining artifacts are moving radially from one SNR map to the other, in a deterministic way (proportional to $(\frac{\lambda_1}{\lambda_2})^2$) so that these two SNR maps could be combined in a smart way to remove these specific artifacts (see Sect. 6.5 for an example of combination using multispectral images).

The Fig. 6.13 shows the corresponding detection limits for H2, H3 and H2-H3 bands. Once again, at short separations (below $1.2''$), the detection limit in SADI mode is lower than the one in ADI-only mode, showing that SADI is more efficient at short separations. This trend is inverted from $1.2''$ where the dominant noise is the detector noise. In that case, the SDI process does not help the detectability, (as seen with the SNR value of HR8799b in Tab. 6.10). Indeed in this region, the dominant noise in the image is the detector noise, so when performing the spectral difference *and* the angular difference, the noise level increases. Thus the SADI curve (red line) shows a contrast typically higher than the ADI curves (blue lines) and is lower than the raw contrast, by factor two. On this graph, I also placed the location of the four companions, in black in ADI-only mode and in orange for the SADI mode. As

a result, the closer to the star, the higher the self-subtraction of the signal since the distance between the two points (in the rescaled and reduced images) is smaller. At first order, the separation of the detected companion is preserved during the process (the red and orange points are aligned). The difference in the separation estimated in ADI or SADI can be determined in advance and taken into account.

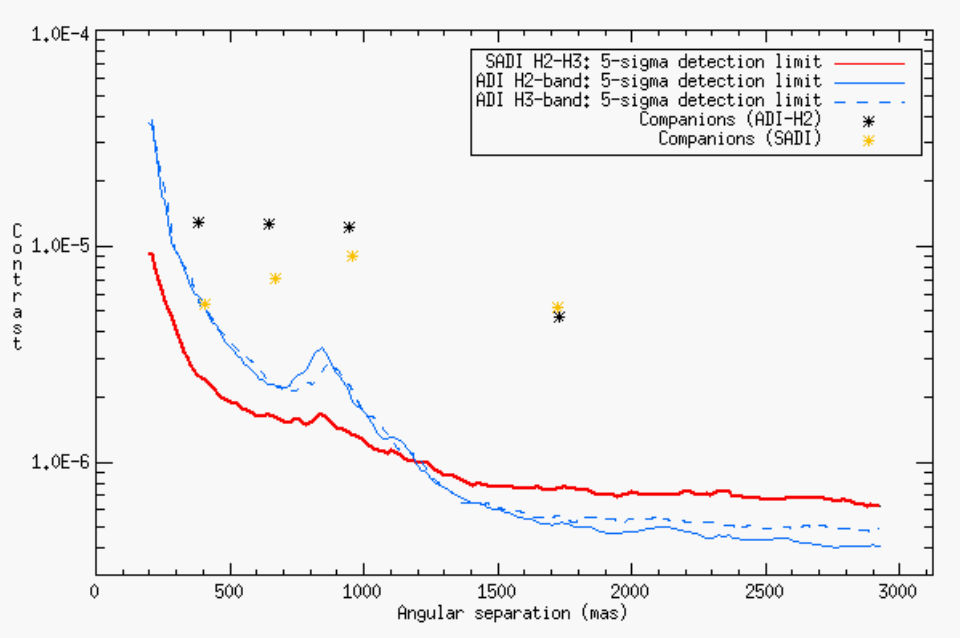

Figure 6.13 – Detection limits at 5σ provided by ANDROMEDA when processing the HR8799 data described in Tab. 6.8 with the parameters set described at Tab.6.9.

Also, when using the SADI process, one has to be careful of the effect pointed out in Rameau et al. (2015): Not only the separation of the companion has to be taken into account, but also its spectral properties in order to derive a correct flux and detection limit estimate. Then when the detection limits are to be converted into mass and temperature properties, it is not accurate enough to only take into account the flux loss due to the self-subtraction.

Conclusion on the SADI mode of ANDROMEDA

In this section, I presented preliminary results from the SADI mode of ANDROMEDA applied to experimental data in two different particular cases. This SADI mode first performs a pre-SDI process then runs the classic ADI mode of ANDROMEDA on the spectrally subtracted cube. From these applications, several conclusions and perspectives can be drawn out:

- If one wants to probe companions at large separation, where the detector noise becomes the dominant noise, the SADI mode proposed by ANDROMEDA is reliable to perform both the detection and the characterization but has worse performance than in ADI-only mode (the SNR is lower and the contrast estimation slightly biased).
- If the companion has a known strong absorption line in one of the two bands, the SADI mode proposed by ANDROMEDA is efficient and reliable to perform both the detection and the characterization.
- If the target applies in none of these two cases, two solutions can be followed: (1) performing a pre-SDI process but modifying the planetary signature model (with or without adding a new unknown if one wants to estimate the contrast in the two bands) or (2) without performing a pre-SDI process and by combining the two output SNR maps obtained in ADI to increase the detection confidence (in that case, one must find a way of computing the corresponding detection

limits. The latter solution avoids the rescaling in wavelength. Indeed, the implemented rescaling is only a first order approximation and its reliability depends on the aberration level.

The same reasoning can be followed to process multispectral data such as the one delivered by SPHERE-IFS. In the next section, I will present preliminary results from the application of ANDROMEDA in its current state on multispectral data, in order to point out the main stakes.

6.5 Processing SPHERE-IFS data with ANDROMEDA

One of the major challenges and objectives of exoplanets imaging is to obtain the spectra of the planetary companions. The last generation of high-contrast instruments are equipped with IFUs, delivering multispectral cubes, from which such spectra can be derived. As it is expected that the planetary atmospheres have several absorption bands, one must now separate the detection aspect from the characterization aspect. In this section, I present preliminary work to perform, on the one hand, the detection and, on the other, the characterization by using the ANDROMEDA pipeline in its current state. This work leads to ideas which could guide future work to adapt ANDROMEDA to specifically process multispectral images.

To perform such tests, I use SPHERE-IFS data of the 51 Eri star described in Sect. 6.3.1 since its planetary companion is a challenging detection whose spectrum has been retrieved earlier by the GPI instrument team (Macintosh et al., 2015).

6.5.1 Multispectral cubes properties and user-parameters set for ANDROMEDA

The Tab. 6.13 summarizes the main properties of the SPHERE-IFS multispectral data cube of 51Eri in both YJ and YH bands on which ANDROMEDA has been applied.

Property	**Value**	
	YJ bands	YH bands
Observation date	2015/09/26	2015/09/25
Atmospheric conditions	average to good (seeing of 0.85″)	good (seeing of 0.95″)
Wavelength of observation	$0.95\mu m \rightarrow 1.35\mu m$; $R \sim 50$	$0.95\mu m \rightarrow 1.65\mu m$; $R \sim 30$
Number of images	64×39	60×39
DIT image	64 sec	16 sec
Total field rotation	$43.05°$; $(-240.394 \rightarrow -197.345°)$	$43.17°$; $(-238.268 \rightarrow -195.095°)$

Table 6.13 – Table summarizing the characteristics of the observation of the star 51Eri with SPHERE-IFS, on which ANDROMEDA has been applied.

The Tab. 6.14 gathers the set of user-parameters applied to run ANDROMEDA on the 51Eri multispectral images described in Tab. 6.13.

6.5.2 Collapsing the images to obtain the detection

In order to detect the companion in the multispectral cubes, one first idea is to collapse the images in order to obtain only one temporal cube to be processed in single-ADI mode (without rescaling so it is equivalent to a broad-band image cube). One image of the collapsed cubes in YJ or YH bands is shown at Fig. 6.14. The reference PSF cube must also be collapsed the same way. The oversampling factor used is the one corresponding to the mean wavelength of the collapsed images.

The SNR maps provided by ANDROMEDA are shown in Fig. 6.15. In the YJ band SNR map, the signal is hardly distinguishable and shows a SNR of 1.8σ. In the YH band SNR map, the expected pattern appears at the location of 51Eri b, with a SNR of 4.8σ. This signal is the highest signal in the SNR map.

User-defined parameter	Value
Size of the images, N_{img}	190×190 pixels
Size of the reference PSF frames, N_{PSF}	16×16 pixels
Inner Working Angle, IWA	$2\lambda/D$
Filtering fraction, F	$1/4$
Size of annuli, d_r	$1.0\lambda/D$
Minimum separation for ADI, δ_{min}	$1.0\lambda/D$
Optimization method for ADI	No Optimization
Smoothing of the normalization profile, N_{smooth}	8 pixels

Table 6.14 – User parameters set to run ANDROMEDA on the SPHERE-IFS images of the star 51Eri whose observation conditions are gathered in Tab. 6.13.

In YH band, the estimated position and relative contraste of the companion can be found in Tab. 6.15 in comparison with the H2-band (narrow IRDIS filter) estimations.

Wavelength	SNR	Separation	Position angle	Contrast
Collapsed IFS YH	4.8	458.8 ± 6.1 mas	166.04 ± 0.19 deg	$14.8 \pm 1.2s$ mag
IRDIS H2	3.7	446.3 ± 14.7 mas	164.73 ± 1.02 deg	$14.1 \pm 0.8s$ mag

Table 6.15 – Estimated position and contrast of the companion 51Eri b in the 39 collapsed IFS images covering the YH bands. As a comparison, the same estimated values on the IRDIS H2-band images are shown in the table.

This method does not take into account the companion spectral signature and provides a small SNR for the companion in the YJ band. In addition, the estimated flux is over the whole wavelengths range and the spectral resolution is lost in the process. As a conclusion, even though it provides a first idea of the possible detections, this technique is not efficient enough to fully exploit multispectral data using ANDROMEDA.

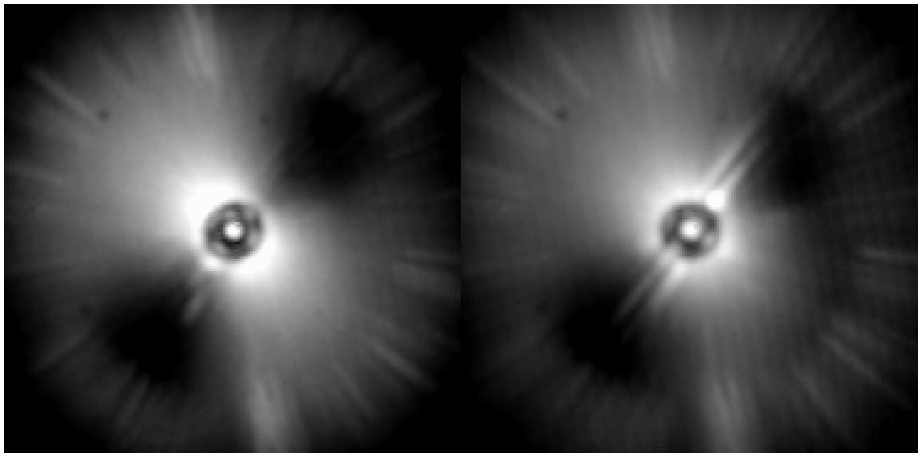

Figure 6.14 – Reduced images from SPHERE-IFS data of the star 51Eri, collapsed on all wavelength in YJ bands (left) and YH bands (right).

Note that one of the observing modes of SPHERE-IRDIS is the broad band imaging (BBI, also called classical imaging). Collapsing the 39 channels of the IFS data cube is equivalent to deal with very BB images (with a relative resolution $\frac{\Delta\lambda}{\lambda} \sim 46\%$ in YH-band and $\sim 26\%$ in YJ-band). During my PhD, I ran ANDROMEDA on BB images from SPHERE, showing a relative resolution $\frac{\Delta\lambda}{\lambda} \sim 17.9\%$ in H-band, resulting in a different conclusion (to give an order of magnitude, in DB the resolution in H2 is of 3.3%): ANDROMEDA succeeds in detecting the companion with a SNR of 6.2 and provides an estimated flux consistent with the one obtained using the PCA method. The NaCo BB data in L' band, showing a resolution of 16.3% also showed convincing results (published in Cantalloube et al.,

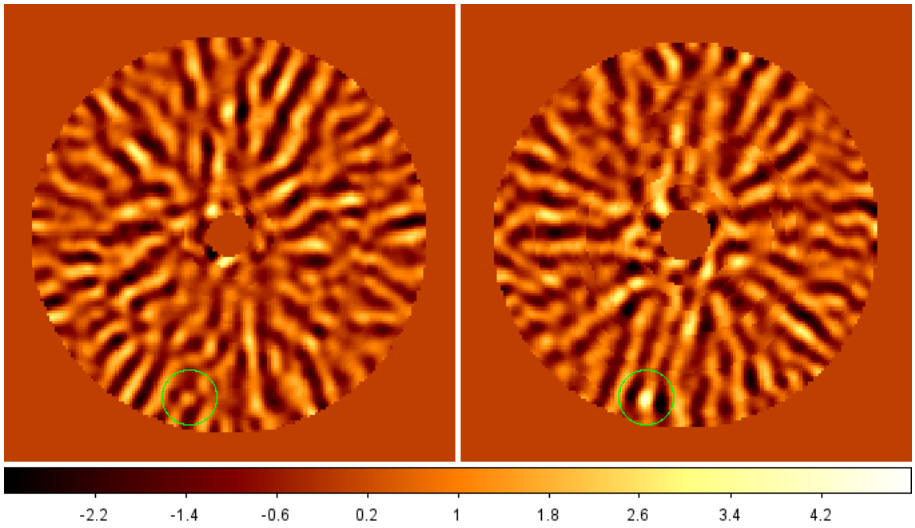

Figure 6.15 – SNR map obtained by running ANDROMEDA on the spectrally collapsed images from SPHERE-IFS data of the star 51Eri, in YJ bands (left) and YH bands (right). The companion 51Erib is visible only in the YH bands SNR map (green circle on right panel).

2015), as well as on Keck/NIRC2 images in K band with a resolution of 15.3%. ANDROMEDA being dedicated to point source extraction, it seems, as expected, robust to extracting planetary companions within broadband images showing radially elongated speckles (see Fig. 6.14).

In order to increase the band per band detectability with the multispectral data, instead of collapsing the whole cube, one can collapse a certain amount of adjacent channels. Indeed, in a detection approach, it is possible to include reasonable hypothesis on the planetary spectrum trend (such as absorption lines in methane or using more elaborated atmospheric models).

6.5.3 Multi-channel detection and channelwise spectrum estimation

In order to characterize the companions, a first idea is to process each spectral channel separately by a simple ADI.

Detection The 39 SNR maps obtained by running ANDROMEDA in ADI mode on each channel show a fair level of residuals and the companion appears above a 5σ threshold in very few channels. From the SNR maps where the companion is the only detected signal above a 5σ threshold, it is easy to run the detection module and obtain the precise position of the companion. The accuracy on the estimated astrometry of the companion is even reinforced by the spectral diversity offered by the IFS data.

Another better idea to detect the companion is to collapse astutely the 39 SNR maps obtained from the channel per channel ANDROMEDA (and not the raw images as in the previous section). Thiebaut et al. (2016) have shown that an optimal SNR combination for multispectral images in the Gaussian case (as it is with ANDROMEDA), is given by: $\frac{1}{N_\lambda}\sum_\lambda (SNR(\lambda)|_{\tau>0})^2$ where N_λ is the total number of spectral channels and $SNR|_{\tau>0}$ is the SNR on which a zero thresholding is applied. Such a combination is presented on Fig. 6.16. The companion can be detected on the YH collapsed map by thresholding it to a high threshold (about 10σ in this case) but it is difficult to spot it on the YJ collapsed map since it has a very poor SNR. A first estimation of the companion position can be extracted from such maps.

Characterization To characterize the companion, I simply read the flux on each flux maps provided by ANDROMEDA at the estimated location of the companion and plotted the resulting a spectrum. In order to visualize the detection confidence in each channel, I over-plotted on the spectrum the 5σ,

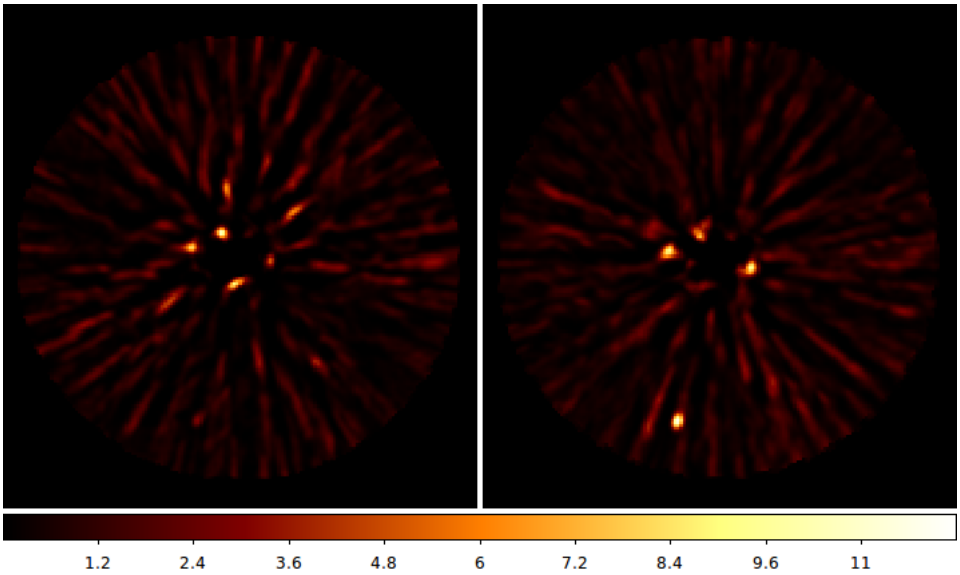

Figure 6.16 – Maps obtained by combining the 39 SNR maps obtained by running ANDROMEDA in ADI (channel per channel) on the SPHERE-IFS data of 51Eri, as in Thiebaut et al. (2016). Left: YJ-bands ($SNR_{51Erib} = 3\sigma$). Right: YH band ($SNR_{51Erib} = 11.5\sigma$). In both maps, the SNR of the highest residuals, located at ~ 75 mas from the star, are of about 10σ: Eri51 b is the highest signal in the YH map but not in the YJ map.

3σ and 1σ detection limits at this location (by simply reading the map of the standard deviation of the flux on each maps provided by ANDROMEDA, at the estimated position of the companion). For instance, on the spectra presented at Fig. 6.17, every point above the red dashed line are above a 5σ threshold and thus have the corresponding probability of presence and the same applies with the red and blue dashed lines which are respectively the 3σ and 1σ detection limit. Obviously the contrast estimated below zero should not be taken into account (the positivity constraint in ANDROMEDA cannot be used when performing a post-normalization of the SNR map, which is the case here).

In the 51Eri case, such a spectrum is shown at Fig. 6.17: No detection is made in YJ bands above the 5σ threshold and only few detections stand above a 3σ threshold at large wavelengths. In YH bands, the companion 51Eri b is detected above the 5σ threshold only in a few channels. This method to exploit IFS data is not efficient enough in terms of detection confidence if the companion is not known.

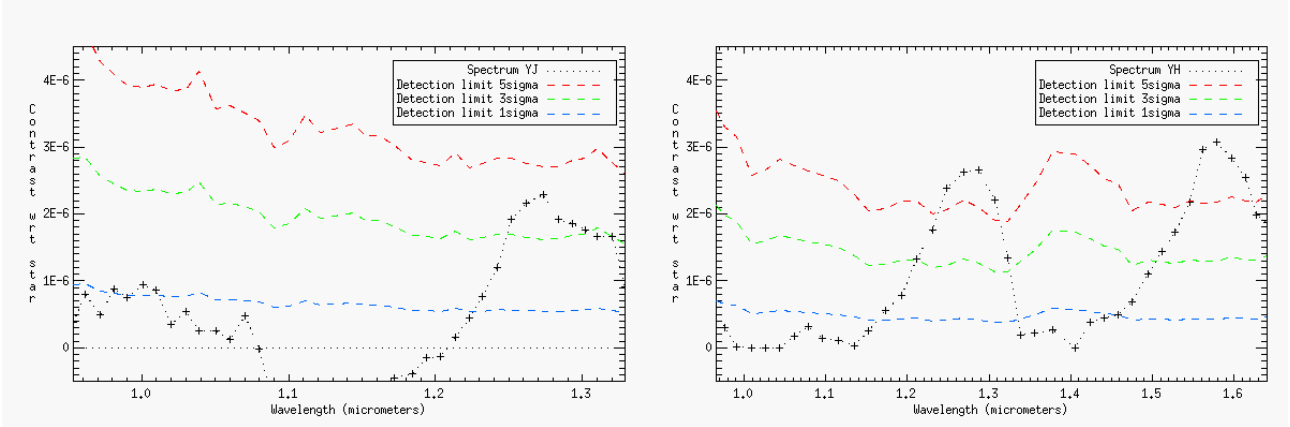

Figure 6.17 – Spectrum and associated probability of presence of the 51Eri b companion, retrieved in YJ bands (left) and YH bands (right) when processing the SPHERE-IFS data in ADI mode. The companion 51Eri b is visible above a 5σ threshold only when it is above the red dashed line.

The Fig. 6.18 shows the same spectrum but on which the 1σ error bars on the contrast estimations

are over-plotted. Globally, the error bars are larger at shorter wavelengths, as expected since the reference PSF used to estimate the relative contrast has a Strehl ratio lower at shorter wavelengths and usually shows more temporal variability at shorter wavelengths. ANDROMEDA thus provides consistent results with the actual instrumental limitations, as previously investigated.

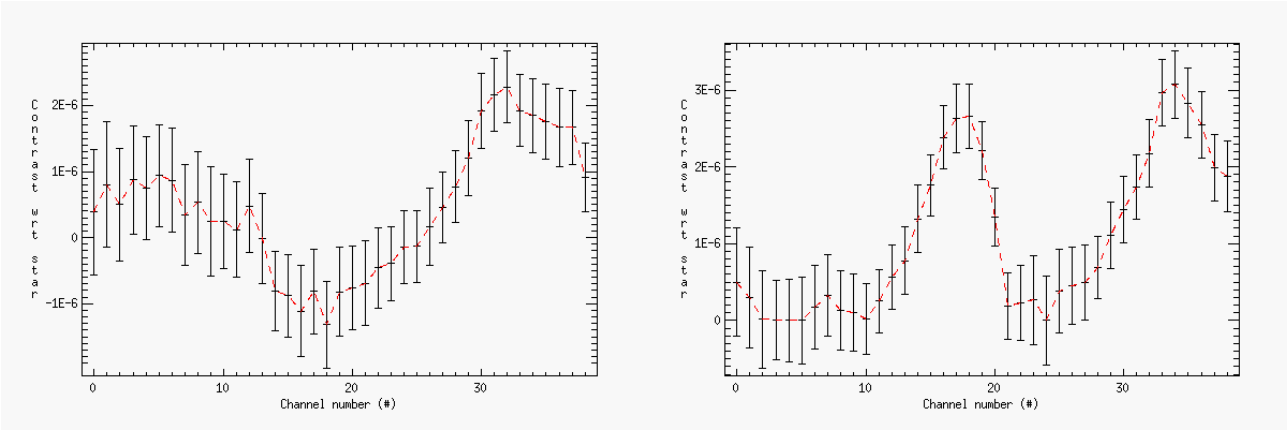

Figure 6.18 – Spectrum and associated 1σ error bars of the 51Eri b companion in YJ bands (left) and YH bands (right) when processing the SPHERE-IFS data in ADI mode.

Overlap of the spectra To assess the qualitative reliability of the retrieved spectra, it is possible to over-plot the two spectra since the YH and YJ modes of the SPHERE-IFS instrument have overlapping wavelengths. The Fig. 6.19 shows these two spectra with their corresponding 5σ detection limit. A rather good agreement on the trend is observed between the overlapping wavelengths at larger wavelength but at short wavelength it is not exact since the signal is fainter. Also, the spectral resolution in the YJ bands is higher at short wavelengths (which could explain the small discrepancies since the signal is not averaged in these zones). However this graph shows that the estimated spectra are not completely reliable due to the lack of detectability in the corresponding images: the signal is too faint and the error bars are too large.

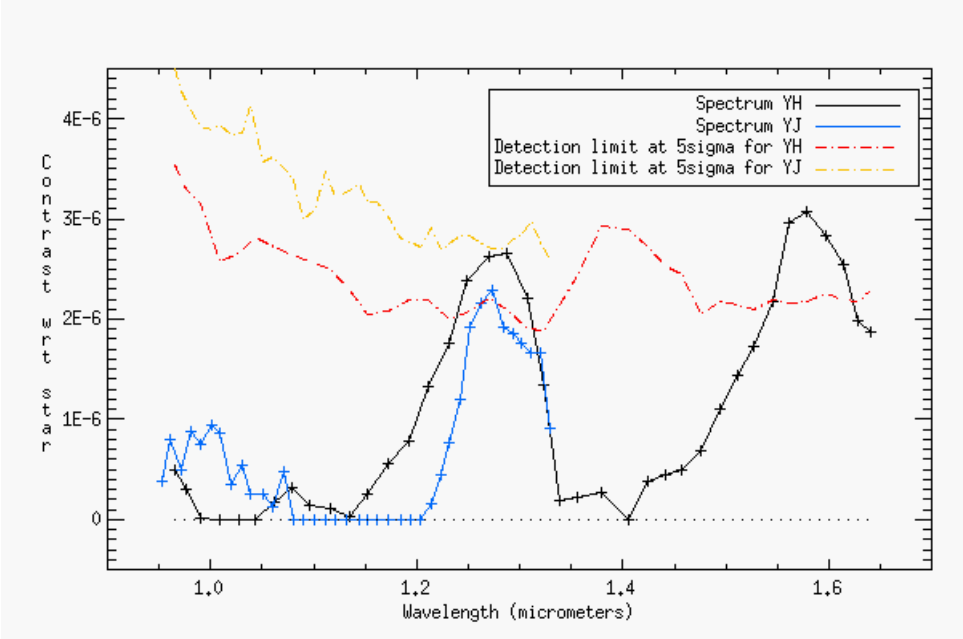

Figure 6.19 – Spectrum and associated 5σ detection limit of the 51Eri b companion in YJ bands and YH bands when processing the SPHERE-IFS data in ADI mode.

Detection limits Another interesting information to visualize these results, but on the whole field of view, is to plot the corresponding detection limits for each spectral channel of the SPHERE-IFS instruments. Fig. 6.20 shows the computed detection limits by ANDROMEDA for the different spectral channels. For the YH bands, the detection limit increases with the wavelength in the corrected zone (further on, the trend is inverted) as it is harder to detect companions at large wavelengths (see Sect. 6.1). This trend is less obvious for the YJ bands, but it follows roughly the same rule.

Another interesting note is that at close separation, the detection limits show a double-bump bulge due to the coronagraph response (the small ring surrounding the center of the image at Fig. 6.1) whose size is wavelength dependent (obviously, the same coronagraph is used to obtain the multispectral images within the IFS). Also, the adaptive optics cutoff frequency is visible as a rise emerging at $20\lambda/D$ (so at large wavelength, the bump is not even visible).

The two sets of detection limits are thus consistent to each other and consistent with the global imaging performance of the SPHERE instrument. The link between the raw contrast achieved by SPHERE and the detection limit obtained from a post-processing is not linear and straightforward, but the global trend in terms of performance is recorded by ANDROMEDA, which makes ANDROMEDA a good gauge of the overall sensitivity.

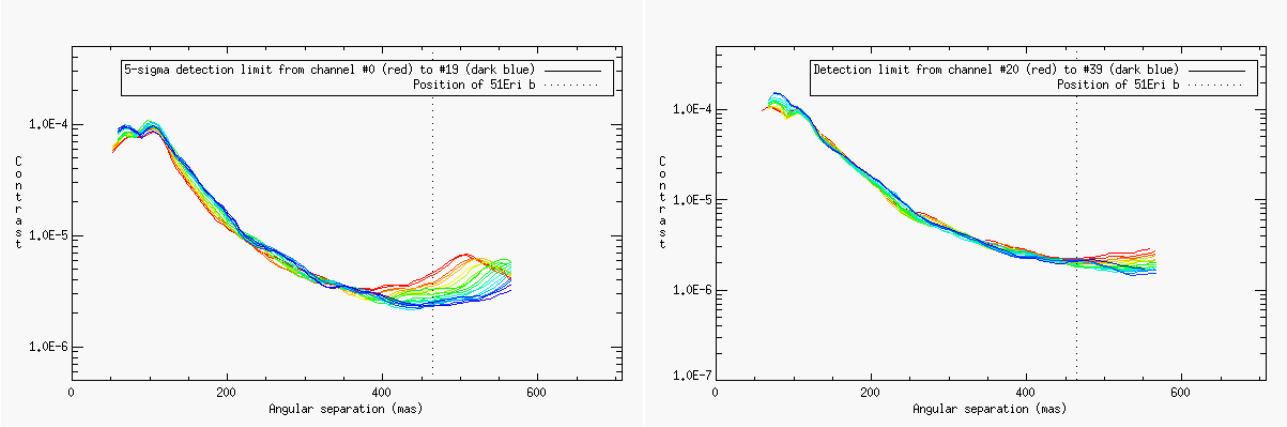

(a) : 3σ detection limits in YJ bands. *Left:* From channels #1 to #19. *Right:* From channels #20 to #39.

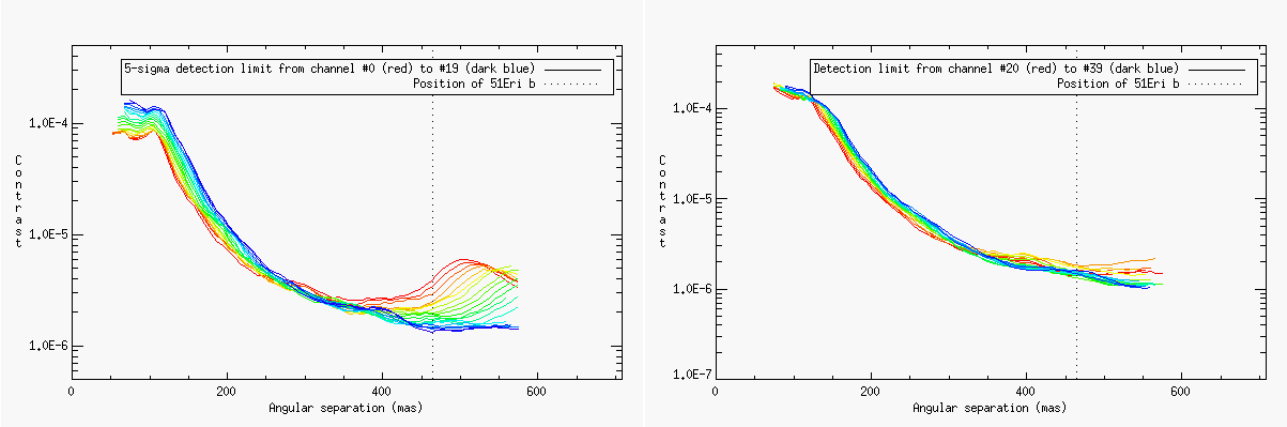

(b) : 3σ detection limits in YH bands. *Left:* From channels #1 to #19. *Right:* From channels #20 to #39.

Figure 6.20 – Detection limits at 3σ computed by ANDROMEDA, using the user-parameters set of Tab. 6.14, for each spectral channel of the 51Eri SPHERE-IFS data described in Tab. 6.13.

At this stage, I have shown in this example that it is not easy with the band to band analysis (neither with the collapsed images) to highly increase the detection capability. However, if the companion is bright enough to be above the detection limit in one or few channels only, then the ANDROMEDA flux map at this identified position for all channels provide very valuable and consistent spectral information and uncertainty estimates, even if the SNR is poor. The next section propose

another technique to better subtract the speckles in each band by performing a spectral subtraction added to the ADI process (SADI mode). Note that it takes about 15 minutes to perform this band to band processing.

6.5.4 Using SADI to increase the detectability and sensitivity

Another track is to use an SDI subtraction before the ADI subtraction to increase the visibility of the companion, as shown at Sect. 6.4.

If the companion has a strong known absorption band, a clever way to perform a clean SDI process is to consider the image at the wavelength corresponding to this absorption band (where the companion should not be present) and rescale and subtract this image to all the other spectral channels images. The result is a temporal cube in which each image has been pre-subtracted of the image in which the companion is absent. Running a simple band per band ADI process on this resulting image cube should substantially increase the visibility of the companion in the final processed images (SNR maps in the case of ANDROMEDA). To check where the absorption band is, the spectra provided in ADI-only mode can be used (it is a generalization of what is presented on DBI data at Sect. 6.4).

Choosing the channels to be spectrally subtracted For instance, in the case of the 51Eri data, on Fig. 6.17, the YJ bands spectrum shows an estimated contrast below zero in the channels #17 to #23 (that is to say from 1.12136μm to 1.18410μm) and the YH bands spectrum shows an estimated contrast below zero in the channel #24 (1.40555μm). In YJ band the images of the channels from #17 to #23 are rescaled at the wavelength corresponding to image #X, then their median is made and the resulting median frame is subtracted to the frame #X. This operation is repeated for all the 39 frames of the multispectral cubes. The resulting spectrally subtracted data cube has been generated and kindly provided by A. L. Maire (MPIA). In YH band, I picked the frame #24 and rescaled it to the frame #X before subtracting it to the frame #X. I repeated this operation for every frame except, obviously for the frame #24 which is thus null. I then ran ANDROMEDA in ADI mode on the 39 resulting YJ and YH cubes.

Detection The 39 SNR maps obtained by running ANDROMEDA in ADI mode on these pre-subtracted image cubes show a lower level of residuals and the companion appears clearly, above a 5σ threshold in several bands. With this method it is thus possible to perform the detection in a more efficient and reliable way than collapsing the images or processing a band per band ADI.

To better visualize this gain, Fig. 6.21 shows the collapsed SNR maps obtained in YJ and YH: the companion is the only signal above a 3σ threshold in the two bands.

Characterization As for the ADI procedure, the position of 51Eri b is estimated and its flux is read on each flux maps provided by ANDROMEDA at this estimated position to obtain the corresponding spectrum. As for the Fig. 6.17, to visualize the corresponding detection capabilities in each SNR map, I over-plotted on the spectra in Fig. 6.22 the 5σ, 3σ and 1σ detection limits at this location. This time, the companion 51Eri b is revealed above a 5σ threshold in 8 spectral channels of the YJ bands (though there were no detection above 5σ with the ADI-only method). In the same way, more detections of the 51Eri b companion are above a 5σ threshold in the YH bands SNR maps. Also, the spectra obtained in both cases are consistent with the ones obtained in ADI-only mode (see Fig. 6.17).

The Fig. 6.23 shows the same spectra as Fig. 6.18, but on which the 1σ error bars on the contrast estimations are over-plotted. Globally, the error bars are smaller than the ones derived in ADI-only mode since the SNR is higher (see Fig. 6.18).

Overlap of the spectra Once again, to assess the qualitative reliability of the spectra retrieved, it is possible to over-plot the two spectra in YH and YJ to check if they match at the overlapping wavelengths. The Fig. 6.24 shows these two spectra with their 5σ detection limit. A good agreement is

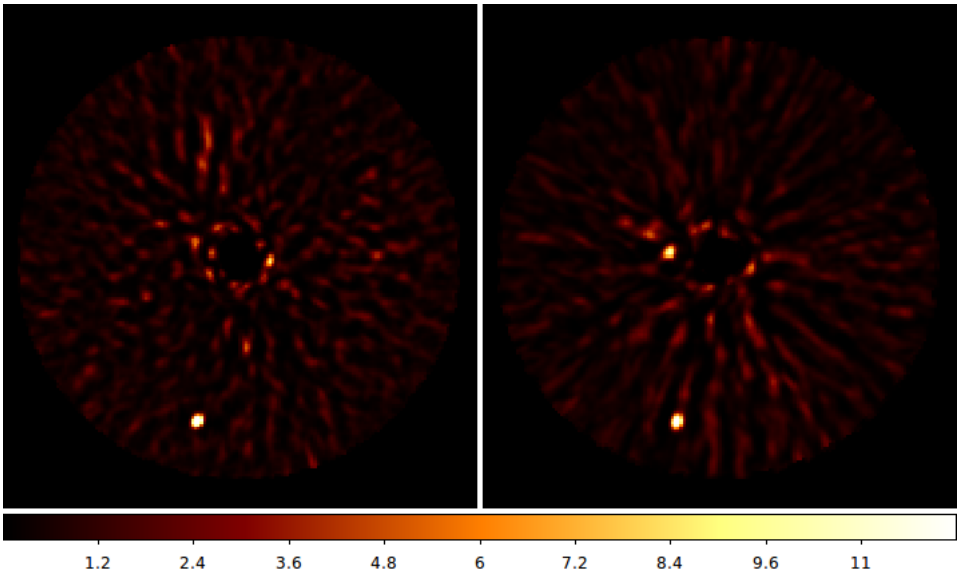

Figure 6.21 – Maps obtained by combining the 39 SNR maps obtained by running ANDROMEDA in SADI-mode on the SPHERE-IFS data of 51Eri, as in Thiebaut et al. (2016). Left: YJ-bands ($SNR_{51Erib} = 18.5\sigma$). Right: YH band ($SNR_{51Erib} = 15\sigma$). The companion 51Eri b is the only signal standing above a 10σ threshold.

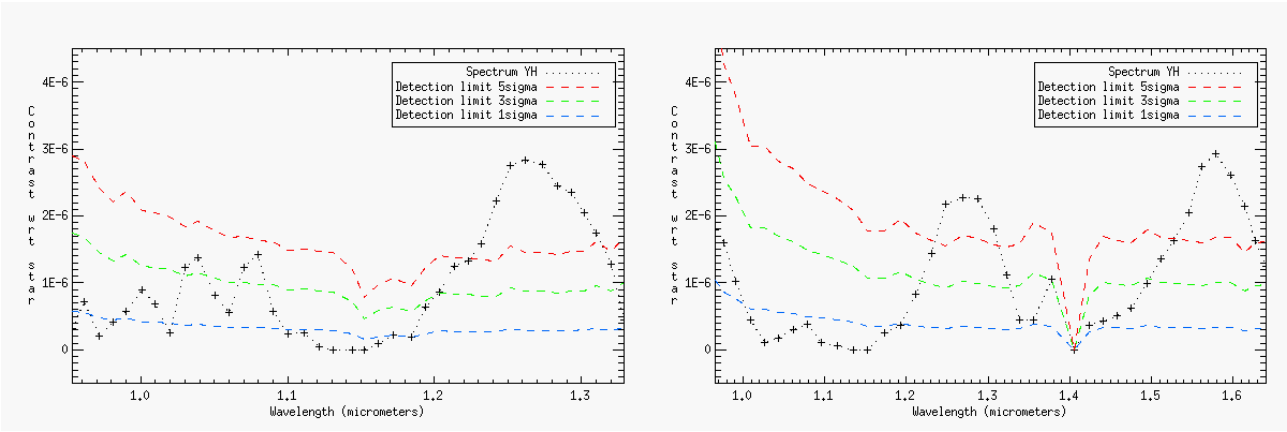

Figure 6.22 – Spectrum and associated probability of presence of the 51Eri b companion, retrieved in YJ bands (left) and YH bands (right) when processing the SPHERE-IFS data in SADI mode.

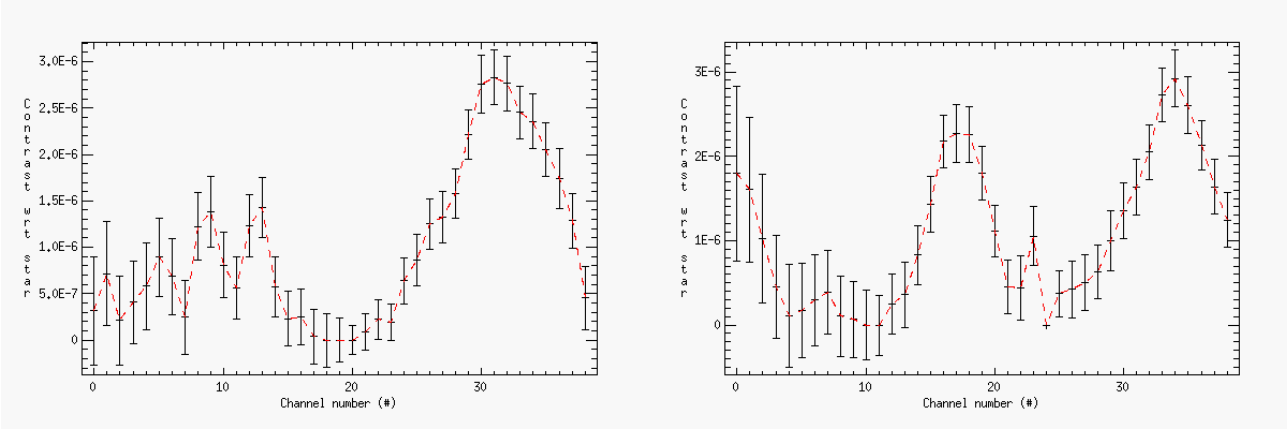

Figure 6.23 – Spectrum and associated 1σ error bars of the 51Eri b companion in YJ bands (left) and YH bands (right) when processing the SPHERE-IFS data in SADI mode.

observed between the overlapping wavelengths (better than in ADI-only mode, as on Fig. 6.19) except

at very short wavelength where the signal is fainter. Also a discrepancy is visible in the channels #17 to #23 in YJ bands (blue line on Fig. 6.24), which is due to the fact that part of the signal is self-subtracted in these channels due to the pre-SADI process. One has to keep this aspect in mind: the YJ spectrum in these channels is not reliable. A solution would be to use only the adjacent modes for these specific channels.

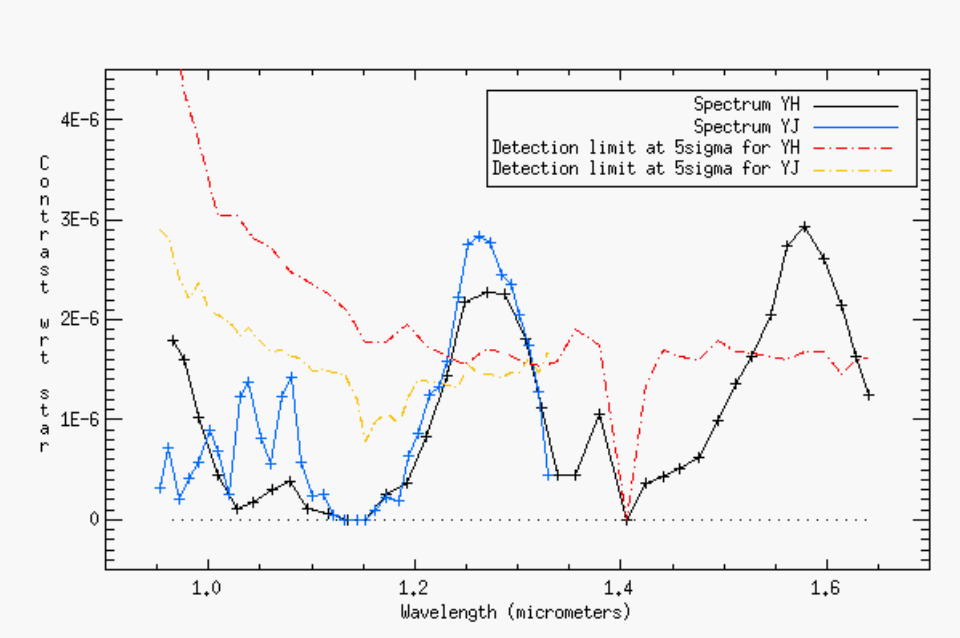

Figure 6.24 – Spectrum and associated 5σ detection limit of the 51Eri b companion in YJ bands and YH bands when processing the SPHERE-IFS data in SADI mode.

Detection limits The corresponding detection limits for each spectral channel of the SPHERE-IFS instruments are shown on Fig. 6.25. In the corrected zone, the computed detection limits for the different channels are in agreement with the spectral subtraction capability, that is to say with the distance between the rescaled wavelength and the subtracted wavelength: the detection limit is lower when the regarded channel is close to the rescaled channel. As a result, for the YH bands the trend is inverted before and after the frame used to spectrally subtract each image of the multispectral cubes (#24). For the YJ bands, the rescaled channel is a median combination of channels #17 to #23 which explains why the detection limit for the frame #20 is extremely low and is not realistic (almost all the light is subtracted). The detection limits provided by ANDROMEDA in SADI mode are biased by the chosen channel used to perform the spectral subtraction and should be regarded with care.

As a conclusion, the SADI method proposed in this section to process IFS data provides good results if one is sure that the companion is not present in the spectrally subtracted frame. With this method, it is possible to perform both the detection in a more efficient and reliable way than collapsing the images or performing a band to band ADI process. More accurate spectra can also be retrieved with this method. Note that it takes about 22 minutes to run the 51Eri data cubes described at Sect.6.5.1 in this SADI-mode with ANDROMEDA. One still must be certain that the pre-SDI subtraction does not affect the adjacent channels.

Note that for the final draft of the publication Samland et al., we notably improved these results by using two SDI references in order to avoid subtracting two wavelengths which are too far away from each other. We thus chose two channels, one at short wavelength and one at long wavelength, where the planetary companion present absorption bands. We then processed the first part of the channels using the shorter wavelength as a reference and the second part of it using the larger wavelength as a reference. The estimated spectrum in YJ and YH bands are matching better in the overlaped bands and we checked that the spectral correlation matrix (as defined in Greco and Brandt, 2016) shows less

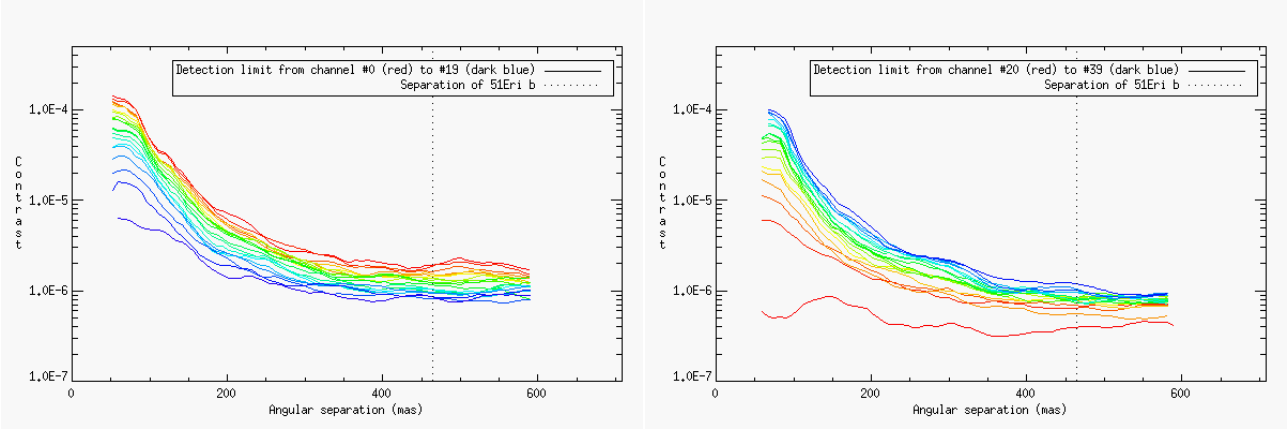

(a) : 3σ detection limits in YJ bands. *Left:* From channels #1 to #19. *Right:* From channels #20 to #39.

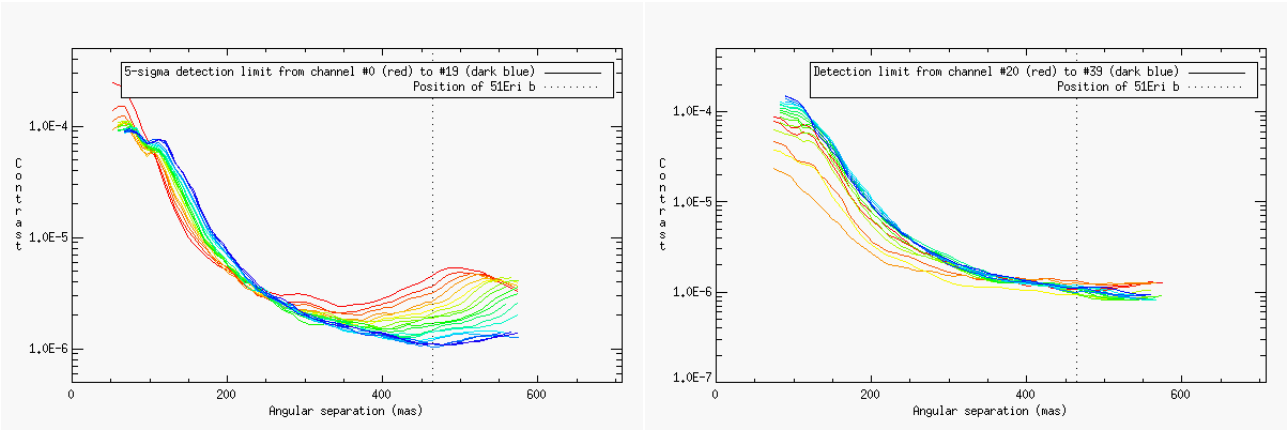

(b) : 3σ detection limits in YH bands. *Left:* From channels #1 to #19. *Right:* From channels #20 to #39.

Figure 6.25 – Detection limits at 3σ computed by ANDROMEDA in SADI-mode, using the user-parameters set of Tab. 6.13, for each spectral channel of the 51Eri SPHERE-IFS data.

channel to channel correlation which indicates a better processing with less spectral self-subtraction (see Samland et al. 2016 for further details).

6.5.5 Preliminary spectra retrieved by ANDROMEDA

In this section, simple methods are proposed to detect and characterize companions using multispectral data such as the ones provided by SPHERE-IFS. Analysis of the results show that the first spectra obtained by using ANDROMEDA in its current state are quite promising. There is still some room for improvements that are proposed in the perspectives of this part (Chap. 6.5.5), but ANDROMEDA can really be considered as an efficient tool to process IFS data and deliver spectra.

In particular, we compared the obtained spectra with the spectra derived from the GPI instrument on this object, published in Macintosh et al. (2015). Within some minutes, ANDROMEDA provided spectra similar to the one published by GPI at large wavelength. The bias observed at short wavelengths is still being investigated. The Fig. 6.26 shows the spectra obtained with ANDROMEDA (ADI-only mode), PCA (processed by M. Samland, MPIA) and the one from the GPI publication.

As a conclusion the retrieved spectra by ANDROMEDA in its current state make sense. Even if the presented work on these data is preliminary and that adaptation of the pipeline should be considered since the current performance are more reliable than other state-of-the-art pipelines. This is due to the specific formalism of ANDROMEDA which estimates the flux in an unbiased way. Updates of this work and comparison with PCA and TLOCI estimated spectra can be found in the paper Samland et al. (in prep).

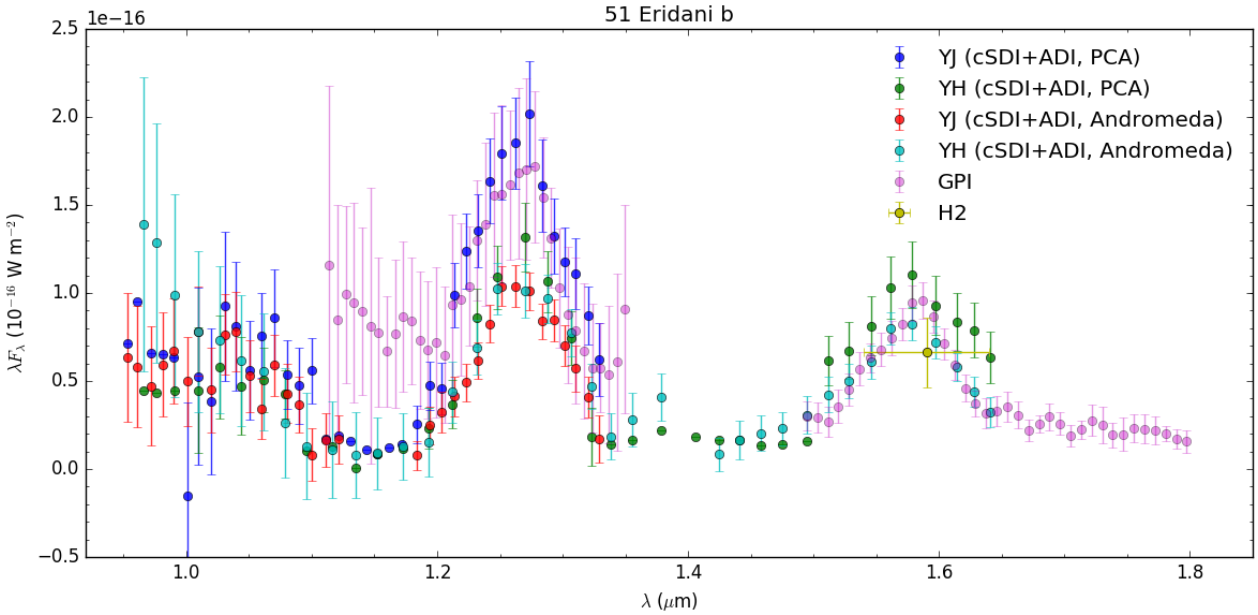

Figure 6.26 – Retrieved spectra of the companion 51Eri b, using ANDROMEDA and PCA on the SPHERE-IFS data of 51Eri described in Tab. 6.13 and spectra of 51Eri b retrieved from the GPI observations Macintosh et al. (2015). These results will be published in Samland et al. (in prep.).

Conclusion: processing SPHERE-IFS data with ANDROMEDA

At first order, this technique allows one to retrieve spectra which make sense. However, the detection and characterization procedures must be separated and exact performance are highly dependent on the companion spectrum assumptions. Also, this method only works for point sources and cannot investigate extended sources such as debris disks or proto-planetary disks.

The next part of this manuscript deals with a method which would avoid these dependencies. This method, called MEDUSAE also relies on inverse problem solving but directly exploit the multispectral information, regardless of the field rotation.

Conclusion: ANDROMEDA operational on various data-sets

Many lessons were learned from the application of ANDROMEDA to various data from the SPHERE instrument. First of all, the SPHERE data are quite different from the NaCo data which makes ANDROMEDA less sensitive to the user-defined parameters when processing SPHERE images. Not only ANDROMEDA does provide reliable results in an efficient and quasi-systematic way but its performance in terms of signal extraction is fully in line with the extrinsic instrumental features. Moreover ANDROMEDA proved to be a versatile tool, easily adaptable to process dual-band or multispectral data, increasing the extraction capabilities within such data. This ability mainly comes from the original way of estimating the flux and the SNR of the companions, by using a MLE, which makes it possible to perform an objective detection based on the thresholding criterion and a direct estimation of the flux. This makes ANDROMEDA appropriate and easy to process such data in typically 15 minutes for 60 SPHERE-IFS multispectral cubes ($190 \times 190 \times 39$).

From these various applications, I could also improve the ANDROMEDA pipeline in terms of input format, default user-parameters and output to make it more suitable to process SPHERE data and more adapted to the needs of the astronomers who will hopefully also use this algorithm from now on.

I would like to thank collaborators for having provided me the reduced data sets used in this chapter, as well as for the useful and interesting discussions raised from the ANDROMEDA application on these fascinating data sets: A. Vigan and A. Zurlo (LAM) for the HR8799 data, M. Bonnefoy (IPAG) for

the GJ504 data and M. Samland (MPIA) for the 51Eri data.

ANDROMEDA: perspectives

Following my work to make ANDROMEDA an operational and effective tool, I identified several perspectives on either short-term or long-term. In the following, I present some specific tracks that could be implemented or explored to make this ANDROMEDA method more suited to the different instruments and/or objects sought in the field of exoplanet imaging.

Short-term perspectives of ANDROMEDA

From the work presented in this part, some improvements could be easily implemented in ANDROMEDA to increase its extraction performance and improve the whole pipeline.

Reducing the computing time by parallelizing the ML search: In ANDROMEDA, the companion tracking is made for every distance to the star within annuli of thickness determined by the user-defined d_r parameter. In order to decrease the computing time (which is typically of 15 to 20 minutes for a $512 \times 512 \times 100$ images cube, depending on the computer used), it is possible to parallelize the subtraction and MLE track that are independent. Once the computation is made for every annulus, the results are combined into the flux, snr and standard deviation of the flux maps. In IDL, it is possible to replace the `FOR` loop by such a parallel computation[8]. This operation would enable to divide the computation time by the amount of parallelized loops / cores used.

Including the potential temporal variation of the companion PSF: In this version of the ANDROMEDA pipeline, the model of the planetary signature is built thanks to one single reference PSF taken either before or after the observation session. The final contrast is estimated from the flux of this reference PSF. To increase the precision of the estimated contrast, a temporal follow-up of the PSF could be implemented in the model defined at Eq. 2.13. The reference PSF h can be replaced by $h(t)$ with t corresponding to the couple of images used for the PSF subtraction following:

$$m_k(a, \mathbf{r_0}) = a.[\delta(r, \theta_{t_0}) * h(\mathbf{r}, \mathbf{t_0}) - \delta(r, \theta_{t_1}) * h(\mathbf{r}, \mathbf{t_1})] \tag{6.1}$$

In order to access the temporal variation, several tracks could be explored: (1) by scaling the reference PSF by the Strehl ratio if we have access to a reliable SR value, (2) by using the information provided by the AO RTC (SPARTA on SPHERE), (3) by using the information from the DTTS monitor or (4) by exploiting the PSF replicates from the four satellite spots (that can be produced by a waffle pattern on the DM at the convenience of the user). This operation would increase the detectability of the pipeline (for faint objects) and significantly increase the precision on the estimated contrast. Not taking into account the temporal variation of the reference PSF affects all the different pipelines based on ADI. Thus if we could access this information the gain would be non-negligible.

Modifying the angular differential images construction: Instead of performing a classical ADI before the MLE one could implement a more efficient speckle subtraction such as a LOCI or a PCA subtraction. In that case, the model must be adapted so that the reference PSF undergoes exactly the same flux subtraction as the resulting differential images. For instance, if a PCA subtraction is used, the model must take into account the C_{max} subtracted modes with the correct coefficients.

[8] By using IDL procedures available for the users' community such as `split_for.pro` or `multithread.pro`.

For example the x-th image of the cube, the corresponding differential image must be modeled as: $\Delta = i_x - \sum_{c=0}^{C_{max}} \alpha_c^x \ \mathcal{I}_c$ (in the effective subtraction zone if a mask is applied). This modification only affects the speckle subtraction (and consequently the model of the companion signature) but the detection formalism remains the same.

Adaptation to DBI data: More specifically, as explained at Chap. 6, ANDROMEDA could be adapted to process DBI data and take advantage of the spectral redundancy provided by such data. The current version of ANDROMEDA already has a simple SADI mode implemented which consists in rescaling then subtracting two channels one to another and which assumes that the companion is fully absent in the subtracted channel. This technique proved useful efficient at better subtracting speckles than a simple ADI process but it is not useful neither at large separation (where the photon and detector noise are dominant) nor at close separation (where the spectral self-subtraction is too important, typically at closer separation than $\frac{\lambda_1}{|\lambda_2 - \lambda_2|}$). Moreover, this technique biases the flux and the detection limit estimations in particular when the companion is not completely absent in one of the two bands. Thus in a more general way (where the companion spectrum is not known in advance) two major leads can be followed to fully exploit the spectral diversity and avoid the latter bias. (1) a very simple solution is to a posteriori combine the SNR maps so as to reject the detection that are radially moving. This solution does not enable to decrease the speckle noise level at close separation (compared to a SADI) but it can be used either with a very low threshold in order to probe fainter sources all over the field (such as for the GJ504b companion in J2 band which has a threshold of 3σ - see Sect. 6.1.4), or with data in which the speckle field is particularly stable. One must thus find a way to derive a consistent detection limit when using this technique. (2) by modifying the model to account for the new planetary signature which has deterministic radial features. This method would enable to better subtract the speckle field (in the speckle dominant regime) and to directly estimate the flux of the companions and the corresponding detection limit. Moreover, it is possible to estimate the contrast a in the two bands by adding an unknown in the model to be inverted by ANDROMEDA:

$$\begin{aligned} m_k(a, \mathbf{r_0}) = & [a^{\lambda_1}.(\delta(r, \theta_{t_0}) * h^{\lambda_1}(\mathbf{r}, \mathbf{t_0}) - \delta(r, \theta_{t_1}) * h^{\lambda_1}(\mathbf{r}, \mathbf{t_1})] \\ & - [a^{\lambda_2}.(\delta(r', \theta_{t_0}) * h^{\lambda_2}(\mathbf{r'}, \mathbf{t_0}) - \delta(r', \theta_{t_1}) * h^{\lambda_2}(\mathbf{r'}, \mathbf{t_1})] \end{aligned} \tag{6.2}$$

where r' is the position of the companion after wavelength rescaling: $r' = r \times \frac{\lambda_2}{\lambda_1}$. This extension of ANDROMEDA is quite easy to implement and would bring a non-negligible gain, useful for the exoplanet imaging community, as shown in Chap. 6.

Longer-term research axis to improve ANDROMEDA

Along this part, we saw that the key-points of the ANDROMEDA method are: (1) the differential images construction and (2) the model of these differential images. On a longer-term perspective, I propose explorations on how to adapt these steps, so that they are more consistent with the real data properties, in order to improve the performance of ANDROMEDA. Moreover, in its current state, ANDROMEDA is only dedicated to point source extraction but its approach could be adapted to extended source extraction.

Finding the optimal frame correlation: In the current version of ANDROMEDA it is assumed that the most correlated frames to be subtracted are the closest in time, which is not necessarily true. To go further, we may consider more elaborate ways of building up the differential images. Identifying the most relevant information to be taken into account requires a better understanding of the correlation of the images, which is far from trivial. For instance, specific study of the frame to frame correlation as made in Milli et al. (2016) could give insights on which frame to combine in order to better subtract the speckles. The ANDROMEDA approach, which is to look for a specific signature given by the parallactic angles, can include any subtraction as long as the model matches this operation. Such an improvement could enable a non negligible gain in terms of detectability. In the same direction, it is possible to replace the ADI operation of ANDROMEDA by a RDI operation, by

looking for the most correlated frames from a PSF library. This solution is also easily implementable in ANDROMEDA and would enable to scrutinize regions closer to the star that are currently limited by the field rotation when using ADI and by the spectral self-subtraction when using SDI. Moreover, as the coronagraph prevents, by its throughput, from investigating sources at very short distance (less than 200mas), this RDI solution might turn really useful in the future.

Frame selection: Moreover, one of the major problem identified to process the high contrast images in an automatic way is the frame selection. During the observation, some images might be of bad quality and no reliable method enables to sort out the frames. Experience has shown that, when using basic rejection criteria, almost half of the frames were currently removed which is extremely costly in telescope time. Solution could be either to integrate an efficient frame selection method or to develop image processing techniques which are insensitive to the bad frames.

Implementing an evolutionary model of the speckle field: Instead of performing an ad hoc differential imaging (which is limiting at close separation), another track is to use an approximate temporal model of the speckle field by saying that the speckle field at a time $t_1 > t_0$ is a fraction of the speckle field at t_0 plus a small variation which can be embodied in an Auto-Regressive model of the speckles. In order to use such an approach, the speckle field still has to be quite stable, which is possible with SPHERE images. This approach is thus similar to work published by Smith et al. (2009) but by taking into account the temporal variation of the speckle field.

Robust detection criterion: As the concept of ANDROMEDA is to look for a given pattern within noise structure, advanced signal processing can be used to find the specific planet signature in the differential images in a robust way. Denis et al. (2016) have for instance developed a detection criterion insensitive to outliers which does not require a too long computing time (based on the theory of locally optimal detectors). In ANDROMEDA this detection criterion can be implemented for the specific case of a white and Gaussian residual noise distribution as it is already approximated. This technique could bring a significant gain to remove the remaining false alarms in the SNR maps.

Modifying the model of noise: In the current version of ANDROMEDA, one strong assumption is to consider the residual noise in the differential images as white and Gaussian. Finding a way of deriving and implementing the true pdf of this residual noise would reinforce the link between the SNR value of a detection and its PFA. To do so, one could derive a empirical model with parameters accounting for the starlight distribution in the images. Such a study is made possible thanks to the stability of the recent high-contrast instruments. This operation could significantly increase the skills of ANDROMEDA also because the post-normalization procedure would no longer be useful, thus getting rid of the only user-defined parameter that is currently sensitive.

Probing extended sources: The ANDROMEDA concept could be adapted to look for extended sources depending on the shape of the circumstellar disk. If the disk is annular, ANDROMEDA could be adapted by modifying the model in order to take into account the signature due to an extended source and tracking this signature within small areas. This solution is similar to the current *forward modeling* technique used but would be more systematic. Another solution is to find a subspace such as Fourier space or any orthogonal modes subset in which the ring has a specific signature and track this signature thanks to the MLE approach. If the disk is edge on, then it is also easy to implement a way of creating a model to characterize the specific features due to an edge-on disk. The main difficulty comes from the continuities between the disk and the background noise that we can see for spiral disks or edge-on disks with fuzzy outlines. In this case, ANDROMEDA is not suited to such features.

Exploiting ANDROMEDA on real data

Now that ANDROMEDA is operational, it can be used by the exoplanet imaging community. It is planned to implement ANDROMEDA in the SPHERE Data Reduction and Handling pipeline. It is

also planned to implement ANDROMEDA in python within the VIP package Gomez Gonzalez et al. (2016b), in collaboration with the Liège university.

ANDROMEDA could also be used to revisit older NaCo data (or any other instrument equipped with an AO system and a pupil tracking mode) in a systematic and fast way to check for new detections that could not be visually detected or to refine the contrast estimations of know companions as well as the detection limits derived from large surveys.

In any case, ANDROMEDA is completely suited to process data from large surveys since it is a tool which enables an objective detection.

Résumé en français de la partie 1 : l'algorithme ANDROMEDA

Dans ce chapitre, je résume en langue française les points clés de chaque chapitre constituant la première partie du manuscrit. Cette partie concerne l'algorithme ANDROMEDA (pour *ANgular DiffeRential OptiMal Exoplanet Detection Algorithm*) dont le but est de détecter et caractériser des points sources dans des images haut contraste prises en suivi de pupille. Cette méthode exploite la diversité temporelle de ces images en utilisant une méthode de résolution de problèmes inverses.

Le concept de cette méthode a été publié par Mugnier et al. (2009), puis mis en place par Cornia (2010) pendant sa thèse de doctorat. Cependant l'algorithme n'était pas validé sur données ciel, en particulier car le modèle utilisé dans l'inversion ne correspond pas parfaitement aux propriétés des images réelles (Chap. 2). Mon travail de thèse a donc consisté à trouver et implementer des solutions afin de contourner ces différences. J'ai ensuite vérifié, et amélioré si besoin, chaque étape de l'algorithme afin de le rendre le plus correspondant possible aux images en jeu (Chap. 3). Une fois la méthode ANDROMEDA opérationnelle, j'ai réalisé des tests de sensibilité aux paramètres utilisateurs afin, d'une part de caractériser ses performances en détails, et d'autre part d'évaluer l'impact des paramètres utilisateurs en vue de rendre son utilisation quasi-systématique (Chap. 4). J'ai ensuite mené à bien une comparaison détaillée entre la méthode ANDROMEDA et les trois méthodes les plus utilisées à ce jour dans le domaine de la détection d'exoplanètes dans des images à haut contraste (Chap. 5). Dans un dernier chapitre, j'applique ANDROMEDA à différents jeux de données de l'instrument VLT/SPHERE afin de mettre en valeur sa versatilité, puis j'étends et discute son utilisation à des données multispectrales (Chap. 6).

Principe de l'algorithme ANDROMEDA

L'idée principale de l'algorithme ANDROMEDA, se résume en deux grandes étapes : (1) une étape d'imagerie différentielle angulaire qui consiste à choisir deux images du cube temporel pour lesquelles le champ de speckles a le moins varié possible (ici nous choisissons les images les plus proches en temps) tandis que la planète a bougée suffisamment (d'au moins un demi élément de résolution). Ce processus permet de soustraire un maximum les speckles tout en faisant apparaître une signature spécifique en cas de présence d'un compagnon (un pic positif et un pic négatif). (2) Grâce à la connaissance des angles parallactiques de chaque image, il est possible de construire le modèle de cette signature à l'aide de l'image de l'étoile non-saturée ou sans coronographe. La seconde étape consiste à estimer les paramètres d'intérêt (ici la position et le contraste du compagnon planétaire) : étant donné que le bruit résiduel dans l'image différentielle peut être considéré comme blanc et gaussien au premier ordre, une estimation par maximum de vraisemblance est appropriée (Eq. 2.17). Ce maximum de vraisemblance peut se résoudre de façon analytique et est donc facilement mis en pratique. Les sorties sont quatre cartes 2D : (i) une carte de flux (qui donne en chaque pixel, le flux estimé de la planète, si la planète est à la position de ce pixel), (ii) une carte d'écart-type du flux (qui donne l'incertitude à 1σ sur le flux estimé si il y a une planète, et la limite de détection à 1σ si il n'y a pas de planète), (iii) une carte de SNR (qui est la carte de flux divisée par la carte d'écart-type du flux) et (iv) une carte de la log-vraisemblance (plus la valeur d'un pixel est élevée, plus la probabilité de présence d'un compagnon sur ce pixel est grande). Analytiquement, la carte de SNR est équivalente à la carte de log-

vraisemblance sous contrainte de positivité. Ainsi, la détection peut se faire de manière automatique directement à partir de la carte de SNR en seuillant cette dernière (puisque lié à la probabilité de présence d'un compagnon) et le flux est estimé analytiquement, ainsi que son incertitude à partir des cartes de flux et d'écart-type du flux respectivement.

Dans le chapitre correspondant, je détaille le principe de la méthode et les calculs sur lesquels elle est fondée, tout en justifiant les choix réalisés et en discutant les potentielles alternatives (Sect. 2.1). Je décris ensuite l'état de l'algorithme tel qu'il était lorsque j'ai commencé ma thèse (Sect. 2.2). Dans une dernière partie, j'applique la méthode à des données issues de l'instrument VLT/NaCo afin de révéler les principaux problèmes à résoudre pour permettre la détection de compagnons à courte séparation de façon automatique via l'application d'un seuil à la carte de SNR. En particulier, beaucoup de compagnons proches ne sont pas détectés et beaucoup de fausses alarmes sont détectées parmi de nombreux artefacts résiduels (Sect. 2.3).

Modifications pour rendre ANDROMEDA opérationnel

Un point clé est la présence d'inhomogénéités spatiales basses fréquences, qui ne sont pas prises en compte dans le modèle, et qui varient lentement dans les images, et donc ne sont pas soustraites lors de l'étape d'imagerie différentielle. Un moyen de contourner ce problème est de filtrer ces basses fréquences spatiales en effectuant un filtrage passe-haut dans l'espace de Fourier. En appliquant le même filtrage au modèle de la signature de la planète qui est recherchée dans les images, l'algorithme reste cohérent, et le flux estimé n'est pas biaisé.

Un autre point clé est l'hypothèse du bruit résiduel considéré comme blanc et gaussien dans les images différentielles. Même filtrées, il reste dans ces images la partie décorrélée temporellement des speckles. Proche de l'étoile, les résidus sont intenses et colorés. Loin de l'étoile les speckles sont bien soustraits et l'hypothèse de bruit blanc gaussien est bien vérifiée. En conséquence, le seuil imposé loin de l'étoile n'est pas le même que celui à imposer près de l'étoile : dans ce dernier cas, il faut un seuil beaucoup plus élevé pour voir apparaitre seulement les compagnons probables et non des résidus de speckles. Une solution consiste à créer un profile typique qui tient compte de cette différence de seuil selon la distance à l'étoile. Ce profil est généré de façon empirique via l'écart-type des résidus contenus dans chaque anneau entourant l'étoile (qui est donc plus élevé dans les anneaux proches de l'étoile). La carte de SNR est ensuite divisée par ce profil afin de se débarrasser de cette tendance radiale. À la suite de cette opération, il est possible de seuiller cette carte de SNR normalisée par une seule et même valeur, quelque soit la distance à l'étoile, et donc de re-connecter les valeurs de la carte de SNR à une probabilité de fausse alarme.

D'autre part, plusieurs façons de créer les images différentielles avaient déjà été explorées avant ma thèse. En particulier, plutôt qu'une simple soustraction, une soustraction où l'une des images est pondérée par la différence d'intensité entre les deux images permettait de prendre en compte les différences de niveau pouvant exister entre les deux images. Cependant, la variation de flux n'est pas forcément linéaire et la façon de calculer le poids correspondant n'était pas robuste à un signal intense dans l'une des deux images. J'ai ainsi mis en place une méthode pour créer des images différentielles affines de façon robuste afin de répondre à ces deux points. Selon la distribution du bruit résiduel qui domine dans les images traitées, l'une ou l'autre de ces méthodes peut être choisie.

Enfin, une dernière étape est d'exploiter les cartes de SNR, de flux et d'écart-type du flux obtenues afin de fournir directement aux utilisateurs les données d'intérêt astrophysique. Pour rendre l'analyse des sorties d'ANDROMEDA complètement automatique, j'ai crée un module qui analyse les détections et rejette les potentiels artefacts (dus au filtrage réalisé sur les images ou aux résidus de speckles qui restent toutefois au dessus du seuil de détection). Cette rejection d'artefacts se fonde essentiellement sur des critères morphologiques et son efficacité a été vérifiée sur différents jeux de données.

En conclusion, ANDROMEDA est maintenant un pipeline de traitement d'images à haut contraste opérationnel sur des données réelles et qui permet de détecter automatiquement et caractériser les points sources présents dans le champ image. À partir des images coronographiques (ou saturées),

des angles parallactiques correspondants et d'une image de l'étoile non-coronographique (ou non-saturée), ce pipeline fournit une carte de détection avec la position sub-pixel, le SNR et le flux estimé des compagnons planétaires probables (avec les incertitudes correspondantes), ainsi que la limite de détection du cube d'images, en tenant compte des biais statistiques à courte séparation.

Sensibilité aux paramètres utilisateurs

Afin d'examiner les réponses de l'algorithme en fonction des paramètres utilisateurs, j'ai choisi un cube d'images de l'instrument VLT/NaCo en bande H dont l'étoile centrale est entourée de sources de fond qui peuvent être utilisées comme cas test de compagnons à détecter. Afin d'analyser plus finement les performances d'ANDROMEDA, 20 compagnons synthétiques ont été injectés dans les images, à des positions et contrastes connus.

Les paramètres utilisateurs d'ANDROMEDA sont au nombre de 7 et sont indépendants. J'ai donc choisi de les faire varier un par un et de comparer les résultats à un cas de référence. La comparaison inspecte l'impact sur la forme du signal dans la carte de SNR, le nombre de vraies et fausses détections, le SNR des vraies détections, la caractérisation (position et contraste estimés), la courbe de limite de détection et le temps de calcul pour arriver aux résultats. Avec le cas de référence, j'ai aussi discuté la notion de seuillage de la carte de SNR en comparant le nombre de détections réalisées par rapport au nombre de détections manquées ou de faux positifs en fonction du seuil imposé. Les résultats obtenus permettent de définir un jeu de paramètres par défauts inscrits dans le code. Il s'avère qu'un seul paramètre utilisateur peut avoir un impact critique sur les résultats et concerne le post-traitement (normalisation de la carte de SNR). Ayant compris en quoi ce paramètre est critique, une façon de gérer ce paramètre à la main est définie.

Ainsi, en termes de performances, la méthode ANDROMEDA dans son ensemble a les propriétés suivantes : (i) concernant la détection automatique, ANDROMEDA est très efficace mais toujours limitée à courte séparation due au manque de rotation de champ et au niveau de speckles quasi-statiques (ce qui est la limitation de toutes les méthodes basées sur de l'ADI); (ii) l'estimation de la position sub-pixel des compagnons est exacte et précise; (iii) l'estimation directe du contraste des compagnons est aussi très juste et les erreurs sur le contraste estimé sont bien en accord avec les incertitudes calculées par ANDROMEDA; (iv) la limite de détection fournie directement par ANDROMEDA est en accord avec les compagnons effectivement détectés dans le champ; (v) ANDROMEDA est très peu sensible aux paramètres utilisateurs, qui peuvent être laissés aux valeurs par défaut, sauf un paramètre concernant le post-traitement; (vi) la rejection d'artefacts résiduels sur critères morphologiques, connaissant le fonctionnement d'ANDROMEDA, est efficace; (vii) enfin, la méthode est très rapide (10 minutes pour 64 images de taille 512×512 pixels) et ne demande que deux grandes étapes non-supervisées.

Comparaison aux autres méthodes couramment utilisées

Trois autres méthodes (cADI de Chauvin et al., 2012; Marois et al., 2006, PCA de Amara and Quanz, 2012; Soummer et al., 2012 et T-LOCI de Marois et al., 2014 dont les principes sont détaillés aux parties 5.2.1, 5.2.3 et 5.2.2 respectivement) sont largement utilisées pour traiter les données des instruments haut contraste afin d'y détecter de potentiels compagnons stellaires. Afin de comparer ces méthodes, j'ai utilisé des données de l'instrument VLT/SPHERE dans lesquelles des compagnons sont injectés à des distances et contrastes connus. Chaque méthode est appliquée aux données en ignorant ces injections[9].

Connaissant la structure des images et les difficultés spécifiques à leurs propriétés, j'ai établi des métriques permettant de comparer ces méthodes selon différents aspects : (1) sur l'aspect détection, sachant qu'il est plus facile de trouver des compagnons loin et brillants, (2) sur la caractérisation, en tenant compte des incertitudes calculées et de leur pertinence, (3) sur les limites de détections fournies

[9]Le traitement de ces images par les différentes méthodes a été fait en collaboration avec des chercheurs utilisateurs de ces méthodes.

et (4) sur différents aspects pratiques choisis d'expérience (le temps de calcul total et le nombre d'étapes requises pour arriver aux résultats finaux ainsi que le nombre de paramètres utilisateurs à faire varier).

En conclusion, ANDROMEDA est le seul pipeline qui permet une détection objective et non-supervisée (les autres requérant une inspection visuelle des images) et dont le signal est relié à une probabilité de fausse alarme. Ses capacités en terme de caractérisation sont comparables aux autres mais le flux est obtenu de façon directe (sans post-traitement intensif) avec des incertitudes cohérentes avec le SNR de la détection et cohérentes avec les propriétés des données. Aussi, la limite de détection indique qu'ANDROMEDA est plus sensible que les autres algorithmes à très grande séparation (une interprétation est que cet effet est dû au fait qu'ANDROMEDA ne soustrait pas seulement les speckles mais recherche le signal spécifique de la planète). C'est aussi le pipeline le plus rapide (de 3 à 70 fois plus rapide que les autres méthodes), qui de plus ne demande que deux étapes (étape générale avec l'imagerie différentielle et le calcul du maximum de vraisemblance puis l'étape de post-traitement suivie directement par l'analyse des cartes fournies par ANDROMEDA) avec seulement un paramètre utilisateur à régler (qui peut être modifié après la première étape qui est la plus longue).

Application à des données de l'instrument VLT/SPHERE

Dans le dernier chapitre, afin d'anticiper les potentielles limitations de la méthode et d'étendre son fonctionnement à différents types de données, j'applique ANDROMEDA à plusieurs cas spécifiques pour étudier :
-La structure des résidus selon différentes longueurs d'onde (cas d'un objet loin de l'étoile, Sect. 6.1);
-La réponse de l'algorithme à différentes conditions d'observation (cas d'un objet loin de l'étoile Sect. 6.2);
-Le cas d'un compagnon proche de l'étoile et peu brillant (Sect. 6.3);
-Le mode incluant une différence d'image spectrale avant l'utilisation classique d'ANDROMEDA (deux jeux de données, avec ou sans absorption dans l'une des deux bandes, Sect. 6.4);
-Le cas de données multispectrales (sur une source difficile, Sect. 6.5).

D'après ces différentes applications, ANDROMEDA est très robuste et appropriée à une application massive. Ce résultat est particulièrement vérifié dans le cas de données de l'instrument SPHERE, dont les images sont de bien meilleures qualités et plus stables que les autres instruments. Les capacités de détection d'ANDROMEDA sont par ailleurs en accord avec les capacités de l'instrument (étant donc la principale limitation).

D'autres résultats importants apparaissent. Pour la première fois, le compagnon GJ504b est détecté en J2 (avec un SNR de 3) et son contraste a pu être extrait une fois le compagnon identifié. La combinaison ADI et SDI fonctionne avec les limitations connues dues au principe de la méthode. Dans le cas de données multispectrales, il est possible d'augmenter les capacités de détection en combinant de manière astucieuse les cartes de SNR obtenues à chaque longueur d'onde. Dans une seconde étape, connaissant la position du compagnon grâce à cette combinaison des cartes de SNR, le spectre du compagnon peut être extrait avec des incertitudes homogènes au SNR du signal dans chaque bande.

Conclusion de la partie 1

Cette partie présente les évolutions et résultats de l'algorithme ANDROMEDA qui est aujourd'hui opérationnel avec des performances très intéressantes qui le rendent complémentaire aux autres méthodes utilisées à ce jour. En particulier, ANDROMEDA répond avec succès aux motivations principales de ce travail de thèse, exposées en introduction. ANDROMEDA est un outil ajustable qui propose une approche innovatrice et originale par rapport aux autres méthodes qui font l'état de l'art. Son objectivité à détecter des compagnons stellaires et à en estimer la position, le contraste et la limite de détection via une approche problème inverse, ainsi que sa rapidité et sa facilité d'utilisation en font une méthode compétitive, en particulier dans le contexte des données considérables venant des grands relevés.

D'autre part, la méthode ANDROMEDA peut être étendue au traitement d'images multispectrales. La redondance spectrale est alors exploitée pour augmenter le SNR des potentiels compagnons présents dans le champ image. Ensuite, la capacité d'ANDROMEDA à estimer le contraste directement est utilisée pour extraire un spectre avec des incertitudes correspondant à la détectabilité du compagnon dans chaque bande.

Part II

MEDUSAE: Exploitation of the spectral diversity in the images.

The goal of this second part of the thesis is to present the work I have done during my PhD on the MEDUSAE algorithm, which is a method dedicated to process multispectral high-contrast images from IFUs equipped with a coronagraph.

Even though this ANDROMEDA algorithm addresses the main issues dealt with in introduction (namely the direct and objective detection and characterization), there is still strong limitations in practice.

- For now, ANDROMEDA is only adapted to point source extraction. Planet detection in young system is very related to the presence of dust disks, both for the theoretical persectives and in the observational exemples: many of the detected young giant exoplanets belong to systems with dust disks (e.g. the Beta Pictoris b companion Lagrange et al. (2009), the HR8799 quadruple system Marois et al. (2010b) and the numerous discoveries enabled by SPHERE).
- Even if its application on multispectral data is promising in the current landscape, the results rely on the hypothesis made on the exoplanet spectra. The recent generation of high-contrast instruments dedicated to exoplanet imaging are all equipped with IFUs and there is a need in developing image processing methods to retrieve objective exoplanetary spectra from these IFS.
- As any other ADI-based image processing operational so far, this method is limited in terms of IWA: at short separation, it is impossible to detect faint companions due to the quasi-static speckle which is particularly high and neither the spectral nor the temporal diversity bring enough information to be exploited.
- Moreover most image processing techniques do not take into account all the a priori information available on the data.

These three aspects are directly linked with the three major topics of the exoplanet research field: (1) the study of the connection between the disks and the exoplanets, (2) the extraction of exoplanetary spectra to study the atmospheric composition and (3) probing fainter companions at shorter separation to fill the mass-distance diagram of the exoplanet discoveries and better understand the nature of these objects. In this context, developing advanced image processing tools dedicated to high-contrast imaging is crucial to meet these needs.

As evoked in introduction, three main algorithms are meant to exploit multispectral images: SDI (Racine et al., 1999), spectral deconvolution (Sparks and Ford, 2002) and the wavelength diversity (Burke and Devaney, 2010). The major limitations of these algorithms are the following:

1. Algorithms based on differential imaging are substracting part of the signal of interest and usually rely on a model of planetary spectrum;
2. The rescaling in wavelength is a first order approximation which depends on the level of the aberrations;
3. The wavelength diversity proposed by Burke and Devaney (2010) does not take into account the coronagraph in the instrument.

The next part of the thesis present the work achieved on the MEDUSAE algorithms, which aims at addressing these limitations. In MEDUSAE, the quasi-static speckles are no longer regarded as noise to be removed but as information to be carefully estimated. This idea is fundamental for the development of future algorithms to avoid self-subtraction due to the differential imaging techniques and thus probe the very close environment of the target star, which is currently limited by the starlight leakages not stopped by the coronagraph that are due to the remaining instrumental aberrations. This issue becomes crucial with the recent instruments since the images are no longer limited by the diffraction but by the instrumental residual aberrations. This will be even more important for the ELTs instruments whose main limitation will be clearly due to these optical aberrations.

Chapter 7

The MEDUSAE approach and initial status

Contents

7.1 The MEDUSAE approach: image model and inversion 206
7.1.1 Model of the multispectral images 206
7.1.2 Inversion criterion 210
7.1.3 Methods to estimate the three unknowns 210
7.1.4 Minimization algorithm used for the phase retrieval in MEDUSAE 212
7.1.5 Inversion scheme to run MEDUSAE 212
7.2 Main hypothesis used in MEDUSAE 213
7.3 Previous work on the MEDUSAE method 214
7.3.1 Simulated data to validate the MEDUSAE concept 214
7.3.2 Tests and conclusion from the inverse crime MEDUSAE application 215

In order to address the issues mentioned in the previous chapter, an original idea[1] published by Ygouf et al. (2013), consists in jointly estimating the instrumental aberrations and the circumstellar objects by using the diversity provided by the multispectral images. This method, hereafter called MEDUSAE for *Multispectral Exoplanet Detection Using Simultaneous Aberration Estimation* is the subject of this part of the thesis.

The key point of this algorithm is that the speckles are no longer considered as part of the noise but as information to be carefully assessed in order to disentangle them from the off-axis signals of interest. In order to estimate the speckles, the innovative idea of this method is to make use of an analytical model of the post-AO *coronagraphic PSF* describing the speckle field. The spectral diversity is used to, on the one hand, constrain the estimation of the speckles via this analytical parametric model and, on the other hand, to constrain the circumstellar objects since their position is fixed in the images. Moreover, it will also be possible to include a specific regularization to take into account priors on the companion vs stellar spectra.

Inverse problem solving is used to estimate the astrophysical objects surrounding the target star. The model to be inverted is to consider that each image of the multispectral cube is composed of (1) the speckle field, (2) the image of the objects and (3) the residual noise (photon, detector or other instrumental noise) as shown in Fig. 7.1. In practice, the chosen strategy to jointly estimate these two first components is to alternately estimate the speckle field and the object map until minimization of the penalized distance between the model and the real data.

This chapter describes the status of the MEDUSAE method before I started working on it to investigate the possibility of making it able to process real data from IFS. I will first present the theoretical concept on which MEDUSAE is based on, that is to say the imaging model it uses and

[1]Note that premises of this method have been published in Sauvage et al. (2010) and Ygouf et al. (2013) have implemented this principle in practice and validate its concept on simulated data.

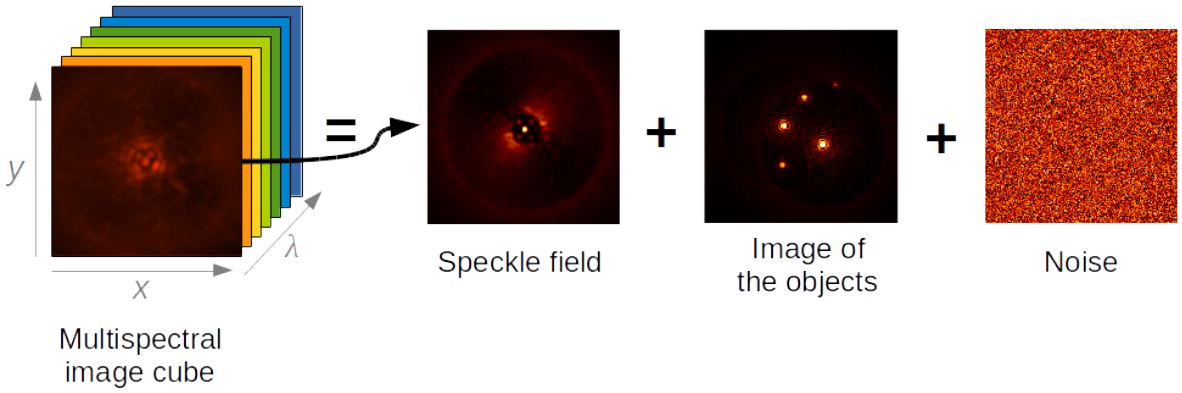

Figure 7.1 – Schematic image model used by MEDUSAE: the images of the multispectral cube are assumed to be constituted of a speckle field on which circumstellar objects and noise are added.

the corresponding criterion to be inverted (Sect. 7.1). Secondly, I will discuss the hypothesis on which this whole algorithm relies (Sect. 7.2). Eventually I will summarize the previous work achieved and the main conclusions drawn from it (Sect. 7.3).

7.1 The MEDUSAE approach: image model and inversion

In this section, I will describe the principles on which the MEDUSAE image processing method relies. As MEDUSAE is a method relying on inverse problem solving, the first step is to define an accurate imaging model (Sect. 7.1.1). From this model, a criterion to be minimized is derived from which the unknowns of the imaging model are estimated (Sect. 7.1.2). According to this criterion, an optimization scheme is established to estimate all the unknowns of the problem (Sect. 7.1.3). Eventually, the criterion is minimized along the chosen strategy, by using a specific method to reach its minimum (Sect. 7.1.4).

7.1.1 Model of the multispectral images

As mentioned in introduction of this chapter, each image of the multispectral cube, i_λ can be considered as the sum of three components: (1) the speckle field, (2) the focal plane image of the circumstellar objects and (3) the noise (see Fig. 7.1). Each component is dependent upon the wavelength λ but has a deterministic behavior as a function of the wavelength. The speckle field is given by the on-axis PSF of the system (called *coronagraphic PSF* in the following), denoted h^c_λ, multiplied by the on-axis star intensity, denoted f^*_λ. The image of the circumstellar objects are given by the off-axis PSF of the system (non-coronagraphic PSF), denoted h^{nc}_λ, convolved with the astrophysical object map, denoted o_λ. The noise is the photon noise, the detector noise or any other background noise and is denoted n_λ. The speckle field and the object map are jointly estimated by performing an alternate estimation of these unknowns.

Thus the multispectral images model $m_\lambda(\alpha)$ can be written, as in Ygouf et al. (2013):

$$m_\lambda(\alpha) = f^*_\lambda \times h^c_\lambda(\alpha) + [o_\lambda * h^{nc}_\lambda](\alpha) + n_\lambda(\alpha) \tag{7.1}$$

Where α denotes the angular position in the images and λ are the imaging wavelengths constituting the multispectral cube.

7.1.1.1 Model of the speckle field: $f^*_\lambda \times h^c_\lambda$

Coronagraphic images are not the product of a convolution process. The key point of the MEDUSAE method is to use a parametric model of the coronagraphic PSF in order to estimate the instrumental

aberrations from which the observed speckle field originates. In order to determine this model of coronagraphic PSF, the idea is to propagate the light from plane to plane in the coronagraphic setup. Two regions are considered in this model, the region before the coronagraph, called *upstream* and the region after, called *downstream*. The aberrations are then separated into their quasi-static component and their time-dependent component. Over one exposure, the quasi-static component is considered static.

The coronagraphic setup is defined as on Fig. 7.2, with an entrance pupil, $\mathcal{P}_{up}$ of surface $\mathcal{S}$ from which the optical wavefront enters with a certain phase ϕ which is due to the static aberrations and the time-dependent aberrations. It is considered here that the time-dependent aberrations are only due to the post-AO turbulence residuals, inducing a phase $\phi_{res}(t)$. The static upstream phase, due to the instrument itself, is denoted ϕ_{up}. After the coronagraph, in the Lyot stop plane of aperture $\mathcal{P}_{down}$, the wavefront undergoes a downstream phase ϕ_{down}which is assumed to be constant during the long exposure time. The amplitudes in the pupil planes are written ψ_x and the amplitudes in the focal planes are written $\mathcal{A}_x$.

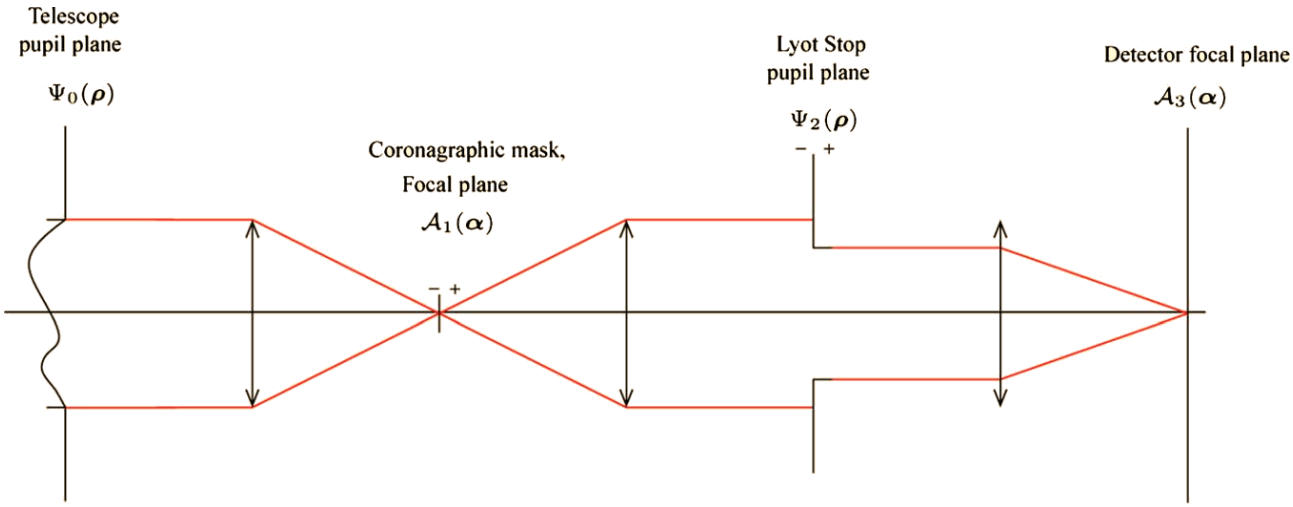

Figure 7.2 – Description of the plane to plane coronagraph configuration used to derive the analytical expression of the long exposure coronagraphic PSF on which the imaging model of MEDUSAE relies. Figure from Sauvage et al. (2010).

Several assumptions are used for the calculations:

- The light comes from a perfectly centered on-axis point source;
- The computations are made in the framework of the Fraunhofer diffraction, which implies that all the aberrations are introduced in the pupil planes (no Fresnel effects are taken into account);
- The entrance pupil is uniform (no apodization) and centro-symmetrical (the spider of the telescope are not taken into account), in other words, no amplitude defects are taken into account;
- The upstream aberrations may contain the tip-tilt aberrations;
- The non-static phase (originating from the turbulence residuals) is assumed to be random within a centered normal distribution, stationary, of uniform variance all over the pupil plane and ergodic wrt time.

In this model, three types of phases are considered to be responsible for the wavefront distortion:

- The upstream static phase, ϕ_{up}: it is the most critical component, since it is responsible for most of the features arising in the speckle field with the same spatial scale as potential companions;
- The upstream time-dependent phase due to turbulence residuals, $\phi_{res}(t)$: this contribution is expected to vary very fast ans induces a smooth halo, characterized by the statistical properties only (its structure function), and not by each of its instantaneous realizations;

- The downstream static phase, ϕ_{down}: they are by definition located *after* the focal plane mask where no rotating optical devices are found (such as the pupil derotator or the ADC) so it can be considered as static to a good approximation.

In the whole development of MEDUSAE it has been chosen to estimate separately the two last unknowns (by calibration or so) and to provide them as an input of the method. Also, the upstream phase might not be accurately calibrated since it can vary significantly throughout the night, contrary to the static downstream phase. In the end, *only the upstream static phases at each wavelength are estimated in this current version of MEDUSAE*[2].

The model used in MEDUSAE assumes an *ideal* coronagraph, that is to say, which removes all the coherent part of the input beam (e.g., if the input wavefront was perfectly plane and perpendicular to the optical axis, no light would be left in the focal plane), as presented in Sauvage et al. (2010).

Short exposure expression: Under these assumptions, the amplitude in the entrance pupil plane (following notations of Fig. 7.2) writes $\psi_0(\rho,t) = \mathcal{P}_{up}(\rho).e^{j(\phi_{res}(\rho,t)+\phi_{up}(\rho))}$, where j is the imaginary unit such that $j^2=-1$. Then, by simply propagating the light from plane to plane, and by choosing the convention that the inverse Fourier transform is used to propagate the light from the pupil to the focal plane, the short exposure coronagraphic PSF, h^c_{SE}, writes:

$$h^c_{SE}(\rho,t) = h^{nc}(\rho,t) + |\eta_0(\rho,t)|^2\ h_{do}(\rho) - 2\Re(\eta_0^*(\rho,t).\mathcal{A}_{nc}(\rho,t).\mathcal{A}^*_{do}(\rho)) \tag{7.2}$$

With h^{nc} the non-coronagraphic PSF of the system: $h^{nc}(t) = |\mathcal{A}_{nc}(t)|^2 = |FT^{-1}(\mathcal{P}_{down}.e^{j.\phi_{tot}(t)})|^2$, where $\phi_{tot} = \phi_{up} + \phi_{res}(t) + \phi_{down}$. And h_{do} the PSF only due to the downstream aberrations: $h_{do} = |\mathcal{A}_{do}|^2 = |FT^{-1}(\mathcal{P}_{down}.e^{j.\phi_{down}})|^2$. The variable η_0 is the most important parameter which codes for the part of the incident wave which is actually subtracted by the coronagraphic mask. In the detector plane, the field can be written: $\mathcal{A}_c = \mathcal{A}_{nc} - \eta_0\ \mathcal{A}_{do}$. In the case of an ideal coronagraph, the part of the incoming wavefront which is perpendicular to the optical axis is fully suppressed, hence η_0 can be written:

$$\eta_0 \doteq \langle\psi_0|\mathcal{P}_{up}\rangle = \frac{1}{S}\int\int \psi_0^*(\mathbf{r},t)\mathcal{P}_{up}(\mathbf{r})d^2\mathbf{r} = \frac{1}{S}\int\int |\mathcal{P}_{up}|^2(\mathbf{r})\ \exp^{-j(\phi_{res}(\mathbf{r},t)+\phi_{up}(\mathbf{r}))}\ d^2\mathbf{r} \tag{7.3}$$

Long exposure expression: In order to obtain the corresponding long exposure h^c_{LE}, the idea is to average in time this short exposure expression: $h^c_{LE} = \langle h^c_{SE}\rangle_t$. By doing so, it results in the expression derived by Sauvage et al. (2010):

$$h^{LE}_c = \langle h^{nc}(t)\rangle + \langle|\eta_0(t)|^2\rangle\ h_{do} - \frac{2}{S}\Re\{FT^{-1}[\psi_{u+d}.(\exp^{-\frac{1}{2}D_{\phi_{res}}} * \psi_{up})].\mathcal{A}^*_{do})\} \tag{7.4}$$

Where $\psi_{u+d} = \mathcal{P}_{up}.e^{j(\phi_{down}+\phi_{up})}$ (the dependences upon ρ are ignored for more readability).

Note that compared to the expression derived in Sauvage et al. (2010) ψ_{up} replaces ψ^*_{up} due to a sign mistake at Eq. (18) which had been propagated in the published expression. The difference between the two expressions is minor and does not significantly impact the results.

Multispectral adaptation: The phases can be parametrized by the optical path difference (*opd*), δ describing the optical aberrations. An important assumption used in MEDUSAE is that these *opd*'s are considered achromatic (which is a correct approximation at first order). This assumption enables to reduce the number of parameters to be estimated: if we are able to estimate the aberrations δ from which the phases at each wavelength are computed by $\phi = \frac{2\pi}{\lambda}\delta$ then it is possible to describe the full multispectral speckle fields by incorporating these phases in the model at Eq. 7.4. As a consequence, the number of unknowns to be estimated to describe the speckle field is divided by N_λ.

In this model, the optical aberrations that the starlight undergoes and from which the speckles originate are thus separated into three contributions:

- The upstream static aberrations, δ_{up};

[2]Note that it is possible to also estimate the downstream phases and the residual phases but in order to decrease the number of unknowns added to the reason explained above, it has been chosen to only estimate the upstream phase.

- The upstream aberrations due to post-AO atmospheric turbulence residuals, $\delta_{res}(t)$;
- The downstream static aberrations, δ_{down}.

During her PhD, M. Ygouf tried to simplify this long exposure coronagraphic PSF model in order to understand it more deeply and to explore ways of making its implementation easier and/or the inversion running time shorter. To do so, she performed a Taylor expansion of Eq. 7.4 by assuming that the phases were small. The simplified model she obtained was not precise enough for the inversion (as it does not account for the non-centro symmetrical speckles or for the real evolution of the speckles with the wavelength as in Denis et al. (2016)). However, this model showed two important aspects. First, the simplified model gets back to the dilation of the speckles with the wavelength, which means that working with such a model would give MEDUSAE the same limitations as the other multispectral image processing methods, which are problematic in particular if (i) the phase is important, (ii) the object is faint and (iii) the wavelength extension of the multispectral cube is large. Second, the simplified model explicitly confirm that the downstream phases have a very little impact on the final speckle field. Thus, as the downstream aberrations are low and static, they can be calibrated beforehand and injected in the model without needing to estimate finely this contribution[3]. The simplified model has been published in Ygouf et al. (2010).

As a conclusion, in order to describe the speckle field in every image of the multispectral cube, MEDUSAE has to estimate one single aberration map, δ_{up} corresponding to the static aberrations upstream the coronagraph. This assumes that the downstream aberration map δ_{down} and the residual phase structure function $D_{\Phi_{res}}$ are given as inputs.

Main difficulty arising from the use of this model: This analytical expression is non-linear which induces degeneracy: one given speckle field can be due to different phases. This can lead to problems when estimating the aberration map by the method explained at Sect. 7.1.3 since the inversion can lead to a local minimum and struggle in converging.

Other models explored: Other models have been explored to try minimizing the number of parameters and/or make the model more realistic:

-By performing a Taylor expansion of Eq. 7.4 under the small phase approximation, as in Ygouf et al. (2010) (too simplified to be used in MEDUSAE);

-By changing η_0 into $\eta = (1-\epsilon)\eta_0$ to account for a non-perfect coronagraph, as in Appendix A Ygouf, 2012 which had missing terms.

-At last by trying to derive an analytical expression of a realistic coronagraph which takes into account the spatial extension of the coronagraphic focal plane mask, including its induced diffraction. This solution, is very difficult to implement numerically and has not yet been taken into account for MEDUSAE. An exploitable expression of realistic coronagraphic model is being derived and implemented in IDL by O. Herscovici during his PhD at Onera. First results are published in Hercovisci et al. (2016).

I mentioned this work here since, it had been realized previously that the discrepancy between the model of coronagraphic PSF and the real speckle field impacted the performance of the method so implementing a more sophisticated model should significantly improve the method. Thus, at the very beginning of my PhD, my work was focused on exploring the different analytical expressions of the long-exposure coronagraphic PSF which could be used in MEDUSAE. In the Chap. 8, I will specifically work on these limitations.

7.1.1.2 Model of the circumstellar objects image: $o_\lambda * h_\lambda^{nc}$

To extract the circumstellar objects, a 2D-map containing the objects must be estimated at each wavelength. In the MEDUSAE algorithm, it is a classical case of deconvolution in which the off-axis PSF of the system h^{nc} is derived classically similarly to the ideal model of coronagraph (only

[3]Note that the correction on the published expression of h_c^{LE} does not impact the conclusions obtained by M. Ygouf.

the diffraction is taken into account and the aberrations are assumed to be in the pupil planes). Thus, the estimated aberration map $\hat{\delta}_{up}$ is also consistently used to derive the non-coronagraphic PSF model. Note that the so-called *non-coronagraphic PSF* is less sensitive to the aberrations and thus the accuracy of the estimated upstream aberration map does not have a critical impact on the object estimation. As a consequence, *for given aberration maps*, that is to say within one specific iteration of the alternate algorithm, a non-myopic deconvolution is performed, that is to say which uses this derived non-coronagraphic PSF calculated with these given aberration maps. However, generally speaking, the whole MEDUSAE algorithm performs a myopic deconvolution since the PSF is not a priori known and provided to MEDUSAE but it is estimated by the algorithm itself.

7.1.1.3 Model of the noise: n_λ

This term is constituted of the different noises which are affecting the images: the photon noise (due to the star, the planets and the background) and the detector noise. The detector noise has a Gaussian distribution and the photon noise in post-AO images can be approximated by a Gaussian noise whose variance is given by the image (as used in the development of the MISTRAL algorithm Mugnier et al., 2004, which proved to be a reliable hypothesis to describe the noise in post-OA images). The sum of Gaussian noises is Gaussian whose variance is given by the sum of the detector noise variance and the photon noise variance.

7.1.2 Inversion criterion

Eventually, the three unknowns to be estimated are:

1. the spectrum of the observed star f^*_λ,
2. the upstream aberration map δ_{up},
3. the object maps o_λ.

To invert the problem, it consists in minimizing, in the least-square sense, the distance between the multispectral images i_λ and its model m_λ defined at Eq. 7.1, weighted by the noise variance σ^2. This criterion to be minimized is denoted J_{data}. Moreover, in order to constraint the inversion and avoid the numerous local minimums, regularization terms $\mathcal{R}$ are added (Bayesian framework). The corresponding criterion (or penalized likelihood) to be minimized, $J = J_{data} + \mathcal{R}$, writes:

$$J(f^*_\lambda, \delta_{up}, o_\lambda) = \sum_\lambda \sum_\alpha \frac{1}{2\sigma^2_{\lambda,\alpha}} |i_\lambda - [f^*_\lambda \times h^c_{\lambda,\alpha}(\delta_{up}) + o_{\lambda,\alpha} * h^{nc}_{\lambda,\alpha}]|^2 + \mathcal{R}(o) + \mathcal{R}_\lambda(f^*) + \mathcal{R}(\delta_{up}) \quad (7.5)$$

If the data are completely in agreement with the model, then for a noise variance of one, $J_{data} = \frac{1}{2} \times N^2_{pix} \times N_\lambda$. For the 39 channels of the IFS providing 190×190 pixels images, the minimum value of this J_{data} criterion is thus: $J_{data} = 703950$.

7.1.3 Methods to estimate the three unknowns

The chosen optimization scheme implemented in MEDUSAE is to *alternately* estimate the speckle field and the object map image. To estimate the speckle field, the star spectrum and the coronagraphic PSF are *jointly* estimated and the coronagraphic PSF is estimated via the upstream aberration map.

In the following, I will describe the methods implemented in MEDUSAE to estimate each of these three unknowns, including the regularizations applied on these unknowns to constrain the problem.

7.1.3.1 Star flux f^*_λ

It is not necessary to proceed to a criterion descent to obtain the stellar flux. Indeed, for a given couple (o_λ, δ_{up}), the spectrum of the star can be estimated analytically by maximum likelihood. This

step simply consists in differentiating the criterion wrt f^*_λ, all the other parameters being fixed. Its computed value is then injected in J before proceeding to the criterion descent on the δ_{up} parameter.

When minimizing the criterion wrt the star flux by solving $\frac{\partial J}{\partial f^*_\lambda} = 0$, the estimated star spectrum $\hat{f^*_\lambda}$ is proportional to $1/h^c_\lambda$. In order to avoid the divergence when the phase is really small the star flux estimation is regularized. We chose a separated regularization for each lambda, which is Gaussian with a mean f_0 and a variance σ_f^2 (so that the criterion remains differentiable):

$$\mathcal{R}^{f*}_\lambda = \frac{(f^*_\lambda - f_0)^2}{2\,\sigma_f^2} \tag{7.6}$$

The estimated star spectrum obtained by solving this regularized criterion $\frac{\partial J_{MAP}}{\partial f^*_\lambda} = 0$ then writes:

$$\hat{f^*_\lambda} = \frac{\frac{f_0}{\sigma_f^2} + \sum_\alpha \frac{1}{\sigma^2_{n,\lambda}}\, h^c_\lambda \cdot i_\lambda}{\sum_\alpha \frac{1}{\sigma^2_{n,\lambda}} (h^c_\lambda)^2 + \frac{1}{\sigma_f^2}} \tag{7.7}$$

Where i_λ is the image at wavelength λ, $\sigma^2_{n,\lambda}$ is the noise variance in this image and h^c_λ the corresponding estimated coronagraphic PSF (assumed known at this stage).

In practice, $f_0 = 0$ and $\sigma_f^2 \sim 100 \times \sum(i_\lambda)$ is enough to avoid the divergence since the final estimated flux is proportional to $1/\sigma_f^2$. Note that the chosen regularization is separable so the star spectrum f^*_λ is computed separately for each considered wavelength.

7.1.3.2 Upstream aberration map δ_{up} using phase retrieval (for a given object)

For given object maps (o_λ are fixed in the J criterion), the upstream phase is estimated by a multispectral *phase retrieval*. The phase retrieval consists in estimating the aberrations in the pupil plane which would be responsible for the speckle field observed in the data. This phase retrieval is thus dependent on both the star spectrum f^*_λ and the aberration map δ_{up} that are jointly estimated.

To reach the correct aberration map, the criterion J is minimized. This phase retrieval is thus an *iterative descent* which can take several minutes to hours to reach the convergence threshold[4]. The number of iterations is limited by a certain amount which is user-defined. The convergence threshold set is also user-defined.

As this phase retrieval is based on the model of ideal coronagraph, which is non-linear, during the descent, the algorithm might converge in one of the local minimums. The phase retrieval is consequently dependent on the chosen starting point. This phase retrieval step is crucial and it is the most sensitive step in MEDUSAE. I will re-discuss this aspect in Sect. 7.1.5.

The stellar halo is proportional to the star flux and also, at first order and in the small phase regime, to the aberration variance. This means that there is a strong degeneracy between, the aberration variance and the stellar flux used to produce the speckle field in the corrected zone. At larger separation, the uncorrected part of the field (smooth stellar halo) helps disentangling this two components. As a general rule, the stellar smooth halo is mainly described by $D_{\phi_{res}}$, the presence of $D_{\phi_{res}}$ removes the degeneracy between the stellar flux and the estimated upstream phase (the star flux is said to be mainly due to the stellar halo coded by $D_{\phi_{res}}$ and not due to the speckles coded by δ_{up}). As a consequence, provided that the input $D_{\phi_{res}}$ corresponds to the true one, the presence of turbulence residuals constrains the star spectrum estimation, thus leading to a better inversion.

7.1.3.3 Object map o_λ using a non-myopic deconvolution (for a given upstream *opd*)

For a given speckle field, parametrized by δ_{up} and f^*_λ (they are fixed in the J criterion), the object is estimated via a multispectral non-myopic deconvolution. As the resulting criterion is convex, the solution is unique. The deconvolution is said to be *non-myopic* since it integrates the non-coronagraphic

[4]The convergence threshold, or *stopping rule*, is defined as $\epsilon = \frac{|J_i - J_{i-1}|}{|J_i + J_{i-1}|/2}$, where J_i is the value of the criterion at the iteration number i.

PSF calculated from the aberration map previously estimated by phase retrieval. This step lasts only a few seconds.

To better constrain the object map estimation, the positivity constraint is added, as well as a spatial regularization. Assuming the pixel to pixel independence in the images, the object map is estimated under the L1-L2 regularization (see Chap. 1.3.1.5). Indeed, for now, MEDUSAE supposes point sources (such as exoplanets) in the field of view, which means the object map will be sparse. Under this hypothesis, the object map is well constraint by a L1-L2 regularization which smooths the background (where no planets are expected) while sharpening the point source signals (as the planetary signal can be considered as Dirac peaks). In practice, the L1 regularization is currently implemented by using a L1L2 metric but with a very small quadratic region whose presence only aims at making the criterion differentiable.

Note that for now, the object spectrum is assumed to be flat and is not estimated in this version of MEDUSAE. Thus only one object map is provided, on which the location as well as the estimated flux can be read.

7.1.4 Minimization algorithm used for the phase retrieval in MEDUSAE

In order to perform the phase retrieval, the criterion J at fixed object map, denoted J', must be minimized (its derivative must reach zero). In order to reach the global minimum of this J' criterion, an adapted method must be implemented to avoid converging in one of the numerous local minimums due to the very non-linear nature of the phase retrieval problem.

During her PhD, M. Ygouf has chosen to use a *local descent* algorithm which consists in using the analytical expression of the criterion's gradient. Among these methods, she chose to use a *quasi-Newton method* which is an iterative method that does not require to compute the Jacobian of the criterion. The main advantage of this method is that it reaches the minimum quite fast given the numerous data point processed by MEDUSAE (up to 39 channels of 200×200 pixels in SPHERE-IFS). Its main drawback is that it is sensitive to local minimums and thus to the starting point of the descent.

More precisely, she used the *Variable Metric with Limited Memory and Bounds*, VMLM-B, developed by Thiebaut (2002), which has the advantage of incorporating bounds on every parameter to better constrain the descent and contains strategies to converge faster than the conjugated gradients in practice[5]. This local descent method is particularly suited to image reconstruction, given the numerous data points and given the usual positivity constraint that can be added. This method requires an analytical expression of the gradient of the criterion at each of the parameters sought. The corresponding gradients of J given by the Eq. 7.5 at the upstream aberration map δ_{up} has been calculated by M. Ygouf and details about this calculation can be found in her PhD thesis (Appendix A Ygouf, 2012).

7.1.5 Inversion scheme to run MEDUSAE

In order to avoid reaching a local minimum during the phase retrieval process, the inversion strategy used in MEDUSAE goes through two main steps: an initialization stage and a main stage.

Initialization stage: The first step in MEDUSAE is to start from a random aberration map having a very small *rms* value and begin the descent with the object considered null. Once the phase retrieval converges to a first estimated aberration map, δ_{up}, the initialization consists in investigating the so-called *four equivalent aberration maps*: δ_{up}, $-\delta_{up}$, $rot(\delta_{up}; \pi/2)$ and $-rot(\delta_{up}; \pi/2)$. Indeed, it has been noticed that the speckle field computed for a given aberration map δ_{up}, is in a first order approximation, the same as the one computed for the opposite aberration map, the rotated aberration map by 180°, or the opposite of the rotated aberration map by 180°. In order to check which of these four aberration

[5]This method is part of the *OptimPack* IDL library containing several descent algorithms, useful for image reconstruction: https://cral.univ-lyon1.fr/labo/perso/eric.thiebaut/?Software/OptimPack.

maps is the most appropriate, the algorithm begins a descent from each of them until obtaining four aberration maps, $\delta_1 \equiv \delta_{up}$, δ_2, δ_3 and δ_4. The chosen aberration map is the one that minimizes the criterion J. From this chosen aberration map, the alternated object-aberration estimation is started until reaching the convergence threshold.

To increase the robustness, this initialization procedure is performed twice (since using only one spectral channel could still lead to a local minimum):

1. Only one wavelength is considered (usually the shortest since it is easier to extract companions from it);
2. Two wavelengths are considered (usually the shortest and the largest to emphasize the speckle radial motion in the two images).

In between these two initializations, the estimated object is assumed to be not realistic enough and is reset to zero. Moreover, the object is estimated with a L1L2 spatial regularization using hyper-parameters such that the regularization is very low.

Inversion core: After the initialization procedure, the previously estimated object is reset to zero and the main inversion is performed. This inversion core consists in alternatively estimating the upstream aberration map δ_{up} and the object map o. This inversion core starts with two wavelengths (the most distant) and once the convergence is reached, the alternated procedure is performed with one more wavelength. The wavelengths are thus incorporated one by one until the whole multispectral cube is used. When incorporating one more wavelength, the object map is reset to zero. The spatial regularization applied on the object map estimation is crucial during the core of the MEDUSAE process and must be carefully set via the two hyper-parameters tuning the chosen L1L2 regularization (essentially one of the two parameters since we want to be as L1 as possible).

Since the initialization stage is mainly performed to get closer to the real aberration map and in order to avoid the initialization to be too long, the convergence threshold set for the phase retrieval at the initialization stage is lower than for the main inversion: it is set to $\epsilon = 10^{-4}$ in the initialization while it is set to $\epsilon = 10^{-5}$ in the inversion core.

7.2 Main hypothesis used in MEDUSAE

The list below gathers the main hypothesis used in this version of MEDUSAE and discuss their impact and/or how it can be fulfilled.

- **Star spectrum**: No prior is taken into account to estimate the star spectrum though the SPHERE-IFS calibrations provide at least the trend of the star spectrum. One could add this information to decrease the degeneracy between the star spectrum and the upstream phase.
- **Speckle field**: The model of coronagraph used relies on several assumptions, as described at Sect. 7.1.1. One of the most important assumptions is that an ideal coronagraph is considered and the diffraction effects due to the spatial extension of the focal plane mask are not taken into account.
- **Speckle field**: One of the most important hypothesis is that the optical path difference is assumed to be achromatic. This hypothesis is verified at first order but is not fundamentally correct since the speckles arise from the optical elements along the optical path.
- **Speckle field**: The aberrations are introduced in the pupil planes: it is not fully verified in the SPHERE-IFS design since some optics are not exactly located in the pupil plane, before and after the coronagraph. Moreover the amplitude defects are neglected though some might be in the instrument.
- **Speckle field**: The time dependent aberrations only arise from the turbulence residuals. In imaging instrument such as SPHERE, the stability of the system was one of the key-point of its design and this should be verified for exposures of less than a minute. Note that rigorously,

the upstream and downstream aberrations are not static but their variation can be considered as static on the timescale of one exposure.

- **Object map**: For now, only one object map (at one wavelength) is estimated by MEDUSAE because the object is assumed to have a gray spectrum. In order to retrieve the spectrum of the circumstellar objects, a multispectral deconvolution as in Bongard et al. (2011), could be implemented.
- **Noise**: The noise in the multispectral images is assumed to be Gaussian which is responsible for the criterion J expression at Eq. 7.5. This approximation is well verified for the fluxes at hand and should not impact the results.

Moreover, another important assumption is that the downstream aberrations δ_{down} and the turbulence residual structure functions $D_{\phi_{res}}$ are assumed to be known and given as an input to MEDUSAE. In the next chapter, at Sect. 8.4, a deeper discussion is presented about how to estimate these two parameters and how much MEDUSAE is sensitive to them.

In the next section, I will describe the work made by M. Ygouf during her PhD to validate the MEDUSAE algorithm strategy by performing an inverse crime. I will thus present the main conclusions and perspectives drawn from her work and which were the starting point of my PhD. Her work does not discuss the chosen hypothesis, considered settled, but focuses on validating the concept of MEDUSAE. My work consisted in reviewing the strategy chosen in the aim of applying MEDUSAE on real multispectral data.

7.3 Previous work on the MEDUSAE method

The MEDUSAE concept described at the previous section has been laid out by M. Ygouf during her PhD whose defense took place in December 2012 at IPAG. She also implemented in IDL the whole inversion procedure (the phase retrieval calling the VMLM-B optimization, the maximum likelihood to estimate the star spectrum for each estimated upstream phase and the non-myopic deconvolution), including the analytical expression of the gradient of the criterion J. To validate the concept and refine the inversion strategy, she tested the algorithm on an inverse crime: the images are simulated by using the same model as the one used in the inversion.

This work led to numerous conclusions and the main results have been published in Ygouf et al. (2013) whose refinement are presented in her PhD thesis, Ygouf (2012). In this section, I summarize the main conclusions she obtained.

7.3.1 Simulated data to validate the MEDUSAE concept

The data used to test the MEDUSAE concept are data that are simulated using the ideal coronagraphic PSF model of Eq. 7.1. The downstream aberration map δ_{down} and the turbulence residuals structure function $D_{\phi_{res}}$ used to build the images are also the ones given as an input of MEDUSAE.

The images are simulated under typical observation conditions (seeing 0.85″at 0.5μm, 3 turbulent layers with typical C_n^2 profile and wind strength) of a star of magnitude 6 at 950nm during 30 minutes at the VLT. The AO corrections considered here are typical correction by a SH-WFS working at 700nm (for this wavelength the star magnitude is set to 8) with a sampling frequency of 1.2 kHz and constituted of 40×40 micro-lenses, conjugated to a DM constituted of 41×41 actuators. The IDL code to generate the turbulence residuals structure function has been developed by the Onera-DOTA/HRA group.

The entrance pupil is defined as circular and uniform (neither central occultation nor telescope spiders are taken into account) and the Lyot stop diameter is set equal to the entrance pupil diameter (in other terms, $\mathcal{P}_{up} = \mathcal{P}_{down}$).

Method used to produce the multispectral cube In order to build the multispectral cube from the input aberrations, the method used is to define the aberrations in the pupil plane over a

specific pupil diameter which is constant for every wavelength. Then, in order to adapt the focal plane sampling at the different wavelengths, these pupil plane arrays are zero padded (so that the same pupil size is used). The size of the zero padded arrays for each wavelength (which is the size of the image for the Nyquist sampled wavelength) is stored in a variable which is required as an input to MEDUSAE. This variable is used to build the multispectral model by zero padding during the inversion procedure.

Numerical values used to produce the data set Following the method described above, Tab. 7.1 gathers the parameters used to build the simulated data used in this section.

Parameter	Value	Unit
Number of spectral channels N_λ	6	-
Size of images N_{img}	128×128	pixels
Wavelengths	950 - 1083.6 - 1232.0 - 1365.6 - 1514.1 - 1647.7	nm
Nyquist sampling wavelength	950 nm	-
Upstream pupil diameter	64	pixels
Downstream pupil diameter	64	pixels
RMS upstream aberrations	30	nm
RMS downstream aberrations	30	nm
Turbulence residual aberrations	typical conditions	-
Photon noise	yes	-
Detector noise	no	-

Table 7.1 – Parameters used to produce the simulated images used to perform the inverse crime.

Fig. 7.3 shows the aberration map used to produce the speckle field (left) and the speckle field obtained by injecting this aberration map in Eq. 7.4.

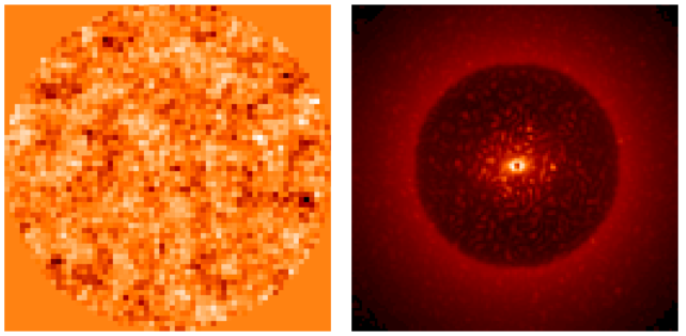

(a) Aberration map (b) Image of the speckle field in the focal plane

Figure 7.3 – Simulated data used in the so-called *inverse crime*. Left: Upstream aberrations used to simulate the images. Right: Corresponding coronagraphic PSF at 950nm obtained with the properties gathered at Tab. 7.1. Figure from Ygouf et al. (2013).

Injected planetary companions In the images, a few planetary signals are injected by convolving the object map constituted of Dirac peaks with the non-coronagraphic PSF. The aberrations used to build this non-coronagraphic PSF are the same as the ones used to build the coronagraphic PSF.

7.3.2 Tests and conclusion from the inverse crime MEDUSAE application

Generally speaking, for the MEDUSAE method, as any other method it is more difficult to extract companions faint and/or close to the host star. Indeed, faint companions are hidden in the speckle noise and hard to spot and for close companions, the radial motion of its surrounding speckle is less important which makes it harder to be disentangled from the speckle noise when using spectral diversity.

Number of spectral channels As expected, increasing the number of images in the multispectral cubes allows to remove the ambiguity between the planetary companions and the surrounding speckles. As a consequence, increasing the number of spectral channels enables to (1) detect fainter planetary companions, (2) estimate their flux more accurately and (3) increase the robustness of the algorithms. In this inverse crime case, incorporating the spectral channels one after the other seemed to be more efficient than using the entire image cube at once.

Distance between the spectral channels The more the spectral channels are distant, the larger the radial motion of the speckles in the images, which makes it easier to disentangle the speckles from the planetary companions. It has been checked that indeed, using distant spectral channels increases the detectability.

Starting point for the upstream phase In order to choose for a good starting point, tests have proven that a random upstream aberration map with a small rms value (way smaller than the real rms value) constituted a good starting point.

Ten different starting points have been tested, using very small rms random aberration maps. As a result, no major impact on the detection capabilities were observed when using these ten different starting points.

Sensitivity to the downstream aberration map given in input If the provided downstream aberration map in input, δ_{down}, perfectly corresponds to the true one, then a large amount of downstream aberrations helps MEDUSAE to converge. Indeed, it constrains the problem and helps disentangling the upstream aberrations contribution to the speckle field. As a consequence less speckle residuals are left in the estimated object map.

Also, if the input downstream aberration map is not accurate (due to its mis-calibration for instance or if it has evolved after the given calibration), it significantly impacts the MEDUSAE's performance. In the framework of the inverse crime, a mis-calibration of 1% does not impact much the MEDUSAE's performance. However, it becomes significant from a 3% error, which makes this input very important for real data application.

Sensitivity to the star flux estimation To follow the reasoning of the previous paragraph, MEDUSAE tries to avoid putting some star signal in the estimated object map. If the star flux is not correctly estimated, it induces the presence of strong residuals in the object map, which are speckles assessed to be part of the object instead of being assessed to be due to δ_{up}. Within the high-contrast images dealt with here, the stellar flux dominates at very close separation (where the aberrations provoke starlight leakages which are not stopped by the coronagraph) and out of the correction zone (where the turbulent residuals are dominant, thus showing a smooth bright halo). Thus the idea is to add a zonal constraint when estimating the object map: we assume that all the light outside of the correction zone and within the very close regions to the star are pure starlight, that is to say no companions can be found in these regions. An annular mask of inner radius $3\lambda/D$ and outer radius $20\lambda/D$ is thus applied to regularize the object map estimation. On the inverse crime, this strategy proved efficient in removing most residual speckles in the final object map and correctly estimate the star spectrum.

Sensitivity to the chosen spatial regularization for the object estimation The regularization used to estimate the object map via a non-myopic MAP deconvolution has a strong impact on both the residual noise in the estimated object and the detection and characterization capabilities. Added to that, the fact that the light not accounted in the object map is accounted in the speckle fields via δ_{up} makes this regularization tuning extremely important. M. Ygouf opted to use a L1L2 regularization (More details about the couple of hyper-parameters chosen can be found in her thesis: Chap.4 Ygouf, 2012).

During the MEDUSAE development, M. Ygouf noticed that a L1 regularization should show better performance since it favors the pixel to pixel independence and thus a sparse object map. However a L1 regularization is no longer differentiable and the VMLM-B descent algorithm does not converge. A specific criterion descent algorithm should be implemented to use a L1 spatial regularization on the object map.

Conclusion: MEDUSAE in its initial status

As a conclusion, the MEDUSAE method has a settled formalism following a solid scheme: a parametric imaging model which is analytically derivable, a criterion to be minimized to invert the problem, a certain number of unknowns with a specific strategy to estimate each of them, including an optimization scheme to minimize the penalizing function. An inversion strategy has been also established to avoid reaching a local minimum during the phase retrieval.

This MEDUSAE concept has been tested on an "inverse crime" data set (the data used are simulated with the model used) which reinforced the inversion scheme. The implemented strategy resulted in the convergence of the algorithm in 90% of the cases. Moreover, in the cases for which the algorithm has not converged, which means some speckles have been estimated as object signals and vice-versa, it is quite obvious when looking at the estimated object map which shows strong speckle residuals. Thus these failing cases can be easily rejected. Moreover, on these simulations, MEDUSAE shows its ability in detecting companions having a contrast of 10^{-6}, located at $0.2''$ from the star. Companions with lower contrast could not be detected, even further from the star.

This MEDUSAE concept validation has been published in Ygouf et al. (2013), and the final strategy chosen to perform the inversion is summarized in Fig. 7.4.

In its current state, three fundamental points have not been approached yet:

1. How to estimate the downstream aberration map δ_{down} and the turbulence residuals structure function $D_{\phi_{res}}$ required as input of MEDUSAE. And how much MEDUSAE is sensitive to the precision on these input.

2. How much the discrepancy between the ideal model of coronagraphic PSF and the real experimental speckle field will affect the ability of MEDUSAE to retrieve the upstream phase and object map.

3. How to extract the object spectrum with this method.

In the following chapters, I will conduct further tests on this inverse crime data set (Chap. 7) before focusing on simulated data using a realistic coronagraphic model (Chap. 8). This work is a step forward necessary to prepare MEDUSAE to real data applications.

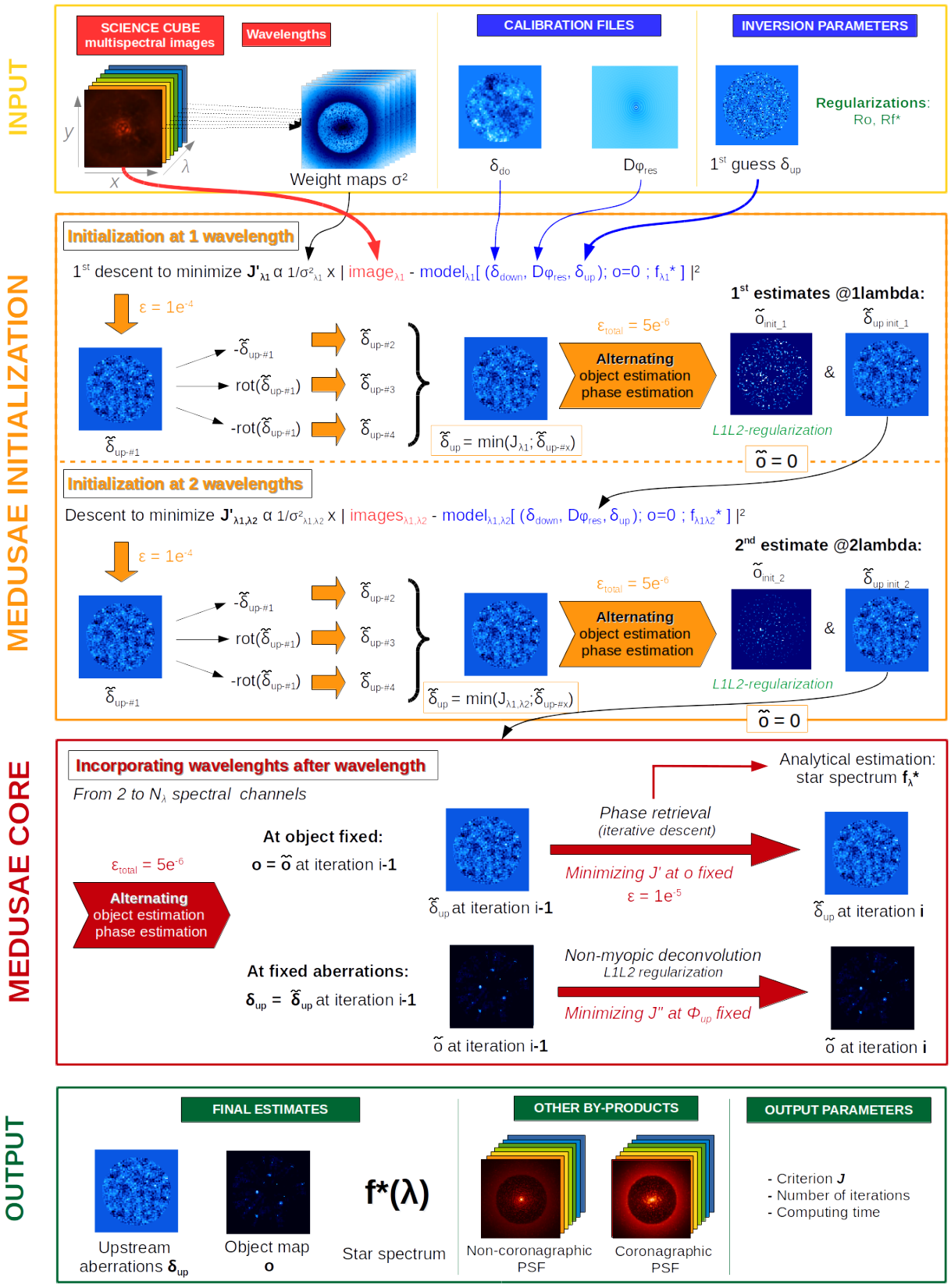

Figure 7.4 – Diagram describing the initial inversion strategy implemented for MEDUSAE, from the input to its output.

Chapter 8

Refining the MEDUSAE strategy on inverse crime

Contents

8.1 Simulated data and analysis criteria 219
8.1.1 Simulated data used for tests 219
8.1.2 Analysis criteria 221
8.2 Inversion scheme: revisiting the strategy 222
8.2.1 Multispectral phase retrieval for a known object 223
8.2.2 Initialization procedure 224
8.2.3 MEDUSAE core 228
8.3 Corruption due to intense planetary signals 230
8.4 Sensitivity to the inputs required by MEDUSAE 231
8.4.1 Error on the downstream aberration map δ_{down} 231
8.4.2 Error on the residual phase structure function $D_{\phi_{res}}$ 234

In order to study the effect of the MEDUSAE parameters one by one, in this chapter I re-use an inverse crime data set to run MEDUSAE. Indeed, to prepare MEDUSAE to its application on real data from SPHERE-IFS, several effects were still to be studied. First of all, I define the simulated data and the metric used throughout the manuscript to analyze the results (Sect. 8.1). Then, I rework on the inversion strategy originally implemented in order to reach the best performance for MEDUSAE while understanding better its behavior (Sect. 8.2). I then check if the whole process can be corrupted by the presence of high intensity signals in the images (Sect. 8.3). In a last section, I investigate the sensitivity to the inputs required by the method: the upstream phase and the turbulent residual phase (Sect. 8.4).

8.1 Simulated data and analysis criteria

In this section, I describe the data used to perform the reconstruction (Sect. 8.1.1) then define the analysis criteria used to assess the MEDUSAE performance throughout this part (Sect. 8.1.2).

8.1.1 Simulated data used for tests

The data used in this section are simulated along the same way as described in Sect. 7.3.1. The Fig. 8.1 shows the aberration maps used to build the coronagraphic images using the model of long exposure ideal coronagraphic PSF defined by Eq. 7.4. The static phases, ϕ_{up} and ϕ_{down}, have a wavefront error of 30nm rms and their power spectra have a f^{-2} trend (f being the spatial frequency). The turbulence residuals structure function has the same properties as described in Sect. 7.3.1. These three terms

are defined at the Shannon wavelength, denoted $\lambda_{Shannon}$, that is to say the wavelength for which the images are Nyquist sampled (here, $\lambda_{Shannon} = 950$ nm).

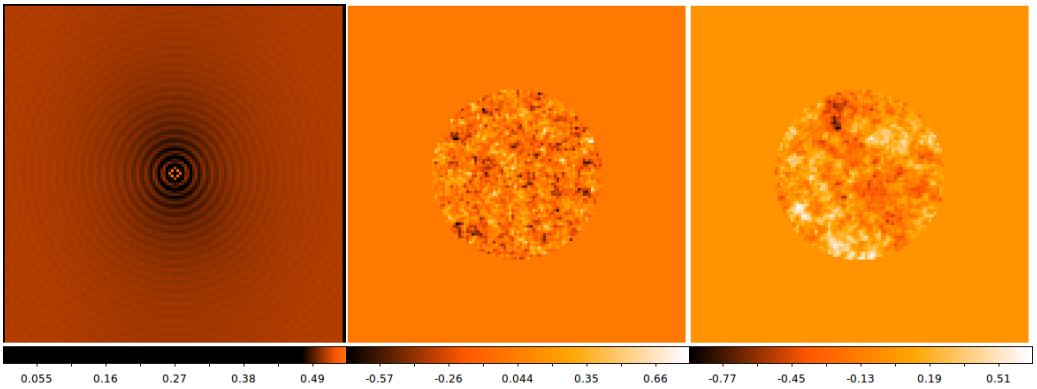

Figure 8.1 – Phase maps used to build the multispectral data cube for the inverse crime. Left: Turbulence residuals phase structure function, $D_{\phi_{res}}$. Middle: Static upstream phase, ϕ_{up} (radians). Right: Static downstream phase, ϕ_{down} (radians). To produce the multispectral cube, these three arrays are zero-padded into bigger arrays whose size are proportional to the wavelength ratio $\lambda_i/\lambda_{Shannon}$.

Five planetary signals have been placed in the object map. Fig. 8.2 shows the location of these 5 planetary signals constituting the object map (Fig. 8.2-Left), as well as the corresponding image at the Shannon/shortest wavelength (Fig. 8.2-Right) obtained by the convolution of the object map with the non-coronagraphic PSF (Fig. 8.2-Middle). The characteristics of the five planetary signals are gathered in Tab. 8.1.

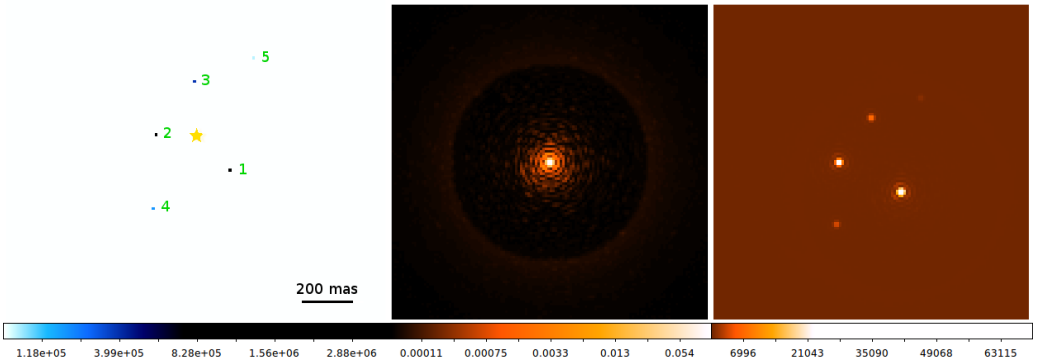

Figure 8.2 – Objects to be estimated. Left: Object map (five Dirac peaks whose characteristics are gathered in Tab. 8.1). Middle: Non-coronagraphic PSF obtained analytically by using the aberrations at Fig. 8.1 (at $\lambda_{Shannon}$). Right: Object map convolved by the non-coronagraphic PSF (at $\lambda_{Shannon}$).

Planet index	Contrast	Separation	Position angle
1	1.10^{-5}	207.8 mas	135°
2	5.10^{-6}	159.3 mas	270°
3	1.10^{-6}	220.5 mas	0°
4	5.10^{-7}	351.0mas	225°
5	1.10^{-7}	401.8 mas	45°

Table 8.1 – Characteristics of the five planetary companions injected in the simulated images to perform the inverse crime.

Finally, the Fig. 8.3 shows the first (at 950 nm) and last image (at 1647 nm) of the six images constituting the resulting multispectral cube.

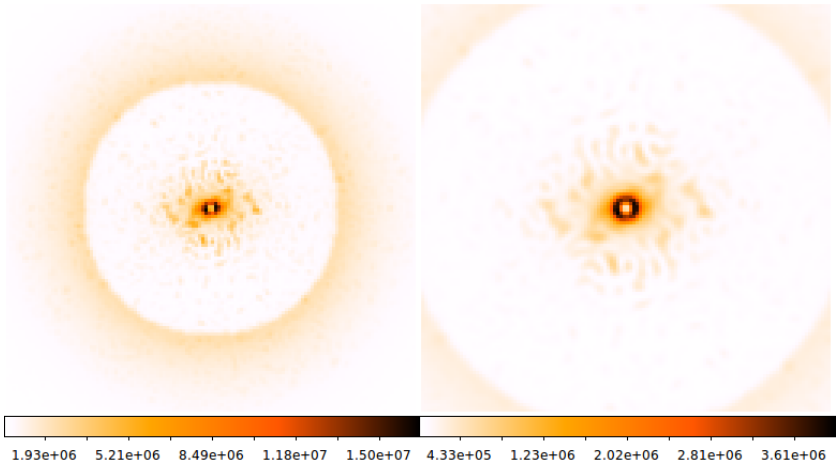

Figure 8.3 – Two images of the multispectral cube. Left: First channel at 950nm (Nyquist sampled). Right: Sixth channel at 1647nm. Colors are inverted.

8.1.2 Analysis criteria

In this section, I define the criteria I will use throughout the following chapters to assess the quality of the estimations. I will focus on four aspects of the MEDUSAE capabilities: the total inversion "efficiency", the planetary signal extraction, the star spectrum estimation and the phase map retrieval. In total, 10 quantitative criteria are used.

In the following, I use the notation $\mathcal{I}(x)$ to describe the image built using x. For instance, $\mathcal{I}_\lambda(\hat{o})$ is the image of the estimated object, obtained by convolving the estimated object with the estimated non-coronagraphic PSF at a wavelength λ (itself being dependent upon the estimated phase $\hat{\phi_{up}}$ and the estimated star flux $\hat{f}^*$).

General inversion efficiency: Four criteria are checked to assess the overall performance of the inversion led by MEDUSAE:

1. **Final criterion**[1]**:** $J_{data} = \sum_\lambda \sum_\alpha \frac{1}{2\sigma_n^2(\lambda,\alpha)} |i(\lambda) - [f^*(\lambda) \times h^c|_{\hat{\delta}_{up}}(\lambda,\alpha) + \hat{o}(\lambda,\alpha) * h^{nc}|_{\hat{\delta}_{up}}(\lambda,\alpha)]|^2$;

2. **Image reconstruction**[2]**:** For each wavelength, the relative mean square error between the estimated image, defined as $\hat{i}_\lambda = \mathcal{I}_\lambda(\hat{\delta}_{up}, \hat{f}^*) + \mathcal{I}_\lambda(\hat{o})$, and the true image i_λ:

$$\text{rMSE}_\text{i} = \frac{\sqrt{\sum_\mathbf{r} [i_\lambda(\mathbf{r}) - \hat{i}_\lambda(\mathbf{r})]^2}}{\sqrt{\sum_\mathbf{r} i_\lambda^2(\mathbf{r})}} \times 100 \tag{8.1}$$

3. **Image reconstruction in the corrected zone:** The exact same metric but only within the correction zone (between a radius from $3\lambda/D$ to $20\lambda/D$), denoted rMSE_corr;

4. **Computing time:** The total computing time to run the MEDUSAE algorithm on the multispectral cube.

Estimated star spectrum $\hat{f}^*_\lambda$: For each wavelength, the relative disparity between the estimated star flux, $\hat{f}^*_\lambda$, and the true star flux, f^*_λ, is computed:

$$\mathscr{M}_{f^*} = \frac{|\hat{f}^*_\lambda - f^*_\lambda|}{f^*_\lambda} \times 100 \tag{8.2}$$

[1] i.e., without taking into account the regularization terms.

[2] Note that this is almost the same information than J_{data} but it is possible to have this information for each wavelength independently.

Estimated object map $\hat{o}_\lambda$: Three criteria are checked to assess the performance in terms of object map estimation:

1. **Companion detection**: The number of companion detected in the estimated object map wrt the true one and if it is easy to disentangle them from the residuals (at least visually);
2. **Companion flux accuracy, $\mathscr{M}_{fp}$**: For each wavelength and each planet visually detected, the relative disparity between the estimated flux of the planets $\hat{f}^p_\lambda$ wrt the true one, f^p_λ:

$$\mathscr{M}_{fp} = \frac{|\hat{f}^p_\lambda - f^p_\lambda|}{f^p_\lambda} \times 100 \tag{8.3}$$

   However, in this version of MEDUSAE, the object is assumed to have a gray spectrum so this value is estimated on average for all wavelengths. Note that the flux is integrated over the whole planetary signal in the object map (whose shape depends on the applied spatial regularization);
3. **Residuals in the object map, f^o_{res}**: The residuals in the object map are assessed by removing the planetary signals and integrating the remaining flux, f^o_{res}.

Estimated upstream aberration map $\hat{\delta}_{up}$: Three criteria are checked to assess the performance of the phase retrieval performed by MEDUSAE:

1. **Estimated speckle field accuracy, rMSE_{SF}:** For each wavelength, the relative mean squared error between the estimated speckle field $\mathcal{I}_\lambda(\hat{\delta}_{up}, \hat{f}^*)$ and the true one $\mathcal{I}_\lambda(\delta_{up}, f^*)$:

$$\mathrm{rMSE_{SF}} = \frac{\sqrt{\sum_{\mathbf{r}}[(\mathcal{I}_\lambda(\delta_{up}, f^*))(\mathbf{r}) - (\mathcal{I}_\lambda(\hat{\delta}_{up}, \hat{f}^*))(\mathbf{r})]^2}}{\sqrt{\sum_{\mathbf{r}}[(\mathcal{I}_\lambda(\delta_{up}, f^*))(\mathbf{r})]^2}} \times 100 \tag{8.4}$$

2. **Residuals level between the true phase map and the estimated one, Φ^{up}_{res}:** The absolute rms value of the residuals between the estimated phase map at the Shannon wavelength (0.95μm), $\hat{\Phi}_{up}$, and the true phase map Φ_{up} (in radians);
3. **Estimated phase accuracy, rMSE_Φ:** The relative mean squared error between the estimated phase map $\hat{\Phi}_{up}$ and the true one Φ_{up} (both defined at the Shannon wavelength):

$$\mathrm{rMSE}_\Phi = \frac{\sqrt{\sum_{\mathbf{r}}[\Phi_{up}(\mathbf{r}) - \hat{\Phi}_{up}(\mathbf{r})]^2}}{\sqrt{\sum_{\mathbf{r}} \Phi_{up}(\mathbf{r})^2}} \times 100 \tag{8.5}$$

According to their definition, we want each of these ten criteria to be the smallest as possible (but the number of detections over the number of injected companions). Throughout this chapter, I will present several images to show the performance obtained with MEDUSAE: (1) the residual phase maps, $\Phi_{up} - \hat{\Phi}_{up}$ (defined at the Shannon wavelength), (2) the estimated object map $\hat{o}$, (3) the residual speckle field $\mathcal{I}(\delta_{up}, \hat{f}^*) - \mathcal{I}(\hat{\delta}_{up})$ and (4) the residual images $i_{input} - [\mathcal{I}(\hat{\delta}_{up}, \hat{f}^*) + \mathcal{I}(\hat{o})]$, where i_{input} is the original image cube.

8.2 Inversion scheme: revisiting the strategy

The goal of this section is to revisit the MEDUSAE method on this inverse crime data-set in order to (1) refine the strategy implemented to run MEDUSAE, (2) reduce the computing time (two hours in the original case) and (3) increase the MEDUSAE performance.

To introduce the complexity of the phase retrieval, I first present a simple multispectral retrieval on images without planetary companions. I then focus on the initialization stage described in Sect. 7.1.5 before revisiting the main inversion procedure (called *MEDUSAE core*).

8.2.1 Multispectral phase retrieval for a known object

Before investigating in details the initialization procedure, I first tested the multispectral phase retrieval alone which is the most difficult part of MEDUSAE since the phase retrieval does not show a convex criterion. I ran it on the multispectral cube (six different wavelengths) in which I removed the planet images (Fig. 8.2-Right). Given that one of the critical point in the phase retrieval process is the choice of the starting point, in this section, I chose to run the phase retrieval at known object for four different starting points of the upstream aberration map:

(i) a null aberration map;

(ii) an extremely small aberration map of 1pm *rms*;

(iii) a very small aberration map of 1nm *rms*;

(iv) a random aberration map whose *rms* value is close to the real one, that is to say 30 nm *rms* with these data.

These aberration maps are created from a random, white and normal distribution, using the same seed. To compare the results, I will also run the phase retrieval in the case (o) which uses the real upstream aberration map as an input. In the latter case, the phase retrieval is only limited by the noise in the images (in these data, only the photon noise is taken into account).

The results presented in this section are by setting a convergence threshold at $\epsilon = 10^{-5}$ and imposing a limit number of iterations, $N_{iter}^{max} = 10,000$ for the phase retrieval descent. Tab. 8.2 gathers the main results from the phase retrieval as a function of the starting point set.

Starting point	**Processing time [min]**	**Criterion J_{data}**	rMSE$_\Phi$	rMSE$_{SF}$
(o) true phase	2	47,275	0.41%	0.014%
(i) null	64	18,396,630	59.23%	2.16%
(ii) 1pm *rms*	62	18,149,204	58.18%	2.16%
(iii) 1nm *rms*	45	20,568,052	62.28%	2.22%
(iv) 30nm *rms*	32	17,565,530	62.73%	1.59%

Table 8.2 – Processing time, value of the criterion J_{data} and mean squared error on the phase map Φ_{up} and of the corresponding speckle fields (SF), averaged on the 6 λ, obtained after the phase retrieval performed on the images on which the image of the planets has been fully removed. Note that the minimum value of the criterion is $J_{data} = 48,996$ for these simulated data which means that some noise is fitted by the phase retrieval in the case (o).

The Fig. 8.4 shows the residuals between the real upstream aberration map and the estimated ones as a function of the starting point. The residuals show a typical *rms* of 0.12 nm, whatever the starting point, but the case (o) which shows a very small *rms* value (less than 0.001 rad).

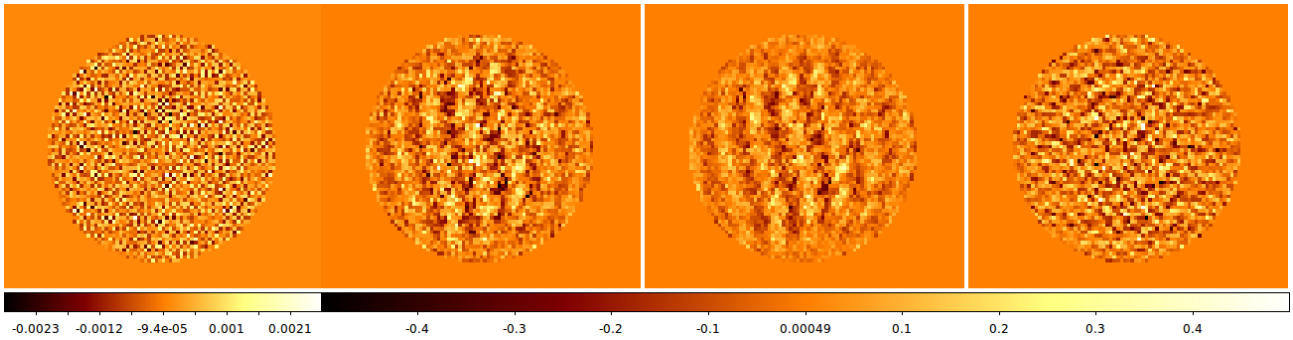

Figure 8.4 – Subtraction of the true aberration map and the estimated one as a function of the starting point. Left: Case (o) with the true upstream aberration map as a first guess. Middle-Left: Case (i) with a null aberration map. Middle-Right: Case (ii) with a random aberration map of 1pm *rms* Right: Case (iv) with a random aberration map of 30nm *rms*. Note that I do not show the case (iii) which leads to similar residuals to the case (ii).

The Fig. 8.5 shows the residuals between the real speckle field input in the phase retrieval procedure and the estimated one as a function of the starting point. Fig. 8.5-Left, showing the case (o), using the

true phase as a starting point, shows very low level residuals with specific elongated features. These features are probably due to the achromatic hypothesis used in the MEDUSAE phase retrieval, which states that one single aberration map can represent the speckle field at every wavelength. The residual noise in each image (here only the photon noise) being different, it can be partly fitted by the phase and not properly taken into account at each wavelength.

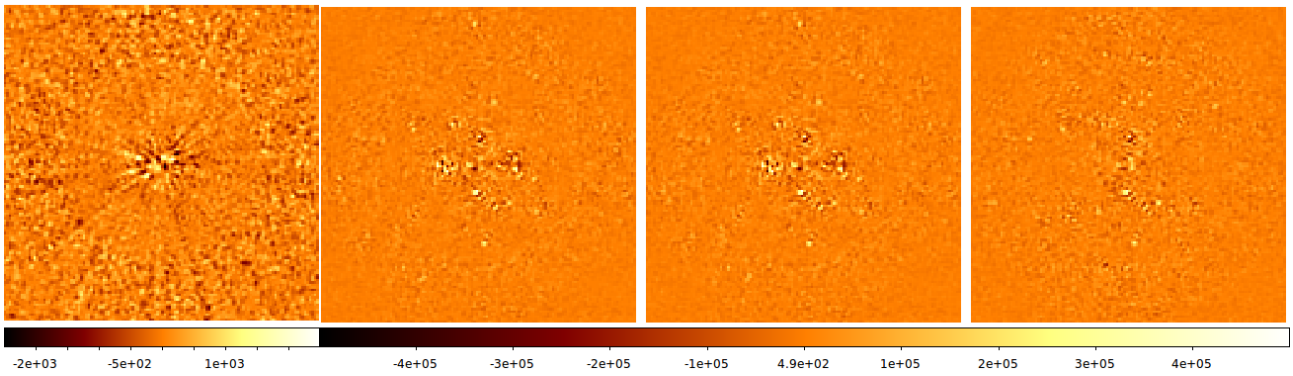

Figure 8.5 – Subtraction of the true speckle field and the estimated one at the shortest wavelength (Nyquist sampled), as a function of the starting point. Left: Case (o) with the true upstream aberration map as a first guess. Middle-Left: Case (i) with a null aberration map. Middle-Right: Case (ii) with a random aberration map of 1pm *rms* Right: Case (iv) with a random aberration map of 30nm *rms*. Note that I do not show the case (iii) which leads to similar residuals to the case (ii). The images are given in ADU units.

The Tab. 8.3 gives the average contrast achievable within the AO correction zone, as a function of the case.

Starting point	(o) true phase	(i) null	(ii) 1pm *rms*	(iii) 1nm *rms*	(iv) 30nm *rms*
Reachable contrast	9.23^{-6}	83.2^{-3}	1.9^{-3}	2.2^{-3}	1.9^{-3}

Table 8.3 – Average achievable contrast in the AO corrected zone (below $20\lambda/D$) and outside of the zone where the coronagraph has a chromatic behavior (above $3\lambda/D$).

In any of these cases, the estimated aberration map is quite different from the true one. The corresponding speckle field is not accurate enough to perform signal extraction below a 10^{-3} contrast in the correction zone. Moreover, on cases (i), (ii) and (iii), ripples can be observed in the aberration maps (Fig. 8.4-Middle), which correspond to the peculiar structure that can be observed around $3\lambda/D$ in the corresponding speckle fields (Fig. 8.5-Middle).

As a conclusion, the multispectral phase retrieval applied directly on the image cube at six wavelengths does not succeed in estimating a correct phase map in order to reach the required contrast. As previously found by M. Ygouf during her PhD, it is necessary to establish an initialization procedure to converge toward the true upstream phase. The established strategy, described in Sect. 7.1.5, is to (1) incorporate the wavelengths one by one and starting with a phase retrieval at one wavelength and (2) exploring the four equivalent phases each time a new wavelength is incorporated Ygouf et al. (2013). In the code, the object and phase are alternately estimated during the initialization procedure, contrary to what is written in the publication. In the following, I thus revisit the main steps of this initialization procedure in order to check if it is possible to increase the performance of the method, reduce the computing time and if each step is truly necessary.

8.2.2 Initialization procedure

The initialization procedure has been established in order to avoid reaching a local minimum during the phase retrieval. This initialization procedure contains three aspects: (1) the inversion is ran at one then two wavelengths, with the alternate object-phase estimation, (2) for each new incorporated wavelength, the four equivalent phase maps are explored and (3) before running the inversion with a new wavelength, the object map is reset to zero. During this initialization step, the object is

estimated with a support constraint but with a L2 under-regularization (so almost without spatial regularization). The goal of this section is first of all to check if this initialization is indeed useful and to revisit this initialization procedure in order to decrease the processing time and increase the overall performance.

In this section, I will provide the results according to the criteria defined at Sect. 8.1.2. Given that the goal of the initialization procedure is to have a first estimate of the upstream aberration map, δ_{up}, before starting the main MEDUSAE descent (called MEDUASE core), I will focus on the criteria to assess the performance of the speckle field retrieval: $\mathcal{M}_{f^*}$ (Eq. 8.2), Φ^{up}_{res} (in rad rms), rMSE$_\Phi$ (Eq. 8.5) and rMSE$_{SF}$ (Eq. 8.4).

8.2.2.1 The four equivalent phase maps

At each first iteration, after incorporating a new spectral channel, the four quasi-equivalent phase maps are explored (see Sect. 7.1.5). This short section aims at checking if this step is necessary and leads to better performance. Note that although I discuss here this aspect, this stage was also present in the MEDUSAE core in the original version of the algorithm.

Fig. 8.6 shows the four equivalent residual phase maps obtained from a random first guess of ϕ^{guess}_{up}, generated with a certain seed. For the first wavelength, the first estimated phase maps, $\phi_1 \equiv \hat{\phi}_{up}$ is clearly the one showing less residuals. At two wavelengths, this is even more obvious.

Tab. 8.4 presents the rms of the residuals and the mean standard deviation for each of these 8 phase maps. The first phase map, $\phi_1 \equiv \hat{\phi}_{up}$ is the only one which has a different rms residuals value and rMSE$_\phi$ from one to two wavelengths. All the other equivalent phase maps show the same characteristics.

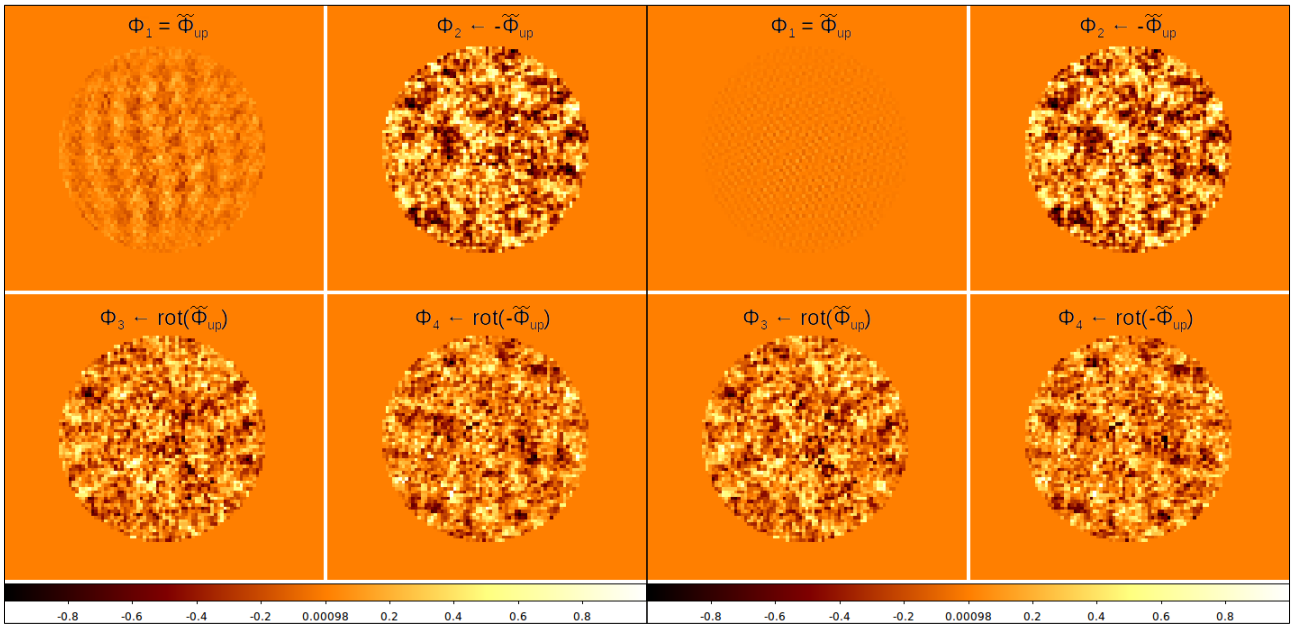

Figure 8.6 – Residual upstream phase maps, $\phi_{up} - \hat{\phi}_{up}$, for the four equivalent phase maps. Left: From the first initialization stage at one wavelength. Right: From the second initialization stage at two wavelengths.

Initialization stage	*At one wavelength*		*At two wavelengths*	
Aberration map	ϕ^{up}_{res} [rad]	rMSE$_\Phi$	ϕ^{up}_{res} [rad]	rMSE$_\Phi$
$\phi_1 \equiv \phi_{up}$	0.092	47.04%	0.028	14.59%
$\phi_2 \leftarrow -\phi_{up}$	0.362	185.91%	0.368	189.38%
$\phi_3 \leftarrow rot(\phi_{up})$	0.279	143.05%	0.280	145.21%
$\phi_4 \leftarrow rot(-\phi_{up})$	0.280	143.85%	0.280	143.79%

Table 8.4 – Characteristics of the four equivalent phase maps obtained at one then two wavelengths.

I performed this test for several starting points (using ten different seeds) and it led to similar results: once the first phase map estimate is found (thanks to the phase retrieval at one wavelength), it is useless to explore the four equivalent phase maps at two or more wavelengths.

As a conclusion, at the very first iteration of the phase retrieval at one wavelength, this exploration might be useful. However it turns out that the first phase map estimated is usually the correct starting point. In any case, at more than one wavelength, once this first guess has been found, it turned out that there is no point in exploring the four equivalent phase maps since the first one is still the correct one as it derived from the previous step.

8.2.2.2 Alternated estimation of the object and the aberration map

As this initialization stage is meant to obtain a first aberration map before starting the main inversion procedure, one first idea is to avoid estimating the object during this initialization procedure. Avoiding to alternately estimate the object *and* the aberration map would result in a critical gain of computing time.

After running several tests, I can conclude that the first aberration map estimated (only by phase retrieval and not by alternating the phase retrieval with the object deconvolution) is not accurate enough to be input in the MEDUSAE inversion core. Alternatively estimating the object and the speckle field in the initialization procedure is critical to run MEDUSAE correctly.

My interpretation of why estimating the object is critical is that, it enables to relax the phase retrieval procedure. Indeed, converging towards the correct aberration map is really constraining whereas if one let some light going in a *dummy* image (as the object map here), it is easier to reach the aberration map responsible for the main features of the speckle field in the image plane. This trick enables to avoid taking into account tiny residuals in the speckle field that are not due to the upstream aberration map (but potentially from the noise) and cannot be fitted by the latter.

8.2.2.3 Object spatial regularization during the initialization

According to the previous paragraph, the object must be estimated during the initialization procedure as it relaxes the phase retrieval. During the object deconvolution, the spatial regularization applied on the object estimation should account for the residual noise in the speckle field which cannot be fitted via the aberration map. Also, with this new interpretation, the zonal constraint applied on the object estimation should be removed to obtain an even better phase estimation (so that light in the inner and outer regions that cannot be fitted at first by the aberration map can be in the object map during the initialization procedure). However, removing this zonal constraint might affect the star flux estimation as it had been implemented to better constrain the latter. The definition of the regularization and their corresponding hyper-parameters can be found in Sect. 1.3.1.5.

Tab. 8.5 shows the main results on the phase map estimation for various spatial regularization applied:

(i) a L1L2 regularization tending toward a L1-regularization ($\delta = 0.001; scale = 3$);

(ii) a L1L2 regularization using ($\delta = 0.05; scale = 3$) as in the original version of the MEDUSAE core;

(iii) a L2-regularization with a classical regularization;

(iv) a under-regularized L2-regularization ($PSD = 10^{20}$, so it is equivalent to no regularization).

Version	Time [min]	Criterion J_{data}	$\mathcal{M}_{f^*}$	ϕ^{up}_{res} [rad]	rMSE$_\delta$	rMSE$_{SF}$
(i) L1L2 L1-regularized	24	$271,950$	0.069%	0.028	14.60%	0.24%
(ii) L1L2 basic-regularization	19	$2,130,251$	0.292%	0.07	33.4%	1.94%
(iii) L2 basic-regularization	15	2^{10}	0.39%	0.09	47.89%	2.93%
(iv) L2 under-regularized	27	$268,213$	0.063%	0.03	14.61%	0.25%
(iv) without zonal constraint	65	$12,940$	0.33%	10^{-3}	2.18%	0.053%

Table 8.5 – Results obtained at the initialization procedure for various regularizations on the object.

Tests showed that the phase estimation is excellent when removing the zonal constraint (see Tab. 8.5) while the star spectrum is slightly less correctly estimated. However, the star spectrum will be constrained during the inversion core following the initialization. Thus, removing the zonal constraint during this initialization step leads to better performance in the framework of the initialization procedure. This procedure is however three times longer than the original version but it is worth since the phase retrieval is the most critical point of MEDUSAE.

This procedure has been tested with ten different random aberration maps as a starting point, leading to the same results.

8.2.2.4 Wavelengths used for the initialization

In order to decrease the computing time, another idea is to estimate the first aberration map directly at two wavelengths or only with one wavelength. Yet, results show that it is necessary to run the initialization procedure with one wavelength first and not directly with two wavelengths, otherwise the aberration map is not correct enough which makes the MEDUSAE core diverge. Performing twice the initialization, with one then two wavelengths, leads to better results and only takes a few more minutes. It is thus worth performing the initialization procedure with these two stages.

Because the object is not regularized, the first stage (at one wavelength) is stopped not by the convergence rule given by $\epsilon = 10^{-4}$ but by the maximum number of iteration N_{iter} imposed (for the phase-object alternate estimations). The latter is set to 1000 during the initialization procedure. In order to gain some computing time, this maximum number of iteration can be reduced (note that I also tried to input a PSD estimated directly from the images, to L2-regularize the object estimation but the gain in time and the performance were not worth to implement this method). In Tab. 8.6, I also put the results obtained when performing the initialization at one then two wavelengths but setting $N_{iter} = 500$ and for $N_{iter} = 100$ the first stage. The gain in time is of respectively 10% and 46% and the performances are the same (slightly lower for the flux star estimation). The main point is the second stage, at two wavelengths, which reaches convergence after 80 iterations.

The Tab. 8.6 shows the results for the three schemes proposed: (i) with one then two wavelength (as in the original version), (ii) with only one wavelength, (iii) with directly two wavelengths (choosing the most distant spectral channels). The results are obtained by imposing neither zonal constraint nor spatial regularization on the object.

Version	Time [min]	Criterion J_{data}	$\mathcal{M}_{f^*}$	ϕ_{res}^{up} [rad]	rMSE_{Φ}	rMSE_{SF}
(i) One then two wavelengths	65	$12,940$	0.33%	10^{-3}	2.18%	0.053%
(ii) One wavelength	48	$3,687$	3.58%	10^{-2}	5.01%	1.02%
(iii) Directly two wavelengths	42	$3,416,904$	3.43%	9.0	39.96%	2.39%
(i) with $N_{iter} = 500$	58	$12,938$	0.38%	10^{-3}	2.18%	0.053%
(i) with $N_{iter} = 100$	30	$12,938$	0.44%	10^{-3}	2.18%	0.053%

Table 8.6 – Results obtained at the initialization procedure for various regularizations on the object.

Note that at two wavelengths, the criterion J_{data} is not the same as at only one wavelength so the two values are not directly comparable. I still show these values in Tab. 8.6 to give an order of magnitude.

8.2.2.5 Summary of the new initialization procedure

First of all, the initialization procedure is a necessary step, otherwise the whole MEDUSAE procedure does not reach the convergence. Here are the main points about this initialization procedure:

- The object must be estimated in the initialization in order to relax the phase retrieval and to avoid biasing it if an object is really bright;

- The object must not be regularized (neither zonal constraint nor spatial regularization) in order to be mainly used to relax the phase retrieval[3];
- The initialization must be performed twice, at one *then* two wavelengths to reach a correct first estimate of the aberration map before the MEDUSAE core;
- During the first stage of this initialization procedure, the stopping rule is given by the maximum number of iterations (of the alternation phase-object) which can be tuned at the user's convenience;
- The four equivalent aberration maps do not need to be explored at each incorporated wavelength but only during the first iteration of the first stage (at one wavelength) of the initialization procedure.

This whole procedure provides the results gathered at Tab. 8.7, to be compared to the results obtained with the former version of MEDUSAE.

Version	Time [min]	Criterion J_{data}	$\mathcal{M}_{f^*}$	ϕ_{res}^{up} [rad]	rMSE$_\Phi$	rMSE$_{SF}$
New initialization:	65	$12,940$	0.33%	10^{-3}	2.18%	0.053%
Old initialization:	35	$268,213.43$	0.063%	0.03	14.61%	0.46

Table 8.7 – Results obtained at the end of the initialization procedure (along the criteria presented at Sect. 8.1.2) for the former and the new version of MEDUASE.

8.2.3 MEDUSAE core

First the inversion at two wavelengths was repeated twice: the first time during the initialization process and the second time during the inversion core. In order to gain some computing time, I removed the stage at two wavelengths in the MEDUSAE core. Also, to go further, instead of incorporating the wavelengths one by one, I tried to launch the inversion core directly on the whole multispectral cube.

Tab. 8.8 present the results obtained following the three different strategies, compared to the original version strategy of MEDUSAE:

(i) with directly the whole multispectral cube;

(ii) by incorporating the wavelengths one by one, starting from two wavelengths;

(iii) by incorporating the wavelengths one by one, starting from three wavelengths.

Version	Total time	Criterion J_{data}	$\mathcal{M}_{f^*}$	rMSE$_\delta$	rMSE$_i$	rMSE$_{corr}$
Old version:	1h52	$617,248$	0.058%	14.95%	0.4477%	0.3508%
New version (i):	1h14	$98,470$	0.33%	2.14%	0.144%	0.190%
New version (ii):	1h26	$94,951$	0.33%	2.14%	0.077%	0.096%
New version (iii):	1h24	$97,934$	0.33%	2.14%	0.146%	0.195%

Table 8.8 – Results obtained at the end of the whole MEDUSAE procedure (using the six wavelengths), along the criteria presented at Sect. 8.1.2, for the former and the new version of MEDUASE.

From these results, it seems that the method (ii) which was the original method implemented to run MEDUSAE, is the most powerful (according to the criteria described in Sect. 8.1.2) to obtain less residuals in the object map and thus a better subtraction of the speckles in the corrected zone. This methods runs in $\sim 20\%$ more time than when using the whole multispectral cube.

Tab. 8.9 gathers the estimated flux of the planetary companions, according to the different scheme for the MEDUSAE core procedure. No direct conclusion can be deduced from these results, however the lower residuals in the object map is given by the case (ii), which reinforces the previous conclusion.

[3]It is thus exactly the same procedure, for each wavelengths set, as in the MEDUSAE core but (1) without object regularization (neither spatial nor zonal constraint) and (2) by reseting the object before incorporating a new wavelength.

Companion index	#1	#2	#3	#4	#5	Residual flux, f^o_{res}
Old version:	9.06%	20.43%	52.66%	43.80%	99.99%	15, 122
New version (i):	7.50%	25.44%	33.81%	56.68%	99.99%	3, 041
New version (ii):	6.66%	23.84%	33.98%	54.29%	99.99%	1, 899
New version (iii):	8.04%	28.50%	35.83%	52.30%	99.99%	2, 302

Table 8.9 – Estimated flux of the 5 injected companions, as a function of the MEDUSAE core procedure chosen.

8.2.3.1 MEDUSAE core: Object regularization

Within the chosen scheme, an important aspect is to correctly regularize the object deconvolution. I compared different generic spatial regularization[4], while keeping the zonal constraint, in order to have an idea of which regularization could be the most suited to this problem. The regularization hyper-parameters are defined in Sect. 1.3.1.5.

Tab. 8.10 and Tab. 8.11 present the results obtained following the three different regularizations, compared to the original version of MEDUSAE, case (o), including the new initialization procedure:

(o) with a L1L2 regularization using the couple $(\delta = 0.05; scale = 3)$;
(i) with a L1L2 regularization using the couple $(\delta = 0.001; scale = 3)$;
(ii) with a quasi-L1 regularization using the couple $(\delta = 0.001; scale = 1)$;
(iii) using a L2 regularization, under-regularized as during the initialization stages.

Version	Total time	Criterion J_{data}	$\mathcal{M}_{f^*}$	rMSE_δ	rMSE_i	rMSE_{corr}
L1L2 regularization (o):	1h26	94, 951	0.33%	2.14%	0.077%	0.096%
L1L2 regularization (i):	1h14	48, 067	0.33%	2.14%	0.075%	0.084%
L1 regularization (ii):	1h25	51, 004	0.33%	2.14%	0.075%	0.085%
L2 under-regularized (iii):	1h28	46, 616	0.33%	2.14%	0.075%	0.083%

Table 8.10 – Results obtained at the end of the whole MEDUSAE procedure (along the criteria presented at Sect. 8.1.2) for the former and the new version of MEDUASE.

Companion index	#1	#2	#3	#4	#5	Residual flux, f^o_{res}
L1L2 regularization (o):	6.66%	23.84%	33.98%	54.29%	99.99%	1, 899
L1L2 regularization (i):	0.62%	0.44%	5.83%	5.52%	58.2%	499, 102
L1 regularization (ii):	0.85%	0.20%	4.95%	2.19%	64.37%	248, 842
L2 under-regularized (iii):	2.07%	3.35%	6.14%	7.01%	50.9%	694, 708

Table 8.11 – Estimated flux of the 5 injected companions, as a function of the spatial regularization used in the non-myopic deconvolution.

From these results, a L1L2 "almost L1" regularization seems to be the most convenient scheme in terms of planet flux estimation while not presenting too much residual flux in the estimated object map. Note that without any planets, the residuals in the object map are lower when imposing a L1L2 spatial regularization on the object estimation. Also, the object regularization hardly affects the estimated speckle field.

Conclusion on the new MEDUSAE procedure

The new strategy established to run MEDUSAE on multispectral cube is not fundamentally different from the original one but the interpretation of the initialization procedure is different and the new version is critical to obtain excellent results on this inverse crime data set.

Fig. 8.7 shows the results from the new inversion procedure compared to the previous one presented in the previous chapter.

Now that this strategy of MEDUSAE is implemented, the next sections aim to check the sensitivity to the input parameters and to intense planetary signals in order to prepare the application of

[4] A neat comparison of the different spatial regularization to be applied can be found in Ygouf (2012), chap. 5.

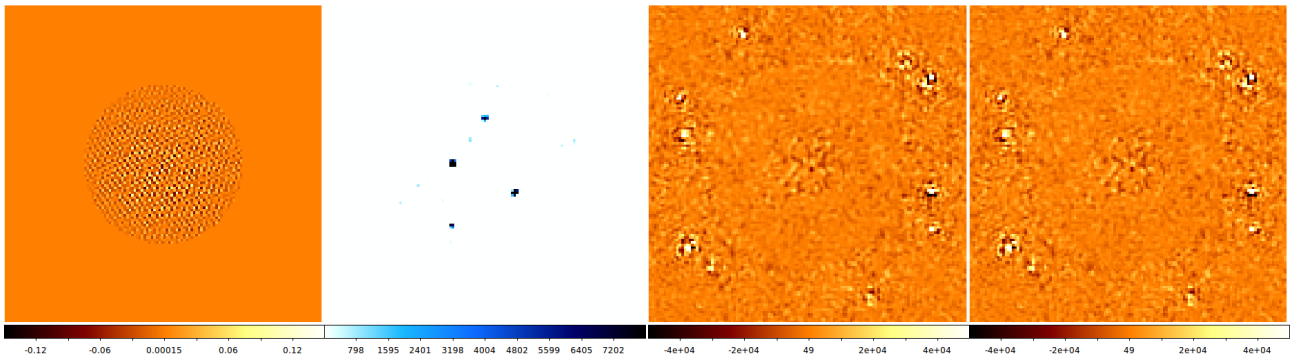

(a) : Old inversion procedure described at Sect. 7.3.1.

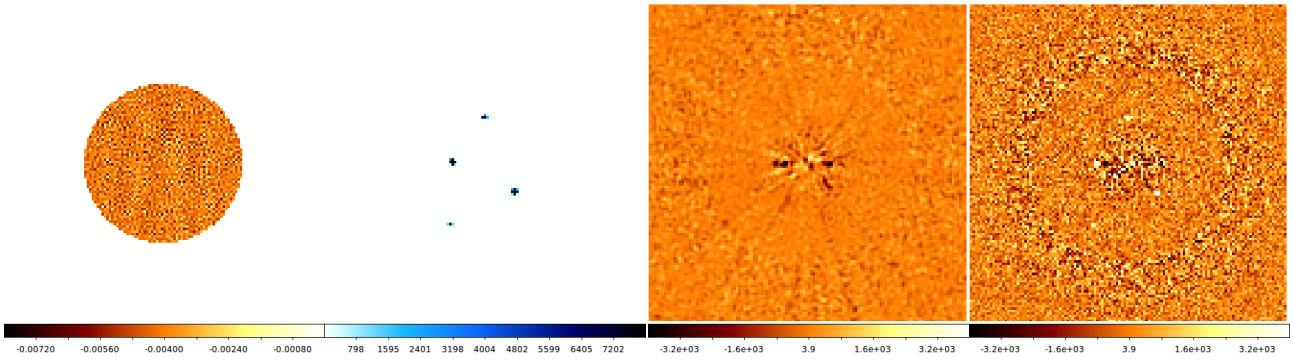

(b) : New inversion procedure described in this section.

Figure 8.7 – Results obtained by running MEDUSAE on the inverse crime data, for the two different inversion procedure. From left to right: residual aberration map, estimated object map (inverted colors), residual speckle field and residual image. The scale is linear but the bounds different for every image.

MEDUSAE on real data. Indeed, the performance obtained above are the best we can reach with MEDUSAE and it is important to be aware of how much we can deviate from the results thanks to this inverse crime problem.

8.3 Corruption due to intense planetary signals

This section aims to check that the strategy implemented to run MEDUSAE is not corrupted when high intensity planetary signals are present in the image field. I thus used the same data set but with two of the five injected planetary companions having a smaller contrast (companions #2 and #4), as gathered in Tab. 8.12.

Planet index	Contrast	Separation	Position angle
6	4.10^{-4}	401.8 mas	45°
7	3.10^{-4}	159.3 mas	135°
8	1.10^{-4}	207.8 mas	225°
9	1.10^{-6}	220.5 mas	0°
10	1.10^{-7}	351.0 mas	270°

Table 8.12 – Characteristics of the four planetary companions injected in the simulated images. See Fig. 8.3-Left for the location of these five companions.

The Tab. 8.13 and Tab. 8.14 gather the results obtained for this second set of images compared to the previous data set used.

Fig. 8.8 shows the residual images obtained by running MEDUSAE on this data set.

As expected, the flux of the brightest companions are better estimated. However, the process is significantly longer with bright companions in the field (twice longer) and the estimations of the speckle field are less accurate than for the data set constituted of fainter companions. Thus, bright

Data set	Total time	Criterion J_{data}	$\mathcal{M}_{f^*}$	rMSE_δ	rMSE_i	rMSE_{corr}
Data w. bright companions (Tab. 8.12):	2h44	221,763	0.40%	2.14%	0.086%	0.13%
Previous data set (Tab. 8.1):	1h25	51,004	0.33%	2.14%	0.075%	0.085%

Table 8.13 – Results obtained at the end of the whole MEDUSAE procedure (along the criteria presented at Sect. 8.1.2) for the images with and without bright planetary companions.

Data set	**Companions index**					**Residual flux,** f^o_{res}
	#6	**#7**	**#8**	**#9**	**#10**	
New data set (Tab. 8.12):	0.03%	0.63%	3.60%	6.36%	10.4%	283,875
	#1	**#2**	**#3**	**#4**	**#5**	
Previous data set (Tab. 8.1):	0.20%	0.85%	4.95%	2.19%	64.37%	248,842

Table 8.14 – Estimated flux of the 5 injected companions, for the two different data sets, with and without bright planetary companions.

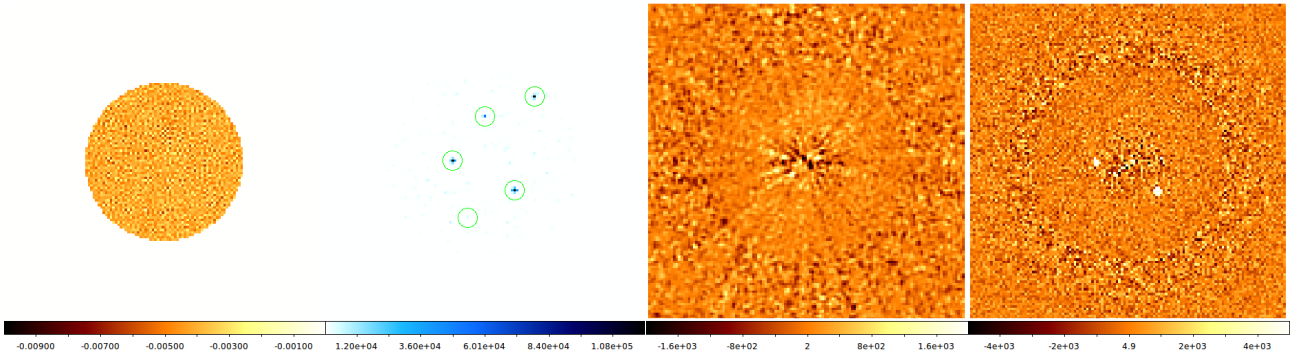

Figure 8.8 – Results obtained by running MEDUSAE on the inverse crime data with five bright planetary signals described in Tab. 8.12. From left to right: residual aberration map, estimated object map (inverted colors), residual speckle field and residual image. The scale is linear but the bounds different for every image.

companions in the field of view indeed impacts the MEDUSAE process, even using the new strategy established. However, we will see in the next section that this is clearly not the dominant impact and this effect, even if it has to be kept in mind to understand how MEDUSAE works, is not of main importance: the planetary companions are easily detected (see Fig. 8.8) and the speckle field estimation is accurate enough to enable a correct contrast estimation.

8.4 Sensitivity to the inputs required by MEDUSAE

In this section, I investigate the impact on MEDUSAE's performance (within the scheme previously established) of the required input: the downstream aberration map (Sect. 8.4.1) and the input turbulence residual structure function (Sect. 8.4.2).

8.4.1 Error on the downstream aberration map δ_{down}

As previously explained, the downstream aberration map must be given as an input to MEDUSAE. The downstream phase should be relatively static, at least over one observation night, and it could be calibrated during the day. However the calibration might be not perfect or the aberrations might evolve between the calibration and the actual observation.

One solution would be to estimate the downstream phase during the inversion process, starting from the calibrated phase, which would perceptibly increase the number of unknowns to be estimated. However if MEDUSAE succeeds in estimating the circumstellar objects spectra from only a few multispectral cubes, the temporal gain would be considerable, which would motivate doing a calibration even during the night. If none of these techniques are working out, one can think of analytically

estimating the downstream phase via solutions such as COFFEE (Paul et al., 2014; Sauvage et al., 2012) based on phase diversity.

The goal of this section is to assess the sensitivity to this input in order to anticipate the real data application of MEDUSAE and discuss the potential solutions according to the results obtained on this inverse crime data-set. Six cases are explored in this section:

(i) the input downstream aberration map is null,

(ii) the input downstream aberration map has an error of 1% in MSE wrt the true one,

(iii) the input downstream aberration map has an error of 10% in MSE wrt the true one,

(iv) the input downstream aberration map has an error of 30% in MSE wrt the true one,

(v) the input downstream aberration map has an error of 50% in MSE wrt the true one,

(vi) the input downstream aberration map is randomly generated using the same rms value and the same spatial spectrum trend.

Tab. 8.15 and Tab. 8.16 show the performance obtained in each of these cases, using the strategy presented at Sect. 8.2.

Test case	Total time	Criterion J_{data}	$\mathcal{M}_{f^*}$	rMSE_Φ	rMSE_i	rMSE_{corr}
(i):	1h50	$37,656,648$	37.17%	144%	3.69%	6.15%
(ii):	1h12	$52,228$	0.33%	2.16%	0.078%	0.09%
(iii):	1h09	$175,358$	0.08%	3.83%	0.23%	0.31%
(iv):	1h05	$1,150,462$	0.10%	9.95%	0.64%	0.89%
(v):	1h06	$3,046,097$	0.09%	17.06%	1.08%	1.41%
(vi):	1h25	$41,591,985$	52.46%	143%	4.20%	6.02%

Table 8.15 – Results obtained at the end of the whole MEDUSAE procedure (along the criteria presented at Sect. 8.1.2) for the different upstream phases chosen as an input.

Companion index	**#1**	**#2**	**#3**	**#4**	**#5**	**Residual flux,** f^o_{res}
(i):	13.35%	185%	235%	388%	-	$42,890,194$
(ii):	1.06%	0.72%	4.66%	3.20%	67.18%	$245,548$
(iii):	0.14%	6.41%	4.89%	4.18%	57.84%	$696,109$
(iv):	0.62%	12.09%	2.69%	1.92%	7.14%	$2,429,063$
(v):	2.49%	21.86%	7.81%	10.90%	26.33%	$3,773,848$
(vi):	37%	145%	150%	333%	148%	$38,670,609$

Table 8.16 – Estimated flux of the 5 injected companions, as a function of the different upstream phases chosen as an input.

Fig. 8.9 shows the residual phase maps, the estimated object map and the residual speckle field and residual images obtained for different cases of input upstream aberration maps.

In case (i): if δ_{do} is null, there are too many residuals appearing in the object map and in the residual image. This method is not a good option and a downstream aberration map must be given as an input.

In case (ii) to (v): if the input δ_{do} is the correct one with an error from 1% to 50% on its MSE, MEDUSAE provides correct results. Obviously, the higher the error, the more the estimated speckle field is affected and it is more and more difficult to detect the planetary signals in the object map (see Fig. 8.9c. These residuals are more and more intense and they are radially distributed in the object map which make them obvious to disentangle from the planetary signals. However the estimated contrast are not well estimated from an error of 50% on the input downstream aberration map.

In case (vi): the input δ_{do} is randomly generated with the same characteristics as the true one (same spatial spectrum and same rms value). As for the case (i), this is not a good option: the estimated upstream aberration map is the same as the one in case (i) and the corresponding results are about the same.

To summarize, the downstream aberration map given in input to MEDUSAE must have the same spatial structure as the true one. Thus it must be estimated beforehand (by calibration or analytical

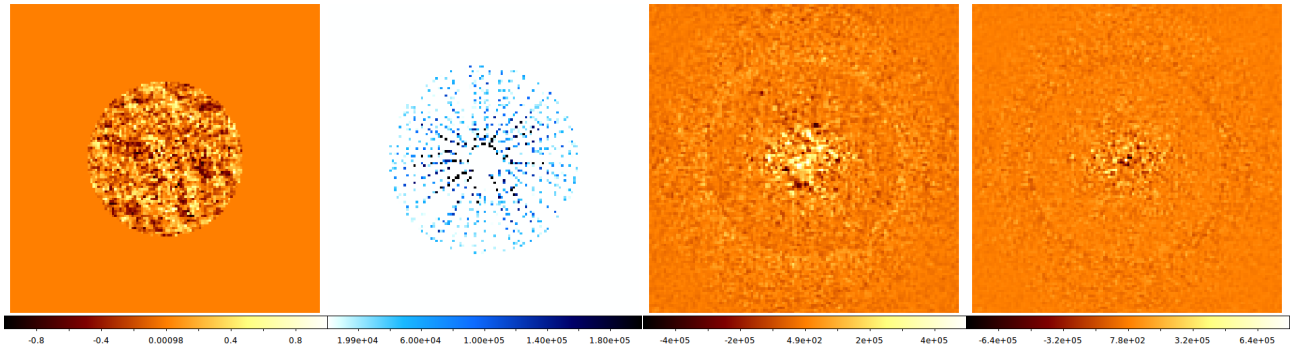

(a) : Case (i), with a null downstream aberration map as an input.

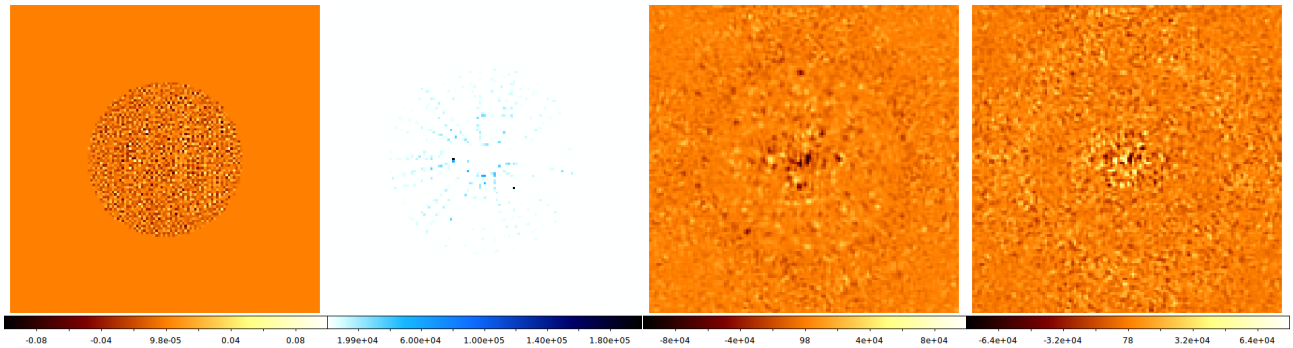

(b) : Case (iv), with a 30% error on input the downstream aberration map.

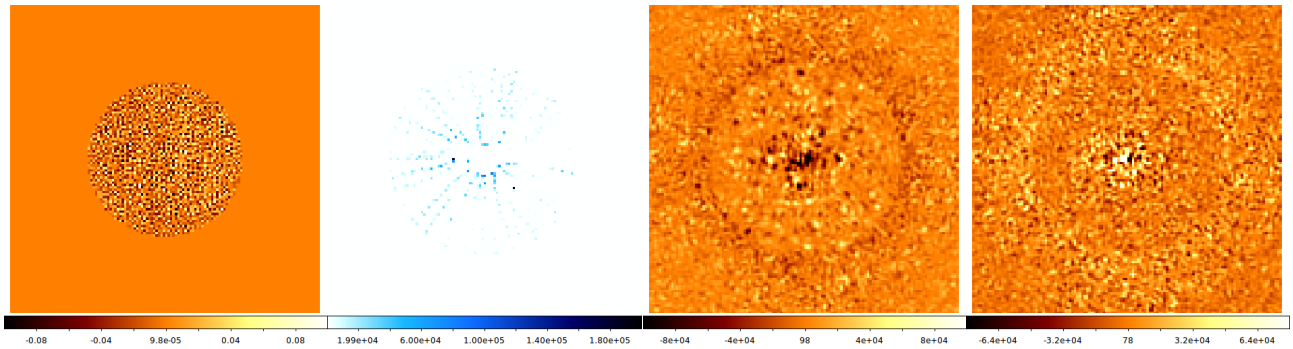

(c) : Case (v), with a 50% error on input the downstream aberration map.

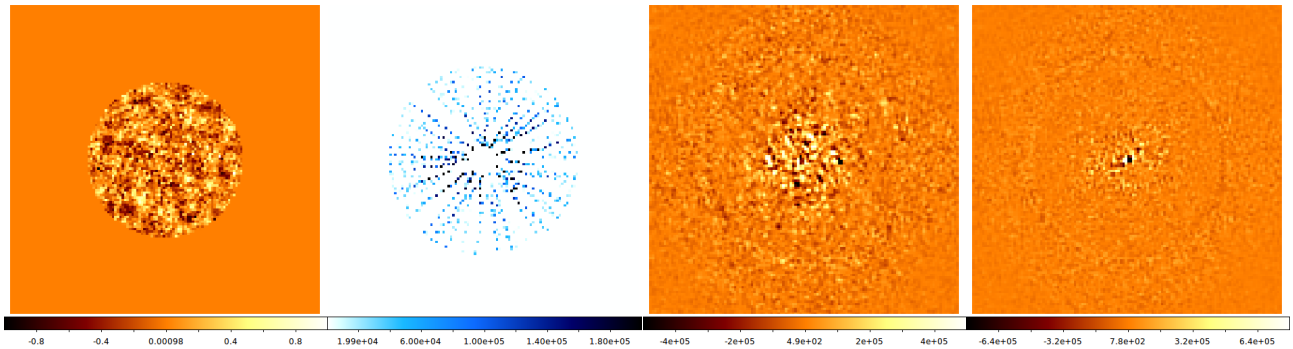

(d) : Case (vi), with an input the downstream aberration map randomly generated with the same characteristics.

Figure 8.9 – Results obtained by running MEDUSAE on the inverse crime data, for different downstream aberration maps provided in input. From left to right: residual aberration map, estimated object map (inverted colors), residual speckle field and residual image. The scale is linear but the bounds different for every image.

solution). However, once its correct spatial distribution is found, a relative error on this map does not really affect the performance of MEDUSAE, when this error is below 50%.

8.4.2 Error on the residual phase structure function $D_{\phi_{res}}$

As previously explained, the turbulence residuals structure function map must also be given as an input to MEDUSAE. This parameters depends on the observation conditions and currently, it is not calibrated during the observation.

Several solutions could be implemented. (1) We could try to remove this contribution by filtering the smooth stellar halo and assuming the phase is fully static during the exposure. (2) We could ignore this parameter and a posteriori remove the light from its contribution in the estimated object. (3) We could calibrate this value with the data from the DIMM or the SH-WFS slopes. (4) We could generate a library of images with various $D_{\phi_{res}}$ values and build a routine to estimate the real value in the images (using, for instance, its spatial frequency distribution, as in Garrel et al., 2012). (5) We could analytically estimate this $D_{\phi_{res}}$, following the reasoning of Sauvage et al. (2006).

The goal of this section is to assess the sensitivity to this input in order to anticipate the real data application of MEDUSAE and discuss the potential solutions according to the results obtained on this inverse crime data-set. Three cases are explored in this section:

(o) the input turbulence residuals structure function is the true one,

(i) the input turbulence residuals structure function is null,

(ii) the input turbulence residuals structure function is generated with very different wind and seeing characteristics.

Tab. 8.17 and Tab. 8.18 show the performance obtained in each of these cases, using the strategy presented at Sect. 8.2.

Test case	Total time	Criterion J_{data}	$\mathcal{M}_{f^*}$	rMSE$_\Phi$	rMSE$_i$	rMSE$_{corr}$
(o):	1h29	$51,004$	0.33%	2.14%	0.075%	0.08%
(i):	1h50	$37,656,648$	37.17%	0.28%	3.69%	6.15%
(ii):	0h53	2.78^8	0.57%	285%	10.9%	13.25%

Table 8.17 – Results obtained at the end of the whole MEDUSAE procedure (along the criteria presented at Sect. 8.1.2) for different residual phase structure functions $D_{\phi_{res}}$ in input.

Companion index	**#1**	**#2**	**#3**	**#4**	**#5**	**Residual flux, f^o_{res}**
(o):	0.84%	0.21%	4.94%	2.18%	64.37%	$248,842$
(i):	98.96%	98.99%	94.08%	92.13%	99.13%	2.82×10^8
(ii):	20.95%	824%	100%	728%	-	1.34×10^8

Table 8.18 – Estimated flux of the 5 injected companions, as a function of the different residual phase structure functions $D_{\phi_{res}}$ in input.

Fig. 8.10 shows the residual phase maps, the estimated object map and the residual speckle field and residual images obtained for different cases of input turbulence residuals structure functions.

In case (i): if $D_{\phi_{res}}$ is null then the upstream aberration map are well estimated but the star spectrum is not, as expected since, as explained at the previous chapter, the main contributor to estimate the star spectrum is the halo in the image. Moreover, some *speckled structures* appear in the estimated image visible on Fig. 8.10b-Middle/Right. The halo is not estimated via δ_{up} and remains in the residual speckle as shown on Fig. 8.10b-Right. Consequently, it is impossible to detect the planetary signals in the object map which shows elongated structures from the center to the edge.

In case (ii): the $D_{\phi_{res}}$ is randomly generated, as previously but with different wind speed, wind direction and seeing conditions. In that case, the estimations are not correct and it is impossible to detect the planetary signals in the object map.

To summarize, the $D_{\phi_{res}}$ is an extremely important input that must be carefully calibrated or computed beforehand. If it is not properly given in input, it completely affects the estimated image which makes it impossible to detect the planetary signals in the estimated object map.

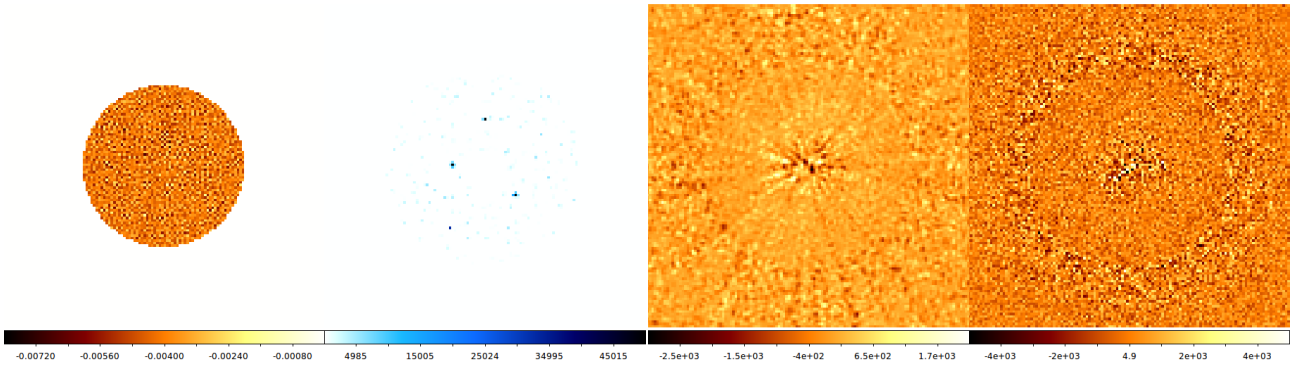

(a) : Case (o), with an input $D_{\phi_{res}}$ generated randomly with the exact same characteristics.

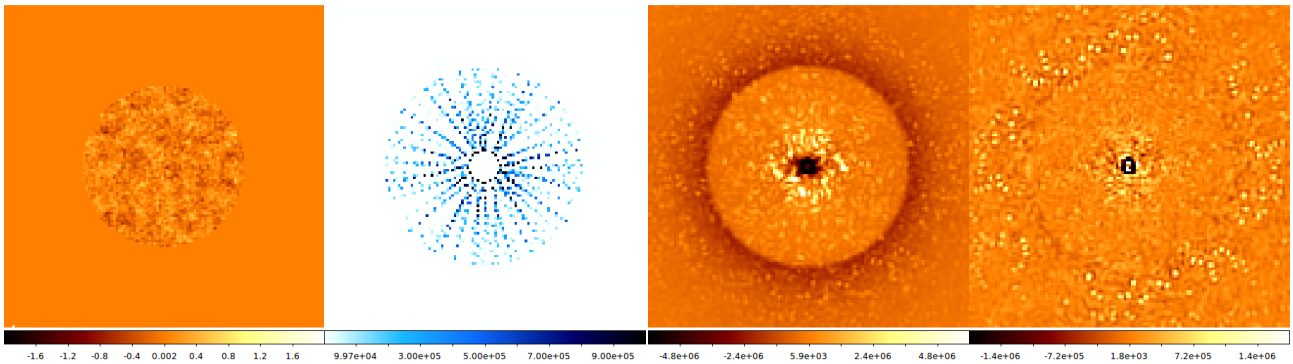

(b) : Case (i), with a null $D_{\phi_{res}}$ map as an input.

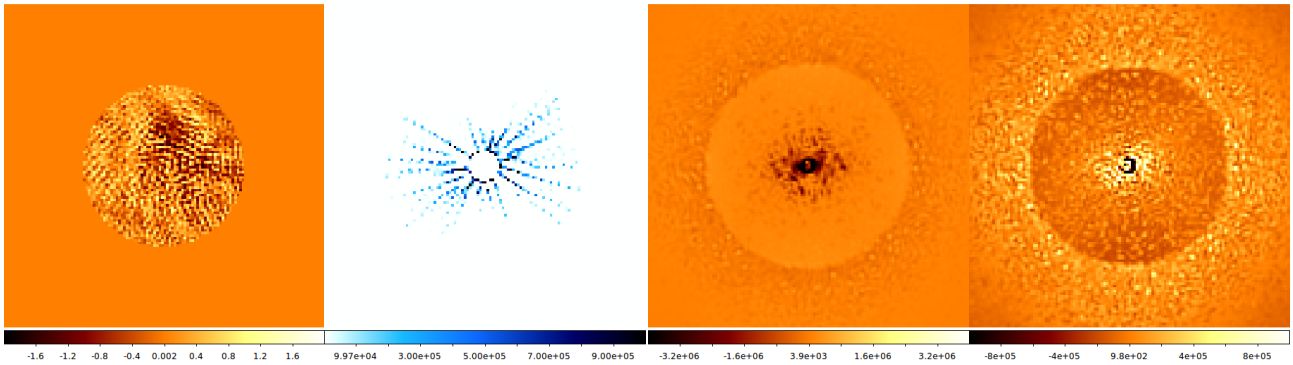

(c) : Case (ii), with an input $D_{\phi_{res}}$ generated randomly with the different characteristics.

Figure 8.10 – Results obtained by running MEDUSAE on the inverse crime data, for different turbulence residual phase structure functions provided in input. From left to right: residual aberration map, estimated object map (inverted colors), residual speckle field and residual image. The scale is linear but the bounds different for every image.

Conclusions from tests on inverse crime

In this chapter, I run the MEDUSAE method on an inverse crime data set, that is to say with images that are generated using the same model than the one implemented in the inversion process of the method. This specific test case enabled me to work under ideal conditions and revisit the strategy to obtain the best performance which can be expected from the MEDUSAE concept.

As a result, I improved and justify the inversion strategy in order to decrease the computing time while increasing the performance of the method. The new inversion strategy consists in an initialization procedure in two stages, at one then two wavelengths, in which the object is estimated but no regularization is applied for its estimation. The four equivalent aberration maps are only explored at the very first iteration at one wavelength. Then the MEDUSAE core is to incorporate the wavelengths one by one, starting at two wavelengths, as implemented in the original version. However, the object is estimated by applying a L1L2 spatial regularization which tends to be a L1 regularization

(the hyper-parameter δ is set to be very small but non zero, else it corrupts the criterion computation and makes the inversion process diverge) added to the zonal constraint.

With this new strategy to run MEDUSAE, bright companions in the image field still impact the performance of the algorithm to a small extent. It is not of great importance but this effect has to be kept in mind for further tests and real data application.

By running MEDUSAE in the ideal case of the inverse crime, it also enabled me to have a deeper understanding on its sensitivity to the input parameters. I thus explored the specific cases of the input downstream aberration map δ_{do} and the input residual phase structure function $D_{\phi_{res}}$. I chose test cases that could be used when applying MEDUSAE to real data. As a result, the $D_{\phi_{res}}$ is by far the most critical parameter that must be carefully estimated beforehand. Else its contribution must be removed or another way of estimating it must be implemented. Concerning the downstream aberration map δ_{do}, it is necessary to input in MEDUSAE the structure of the true downstream aberration map, thus it still provides good results if it is estimated with an error of 50%. This downstream aberration map must be either calibrated or estimated beforehand but its precision is not a major problem as long as its spatial structure is provided.

One important effect that will affect the MEDUSAE method is the model of coronagraphic image implemented in the method. Thus, once tests have been conducted in the ideal case of the inverse crime data set, I perform similar tests on data generated with a different model than the one used in the inversion procedure. Moreover, I generate images that have the same properties as those from the SPHERE-IFS instrument, which implies modifications of the MEDUSAE code to handle such data. The next section describes how the simulated multispectral cube is generated and results obtained by running the MEDUSAE algorithm on this realistic data set.

Chapter 9

Towards application on real data: tests on realistic simulated data

Contents

9.1 Simulation of realistic multispectral high contrast images 238
9.1.1 Short exposure realistic coronagraphic PSF 238
9.1.2 SPHERE-IFS data characteristics 239
9.1.3 Chosen characteristics of the images 240
9.1.4 Generation of a representative $D_{\phi_{res}}$ 241
9.1.5 Resulting realistic simulated images 242
9.2 Application of MEDUSAE on the realistic simulated data 244
9.2.1 First application: Reference case 244
9.2.2 Estimating the speckle field only 247
9.2.3 Estimating the object map with MEDUSAE 252
9.3 Perspectives for the MEDUSAE methods 255

Before applying MEDUSAE on real data, I present in this chapter applications of MEDUSAE on realistic SPHERE-like data. The real SPHERE-IFS image properties are quite different from the images on which MEDUSAE have been applied so far. Fig. 9.1 shows a real SPHERE-IFS image and a simulated image using the ideal model of coronagraph from Sauvage et al. (2010) that has been used previously to run MEDUSAE. Visually three features are notably different: (1) the central part of the coronagraphic image is brighter in the real case (image using an APLC coronagraph) than in the ideal case, (2) low spatial frequencies are visible in the corrected area of the real image and (3) the correction halo shows a broader ring on real data as well as two broad spots on either side of the correction halo (at $\sim -10°$ of the vertical axis) that are due to the DM square actuator grid. Added to that, compared to the inverse crime data set used previously, the real images are obtained with an instrument having the following properties: the telescope pupil has a central obstruction and spiders to hold the secondary mirror, the Lyot mask diameter (downstream pupil) is smaller than the upstream pupil diameter, the image sampling is different, the spectral bandwidth is not infinitely small and of course, the wavelengths constituting the multispectral cube are not the same.

A first action was to adapt the MEDUSAE code in order to make it able to cope with the new image sizes, pupil sizes, wavelengths and oversampling factors. Once the MEDUSAE code was ready to process real data, I first tested it on in-lab data without turbulence whose results are shown in appendix (App. D). The results showed that the major error factor was due to the discrepancy between the model used for inversion (the ideal coronagraphic model) and the real data (imaged with an APLC). In order to specifically probe the impact of this discrepancy, I simulated realistic coronagraphic images, following the characteristics of SPHERE-IFS (Sect. 9.1). I then ran MEDUSAE on these realistic simulated images, knowing all the parameters, while first focusing on the speckle field estimation, then

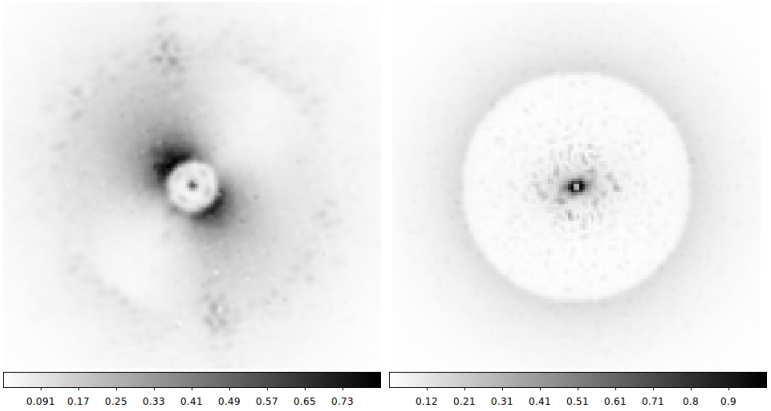

Figure 9.1 – Visual comparison between a real on-sky SPHERE-IFS image of the star 51 Eri and a simulated ideal image, as used in the previous chapter. Left: One experimental image from a SPHERE-IFS multispectral cube (956μm). Right: One simulated image using the ideal coronagraph model for the same wavelength. In the two cases, the aberrations are not exactly the same but are of the same order of magnitude. Inverted colors, normalized to their maximum.

on the speckle field *and* object estimation (Sect. 9.2). The results obtained led to several perspectives on both short term and long term in order to make MEDUSAE able to process real data (Sect. 9.3).

9.1 Simulation of realistic multispectral high contrast images

One of the major issue in inverse problem solving is the accuracy of the model used. As in ANDROMEDA where the model of noise was not fully verified, in MEDUSAE the model of an ideal coronagraphic image might strongly impact the phase retrieval process. In order to probe the impact of this discrepancy, I simulated a realistic data set, similar to the multispectral data cube provided by SPHERE-IFS. The images are simulated by using a "semi-analytical" model of coronagraphic PSF. By doing so, I could tune the parameters and use the correct input to focus only on the coronagraphic model discrepancy while preparing MEDUSAE to real data application.

This section describes how the realistic data-set is created. First I describe the method used to obtain the realistic short-exposure coronagraphic PSF (Sect. 9.1.1). Then the adaptation to obtain SPHERE-like data (Sect. 9.1.2). Eventually the phases and objects that I have chosen to build the images (Sect. 9.1.3). In another section, I specifically present how to generate a $D_{\phi_{res}}$, by tuning the turbulence and AO parameters, in order to generate images with a chosen profile (Sect. 9.1.4). I finally present the resulting realistic simulated data and compare their properties to real data from SPHERE-IFS (Sect. 9.1.5).

9.1.1 Short exposure realistic coronagraphic PSF

In order to obtain a realistic coronagraphic PSF, the code I used, is based on a semi-analytical model: the light is propagated from one plane to the other, following the coronagraphic set-up scheme of Fig. 7.2, in the Fraunhofer framework. The light propagation is numerically computed via a *Matrix Fourier Transform*, MFT, developed by Soummer et al. (2007b). The MFT is a non-FFT based Fourier transform enabling to take into account the spatial extension of the coronagraphic focal plane mask and pupil mask while not requiring too much computation time. This method has been numerically implemented in IDL by B. Paul during his PhD at Onera and used in the publication Paul et al. (2014). With such a method, it is thus possible to insert a coronagraphic focal plane mask (either a phase or amplitude mask), exotic binary pupil masks and an upstream pupil apodizer.

This code directly computes the coronagraphic PSF as a function of the input wavelength so no zero padding is performed and the size of the elements remain the same (only the oversampling factor is taken into account).

This code provides a short exposure coronagraphic PSF. In order to obtain a long exposure PSF, I generated N_{exp} short exposures using N_{exp} different (uncorrelated) turbulence residual phase screens ϕ_{res} randomly generated from the code dealt with at Sect. 9.1.4. I then added the resulting N_{exp} exposures to obtain a long exposure coronagraphic PSF.

9.1.2 SPHERE-IFS data characteristics

In this section, I describe the properties of the real data from SPHERE-IFS that I included in the realistic images simulation. First of all, the images from SPHERE IFS must be cropped in a 190×190 pixels window to not take into account the entire frame including many zeros on the edges (see one reduced image in Fig. 9.2). This implies that the sampling of the pupils must be defined in agreement with this frame size, according to the sampling of each image (formerly $N_{pix} = 128$ pixels and $\varnothing_{\mathcal{P}} = 64$ pixels for the inverse crime data set, using an oversampling factor of 1).

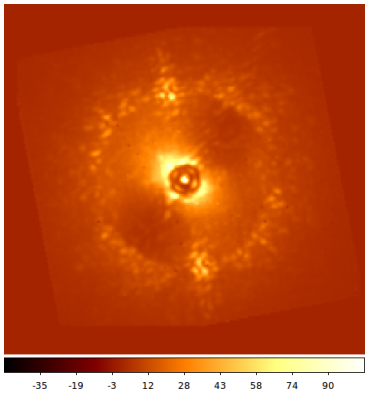

Figure 9.2 – Reduced image at 957.56 nm (first channel in YH-band) from SPHERE-IFS, as it is provided before the application of advanced image processing.

Pixel scale and sampling of the images The reduced images have a pixel scale of 7.46 mas/pixel (whereas the raw images have a micro-lens pitch of 12.25 mas, as explained in 1.2.4.3). The numerical sampling and sizes of the pupil and images are not independent: we have 2 degrees of freedom. We define those values from two constraints to match the real data:

- the real data sampling is 7.46 mas/pixel;
- the real data field of view should be below 190×190 pixels since the outer part of the square reduced SPHERE-IFS images includes zero or NaN values in the peripheric area (as shown on Fig. 9.2). Note that the exact value can be accommodated with appropriate cropping of the data.

For these data, I chose to fix the size of the images to $N_{pix} = 190$ pixels. As a consequence, given that the VLT pupil has a diameter of 8m, the upstream pupil diameter in the simulation are numerically sampled within a 58×58 pixel window.

Channel number and wavelengths In SPHERE-IFS, there are 39 channels, in YH (from 966.01 nm to 1640.70 nm) or YJ bands (from 957.56 nm to 1328.84 nm). The distance between the channels is not constant and has to be taken into account: I thus used the wavelengths file from calibration, giving the wavelength value of each channel in both modes of SPHERE-IFS. The oversampling factor for each channel is computed, knowing the corresponding pixel scale and wavelength.

Pupils of the set up The telescope pupil has a central obstruction and spiders that are taken into account to produce the realistic simulated data. To do so, I used the calibration files showing the upstream pupil and the downstream pupil, as seen by the imaging camera of SPHERE-IRDIS[1]. I had to interpolate these pupil images to make them correspond to the image sizes I am dealing with in this section. In the configuration used, the Lyot stop diameter is 96% smaller than the upstream pupil.

APLC coronagraph characteristics For the SPHERE-IFS images, the most used coronagraph is the APLC coronagraph whose diameter is of 185 mas[2]. The pupil apodizer is also given by a calibration file showing the transmission of the apodizer throughout the pupil plane (and whose size has also to be interpolated according to the image sizes for the simulation). Fig. 9.3 shows the apodizer, the

[1] I used the calibration files obtained during the integration of the SPHERE instrument at IPAG in 2013. These files do not take into account the patches added to hide the dead actuators of the SAXO DM.

[2] In YH band the APLC coronagraph of diameter 240 mas is also generally used (showing a larger IWA), specifically in the configuration where SPHERE-IFS observes in parallel with SPHERE-IRDIS in K band.

upstream pupil and the downstream pupil of SPHERE that I used in these simulations. Note that I used the same apodizer and focal plane mask size for the two IFS modes (YH and YJ).

Figure 9.3 – Pupils used to produce the realistic simulated data. From left to right: Pupil apodizer (linear scale), upstream pupil and downstream pupil. The upstream and downstream pupils are binary masks generated from images of the pupils seen by the SPHERE-IRDIS detector.

Multispectral adaptation In order to obtain the coronagraphic PSF at every wavelength, I computed the short exposure coronagraphic PSF by adapting the focal plane mask size and oversampling factor accordingly.

During the inversion, in order to compute the multispectral coronagraphic PSF, MEDUSAE needs in input the array size to zero-pad the pupil for each wavelength, as explained at Sect. 8.1.1. For instance, at the shortest wavelength, the pupil is coded within a zero-padded array of 192×192 pixel. This array size is then adjusted according to the wavelength in order to fit the image field of view sampling (that is to say the corresponding variable oversampling factor). The vector containing the array sizes of the 39 wavelengths is computed accordingly, directly from the wavelength values.

9.1.3 Chosen characteristics of the images

In this section I describe the process followed to create the multispectral images, including the phases and object map used to build the images.

Static aberrations, ϕ_{up} and ϕ_{do} Both static aberration maps are generated by a random number generation following a Gaussian distribution. The aberration maps have a spatial spectrum in f^{-2} (with f the spatial frequency). For both of them, I chose a wavefront error of 30 nm rms. These maps are then converted into radians, as required by MEDUSAE. Note that the choice of using such a spatial spectrum is rather realistic for the downstream aberrations, but pessimistic for the upstream aberrations as measurements from the primary mirror of the VLT show a PSD varying as f^{-3}. Moreover to be even more realistic, one could have chosen to assume that low frequencies are compensated by calibration (and thus smaller than 30 nm rms) but as the impact of static aberrations is negligible compared to residual turbulence aberrations, I did not take this aspect into account.

Turbulence residuals In order to obtain long-exposures, I added N_{exp} short exposures. Thus, N_{exp} turbulence residual phase screens must be created. The corresponding turbulence residual phase structure function that is required as an input to MEDUSAE in order to build the ideal coronagraphic PSF model, is generated independently with exactly the same characteristics. It has been a posteriori checked that the empirical structure of the residual phase maps is consistent with the corresponding generated $D_{\phi_{res}}$. In order to generate the residual phase ϕ_{res} and the residual phase structure function $D_{\phi_{res}}$, the same code as the one used to create the inverse crime data set is used here. In Sect. 9.1.4, I specifically discuss how to generate a realistic $D_{\phi_{res}}$.

Building the multispectral coronagraphic PSF cube The long exposure images are obtained by stacking N_{exp} short exposures (for instance, I generated two different data sets, using either a number of exposures $N_{exp} = 250$ or $N_{exp} = 2000$). Thus, for each wavelength, N_{exp} short exposures are built

using the same upstream and downstream aberration maps but different residual phase screens. The resulting long exposure coronagraphic PSF is normalized to its maximum, then multiplied by the star flux. I considered here a flat stellar spectrum having a total of 10^8 photons per long exposure. This process is being performed for each of the 39 channels considered here.

Adding planetary signals to the star images Five planets are injected in the images, with the properties gathered at Tab. 9.1. Once again, the spectra of the planetary companions are flat.

Planet index	Contrast	Separation	Position angle
1	1.10^{-4}	246.2 mas	90°
2	5.10^{-5}	211.0 mas	−45°
3	1.10^{-5}	186.5 mas	0°
4	5.10^{-6}	339.3mas	56.7°
5	1.10^{-6}	244.7 mas	−37.6°

Table 9.1 – Characteristics of the five planetary companions injected in the realistic simulated images.

Noise propagation in the set up I added to the generated images at each wavelength the photon noise, computed directly from the image, following a Poisson statistics. From these images, including only the photon noise, I computed the corresponding noise variance maps for each wavelength, $\sigma^2_{\lambda,\alpha}$. The weight map, defined as $\frac{1}{\sigma^2_{\lambda,\alpha}}$ at Eq. 7.5, is a required input to perform the inversion in MEDUSAE.

9.1.4 Generation of a representative $D_{\phi_{res}}$

In order to obtain a specific $D_{\phi_{res}}$, I used the Onera IDL function generating a $D_{\phi_{res}}$ thanks to a Fourier-based simulation, as described in Jolissaint et al. (2006). In this simulation, the AO system is described via the spatial power spectrum of the residual phase. The AO residual power spectral density includes a Kolmogorov turbulence model, servo-lag term, fitting term, RON and photon noise, spatially-filtered SH-WFS and turbulence parameters (seeing, C_n^2 profile, wind speed and strength). This simulation uses a three turbulent layers model that is known to represent a realistic turbulent profile (Fusco, 2000) and whose altitude can be chosen. In order to generate a representative $D_{\phi_{res}}$, I used the SPHERE configuration (as for the inverse crime data set, Sect. 8.1.1) and chose to tune 4 parameters in this simulation to obtain the correct profile: the seeing, the magnitude of the observed star (for the SH-WFS correction, driving the measurement noise), the wind speed and direction (even though no atmospheric turbulence is involved here) and the aliasing. The idea is to match the profile obtained with the ideal coronagraphic model using this $D_{\phi_{res}}$, with the profile of the real SPHERE-IFS images.

Fig. 9.4 shows the different profiles obtained by making these four parameters vary one by one, compared to the typical profile (dark solid line) used in the inverse crime data set for instance.

From these figures, I chose a protocol which consists in tuning these four parameters in order to make the ideal coronagraphic PSF radial profile match the real data radial profile. As the model of ideal coronagraph is significantly different from the real data in the central part (due to the different coronagraph), I focused on the corrected and external areas while ignoring the central area (below a radius of $6\lambda/D$). The different steps to be followed to obtain a representative profile are the following:

1. The seeing must be tuned to make the non-corrected area match the real data;
2. The star magnitude must be tuned to adapt the overall level of the corrected zone;
3. The aliasing must be set in order to adapt the size of the non-corrected bounce at $20\lambda/D$;
4. The wind speed must be set to adapt the profile's slopes.

This method has been used to produce a so-called representative $D_{\phi_{res}}$ in order to run MEDUSAE on in-lab SPHERE-IFS data, as presented in appendix (App. D).

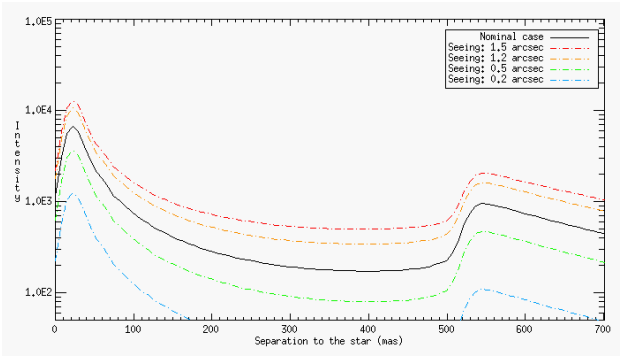

(a) : Variations of the seeing conditions.

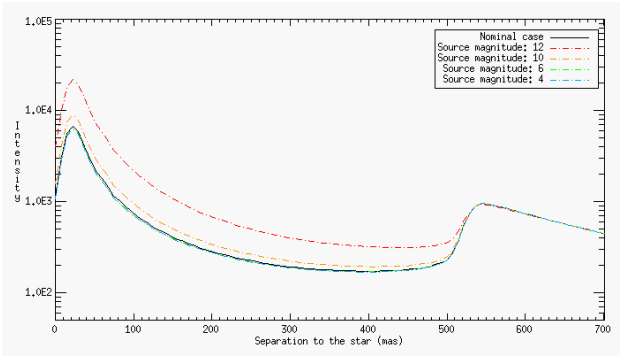

(b) : Variations of the source magnitude.

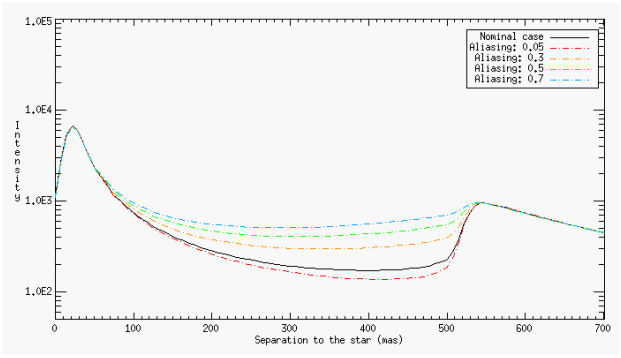

(c) : Variations of the aliasing factor.

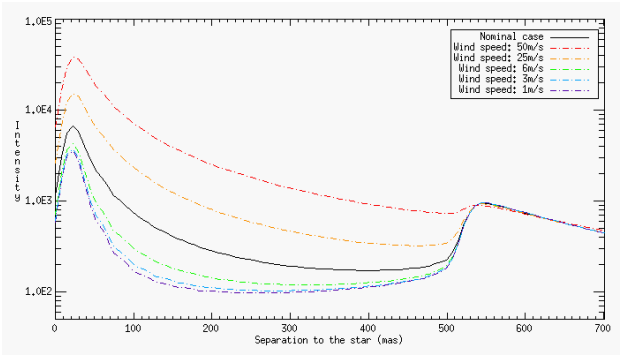

(d) : Variations of the wind speed.

Figure 9.4 – Azimuthal mean profiles of the ideal coronagraphic PSF obtained with null upstream and downstream phase and using a $D_{\phi_{res}}$ generated with different seeing conditions (9.4a), source magnitude (9.4b), aliasing (9.4c) and wind speed (9.4d). On each figure, the black solid line shows the *nominal case* used to generate the inverse crime data set: seeing of 0.8″, source magnitude of 8, aliasing factor of 0.1 and wind speed of 12.5m/s for each layer.

Fig. 9.5 shows the median profiles of one real image from SPHERE-IFS and the corresponding realistic simulated image.

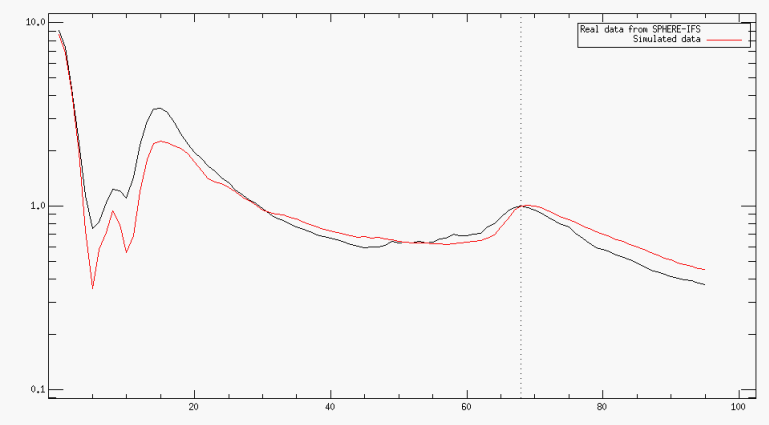

Figure 9.5 – Profile of the real SPHERE-IFS image at 957nm (black solid line) and its corresponding simulated image (red solid line), using $N_{exp} = 250$ in this example. The profile is normalized at the AO cutoff frequency (dashed line).

9.1.5 Resulting realistic simulated images

Fig. 9.6 shows a real image and its corresponding simulated image for the shortest and the largest wavelength.

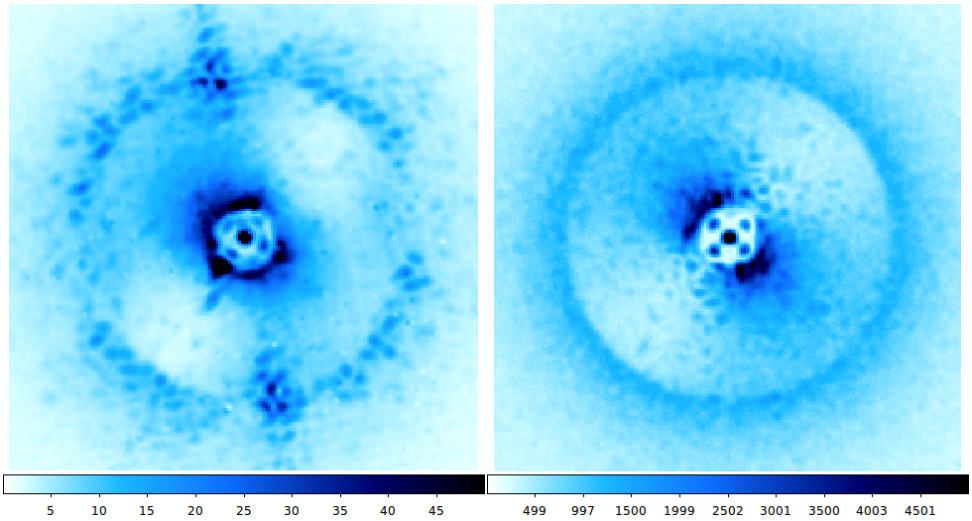

(a) : Shortest wavelength of the multispectral cube: 957.56nm.

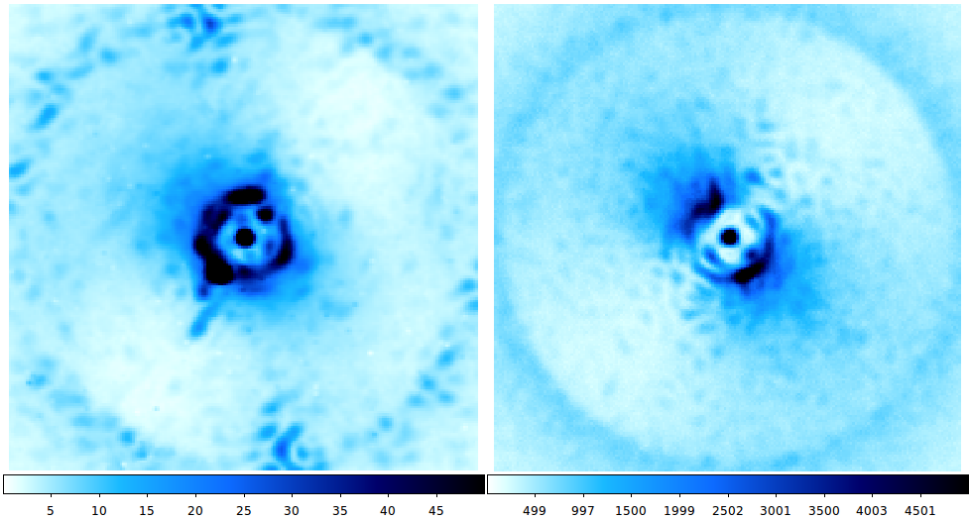

(b) : Largest wavelength of the multispectral cube: 1328.84nm.

Figure 9.6 – Left: Real reduced image from SPHERE-IFS in YJ mode. Right: Corresponding simulated image using a semi-analytical model of long exposure coronagraphic PSF (using $N_{exp} = 250$ in this example).

By following the method described in this section and following the characteristics of the real SPHERE-IFS images, I could simulate images that have the correct spectral and spatial behavior.

Spatial structures of the simulated images The realistic simulated images are very similar to the real SPHERE-IFS images, with the following specific remarks:

-In the central part of the images (below $3\lambda/D$), which is strongly affected by the coronagraph, the two images show very similar structures.

-In the corrected area (between $3\lambda/D$ and $20\lambda/D$), we see that the smooth halo corresponding to the AO residuals (close to the coronagraph edge, in a direction of $\sim -45°$ from vertical) more specifically due to the temporal noise of the correction, can be reproduced. This halo can be adjusted to be similar in terms of intensity, radial and and azimuthal distribution.

-In the outer region (from $20\lambda/D$), we can note that the real images presented here (under fair seeing conditions and high SNR) show a significant amount of not smoothed speckle-like features that are not well reproduced by the realistic simulations. This indicates a higher level of high spatial frequency static aberrations in the instrument. Another feature that is not reproduced in the simulated images is the extra intensity of speckles in the $\sim -10°$ direction from vertical, visible in the real reduced images. This direction actually corresponds to a physical vertical direction in the raw images (in the

IFU plane), aligned with the direction of the DM square actuator grid.

Spectral behavior of the simulated images I checked that the realistic simulated images have the correct spectral behavior, by comparing them to the real SPHERE-IFS multispectral cube and by rescaling each simulated image at a common wavelength, following Eq. 1.18, and checking that they are indeed similar.

As a conclusion I could generate multispectral images that are very similar to those obtained by the SPHERE-IFS instrument. This data set is more appropriate than the inverse crime data set to test the capabilities of MEDUSAE to deal with a different coronagraphic set-up while still having the exact $D_{\phi_{res}}$ and ϕ_{down} required as inputs to run MEDUSAE.

9.2 Application of MEDUSAE on the realistic simulated data

From the simulated data, we have all the inputs needed for MEDUSAE to run: the $D_{\phi_{res}}$ and the ϕ_{down} are exactly known and provided to the algorithm. Thus the only difference with the inverse crime data set is that the simulations are realistic, that is to say they are using a model of coronagraph that is not the one used in the inversion procedure. Moreover, the wavelengths and image sampling are the one of the SPHERE-IFS images.

9.2.1 First application: Reference case

In a first attempt, I launched the MEDUSAE algorithm in its *reference* case described hereafter for a multispectral cube in YJ band and with $N_{exp} = 250$. I only ran the initialization procedure to check the ability of the method to retrieve a good starting point: I first run the algorithm using the shortest wavelength (957.56μm) and then using the shortest and the largest wavelength (1328.84μm). Also, there is no regularization on the object estimation (neither spatial nor zonal constrain). I also used the weight map defined by the inverse of the noise variance (only the photon noise is taken into account here).

The Fig. 9.7 shows the estimated speckle field (i.e. the ideal coronagraphic PSF model using the estimated upstream phase and the estimated star flux), the estimated image of the object (object map convolved with the non-coronagraphic PSF), the estimated image (the sum of the estimated speckle field and the estimated image of the object) and the images residuals (the true image minus the estimated image).

The estimated image presented on Fig. 9.7-Middle-Right has features that are similar to the real input image. However, in order to fit the images and mostly to reproduce the central part of the realistic images that are rather different from the ideal model, the estimated phase shows high values: the estimated phase has a high rms value (3.49 rad rms) compared to the true one (0.20 rad rms), which is not realistic. This induces the presence of dark spots of typical size $1\lambda/D$ that are centro-symmetrical and spread all over the image field. Fig. 9.8 shows the estimated phase compared to the true phase. The estimated upstream phase shows very different spatial structures compared to the true one.

I further investigated the impact of the coronagraphic model onto the estimated upstream phase: Fig. 9.8 shows the ideal coronagraphic PSF obtained using the *real* input phases (the simulated ϕ_{down}, ϕ_{up} , $D_{\phi_{res}}$ and star flux f^*) and the ideal coronagraphic PSF using the *estimated* upstream phase and the *estimated* star flux (and the simulated ϕ_{down} and $D_{\phi_{res}}$). The first image is thus the speckle field that one would estimate if the estimated upstream phase was perfectly equal to the true upstream phase used to build the images.

In addition, even if the global structure is indeed present in the estimated PSF, this constraint on the phase trying to reproduce the central part of the image induces artifacts that are compensated by the object (whose image is shown on Fig. 9.7-Middle-Left) which is also not satisfactory since it is very bright and contains features that clearly belong to the speckle field (even though during this

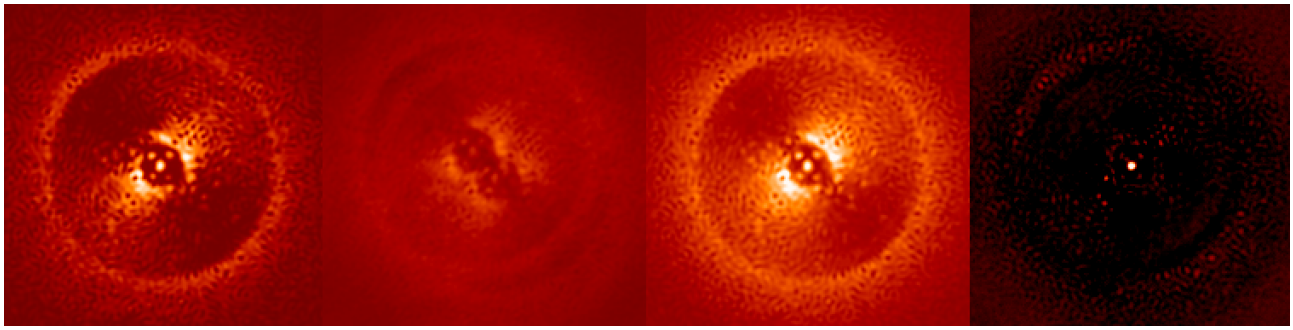

(a) : First initialization stage (at one wavelength).

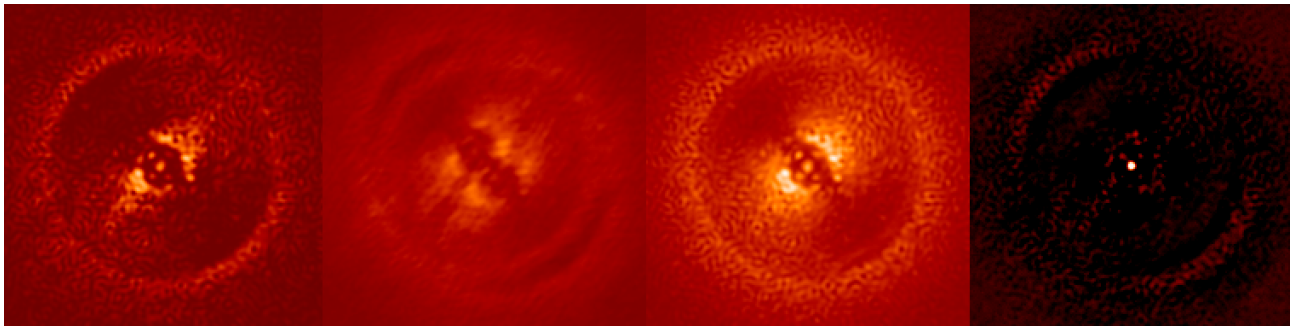

(b) : Second initialization stage (at two wavelengths).

Figure 9.7 – Results from the MEDUSAE inversion procedure for the two initialization stages. From left to right: Image of the estimated speckle field, image of the estimated object map, estimated image (sum of the two images on the left) and residuals wrt the real input image. The images are linearly scaled and to the power 0.2.

initialization procedure, the object is rejected). The image of the object presented on Fig. 9.7-Middle-Left is very peculiar and we did not find interpretation that could explain this shape.

Another aspect visible on Fig. 9.7-Right, showing the residuals between the true input image and the estimated one, is that the very central part cannot be reproduced with the ideal coronagraphic model since by definition the central part of the coronagraphic PSF is null. However, it is not the case for either the realistic simulated image or the true images from SPHERE-IFS as shown on Fig. 9.6.

In order to further visualize the zone of interest (the corrected zone), Fig. 9.9 shows the true corrected zone vs the estimated corrected zone. Even though large scale structures are similar, the images are quite different (in particular due to the presence of the dark spots), having a relative mean squared error of about 30%.

In the Tab. 9.2, I gathered the results of the metrics stated at Sect. 8.1.2 for the two stages of the initialization (at one then two wavelengths). Even in the corrected area, the speckle field is not well fitted by the upstream phase.

Initialization stage	Total time	J_{data}	$\mathcal{M}_{f^*}$	$\hat{\delta}_{up}$	rMSE_{δ}	rMSE_{i}	rMSE_{corr}	rMSE_{SF}^{corr}
One wavelength	0h53	$297,039$	3.46%	3.48 rad	1763%	77%	78%	21%
Two wavelengths	4h	$843,824$	0.01%	4.20 rad	2130%	115%	116%	33%

Table 9.2 – Results obtained at the first and the second stage of the initialization procedure of MEDUSAE (along the criteria presented at Sect. 8.1.2) when applying MEDUSAE to the realistic simulated data presented in Sect. 9.1. The results are given for images at the shortest wavelength.

As a conclusion, the very first problem to solve is the difference between the ideal coronagraphic model used in the inversion and the realistic image features. As this difference mainly affects the central part of the images (below $4\lambda/D$), a first idea is to set a null weight in this central area. Thus, the estimated upstream phase does not try to fit the central part of the images which is not consistent with the model used for the inversion.

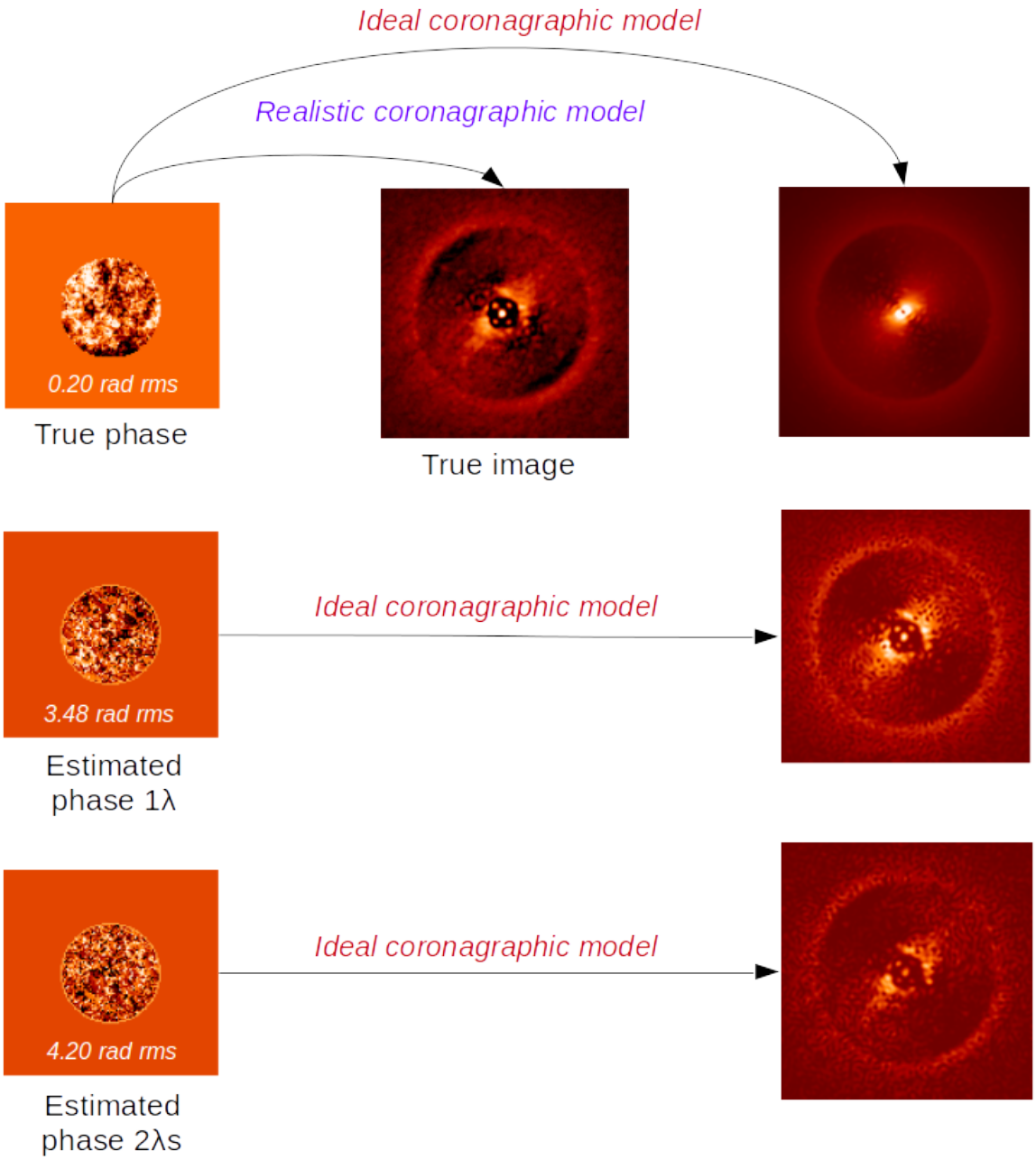

Figure 9.8 – True and estimated upstream phase maps and corresponding images obtained with the two models. The so-called *true image* is the realistic simulated image given as an input to MEDUSAE. If the upstream phase was perfectly estimated, one would obtain with the ideal coronagraphic model the image shown in top right. However, as it is not the same coronagraph used in the input image, it is impossible to converge towards the true phase and the estimated phase is quite different (in both its spatial structure and intensity). In the end, the estimated speckle field (bottom right) shows similar features to the true image but not accurate enough to recover the object map.

In the next section, I focus on the speckle field estimation by running MEDUSAE on the realistic simulated data, without planet. I thus ran MEDUSAE without the planet estimation for each case. In order to prepare the real data application of MEDUSAE, after solving the central part problem, I focus on the main differences that are expected between the real data from SPHERE-IFS and the model used for the inversion: in the model used for inversion, (1) very long exposures are considered (the halo in the non-corrected part is very smooth compared to the real images) and (2) the pupils are circular (no central obstruction, spiders or apodization can be taken into account for now). I then launched MEDUSAE on both YH and YJ bands to check if increasing the spectral diversity helps

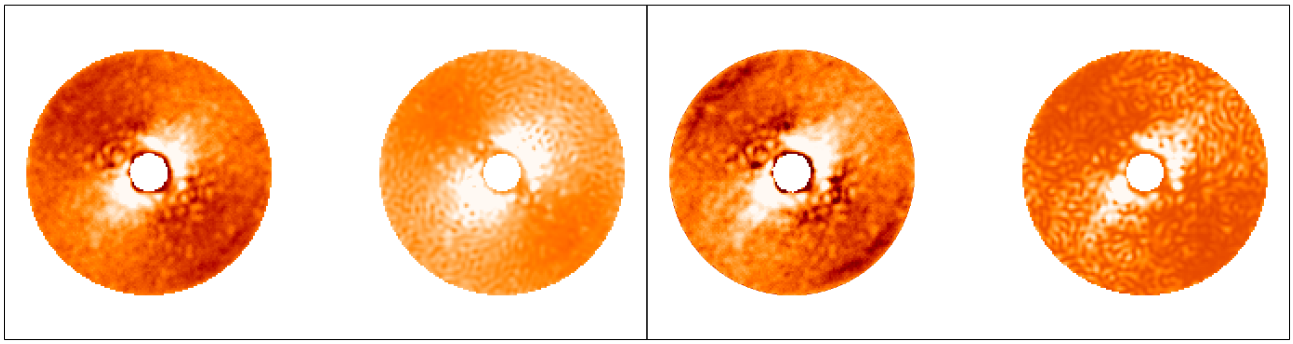

Figure 9.9 – Zoom on the corrected area of interest: real input image and estimated speckle field (obtained by using the ideal coronagraphic model estimated from the estimated upstream phase and the estimated star flux). The relative mean square error of these images are given in Tab. 9.2. Left box: Using one wavelength. Right box: Using two wavelengths.

estimating the speckle field.

9.2.2 Estimating the speckle field only

In this section, I focus on the estimation of the speckle field only. In order to only investigate the ability of MEDUSAE to estimate the speckle field, I ran MEDUSAE on data *without objects* in the field of view and *without estimating the object map*. The results are given for the end of the full MEDUSAE processing, that is to say including the initialization procedure (without object estimation) and the main procedure using six wavelengths of the image cube. The wavelengths used are the following: 957.57, 1020.64, 1091.11, 1164.61, 1236.76 and 1303.19 nm.

In the previous section, we saw that the discrepancy between the ideal coronagraphic model used and the realistic data, mostly affecting the center of the images, prevents from estimating the speckle field in the corrected zone with an accuracy that makes it possible to detect the planetary companions.

The idea of this section is to check the discrepancies between the real SPHERE data and the model used for the inversion. In the following, I first investigate which weight map is the most appropriate to accurately estimate the speckle field in the AO-corrected zone. I then study the effect of the number of exposures chosen to simulate the data: the SPHERE exposures are usually not long enough compared to the model which assumes a very long exposure showing a very smooth stellar halo in the non-corrected zone (see Fig. 9.1). In a third section, I check the difference between the YJ and YH bands data-set as provided by SPHERE, to see if having a wider spectral range does help estimating the speckle field. In a last section, I compare the results obtained with and without the apodization, spiders and central obstruction since real data from SPHERE have these pupils whereas, for now, the model uses full circular pupils (in order to take them into account, the criterion gradient should be calculated with these new pupils).

9.2.2.1 Choice of the weight map

In order to alleviate the difference between the model and the true images it is possible to set a null weight map in the regions where the images are not corresponding.

As seen in the previous section, the central part is the main discrepancy between the model for the inversion used and the simulated data (see Fig. 9.8), which prevents from correctly estimating the speckle field. Moreover, the model used for the inversion assumes a very long exposure, that is to say a very smooth halo in the non-corrected area, coded by $D_{\phi_{res}}$ (see Fig. 9.8). However, on the real SPHERE-IFS images (Fig. 9.6-Left) that I simulated (Fig. 9.6-Right), the outer halo is not as smooth as in the model.

Thus, two different weight maps can be considered: one with only the central part (below $4\lambda/D$) being set to zero or one with both the central part and the outer part (above $20\lambda/D$), as shown on Fig. 9.10 left and right respectively.

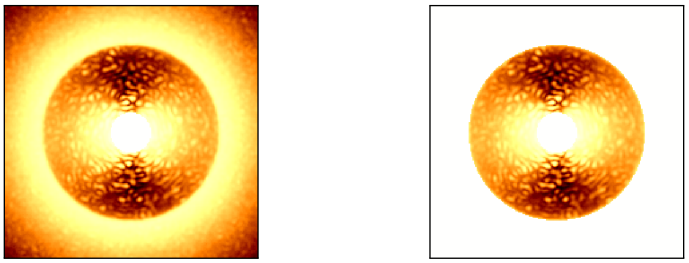

Figure 9.10 – Weight maps used to run MEDSUSAE (for the shortest wavelength at 966μm), accounting only for the photon noise. Left: Case with only the internal part set to zero (below $4.5\lambda/D$). Right: Case with both the internal and external part set to zero (below $4.5\lambda/D$ and above $20\lambda/D$). Inverted color (white is zero).

As the outer area smoothness is linked with the exposure time, I therefore present two cases: one with realistic data simulated using $N_{exp} = 250$ and one with realistic data simulated using $N_{exp} = 2000$. Fig. 9.11 shows the images at the shortest wavelength for these two cases. Knowing that it is possible to temporally bin the images from SPHERE-IFS, this test is to find which strategy is the best to accurately estimate the speckle field: by temporally binning the data or by setting a null weight map in the outer area (above $20\lambda/D$).

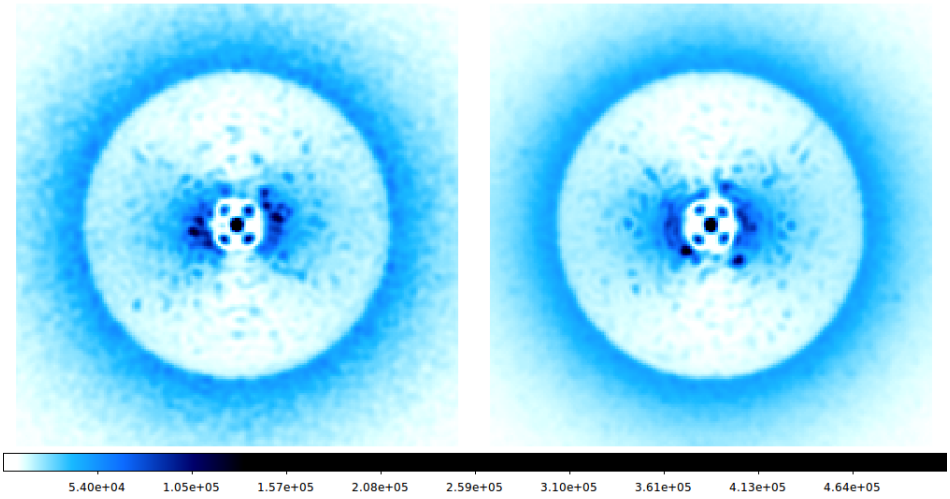

Figure 9.11 – Realistic simulated images at 966μm for two different exposure time. Left: Image obtained by adding $N_{exp} = 250$ short exposures. Right: Image obtained by adding $N_{exp} = 2000$ short exposures, showing a very smooth stellar halo in the non-corrected area (inverted colors).

In this section, I present the results obtained on the realistic simulated data in YJ mode, as in the previous section, but containing no planetary companions. The results obtained at the end of the full MEDUSAE process (including the initialization procedure and the main procedure with six wavelengths) are presented in Tab. 9.3. Fig. 9.12 shows the estimated speckle fields in the corrected zone, at the shortest and largest wavelengths, for each case.

Weight map	**N$_{exp}$**	Time	J_{data}	$\mathcal{M}_{f^*}$	rMSE$_{corr}$	Reachable contrast	Contrast at #1
Inner	250	4h20	9,296,588	0.62%	7.44%	1×10^{-6}	5×10^{-6}
Inner and outer	250	10h	1,698,416	0.44%	4.20%	4×10^{-7}	3×10^{-6}
Inner	2000	4h30	6,082,993	0.52%	6.57%	3×10^{-7}	9×10^{-6}
Inner and outer	2000	9h20	1,265,172	0.58%	3.64%	3×10^{-7}	3×10^{-5}

Table 9.3 – Results obtained when processing the realistic simulated data in YJ bands with MEDUSAE (along the criteria presented at Sect. 8.1.2), according to the different weight map and exposure time. The results are the average over the six wavelengths and are given for the AO-corrected area. The last column indicates the contrast at the brightest companion location (see Tab. 9.1), for the shortest wavelength.

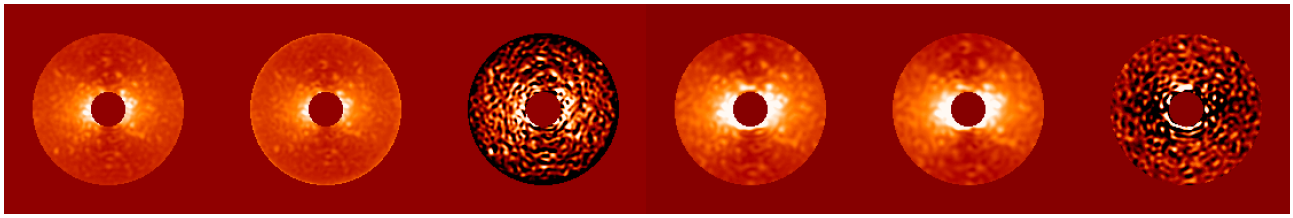

(a) : Results for the inner null weight map and $N_{exp} = 250$ for the shortest (left) and longest wavelength (right).

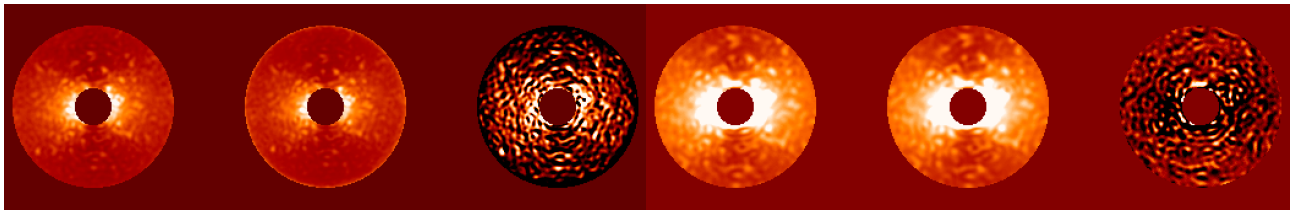

(b) : Results for the inner and outer null weight map and $N_{exp} = 250$ for the shortest (left) and longest wavelength (right).

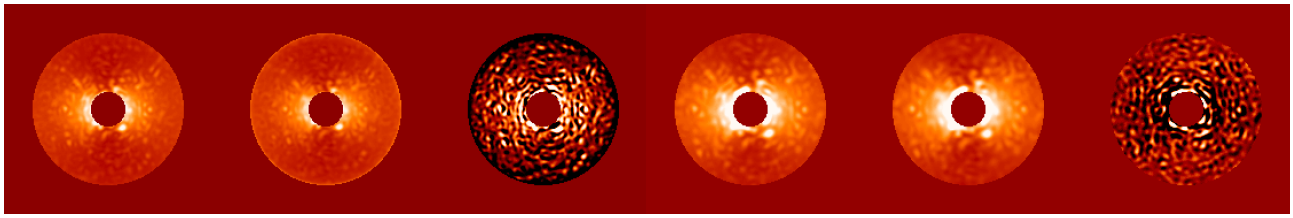

(c) : Results for the inner null weight map and $N_{exp} = 2000$ for the shortest (left) and longest wavelength (right).

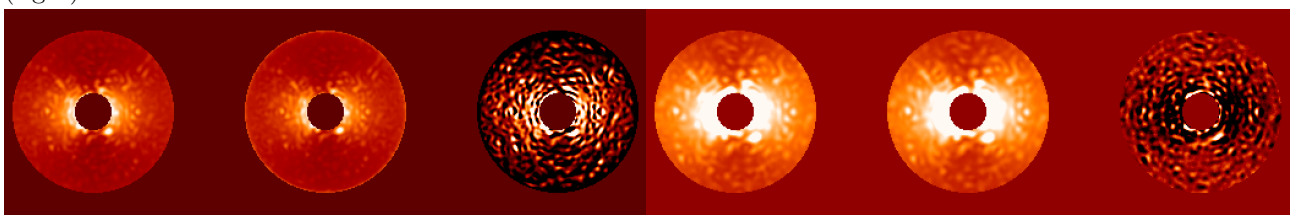

(d) : Results for the inner and outer null weight map and $N_{exp} = 2000$ for the shortest (left) and longest wavelength (right).

Figure 9.12 – Difference when estimating the speckle field with MEDUSAE according to the different weight maps and exposure times. From left to right: image in input, estimated speckle field at the end of the MEDUSAE process and residuals times 10 for better visibility (same color scale).

When using a null weight map in both the inner and outer part, the inversion focuses on reproducing the speckle field in the corrected zone, hence the speckle field is indeed better estimated in this case than in the case with a weight map with only the inner part set to zero. However this procedure is twice longer.

Also, when using a weight map with only the inner part set to zero, the speckle field is indeed better estimated when using $N_{exp} = 2000$, that is to say with a very smooth outer halo since it corresponds more to the ideal model used in the inversion process. In the future, it might be considered to temporally bin the SPHERE-IFS images so as to obtain a smoother outer halo.

In any of these case, the mean reachable contrast all over the corrected zone is above 5×10^{-7}, as in the inverse crime data set. More specifically, the contrast at the location of the brightest companion, at 250 mas enables to detect a planetary signal above a contrast of 10^{-5}.

As a conclusion, with this solution, we succeeded in estimating the speckle field in spite of the different coronagraphic model used in the inversion. The estimated speckle field makes it possible from now on to obtain a residual level that would enable to detect companions of contrast of $\sim 10^{-5}$ at 250 mas from the star. Moreover, the weight map being set to zero in both the central part and the external part helps estimating the speckle field in the AO corrected zone since it focuses only on this part.

9.2.2.2 With a flat pupil as in the model

As said previously, the coronagraphic model used in the inversion assumes flat pupils, that is to say without spider, central obstruction or pupil apodization. In order to take them into account, I ran MEDUSAE on several simulated data-sets: a realistic data set (as previously), a data set using only a pupil apodization but neither central obstruction nor spider and a data set using neither apodized nor obstructed pupils.

As the pupil apodization helps rejecting the residual star light and thus show a speckle distribution closer to the one obtained in the case of the ideal coronagraph, it is expected that the second case provides better results. In the next section, I used data simulated with $N_{exp} = 250$ and using a null weight map only in the inner part in order to run the MEDUSAE algorithm faster.

Tab. 9.4 provides the results obtained in terms of speckle field estimation.

Simulation	J_{data}	$\mathcal{M}_{f^*}$	rMSE_{corr}	Reachable contrast	Contrast at #1
Realistic	9,296,588	0.62%	7.44%	1×10^{-6}	5×10^{-6}
Apodizer only	7,184,116	0.61%	6.55%	7×10^{-7}	6×10^{-6}
Full pupils	9,097,185	0.73%	8.47%	1×10^{-6}	1×10^{-5}

Table 9.4 – Results obtained when processing the realistic simulated data in YJ bands with MEDUSAE (along the criteria presented at Sect. 8.1.2), according to the different pupil simulations. The results are the average over the six wavelengths and are given for the AO-corrected area. The last column indicates the contrast at the brightest companion location (see Tab. 9.1), for the shortest wavelength.

As expected, the case with only the pupil apodizer but without the central obstruction or the spiders taken into account in the model estimates better the speckle field since on the one hand the speckle structure in the input images are more similar to those given by the ideal model used in the inversion and on the other hand, the model used in the inversion does not take into account the pupil features.

Since the analytical model of long exposure coronagraphic PSF established by Sauvage et al. (2010) can take into account the pupil features, one short term perspective in order to increase the MEDUSAE performance is to calculate the corresponding gradients, including any input pupil, and implement them in IDL in the phase retrieval procedure.

9.2.2.3 Spectral diversity: YH vs YJ modes

In this last section, I ran MEDUSAE on realistic SPHERE-like simulated images, that is to say using the apodization, the spiders, the central obstruction and creating long exposures given by adding $N_{exp} = 250$ exposures, as on Fig. 9.6. I created two data sets, one in YJ band and one in YH band and ran MEDUSAE on it. It is expected that increasing the spectral diversity helps estimating the speckle field. Once again, I used a null weight map only in the inner part in order to run the MEDUSAE algorithm faster.

Tab. 9.5 shows the results on the MEDUSAE inversion on these two data sets.

Simulation	J_{data}	$\mathcal{M}_{f^*}$	rMSE_{corr}	Reachable contrast	Contrast at #1
YJ	6,082,993	0.52%	6.57%	3×10^{-7}	9×10^{-6}
YH	9,055,026	0.85%	8.00%	1×10^{-7}	4×10^{-5}

Table 9.5 – Results obtained when processing the realistic simulated data in YH bands with MEDUSAE (along the criteria presented at Sect. 8.1.2), according to the different weight map and exposure time. The results are the average over the six wavelengths and are given for the AO-corrected area.

Fig. 9.13 shows the results of the speckle field estimation for the two data sets.

The case with a larger spectral diversity provides estimated speckle fields that are slightly less accurate and thus leading to a lower reachable contrast in the corrected area. This might come from

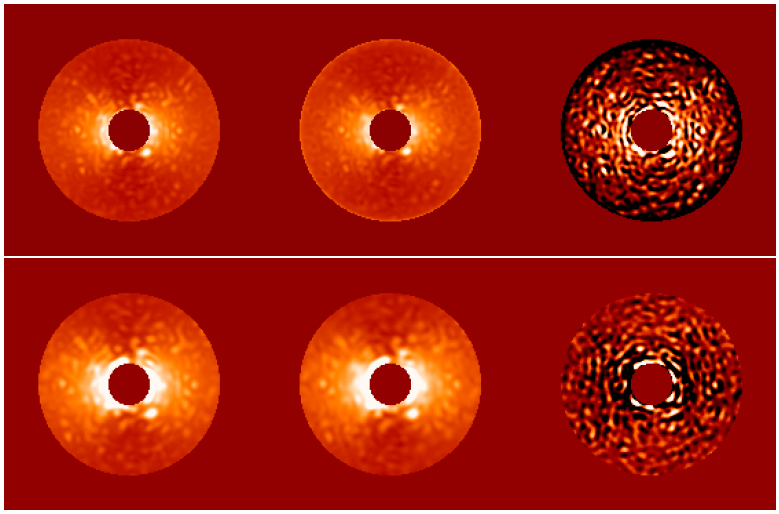

(a) : Results in YJ band at the shortest wavelength (top) and the longest wavelength (bottom).

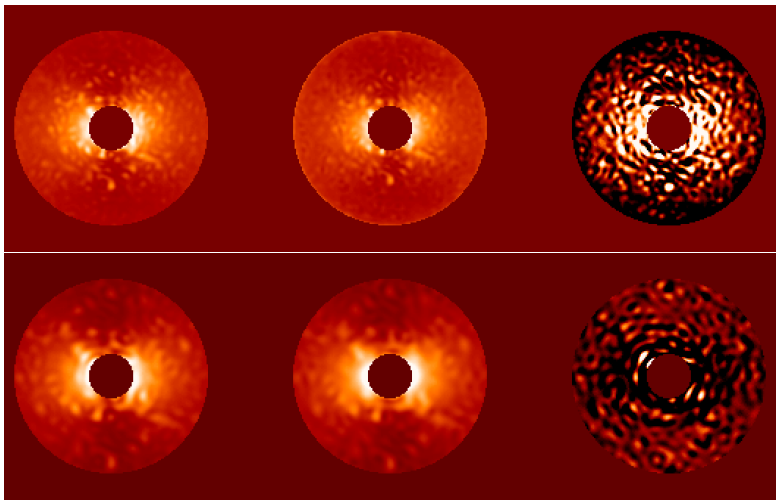

(b) : Results in YH band at the shortest wavelength (top) and the longest wavelength (bottom).

Figure 9.13 – Difference when estimating the speckle field with MEDUSAE in either YH or YJ bands. From left to right: image in input, estimated speckle field at the end of the MEDUSAE process and residuals times 10 for better visibility (same color scale).

the fact that a larger spectral diversity is harder to constrain under the achromaticity hypothesis used in the MEDUSAE model. Note that this test has been performed using the same coronagraph for the two data set whereas it is not optimized for the longest wavelengths of the YH data set.

Conclusions on the tests with a null weight map in the center

First of all, setting a null weight map in the central region (below $4\lambda/D$) helps estimating the speckle field in the AO-corrected area without obtaining aberrant estimated upstream phase due to the model discrepancy. With this technique we could alleviate the problem due to this discrepancy and which prevented to apply MEDUSAE on real data. From further tests performed in this section, several conclusions can be drawn out:

1. Adding a null weight map in the external zone (above $20\lambda/D$) obviously also helps estimating better the speckle field in the corrected area since it focuses only on this region.

2. The coronagraphic PSF model does not take into account the pupil features used to simulate the data which decreases the MEDUSAE performance.

3. Increasing the spectral diversity does not help estimating better the speckle field but on the

contrary decreases the MEDUSAE performance.

In other words, for the real data application, one should probably favor very long exposures with a precise coronagraph and the YJ mode of SPHERE-IFS. On the MEDUSAE algorithm, it is also needed to work on the analytical gradients expression of the inversion model in order to take into account exotic pupils that could modify the previous conclusions.

To give an idea of the residual level, Fig. 9.14 shows the residuals obtained by removing the estimated speckle field from the input images as well as the residuals obtained when removing the estimated speckle field from the same simulated images but *containing* the planetary companions. The brightest companion (contrast of 10^{-4}) is indeed easily visible in the image but the closer and fainter companions are still hidden in the surrounding noise.

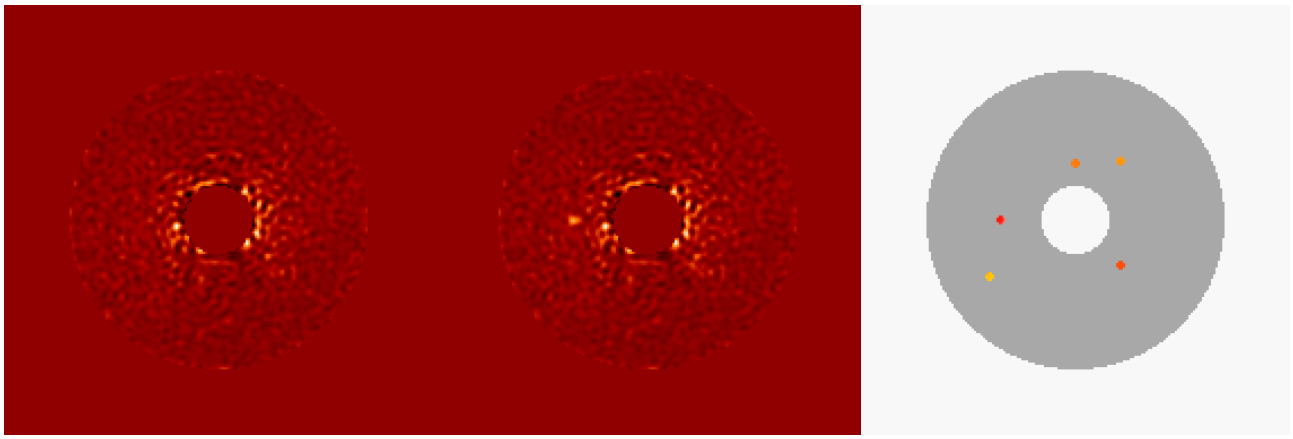

Figure 9.14 – Objects in the field of view: residual image obtained by removing the estimated speckle field to the image of the star from which it is estimated (Left) or to the image containing the planetary signals (Middle). Right: Position of the companions, the redder are the brightest objects.

In the next section, I run the full MEDUSAE procedure, which alternates the object and phase estimation, on the images containing the five planetary signals.

9.2.3 Estimating the object map with MEDUSAE

The data set used in this section is the SPHERE-like data set in YJ band (including the spiders, the central obstruction, the apodization and using $N_{exp} = 250$, as on Fig. 9.6). In order to estimate the object, I used a regularization favoring the L1 norm by choosing the hyper-parameters $\delta = 100$ and scale= 0.05. To run MEDUSAE, I used a null weight map only in the central part (below $4\lambda/D$) so that the process could run faster.

The whole MEDUSAE algorithm ran in 12h for the 6 wavelengths. The star flux is estimated with a relative error of 0.67%. The estimated speckle field is estimated with an average mean square error of 22.44% for the six wavelengths (compared to the images without the planetary companions). However, when estimating the mean square error of the estimated speckle field with respect to the input images (containing the planetary signals), we obtain 7.14%. This means that the estimated speckle field contains part of the planetary signals.

Fig. 9.15 shows the estimated upstream phase at the end of the process and Fig. 9.16 the corresponding speckle field in the corrected zone. It is very difficult to spot the brightest planetary signal in the residual speckle field since it has a very low SNR of about 0.01 at the exact location of the companion and taking the noise variance in an annulus centered around the star and of width 10 pixels arround this location.

Fig. 9.17 shows the evolution of the estimated object when incorporating the wavelengths one by one in the main MEDUSAE procedure (from 2 to 6 wavelengths). The object map shows more and more radial elongated features that clearly belong to the speckle field. None of the injected companions is visible and therefore their flux is not correctly estimated.

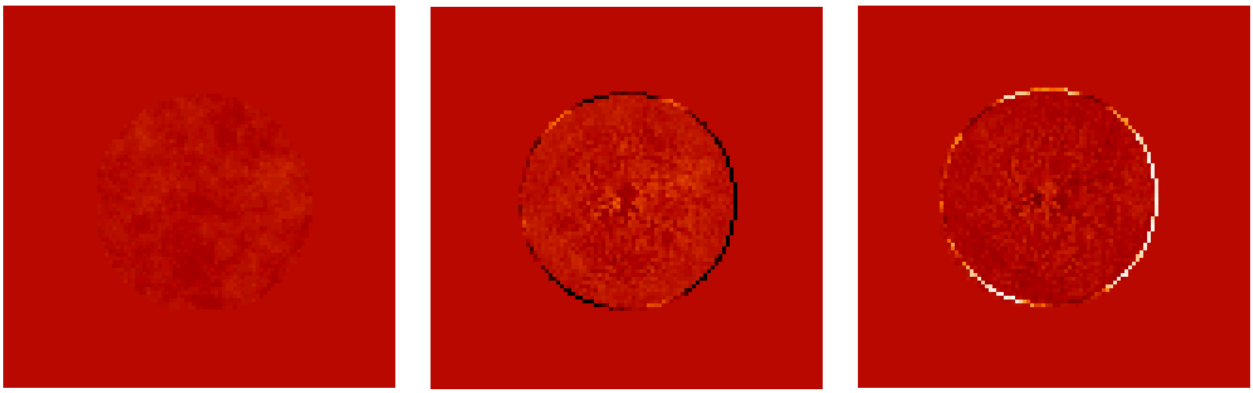

Figure 9.15 – Results from the whole MEDUSAE process. From left to right: Input upstream phase, estimated upstream phase and residuals (same scale).

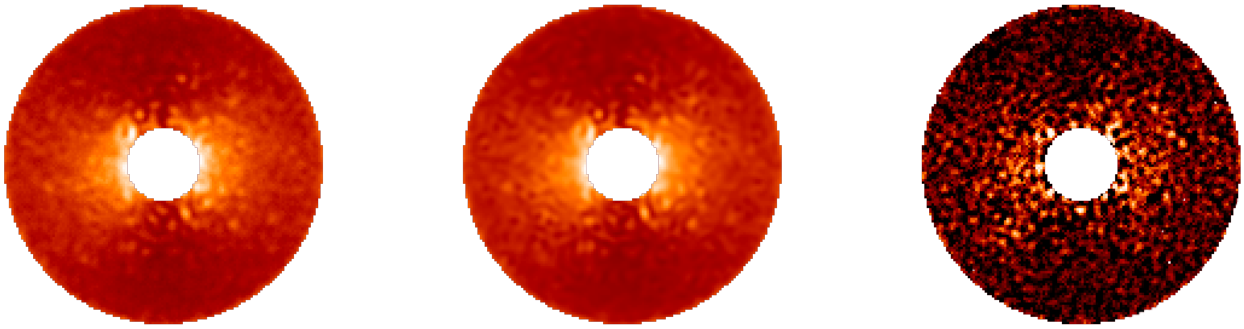

Figure 9.16 – Results from the whole MEDUSAE process. From left to right: Input image, estimated speckle field and residuals (times ten for better visibility).

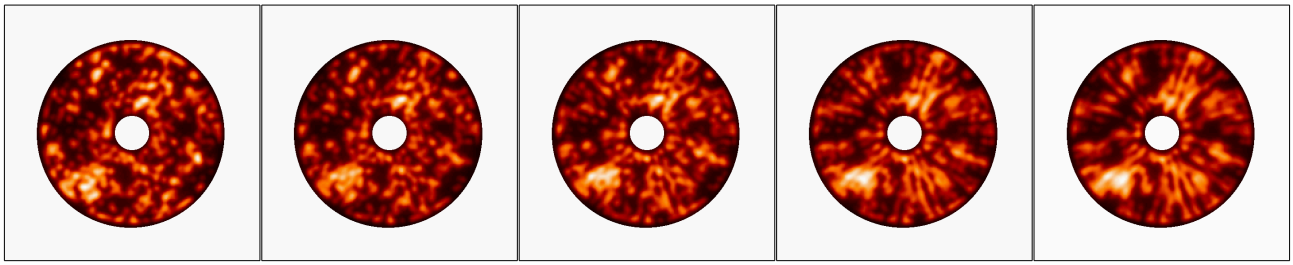

Figure 9.17 – Evolution of the estimated object when incorporating the wavelengths one by one in the main core of MEDUSAE (from left to right).

From these results we can conclude that for now, MEDUSAE does not allow one to estimate the object map since part of the object light is fitted by the phase. Before discussing further the object regularization applied that is not appropriated, one should find a way in better estimating the speckle field to reach a higher contrast.

Conclusions on the MEDUSAE method updates

In this chapter, I produced data sets that are very similar to the real data provided by the SPHERE-IFS instrument. Such realistic data sets allowed me to test several aspects of the PSF reconstruction performed by MEDUSAE. Thanks to the modifications I implemented in the code and in the inversion strategy, it is now possible to reproduce the speckle field with a mean squared error between 5% and 8% from the realistic simulated data. For these data, both the ϕ_{down} and $D_{\phi_{res}}$ are known and

provided as input to MEDUSAE. However, due to the residual noise, these 7% are not sufficient for the algorithm to detect planetary signals of contrast above 10^{-4}. From the results presented in this chapter, several immediate aspects must be investigated thanks to these realistic simulated data:

1. the gradient of the criterion used for the algorithm decent should include the pupils features (apodization, spider and central obstruction);
2. the regularization on the object map deconvolution is not immediate and must be further investigated;
3. the sensitivity to the required inputs $D_{\phi_{res}}$ and ϕ_{down} must also be carefully investigated.

During my PhD, I specifically explored the adaptation of the MEDUSAE inversion procedure to the real on-sky data from the SPHERE-IFS instrument. To do so, I first ran MEDUSAE on the inverse crime data set in order to better understand what are the most important inputs and the sensitivity of the algorithm to the expected real data characteristics. To go further in this direction, I then simulated realistic SPHERE-like data which implied to modify the inversion procedure in order to handle these non-ideal data. I performed several tests on these data and I presented the major results I obtained in the previous chapter. However, during my PhD, I did not revisit the criterion descent procedure which should be the next step towards application on real data.

In the next section, I propose several perspectives on both short and long term, which should increase the performance of the MEDUSAE algorithm while making it ready to process on-sky data from the SPHERE-IFS instrument.

9.3 Perspectives for the MEDUSAE methods

In the light of the preliminary tests presented in this chapter, I identified several perspective on both short and long term.

Short-term perspectives of MEDUSAE

Thanks to the applications of MEDUSAE presented in this manuscript, there are three main points that deserve to be carefully looked at in order to make MEDUSAE suitable to process on-sky data (in the order of importance): the discrepancy between the coronagraphic PSF model used in the inversion and the real coronagraphic PSF, the required residual phase structure function $D_{\phi_{res}}$ and the required downstream phase. In the following, I describe potential solutions that could be investigated to address these points.

The ideal coronagraphic model used in the inversion

Even though setting a null weight map in areas where the model does not match the real input images is efficient, there is still some discrepancies that must be alleviated by modifying the model used for the inversion. On short term, the analytical expression of the gradients must be carefully checked and should include any kind of pupils. This operation would then make it possible to include the spiders, the central obstruction and the pupil apodization in the inversion model.

Testing the sensitivity to the required input $D_{\phi_{res}}$ and ϕ_{down}

Another important aspect is that, thanks to the realistic simulated data, it is now possible to investigate the response of MEDUSAE to different $D_{\phi_{res}}$ and ϕ_{down} provided in input (as on the inverse crime data set, presented in Sect. 8.4).

Dealing with the knowledge of $D_{\phi_{res}}$ According to both inverse crime tests and preliminary tests on in-lab data, the $D_{\phi_{res}}$ must be provided to MEDUSAE with a good accuracy. I elaborated tools and a protocol to generate a $D_{\phi_{res}}$ which empirically corresponds to the real images properties (with a small number of degrees of freedom, as presented in Sect. 9.1.4). Thanks to this method, I generated an ad-hoc $D_{\phi_{res}}$, based on the real data radial profile structure compared to the ideal coronagraphic PSF radial structure (see App. D). In particular, checking if this *representative* $D_{\phi_{res}}$ is an efficient and reliable method would bring a non-negligible step further since the $D_{\phi_{res}}$ unknown is now the most important parameter required to run MEDUSAE on real data. Alternatively, it will also be possible to explore possibilities to avoid needing this input:

(1) We can find a way to remove it from the images (by filtering or smoothing for instance) and ignore it in the PSF reconstruction made by MEDUSAE.

(2) If the upstream phase succeeds in fitting the speckles only (stellar halo above the corrected zone), then the light from the $D_{\phi_{res}}$ should go in the object image. It might be possible to a posteriori remove this contribution in the object map, providing that its characteristics are known (but it would probably prevent from detecting extended structures such as disks). Moreover it might work at one wavelength but it can be problematic at two or more wavelengths.

(3) We can try to analytically estimate the $D_{\phi_{res}}$ from the images, similarly to Sauvage et al. (2006) which is in a non-coronagraphic context.

(4) One could find an instrumental calibration that would help obtaining this $D_{\phi_{res}}$, by for instance using the SH-WFS slopes.

(5) Lastly we could create a library of images generated with different $D_{\phi_{res}}$ and compare these images to the real one to find an appropriate approximated $D_{\phi_{res}}$. In order to automatically find the approximated $D_{\phi_{res}}$, a correlation criterion could be used between the real image and the images of the library.

Dealing with the knowledge of ϕ_{down} According to the inverse-crime tests, this parameter is less critical but it is still required to provide MEDUSAE an accurate downstream aberration map which has less than 50% errors. These downstream aberrations are expected to be quite low and stable over an observation night time scale. Thus an appropriate calibration could provide this input. Several solutions can be investigated to deal with this required input:

(1) The phase diversity can be an option although it is difficult to get a high SNR data over a large range of separation to the star, and thus to obtain accurate measurements for numerous aberration modes.

(2) An estimation of the downstream aberrations as in COFFEE (Paul et al., 2014) which is also based on an inverse problem approach by making use of the phase diversity on coronagraphic images.

(3) In this part, I dealt with one multispectral cube taken at one single moment. However, the SPHERE-IFS instrument, which is used simultaneously to SPHERE-IRDIS provides a certain amount of multispectral cubes in pupil tracking mode. On a longer term perspective, one could make use of the temporal diversity to specifically estimate this input since it is the only parameter that is constant in all these multispectral image cubes.

Finding a correct starting point for ϕ_{up} In order to launch the MEDUSAE algorithm, a good starting point is required. For now, the starting point is a phase map with an extremely small rms wavefront error. One idea would be to use the same approach as in MEDUSAE but on the reference PSF (non-coronagraphic PSF) provided in the reduced data set in order to estimate the upstream phase (while either assuming that the downstream phase is negligible or estimating this downstream phase also from the reference images). Another approach is to use phase diversity to estimate this starting point, directly from the coronagraphic images.

Mid-term perspectives of MEDUSAE

Once MEDUSAE is operational, other general aspects could be modified in the algorithm to provide more accurate estimations.

Modifying the spatial regularization for the object deconvolution As discussed in Sect. 8.3, the object map is estimated by a MAP approach, including a spatial regularization on the object. In order to find a sparse object (a very few planetary signals that are Dirac peaks in the object map), a truly L1 regularization seems more appropriated than the current L1L2 or L2 regularizations implemented. However, a L1 regularization is no longer derivable and the VMLM-B descent algorithm cannot converge. A specific criterion descent algorithm should be implemented to use a L1 spatial regularization on the object map (such as ADMM as in Mourya et al., 2015b or ALBHO, as in Mourya et al., 2015a).

Another interesting perspective is to implement a L0-norm regularization in order to increase the sparsity of the estimated object map. However in that case also, the L0 norm is not continuous at the zero point and it is impossible to compute the gradient of the criterion at this point. Specific descent algorithm to solve this non-convex optimization problem has also to be investigated.

Optimizing the computing time As showed in this section, the MEDUSAE algorithm is quite long to run (up to several hours for one image). In order to reduce this computing time, one can either parallelize some of the calculations or constrain the convergence.

Longer-term research axis to make MEDUSAE operational on real data

To refine the concept of MEDUSAE, further prior knowledge can be implemented in the method thanks to its Bayesian formalism. I propose several starting points to be explored in that framework.

Implementing further knowledge: spectral information on the star For now, no prior is used on the stellar spectrum whereas it is expected to be smooth (following a blackbody shape and the star flux is usually calibrated in one or more spectral bands). Moreover it is very easy to calibrate the trend of the stellar spectrum either directly from the reduced images or from specific calibration files (using the non-coronagraphic reference PSF taken before and/or after the observation). This would help raising the degeneracy between the stellar flux and the upstream phase.

Implementing further knowledge: spectral information on the object Several models of planetary spectra have been derived in the literature (as in Baudino et al., 2015). This knowledge could be implemented to "help constraining" the estimated spectra of the object map. Note that for now, the spectrum is extremely constrained since it is forced to show a gray spectrum. Moreover, for now, only one object map is provided with one star spectrum estimation that is to say the objects of the maps have the same spectrum.

This MEDUSAE algorithm is still very promising since it enables to estimate the speckle field (similar to the model PSF in the differential imaging methods) by taking into account the instrument design instead of relying on an empirical subtraction methods (as for the differential imaging methods). The alternate estimation of the object map and aberrations defined by a reliable criterion is an innovative step in image processing for exoplanetary science. Moreover, for future instruments, the instrument design, calibration protocol and post-processing method could not be separately established and these three aspects have to be co-designed. For these reasons, studies to make the MEDUSAE suitable to process real data should really be carried on.

Résumé en français de la partie 2 : l'algorithme MEDUSAE

Dans ce chapitre, je résume en langue française les points-clés de chaque chapitre constituant la seconde partie du manuscrit. Cette partie concerne l'algorithme MEDUSAE (pour *Multispectral Exoplanet Detection Using Simultaneous Aberration Estimation*) dont le but est de détecter et extraire les spectres d'objets circumstellaires dans des images coronographiques multispectrales. Cette méthode exploite la diversité spectrale des images en utilisant une méthode de résolution de problèmes inverses dans le cadre Bayésien.

Le concept et la mise en place des bases de cette méthode ont été publiés par Ygouf et al. (2013) pendant sa thèse de doctorat. Le principe de l'algorithme a été validé sur des données simulées idéales qui utilisent le même modèle que celui utilisé pour l'inversion (Chap. 7). Le but de mon travail de thèse a été de préparer l'algorithme à une application sur données ciel. Avant l'application à des données réelles, il restait à faire des tests de sensibilité sur ces données simulées idéales (Chap. 8). Par la suite, une étape intermédiaire consistant à étudier les réponses de l'algorithme à des données simulées réaliste (crées avec un modèle différent, qui s'apparente plus aux propriétés des instruments actuels) s'est avérée nécessaire pour mieux comprendre le fonctionnement de MEDUSAE (Chap. 8). Ce travail à mis en valeur de nombreuses perspectives afin de faire correspondre le modèle utilisé dans l'inversion aux propriétés des images réelles et de gérer les informations dont a besoin l'algorithme afin de pouvoir traiter les données (Sect. 9.3).

Principe de l'algorithme MEDUSAE

Chaque image du cube multispectral peut être décrite comme la superposition de l'image de l'étoile (le champ de speckles), l'image des objets circumstellaires (planètes ou disques) et le bruit (considéré comme gaussien car le flux dans l'image est élevé).

L'image de l'étoile est l'image d'un point source à travers le système incluant le coronographe. Pour modéliser l'image de l'étoile, un modèle de réponse impulsionel coronographique longue pose est requis. Dans MEDUSAE, c'est un modèle analytique qui est utilisé, en considérant un coronographe dit *idéal*, c'est-à-dire qui supprime toute la partie cohérente du faisceau incident et qui laisse cependant passer la lumière de l'étoile déviée par les aberrations résiduelles de l'instrument (statiques ou non). Ce dernier est parametrisé par les aberrations statiques avant et après le coronographe et les aberrations variables temporellement (essentiellement les résidus non-corrigés par l'optique adaptative). Seulement les aberrations statiques *avant* le coronographe sont supposées dominantes et inconnues. Ces aberrations dites *upstream* (en aval du coronographe) sont estimées en même temps que les objets d'intérêt. Au lieu d'estimer la phase responsable de ces aberrations dans le plan focal, la différence de chemin optique est estimée car c'est une grandeur achromatique au premier ordre : une seule carte de différence de chemin optique est capable de représenter le champ de speckles à toutes les longueurs d'onde du cube d'images multispectrales.

L'image des objets est la convolution de l'objet avec la réponse impulsionnelle de l'instrument hors axe (donc non-coronographe), dont le modèle dépend aussi des aberrations résiduelles de l'instrument. L'algorithme MEDUSAE n'estime pas chaque objet séparément comme dans ANDROMEDA, mais estime une carte objet bidimensionnelle.

Dans ce cadre, les paramètres d'intérêt Ã estimer sont bien plus nombreux que dans le cas d'ANDROMEDA et peut se fait par maximum a posteriori, c'est-à-dire un critère d'attache aux données (maximum de vraisemblance dans ce cas) auquel des termes de régularisation sont ajoutés pour contraindre l'espace des paramètres explorés. Les régularisations actuellement incluses dans l'algorithme concernent le flux de l'étoile centrale et la forme des objets.

Une fois le modèle défini et le critère à minimiser déterminé, le choix de la stratégie de minimisation s'est reporté sur une minimisation alternée en deux étapes qui se répètent jusqu'à convergence vers un minimum global : (1) à objet supposé connu, le champ de speckles est estimé par diversité de phase (ici une descente locale par gradients conjugués qui sont calculés analytiquement à partir du modèle de réponse impulsionnelle coronographique longue pose idéal évoqué plus haut), qui estime conjointement l'intensité de l'étoile et les aberrations dites upstream; puis (2) à aberrations connues, la carte objet est estimée par une déconvolution non-myope classique.

Le point dur de la méthode est la diversité de phase. En effet, le modèle est très non-linéaire et il existe de nombreux minimum locaux. Afin d'éviter ces minimums locaux, pendant sa thèse de doctorat, M. Ygouf a développé un schéma de minimisation qui en particulier démarre d'une petite phase upstream aléatoire et explore les phases quasi-équivalentes correspondantes (c'est-à-dire qui sont différentes mais qui donne les mêmes champs de speckle). Ce schéma propsé est un bon point de départ pour mon travail de thèse.

Raffinement de la méthode sur données simulées idéales

À ce stade, il reste à vérifier le bon fonctionnement de ce schéma de minimisation et l'impact de la bonne connaissance des autres paramètres à donner en entrée. Pour cela je continue à travailler avec les données simulées idéales qui sont générées en utilisant le même modèle que celui inclu dans l'inversion. Le résultat de ces tests approfondis permet d'obtenir les résultats ultimes que peut fournir MEDUSAE puisqu'il s'agit d'un cas optimal où les données correspondent exactement au modèle.

Après avoir défini les critères sur lesquels les résultats sont jugés (Sect. 8.1.2), je me concentre d'une part sur l'étape de phase retrieval seule puis je revisite chaque étape mise en place dans l'algorithme, en discutant spécifiquement les aspects qui me semblent critiques et que j'ai définis dans le chapitre précédent (Sect. 8.2). Une fois le schéma d'inversion optimisé, MEDUSAE est capable, dans ce cas idéal, de détecter des compagnons de contraste 5.10^{-7} à une séparation de $0.3''$avec une erreur de 2% sur le contraste estimé. Ce résultat est bien plus performant qu'attendu par les méthodes classiques de traitement d'images multispectrales qui sont utilisées aujourd'hui motivant ainsi la poursuite du travail sur cette méthode originale qui traite les données dans leur ensemble.

Par la suite, j'ai condui des tests de sensibilité sur cette version mise à jour de MEDUSAE. Dans un premier temps, j'examine si l'étape de phase retrieval est corrompue par la présence d'un compagnon très intense dont la lumière pourrait être considérée par l'algorithme comme venant de l'étoile (Sect. 8.3). Cela est le cas lorsqu'un compagnon de contraste 1.10^{-4} est injecté à une séparation de $0.4''$: le processus d'inversion est deux fois plus long et l'erreur sur l'estimation de flux augmente (passant de 5% à 6.4% pour un compagnon de contraste 1.10^{-6} situé à $0.22''$). Dans un second temps, j'examine la sensibilité de l'algorithme aux deux paramètres d'entrée requit par l'algorithme (Sect. 8.4). L'un de ces deux paramètres, concernant la fonction de structure de la phase résiduelle turbulente, doit être connu précisément pour pouvoir estimer correctement le champ de speckles et ne peut pas être remplacé par une valeure nulle ou obtenue avec des conditions d'observations différentes (en terme de seeing et de vitesse de vent). Pour le second paramètre, qui est la phase statique après le coronographe, sa structure spatiale doit être connue exactement mais son niveau rms peut varier jusqu'à 50% sans impacter les résultats de façon conséquente.

Cependant, en vue de l'application de MEDUSAE sur données ciel, un effet dominant qui risque d'affecter ces résultats de façon non négligeable est le fait qu'il s'agit d'un cas idéal où le modèle d'image coronographique utilisé correspond parfaitement aux données. Pour tester la réponse de l'algorithme à un coronographe différent du modèle, j'ai dans la suite appliqué MEDUSAE à des données simulées avec un modèle de coronographe différent, plus proche de ce qui est effectivement obtenu avec les

instruments actuels tel que SPHERE/IFS.

Tests sur données simulées réalistes

Le but de ces données simulées réalistes est de travailler uniquement sur la différence entre la réponse coronographique utilisée dans le modèle (idéale) et celle utilisée pour générer les données (réaliste), tout en connaissant parfaitement les autres paramètres (en particulier la fonction de structure de phase résiduelle et la phase statique post-coronographe). Afin d'obtenir de telles données, j'ai utilisé un modèle de coronographe de Lyot apodisé (APLC; comme celui utilisé aujourd'hui dans SPHERE/IFS), en utilisant une propagation de la lumière plan par plan via transformé de Fourier. J'ai ainsi généré des images avec les mêmes propriétés en terme de taille, d'échantillonage et de canaux spectraux que les images de SPHERE/IFS. Le résultat est un cube de 39 images dont le comportement spatial et spectral est très similaire à celui des images réelles obtenues avec SPHERE/IFS (Fig. 9.6).

La première tentative posait un problème fondamentale : MEDUSAE essaye d'ajuster les images via la construction d'une phase (phase retrieval) mais tout en utilisant le modèle idéal. En d'autres termes, même si la vraie phase était parfaitement connue, la minimization ne pourrait converger puisque le modèle ne correspondrait jamais aux données. Or le but de MEDUSAE est d'estimer la phase amont pour décrire correctement le champs de speckle. Cependant MEDUSAE réussit à fournir certaines structures spécifiques du champs de speckle au détriment d'une phase estimée complétement différente. Le but final étant de retrouver le champ de speckles, ceci pourrait ne pas poser de problèmes. Cependant, la phase qui est estimée crée des artefacts hautes fréquences très spécifiques (mouchetures) dans le champ de speckles, qui sont dus à des basses fréquences non incluses dans la phase estimée.

Afin de contourner ce problème, il faut réaliser que la différence principale entre le modèle idéal et le coronographe réaliste est essentiellement due à la partie centrale, en deçà de $3\lambda/D$. Or dans le critère à minimiser, le critère d'attache aux données est pondéré par l'inverse de la variance de bruit qui est une entrée requise de l'algorithme (calculée empiriquement directement à partir des données). Si cette carte de poids est forcée à zéro dans la zone centrale, l'algorithme va ignorer complètement cette région centrale lors de l'inversion. Grâce à cette astuce, le champ de speckles estimé diffère de seulement 4% du vrai champ de speckles et le niveau de résidus à $0.3''$entre ces deux champs est de l'ordre de 3.10^{-6}.

Une fois cette solution trouvée, j'ai pu étudier l'impact de certains paramètres des images tels que le temps de pose et la plage de longueur d'onde parcourue par les images. Comme le modèle analytique suppose une très longue pose, plus les images sont longue pose, plus les estimations sont correctes. Concernant la diversité spectrale, augmenter la plage de longueur d'onde n'aide pas forcément à obtenir de meilleures estimations car le coronograph est adapté pour une longueur d'onde spécifique et l'achromaticité du modèle est plus difficilement vérifiée en pratique. D'autre part, ajouter les éléments tels que l'occultation centrale du télescope et les spiders dans les données reduit les performances puisque ces éléments ne font pas partie du modèle.

Ces tests ont été réalisés sur des données ne contenant pas de planètes afin de vérifier si le champ de speckles pouvait être correctement estimé. Cependant, lorsque des compagnons planétaires sont ajoutés dans les images, MEDUSAE ne réussit pas à récupérer la carte objet correspondante. Une partie de la lumière de l'étoile est considéré comme appartenant à l'objet et corrompt la carte objet estimée. Cependant, avant de travailler sur la régularisation qui est appliquée à l'objet, il faut d'abord pouvoir augmenter la capacité de MEDUSAE à correctement estimer le champ de speckles avec une meilleure précision qu'actuellement.

Conclusion de la partie 2

À ce jour, l'algorithme MEDUSAE n'est pas capable de traiter des données réelles. Il faut dans un premier temps continuer à explorer les obstacles qui existent à l'aide de ce jeu de données simulées réalistes.

Dans un premier temps, il faudrait modifier le modèle utilisé pour qu'il soit le plus proche possible des données (incluant l'apodiseur, les spiders et l'occultation centrale du télescope). Ce point requiert de modifier le calcul des gradients analytiques utilisés pour la minimisation. Dans la même approche, les données doivent êtres prises dans des conditions proches du modèle en particulier, il faut faire de très longues poses et de préférence utiliser un coronographe qui s'approche plus du modèle idéal (tel que le VVC).

Dans un second temps, il faut travailler sur la régularisation spatiale imposée à l'estimation de l'objet. Une fois l'algorithme capable de retrouver les compagnons planétaire présents dans les images simulées réalistes, il faudra mettre en place des simulations où le spectre de la planète n'est pas plat comme dans les données simulées utilisées jusqu'à présent et vérifier que MEDUSAE estime correctement et précisément le spectre des compagnons. Comme pour ANDROMEDA, il sera alors possible de développer une méthode de détection automatique à partir des sorties de MEDUSAE qui trie les détections et fournit les données requises par les astronomes.

Dans un dernier temps, avant l'application à des données ciel, il faudra s'assurer d'avoir en main toutes les entrées nécessaires à l'algorithme. Pour cela, plusieurs solutions logicielles ou matérielles peuvent être examinées. (1) Concernant la fonction de structure de phase résiduelle, on peut par exemple à l'aide d'un simulateur essayer de reproduire cette grandeur. Sinon, la lumière due à la phase résiduelle va se retrouver dans l'objet et pourrait être retirée a posteriori (par un filtrage adapté par exemple). On pourrait aussi estimer analytiquement cette grandeur à partir des images. Ou encore, certaines données venant de l'instrument pourraient être exploitées pour retrouver cette grandeur (comme les pentes du SHWS ou des informations provenant du DDTS). Si aucune de ces solutions n'est efficace, on pourrait créer une libraire avec différentes fonctions de structure de phase résiduelle et choisir dans cette librairie celle qui correspond le mieux aux images. (2) Concernant la phase statique en aval du coronographe, elle peut être estimée par diversité de phase ou avec un analyseur spécifique inclu dans l'instrument qui fournirait ainsi le fichier de calibration requit.

Par son approche innovative, MEDUSAE permettrait d'exploiter au mieux les données venant des instruments à haut contraste, en collaboration étroite avec les instrumentalistes. MEDUSAE se fonde sur un modèle fin d'imagerie qui prend en compte tous les éléments du système. Afin de rendre cette méthode opérationnelle sur données réelles, il reste quelques tests spécifiques à conduire et des modifications à apporter à l'algorithme. Pendant ma thèse de doctorat, j'ai fait avancer ces tests d'une étape importante en réalisant des tests sur données simulées réalistes et en mettant en place un plan de travail pour répondre aux différentes conditions nécessaires pour faire fonctionner MEDUSAE sur des images venant des grands télescopes.

General conclusion

Conclusions of ANDROMEDA

All along the first part of the thesis, I highlighted the original approach of ANDROMEDA, and laid the emphasis on its advantages and drawbacks about its fundamental approach, its practical and numerical implementation and eventually, about its numerous on-sky applications. I summarize here the most important points to be reminded:

- ANDROMEDA relies on an innovative and original approach to the ADI-based methods: the ADI is used as a mean to build differential data (with a lower level of stellar halo, but also, with better statistical properties), and not as an end; the key point of the method being the maximum likelihood estimation of both the position and the flux of any point source present in the field of view.
- ANDROMEDA is operational on real data and shows good performance in terms of detection, comparable to the current state-of-the-art image processing methods. In addition, it is the only method which performs an automatic detection which moreover relies on concrete statistical tools. The detection becomes objective and does not rely on the users acuteness contrary to the other existing methods.
- ANDROMEDA estimates the sub-pixel position of the detected companion and the contrast of the detected companion directly, without bias. This is the first method which does not require tedious post-processing to estimate the companions contrast.
- ANDROMEDA is the only method directly providing the detection limit at the same time and for every pixel of the image field. It has been checked that the latter is fully consistent with the detection capabilities of the algorithm.
- On practical aspects, the ANDROMEDA pipeline runs very fast and its ergonomics brings valuable and convenient information about the truthfulness of the detections.
- ANDROMEDA has been applied on various instruments (NaCo, SPHERE, GPI), under different observation conditions and observation modes (DBI, BB, IFS etc.). Each time, the pipeline has proved very efficient and its applications led to reflections about possible improvements. From a fine analysis on the user-parameters sensitivities, it appears that only one user-parameter needs to be fine tuned. Thus ANDROMEDA can be used in a quasi-systematic way on various data sets.
- At last, thanks to its formalism, it is relatively easy to add prior knowledge in ANDROMEDA to make it more efficient.

Thanks to all of these specificities, ANDROMEDA proved able to detect stellar companions that were not detected by other methods (such as GJ504 b in J2 band or Eri51 b in H2 band) and provided the corresponding contrast estimation even though these companions are very faint. As post-processing is not required to obtain the flux, ANDROMEDA can derive a spectrum even when the companion is very faint. This new operational tool must be considered for further applications on either older data or on-going surveys such as the SPHERE GTO survey SHINE or any surveys using high-contrast

imaging with a relative imaging bandwidth below 17%.

As for the other ADI-based algorithms, the fundamental limitation of ANDROMEDA arises from the diversity used which prevents from detecting companions at very close separation with current instruments: at close separation, the companions are not moving enough azimuthally for the given correlation time of the speckles.

Conclusions of MEDUSAE

In the second part of the thesis, I described preliminary results from an innovative algorithm for exoplanet imaging, called MEDUSAE. My work on this algorithm underlined the necessity of having specific calibrations to make this MEDUSAE concept able to process on-sky data. These calibrations can be obtained by hardware solutions that are currently being considered for their implementation in SPHERE and other high-contrast instruments since they are essential to reach the ultimate capabilities of the instrument. I summarize here the most important points to be reminded:

- The originality of MEDUSAE is that it estimates both the aberrations that are responsible for the speckle field and the objects surrounding the central star. In the future, this joint estimation will be essential to optimally exploit the high contrast instruments.
- This joint estimation relies on an imaging model which takes into account the AO correction and the coronagraph. The spectral diversity is used to disentangle the planetary signal from the speckle field in the images. Moreover, the Bayesian framework makes it possible to include prior knowledge on either the instrument or the astrophysical object.
- Thanks to a crime inverse data set, I revisited the inversion strategy of MEDUSAE in two steps. (1) During the initialization procedure, necessary to obtain a good starting point of the estimated aberration map, the object estimation is used to relax the constraints on the phase estimation by phase retrieval. The object retrieved during the initialization is not realistic and is not taken into consideration. (2) From this estimate of the upstream phase, the companion is estimated using specific regularizations in the main MEDUSAE procedure which uses two or more wavelengths. By doing so, I could recover a synthetic companion of 5.10^{-7} at $0.3''$.
- From tests conducted on simulated data and preliminary tests on real data, the major obstacle with the current version of MEDUSAE is due to the disagreement between the coronagraphic PSF model used and the real data. This problem mainly affects the central part and I proposed solutions to tackle this issue: a null weight map in the central part (below $4.5\lambda/D$) helps estimating the speckle field with a 4 to 7% error.
- A second obstacle is that the algorithm needs inputs that motivate new accurate instrumental calibrations: the downstream phase ϕ_{down} and the residual phase structure function $D_{\phi_{res}}$.

Solutions have to be investigated to address the latter issue. The development of this algorithm motivates working in close collaborations with instrumentalists to find appropriate solutions. More specifically, in the current landscape of instrument design for the ELTs, working on such an algorithm is essential to foresee the needed instrumental specifications and calibrations. Moreover such a solution is worth exploring since the current state-of-the-art post-processing methods are based on differential imaging, which affects the planetary signal.

During this PhD, I studied two different algorithms, one directly replying to the current needs of the exoplanet imaging community and the other being an upstream study for long term solutions to exoplanet imaging. From these aspects, I could work with astronomers and instrumentalists and be aware of the main stakes of exoplanet imaging with high contrast instrument.

Résumé en français de la conclusion

Durant ces trois années de thèse, j'ai travaillé à l'interface entre l'instrumentation et l'astrophysique dans le domaine du traitement d'images pour la détection et à la caractérisation d'objets circumstellaires dans des images venant d'instruments à haut contraste. J'ai commencé mon travail à partir de deux algorithmes, ANDROMEDA et MEDUSAE, dont les bases avaient déjà été mises en place et validées sur des données simulées. Mon but a été de faire le lien entre le modèle théorique mis en place et les propriétés réelles des images afin de rendre ces algorithmes opérationnels sur des données venant d'instruments haut contraste. Pour cela, j'ai suivi une approche systématique consistant à simuler des images pour examiner chaque étape de ces algorithmes, faire des tests pour en analyser les performances, faire une analyse de sensibilité poussée et, une fois la méthode capable de traiter des données réelles, j'ai mené une comparaison détaillée avec les autres méthodes qui font l'état de l'art.

ANDROMEDA est une méthode dédiée à l'extraction de points sources dans des images haut contraste prises en suivi de pupille. Le point-clé de cette méthode est de faire une estimation par maximum de vraisemblance dans des données préalablement soustraites angulairement. Cet algorithme est maintenant complètement opérationnel sur données réelles et permet : (i) de faire une détection non-supervisée, (ii) d'estimer le flux des compagnons de façon non-biaisée, (iii) de fournir des incertitudes et une limite de détection cohérentes avec les données, (iv) d'estimer la position sub-pixel du compagnon et (v) de délivrer très rapidemment les résultats, en seulement deux étapes, et avec seulement un paramètre utilisateur à régler finement. ANDROMEDA a été appliqué sur de nombreuses données venant de différents instruments et a prouvé son efficacité et sa pertinence dans le paysage actuel. En plus des nombreuses applications possibles, des perspectives pourraient permettre d'améliorer notablement la méthode (e.g. l'implémentation du modèle correspondant à une soustraction spectrale puis angulaire, une méthode pour choisir les images les plus corrélées pour les soustraire ou pour éviter la soustraction angulaire qui limite la méthode à petite séparation).

MEDUSAE est une méthode dédiée à l'extraction de spectre des objets circumstellaires présents dans des images multispectrales haut contraste. L'idée-clé est d'estimer à la fois les aberrations responsables du champ de speckle et une carte objet. De plus cette méthode se fonde sur l'exploitation des connaissances de l'instrument (dans un cadre Bayésien) et utilise un modèle d'imagerie précis. Les études en cours sur les images simulées réalistes ont montré que mettre un poids nul au centre de l'image où le modèle et les images réelles ne correspondent pas est une bonne solution pour estimer le champ de speckle. Afin de rendre cette méthode opérationnelle sur des données réelles, de nombreuses perspectives ont été définies et consistant essentiellement à améliorer le modèle d'une part et à trouver un moyen d'obtenir les calibrations nécessaires d'autre part.

En conclusion, la recherche en traitement d'images pour détecter les objets circumstellaires dans des images haut contraste est prometteuse et dynamique, avec l'arrivée de récents instruments tels que Gemini/GPI, VLT/SPHERE et Subaru/CHARIS et la conception en cours des futurs instruments pour les ELTs tels que E-ELT/METIS et E-ELT/MICADO. Comme prouvé par les résultats donnés par ANDROMEDA, l'approche par problème inverse est une solution intéressante pour contourner les problèmes actuels qui se posent en traitement d'images haute dynamique. La recherche pour développer des algorithmes poussés qui utilisent un maximum d'information venant de l'instrument mérite d'être poursuivie : les résultats d'une telle recherche en terme astrophysique ont déjà prouvé l'importance d'avancer dans cette direction (par les découvertes de nouveaux compagnons ou disques dans d'anciens jeux de données et le raffinement des analyses des objets connus) ce qui permettrait un gain non négligeable en modifiant très peu ou pas du tout les instruments existants.

Appendix A

Publication on the ANDROMEDA pipeline applied on VLT/NaCo data

The publication presented hereafter demonstrates the capability of ANDROMEDA to process real data from the VLT/NaCo instrument. In this paper, I first describe the whole algorithm (including the updates I have implemented), as well as the toolbox developed to extract the astrophysical information from the ANDROMEDA output. I then present the performance of the algorithm applied on a test case in which 20 synthetic companions have been injected in order. I finally present a comparison of the ANDROMEDA performance with the PCA algorithm on L' NaCo data of β Pictoris .

Astronomy & Astrophysics manuscript no. Andromeda
August 25, 2015

Direct exoplanet detection and characterization using the ANDROMEDA method: Performance on VLT/NaCo data⋆

F. Cantalloube[1,2,3], D. Mouillet[1,3], L. M. Mugnier[2], J. Milli[1,3,4], O. Absil[5,⋆⋆], C. A. Gomez Gonzalez[5], G. Chauvin[1,3], J.-L. Beuzit[1,3], and A. Cornia[2]

[1] Univ. Grenoble Alpes, IPAG, F-38000 Grenoble, France
e-mail: faustine.cantalloube@obs.ujf-grenoble.fr
[2] Office National d'Etudes et de Recherches Aérospatiales (ONERA), Optics Department, BP 72, 92322 Châtillon, France
[3] CNRS, IPAG, F-38000 Grenoble, France
[4] European Southern Observatory (ESO), Alonso de Còrdova 3107, Vitacura, Casilla 19001, Santiago, Chile
[5] Département d'Astrophysique, Géophysique et Océanographie, Université de Liège, Allée du Six Août 17, 4000 Liège, Belgium

Received December 22, 2014; accepted August 04, 2015

ABSTRACT

Context. The direct detection of exoplanets with high-contrast imaging requires advanced data processing methods to disentangle potential planetary signals from bright quasi-static speckles. Among them, angular differential imaging (ADI) permits potential planetary signals with a known rotation rate to be separated from instrumental speckles that are either statics or slowly variable. The method presented in this paper, called ANDROMEDA for *ANgular Differential OptiMal Exoplanet Detection Algorithm* is based on a maximum likelihood approach to ADI and is used to estimate the position and the flux of any point source present in the field of view.

Aims. In order to optimize and experimentally validate this previously proposed method, we applied ANDROMEDA to real VLT/NaCo data. In addition to its pure detection capability, we investigated the possibility of defining simple and efficient criteria for automatic point source extraction able to support the processing of large surveys.

Methods. To assess the performance of the method, we applied ANDROMEDA on VLT/NaCo data of TYC-8979-1683-1 which is surrounded by numerous bright stars and on which we added synthetic planets of known position and flux in the field. In order to accommodate the real data properties, it was necessary to develop additional pre-processing and post-processing steps to the initially proposed algorithm. We then investigated its skill in the challenging case of a well-known target, β Pictoris, whose companion is close to the detection limit and we compared our results to those obtained by another method based on principal component analysis (PCA).

Results. Application on VLT/NaCo data demonstrates the ability of ANDROMEDA to automatically detect and characterize point sources present in the image field. We end up with a robust method bringing consistent results with a sensitivity similar to the recently published algorithms, with only two parameters to be fine tuned. Moreover, the companion flux estimates are not biased by the algorithm parameters and do not require a posteriori corrections.

Conclusions. ANDROMEDA is an attractive alternative to current standard image processing methods that can be readily applied to on-sky data.

Key words. Methods: data analysis - Techniques: high angular resolution - Techniques: image processing - Planetary systems - Planets and satellites: detection

1. Introduction

Among the thousands of exoplanets known today, less than 2% have been detected by direct imaging. The methods most often used at the present date are indirect, such as Doppler spectroscopy (Marcy & Butler 1993; Walker 1995), transit photometry (Rosenblatt 1971; Borucki et al. 1985), or microlensing (Cassan et al. 2012), that have permitted the population of inner planets (semi-major axis $\lesssim 5\ AU$) of sub-Jovian mass ($\lesssim 2.10^{30}\ g$) to be characterized (Udry & Santos 2007; Schneider et al. 2011). Direct imaging is motivated by its ability to detect massive young exoplanets on wider orbits and also to obtain spectra that provide information about their atmospheric composition. Thus, direct imaging, complementary with other indirect techniques, increases our statistics and understanding of exoplanets.

Very few exoplanets have been imaged up to the present day, and this is essentially due to the difficulty in achieving high contrast at small angular separation, as most giant exoplanets lie within 1″ from their host star with a flux ratio of about 10^5 to 10^8 (depending on mass and age). In order to obtain a high resolution, observation with very large ground-based telescopes is needed, but the resolution is then limited by atmospheric turbulence. This effect can be overcome by the use of an adaptive optics (AO) system, which performs a real-time correction of the incoming distorted wavefront. The second step is to handle the very high contrast that exists between the planet and its host star. The use of a coronagraph greatly helps by removing a large part of the coherent light from the star while preserving its close environment. However, the optics are not perfect, and in long exposures the remaining aberrations are responsi-

⋆ Based on observations made with ESO Telescopes at the Paranal Observatory under programme ID 184.C-0567(D) and 60.A-9800(J).
⋆⋆ F.R.S.-FNRS Research Associate

ble for speckles in the image that vary from less than minutes to hours (Hinkley et al. 2007); the speckles are too slow to be averaged into a smooth halo and too fast to be calibrated and removed a posteriori. These quasi-static speckles make exoplanet detection confusing since they are of the same angular size as the expected planetary signal and are often brighter. Consequently, at this stage it is necessary to apply elaborated image processing methods to disentangle the signal of an exoplanet from the remaining speckle noise.

The image processing methods that are the most widely used by astronomers today are based on the angular differential imaging (ADI) concept (Marois et al. 2006). This technique relies on observations made in pupil tracking mode that fixes the pupil while the image rotates with time. Several algorithms are used to build a *reference* point spread function (PSF) that should reproduce as accurately as possible the speckle pattern to be subtracted, but not the rotating signature of a potential astronomical source around the on-axis star. Among them, Classical ADI (cADI) uses a median image to build the reference PSF, and LOCI (Locally Optimized Combination of Images) (Lafrenière et al. 2007) uses a linear combination of images to build it and locally optimizes the speckle subtraction. The principal component analysis (PCA), in the form of PynPoint (Amara & Quanz 2012) or KLIP (Soummer et al. 2012), uses an expansion of eigenimages to build the reference PSF. Numerous variations of these methods are studied and are used to improve the speckle subtraction.

The ANgular DiffeRential OptiMal Exoplanet Detection Algorithm (ANDROMEDA) methodpresented in this paper is an advanced way of exploiting the ADI technique in the framework of inverse problems. ANDROMEDA uses a maximum likelihood estimation to detect planetary signals and retrieve the projected distance between the planet and the star, as well as the contrast between the two components. From these estimations, and knowing the age of the host star, sophisticated models (e.g., Allard et al. (2012); Spiegel & Burrows (2012); Marleau & Cumming (2014) for young stars) provide estimations of the companions' mass and surface temperature. These results are useful to constrain the current models of star and planetary formation and their evolution.

In this paper we first present and explain in detail the different steps performed by the algorithm ANDROMEDA to properly process real images and we discuss the hypothesis made to check whether it is consistent for real data (Sect. 2). We then explain how to use the output provided by ANDROMEDA to automatically detect the point sources in the images and to extract both their flux and position (Sect. 3). The next section is an application of the full procedure to real VLT/NaCo data, which consists of a bright star (TYC-8979-1683-1) surrounded by numerous background stars acting as point sources to be detected, and in which we injected synthetic companions in order to assess the performance of ANDROMEDA (Sect. 4). The following section shows results using VLT/NaCo data of the well-known case of Beta-Pictoris, imaged under fair conditions and using an AGPM coronagraph (Mawet et al. 2005), thus approaching the quality of future high-resolution and high-contrast imaging systems (Absil et al. 2013). This last part (Sect. 5) compares the performance obtained by using ANDROMEDA with another commonly used method, the PCA.

2. ANDROMEDA's principle

ANDROMEDA uses a statistical approach to discriminate planetary signals from the remaining speckles. The first step is to perform ADI in order to create differential images in which speckles that are stable enough to be distinguished from a rotating companion signature are removed. If a companion is present, a specific signature appears at its location that we can model according to its flux and initial position parameters. The second and original step of the method is to search for such a signature in the differential images by using a maximum likelihood estimation (MLE) of its position and intensity. This estimation is made from a consistent model of the data set, given a statistical model of its noise distribution as first presented in Mugnier et al. (2009), it is similar to the approach proposed for the processing of DARWIN/TPF-I data in Thiébaut & Mugnier (2006) and to the works by Smith et al. (2009) for a perfectly fixed speckle field.

The purpose of this paper is to apply ANDROMEDA to real data from the VLT/NaCo instrument (Lenzen et al. 2003; Rousset et al. 2003). This implied adapting the method described in Mugnier et al. (2009). The different processing steps performed by the upgraded version of ANDROMEDA presented and used in this paper are the following. Section 2.1 describes how and why the artifacts with low spatial frequency are removed from the raw images in a pre-processing step. Section 2.2 describes the angular image difference imaging that is then performed in order to suppress the vast majority of the starlight from the images. Section 2.3 defines the mathematical model corresponding to the resulting differential images along with their dependency with the sought positions and amplitudes of the potential companions. Section 2.4 explains how the problem is inverted between the differential image and its model by using a maximum likelihood which analytically finds an estimation of both the position and flux of the potential companions. Finally, Sect. 2.5 describes the simple and effective post-processing that is performed on the results in order to compensate for the deviation from the noise model (assumed to be white and Gaussian in the differential images) that appears in practice on real data.

2.1. Pre-processing: Filtering out low-frequency artifacts

In both the raw and the reduced images there are some strong inhomogeneities of low spatial frequency that are not stable and thus disturb planetary detection. These large-scale structures in the images, which vary slowly from one frame to another, might originate from temporal variation of the residual turbulence. As they cannot be fully subtracted via the ADI process and they are not included in the image model used to perform the MLE, these low frequencies must be removed.

A pre-processing of the data has thus been introduced in ANDROMEDA to make the detection of point sources easier within the stellar halo. This pre-processing consists in eliminating these disturbing structures by applying a high-pass filter in the Fourier space. Half of a Hann function has been chosen to build this filter's profile in order to avoid Gibbs effects, due to discontinuity, that appear when going from the Fourier to the real space. This filter attenuates the spatial frequencies lower than a chosen cut-off frequency defined as $f_c = F \cdot f_N$, where f_N is the Nyquist frequency and F is a factor in the range 0-1 (hereafter called the filtering fraction). The parameter F is user-defined and must be chosen carefully to efficiently remove the low-frequency artifacts while preserving most of the energy of the point source signals in the images. In order to quantify the signal loss due to this filtering, we took an Airy pattern and applied the filtering to

it. The energy loss is then quantified as follows:

$$E_{loss} = 1 - \frac{\int (airy_{filtered})^2}{\int (airy_{non-filtered})^2}. \quad (1)$$

The obtained results are gathered in a graph showing the energy loss as a function of the filtering fraction (Fig. 1).

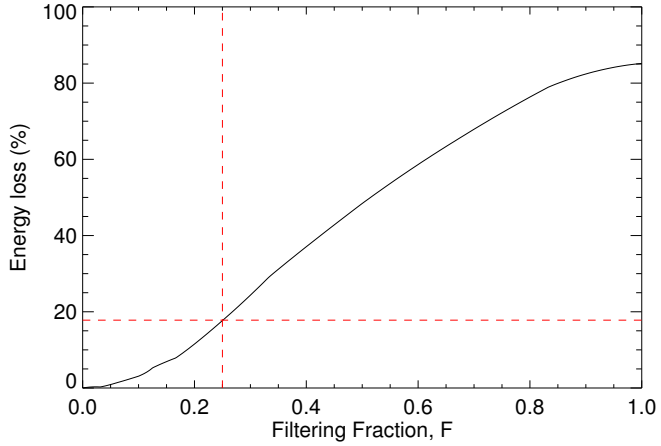

Fig. 1. Energy loss as a function of the filtering fraction when filtering a simple Airy pattern (sampled at the Nyquist rate) with a high-pass Hanning Fourier filter (solid line). Energy loss for a usual filtering fraction of 1/4 is shown with the red dashed line.

Comparisons and tests on simulation and real data show that even though this procedure slightly reduces the intensity of the planetary signal on individual frames, the filtering is worthwhile for planet detection and does not introduce any error on the estimated flux. In practice, a filtering fraction of about one fourth is recommended when dealing with VLT/NaCo data, leading to an energy loss of about 18% (see Fig. 1).

2.2. Construction of differential images

2.2.1. Angular differential imaging (ADI)

The ADI technique consists in taking advantage of the alt-azimuthal mount of the telescope in use: the pupil and the field rotate at different deterministic velocities during the observation. In order to perform ADI, one can choose to fix the pupil (by using a pupil derotator if needed) to stabilize the aberrations in the image, while the observed field rotates as the parallactic angle. Therefore, these images can be later subtracted from each other in an optimized way to reduce as much as possible the speckle noise in the resulting differential image. This method was first introduced by Marois et al. (2006) and is the basis of most image processing methods dedicated to exoplanet detection today.

In order to choose the two images to be subtracted, a compromise has to be made so that (i) the turbulence strength and the quasi-static aberrations do not have time to evolve significantly between the two images, and (ii) the object of interest has rotated enough in the field between the two images in order not to cancel its own signal during the subtraction. Assuming that the most correlated data are the closest in time, we chose two images that are as close as possible in time but within a limitation to avoid the self-subtraction of the companion. This limitation is the minimum distance between the position of the planetary signal in the two images ($\delta_{\min}$), which is a key user-defined parameter whose value must be adjusted according to the speckle lifetime and instrumental stability (typically $1.0\lambda/D$, see Table 2). As the displacement between two images is dependent upon the distance between the star and the object of interest, the ADI is performed over concentric annuli of constant width dr to accommodate this dependency, which is another user-defined parameter (typically $1.0\lambda/D$, see Table 2). For each of these annuli, each image of the cube is subtracted from the first following image (or previous image if needed) that meets condition (ii). If a couple is found, the subtraction results in the creation of a *differential image*, indexed k, where $k \in [1; N_k]$, with N_k the total number of couples found within the cube at the regarded distance from the star. If for a given frame, no other frame satisfies condition (ii), no pair can be built with this frame which is therefore not used. Thus N_k is less than or equal to the total number of images in the cube.

As the two images to be subtracted are likely not to have the same intensity distribution, one of the image needs to be adjusted with respect to the other via a scaling factor, noted γ_k. These intensity variations are primarily caused by variations of the seeing in the course of the observation. Each differential image $\Delta(\mathbf{r}, k)$ resulting from the subtraction of a couple k of images $i(\mathbf{r}, t)$ is then of the form

$$\Delta(\mathbf{r}, k) = i_k(\mathbf{r}, t_1) - \gamma_k\, i_k(\mathbf{r}, t_2)\ . \quad (2)$$

It can be seen in both the simulations and the real data that the flux difference depends on the distance to the star. As a consequence, the scaling factor is computed for each couple of annuli, over an *optimization area* that is slightly wider than the effective *subtraction area* in order to avoid discontinuities between adjacent annuli (Cornia et al. 2010). The ratio optimization to subtraction area (R_A) is a third user-defined parameter, set constant for all annuli (typically 2.0, see Table 2).

Several considerations guided us in the design of the best computation of this scaling factor. Because the high-pass filtered images have a zero mean, it is not possible to compute the scaling factor γ_k with a simple ratio of the total intensities in each image. Instead the scaling factor is better estimated by a least-squares fit that minimizes $\|i_{k(t_1)}(\mathbf{r}) - \gamma_k\ i_{k(t_2)}(\mathbf{r})\|^2$ (Cornia et al. 2010). In the following, we refer to this method as the *LS optimization*. We note that optimization depending on position in the field has been implemented in other methods of exoplanetary detection, as in Marois et al. (2006); Lafrenière et al. (2007). Another way to subtract the images is also presented here, after taking two aspects into consideration: first the PSF may not vary linearly and if there is a sudden evolution in the turbulence strength, the image can be better fitted by an affine law. Thus, the differential image can be constructed by

$$\Delta(\mathbf{r}, k) = i_{k(t_2)}(\mathbf{r}) - \gamma_k\, i_{k(t_1)}(\mathbf{r}) - \gamma'_k. \quad (3)$$

Second, the least-squares is sensitive to outliers and if, from one image to the other, a speckle or a planetary signal intensity has varied significantly, their high signal is taken into account to compute the scaling factor, which results in a flux offset in the differential image. In order to avoid the latter bias, we additionally implemented a robust fit, using a L_1 norm that can be chosen instead of the L_2 norm. The scaling factors γ_k and γ'_k are then computed by minimizing: $\|i_k(\mathbf{r}) - \gamma_k\,.\,i_k(\mathbf{r}) - \gamma'_k\|_{L_1}$. In case there are such outliers corresponding to high flux and variable signals (either speckles or planetary signals), this way of combining the image pair – hereafter called *L1-affine optimization* – has proven equally or more efficient at reducing the speckle noise on both simulated and real data, while preserving the planetary signal, if any. This L1-Affine optimization is particularly good at very

close separation where the intensity of the numerous speckles varies a lot from one image of the couple to the other due to the poor rotation field velocity.

After this operation, the differential images $\Delta(\mathbf{r}, k)$ are obtained for every distance to the star. We note that even if the image couples are determined for specific annuli and the optimizations are computed over annular areas including these annuli, the whole images are actually subtracted one from another to build the differential images. By minimizing the residuals in these data, the noise has been partly whitened spatially (Cornia et al. 2010; Mawet et al. 2014). Since ANDROMEDA relies on solving an inverse problem, it is also useful to estimate the variance map $\sigma^2_\Delta(\mathbf{r})$ of the differential images. Currently it is estimated empirically over the time dimension k as a function of the position $\mathbf{r}$:

$$\sigma^2_\Delta(\mathbf{r}) = \langle[\Delta(\mathbf{r}, k)]^2\rangle_k - [\langle\Delta(\mathbf{r}, k)\rangle_k]^2. \quad (4)$$

We note that when the observer has other independent ways to estimate the variance map, in particular taking the temporal variations into account, it could be introduced here. In the following, it is nevertheless assumed that the noise variance is stationary in time and the definition of the variance map given above is used, which is satisfactory for our study.

2.2.2. Other possible combinations of images

Because ANDROMEDA was developed with the objective of being used to process large amount of survey data from second-generation instruments, it was proposed with a simple ADI subtraction to whiten the noise. This allows the algorithm to run quickly (in particular, it is possible to parallelize the computation of each operation), and to have a very low number of user-parameters to be adjusted. However, many other approaches can be considered to build up differential images that could also be included in the ANDROMEDA scheme, as long as the impact on the potential companion signature can be evaluated and inserted in the model. For instance, it would be possible to merge this method with other subtraction algorithms, such as LOCI or PCA, that are known to be able to reduce the speckle noise very efficiently.

Other techniques can be used to whiten the noise: instead of exploiting only the temporal information, ANDROMEDA could deal with spectral or polarization redundancy, for instance, and perform, respectively, spectral differential imaging (SDI) (Racine et al. 1999; Marois et al. 2000) or polarimetric differential imaging (PDI) (Kuhn et al. 2001) in addition to the ADI. An optional SDI for ANDROMEDA has been implemented and discussed in Cornia et al. (2010) and simple tests have been led on images taken either with a dual band imager (DBI) or an integral field spectrograph (IFS), such as IRDIS or IFS on the VLT/SPHERE instrument, but this work is beyond the scope of this paper.

2.3. Building a model of the differential images

Once the differential images have been created, evidence of the presence of a planetary signal in the original image is sought inside all of these differential images. After performing the ADI, if a companion is indeed present in the field of view, a peculiar signature appears in the differential images. This so-called planet signature is naturally the difference of two planetary signals separated by at least $\delta_{\min}$. Figure 2 illustrates the shape of the expected planet signature obtained either with or without high-pass filtering of the raw data. In order to properly estimate the position and flux of a potential exoplanet using a maximum likelihood approach, we now define a model for these differential images. Assuming that the stellar halo is fully suppressed by the subtractions and that a planet is present in the field of view, each differential image can be modeled as

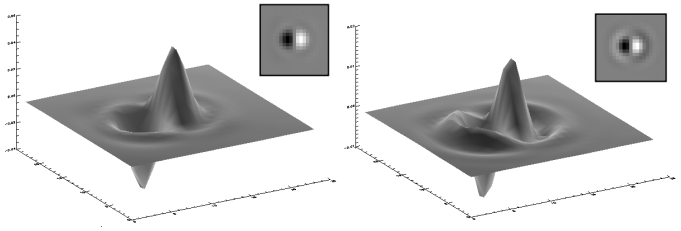

Fig. 2. Illustration of the planet signatures obtained when performing the ADI, setting $\delta_{min} = 0.5\lambda/D$. These have been obtained by simulating two identical noiseless planetary PSF, separated by δ_{min} and then subtracted one from the other. *Left:* Planet signature obtained without high-pass filtering of the raw data. *Right:* Planet signature obtained when the raw data have been filtered of their low frequencies ($F = 1/4$). This time secondary opposite lobes surround the main lobe.

$$\Delta(\mathbf{r}, k) = a \cdot \mathbf{p}(\mathbf{r}, k; \mathbf{r}_0) + \mathbf{n}(\mathbf{r}, k)\ , \quad (5)$$

where the planet's flux a and the position of the planet on the first image of the sequence (initial position) $\mathbf{r}_0$ are the two unknown parameters, $\mathbf{n}(\mathbf{r}, k)$ denotes the residual noise, and $\mathbf{p}(\mathbf{r}, k; \mathbf{r}_0)$ is the planet signature.

The model can be built by placing two PSFs, one positive and one negative, properly positioned in the field of view to correspond to the field rotation at times t_1 and t_2 of a certain couple k. We assume here that the exposure time is short enough that the companion does not undergo any azimuthal smearing, but it could be added if the smearing becomes significant. As we have only one representative PSF for all the images of the cube, we also assume that the PSF is known and does not vary with time. As was true for other ADI approaches, if the instrument PSF does vary during the sequence, it directly affects the companion flux estimate. The main limitation here is related to monitoring the PSF Strehl ratio along the sequence. If it were known, this knowledge could be included to rescale the searched companion signature in ANDROMEDA within the succesive differential images. In the current paper, we also work under the hypothesis that the companion PSF core is temporally stable. In this case, the scaling factor γ_k used to build up the differential images, which is related to the variability of the star halo, must be taken into account to build the model of the planet signature,

$$\mathbf{p}(\mathbf{r}, k; \mathbf{r}_0) = h(\mathbf{r} - \mathbf{r}'(t_1, \mathbf{r}_0)) - \gamma_k\ h(\mathbf{r} - \mathbf{r}'(t_2, \mathbf{r}_0)), \quad (6)$$

where h is the PSF of the system that can be estimated by providing an empirical PSF to the algorithm simply obtained by imaging the star (unsaturated image or without coronagraph). This PSF is shifted at a position $\mathbf{r}'(t_x, \mathbf{r}_0)$ that the planet will have at a time t_x if its position in the first frame is $\mathbf{r}_0$. If, however, it turns out that the intensity of the planetary signal and the PSF vary the same way in every image, the scaling factor should not be taken into account to build this model.

If another kind of method is used to perform the speckle subtraction, as suggested in Sect. 2.2.2, the model must be modified according to the subtraction performed. For instance, if the previously mentioned methods LOCI or PCA are used, the coefficients found to perform the subtraction must be recorded for each zone in order to build a consistent model.

Since ANDROMEDA models differential images through Eq. (5), the filtering procedure must also be applied to the reference PSF used to build the planet signature. In this way, the model remains consistent with the data and ANDROMEDA tracks the proper filtered planet signature in the filtered data sequence.

2.4. Estimation of position and flux via maximum likelihood

ANDROMEDA's goal is to estimate the position and the flux of a potential planet orbiting around the target star using a probabilistic approach. This estimation is based on a MLE under the hypothesis that the residual noise inside the differential images is a Gaussian and white. Far from the star, this hypothesis is fulfilled if the star PSF does not vary during the exposure because there is only photon and detector noise in the images (Mugnier et al. 2004). Closer to the star, quasi-static speckles are predominant and they follow modified Rician statistics (MR) (Goodman 1985; Soummer & Aime 2004; Fitzgerald & Graham 2006), which are neither Gaussian nor totally white.

However, ANDROMEDA deals with high-pass filtered image differences. First, it appears that the filtering process of the raw images increases the Gaussianity of the residual distribution in the images since it removes the slowly evolving structures while preserving the high spatial frequencies that evolve quickly. As the remaining noise inside an annulus is with a good approximation independant, according to the central limit theorem, its distribution should follow a normal distribution. Second, the speckle noise is temporally correlated from one frame to another. By performing the difference between close images, only the variation between the speckle fields in the two frames will remain in the differential image. That is to say the created differential image will contain the time derivative of the speckle and the power spectral density (PSD) of a derivative tends toward a constant so the differential imaging process "whitens" the noise. This whitening is a well-known consequence of the ADI (Marois et al. 2008), which is true mostly because we consider the reference frame of the sky. This property is verified empirically on real NaCo data in Sect. 4.2.2. To conclude, the noise in the differential images created to perform the MLE is, to a good approximation, Gaussian and white, thanks to the filtering and differential imaging performed. At the end of this section there is further discussion of this hypothesis.

Under the assumption that the residual noise in the differential images is white (in time and space), Gaussian, and non-stationary, the likelihood can be written

$$L(\mathbf{r_o}, a) \propto \exp\{-\frac{1}{2}\sum_k \sum_{\mathbf{r}} \frac{|\Delta(\mathbf{r},k) - a\, p(\mathbf{r},k;\mathbf{r_o})|^2}{\sigma^2_\Delta(\mathbf{r})}\}. \quad (7)$$

For each annular zone, at a certain distance from the star, this likelihood is computed for any possible initial position $\mathbf{r}_0$: the sum is made over all the N_k couples found for this distance from the star and over all the pixels in the image field.

ANDROMEDA analyzes the sequence of differential images $\Delta(\mathbf{r}, k)$ by seeking the optimal values $(\hat{\mathbf{r}}_0, \hat{a})$ that maximize the logarithm of the likelihood,

$$J(\mathbf{r}_0, a) \triangleq \ln L(\mathbf{r}_0, a) \propto -\sum_{\mathbf{r},k} \frac{|\Delta(\mathbf{r},k) - a \cdot p(\mathbf{r},k;\mathbf{r}_0)|^2}{2\sigma^2_\Delta(\mathbf{r})}. \quad (8)$$

Equation (8) shows that maximizing the log-likelihood is equivalent to minimizing the sum of squared residuals between the differential image and the model, weighted by the variance of the residual noise. We note that the definition of the variance σ^2_Δ at Eq. 4 means that the weight is lower when there is a planet in the studied differential image (and the noise is more overestimated to a higher degree when the planet is brighter and at closer separation). This bias induces an overestimation of the error, but this does not affect the estimation itself.

The optimal flux value $\hat{a}$ for each possible initial position of the planet is easily computable analytically and is given by

$$\hat{a}(\mathbf{r}_0) = \frac{\sum_{\mathbf{r},k} p(\mathbf{r},k;\mathbf{r}_0)\Delta(\mathbf{r},k)/\sigma^2_\Delta(\mathbf{r})}{\sum_{\mathbf{r},k} p^2(\mathbf{r},k;\mathbf{r}_0)/\sigma^2_\Delta(\mathbf{r})}\,. \quad (9)$$

This equation shows that the estimated flux can be regarded as a cross-correlation between the planet signature and the differential image, weighted by the noise variance averaged on every differential image, the denominator being a normalization constant. In the ANDROMEDA code, after a processing per annuli, the data are combined in a single 2D map called a flux map, giving at each pixel the flux of the object, if the object has this pixel position.

By inserting this expression of $\hat{a}(\mathbf{r}_0)$ into the metric J, it is possible to obtain an expression for the log-likelihood that depends from now on only on the initial planet position $\mathbf{r}_0$,

$$J'(\mathbf{r}_0) \triangleq J[\mathbf{r}_0, \hat{a}(\mathbf{r}_0)] = \frac{\left(\sum_{\mathbf{r},k} p(\mathbf{r},k;\mathbf{r}_0)\Delta(\mathbf{r},k)/\sigma^2_\Delta(\mathbf{r})\right)^2}{\sum_{\mathbf{r},k} p^2(\mathbf{r},k;\mathbf{r}_0)/\sigma^2_\Delta(\mathbf{r})} + C, \quad (10)$$

where C is a constant. The criterion $J'(\mathbf{r}_0)$ is a measure of the probability that there is a point source at position $\mathbf{r}_0$ on the first image of the sequence. This formula is easily interpretable by saying that the planet has a high probability of being found at the position where the correlation between the model and the differential image is the closest to one. In practice $J'(\mathbf{r}_0)$ is computed for each possible initial position of the planet on a grid chosen as the original pixel grid of the images. The results are then a so-called likelihood map which has higher values at positions where the presence of a companion is more probable.

Once the likelihood and flux maps are computed, one purpose is to link the intensity of a likelihood peak to a probability of false alarm in order to assess whether it is indeed a true planetary signal. One way to proceed is to compute the standard deviation of the estimated flux, $\sigma[\hat{a}(\mathbf{r}_0)]$, for each possible initial position, which describes how the noise propagates from the differential image toward the flux map. The standard deviation of the estimated flux is given by

$$\sigma^2[\hat{a}(\mathbf{r}_0)] = \left[\sum_{\mathbf{r},k} p^2(\mathbf{r},k;\mathbf{r}_0)/\sigma^2_\Delta(\mathbf{r})\right]^{-1}. \quad (11)$$

It is then possible to define the signal-to-noise ratio of the estimated flux, S/N, as

$$\mathrm{S/N}(\mathbf{r}_0) \triangleq \frac{\hat{a}(\mathbf{r}_0)}{\sigma[\hat{a}(\mathbf{r}_0)]}\,. \quad (12)$$

The so-called *detection limit*, that is to say the faintest detectable companion flux as a function of the separation from the star, at chosen threshold $N\sigma$ is thus given by $N \times \sigma[\hat{a}(\mathbf{r}_0)]$. In other words, the standard deviation of the flux map is the detection limit at 1σ.

It is straightforward to show that the S/N can be rewritten as

$$\mathrm{S/N}(\mathbf{r}_0) = \frac{\sum_{\mathbf{r},k} p(\mathbf{r},k;\mathbf{r}_0)\Delta(\mathbf{r},k)/\sigma^2_\Delta(\mathbf{r})}{\sqrt{\sum_{\mathbf{r},k} p^2(\mathbf{r},k;\mathbf{r}_0)/\sigma^2_\Delta(\mathbf{r})}}. \quad (13)$$

Showing that the log-likelihood is simply the square of the S/N. This means that maximizing the likelihood map is equivalent to maximizing the S/N map to find the most-likely position of a potential companion. The S/N thus gives a physical meaning to the log-likelihood $J'(\mathbf{r}_0)$. Moreover, thresholding the S/N to zero is equivalent to computing $\hat{a}(\mathbf{r_0})$ under the constraint that it is non-negative, and the log-likelihood then obtained through Eq 13 incorporates this positivity constraint (see Mugnier et al. 2009). In summary, the likelihood and S/N maps contain the same information, and we chose to use the S/N map to perform detection since it directly yields the statistical significance of each detection.

It is then possible to define a threshold τ, to be applied to the S/N map, which corresponds to a certain confidence level of the detection. Assuming that there is no planet anywhere in the images (hypothesis H_0) our model shows that the differential images equal the residual noise. If our hypothesis were strictly fullfilled, the residuals in the S/N map would have the same statistics as the noise in the differential images (because each pixel of the S/N map is a linear combination of pixels from the differential images (via Eq. (9) and (12)), which is assumed to be white and Gaussian, with a probability density function (PDF), $p_{\mathrm{S/N}}$ that is normal, zero-mean, and of unit variance. Under the assumptions on the noise, the probability of false alarm (PFA), defined as the probability that the S/N shows a signal above the chosen threshold τ under the hypothesis H_0, writes

$$\begin{aligned}\mathrm{PFA}(\tau) &= Pr(\mathrm{S/N} > \tau)|_{H_o} \\ &= 1 - \frac{1}{\sqrt{2\pi}} \int_{-\infty}^{\tau} \exp(-\tau'^2/2)\, d\tau' \\ &= 1 - erf(\tau), \end{aligned} \tag{14}$$

where *erf* is the so-called error function. The applicability and relevance of such a threshold τ is important as further discussed in Sect. 2.5 and when applying ANDROMEDA over real data in Sect. 4.

However, these considerations are for the ideal case of a white, Gaussian, and non-stationary noise in the differential images, for which the connection between PFA and threshold is perfect. For real data, even if the filtering permits an increase in the Gaussianity of the noise and allows the differential imaging to remove an important fraction of its correlated component, the actual noise distribution still slightly deviates from our assumptions. The real noise distribution is closer to a MR distribution, which increases the PFA. Because of its structure, the MR distribution evolves radially: the quasi-static speckles have the same mean and variance only for a specific annulus. Close to the star, the speckle noise is dominant (and the noise is more correlated), whereas far from the star the photon noise, the readout noise, and the dark current prevail. The threshold should thus be increased according to the separation from the star where the companion is sought (Marois et al. 2008).

Another effect that is worth pointing out here is that for annuli close to the star, the field has not rotated as much as at large separations. At small separations, not only are there a small number of pixels contained in the annulus, there are also few images to be subtracted. These two effects reduce the number of degrees of freedom (in ANDROMEDA, the number of points inside the annulus, $\mathbf{r}$, plus the number of ADI couples, k) and corrupt the statistics: we are in a small sample statistics regime. In that case, Mawet et al. (2014) have shown, using a frequentist approach, that the PFA is underestimated to an even greater extent. To correct for this bias, close to the star, the noise statistics no longer follow a MR distribution, but a robust Student's t-distribution, which is valid only if the sample is independent and identically distributed (which is the case if processes to whiten the noise, such as differential imaging, have been applied to the images). In practice, when correcting for this bias, we calculate the equivalent threshold that should be applied to provide the same PFA that Gaussian statistics would give at the actual chosen threshold.

As a consequence, the PDF chosen in Eq. (14) is no longer the normal law, $\mathcal{N}$, and should be replaced by the appropriate law: a MR PDF at large separation (Marois et al. 2008) and a Student t-distribution PDF at small separation (Mawet et al. 2014). The detection limit calculation should then be modulated to take into account these two considerations. The next section is about how to take the deviation into account from our model, in order to set a constant threshold throughout the whole S/N map. Setting a constant threshold enables the probable point sources in the field to be automatically and systematically detected with a relevant confidence level.

We note that the discrepancy between the model of noise made with respect to the real noise distribution does not affect the flux estimation in itself, but will affect the error on the flux estimation.

2.5. Post-processing: normalization of the S/N map

To complete the presentation of the method within this section, we can already indicate that the first tests performed on real data showed that the deviation from the noise model prevents one from applying a constant threshold to the S/N map and building an automatic procedure to detect companions. We can vizualize this deviation effect in Fig. 9-*left*, which notably shows a radial dependancy so the threshold should indeed be modified as a function of the separation.

This is not unexpected since if the noise model (white, Gaussian, and non-stationary) were consistent with the real values, the output S/N map from ANDROMEDA would have a zero mean and a standard deviation of one when, of course, excluding the pixels containing the signal from a companion. In this case, the threshold could be uniform all over the field. However, as explained in the previous section, in real images, the noise clearly deviates from this model and the standard deviation of the residual noise in the S/N map generally has a standard deviation larger than one which increases from the center to the edge and a mean of zero very far from the star that increases when going closer to the star.

Knowing that we would like to obtain a S/N map that has a zero mean and a standard deviation of one, we propose a simple solution to preserving the PFA, which consists in normalizing radially the S/N map by its own empirical radial standard deviation. This operation removes the radial dependency and allows one to apply a constant threshold to the S/N map, regardless of the distance from the star. To normalize the S/N map, it is necessary to build an empirical radial profile of the standard deviation from the S/N map, without taking into account any peaks due to planetary signals. A method from Hoaglin et al. (1983) and Beers et al. (1990) to estimate this standard deviation, hereafter called robust standard deviation, has been implemented in ANDROMEDA. This method consists in calculating the median absolute deviation divided by a normalization factor enabling a robust estimate of the standard deviation. The factor is chosen so that the regular standard deviation and the robust value are identical in the case of a Gaussian distribution. Because only the global trend is needed, the mean radial robust standard deviation profile is smoothed over a certain number of pixels, N_{smooth},

which is a user-defined parameter that has to be set empirically according to the pixel scale and the size of the images. Once a satisfactory profile that does not take into account the small variations from one annulus to its neighbor is obtained, the normalized S/N map is obtained by dividing the S/N map by this radial trend.

This method is reproducible and independent of the data set. The post-processed S/N map thus gives the confidence level for a point source detection on each pixel of the image grid. Thresholding this map by a constant value throughout the field of view provides a list of positions where a probable companion candidate is detected. As a result, in the following we work exclusively with the normalized S/N map and from now on "S/N map" stands for the normalized S/N map. Through Eq. 12, as the S/N map has been normalized, the standard deviation flux map must also be normalized in a coherent manner to obtain a consistent relation between the normalized S/N and the standard deviation of the flux. The normalization process does not significantly affect the position and flux estimations (the impact is lower than the given errors on these estimations) but normalizing too much (smoothing the profile too much) artificially lowers the error on the flux estimation.

ANDROMEDA provides four 2D maps for analysis: the likelihood map, the S/N map, the flux map, and the flux standard deviation map. The two most useful outputs for detection and characterization are the S/N map, in which we can look for planetary signals and estimate their most likely position $\hat{r_0}$, and the flux map, in which we can read the corresponding estimated flux $\hat{a}(\hat{r_0})$. The map of the flux standard deviation is the detection limit at 1σ. The following section deals with the analysis of the ANDROMEDA output to accurately compute the position and flux of potential companions present in the image field based on applications on real VLT/NaCo images to show concrete illustrations.

3. Extracting companion information from the ANDROMEDA outputs

In this section we explain how to systematically and efficiently extract a list of likely companions with their subpixel position and estimated flux in terms of contrast. Once the S/N and flux maps are at hand, a complementary module is developed that automatically detects and analyzes the point sources present in the images. This module simply finds the signals above threshold in the S/N map and, knowing the expected shape of a planetary signal in the S/N map (Sect. 3.1), assesses their subpixel positions and then estimates their corresponding flux thanks to the flux map (Sect. 3.2). Also, during the analyses, some tests are performed to discriminate probable planetary signals from artifacts (Sect. 3.3).

3.1. Resulting pattern from a planetary signal

If there is indeed a planetary signal, a specific pattern appears in both the S/N and flux maps. This pattern is well known and derived from Eq. (10) and Eq. (13): under the hypothesis that there is no noise in the data, it can be seen essentially as the autocorrelation of the planet signature $p(\mathbf{r}, k; \mathbf{r_0})$ shown in Fig. 2, multiplied by the intensity of the candidate companion. Such a pattern is illustrated in Fig. 3, either with or without pre-filtering of the data.

As expected, this pattern is made up of a main positive lobe surrounded by two negative lobes positioned perpendicular to the star-companion direction. The main lobe of the pattern is oval with its longest side along the radial direction with a typical length of λ/D, whereas the length of its perpendicular direction is dependent upon the chosen distance δ_{min}. In the case without pre-filtering, positively thresholding the S/N map retains only the main lobe. On the other hand, the filtering induces the appearance of two tertiary sickle-shaped positive lobes surrounding the main lobe as well as two tiny fourth negative lobes. Consequently, when applying a positive threshold, the tertiary lobes may remain in the thresholded map if the S/N is high enough.

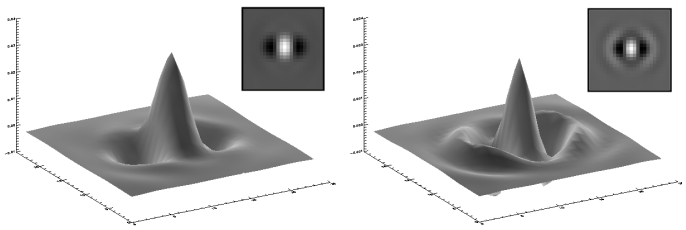

Fig. 3. Illustration of the pattern (autocorrelation of the planet signature, Fig. 2) appearing in the maps as evidence of a planetary signal. *Left:* Pattern obtained without filtering the raw images. *Right:* Pattern obtained with high-pass filtering of the raw images ($F = 1/4$).

3.2. Identification, position, and flux retrieval of candidate companions

The S/N map permits the identification of the most likely companions and the extraction of their subpixel position in the first image. The signals above the user-defined detection threshold are identified and classified according to decreasing peak S/N values. For each of them, a subwindow is extracted that fully encloses the central part of the candidate signal, as shown for instance in Fig. 4, and whose size is about $4\lambda/D$. To evaluate the subpixel position $\hat{r_0}$ of a candidate companion in a simple way, the planetary signal is interpolated to find the subpixel position of the maximum S/N, coinciding with the position of the planetary signal. The main lobe of the pattern expected from a planet is approximated by a Gaussian (this approximation is quite reliable in the very central part and less valid at the edges), and the subpixel position is identified at the maximum position of the 2D Gaussian fit of this main lobe. The error on the position estimation is simply given by the Gaussian fit uncertainty taken at 3σ. If needed, this error is corrected for the surrounding noise when it is too intense and might bias the error estimation.

To read the corresponding estimated flux $\hat{a}(\hat{r_0})$, the same approach is used by performing a 2D Gaussian fit of the planetary signal, but this time using the flux map provided by ANDROMEDA. The extracted flux of the companion is then the value of the fitted Gaussian at the subpixel position, $\hat{r_0}$, previously retrieved on the S/N map. At this stage, ANDROMEDA returns the flux of the detection with respect to the flux of the input PSF. From this value, it is easy to derive the contrast between the two components by using all the information about how the input PSF has been imaged, such as the integration time of the PSF with respect to the integration time of each image of the cube, any normalization factor, or the neutral density transmission if one was used to image the star. We emphasize here that this approach intrinsically takes all the pre-processing applied to the data into account: the companion signature that is sought takes into account the pre-filtering, and then the subtraction applied on image pairs separated by a small rotation difference. As a consequence the estimated flux does not depend on

such parameters, and contrary to other approaches such as PCA or LOCI, there is no companion flux loss. The error at 1σ on the flux estimation is directly read on the flux standard deviation map at the location $\hat{r_0}$ retrieved earlier. The error bars provided by the algorithm are the corresponding values at 3σ.

3.3. Rejection of known sources of artifacts

The method described so far, based on thresholding the S/N map, does not prevent the detection of artifacts whose signals are nevertheless above the threshold. Any signal temporally varying in the images is not fully subtracted and may leave some high-level residuals in the differential images, which could mimic the expected planet signature. This kind of artifact appears in particular if the pupil field is not well stabilized or if the star is not well centered in the image during the observation. Therefore, it is needed to discriminate a posteriori probable planetary signals from remaining artifact signals. The rejection criterion setup is based on the morphological properties of the pattern expected from a planetary signal (Sect. 3.1).

Three main sources of errors have been identified that can be used to efficiently reject these false detections. To illustrate these sources, practical examples are pointed out in the images of Fig. 4 that were produced thanks to data provided by NaCo (see Sect. 4 for more details on the data processed). The subimages cut in the S/N map and classified by decreasing S/N signals are displayed in Fig. 4-*left*. Below are listed the three sources of false detection that have been diagnosed:

1. The expected pattern contains tertiary positive lobes induced by the filtering procedure (Fig. 3-*right*). If the S/N of the signal is high enough, it these tertiary lobes may be above the threshold too and may thus be regarded as detections. These detected tertiary lobes are indeed surrounding only the very high S/N signals, such as #1, #2, and #3 visible in Fig. 4-*right* via the dark blue symbol @. Three criteria are used to spot and reject these artifacts: their proximity to a high S/N signal, the S/N ratio between the regarded signal and its neighbor, and their peculiar sickle shape which prevents the 2D Gaussian fit from converging. Such signals can be seen in Fig. 4-*left* such as #18 (surrounding signal #1) and #25 (surrounding signal #3 - we note that some pixels are missing in the subimage because they had already been erased after detecting the contingent part of this tertiary lobe).
2. The filtering may reveal the spider diffraction pattern in the S/N map that are not completely subtracted during the ADI (probably owing to the bad centering of the star or pupil tracking). Consequently, some signals can be found above the threshold that are actually artifacts due to this diffraction pattern. However, if this is the case, the signal is quite elongated along the radial direction and it is thus possible to constrain the fit parameters to reject such signals. This kind of signal can be seen in Fig. 4-*left*, such as signal #31, which is clearly located in the spider diffraction pattern visible in Fig. 4-*right*.
3. In areas where the speckle noise is quite high (close to the star), we might detect signals that originate from the speckle noise. This kind of signal is usually quite irregular compared to the expected pattern and can thus be rejected by constraining the 2D Gaussian fit to be neither too wide nor too shifted in the subimage.

Some other sources of instrumental error (hot pixels, etc.) can induce the detection of an actual artifact. To find all these artifacts and reject them, three of the fit parameters are constrained (by using the IDL function `mpfit2Dpeak.pro` developped by Craig B. Markwardt, for instance): (i) The distance between the fit maximum and the center of the subwindow must be of less than a pixel, (ii) the FWHM of the fit must be consistent with the one expected from the pattern, and (iii) the long-axis orientation must be close to the radial direction. In the following, a detection whose fit has not converged or that does not respect one of the constraints listed above is referred as an "ill-fitted" companion and is therefore rejected. In Fig. 4, when the 2D Gaussian fit is unsuccessful one asterisk is placed above the subimage (such as the detections indexed #17 and #25). When the S/N decreases, the shape of the signals is less and less regular and is consequently often not well fitted. Indeed, the lower the S/N, the less probable it is for the signal to be real, hence the frequency of strangely shaped signals increases (e.g., we can see this effect in signal #31, which has a S/N value of 5.4σ and lower). If the signal found is too close to the edge of the image, so its signal might be incomplete, it is impossible to obtain a correct 2D fit and in that case three asterisks are marked above the subimage (e.g., signal #8).

4. Application to NACO data: Test case with TYC-8979-1683-1 data

In order to assess the performance of the entire method, we ran ANDROMEDA on real data from the VLT/NaCo instrument. We applied ANDROMEDA to data collected by the NaCo Large Programme, which aimed at dectecting planets on wide orbits (Chauvin et al. 2015). The data we used consisted in observing a bright star surrounded by numerous background stars that are natural point sources acting as companions to be detected by the algorithm. Synthetic companions were then added inside the images in order to better quantify the ability of ANDROMEDA to accurately retrieve the position and contrast of the point sources present in the images.

4.1. Data used for the test

The data collected are sequences of saturated exposures (there is no coronagraph in that setup) taken in pupil tracking mode. The chosen star is TYC-8979-1683-1 (also called CD-62-657) observed in 2011 on May 5 within the ESO program 184.C-0567(D) (PI: J.-L. Beuzit). This star is a G7 star of 17 Myr (V = 9.36, H = 7.47) located at 75.6 pc from the Sun. The observation was made in H-band (filter centered around $1.66\mu m$) and stored in a 1024×1024 pixel frame (S13 camera inside the CONICA imager having a field of view of $13.6'' \times 13.6''$), the pixel scale being 13.22 mas/pixel.

4.1.1. Observation conditions

The star was observed during a total integration time of 36 min (giving 11 cubes of 29 frames each with an exposure time of 6.8 sec) and for a total field rotation of 18.5°. Seeing conditions were good but variable (seeing of 0.57″to 1.15″; coherence time of 4-9 ms; Strehl ratio of the reference PSFs: 21% and 26%). The empirical PSF core FWHM is estimated to be of 4.75 ± 0.05 pixels. The target was observed close to meridian crossing, the PSF core is saturated inside a radius of 10-15 pixels (0.13″-0.20″), and integration times are set short enough so that the angular smear of potential companions is small, especially in the inner part of the field. The data reduction of saturated exposures included sky subtraction (sky frame constructed from the median

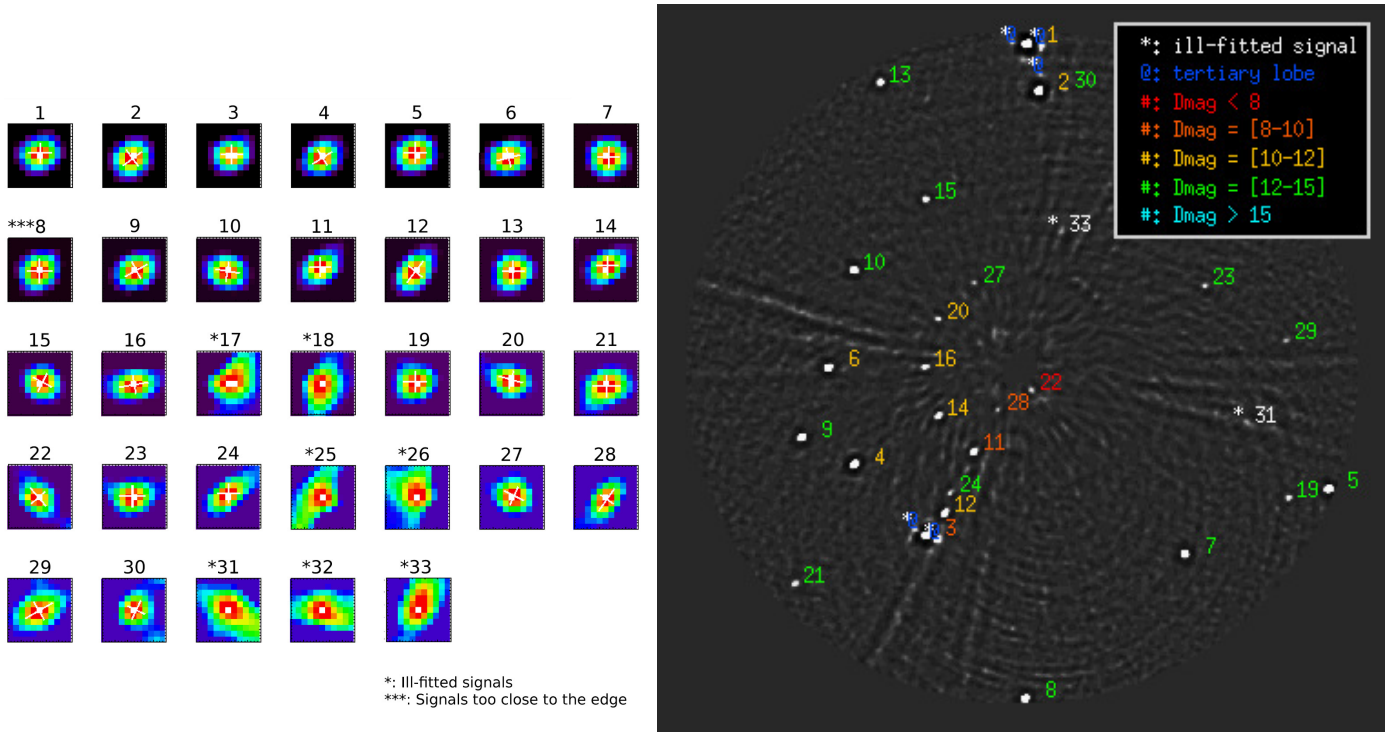

Fig. 4. Images obtained by running the automatic detection module on the output provided by ANDROMEDA applied to the images of TYC-8979-1683-1 taken with the VLT/NaCo instrument (see Sect. 4). The threshold is set at 5σ. *Left:* S/N map subwindows (11×11 pixels) in which the 2D Gaussian fits are performed for each detection. The subimages are classified by decreasing S/N and indexed by an increasing integer from one to the total number of detections above threshold. If the fit could not converge, one asterisk is placed above the corresponding subimage. Otherwise, the two axes of the fitted Gaussian are superimposed and their lengths are equal to the FWHM. *Right:* S/N map showing the location of each detection in the first image (labeled by their index of detection) as well as their flux range (color of the index) and whether it is an artifact (one asterisk means that the 2D Gaussian fit did not converge; the @ symbol means that it is assessed as a tertiary lobe artifact).

combination of exposures obtained at the five different jitter positions: on minute timescales, the image center is moved by ±3 arcsec in x or y on the detector field.), flat fielding, bad pixels correction, and rejection of poor-quality exposures. The location of the star center on each frame is determined by fitting the unsaturated portion of the saturated PSF with a 2D Moffat function. Individual frames are then shifted and registered to a common image center in between four pixels.

A short series of exposures with the unsaturated star was taken before and after the main saturated sequence in order to build the reference PSF required as an input for ANDROMEDA. These unsaturated sequences were acquired with an exposure time of 1.7927 seconds in autojitter mode, using a neutral density filter (ND_Short) of 1.19±0.05% transmission factor. The first unsaturated image obtained for these data is shown in Fig. 5-*right*.

The parallactic angle associated with each frame of saturated images is computed from the observing time (converted from UTC to LST), assuming that individual exposures are recorded at constant time intervals within each data cube (time information is available only for the beginning and end of each data cube).

We thus obtained the three necessary inputs for ANDROMEDA: a reduced image cube, a PSF of reference, and a vector containing the parallactic angles of each image of the cube.

4.1.2. Introduction of synthetic companions

To better quantify and optimize the detection performance of ANDROMEDA using NaCo data, we implanted 20 additional synthetic substellar companions in the image cube. The signal of each synthetic companion was modeled using the unsaturated PSF image and inserted in the individual reduced frames, taking into account the field rotation that occurred between the exposures. The procedure used to inject synthetic planets in the images of the data cube is explained in Chauvin et al. (2012).

The twenty synthetic companions were introduced along five radial directions of respective position angles of 30°, 60°, 90°, 120°, and 150° on the first image for each of these angle, at five angular separations of 0.26″, 0.53″, 1.06″, and 2.12″. The synthetic companions of the same position angle are of equal flux, each with peak intensities corresponding to magnitude differences of respectively 12.85, 12.10, 11.35, 10.60, and 9.85 for the five position angles in increasing order. An example of one saturated image of TYC-8979-1683-1 on which the location of these introduced synthetic companions are added is shown in Fig. 5-*left*. In order to verify the detection capability at close separation, we also added a companion at 0.26″, with a PA of 220° and a magnitude of 6.8 (contrast of about 2.10^{-3}).

4.2. ANDROMEDA's output

We applied ANDROMEDA to the data described above and obtained the four output detailed in Sect. 2. To process these data, we have chosen the user-defined parameters values gathered in Tab. 1 and whose suitability is discussed in detail in Sect. 4.2.3.

The S/N map obtained is shown in Fig. 6 according to different filtering fractions. It can be seen that when the low frequencies are removed, the companion candidates appear more distinctly, mostly those close to the star. The diffraction patterns

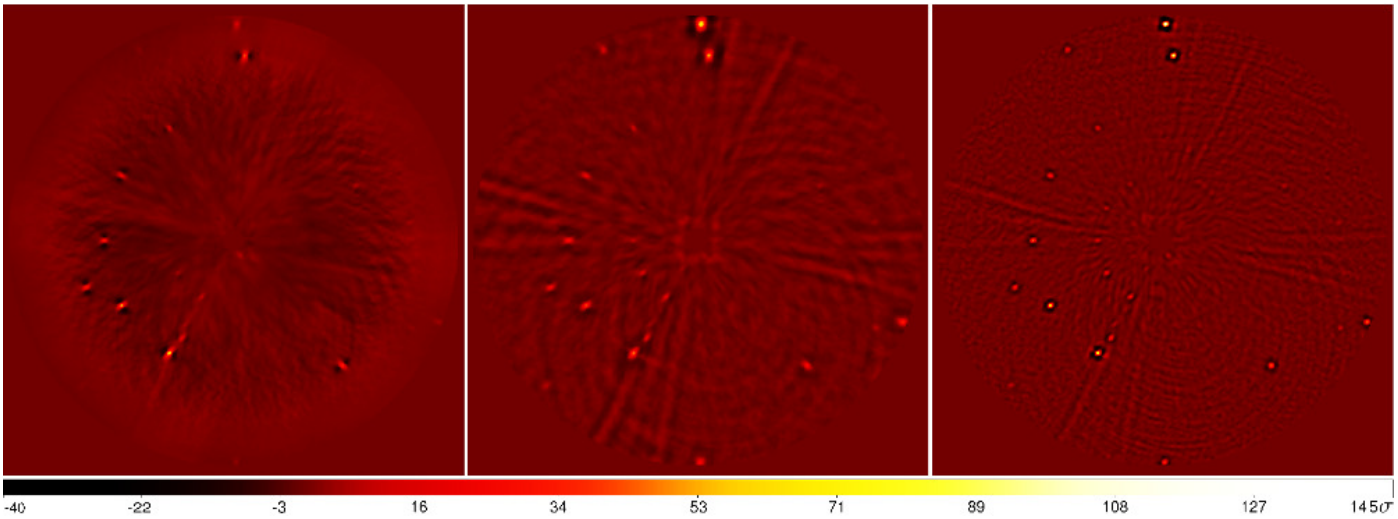

Fig. 6. Effect of the pre-processing (spatial high-pass filtering of the raw data) on the output S/N map obtained by processing the TYC-8979-1683-1 NaCo data (including both real and injected synthetic companions) with ANDROMEDA. *Left:* S/N map obtained without pre-filtering. *Middle:* S/N map obtained with high-pass pre-filtering, using $F = 1/16$. *Right:* S/N map obtained with high-pass pre-filtering using $F = 1/4$. All these S/N maps are normalized following the procedure in Sect. 2.5

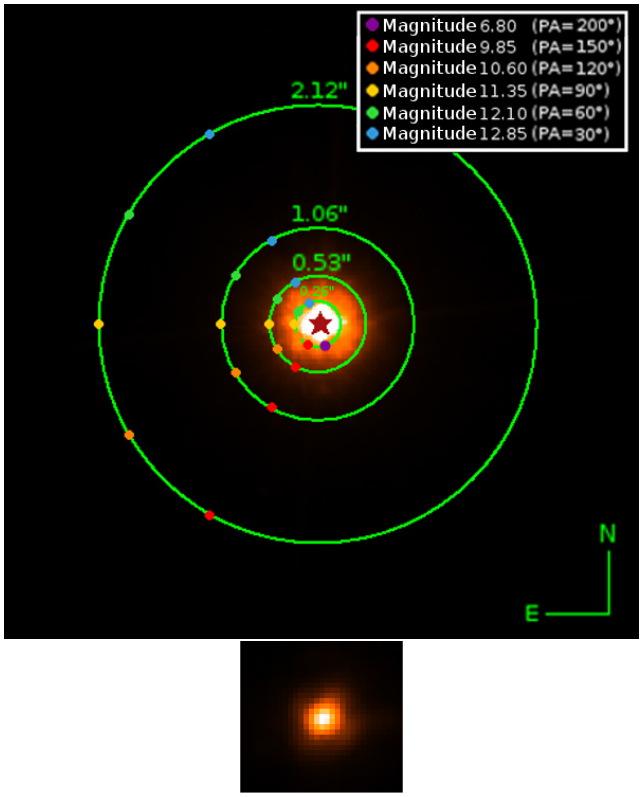

Fig. 5. NaCo data of TYC-8979-1683-1. *Top:* One reduced saturated image of the raw data cube (600 × 600 pixels, linear scale). The position of the injected synthetic planets is indicated with colored dots on the green circles. *Bottom:* Reduced unsaturated image used as a reference PSF to perform ANDROMEDA (32 × 32 pixels).

induced by the spider of the telescope are revealed as two blurry lines crossing at the center (their cone shape is due to the ADI process per annulus and shows the expected pattern, negative-positive-negative); the patterns remain despite the ADI procedure, probably due to the smearing of the star in the field. If not filtered enough, the number of false detections increases, especially close to the star, and many companions that are close to the star and faint are missing. Moreover, the accuracy of the estimated position and flux decreases since the planetary patterns are wider and less regular. We consequently chose to set the filtering fraction to $F = 0.25$: a quarter of the low frequencies are removed. This value is a trade-off between not losing too much companion flux (see Sect. 2.1), detecting as many true companions as possible, and decreasing the overall number of false alarms. We note that the oversampling of this data set is of 1.6, and so the filtering fraction must be smaller than $F = 0.6$.

Table 1. User-defined parameter values chosen to run ANDROMEDA on the TYC-8979-1683-1 VLT/NaCo data.

User-defined parameter	Used value
Filtering fraction, F	1/4
Minimum distance for subtraction, $\delta_{\min}$	1.0 λ/D
Width of the annuli for ADI, dr	1.0 λ/D
Ratio optimization to subtraction area, R_A	2
Size of the input PSF window, N_{psf}	32 × 32 pixels
Normalization profile smoothing, N_{smooth}	18 pixels

In Fig. 7, from left to right, are the flux map, the likelihood map, and the standard deviation of the flux map obtained with the parameters listed in Tab. 1. As expected, the flux and the likelihood maps look similar to the S/N map, and the standard deviation of the flux shows a clear radial decreasing trend from the center to the edge, as does the residual speckle noise distribution in the differential images.

4.2.1. Effect of the normalization process

In order to correctly normalize the S/N map, we have plotted the radial profile of the robust standard deviation per annulus of the S/N map, according to different smoothing values. We then chose the best profile, the one that smoothed tiny irregularities and kept the global trend. Some profiles are presented in Fig. 8 to compare the robust versus regular standard devia-

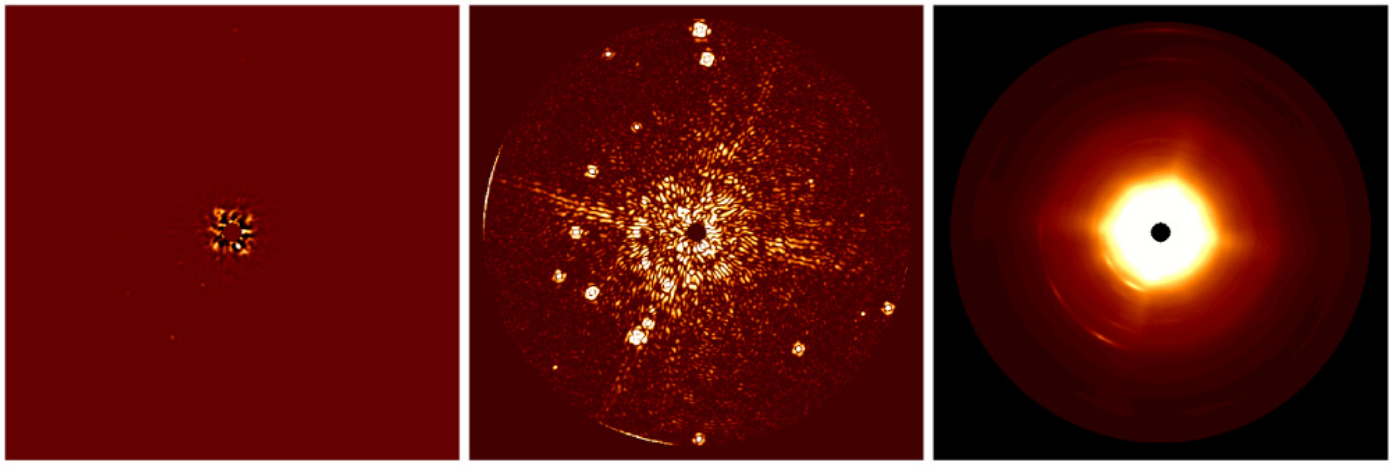

Fig. 7. Output obtained by processing the TYC-8979-1683-1 NaCo data (including both real and injected synthetic companions) with ANDROMEDA. *Left:* Flux map. *Middle:* Likelihood map. *Right:* Map of the standard deviation of the flux. For each of these maps (as for the S/N maps in Fig. 6) the central region corresponding to the star has been masked. The intensity scale is logarithmic for the likelihood and the standard deviation of the flux maps, and linear for the flux map. White corresponds to the highest value and black to the minimum value.

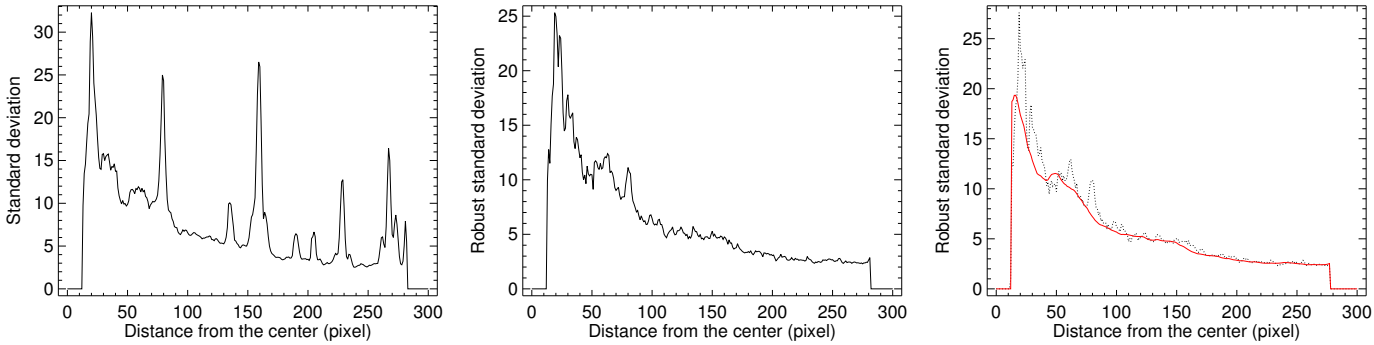

Fig. 8. Azimuthal mean standard deviation of the S/N map as a function of the distance to the star TYC-8979-1683-1. *Left:* Regular radial profile of the S/N standard deviation. We can visualize the high peaks indicating the presence of companions at certain separations. *Middle:* Radial profile of the S/N robust standard deviation. The highest peaks have disappeared but the profile is still jagged. *Right:* Radial profile of the S/N robust standard deviation smoothed over 28 pixels to obtain the global trend of the S/N map standard deviation deprived of its companions. The ANDROMEDA process reduces the exploitable zone between the IWA (at 13 pixels here since $IWA = 4\lambda/D$) and the OWA (at 281 pixels here since $OWA = \mathrm{Size}_{image}/2 - N_{PSF}/2 - dr$).

tion and smoothed versus unsmoothed profiles, thus justifying the choices that were made to build the normalized S/N map.

The maps in Fig. 9 show the raw S/N map (left) and the normalized S/N map (right) both thresholded to 5σ. The non-normalized S/N map (left) does not provide any workable information and just illustrates that its radial profile decreases toward the edge; however, the normalized S/N map reveals only the probable point sources in the map and therefore enables the automatic detection of companions.

4.2.2. Interest of the filtering and normalization process

In order to verify the consistency of the filtering and normalization procedure, we plotted the histograms of the residuals in the S/N map. This permits us to check if the PDF of the residuals has the expected shape, that is to say, Gaussian and white.

The histograms shown in Fig. 10 have been produced from the normalized S/N map obtained by processing the filtered images with ANDROMEDA on TYC-8979-1683-1, using the parameters gathered in Tab. 1. It can be checked that the residual noise in the S/N-map has been made Gaussian thanks to the high-pass filtering (Sect. 2.1) and also that, thanks to the normalization process, this Gaussian distribution is centered on zero, which means that the residuals have a mean value of zero, and its FWHM is equal to two, which corresponds to a standard deviation of about one.

4.2.3. Impact of the user-defined parameters

This part is a short discussion of the influence of each of the user-defined parameters on ANDROMEDA's output. The optimal values of the user-defined parameters found from these investigations are set as default in the algorithm, though it is appropriate only for this particular TYC-8979-1683-1 data set. The parameters are discussed in the order they are used in the algorithm. We note here that most user-defined parameters do not have a major impact on the estimation performance. Their optimal values *for this data set*, as well as the strength of their impact in terms of detection are gathered in Tab. 2.

Performing ADI: To perform the ADI according to the technique explained in Sect. 2.2.1, the parameter δ_{min} must be cho-

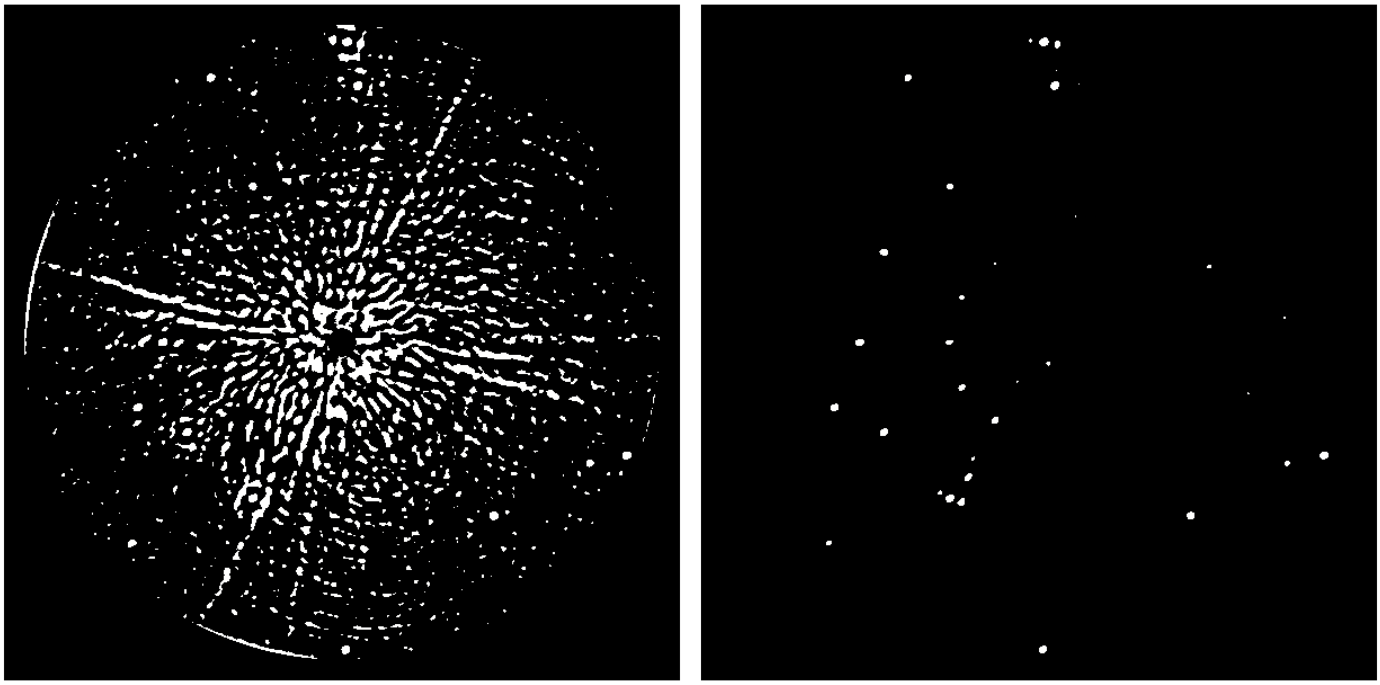

Fig. 9. S/N maps that have been thresholded to 5σ. *Left:* Non-normalized thresholded S/N map. We observe that many signals are above threshold (white), mostly close to the center and along the spider diffraction pattern. *Right:* Normalized thresholded S/N map. Here only the probable planetary signals are found above the threshold. It is possible to perform an automatic detection on this map.

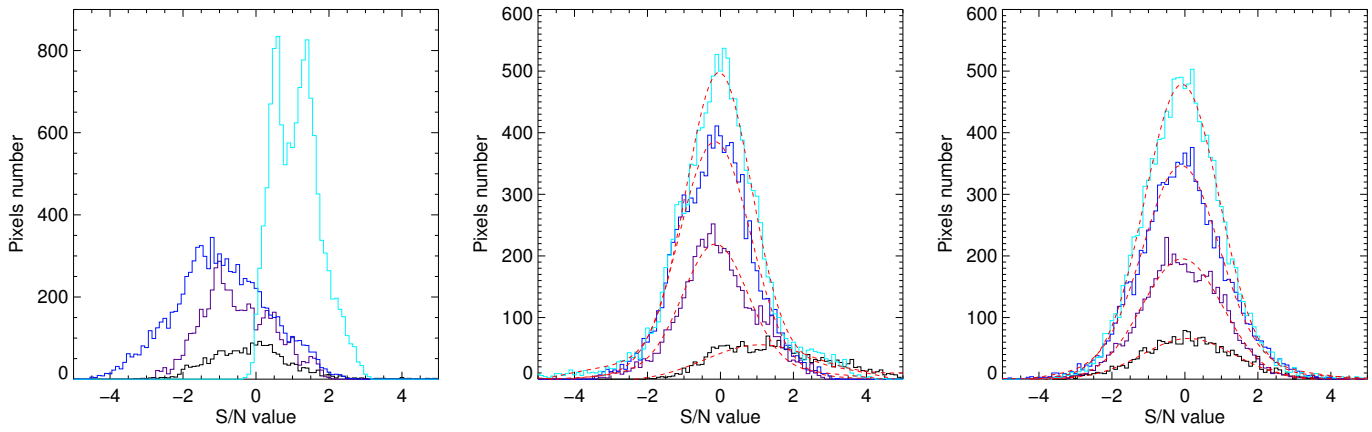

Fig. 10. Histograms of the residuals in the normalized S/N map, obtained using the NaCo data of TYC-8979-1683-1, inside four different annuli centered on the star: black solid lines are for an inner radius of 15 pixels ($\sim 5\lambda/D$), purple solid lines for 50 pixels ($\sim 17\lambda/D$), dark blue solid lines for 95 pixels ($\sim 32\lambda/D$), and light blue solid lines for 247 pixels ($\sim 90\lambda/D$). Each annulus has a width of 15 pixels except for the largest, which only has a width of 8 pixels. No obvious planetary-like signal can be found inside these annuli. *Left:* without filtering. *Middle:* with a pre-filtering, using $F = 1/16$. *Right:* with a pre-filtering, using $F = 1/4$. Gaussian fits of the histograms are overplotted in red dashed lines.

sen carefully to avoid self-subtraction of the companion while subtracting images as temporally correlated as possible. For this data set, the best compromise is obtained when using $\delta_{min} = 1.0\lambda/D$.

Since the displacement between two given images varies with the separation from the star, the ADI is performed over an annulus of user-defined width dr that should be the thinnest. Indeed, there are slightly fewer artifacts detected when dr decreases. However, the width of the annuli should not be too small because it increases the processing time. A compromise is to set $dr = 1\lambda/D$ as default.

When choosing to perform the image subtraction with either a least-squares fit or a L1-affine fit, the width of the annulus over which γ_k is calculated has a certain ratio R_A with respect to the width dr of the subtracted annuli (see Sect 2.2.1). There is a compromise to make when choosing the optimization area so that it can avoid discontinuities (being thicker) while minimizing the flux difference within the annulus taken into account (being close to the subtraction area). As expected, when R_A is too large many artifacts may be detected, but when R_A is too close to one there are discontinuities appearing between adjacent annuli. Under these considerations, the optimal value is set to $R_A = 2$.

Maximum likelihood: The size of the PSF window, N_{psf}, must completely enclose the full signal, otherwise it induces strong errors on the flux estimation. On the other hand, the larger the

window, the longer it takes to run ANDROMEDA. Thus, this parameter can be optimally set so that the first bright ring fits inside the PSF window.

We note that the four parameters talked about previously (δ_{min}, dr, R_A, and N_{psf}) are parameters that have been pointed out from the first developments of the ADI method. Some algorithms such as TLOCI (Marois et al. 2014) or PCA (Amara & Quanz 2012; Soummer et al. 2012), which are improvements of ADI, try to reduce the number of parameters for this part of the algorithm.

Normalization of the S/N: The number of pixels on which the S/N robust radial standard deviation profile is smoothed, N_{smooth}, is another important parameter. Too much smoothing biases the normalization and provokes the appearance of artifacts detected at less than 0.5″ from the star but that can be easily rejected a posteriori. On the other hand, a low smoothing may result in missing faint close signals. Thus, a good value is to smooth the profile over about 28 pixels, but this value is strongly dependent upon the oversampling and upon the quality of the images. It is the only parameter that must currently be chosen by hand after visualizing the trend of the profile with different values. We note that the chosen value does not need to be very precise: for this data set, it can vary from about 26 to about 50 pixels without adding too many artifacts above threshold.

To conclude, along with a correct normalization, ANDROMEDA provides workable output that allow an automatic detection procedure to be built. The results obtained with the automatic procedure, developed to extract the position and flux of the candidate companions from the output maps, are presented in the next section.

4.3. Analysis of the planetary signals detected

In a second step, the automatic detection module was applied on the maps, using a threshold of 5σ. The subimages extracted from the S/N map in which the fits are performed are shown in Fig. 4-*left*. On account of the pixel scale of the imaging camera, the size of the subwindows is set to 11 *pixels*, which is the expected planetary pattern size ($\sim 4\lambda/D$) that encloses the whole planetary signal. The S/N map on which the position of the detected signals is visible and labeled by their index of detection is shown in Fig. 4-*right*.

The program detected 39 signals above this threshold, including 25 reliable detections (Sect. 3.3). Of course the number of detections found in the S/N map depends on the threshold set; this dependence is dealt with in detail in Sect. 4.4. As expected, only the highest S/N signals are found surrounded by tertiary lobes that are detected (detections #1, #2, and #3, having S/N values of respectively 150σ, 105σ, and 95σ). It is also noticeable that, as expected again, all the fits that have converged in the S/N map have also converged in the flux map and vice versa. Thanks to the criteria classiying the detections laid down in Sect. 3.3 , the automatic detection procedure efficiently separates probable true companions from artifacts.

4.3.1. Performance in terms of detection and analysis

To better quantify for the performance of the method in terms of detecting point sources present in the image field and in estimating their positions and flux, it is possible to use the knowledge we have about the injected synthetic planets. Knowing their exact position and contrast, it is possible to compare them with the values obtained by the algorithm. It is also important to check that all the planetary companions found are indeed above the detection limit derived from this data set.

Figure 11 shows the contrast in terms of magnitude of the detected point sources as a function of the angular separation between the detected signal and the central star. On this graph, six horizontal lines represent the original contrast of the synthetic companions and four vertical lines are placed at their theoretical separation from the star. Consequently, we know that signals from the synthetic planets ought to be found at every crossing between the horizontal and vertical lines, except for the upper horizontal line, which only has one synthetic companion at the closest separation. The detection limit is overplotted on the graph (solid line) and the error bars in terms of 3σ error on the contrast estimation are added to the graph.

We first notice that, apart from the brightest synthetic companion that we injected just above the detection limit, none of the five synthetic planets that had been injected at 0.26″ from the star is detected. Moreover, only the brightest synthetic planet located at 0.53″is detected. This result is expected since each of these undetected synthetic planets is located under the detection limit curve. The detection limit shows the following trend: close to the star only bright companions can be detected, whereas going farther from the star enables fainter signals to be detected. Of course, the detection limit is dependent upon the chosen threshold, but even with a very low threshold, it is impossible to detect these faint and close signals. As all image processing methods, ANDROMEDA is limited by the observation conditions.

The estimated positions of the detected synthetic planets match the theoretical values, even very close to the star. The error bars in position due to the Gaussian fit uncertainty at 3σ are of about 2.0 mas (from 0.02 mas for the highest signal to 6.0 mas for the faintest). These errors in position are not shown in Fig. 11 since they are smaller than the symbol size. As expected, the flux is better estimated when the companion is bright and far from the star. A good agreement is still observed between the theoretical contrast and the estimated value, knowing that the error bars shown in Fig. 11 are only the ones given by the map of the flux standard deviation but without taking into account the instrumental errors or the algorithm's intrinsic errors.

To assess the errors intrinsic to the algorithm, one approach is to slightly move the user-defined parameters (which might influence the estimations) from their optimal value. The boundaries within which such user-defined parameter are made to vary are the following: $\delta_{min} \in [0.2; 2.0]\lambda/D$, $dr \in [0.5; 3]\lambda/D$, $R_A \in [1; 4]$, and N_{smooth} must be varied experimentally from no smoothing to what can be reached with the data at hand. In this way, we obtained an error of about 5.0 mas in position and of about 0.25 magnitude, depending on the intensity of the signal. Accounting for this deviation, the real position and contrast values of the injected fake companions are within the error bars of the ANDROMEDA estimations.

In exoplanet imaging, the dominant errors on the position and flux estimations are usually due to instrumental sources. But in the case of poor quality data, it must be verified which of the instrument calibration errors or the algorithm unstability errors are dominant.

4.4. Threshold sensitivity

This section discusses the optimal threshold range that would reveal as many true companions as possible, while not missing any. In particular, it is tested whether a constant detection threshold is efficient all over the field of view. This discussion re-

Table 2. User-defined parameters set as defaults in the ANDROMEDA pipeline and their respective significance.

Parameter	Definition	Units	Default value	Impact
F	Filtering fraction (Sect. 2.1)	-	1/4	low
$\delta_{\min}$	Minimum separation to build the differential images (Sect. 2.2.1)	λ/D	1.0	high
dr	Width of annuli on which ADI is performed (Sect. 2.2.1)	λ/D	1	low
R_A	Ratio optimization to subtraction areas (Sect. 2.2.1)	-	2	low
N_{psf}	Size of the square PSF image (H-band filter of NaCo)	pixels	32	see text
N_{smooth}	Smoothing of the S/N robust standard deviation profile (Sect. 2.5)	pixels	18	high

Notes. The right column shows the impact of the user-defined parameters over the whole process: If *low*, the value can remain fixed and if *high*, it should be tuned according to the data set.

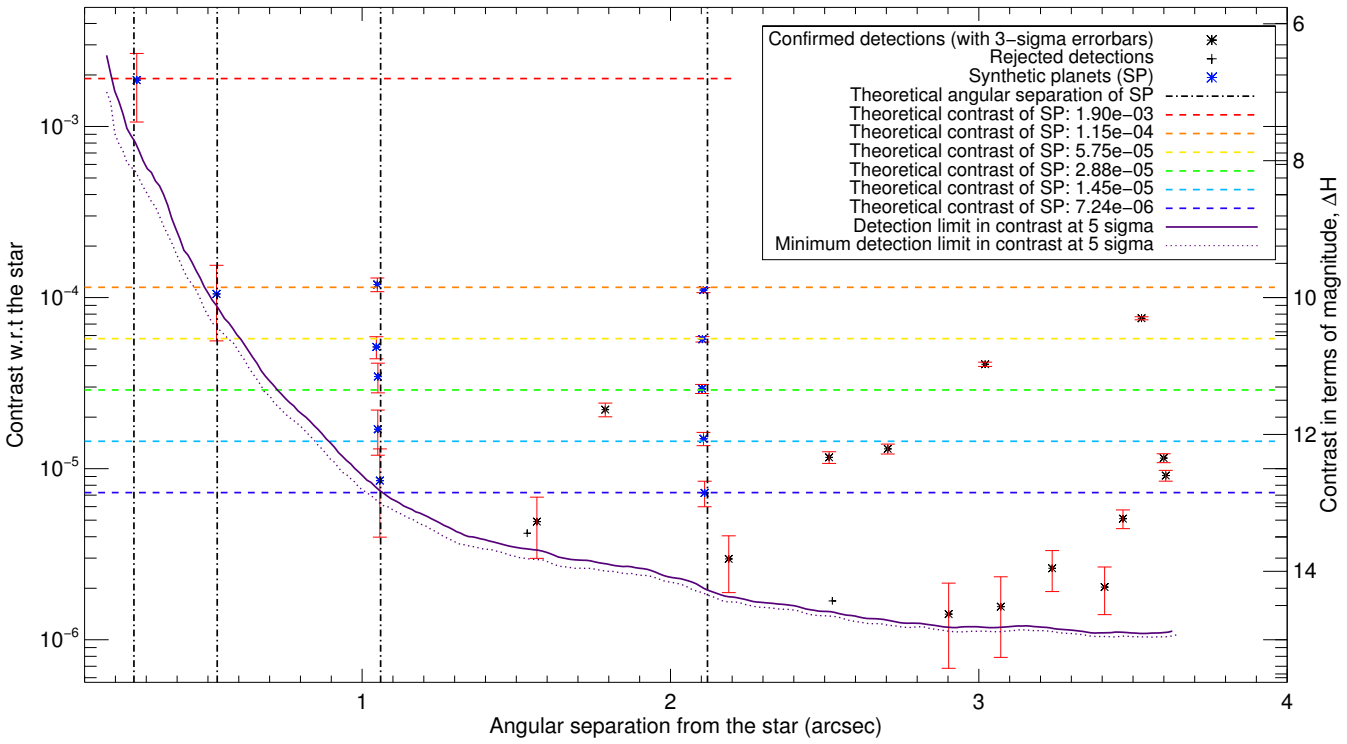

Fig. 11. Contrast of the detections as a function of their distance to the star TYC-8979-1683-1. The theoretical contrasts and distances of the 20 injected synthetic planets are shown as vertical and horizontal lines: we should have found a planetary signal at every crossing. One synthetic companion has also been added at the closest separation just above the detection limit in order to check its consistency (red dashed line). The detection limit at 5σ is overplotted (solid line). This detection limit curve is corrected for the underestimation of the small sample statistics at close separation from the star (see Sect. 2.4). The minimum value of the flux standard deviation map at 5σ for each separation is overplotted for information (dotted line). The radial median of the flux standard deviation map at 5σ, however, provides a realistic estimation of the detection limit. The detected signals assessed to be tertiary lobes are not shown on the graph.

lies upon a study of the behavior of the number of detections as a function of the threshold. Discussing missed detections and false positives requires assumptions on the actual number of companions present in the field. The series of fake companions is a firm basis. The number of astronomical background stars produces additional test cases to check the detection capability homogeneity, and can be tested in comparison to other ADI approaches. We assume in the following that the exact number of detectable point sources for this data set is 25. The graph in Fig. 12 was obtained by running ANDROMEDA under the same conditions as before (Tab. 1), and represents the number of detections as a function of the threshold which varies from 3σ to 6σ. On this graph, both the total number of detections and the number of so-called reliable detections are indicated.

This graph shows the existence of a short optimal threshold range, between 4.7σ and 5.1σ, for which the number of detections is exactly the one suspected of being the true one. When increasing the threshold above this range, the faintest signals (like #39) and/or the ones very close to the star (like #33) are the first to be missed by the automatic detection process, whereas several tests have proved that these are most likely to be real point source signals. When decreasing the threshold, some detections that are actually not true signals are detected and still pass the test that is supposed to sort out artifacts from potential real signals. These detections are usually faint signals ($\Delta H \sim$ 14-16), located far from the star where the algorithm should show better performance, that are most likely to be false alarms due to residual speckles. Moreover, a careful examination of the shape of this graph brings useful insights to help the user choose the threshold. An initial inspection shows that lowering the threshold increases the number of detections exponentially and that there is a plateau, from $\sim 4.5\sigma$ to $\sim 5.0\sigma$, where the number

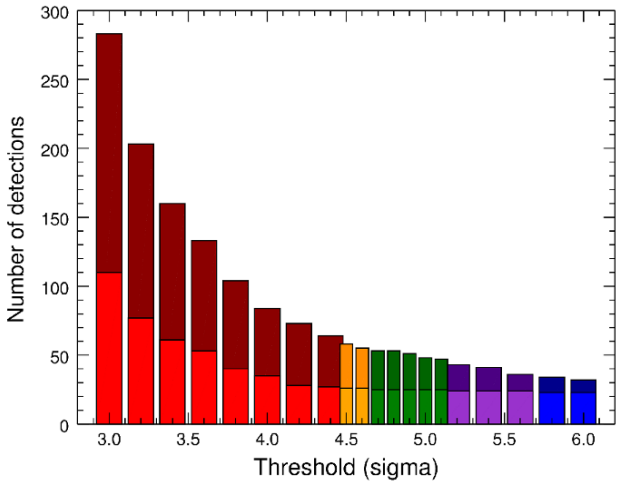

Fig. 12. Number of total detections (dark color) and of confirmed detections (light color) as a function of the threshold set for the TYC-8979-1683-1 NaCo images. The optimal zone (where all 25 companions are detected) is shown in green. A false alarm zone is shown in red (more than one false detection) and orange (one false detection) and a loss zone in blue (more than one true companion is not detected) and purple (one true companion is not detected).

of detections is quite stable as it is for the number of true detections. Also, by looking at the ratio of true detections versus ill-fitted ones, below a threshold of 4.5σ, the number of ill-fitted detections becomes significantly higher than the number of true detections, whereas above the threshold this ratio remains quite constant. This study is of course strictly valid only for this data set, which has the advantage of containing many point sources, but it should still give a fair idea of the behavior of the algorithm as a function of the threshold.

Even if this test case is very advantageous, the goal of this section is to check the overall method skills. This procedure proved to be very efficient in terms of detection ability and in terms of position and contrast estimations with low error bars. We noticed that thresholding the S/N map was not enough to provide only real probable planetary signals so we added an a posteriori classification of the detections, which also proved its efficiency in discriminating artifacts from very probable true point source signals. We note that ANDROMEDA does not provide more information than can be reached given the observation conditions (according to the detection limit trend), but the algorithm does provide, within some minutes, reliable information in terms of position and flux of the detected companions. Of course where the noise is higher (toward the star), the estimation is slightly less accurate, but the errors still remain under the observational errors such as the PSF centering or the tip-tilt correction. Section 5 is a comparison of the results obtained by processing the well-known case of Beta-Pictoris using the PCA methods or ANDROMEDA.

5. Results on β Pictoris and comparison with the PCA-KLIP method

In addition to testing the method on the previous field, populated with both numerous background stars and additional synthetic companions, we also applied it to the emblematic and well-known case of β Pictoris. This star is surrounded by a debris disk inside which only one planet, β Pictoris b, has been detected by imaging. This close companion is located at $\sim$ 9 AU from its host star and was first detected by Lagrange et al. (2009). This companion has since been observed repeatedly because of its outstanding astronomical interest for many reasons. It is a moderate-mass giant planet at close physical separation, making it a good candidate for having been formed within the disk. Its interactions with the remaining debris disk can still be witnessed and dynamical constraints can also be derived from the orbital motion and from numerous falling evoporating bodies as observed in spectroscopy (see Lagrange-Henri et al. 1988; Beust et al. 1990). In the context of this paper, observations of this companion provide an excellent test case of our method in the challenging case of the detection of a companion at very short separation ($< 0.5''$) with appropriate high-quality coronagraphic images; the images processed by ANDROMEDA should be compared to those processed thanks to other methods representing the state of the art.

The β Pictoris data on which we applied ANDROMEDA are described in Absil et al. (2013). The goal of this data set was to search for closer planetary companions (down to 2 AU from the star), which would be at the origin of the dynamical excitation in the planetary system. This search required the use of a newly developed coronagraph that allows detections at angular separation as close as $0''.1$.

5.1. Data used for comparison

β Pictoris was observed on 31 January 2013 for 3.5h at the Very Large Telescope (Chile) using the NaCo instrument (ESO programme ID 60.A-9800). The images were recorded in the L' band (centered on 3.8μm), which is commonly used to work in a more favorable planet/star contrast regime compared to shorter wavelengths, and to obtain an image quality close to that delivered by extreme adaptive optics (XAO) systems in the near-infared. To minimize the impact of starlight in the images, the newly commissioned L'-band Annular Groove Phase Mask (AGPM, Mawet et al. 2005, 2013) vector vortex coronagraph was used. This kind of coronagraph provides an inner working angle and an achromaticity over the bandwidth of interest as good as any other phase mask developed so far.

The data are constituted of ten blocks of 200 successive frames of 0.2s, each taken under fair turbulence conditions. The observing sequence was obtained in pupil-tracking mode, showing a total field rotation of 83°. Two non-coronagraphic PSFs were taken before and after the observing sequence by moving the star far from the vortex center. The pixel scale of the camera used is 27.15 mas/px and the PSF FWHM is empirically measured to be 4 pixels. All the information concerning the data set used in this section and the pre-processing steps applied before running image processing algorithms such as ANDROMEDA (basic cosmetic treatment, recentering, frame selection, etc.) can be found in Absil et al. (2013).

5.2. ANDROMEDA results and comparison with PCA

This section compares the quality of the detection, photometry, and astrometry obtained by ANDROMEDA with respect to the output of a principal component analysis (PCA Soummer et al. 2012; Amara & Quanz 2012), as presented in Absil et al. (2013). We thus ran ANDROMEDA on the exact same data cube and the automatic detection module on its output.

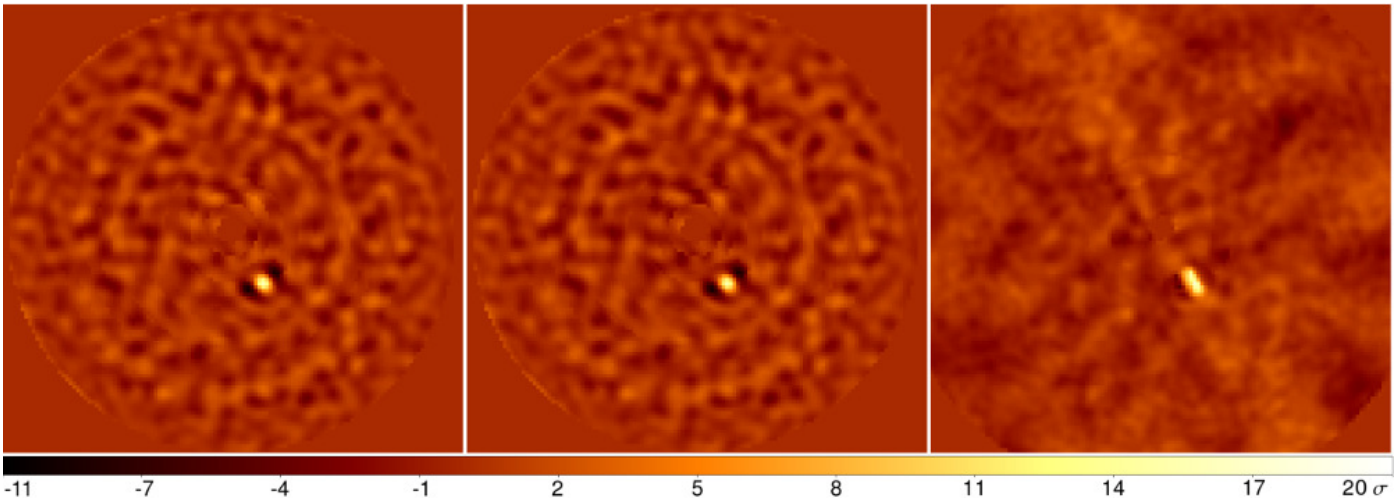

Fig. 13. Resulting S/N map of β Pictoris according to two different image processing methods applied on the reduced data. *Left:* S/N map obtained from ANDROMEDA, using a least-squares optimization for the ADI subtraction. *Middle:* S/N map obtained from ANDROMEDA, using a L1-affine optimization for the ADI subtraction. The residuals are slightly lower, mostly close to the central part, as explained in Sect. 2.2.1. *Right:* S/N map obtained with the PCA-KLIP algorithm (see text). All images are linearly scaled. No signal is found above the 5σ threshold in any of the maps, except for the companion β Pictoris *b*.

Table 3. Relative astrometry and photometry of β Pictoris *b* retrieved from the VLT/NaCo-AGPM data processed with PCA-KLIP and ANDROMEDA methods.

Parameters	**Estimated value using ANDROMEDA**	**Estimated value using PCA**
Peak S/N (σ):	17	17
Separation from the star *sep* (mas):	455 ± 8.7	452 ± 9.6
Position angle *PA* (°):	210.7 ± 0.8	211.2 ± 1.3
Contrast $\Delta L'$ (mag):	8.09 ± 0.21	8.01 ± 0.16

Given that for this study we have selected a region of 150×150 pixels around the star, and knowing the pixel scale of the L' camera (27.15 mas/pixel), the user-defined parameter values chosen to run ANDROMEDA and the detection module are listed in Tab. 4.

Table 4. Parameters used to run ANDROMEDA on the β Pictoris VLT-NaCo-AGPM data set.

Parameter	**Used value**
F	1/4 (default)
dr	1 λ/D (default)
R_A	2 (default)
$\delta_{\min}$	1 λ/D (default)
N_{psf}	20×20 pixels
N_{smooth}	10 pixels
IWA	1 λ/D
Threshold	5σ
Subwindow size	9×9 pixels

The resulting S/N map is shown in Fig. 13-*Left* where the expected companion β Pictoris *b* is clearly visible as a sharp bright spot, southeast of the star (located at the center of the frame).

The same data set has been processed with a home-grown PCA algorithm, based on the KLIP implementation (Soummer et al. 2012). The KLIP algorithm uses a truncated basis of eigenvectors created by a Karhunen-Loève transform of the initial set of images, to perform the subtraction of the star residuals. To follow the original KLIP algorithm, the image processing was performed on the full 150×150 pixel frames at once, and no frame was excluded from the ADI image library based on the amount of parallactic angle variation (unlike in Absil et al. 2013). From the final image of the PCA processing, we compute a S/N map by testing resolution elements centered on each pixel of the map against all the other resolution elements located at the same angular distance from the star, as described in Mawet et al. (2014). The number of principal components used in KLIP was tuned to maximize the S/N of the planet in the final image, resulting in the use of 18 principal components instead of 30 in Absil et al. (2013). The S/N map is illustrated in Fig. 13-*Right*, showing a peak S/N ~ 17 on the planet, i.e., the same as in the case of ANDROMEDA. We note that more advanced implementations of the KLIP algorithm, working on well-defined subregions (e.g., annuli or parts of annuli) in the images and including a frame rejection criterion based on the parallactic angle, can reach a peak S/N of up to ~ 20, although at the expense of a drastically increased computation time (a few minutes instead of ~ 1 second for the classical KLIP algorithm). Using ANDROMEDA, we could reach this S/N value by smoothing the profile over 20 pixels instead of ten, as used here. This does not affect the computation time, but for this value of N_{smooth} one artifact appears above the 5σ threshold.

The errors on the photometric and astrometric estimations are mostly limited by instrumental calibration errors, which can be decomposed into three main contributions: the error on the position of the source (8.5 mas), the PSF centering error in the images (0.1 mas), and the plate scale error (0.04 mas). As these errors are independent, the resulting error is the quadratic sum, giving in this case a total of 8.5 mas. Adding the 3σ error on the position estimation with ANDROMEDA (1.7 mas), the total error on the position is of 8.6 mas and the algorithm's intrinsic error is evaluated within this error bar. For the position angle,

the main errors are due to the true north direction knowledge (0.09°) and the offset of the derotator (0.01°), as discussed by Chauvin et al. (2012). ANDROMEDA gives the PA with a 3σ precision of 0.8° and a negligible intrinsic error. The errors on the flux estimation are mainly due to the variation of the PSF along the observation (0.05 mag). ANDROMEDA estimates the flux with a 3σ statistical error of 0.2 mag and a negligible intrinsic error, and as these three sources are independent again, the total error is the quadratic sum of each error. The estimated position and contrast with both methods and their corresponding error bars are found in Tab. 3, where the photometric and astrometric estimations for the PCA pipeline are directly taken from the publication of Absil et al. (2013). The two estimations agree with each other within error bars.

We emphasize once again here that the photometry and astrometry can be recovered much more easily with ANDROMEDA than with PCA, in particular, because the estimation is direct and precise without needing to inject fake companions. The same applies for the detection limit computation, which is given directly by the map of the standard deviation of the flux provided by ANDROMEDA and does not need, for instance, numerous synthetic planet injections as for other methods.

5.3. Sensitivity comparison and discussion

Another way of comparing the performance of the two methods is to plot their 5σ detectability limits in terms of contrast.

For the PCA-KLIP method, the computation of the detection limits is based on the hypothesis that the noise is Gaussian (Marois et al. 2008), which was checked empirically in Absil et al. (2013). Several methods have been used in the literature to derive detection limits. Here, we use the statistical framework presented in Mawet et al. (2014), where test speckles are compared to the statistics of the flux within all other resolution elements located at the same angular distance from the center. This framework assumes that the noise statistics varies with the distance from the star but not with the azimuth, and it takes into account the effect of small sample statistics on the noise estimations. More specifically, the computation of the contrast curve consists in normalizing the flux in the final PCA-processed image by the integrated flux contained inside the (off-axis) stellar PSF core, then in calculating the standard deviation of the fluxes enclosed in all the non-overlapping apertures of diameter equal to the FWHM of the PSF that can be placed at a given distance from the center. The same procedure is repeated at all radial distances. During the process, any known companion can be masked out , which we did here in order not to bias our noise estimation at the distance of β Pic b. This estimation of the contrast curve provides more realistic results than the pixel-to-pixel standard deviation noise estimation that has frequently been used in the literature in the past.

We chose to use here a "smart" version of the PCA-KLIP algorithm (sPCA), where the images are decomposed in annuli and where a frame rejection criterion is included based on the parallactic angle, in order to avoid self-subtraction of the possible planetary signals. We used the same smart PCA parameters as for the computation of the detection limits in Absil et al. (2013). The final contrast curve, plotted in Fig. 14, takes into account the algorithm throughput, estimated at several radial distances (and azimuths) by injecting fake companions in the original data cube, running the PCA pipeline with the exact same parameters, and comparing the flux of the fake companions in the final PCA-processed image with the flux of the injected companions. We note that the PCA contrast curve presented here is a factor of two higher than the one presented in Absil et al. (2013), where an improper convolution by a Gaussian kernel led to a factor of two underestimation of the contrast curve.

Figure 14 shows the different detection limit curves obtained with the sPCA algorithm and with ANDROMEDA using the methods noted above, all corrected for the small sample statistics. The location of β Pictoris b in terms of angular separation and contrast is also indicated on the graph for comparison. In this figure, we can see that at angular separations ranging from 0.1″to 2″, ANDROMEDA and PCA provide similar detection limits.

To give a rough idea, we mention here that ANDROMEDA takes about 180 seconds to process the 612 150×150 pixels images on a quadri-pro six-core Intel Xeon. This computing time includes the time to obtain the three main outputs from ANDROMEDA (estimated flux map, S/N map, and the map of the standard deviation of the estimated flux) plus the detection described in Sect. 3 (detection of probable point source, sorting out, subpixel position estimation, flux estimation, and corresponding derivation of the 3σ error bars and the computation of the detection limit curve). This latter detection is obtained from the ANDROMEDA output within a few seconds. For the PCA-KLIP method, it takes about 1 second to produce the final reduced image using the original KLIP algorithm. Building the S/N map in Fig. 13 from this reduced image along the Mawet et al. (2014) prescription takes an additional few tens of seconds. We note that the annulus-wise, "smart" PCA (sPCA) processing used to compute the detection limits in Sect. 5.3 takes about 10 minutes on a recent core-i7 laptop. Also, we emphasize here that the photometry and astrometry are included in ANDROMEDA while PCA needs dedicated, computationally intensive methods to get an accurate estimation (such as the negative fake companion technique, which requires running many PCAs to obtain the photometric and astrometric estimations together with their error bars). The latter figures must be taken with care since there are still ways to optimize the computation time for both algorithms (for instance parallelizing the ADI plus MLE with ANDROMEDA), but they are mentioned here to give a rough order of magnitude of the processing time.

The two algorithms that we have used to process the VLT/NaCo-AGPM data of β Pictoris both efficiently detect the close companion β Pictoris b. However, ANDROMEDA does the detection automatically, by giving direct access to the S/N map (which is only a by-product in the PCA algorithm). The approaches that the two algorithms use to estimate the position and flux of the companion are quite different, but result in compatible values. ANDROMEDA potentially shows better accuracy in terms of separation and contrast estimation since it directly relies on the detection probability derived from a strong hypothesis about the image formation and the residual noise in the images, which are well verified. To conclude, the two methods are complementary since they do not rely on the same inner concept and it is better to use several methods that are significantly different to better judge of the truthfulness of a detection.

6. Conclusion and perspectives

The ANDROMEDA method is designed to detect planetary-like signals in high-resolution and high-contrast images. In this paper we have described the improvements brought to the original method when applied to on-sky VLT/NaCo data, in order to make it more robust. This included the implementation of a pre-processing (high-pass filtering of the data), a post-processing (normalization of the S/N map), and the use of a robust method

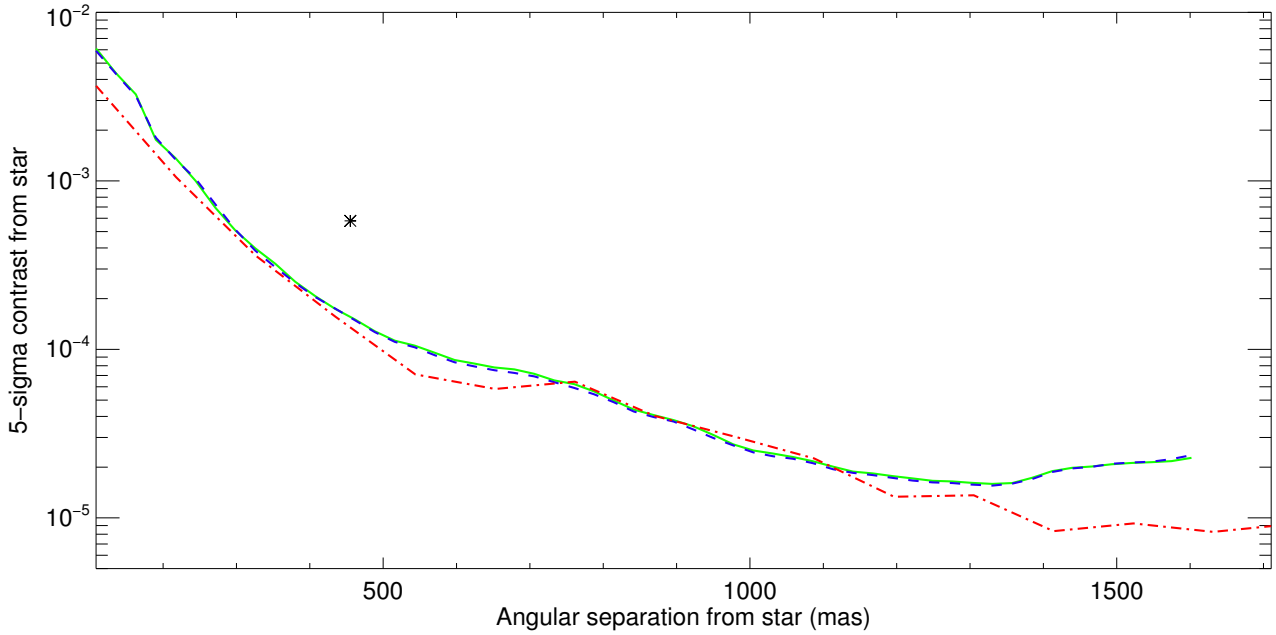

Fig. 14. Detection limits at 5σ obtained by processing the β Pictoris data from VLT/NaCO-AGPM with ANDROMEDA (green solid line, when using a L1-affine optimization or blue dashed line when using a LS optimization) or sPCA (red dash-dotted line). The asterisk symbol shows the location of the detected signal above the 5σ threshold set (only β Pictoris b is detected here).

to perform the image difference. As a result, this method proves to be highly efficient at processing experimental data from the VLT/NaCo instrument taken in pupil-tracking mode. In particular the produced normalized S/N map can be thresholded with a constant value throughout the field of view so as to provide detectability and false alarm levels that are homogeneous over the field. This allows one to automatically detect the candidate companions present in the image, and classify them according to their S/N values. Artifacts can then be rejected based on morphogical criteria expected for a true companion. We then showed on synthetic companions and on the well-known case of β Pic b that ANDROMEDA accurately estimates the subpixel position and the contrast of these companions. Notably, and unlike most other methods, the selection of the data reduction parameters (like filtering or minimum angular separation used for image differences) is fully taken into account in the search for the companion signature, and thus it does not bias the companion flux estimate. In particular, the analysis of the result does not require subsequent tests with synthetic planet injections to estimate a companion flux loss.

The second generation of instruments dedicated to exoplanetary detection and characterization, such as VLT-SPHERE, (Beuzit et al. 2008), Gemini-GPI, (Macintosh et al. 2008), and Subaru-SCeXAO, (Martinache & Guyon 2009; Jovanovic et al. 2013), is about to deliver a large amount of data that will require massive, homogenous, and efficient companion extraction. The capabilities of ANDROMEDA in terms of performance and automatic detection will be very beneficial in this context.

Though ANDROMEDA is operational in its current state, any further experience on these new instruments may motivate the evolution of this algorithm[1]. In particular, its probabilistic formalism directly enables one to include any a priori knowledge of the noise structure of the data or on the sought companions. Evolutions can be considered in various ways to build differential images (for instance, if it appears that the closest images in time are not necessarily the most correlated). Finally, the non-coronagraphic PSF, defining the companion's expected signature, is currently assumed to be stable along the data sequence, as measured before or after the coronagraphic or saturated data set. If the evolution of the PSF and in particular the evolution of the Strehl ratio are known, this variability can be easily included in the algorithm for a better flux estimate fidelity.

[1] The authors of the ANDROMEDA code are open to working in collaboration in order to apply the code to other data and thus gain further experience.

Acknowledgements. The authors thank A. Eggenberger for preliminary work made on applying ANDROMEDA to real VLT/NaCo data. We would also like to especially thank D. Mawet, R. Galicher, C. Lefevre, A. Vigan and T. Fusco for their careful reading and relevant comments. F. Cantalloube and L. Mugnier thank the European Commission under FP7 Grant Agreement No. 312430 Optical Infrared Coordination Network for Astronomy and the French Aerospace Lab (ONERA) (in the framework of the NAIADE Research Project) for partly funding this work. O. Absil and C. A. Gomez Gonzalez acknowledge funding from the European Research Council Under the European Union's Seventh Framework Programme (ERC Grant Agreement n. 337569) and from the French Community of Belgium through an ARC grant for Concerted Research Action.

References

Absil, O., Milli, J., Mawet, D., et al. 2013, A&A, 559, L12
Allard, F., Homeier, D., & Freytag, B. 2012, Royal Society of London Philosophical Transactions Series A, 370, 2765
Amara, A. & Quanz, S. P. 2012, MNRAS, 427, 948
Beers, T. C., Flynn, K., & Gebhardt, K. 1990, AJ, 100, 32
Beust, H., Vidal-Madjar, A., Ferlet, R., & Lagrange-Henri, A. M. 1990, A&A, 236, 202
Beuzit, J.-L., Feldt, M., Dohlen, K., et al. 2008, in Society of Photo-Optical Instrumentation Engineers (SPIE) Conference Series, Vol. 7014, Society of Photo-Optical Instrumentation Engineers (SPIE) Conference Series
Borucki, W. J., Scargle, J. D., & Hudson, H. S. 1985, ApJ, 291, 852
Cassan, A., Kubas, D., Beaulieu, J.-P., et al. 2012, Nature, 481, 167
Chauvin, G., Lagrange, A.-M., Beust, H., et al. 2012, A&A, 542, A41
Chauvin, G., Vigan, A., Bonnefoy, M., et al. 2015, A&A, 573, A127

Cornia, A., Mugnier, L. M., Mouillet, D., et al. 2010, in Society of Photo-Optical Instrumentation Engineers (SPIE) Conference Series, Vol. 7736, Society of Photo-Optical Instrumentation Engineers (SPIE) Conference Series
Fitzgerald, M. P. & Graham, J. R. 2006, ApJ, 637, 541
Goodman, J. W. 1985, Statistical optics
Hinkley, S., Oppenheimer, B. R., Soummer, R., et al. 2007, ApJ, 654, 633
Hoaglin, D. C., Mosteller, F., & Tukey, J. W. 1983, Understanding robust and exploratory data anlysis
Jovanovic, N., Martinache, F., Guyon, O., Clergeon, C., & Garrel, V. 2013, in American Astronomical Society Meeting Abstracts, Vol. 221, American Astronomical Society Meeting Abstracts, 305.05
Kuhn, J. R., Potter, D., & Parise, B. 2001, ApJ, 553, L189
Lafrenière, D., Marois, C., Doyon, R., Nadeau, D., & Artigau, É. 2007, ApJ, 660, 770
Lagrange, A.-M., Gratadour, D., Chauvin, G., et al. 2009, A&A, 493, L21
Lagrange-Henri, A. M., Vidal-Madjar, A., & Ferlet, R. 1988, A&A, 190, 275
Lenzen, R., Hartung, M., Brandner, W., et al. 2003, in Society of Photo-Optical Instrumentation Engineers (SPIE) Conference Series, Vol. 4841, Instrument Design and Performance for Optical/Infrared Ground-based Telescopes, ed. M. Iye & A. F. M. Moorwood, 944–952
Macintosh, B. A., Graham, J. R., Palmer, D. W., et al. 2008, in Society of Photo-Optical Instrumentation Engineers (SPIE) Conference Series, Vol. 7015, Society of Photo-Optical Instrumentation Engineers (SPIE) Conference Series
Marcy, G. W. & Butler, R. P. 1993, in Bulletin of the American Astronomical Society, Vol. 25, American Astronomical Society Meeting Abstracts #182, 916
Marleau, G.-D. & Cumming, A. 2014, MNRAS, 437, 1378
Marois, C., Correia, C., Véran, J.-P., & Currie, T. 2014, in IAU Symposium, Vol. 299, IAU Symposium, ed. M. Booth, B. C. Matthews, & J. R. Graham, 48–49
Marois, C., Doyon, R., Racine, R., & Nadeau, D. 2000, PASP, 112, 91
Marois, C., Lafrenière, D., Doyon, R., Macintosh, B., & Nadeau, D. 2006, ApJ, 641, 556
Marois, C., Lafrenière, D., Macintosh, B., & Doyon, R. 2008, ApJ, 673, 647
Martinache, F. & Guyon, O. 2009, in Society of Photo-Optical Instrumentation Engineers (SPIE) Conference Series, Vol. 7440, Society of Photo-Optical Instrumentation Engineers (SPIE) Conference Series
Mawet, D., Absil, O., Delacroix, C., et al. 2013, A&A, 552, L13
Mawet, D., Milli, J., Wahhaj, Z., et al. 2014, ApJ, 792, 97
Mawet, D., Riaud, P., Absil, O., & Surdej, J. 2005, ApJ, 633, 1191
Mugnier, L. M., Cornia, A., Sauvage, J.-F., et al. 2009, Journal of the Optical Society of America A, 26, 1326
Mugnier, L. M., Fusco, T., & Conan, J.-M. 2004, Journal of the Optical Society of America A, 21, 1841
Racine, R., Walker, G. A. H., Nadeau, D., Doyon, R., & Marois, C. 1999, PASP, 111, 587
Rosenblatt, F. 1971, Icarus, 14, 71
Rousset, G., Lacombe, F., Puget, P., et al. 2003, in Society of Photo-Optical Instrumentation Engineers (SPIE) Conference Series, Vol. 4839, Adaptive Optical System Technologies II, ed. P. L. Wizinowich & D. Bonaccini, 140–149
Schneider, J., Dedieu, C., Le Sidaner, P., Savalle, R., & Zolotukhin, I. 2011, A&A, 532, A79
Smith, I., Ferrari, A., & Carbillet, M. 2009, Signal Processing, IEEE Transactions on, 57, 904
Soummer, R. & Aime, C. 2004, in Society of Photo-Optical Instrumentation Engineers (SPIE) Conference Series, Vol. 5490, Advancements in Adaptive Optics, ed. D. Bonaccini Calia, B. L. Ellerbroek, & R. Ragazzoni, 495–503
Soummer, R., Pueyo, L., & Larkin, J. 2012, ApJ, 755, L28
Spiegel, D. S. & Burrows, A. 2012, ApJ, 745, 174
Thiébaut, E. & Mugnier, L. 2006, in IAUC 200, Direct Imaging of Exoplanets: Science & Techniques, oct. 2005, Nice, France
Udry, S. & Santos, N. C. 2007, ARA&A, 45, 397
Walker, G. A. H. 1995, Ap&SS, 223, 103

Appendix B

User Manual for the ANDROMEDA pipeline

This user manual is included in the ANDROMEDA package. I wrote this user manual in a way that each part is self-consistent and can be read independently. If a user is looking for a specific information, I took a particular care in making it easy to find the information. Feedbacks from collaborators improved this document which can also be updated directly by the users.

ANDROMEDA: User-manual
Version-1.0

Faustine Cantalloube (IPAG & Onera)
contact: faustine.cantalloube@univ-grenoble-alpes.fr

April 28, 2016

Contents

1 ANDROMEDA: Summary of the different steps **2**

2 Required input to run ANDROMEDA **3**
2.1 Science frames: `IMAGES_1_INPUT` . . . 3
2.2 Reference PSF: `PSF_PLANET_INPUT` . . . 3
2.3 Parallactic angles: `ANGLES_INPUT` . . . 4
2.4 Oversampling factor: `OVERSAMPLING_1_INPUT` . . . 4
2.5 User-defined parameters to run the ANDROMEDA function. . . . 4

3 Output provided by the ANDROMEDA function. **8**
3.1 SNR map: `SNR_OUTPUT` . . . 8
3.2 Flux map: `FLUX_OUTPUT` . . . 8
3.3 Flux standard deviation map: `STDDEVFLUX_OUTPUT` . . . 8
3.4 Other useful output . . . 8
3.5 SADI mode of ANDROMEDA . . . 9
3.6 Multispectral data processed with ANDROMEDA . . . 10

4 Automatic detection and characterization procedure **11**
4.1 Input needed for the analysis module . . . 11
4.2 Output given by the detection and characterization procedure . . . 12

5 Example: *TYC-8979-1683-1* observed with VLT/NaCo in H-band **16**
5.1 Data TYC-8979-1683-1 . . . 16
5.2 Input to process this data set . . . 17
5.3 Output and results from the analysis procedure . . . 17

6 Conclusion **17**

List of the files included in the package:
- README containing a summary of instructions and important information for quick hands on;
- IDL library, *libANDROMEDA*, containing all the needed functions and procedures to run ANDROMEDA;
- Batch to process images from VLT/NaCo (TYC-8979-1683-1) which are inside the example folder;
- This user-manual containing detailed information on how to use the input, output etc.;
- The papers *Mugnier et al., 2009* and *Cantalloube et al., 2015* containing a respectively theoretical and practical description of the ANDROMEDA method.

If you are willing to use this software, please contact the authors: faustine.cantalloube@univ-grenoble-alpes.fr and/or laurent.mugnier@onera.fr and/or david.mouillet@univ-grenoble-alpes.fr.

1 ANDROMEDA: Summary of the different steps

ANDROMEDA is an ADI-based algorithm which analytically estimates the position and flux of point sources present in the field of view thanks to a maximum likelihood estimation (MLE). This algorithm thus allows the user to perform an automatic detection, and the detected point sources are associated with a probability of presence. It also provides a direct estimate of the flux without any bias due to subtraction. The detection limit can be directly computed from the ANDROMEDA output, without needing extensive processing of the images. To give a rough idea, ANDROMEDA runs in about 20 minutes for a 512x512x128 images cube. Its overall performance in terms of detection capabilities is limited by the ADI process so it shows the same acuteness than common ADI-based methods such as LOCI or PCA.

Two main calls are made by the software:

-The function `ANDROMEDA.PRO` delivers three main output: a *flux map*, a so-called *SNR map* and a *flux standard deviation map* (see Sect. 2 for details about its input and Sect. 3 for details about its output).

-The procedure `DETECTION_ANDROMEDA.PRO`, uses these output to perform the detection, to derive the astrometry and photometry of the probable companions and to compute the detection limit. The latter was developed in line with the characteristics of the ANDROMEDA function, but could be used for other purposes if similar input are given (see Sect. 4).

Fig.1 is a summary of the different steps performed by the method to process on-sky data.

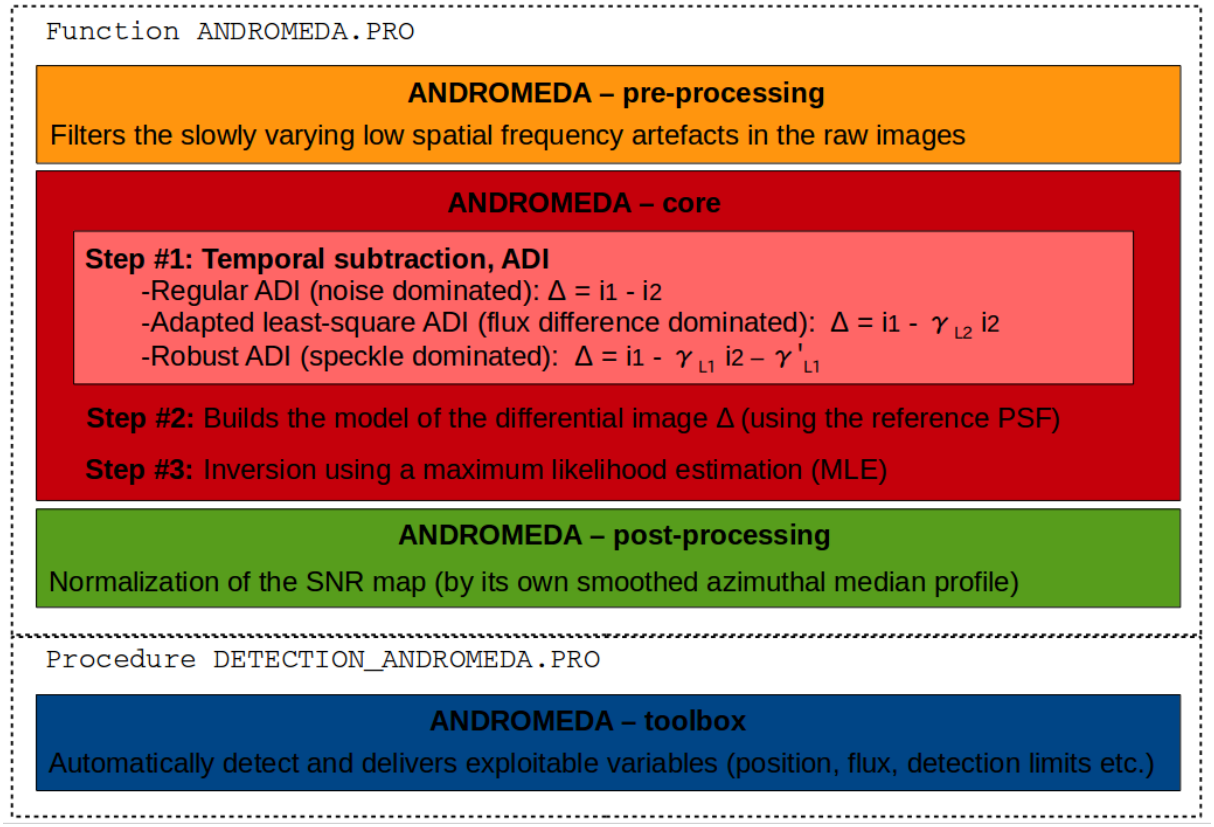

Figure 1: Detailed description of the different steps performed by the ANDROMEDA software.

The whole operational algorithm is described in Cantalloube et al. 2015, including the description of additional steps that are necessary to run ANDROMEDA on real data.

2 Required input to run ANDROMEDA

The classical use of ANDROMEDA is ADI only. Below is the description to run ANDROMEDA in ADI only, see the last subsection for hints to run the SDI+ADI mode of ANDROMEDA.

2.1 Science frames: `IMAGES_1_INPUT`

The images must be either saturated or coronagraphic and taken in pupil tracking mode.
Its dimension should be: $(N_{pix}, N_{pix}, N_{img})$, where N_{img} is the total number of images in the cube and N_{pix} the number of pixels along the x and y axis.

-The images must be square and N_{pix} even.

-The images must be centered in between four pixels.

That is to say (in IDL), if the images size are of $N_{pix} \times N_{pix}$ (eg. 600 x 600 px) then the center must be set in between the pixel number $N_{pix}/2. - 1$ and $N_{pix}/2.$ (eg. 299 and 300). The computations are made assuming that the center lays at $(N_{pix} - 1)/2.$ (eg. at 299.5).

If the images are not centered, the Onera function *images_ centered.pro* can be used to shift the image of a subpixel amount. This function uses Fourier transforms to avoid interpolation between pixels. For instance, if the images are centered on the central pixel $[N_{pix}/2.; N_{pix}/2.]$ (eg. [300;300]) -as it is the case with the SPHERE data reduced with the DRH client-, its use is the following to shift the images in between four pixels:

$$\begin{array}{l} images\_centered = dblarr(Npix, Npix, Nimg) \\ FOR\ \ i = 0,\ \ Nimg - 1\ \ DO\ \ \$ \\ images\_centered[0, 0, i] = SUBPIXEL\_SHIFT(images[*, *, i], x = -0.5, y = -0.5) \end{array} \quad (1)$$

Otherwise, it is also possible to use the built-in option in andromeda.pro by adding the coordinate of the centers of *each* frame within the cube as an input of the function: `COORD_CENTRE_1_INPUT = center_image` with the following definition of the center:

$$\begin{array}{l} center\_image = dblarr(2, Nimg) \\ center\_image[0, n_i] = x\_cent \\ center\_image[1, n_i] = y\_cent \end{array} \quad (2)$$

Where $Nimg$ is the total number of images in the cube, x_cent and y_cent the fraction of pixels from which the center is shifted respectively along the x and y direction in the regarded image n_i.

Note that images might have /NaN or outliers (usually on the edges) that could corrupt the MLE (since the model of noise is then completely inconsistent). Thus it is advised to check the edges and, if needed, to crop the images to get rid of these /NaN values (which usually do not impact other algorithms such as c-ADI).

2.2 Reference PSF: `PSF_PLANET_INPUT`

The so-called *reference PSF* is used to build the model of a planetary signature which is then sought by performing a MLE. This reference PSF is the non-coronagraphic image of the star or the unsaturated image of the star (so that the star is the dominant object in the image, hence the "PSF" denomination). The time when this reference PSF is taken wrt to the observations does not matter since this version of ANDROMEDA does not include a follow-up of the PSF quality with time. Of course it is however better to have a PSF whose Sthrehl ratio (SR) is as close as possible to the mean SR of the science cube frames.

-The reference PSF must be in a square window of even size N_{psf}.

-The reference PSF must be centered in between four pixels.

-The size of the PSF window must be small enough to reduce the running time and large enough to include at least the central core. It is advised to include the secondary ring within the window.

To crop the PSF around its center, the function *centering_ max.pro* can be used. It works as follow:

$$psf\_planet = centering\_max(psf, Npsf) \quad (3)$$

Where $Npsf$ is the new dimension of the PSF used as an input for ANDROMEDA.

Note that if the PSF centering is shifted of 3 pixels, it biases the astrometry by up to 3 pixels (depending on the position of the companion in the field and the direction of the PSF core shift). **Thus, the reference PSF and images centering must be carefully made before running the ANDROMEDA function**.

2.3 Parallactic angles: ANGLES_INPUT

The angles must be given as a vector of dimension $Nimg$ and should follow the same order than the image cube (eg. images_input[*,*,1] have the parallactic angle given by angles_input[1]).

If there is a corresponding offset angle wrt to the true North direction, it is possible to include it in the ANDROMEDA function via the keyword ROTOFF_INPUT which takes this offset angle as an input.

Both the parallactic angles and the rotoffset must be given in degrees.

Note that some reduction pipelines give the inverted set of angles compared to the one needed by ANDROMEDA. ANDROMEDA has been set to handle the data output by the DRH client of SPHERE but if one is using another reduction pipeline, it happens that -angles should be input instead of +angles (it is the case with the NaCo data of TYC-8979-1683-1 given in the Example folder of the package). Thus, if ANDROMEDA does not seem to provide the correct SNR maps, it is advised to try running the algorithm on a well known target to check the angles sign.

2.4 Oversampling factor: OVERSAMPLING_1_INPUT

The oversampling factor is needed to convert from pixels to lambda/D units within the ANDROMEDA process. We recall that the oversampling factor is one at Shannon, else it is greater than one. This factor can be computed knowing the wavelength of the images (*lambda*, given in meters) and the pixel scale of the camera under use (*pixscale*, given in mas/px), following:

$$\begin{aligned} pixscale\_nyquist &= (1/2. * lambda/D)/!dpi * 180. * 3600. * 1.e3 \\ OVERSAMPLING\_1\_INPUT &= pixscale\_nyquist/pixscale \end{aligned} \tag{4}$$

With D the diameter of the telescope entrance pupil in meters (for the VLT, $D = 8.0$m).

2.5 User-defined parameters to run the ANDROMEDA function.

There is *seven* user-defined parameters needed to run ANDROMEDA, within which only two have to be fine tuned. Here is a description of these parameters in the order of their use in the ANDROMEDA call.

2.5.1 High-pass filtering of the raw data: FILTERING_FRACTION_INPUT

The filtering fraction, that is to say the amount of low spatial frequencies removed from the raw images, must be specified. This parameter stands between 0 (no filtering) and 1 (everything is removed). Its highest theoretical value is limited by the cutoff spatial frequency, that is $1/oversampling$.

FILTERING_FRACTION_INPUT default value is set to 1/4 (if this keyword is not provided or set to 0).
If FILTERING_FRACTION_INPUT = 1, no filtering is performed.
If FILTERING_FRACTION_INPUT has a value less than 0 or greater than 1, an error message is returned.

To remain consistent with the ANDROMEDA's principle, the ANDROMEDA function filters the PSF used to build the model for the MLE *in the exact same way* as the filtering applied to the images. This way, the flux estimation is not biased and can be directly retrieved.

2.5.2 Inner working angle: IWA_INPUT

The distance to the star from which the search for companions is started (given in λ/D unit). This value is limited by the total field rotation of the frames (Δ_{parang}): If the frames do not have enough field rotation, either this value should be increased or the value δ_{min} decreased (see following subsection).

IWA_INPUT default value is set to 1.0 lambda/D (if this keyword is not provided or set to 0).

2.5.3 Parameters for the ADI: MINIMUM_SEPARATION_INPUT and ANNULI_WIDTH_INPUT

Any ADI-based method is limited by the choice of the minimum angular separation, δ_{min} between the companion in the first frame and its position in the frame to be subtracted. This angular separation (given in λ/D unit) should be as close as possible for the speckles to be stable enough between the two frames and, at the same time, it must be large enough to avoid the self-subtraction of the companion. This value might have a major impact if the quasi-statics speckles are quickly moving in the field. If the speckle field is temporally stable, then it is advised to favor a large δ_{min} to efficiently separate the two signals, which will be beneficial for the ANDROMEDA MLE.

`MINIMUM_SEPARATION_INPUT` default value is set to 0.5 lambda/D (if this keyword is not provided or set to 0).

As this value varies with the distance from the star, ANDROMEDA performs the image differences for annuli centered around the star. The width of these annuli, d_r, (also called *subtraction area*) must be given as an input (in λ/D unit). The size of the annuli does not have a major impact in the process.
`ANNULI_WIDTH_INPUT` default value is set to 1.0 lambda/D (if this keyword is not provided or set to 0).

Note that the whole images are subtracted one to another (resulting in a so-called *differential image*, and that the MLE is done over the whole field of view. Only the determination of couples to be subtracted within the limit given by δ_{min} are considered, at each distance from the star, separated of d_r.

2.5.4 Optimization method for the ADI: `OPT_METHOD_ANG_INPUT` and `RATIO_OPT_AREA_INPUT`

Several methods can be used to perform the ADI of the images $i(t_1)$ and $i(t_2)$. The parameter `opt_method_ang_input` is an integer which calls for one of these methods:
-If `opt_method_ang_input = 1`: no optimization is performed.
The differential image is simply $\Delta = i(t_2) - i(t_1)$. This basic subtraction is advantageous when the noise (other than speckle noise) is dominant in the images.
-If `opt_method_ang_input = 2`: a so-called 'total ratio' optimization is performed.
The differential image is created following $\Delta = i(t_2) - \gamma_{TR}\, i(t_1)$, with $\gamma_{TR} = \sum_{(x,y)} i(t_1) / \sum_{(x,y)} i(t_2)$. This method must not be used if the images have been pre-filtered since the mean of the filtered images is set to zero, which makes the computation of γ_{TR} diverge.
-If `opt_method_ang_input = 3`: a so-called 'least-square' optimization is performed.
The differential image is $\Delta = i(t_2) - \gamma_{LS}\, i(t_1)$, with $\gamma_{LS} = \sum_{(x,y)} i(t_1).i(t_2) / \sum_{(x,y)} i(t_2)^2$. This method is advantageous when the average flux difference between the two annuli is dominant. However this fit can be biased by the presence of high intensity signals (either from planets or speckles) in one of the images. Moreover the radial flux evolution of the star PSF is not spatially linear, as assumed by this fit.
-If `opt_method_ang_input = 4`: a so-called 'L1-affine' optimization is performed.
The differential image is $\Delta = i(t_2) - \gamma i(t_1) - \gamma'$, with γ and γ' computed using a robust estimation (using bracketing and bisection, see Numerical Recipes 3rd edition (2007) - p.818). This method is advantageous when the flux of some residual speckles varies a lot from one image to another.
`OPT_METHOD_ANG_INPUT` default value is set to 3 (least-square optimization).

As the optimized subtraction can induce discontinuities between adjacent annuli (if gamma varies a lot), the optimization (the computation of the gamma factors) is made over an *optimization area* which is equal or wider than the effective *subtraction area*. The ratio between the subtraction to the optimization area, R_A, must be set equal or greater than 1.
`RATIO_OPT_AREA_INPUT` default value is set to 2.

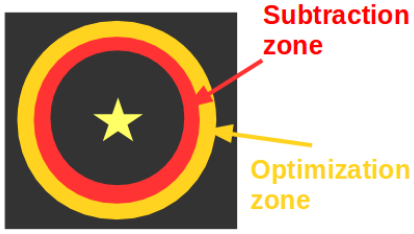

Figure 2: Description of the subtraction zone (red annulus) and the optimization zone (red and orange annuli).

2.5.5 Normalization of the SNR map: `NSMOOTH_SNR_INPUT`

As the model of noise is inconsistent with the real residual noise distribution in the differential images (assumed to be white and Gaussian), mostly at short separation, there is a discrepancy between the given threshold and the probability of false alarm. Instead of tunning the threshold as a function of the distance to the star, one idea is to empirically get rid of this radial trend by normalizing the SNR map by its own radial profile. This profile is obtained by computing the azimuthal variance at each distance from the star. The robust variance is actually

computed to avoid taking into account outliers (such as substellar companions).
The profile is then smoothed over a certain number of pixels given by the value N_{smooth}. This smoothing allows the user to take into account the global radial trend and not the detailed variance profile. Also one considered pixel is smoothed wrt to the pixels at larger separation (and not to pixels before *and* after).

If N_{smooth} is too large, then the information about the radial trend is lost (since it becomes an almost flat profile) and consequently, too many artifacts could appear above threshold and regarded as detections. If N_{smooth} is too small, the normalization profile may be quite jagged (if the speckle field is varying a lot through time) though only the global trend is needed for the normalization. Thus this normalization factor depends on the quality of the data.

For basic SPHERE data, N_{smooth} can be quite low since the speckle field is stable and the ADI subtraction is quite homogeneous.

`NSMOOTH_SNR_INPUT` default value is set to 18 pixels (if this keyword is not provided).
If `NSMOOTH_SNR_INPUT = 1`, no normalization is performed.

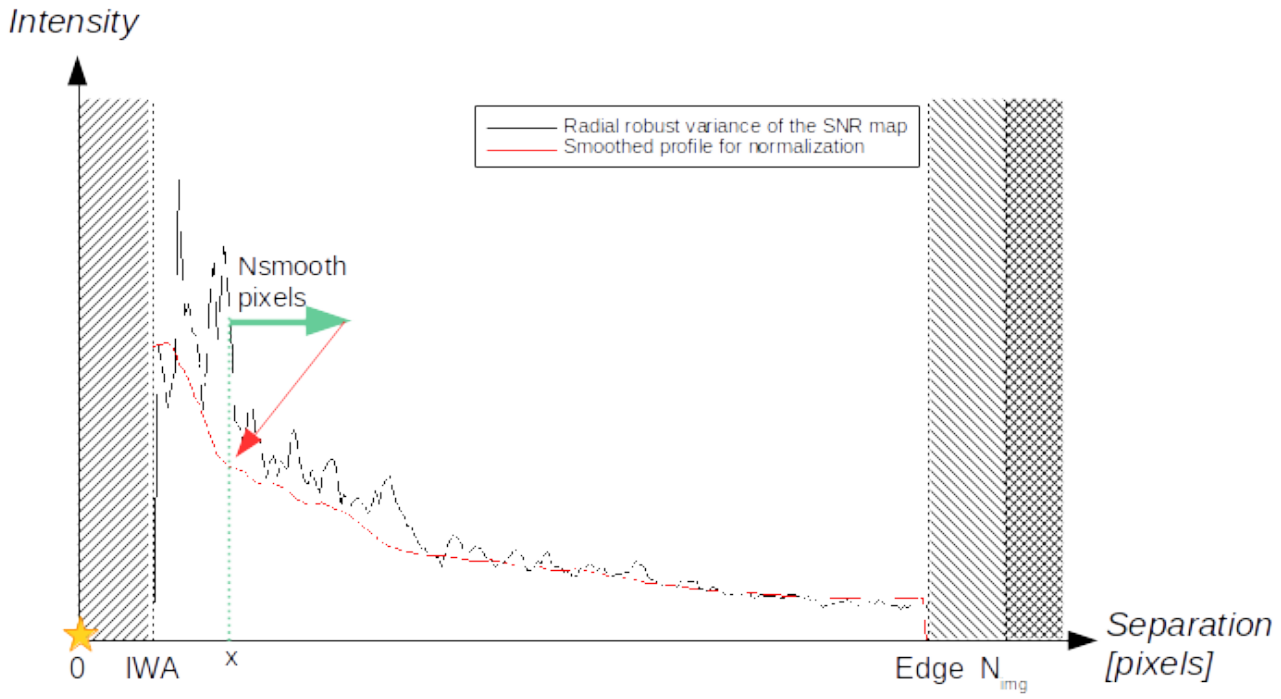

Figure 3: Schematic drawing of the smoothing made to build the normalization profile (red curve).

It is advised in a first step to perform the normalization *after* the ANDROMEDA function ran. The normalization can be done by using the function `normalize_snr.pro` which needs as input: the SNR map, the chosen N_{smooth}, the IWA and OWA (via respectively the keywords `dmin_input` and `dmax_input`, both given in pixels). It is thus possible to change the N_{smooth} value quickly and visualize the profiles used (by using the keyword `/SHOW`), to check if it is consistent with the data. (Note that it is possible to perform a polynomial fit of the 4th order, by using the keyword `/FIT`, but it is not efficient in practice). This function also provides the 2D image of the smoothed profile, via `snr_stddev_output`, which must be used to normalize the standard deviation of the flux map in the same way. **The detection procedure must be launched using the normalized SNR map and on the normalized flux standard deviation map.**

NB: This normalization procedure artificially increases the SNR close to the star, but since $SNR = \hat{a}/\sigma(\hat{a})$, *this is taken into account inside the estimated flux error-bars (which therefore increases). That is why the flux standard deviation map* ***must*** *be normalized by the same profile than the one used to normalize the SNR. However, the normalization* ***does not*** *impact the flux estimation which remains the same. In other words, this normalization procedure 'helps' to detect companions close to the star and the associated probability of presence should be read with care.* ***However, the flux estimation is not biased by this method.***

2.5.6 Summary of the user-defined parameters and their impacts

The table below recalls the user-defined parameters and their impact on the companion extraction with ANDROMEDA for either NaCo like or SPHERE like data. For the NaCo data, more details about these parameters can be found in Cantalloube et al. (2015).

Table 1: Summary of the user-defined parameters default values and their respective significance.

Parameter	**Definition**	**Units**	**Default value**	**Impact**
F	Filtering fraction	-	NaCo: 1/4	low
			SPHERE: 1/6	low
$\delta_{\min}$	Minimum separation to build the differential images	λ/D	NaCo: 0.5	high
			SPHERE: 0.5	low
dr	Width of annuli on which ADI is performed	λ/D	1	low
Opt_meth	Optimization method used for ADI	#	NaCo: 3	high
			SPHERE: 1	low
R_A	Ratio optimization to subtraction areas	-	2	low
N_{psf}	Size of the square PSF image	pixels	see text	low
N_{smooth}	Smoothing of the S/R robust standard deviation profile	pixels	NaCo: 18	high
			SPHERE: 2	low

3 Output provided by the ANDROMEDA function.

In this section, the output are described, regardless of the user-parameters used to run ANDROMEDA. This section intents at giving an idea of how to interpret images in the ideal use of the software.

3.1 SNR map: `SNR_OUTPUT`

This is a 2D image, given in sigma units. *Its value at a given pixel position is linked with the probability of presence of a point source to be at this exact pixel position.* That is to say, the higher the value, the higher the probability of presence of a planetary companion.

This map is thus used to perform the **detection**, by simply thresholding it by a constant value (usually 5-sigma). Hence the automatic detection that the ANDROMEDA solution enables.

The usual shape of a planetary signal is oval, its major axis within the star-companion direction (see Fig. 4b-*Left*). This map is also used to derive the **astrometry** of the detected point sources by performing a 2D Gaussian fit of the planetary signal. The estimated sub-pixel position of the companion is given by the maximum of the Gaussian fit.

3.2 Flux map: `FLUX_OUTPUT`

This is a 2D image given in ADU units. *Its value at a given pixel position is the value of the flux that would have a signal at this exact pixel position.* The flux is given with respect to the PSF flux given as an input (`PSF_PLANET_INPUT`).

This maps is thus used to derive the **photometry** of the detected point sources by performing a 2D Gaussian fit of the planetary signature and retrieving the value of the flux at the sub-pixel position estimated earlier in the SNR map.

3.3 Flux standard deviation map: `STDDEVFLUX_OUTPUT`

This is a 2D image given in ADU units. *Its value at a given pixel position is the 1-sigma error on the estimated flux.* This map thus gives the errorbars on the companions estimated flux by simply reading the value at the subpixel position retrieved earlier.

This maps is thus used to derive the **detection limit** of the data set by averaging the azimuthal values to build its radial profile which is the detection limit at 1-sigma.

We thus have `SNR_OUTPUT` = `FLUX_OUTPUT` / `STDDEVFLUX_OUTPUT`, hence the similarity between the SNR and the flux map.

3.4 Other useful output

3.4.1 Likelihood map: `LIKELIHOOD_OUTPUT`

The 2D map of the computed likelihood. This output is not useful for the planetary companions extraction.

3.4.2 Information about the scaling and affine factors: `GAMMA_INFO_OUTPUT`

If asked in output, this value contains information about the scaling factor(s) that can be useful to better understand the noise distribution in the data (and choose for the most relevant ADI method).
`GAMMA_INFO_OUTPUT`[0,*,k] = min(factor)
`GAMMA_INFO_OUTPUT`[1,*,k] = max(factor)
`GAMMA_INFO_OUTPUT`[2,*,k] = mean(factor)
`GAMMA_INFO_OUTPUT`[3,*,k] = median(factor)
`GAMMA_INFO_OUTPUT`[4,*,k] = variance(factor)

Where '*' is 0 (linear factor, γ) or 1 (affine factor, γ') and k the index of the couple of images that have been subtracted (ie. index of the differential image).

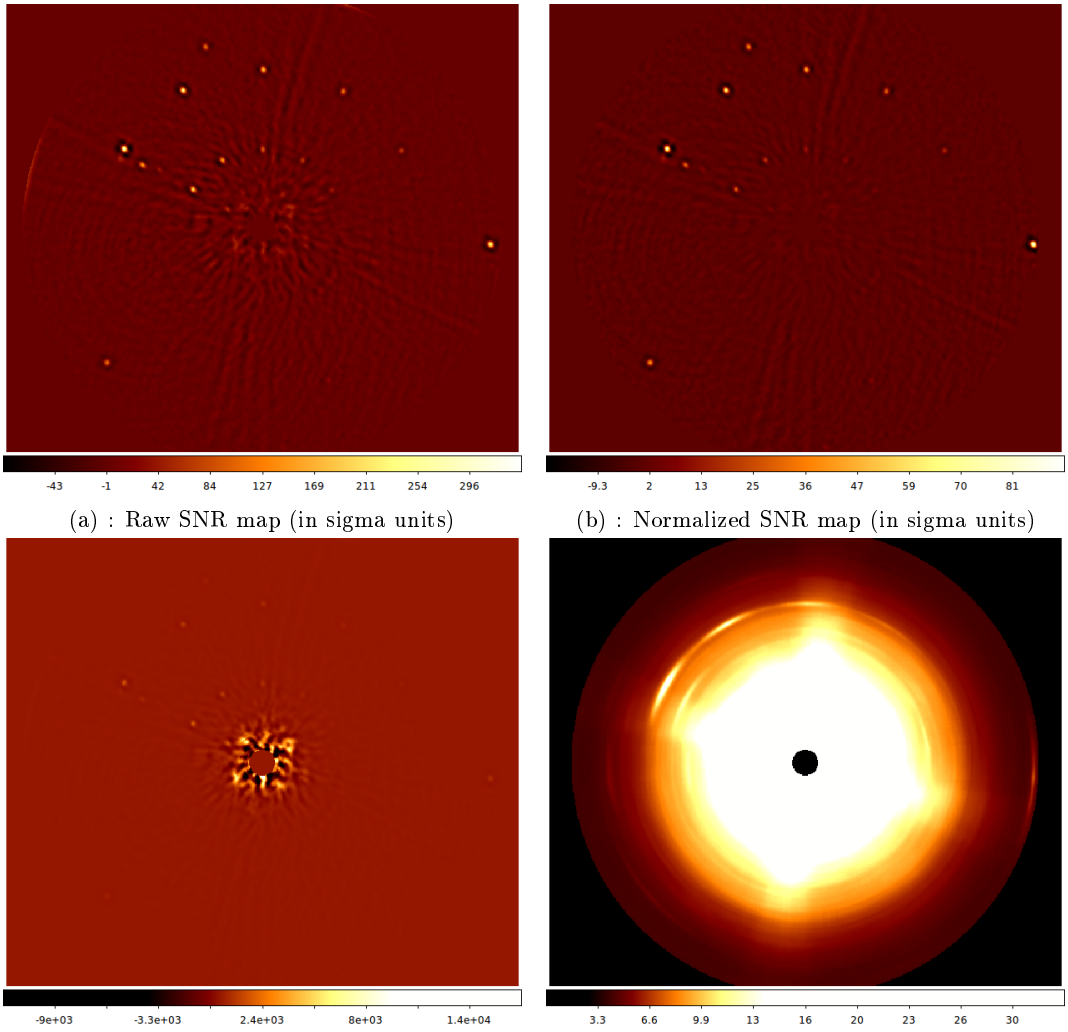

(a) : Raw SNR map (in sigma units)

(b) : Normalized SNR map (in sigma units)

(c) : Flux map (in ADU units, to be translated in contrast terms)

(d) : Normalized map of the standard deviation of the flux (in ADU units)

Figure 4: Maps output by the ANDROMEDA function and from which are made the detection, the astrometry, the photometry and the detection limit estimation.

3.4.3 Maximum investigated distance from the star: `EXT_RADIUS_OUTPUT`

Given the size of the psf used as a model and the width of each investigated annuli, this output gives the value (in lambda/D) of the farthest annulus investigated by ANDROMEDA (See Fig. 3). This output is useful to be aware of the range of distance from the star where a planetary companion is looked for (from IWA to this OWA value) and is used as an input of the function `normalize_snr.pro`.

3.5 SADI mode of ANDROMEDA

There is an SDI+ADI mode included in ANDROMEDA, which is intended to process images taken in pupil tracking simultaneously at two wavelengths.

This SDI mode simply spatially shrinks one of the image to correspond to the wavelength of the other, by using a basic rescaling model in λ^2. The shrank image is then subtracted to the other image. After this step, ANDROMEDA runs in basic ADI mode, as described in the previous sections, on the spectrally subtracted image. As a consequence this ANDROMEDA-SADI mode is fully adapted in the two following cases:

1. In one of the image, the companion is *completely absent* (it corresponds to an absorption band in the planet atmosphere). This image is the one that must be rescaled in wavelength and subtracted to the other;

2. Or the companion angular separation to the star is great enough to have at least a $1\lambda/D$ radial shift in the two images when rescaling in wavelength.

Thus this option performs a very basic SDI, not fully adapted to ANDROMEDA, yet very efficient to better subtract the speckles and reveal detections in the field of view, particularly in the two cases mentioned above.

Only two more keywords are required to run ANDROMEDA in this mode:

`-IMAGES_2_INPUT`, which contains the image cube to be rescaled in wavelength.

`-OVERSAMPLING_2_INPUT`, the oversampling factor at the wavelength to be subtracted.

These input must have the same characteristics than the input at the main wavelength (centered in between four pixels, same parallactic angles etc.). The reference PSF used to build the model for the MLE, `PSF_PLANET_INPUT`, is thus the one corresponding to the 1st wavelength (of `IMAGES_1_INPUT`, not rescaled).

Note that the optimized subtraction evoked at Sect. 2.5.4 are possible to perform the spectral subtraction via the keyword `opt_method_spec_input` whose input are defined the same way (but for the images at the main wavelength and the rescaled images). By default the chosen optimization method for the spectral subtraction is the same than the optimization method chosen for the temporal subtraction.

3.6 Multispectral data processed with ANDROMEDA

For now, no specific work has been done to adapt ANDROMEDA to multispectral data. However, simply making a `FOR loop` on all the wavelengths of the multispectral cube to run ANDROMEDA, had proved efficient to retrieve the companions spectrum.

The N_λ SNR maps obtained can be combined (stack or correlation map) to perform the detection. Once the detection is made and the astrometry retrieved, it is possible to simply read the flux of the detections on the N_λ flux maps obtained to derive the full spectrum of the detection. This spectrum must be associated with the standard deviation spectrum at each wavelength by following the same procedure but reading the standard deviation of the flux map instead of the flux map (at a given threshold). This last step directly gives the confidence of level of the flux estimation, in line with the detection capabilities of ANDROMEDA.

In other words, if the companion is not visible in the SNR map, the flux is however retrieved in the flux map (along with the errorbars given by the standard deviation of the flux map). That is why it is necessary to note the SNR of the companion in each band.

4 Automatic detection and characterization procedure

This section describes how to exploit the previously described output by using the `detection_andromeda.pro` procedure to automatically extract the companions information. It also describes how to interpret the files produced by this procedure.

Important: *Before launching the characterization (and the post-processing, if this step is done afterwards), you sometimes must redefine the variables defined before the ANDROMEDA function call. This is due to IDL which does not handle properly the calls to several variables having the same name inside the functions called.*

4.1 Input needed for the analysis module

The required input for the analysis of the maps provided by the Andromeda functions are the following:

4.1.1 SNR map: `SNR_MAP_INPUT`

The normalized SNR map (see ANDROMEDA output).
This map is used to perform the automatic detection and to retrieve the position of the detections (at the maximum of the detected signal, ie: where its probability of presence is higher). On this map, the SNR of a detected signal is simply read (in units of sigma) but as reminded above, close to the star, this retrieved value should be interpreted with care since the normalization procedure artificially biases it.

4.1.2 Flux map: `FLUX_MAP_INPUT`

The flux map (see ANDROMEDA output).
On this map, the estimated flux of the detected signals are simply read, at the estimated subpixel position.

4.1.3 Flux standard deviation map: `STDDEVFLUX_MAP_INPUT`

The normalized map of the flux standard deviation (see ANDROMEDA output).
This map is used to compute the detection limit (given by performing an azimuthal median of this map) and to compute the errorbars on the flux estimations (since this map gives the 1σ errors on the flux estimation).

4.1.4 Reference PSF: `PSF_PLANET_INPUT`

The cropped and centered reference PSF used as an input of the Andromeda function (see ANDROMEDA input).

4.1.5 Chosen threshold: `THRESHOLD_INPUT`

The value by which the normalized snr map will be thresholded (given in sigma). In other words, *any signal inside the SNR map whose value is greater than the threshold will be regarded as a detection.* These detections will be later sorted out upon morphological criteria to reject potential remaining artifacts.

Default is set to 5σ since it is linked with a substantial probability of presence. However, in case signals are faint, one should try a lower threshold.

4.1.6 Size of the subimages for the detected signal analysis: `SIZE_SUBWINDOW_INPUT`

Size of the subwindow in which the detected signal will be analyzed (in the SNR map and in the flux map): The planetary signal pattern must be fully enclosed in the subwindow (see Fig. **??**). The size of the subimages must be given in number of pixels and must be odd (the sub-window is then automatically made square) else it is automatically set to `SIZE_SUBWINDOW_INPUT`+1.

`SIZE_SUBWINDOW_INPUT` default value is set to: 3lambda/D (typical window size needed).

4.1.7 Distance to tertiary lobes artifacts (if image filtering has been applied): `DIST_NEIGHBOURS_INPUT`

Distance at which two very close signals could be a primary and a tertiary lobe due to the pre-filtering procedure (in pixels) - see paper for more details.

`DIST_NEIGHBOURS_INPUT` default value is set to: 5lambda/D (typical distance to a third lobe artifact).

4.1.8 Chosen threshold: DITIMG_INPUT

Exposure time of the science images (in seconds).
DITIMG_INPUT default value is set to: 1 second.

4.1.9 Chosen threshold: DITPSF_INPUT

Exposure time of the reference PSF image (in seconds).
DITPSF_INPUT default value set to the same than DITIMG_INPUT.

4.1.10 Chosen threshold: TND_INPUT

If a neutral density was used to image the reference PSF, then this is the transmission factor of this neutral density (between 0 and 1).
TND_INPUT default value set to: 1 (ie: transmission factor of 100%).

Note that this input can also be used to put any other factor that would affect the image flux to reference PSF flux ratio (e.g: the transmission factor of the coronagraph, the airmass etc.)

4.1.11 Other parameters:

The following parameters are also needed to perform the automatic detection:
- PIXSCALE_INPUT: Pixel scale of the camera under use, in units of mas/pixel.
- IWA_INPUT: See ANDROMEDA.pro input. Closest distance to the star investigated, in lambda/D units.
- EXT_RADIUS_INPUT: See ANDROMEDA.pro output. Farthest distance to the star investigated, in lambda/D units.

4.1.12 Filenames:

The filenames in which results will be stored must be given as an input (string arrays).
The following keywords must refer to:

- FILENAME_DETECTION: the name of the '.dat' file containing the detection estimations (see next section).
- FILENAME_ERRORS: the name of the '.dat' file containing the errorbars of the detection estimations (see next section).
- SUBIMAGES_NAME: the name of the '.png' image created showing the subimages containing the potential planetary signal and in which the detection analysis is made (see Fig. 8a).
- DETECTION_MAP_NAME: the name of the '.png' image created showing the SNR map with each detection indexed (see Fig. 8b).
- DETLIM_PNG_NAME: the name of the '.png' image created showing the detection limit curve and the detections at the given threshold (see Fig. 5a).
- DETLIM_FITS_NAME: the name of the '.fits' file containing the detection limit curve at the given threshold.

4.2 Output given by the detection and characterization procedure

This section describes the output of the detection module and how to interpret them.

4.2.1 Images and screen display

Three images are displayed and recorded when launching the detection procedure:

1. The subimages, recorded in the '.png' file SUBIMAGES_NAME, (see the Fig. 8a for an example). Each detection is analyzed within such a subwindow (whose size is given as the user-parameter SIZE_SUBWINDOW_INPUT in pixels) which should fully enclose the planetary like signal. A 2D Gaussian fit of the detected signal is performed and the semi-major axis and semi-minor axis of the fitted Gaussian are printed on the subwindow (the center thus corresponds to the estimated position).

2. The detection map, recorded in the '.png' file `SUBIMAGES_NAME`, (see the Fig. 8b for an example). This is the SNR map (with a peculiar color scaling so as to spot the detections easily), on which each detection is denoted by an index whose lowest value correspond to the highest SNR and whose color corresponds to a range of contrast wrt the star. If the signal is likely to be an artifact (if the 2D Gaussian fit could not converge and/or the constraints were not respected), the index is white and accompanied by an asterisk. If the detected signal is assessed to be a tertiary lobe due to the pre-filtering of the raw images, the signal is replaced by a dark blue symbol @. (see Cantalloube et al. 2015 for more details on how to determine these particular cases).

3. The detection limit curve, recorded in the '.png' file `DETLIM_PNG_NAME`, (See the Fig. 5a for an example). The detection limit at the threshold chosen by the user is plotted as a solid line. This detection limit is the azimuthal median of the standard deviation of the flux map, multiplied by the chosen threshold. The azimuthal minimum of the standard deviation of the flux map is over-plotted as a dashed line (still at the given threshold). It means that, for the given threshold, a signal could *never* be found below the dashed line but the azimuthal median gives a better idea of the detection limit for the whole data set.

4.2.2 Estimation files .dat

Two '.dat' files are created and stored within the path provided by the user.

1- The files containing the results, under the name given in `FILENAME_DETECTION`: From the numerous tests

Parameter name	Meaning	Units
Index	Index of the detection (the lower, the higher SNR)	integer
coord_x	x position in the map (IDL coordinates)	pixel
coord_y	y position in the map (IDL coordinates)	pixel
sep-[mas]	estimated separation from the star	mas
err_sep	3-sigma errorbar on the estimated separation	mas
PA-[deg]	position angle from true North	degree
err_PA	3-sigma errorbars on the estimated position angle	degree
SNR	estimated SNR of the detection	sigma
nb_px>thresh	number of pixels of the signals above the threshold set	integer
Flux-[ADU]	estimated flux of the companion	ADU
Contrast	estimated flux translated into contrast wrt the star	-
Contrast-[mag]	estimated contrast of the companion in terms of magnitude	mag
Err_mag	3-sigma errorbars on the contrast in terms of magnitude	mag
flag_pos	**0**: The fit of the signal in the SNR map converged within the given constraints **1**: The 2D-Gaussian fit does not converge The recorded signal position is the one of the pixel having the maximal value **2**: The 2D-Gaussian fit does not respect the imposed constraints The fit is however forced and the estimated subpixel position recorded **3**: The detected signal is too close to the edge and cannot be analyzed	
flag_flux	**0**: The fit of the signal in the flux map converged within the given constraints **1**: The 2D-Gaussian fit does not converge. The recorded signal flux is the one read at the previously estimated position **2**: The 2D-Gaussian fit does not respect the imposed constraints. The fit is however forced and the flux estimated at the recorded position	
flag_lobe	**0**: No detection is found in this signal's nearby area **1**: There is a detection close-by but its SNR is either lower or comparable **-X**: The detection is assessed to be the tertiary lobe of the signal indexed **X**	

performed, no signals having a flag different from 0 was an actual planetary signal. However, a signal may not be assessed as an artifact but could be one. In that case, other methods should be used to confirm or infirm the companion existence. It is also possible to run ANDROMEDA with another set of user-parameters (optimization method used for ADI wrt δ_{min}) to check if the signal remains or use another diversity (such as SDI) if the signal is persistent.

2- The files containing the range of the estimations, under the name given in `FILENAME_ERRORS`:

Parameter name	Meaning	Units
Index	Index of the detection (the lower, the higher SNR)	integer
Err_sep_pos	Maximum estimated separation from the star	mas
Err_sep_neg	Minimum estimated separation from the star	mas
Err_pa_pos	Maximum estimated position angle	degree
Err_pa_neg	Minimum estimated position angle	degree
Err_contrast	3-sigma errorbars on the estimated contrast wrt the star	contrast
Err_mag	3-sigma errorbars on the estimated contrast in terms of magnitude wrt the star	mag

4.2.3 Computation of the detection limits

In case there is no detection (ie. no signal is found above the threshold set), it is still possible to derive the detection limit by using an independent IDL procedure called `DETECTION_LIMIT.PRO`. This procedure displays and record as a *.png* image and as a *.fits* file the detection limit. This detection limit is computed as the azimuthal median of the (normalized) standard deviation of the flux map, at the given threshold. Moreover, this function has three options:

-If the keyword `\MIN` is set: the minimum value of (normalized) standard deviation of the flux map at each distance from the star is over-plotted at the given threshold (dashed curve). It means that planetary companions could be found in between the two curves but never below this dashed curve (see Fig. 5a).

-If the keyword `\MEAN` is set: the detection limit at threshold+1 and threshold-1 are over-plotted to the main curve (see Fig. 5b).

-If the keyword `\SSS` is set: the detection limit taking into account the small sample statistics is over-plotted to the main curve (as described in Mawet et al. 2014), (see Fig. 5c).

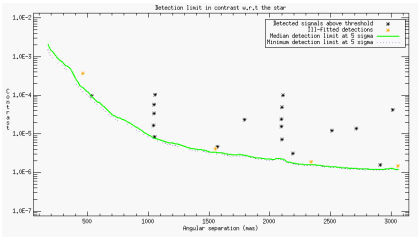

(a) : Detection limit obtained with the `/MIN` option.

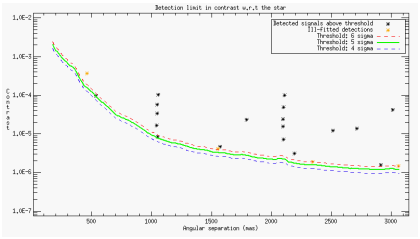

(b) : Detection limit obtained with the `/MEAN` option.

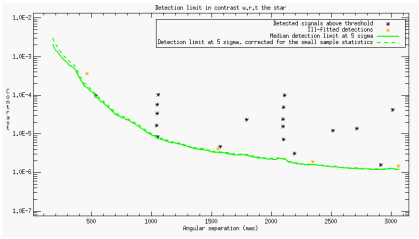

(c) : Detection limit obtained with the `/SMALL` option.

Figure 5: Detection limits obtained with the data set presented in Sect. 5.

ANDROMEDA package: Conclusion

The ANDROMEDA package contains the necessary IDL procedure and a batch to process high contrast images taken in pupil tracking mode. This methods as the following notable advantages:

- It performs an objective detection based on the SNR map thresholding.
- It estimates the sub-pixel position of the detected signals.
- It estimates the flux of the detected signals without bias self induced by the method.
- The toolbox permits to automatically sort out potentially true planetary companions from potential artifacts.
- The whole process runs quite fast (e.g: 30 minutes for an image cube of 150 images of 512×512 pixels and from a IWA of $2\lambda/D$).

Fig.6 is a summary of the different input needed to process on-sky data with ANDROMEDA.

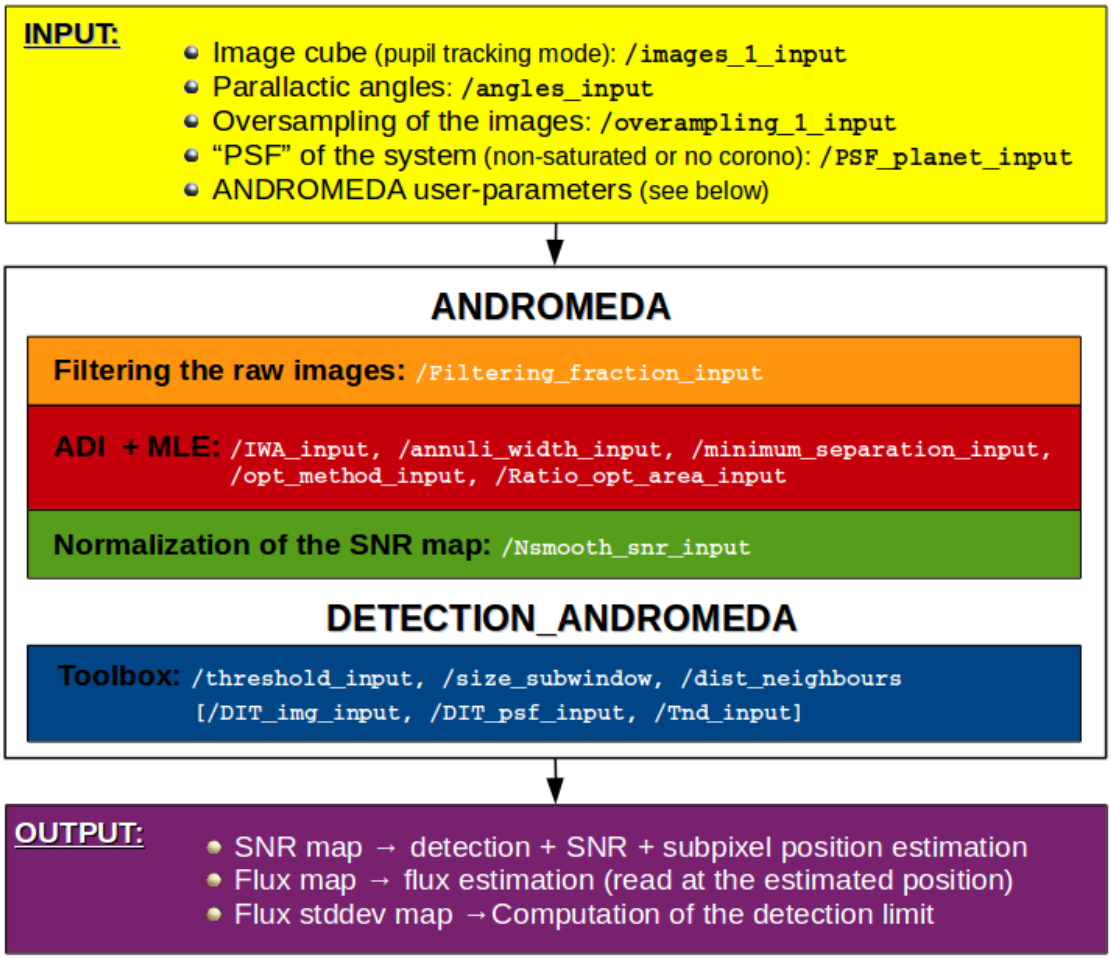

Figure 6: Input and output of the ANDROMEDA method and names of the variables as in the IDL code.

5 Example: *TYC-8979-1683-1* observed with VLT/NaCo in H-band

5.1 Data TYC-8979-1683-1

The data used to run the batch and test the ANDROMEDA method are described in details in the Section 4.1 of Cantalloube et al., 2015.

The central star is TYC-8979-16683-1 (called TYC-8979 hereafter in this manual) observed on 2010 February the 18th within the ESO program 184.C-0567 (PI: J.-L. Beuzit). These data are non-coronagraphic (they are sequences of saturated exposures) and taken in pupil tracking mode with VLT/NaCo (total field rotation of 18.5 degree) using the H-band filter of NaCo which is centered around $1.66\mu m$. The data provided in the DATA_TYC8979 folder have been previously reduced (essentially sky subtraction,flat fielding, bad pixels correction and rejection of poor-quality exposures). One unsaturated exposure was taken before the main observation sequence to serve as a reference PSF to build the model of the planet signature (`PSF_PLANET_INPUT`).

Twenty additional synthetic substellar companions have been inserted in the image cube in five rows of respective position angles of 30, 60, 90, 120 and 150 degree on the first image and at angular separations of $0.26arcsec$, $0.53arcsec$, $1.06arcsec$ and $2.12arcsec$. Each row of synthetic companions contains objects of equal flux, with peak intensities corresponding to magnitude differences of 12.85, 12.10, 11.35, 10.60, and 9.85, as shown in Fig. 7.

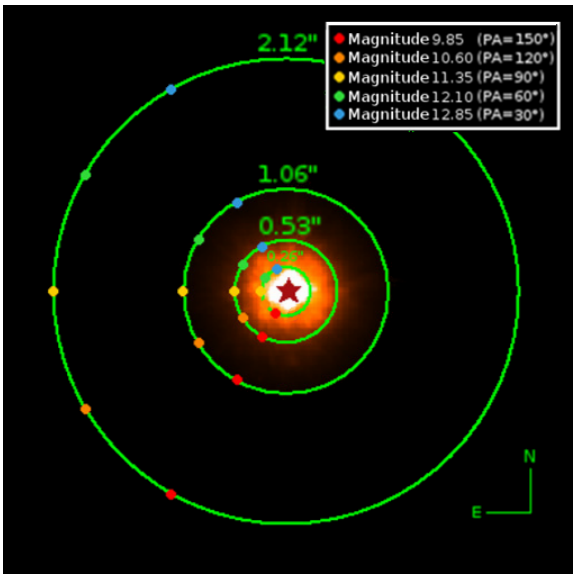

Figure 7: One of the reduced images of TYC8979, cropped in a 512×512 pixels frame, from the example data cube on which is indicated the locations and magnitude of the synthetic planetary signals injected.

The main characteristics of this data-set are gathered in the table 2.

Images size ($Npix \times Npix$)	512×512 px
Total number of images ($Nimg$)	296
Total field rotation ($\Delta Parang$)	18.525° (−22.2470°→ −3.72198°)
Filter	H (1.66μm)
Pixel scale of the camera used ($PIXSCALE$)	13.22 mas/px
Oversampling factor	1.58287
Offset angle from true North direction ($ROTOFF$)	90.4°
Integration time of each frame (DIT_{IMG})	6.8sec
Integration time of the reference PSF (DIT_{PSF})	1.7927
Transmission of the neutral density used for the reference PSF	1.19% (ND_{short})
Turbulence conditions	seeing: $0.57 \sim 1.15$; τ_0: $4-9ms$; SR_{PSF} : 21%

Table 2: Summary of the main characteristics of the data TYC-8979.

5.2 Input to process this data set

The center of the images must be set in between four pixels. This is done by hand using the `SUBPIXEL_SHIFT` function and checking by looking at the center of the median stack of the images.

In H-band, a good compromise is to crop the PSF in 32×32 window.

There is several user-defined parameters that can be modified at the convenience of the user to perform tests.

The optimized user-defined parameters on this test case, that are used to run ANDROMEDA on this data set, are gathered in the following table:

Parameter	**Definition**	**Used value**
`FILTERING_FRACTION_INPUT`	Filtering fraction	1/4
`MINIMUM_SEPARATION_INPUT`	Minimum separation to build pseudo-data	0.5 λ/D
`ANNULI_WIDTH_INPUT`	Radial width of annuli for performing ADI	1 λ/D
`OPT_METHOD_ANG_INPUT`	Least square optimization	option #3
`RATIO_OPT_AREA_INPUT`	Ratio optimization to subtraction areas	2
`NSMOOTH_SNR_INPUT`	Smoothing of the SNR robust standard deviation radial profile	18 pixels
`IWA_INPUT`	Separation from which the planetary signals are being sought	4 λ/D
N_{psf}	Size of the reference PSF image	32×32 pixels

Table 3: User-defined parameters used to run ANDROMEDA in order to obtain the results presented in the article.

It takes about 30min to run ANDROMEDA under these conditions.

5.3 Output and results from the analysis procedure

The 3 maps output by ANDROMEDA on this test-case are the flux map (Fig. 4c), the SNR map (Fig. 4b, already normalized) and the standard deviation of the flux map (Fig. 4d).

From these three map, the detection procedure is ran using the following default parameters:

Parameter	**Definition**	**Used value**
`THRESHOLD_INPUT`	Threshold above which any signal is regarded as a detection	5 sigma
`SIZE_SUBWINDOW_INPUT`	Size of the subwindow in which signal analysis is performed	11 pixels ($3.4\lambda/D$)
`DIST_NEIGHBOURS_INPUT`	Distance of a potential tertiary lobe artifact	16 pixels ($5\lambda/D$)

Table 4: User-defined parameters used to run DETECTION_ANDROMEDA.PRO on the test-case.

The package contains, in the *Example* folder, the two files '.dat' containing the information about the detections, for a threshold of 5-sigma. Notably on a total of 24 signals detected above threshold in the field of view, there is 19 true potential planetary signals, 2 detections regarded as tertiary lobes and 3 detections assessed to be artifacts (residual speckle noise like #22 or diffraction pattern like #21 and #23); See Cantalloube et al. 2015, Sect. 3 for more details.

Performance with respect to the injected fake companions can be found in Cantalloube et al. 2015, Sect. 4

6 Conclusion

ANDROMEDA has been tested on VLT/NaCo data (with and without coronagraph), on VLT/SPHERE data and Gemini/GPI data under different observation conditions. This method has also been successfully tested on different type of data (such as narrow band filters, dual band images, broadband filter and multispectral images).

As a conclusion, this algorithm proved to be very efficient in extracting in a systematic way the point source present in the field of view. It is also a very convenient method since it relies on very few user parameters and provides non-subjective detections and unbiased flux estimation. For these reasons, ANDROMEDA is a very good tool for a quick look. However it does not have better but comparable extraction capabilities than other widely used algorithm since its performance are also limited by the ADI process prior to the MLE estimation.

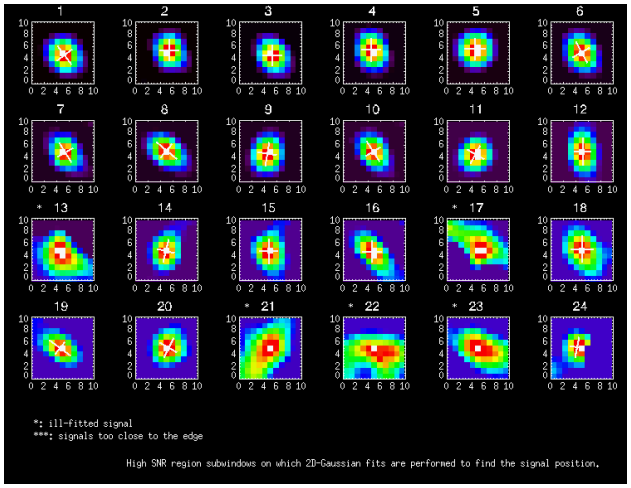

(a) : SNR subimages enclosing all the detected signals above the threshold set in which the analysis is made. When the 2D Gaussian fit could converge, its parameters are in-printed on the subwindow (maximum, semi major axis and semi minor axis.

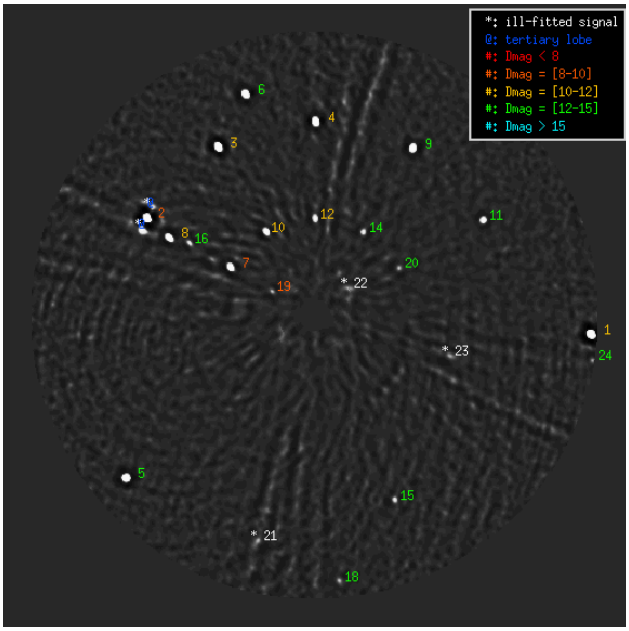

(b) : SNR map displaying the detections and their properties (position, SNR rank, flux range and if it is an artifact)

Figure 8: Images displayed when analyzing the ANDROMEDA output (Fig. 4) with the provided detection module.

Appendix C

Analytical models of long exposure coronographic PSF

This appendix presents the analytical models of coronagraphic PSF that I investigated during my PhD. This work is beeing followed by O. Herscovici, 2nd year PhD at Onera, under the supervision of L. M. Mugnier.

C.1 Notations and hypothesis:

the notations used in this coronagraphic PSF model are indicated in the following scheme from (Sauvage et al., 2010):

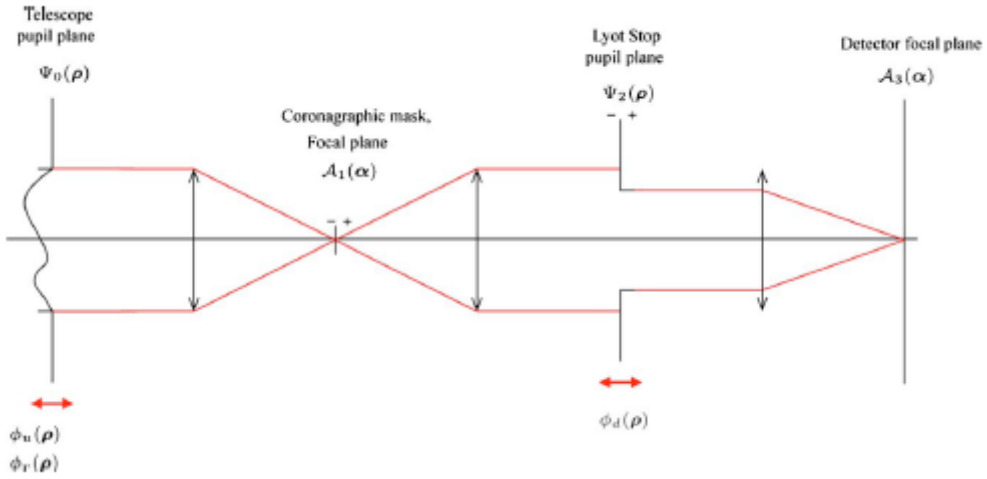

Figure C.1 – Schematic representation of a coronagraphic set up (From Sauvage et al., 2010).

C.1.1 Notations for the coronagraph setup:

In the following, the inverse Fourier transform (defined at Eq. 1.4) is used to define the light propagation from the pupil to the focal plane. The direct Fourier transform is used to the light propagation from the focal plane to the pupil plane.

Amplitude: The pupil plane amplitudes are denoted by Ψ_x. The focal plane amplitudes are denoted by A_x.

Aberrations: The aberrations *before* the coronagraph are constituted of: the upstream static aberrations δ_u and the turbulence residual aberrations $\delta_r(t)$. The aberrations *after* the coronagraph are

constituted of: the downstream static aberrations δ_d. The total upstream phase is: $\Phi_t = \Phi_u + \Phi_r$. The phase $\Phi_r(\rho, t)$ is assumed to be of null temporal mean, stationary and ergodic with a power spectral density $S_{\Phi_r}(\alpha)$.

C.1.2 Definition of the residual turbulence phase structure function:

The structure function of the residual turbulence phase is denoted by D_{Φ_r}, defined at Eq. 1.5.
This is a symmetrical function if Φ_r is stationary and with a centered Gaussian distribution.
This definition is: $D_{\Phi_r}(\mathbf{r}) =< |\Phi_r(\mathbf{r}) - \Phi_r(\mathbf{r}+\rho)|^2 >_t$.
We also have:

$$D_{\Phi_r}(\mathbf{r}) = 2 \times [Autocorr(\Phi_r(\mathbf{0})) - Autocorr(\Phi_r(\mathbf{r}))] \tag{C.1}$$

where $Autocorr(\Phi_r(\mathbf{r})) = \int DSP_{\Phi_r}(\mathbf{k}) \exp(i\mathbf{k}.\mathbf{r})\ d\mathbf{k}$, with $\mathbf{k}$ the conjugated variable of $\mathbf{r}$ in the Fourier domain.

C.1.3 Definition of convolution, inter-correlation and auto-correlation:

Formula from Lena et al. (2012)

Convolution:

$$(f * g)(\mathbf{r}) = \int_{\mathbf{k}} f(\rho)\ g(\mathbf{r}-\rho)\ d\rho \tag{C.2}$$

Auto-correlation:

$$Autocor(f)(\mathbf{r}) = (f \otimes f)(\mathbf{r}) = \int_{\rho} f^*(\rho)\ f(\rho+\mathbf{r})\ d\rho \tag{C.3}$$

Inter-correlation:

$$f(\mathbf{r}) \otimes g(\mathbf{r}) = \int_{\rho} f^*(\rho)\ g(\rho+\mathbf{r})\ d\rho \tag{C.4}$$

C.2 Ideal coronagraph (Sauvage et al., 2010)

The corrected expression of the ideal coronagraphic long exposure PSF published in Sauvage et al. (2010) is the following:

$$h_c^{LP} = \langle h_{nc} \rangle + \langle |V|^2 \rangle\ h_d - 2\Re\{TF^{-1}[\psi_{u+d}(\mathbf{r}).(\exp^{-\frac{1}{2}D_\phi} * \psi_u(\mathbf{r}))].\psi_d^*)\} \tag{C.5}$$

C.2.1 Difference between the two models

The Fig. C.2 shows the PSF profile generated with the ideal coronagraph as published in Sauvage et al. (2010) and used in the MEDUSAE algorithm vs the corrected version. The difference only affects the deepness of the corrected zone just before the AO cutoff frequency (which is equivalent to have more aliasing in the AO correction).

C.3 Almost perfect coronagraph (Ygouf, 2012)

The idea of the almost perfect model is to use η_0' to replace the η_0 in the ideal coronagraphic PSF formula, such that:

$$\eta_0 \longrightarrow \eta_0' = (1-\epsilon)\eta_0 \tag{C.6}$$

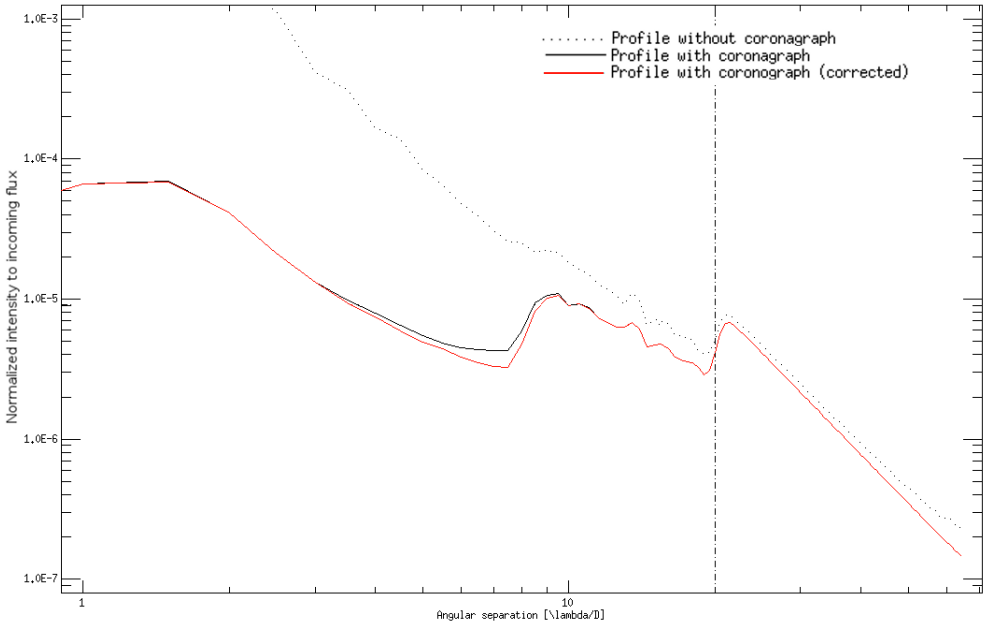

Figure C.2 – Profiles of long-exposure star images without coronagraph (dashed line), without the correction (black solid line) and with correction (red solid line). Similar to Fig.4 in Sauvage et al. (2010).

The formula derived in the manuscript is not correct. The corrected formula is the following:

$$\begin{aligned} h_{NP}^{c} =& (1-\epsilon)^2 |\tilde{P_d} * (\tilde{\Phi_u} + \tilde{\Phi_r})|^2 \\ &+ (2\epsilon - \epsilon^2) |\tilde{P_d} * \tilde{\Phi_{tot}}|^2 \\ &+ \epsilon^2 \tilde{P_d}^2 \\ &+ (\epsilon - \epsilon^2) \times [-2\Re\{(\tilde{P_d} * \tilde{\Phi_{tot}})(\tilde{P_d} * \tilde{\Phi_d})\} \\ &\qquad + 2\Im\{\tilde{P_d}(\tilde{P_d} * \tilde{\Phi_d})\} \\ &\qquad + \Re\{\tilde{P_d}(\tilde{P_d} * \tilde{\Phi_d} * \tilde{\Phi_d})\} \\ &\qquad + \tilde{P_d}^2 (\sigma^2_{\Phi_r} + \sigma^2_{\Phi_u} + \frac{2}{S} \int\int_S \Phi_r \Phi_u d^2\rho)] \\ &+ \epsilon \, [2\Im\{\tilde{P_d}(\tilde{P_d} * \tilde{\Phi_{tot}})\} - \Re\{\tilde{P_d}(\tilde{P_d} * \tilde{\Phi_{tot}} * \tilde{\Phi_{tot}}\}] \end{aligned} \tag{C.7}$$

This expression is derived from the approximated expression (the Taylor expansion of the ideal model).

C.4 The Fourier coronagraph (Hercovisci et al., 2016)

the idea of this coronagraph is to develop the plane to plane propagation of the light (in the Fraunhofer framework) by taking into account the presence of the diffracting focal plane mask. By following the notations of Fig. C.1 and by deriving plane to plane:

$$A_1^- = TF^{-1}(\Psi_0) = TF^{-1}(P_u \exp(j\Phi_t)) \tag{C.8}$$

$$A_1^+ = A_1^- \times P_m = P_m . TF^{-1}(P_u \exp(j\Phi_t)) \tag{C.9}$$

$$\Psi_2^- = TF(A_1^+) = TF(P_m . TF^{-1}(P_u \exp(j\Phi_t))) = TF(P_m) * (P_u \exp(j\Phi_t)) \tag{C.10}$$

$$\Psi_2^+ = \Psi_2^- \times \Psi_d = \Psi_2^- \times P_d \exp(j\Phi_d) = (P_d \exp(j\Phi_d)) \times (TF(P_m) * (P_u \exp(j\Phi_t))) \tag{C.11}$$

$$A_3 = TF^{-1}(\Psi_2^+) = TF^{-1}(P_d \exp(j\Phi_d)) * (TF^{-1}(TF(P_m) * (P_u \exp(j\Phi_t)))) \tag{C.12}$$

$$\tag{C.13}$$

From which it is possible to obtain the expression of the amplitude at the detector, A_3 :

$$\boxed{A_3 = (A_d) * (P_m \times TF^{-1}(P_u \exp(j(\Phi_u + \Phi_r))))} \tag{C.14}$$

where $A_d = TF^{-1}(P_d \exp(j\Phi_d))$

The corresponding short exposure PSF, $h^{CP}_{PSF-Fourier}$, is thus:

$$h_3 = h^{CP}_{PSF-Fourier} = |(A_d) * (P_m \times TF^{-1}(P_u \exp(j\Phi_t)))|^2 \tag{C.15}$$

and the corresponding long exposure PSF, $h^{LP}_{PSF-Fourier}$ is the temporal mean of the short-exposure:

$$\langle h_3 \rangle_t = h^{LP}_{PSF-Fourier} = \langle |(A_d) * (P_m \times TF^{-1}(P_u \exp(j\Phi_t)))|^2 \rangle_t \tag{C.16}$$

As for the Roddier calculation, it is possible to calculate the optical transfer function of this long exposure coronagraphic PSF:

$$\tilde{h}_3 = Autocorr\{TF(A_3)\} = Autocorr\{TF(A_d) \times (TF(P_m) * P_u.\exp(j\Phi_t))\} \tag{C.17}$$

Thus we have:

$$\begin{aligned}
\tilde{h}_3 &= Autocorr\{P_d.\exp(j\Phi_d) \times [\tilde{P_m} * P_u.\exp(j(\Phi_u + \Phi_r))]\} \\
&= \iint_{\mathbf{r}} P_d^*(\mathbf{r}) P_d(\mathbf{r}+\mathbf{r}').\exp(j(\Phi_d(\mathbf{r}+\mathbf{r}') - \Phi_d(\mathbf{r}))\, d\mathbf{r} \\
&\times \{\tilde{P_m} * P_u.\exp(j(\Phi_u + \Phi_r)\}^*(\mathbf{r})\ \{\tilde{P_m} * P_u.\exp(j(\Phi_u + \Phi_r)\}(\mathbf{r}+\mathbf{r}') \\
&= \iint_{\mathbf{r}} P_d^*(\mathbf{r})\ P_d(\mathbf{r}+\mathbf{r}').\exp(j(\Phi_d(\mathbf{r}+\mathbf{r}') - \Phi_d(\mathbf{r}))\, d\mathbf{r} \\
&\times \iint_{\mathbf{r}''} \widetilde{P_m}^*(\mathbf{r}-\mathbf{r}'')\ Pu^*(\mathbf{r}'').\exp(-j(\Phi_u(\mathbf{r}'') + \Phi_r(\mathbf{r}''))\, d\mathbf{r}'' \\
&\times \iint_{\mathbf{r}'''} \widetilde{P_m}(\mathbf{r}+\mathbf{r}'-\mathbf{r}''')\ P_u(\mathbf{r}''').\exp(j(\Phi_u(\mathbf{r}''') + \Phi_r(\mathbf{r}'''))\, d\mathbf{r}'''
\end{aligned} \tag{C.18}$$

Note that P_u is real so $P_u^* = P_u$.

If we take the temporal mean, the first line which takes only into account the static terms:

$$\begin{aligned}
\langle \tilde{h}_3 \rangle_t(\mathbf{r}') &= \iint_{\mathbf{r}} \iint_{\mathbf{r}''} \iint_{\mathbf{r}'''} P_d^*(\mathbf{r})\ P_d(\mathbf{r}+\mathbf{r}').\exp(j(\Phi_d(\mathbf{r}+\mathbf{r}') - \Phi_d(\mathbf{r})) \\
&\times \widetilde{P_m}^*(\mathbf{r}-\mathbf{r}'')\ \widetilde{P_m}(\mathbf{r}+\mathbf{r}'-\mathbf{r}''')\ P_u^*(\mathbf{r}'')\ P_u(\mathbf{r}''') \\
&\times \langle \exp(-j(\Phi_u(\mathbf{r}'') + \Phi_r(\mathbf{r}''))\ \exp(j(\Phi_u(\mathbf{r}''') + \Phi_r(\mathbf{r}')))\rangle_t\, d\mathbf{r}\, d\mathbf{r}''d\mathbf{r}''' \\
&= \iint_{\mathbf{r}} \iint_{\mathbf{r}''} \iint_{\mathbf{r}'''} P_d^*(\mathbf{r})\ P_d(\mathbf{r}+\mathbf{r}').\exp(j(\Phi_d(\mathbf{r}+\mathbf{r}') - \Phi_d(\mathbf{r})) \\
&\times \widetilde{P_m}^*(\mathbf{r}-\mathbf{r}'')\ \widetilde{P_m}(\mathbf{r}+\mathbf{r}'-\mathbf{r}''')\ P_u^*(\mathbf{r}'')\ P_u(\mathbf{r}''')\ \exp(j(\Phi_u(\mathbf{r}''') - \Phi_u(\mathbf{r}''))) \\
&\times \langle \exp(j(\Phi_r(\mathbf{r}''') - \Phi_r(\mathbf{r}'')))\rangle_t\, d\mathbf{r}\, d\mathbf{r}''d\mathbf{r}'''
\end{aligned} \tag{C.19}$$

It then comes to the final expression where the non-static component is separated from the others:

$$\boxed{\begin{aligned}
\langle \tilde{h}_3 \rangle_t(\mathbf{r}') = \iint_{\mathbf{r}} \iint_{\mathbf{r}''} \iint_{\mathbf{r}'''} & P_d^*(\mathbf{r}) P_d(\mathbf{r}+\mathbf{r}')\ \exp(j(\Phi_d(\mathbf{r}+\mathbf{r}') - \Phi_d(\mathbf{r}))) \\
&\times \widetilde{P_m}^*(\mathbf{r}-\mathbf{r}'')\ \widetilde{P_m}(\mathbf{r}+\mathbf{r}'-\mathbf{r}''') \\
&\times P_u^*(\mathbf{r}'')\ P_u(\mathbf{r}''')\ \exp(j(\Phi_u(\mathbf{r}''') - \Phi_u(\mathbf{r}''))) \\
&\times \exp(-\frac{1}{2} D_{\Phi_r}(\mathbf{r}''-\mathbf{r}'''))\ \ d\mathbf{r}\, d\mathbf{r}''\, d\mathbf{r}'''
\end{aligned}} \tag{C.20}$$

The problem of this expression is that there is three integrals which is very long to compute (for instance, for a 128×128 pixels image, 10^{16} points must be calculated). This expression must be simplified. O. Herscovici started from this expression to implement a simplified version in IDL, which is published in Hercovisci et al. (2016).

From this equation, I derived the special cases to check if it is consistent. In the following, I use the notation $\Pi_x = P_x \exp(j\Phi_x)$.

C.4.1 Special case of Eq. C.20: without coronagraph

In that case, $P_m = 1$ and $\tilde{P_m} = \delta_m$. We thus obtain:

$$\langle \tilde{h}_3 \rangle_t = \iint_{\mathbf{r}} \iint_{\mathbf{r}''} \iint_{\mathbf{r}'''} \Pi_d^*(\mathbf{r}) \Pi_d(\mathbf{r}+\mathbf{r}') \times \Pi_u^*(\mathbf{r}'') \; \Pi_u(\mathbf{r}''') \times \exp(-\frac{1}{2} D_{\Phi_r}(\mathbf{r}'''-\mathbf{r}'')) \times \delta(\mathbf{r}-\mathbf{r}'') \; \delta(\mathbf{r}+\mathbf{r}'-\mathbf{r}''') \; d\mathbf{r} \, d\mathbf{r}'' \, d\mathbf{r}''' \tag{C.21}$$

From this expression, it is possible to integrate over $\mathbf{r}''$ and $\mathbf{r}'''$ to remove the Dirac functions:

$$\langle \tilde{h}_3 \rangle_t = Autocorr(\Pi_d)(\mathbf{r}') \times \iint_{\mathbf{r}''} \iint_{\mathbf{r}'''} \Pi_u^*(\mathbf{r}'') \; \Pi_u(\mathbf{r}''') \times \exp(-\frac{1}{2} D_{\Phi_r}(\mathbf{r}''' - \mathbf{r}'')) \; d\mathbf{r}'' \, d\mathbf{r}''' \tag{C.22}$$

It is then possible to in order to make the autocorrelation of the upstream PSF show up, $\tilde{h}_u$: $\mathbf{R} \rightarrow \mathbf{r}''' - \mathbf{r}''$.
Then we have: $\iint_{\mathbf{R}} \iint_{\mathbf{r}'''} \; \Pi_u^*(\mathbf{r}'') \; \Pi_u(\mathbf{R} + \mathbf{r}'') \times \exp(-\frac{1}{2} D_{\Phi_r}(\mathbf{R})) \; d\mathbf{r}'' \, d\mathbf{R}$. That it is possible to integrate over $\mathbf{r}''$.

Which comes to the Roddier formula:

$$\boxed{\tilde{h}_3^{LP} = \tilde{h}_d \times \tilde{h}_u \times \exp(-\frac{1}{2} D_{\Phi_r})} \tag{C.23}$$

C.4.2 Special case of Eq. C.20: without turbulence

In that case, $D_\Phi = 0$. We thus obtain:

$$\langle \tilde{h}_3 \rangle_t(\mathbf{r}') = \iint_{\mathbf{r}} \Pi_d^*(\mathbf{r}) \Pi_d(\mathbf{r} + \mathbf{r}') \times \iint_{\mathbf{r}''} \widetilde{P_m}^*(\mathbf{r} - \mathbf{r}'') \; \Pi_u^*(\mathbf{r}'') \times \iint_{\mathbf{r}'''} \widetilde{P_m}(\mathbf{r} + \mathbf{r}' - \mathbf{r}''') \; \Pi_u(\mathbf{r}''') \; d\mathbf{r} \, d\mathbf{r}'' \, d\mathbf{r}''' \tag{C.24}$$

it is possible to integrate over $\mathbf{r}''$ then over $\mathbf{r}'''$. To then obtain:

$$\langle \tilde{h}_3 \rangle_t(\mathbf{r}') = \iint_{\mathbf{r}} \Pi_d^*(\mathbf{r}) \Pi_d(\mathbf{r} + \mathbf{r}') \times (\Pi_u^* * \widetilde{P_m}^*)(\mathbf{r}) \times (\Pi_u * \widetilde{P_m})(\mathbf{r} + \mathbf{r}') \; d\mathbf{r} \tag{C.25}$$

Which comes to the analytical expression of the coronagraphic PSF:

$$\boxed{\tilde{h}_3^{LP} = Autocorr\{\Pi_d \times (\Pi_u * \widetilde{P_m})\}} \tag{C.26}$$

Appendix D

Preliminary results: Application of MEDUSAE on in-lab data

In this chapter, I present results obtained by running MEDUSAE on real in-lab data. I chose this data set for preliminary tests of the method since there is no turbulence and neither central obstruction nor spider (as in the model of ideal coronagraphic PSF used inside MEDUSAE). The main goal is to verify whether MEDUSAE is able to reproduce the speckle field by using the spectral diversity, in spite of the different model used in the inversion and the lack of information about the residual phase structure function ($D_{\phi_{res}}$) and the downstream static phase (ϕ_{down}).

D.1 Description of the in-lab data

The in-lab data set I present in this chapter, have been taken by the SPHERE-IFS instrument on February the 5^{th} 2013 during the integration of SPHERE at IPAG. These data are taken on an internal source, that is to say without turbulence and without the central obstruction nor the spiders in the pupils. However, the corrected zone is still visible, as shown on Fig. D.1, which may require a $D_{\phi_{res}}$ as input. The idea of this part is to check if this faint turbulence residuals can be taken into account, either via the estimated upstream phase or the estimated object. In this data set, no object is present in the field of view. The images have been made by using an APLC coronagraph. The image cube is constituted of 39 images whose wavelengths are spread between 955.90μm and 1362.22μm (in YJ mode). The exposure time is of 4 seconds.

As some images of the multispectral cube were of bad quality (showing many bad and hot pixels or revealing too much the detector grid), I cropped, cleaned the remaining bad pixels and sorted out the images into a $190 \times 190 \times 23$ image cube (note that the rejected frames were essentially the first and last frames of the multispectral cube). Fig. D.1 shows the images at the shortest and longest wavelengths, at respectively 1013.83μm and 1246.55μm.

D.2 Results from MEDUSAE applied on in-lab data

As neither the $D_{\phi_{res}}$ nor the ϕ_{down} are known, I decided to first run several cases using different couples of $D_{\phi_{res}}$ and ϕ_{down} to be provided in input of MEDUSAE. From the results obtained, I present preliminary results obtained from simple solutions I implemented in order to estimate the speckle field.

D.2.1 Different couples of ϕ_{down} and $D_{\phi_{res}}$ input

D.2.1.1 Input upstream phase ϕ_{down}:

Concerning ϕ_{down}, we know that it is non-null and we roughly know its variance and power spectral density but not its specific realization. In the following, I provided MEDUSAE three different

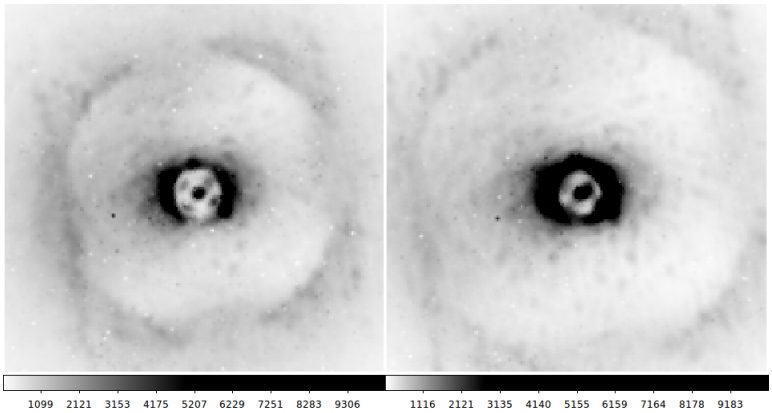

Figure D.1 – Reduced images of the in-lab multispectral data cube used in this section. Left: shortest wavelength (1014μm). Right: largest wavelength (1246μm). (Inverted colors).

downstream phase ϕ_{down}, randomly generated from a Gaussian distribution and having a f^{-2} spatial spectrum (as for the simulated inverse crime data). I used several wavefront error levels: (i) a null upstream aberration map (the smallest usable floating-point value in IDL), (ii) a very small random aberration map having a wavefront error of 10^{-3} nm rms and (iii) a random aberration map with a realistic level wavefront error of 30 nm rms.

D.2.1.2 Input residual phase structure function $D_{\phi_{res}}$:

For each case, I tried two different $D_{\phi_{res}}$ provided as an input: (i) a null $D_{\phi_{res}}$ (the smallest usable floating-point value in IDL) and (ii) a so-called *representative* $D_{\phi_{res}}$. To do so, I did not take into account the potential true value of the wind, seeing or so (which are supposed to be very low for these in-lab data). The representative $D_{\phi_{res}}$ is generated in a purely ad-hoc way. Following the method proposed at Sect. 9.1.4, I finally chose a seeing of $1.14''$, a star magnitude of 8, an aliasing factor of 0.4 and a wind speed of [22,20,35] m/s in the directions [0,10,90]° for the three layers respectively. Of course these values are not realistic but the obtained profile is similar to the real one.

Fig. D.2b shows the azimuthal profile of the real in-lab image at the shortest wavelength (955 nm) and the azimuthal profile of the simulated image (using the ideal model of coronagraphic PSF) using *only* this empirical representative $D_{\phi_{res}}$. Fig. D.2a shows the ideal coronagraphic PSF obtained as well as the real image from SPHERE-IFS (from which the profiles of Fig. D.2b are derived). On each profile, the two orange dashed-line show the region on which I focused to make the two profiles match.

Fig. D.3 shows the profile of the real in-lab image at the shortest wavelength (955 nm) and the profile of the simulated image (using the ideal model of coronagraphic PSF) using *only* this empirical representative $D_{\phi_{res}}$in the x and y-directions: the two profiles are rather different, hence the difficulty in finding a representative profile for both directions (and the average profile shown on Fig. D.2b).

The obtained profile, even if it is not perfect, provides a good starting point to test if it is possible to generate a similar $D_{\phi_{res}}$ in order to manage the lack of knowledge on this required input. Note that the main discrepancy being that the exposure *is not long enough* for the real in-lab data whereas the $D_{\phi_{res}}$ concerns really long exposures for which the stellar halo in the uncorrected zone is really smooth. In MEDUSAE one has to keep in mind that the exposures must be long enough in order to correspond to the coronagraphic PSF model on which the algorithm relies.

D.2.1.3 Other parameters used to run MEDUSAE:

In this section, the goal is to verify if it is possible to launch MEDUSAE as it is on the multispectral cube with these different $D_{\phi_{res}}$ and ϕ_{down} in input. I thus ran only the initialization procedure described in the Sect. 8.2.2.

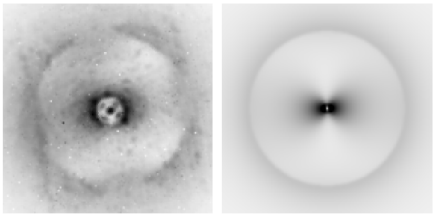

(a) : *Left:* Real in-lab image from SPHERE-IFS from which the profile is extracted. *Right:* Simulated image using the ideal coronagraphic model with null upstream and downstream phases and the representative $D_{\phi_{res}}$.

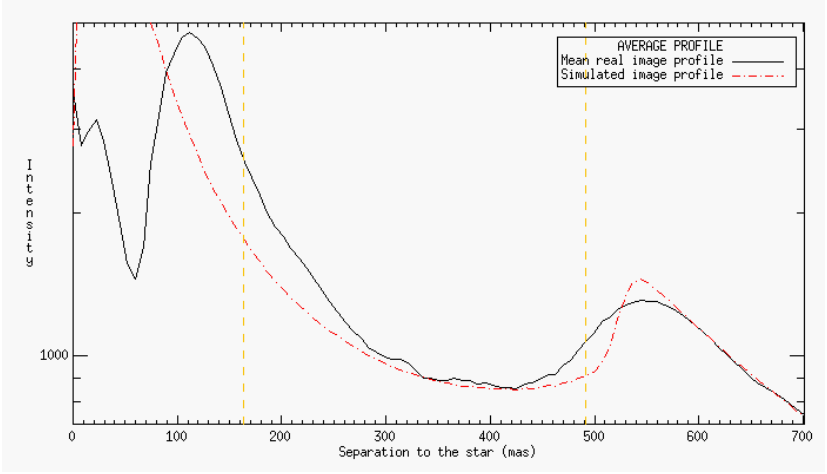

(b) : Average azimuthal profiles of the real in-lab image (black solid line) and the generated image using a representative $D_{\phi_{res}}$ (red dashed line) at 955μm.

Figure D.2 – Generation of a representative $D_{\phi_{res}}$: images (D.2a) and corresponding radial profiles (D.2b) at the shortest wavelength (955μm) of the real in-lab image and the generated ideal image using the representative $D_{\phi_{res}}$.

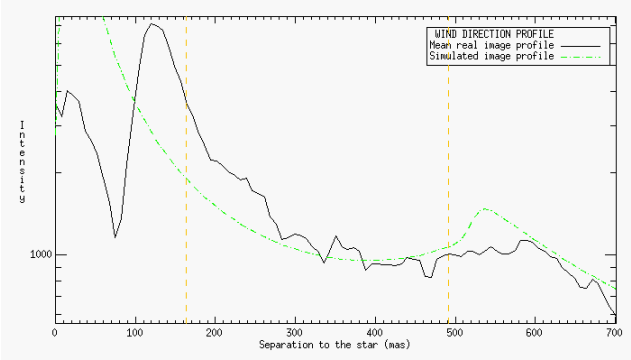

(a) : x-direction profiles.

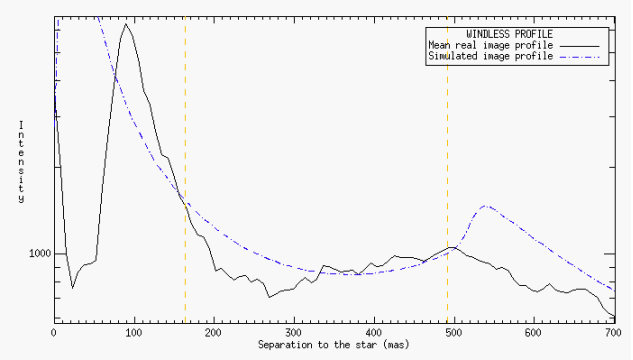

(b) : y-direction profiles.

Figure D.3 – Generation of a representative $D_{\phi_{res}}$: x and y-direction profiles at the shortest wavelength (955μm) of the real in-lab image (black solid line) and the generated ideal image using the representative $D_{\phi_{res}}$ (green and blue dashed lines) .

Weight maps The variance of the noise in the images at each wavelength ($\sigma^2_{\lambda,\alpha}$ in Eq. 7.5) is estimated empirically from the images by accounting for the photon noise only. The corresponding weight maps for each channel, defined as the inverse of this variance must be provided as an input to MEDUSAE.

Wavelengths In this section, I focused on the initialization procedure of MEDUSAE. The algorithm is thus run at one wavelength (the shortest) then two wavelengths (the shortest and the largest).

Object regularization As I focus only on the initialization stages, neither zonal constrain nor a spatial regularization are applied to the object, which can therefore have any distribution possible. Note that after the initialization procedure, the object is rejected and its estimation in the alternate process during the initialization procedure is present in order to relax the phase estimation (see Sect. 8.2.2).

D.2.1.4 Results of the MEDUSAE application on the in-lab data

Tab. D.1 shows the performance of MEDUSAE in terms of estimating the speckle field, as a function of the chosen $D_{\phi_{res}}$ and ϕ_{down} input to the algorithm.

	Input test		Criteria						Init. stage
Test	$D_{\phi_{res}}$	ϕ_{down}	Time [min]	Criterion J	$\mathcal{M}_{f^*}$	ϕ_{res}^{up} [rad]	rMSE$_i$	rMSE$_{SF}$	Nb λ
#1	null	null	4h	8,172	6081%	0.21	101.13%	72.06%	1
#2	null	10^{-3} nm	17h	138,022	1469%	$> 10^6$	14.08%	110.65%	2
#3	null	30 nm	8h	21,158	1056%	$> 10^6$	82.69%	62.19%	1
#4	rep.	null	-	-	-	-	-	-	0
#5	rep.	10^{-3} nm	7h	1,793,117	65.46%	1.16	40.84%	96.56%	2
#6	rep.	30 nm	3.6h	1,645,382	62.51%	0.87	36.29%	94.36%	2

Table D.1 – Results obtained at the second stage (or the first one when the algorithm did not converge, as indicated in the last column) of the initialization procedure of MEDUSAE (along the criteria presented at Sect. 8.1.2) when applying MEDUSAE to the in-lab data presented in Sect. D.1. "rep." stands for the generated representative $D_{\phi_{res}}$. The ϕ_{down} column provides the wavefront error of the downstream aberration map in nm rms.

First of all, the inversions are very long and sometimes, the algorithm does not reach convergence. When the $D_{\phi_{res}}$ is null, the estimated star flux is completely different from the real star flux estimated directly from the true images. Moreover, when ϕ_{down} is not null, the estimated upstream phase is very high and shows very different spatial distribution. In any of these case, the estimated upstream phases and the estimated object do not enable to reproduce the real images. As expected, when no $D_{\phi_{res}}$ is provided in input, the upstream phase tries to reproduce the smooth stellar halo whereas when it is present, the upstream phase mainly fits the speckle structures.

To investigate the estimated speckle field as a function of the different tests, Fig. D.4 shows the estimated speckle fields (obtained from the ideal coronagraphic model and using the estimated upstream phase and estimated star flux as well as the input $D_{\phi_{res}}$ and ϕ_{down}).

Fig. D.5 shows the estimated speckle field (i.e. the ideal coronagraphic PSF model using the estimated upstream phase and the estimated star flux), the estimated image of the object (object map convolved with the non-coronagraphic PSF), the estimated image (the sum of the estimated speckle field and the estimated image of the object) and the images residuals (the true image minus the estimated image) for the five different tests. When the algorithm converged, this figure shows the results of the inversion with two wavelengths, otherwise, with one wavelength.

The test #2, #5 and #6 have converged at two wavelengths. However in these three cases, the image of the object is extremely bright: almost all the image is fitted by the object and not by the phase as expected. Even if the object is rejected after the initialization procedure, this effect is really problematic since the estimated phase is not realistic and therefore is not a good starting point for the MEDUSAE core.

In all of these six different cases, at one wavelength, the central part of the image are mostly fitted by the phase and not by the object. Thus one must find a way to prevent the phase from fitting the central part of the image since the ideal model used for inversion is very different from the real data in this region. A very simple idea is to set a null weight in this central zone (diameter of $6\lambda/D$). The next section present the results obtained with such a weight map.

D.2.2 Results of further tests for the MEDUSAE application on the in-lab data

From these first results, further preliminary tests have been conducted since from the previous tests cases it seems that the main problem arises from the difficulty in fitting the central part of the image. In this short section, I present the results obtained with a null $D_{\phi_{res}}$(case (i)) and a null ϕ_{down}(case (i)) but using a null weight map in the central regions (below a radius of $3\lambda/D$)

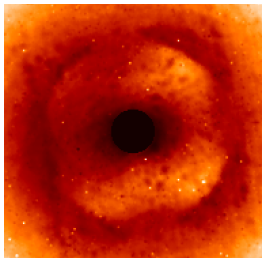

Figure D.6 – Weight map used to run MEDUSAE on the in-lab data described in Sect. D.1.

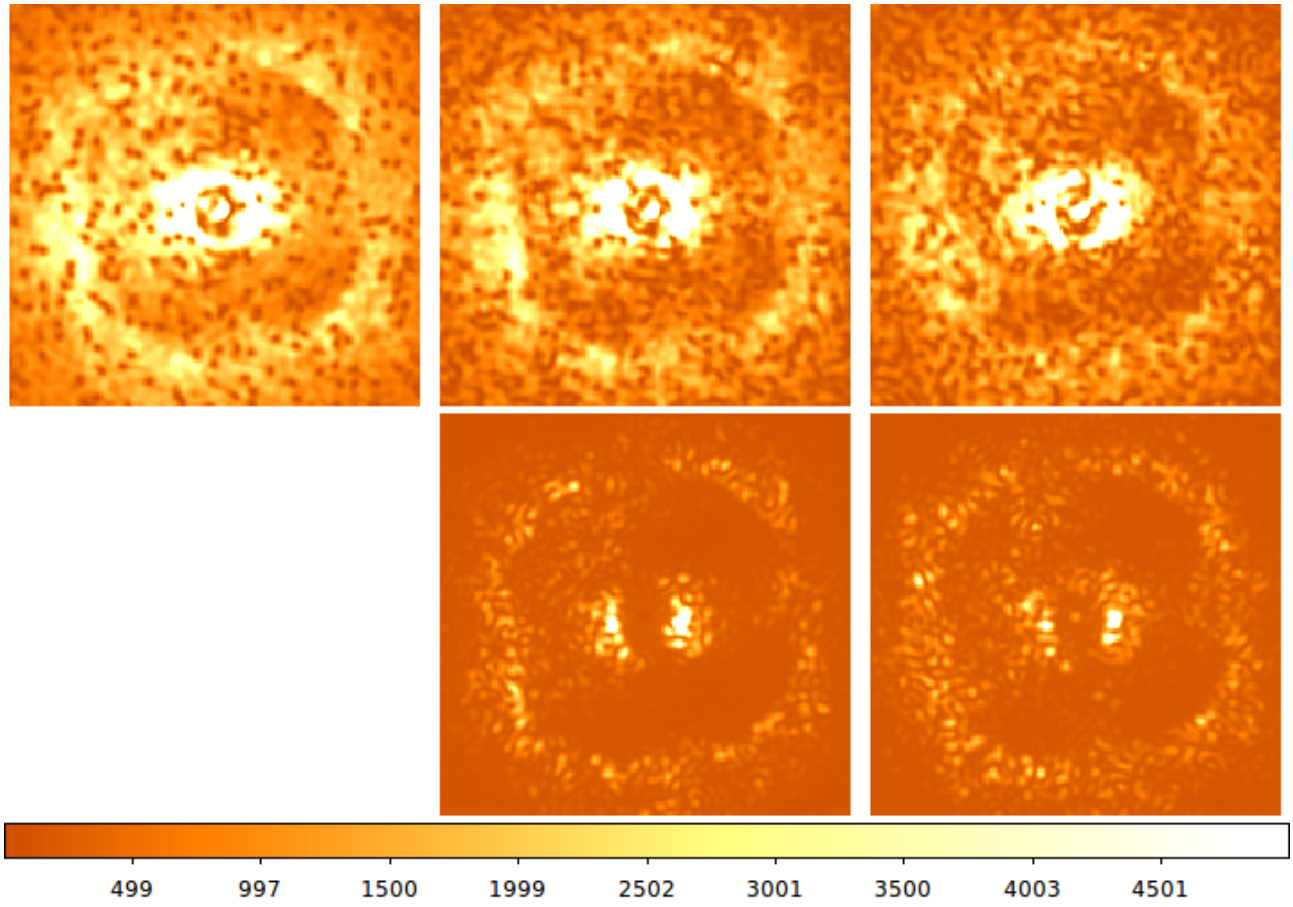

Figure D.4 – Estimated speckle field derived from the estimated upstream phase and the estimated stellar flux. Top row: tests with a null $D_{\phi_{res}}$. Bottom row: tests with a representative $D_{\phi_{res}}$. From left to right: Tests with the input ϕ_{down} corresponding to cases (i), (ii) and (iii) respectively.

in order to avoid fitting the central part of the images where the model used for inversion is not consistent with the spatial structures present in the images (below $3\lambda/D$ from the star). This simple approach is to investigate if the previous results are mainly due to this discrepancy or if the $D_{\phi_{res}}$ and ϕ_{down} also have to be investigated.

Tab. D.2 gathers the results obtained in this case. Compared to the results of test #1 presented at Tab. D.1, only the estimated flux is better estimated. Otherwise, the estimated phase also shows intense values and the estimated speckle field is not satisfactory. Fig. D.7 shows the estimated speckle field, the estimated image of the object, the estimated image and the residuals for the two initialization stages. Compared to the previous tests, the object tries to reproduce the central part of the image. To have a closer look at the estimated speckle fields, Fig. D.8 shows the estimated speckle field at each initialization stage.

Test	Initialization stage	Time [min]	Criterion J	$\mathcal{M}_{f*}$	ϕ_{res}^{up} [rad]	rMSE$_\delta$	rMSE$_{SF}$
#7	1λ	5.15h	197224.66	82.87%	0.62	128.96%	88.10%
#7	2λ	9.38h	526579.28	72.00%	249.50	153.19%	103.35%

Table D.2 – Results obtained at the first and the second stage of the initialization procedure of MEDUSAE (along the criteria presented at Sect. 8.1.2) when applying MEDUSAE to the in-lab data presented in Sect. D.1.

At one wavelength, we can see that it is impossible to find an upstream phase which succeeds in reproducing, even approximately, the image. This estimated upstream phase at one wavelength is so different from the true one that its application at another wavelength is completely inappropriate,

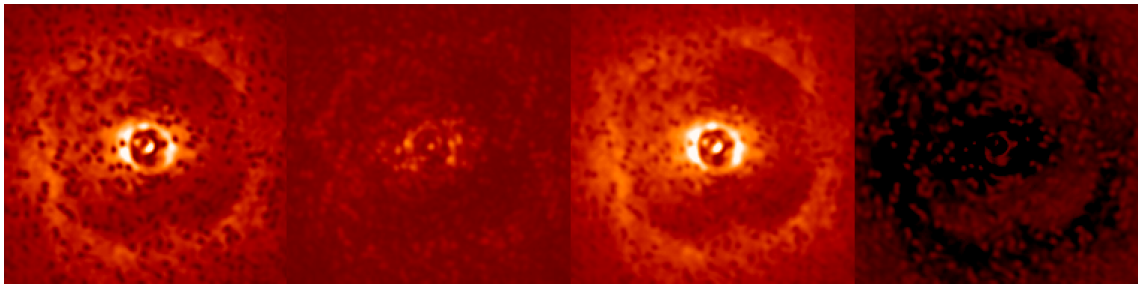

(a) : Test #1 (after initialization at only one wavelength).

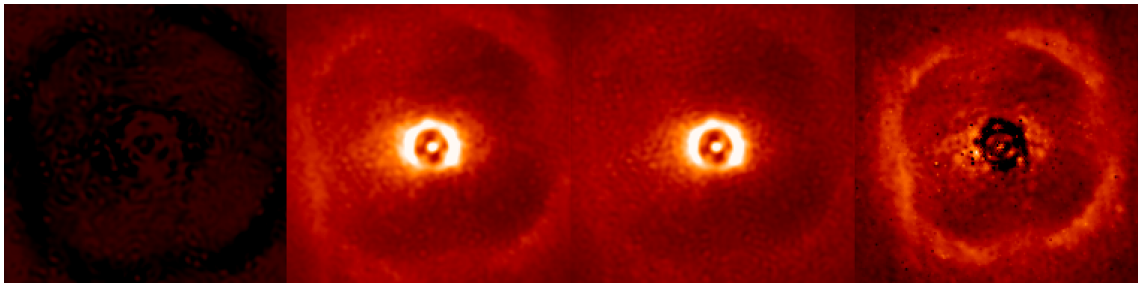

(b) : Test #2 (after initialization at two wavelengths).

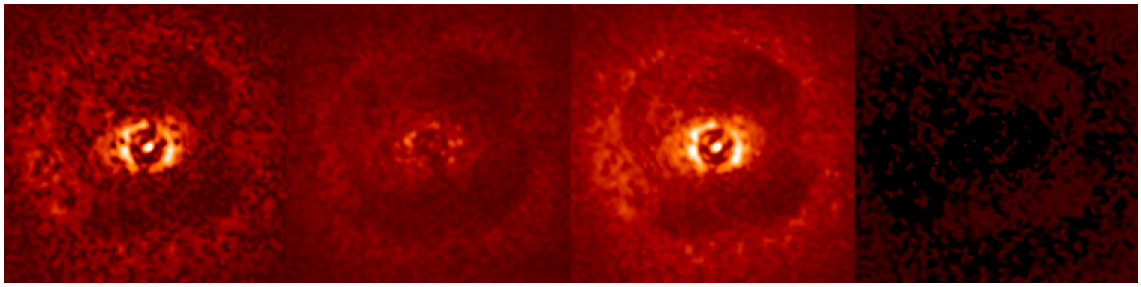

(c) : Test #3 (after initialization at only one wavelength).

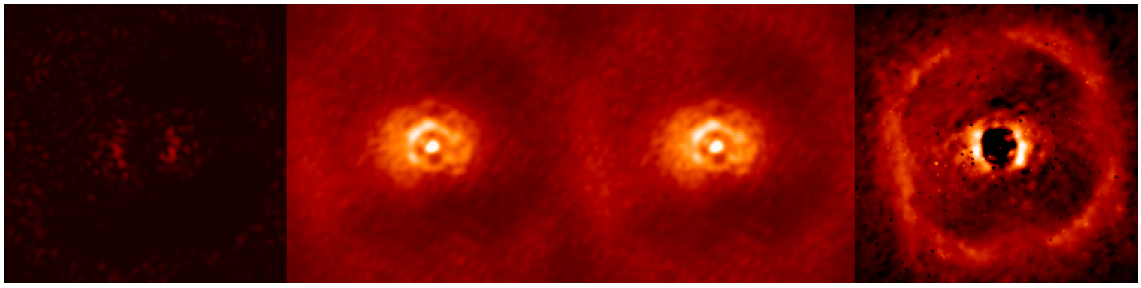

(d) : Test #5 (after initialization at two wavelengths).

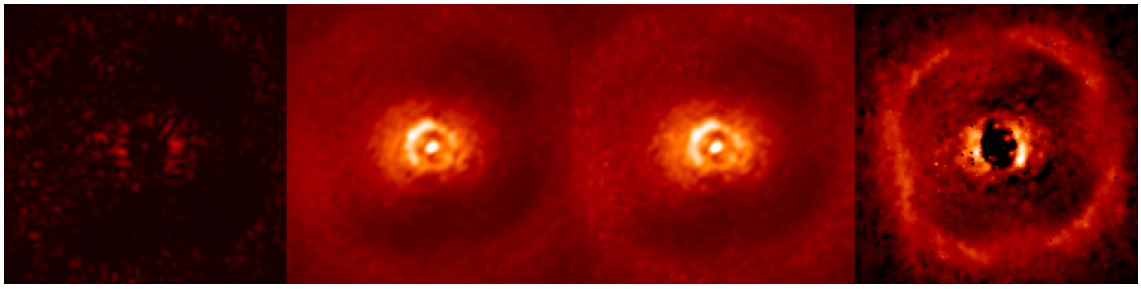

(e) : Test #6 (after initialization at two wavelengths).

Figure D.5 – Results from the MEDUSAE inversion procedure for the six different tests. From left to right: Image of the estimated speckle field, image of the estimated object map, estimated image (sum of the two images on the left) and residuals wrt the real input image. For each test, the colorbars are the same.

which is revealed by all the tests at two wavelengths. Thus, not only the two wavelengths case does not help but it reveals that the estimated phase found to fit the images is far from being the true

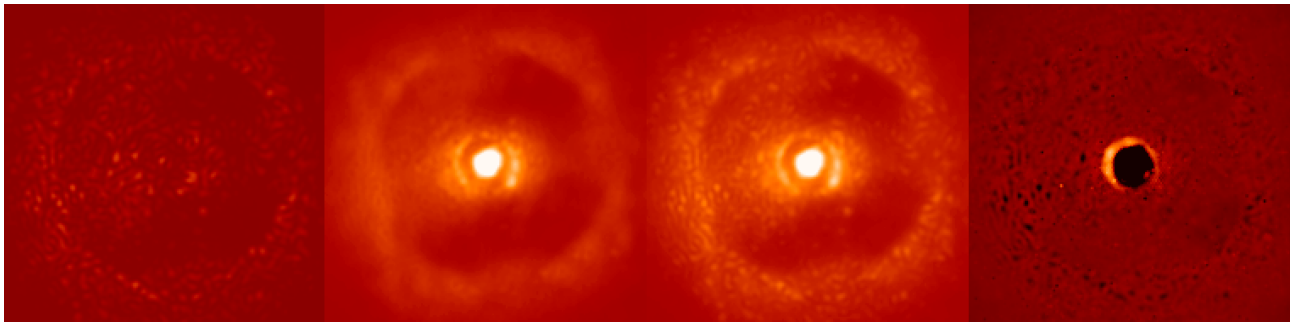

(a) : Results of the first stage of the initialization (only the shortest wavelength)

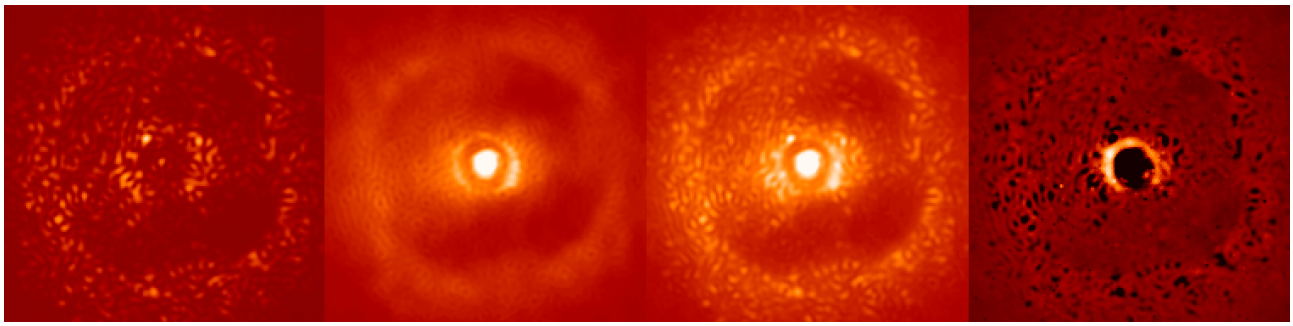

(b) : Results of the second stage of the initialization (two wavelengths): shortest wavelength (955.5nm).

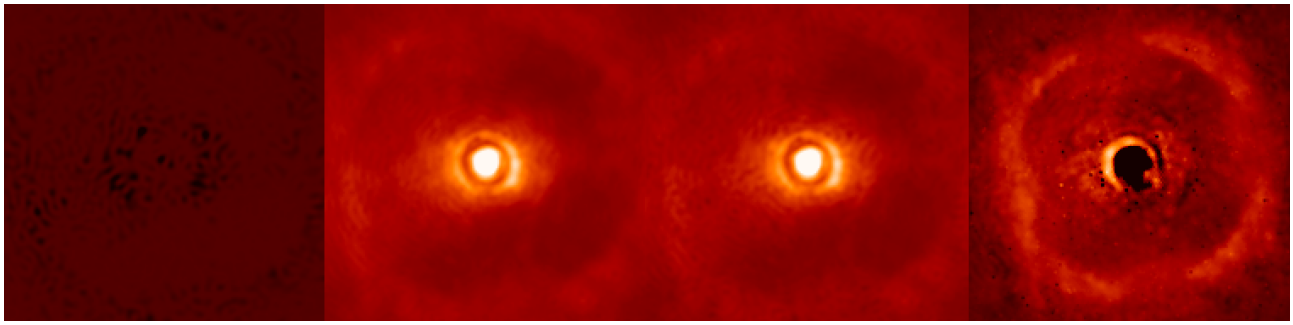

(c) : Results of the second stage of the initialization (two wavelengths): largest wavelength (1328.84nm).

Figure D.7 – Results from the MEDUSAE inversion procedure for the test #7, similar to the test #1 but using a null weight in the central part of the image (below $3\lambda/D$). From left to right: Image of the estimated speckle field, image of the estimated object map, estimated image (sum of the two images on the left) and residuals wrt the real input image. For each test, the colorbars are the same.

solution.

D.2.3 Conclusions on preliminary tests on the in-lab data

These results do not guarantee that no solution exist but as too many unknown ingredients remain it motivated to simulate realistic data, with the same properties as SPHERE-IFS data, which uses an APLC coronagraphic model. In this case, it is possible to focus on the main discrepancy between the model used in the inversion (the ideal coronagraph) and the true image (usually an APLC coronagraph) while knowing perfectly the other parameters.

From the preliminary tests performed in this section, several conclusions arose:

1. A null $D_{\phi_{res}}$ in input forces the estimated upstream phase to try reproduce the stellar halo (showing the correction zone) which biases its estimation and make arise specific speckles structure in the corresponding estimated speckle field (see Fig. D.4);
2. A small $D_{\phi_{res}}$ (generated with a low seeing) does not enable to estimate a ϕ_{up} such that the estimated speckle field is close to the real one;
3. A small downstream phase in input induces that the estimated upstream phase has a high level;

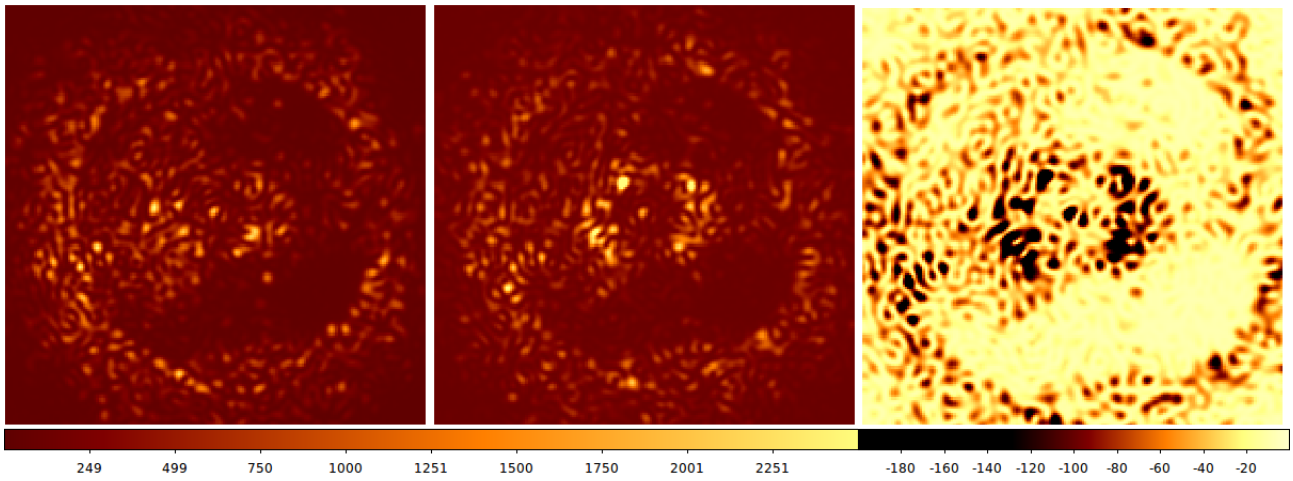

Figure D.8 – Estimated speckle field derived from the estimated upstream aberration map. From left to right: first stage of the initialization (only the shortest wavelength), second stage of the initialization at the shortest wavelength and second stage of the initialization at the largest wavelength.

4. Increasing the number of wavelengths does not necessarily improve the speckle field estimation.

Appendix E

List of communications

Refereed journal publications

- Cantalloube F., Mouillet D., Mugnier L., Milli J., Absil O., Gomez Gonzalez C. A. Chauvin G., J.-L. Beuzit and A. Cornia, *Direct exoplanet detection and characterization using the ANDROMEDA method: Performance on VLT/NaCo data*, A&A, **2015**.

- A. Zurlo, A. Vigan, R. Galicher, A.-L. Maire, D. Mesa, R. Gratton, G. Chauvin, M. Kasper, C. Moutou, M. Bonnefoy, S. Desidera, L. Abe, D. Apai, A. Baruffolo, P. Baudoz, J. Baudrand, J.-L. Beuzit, P. Blancard, A. Boccaletti, F. Cantalloube, M. Carle, E. Cascone, J. Charton, R. U. Claudi, A. Costille, V. de Caprio, K. Dohlen, C. Dominik, D. Fantinel, P. Feautrier, M. Feldt, T. Fusco, P. Gigan, J. H. Girard, D. Gisler, L. Gluck, C. Gry, T. Henning, E. Hugot, M. Janson, M. Jaquet, A.-M. Lagrange, M. Langlois, M. Llored, F. Madec, Y. Magnard, P. Martinez, D. Maurel, D. Mawet, M. R. Meyer, J. Milli, O. Moeller-Nilsson, D. Mouillet, A. Origné, A. Pavlov, C. Petit, P. Puget, S. P. Quanz, P. Rabou, J. Ramos, G. Rousset, A. Roux, B. Salasnich, G. Salter, J.-F. Sauvage, H. M. Schmid, C. Soenke, E. Stadler, M. Suarez, M. Turatto, S. Udry, F. Vakili, Z. Wahhaj, F. Wildi and J. Antichi, *Spectrophotometry and astrometry of the HR8799 exoplanetary system with VLT/SPHERE*, A&A, **2016**.

- M. Bonnefoy, A. Zurlo, J. L. Baudino, P. Lucas, D. Mesa, A.-L. Maire, A. Vigan, R. Galicher, D. Homeier, F. Marocco, R. Gratton, G. Chauvin, F. Allard, S. Desidera, M. Kasper, C. Moutou, A.-M. Lagrange, J. Antichi, A. Baruffolo, J. Baudrand, J.-L. Beuzit, A. Boccaletti, F. Cantalloube, M. Carbillet, J. Charton, R. U. Claudi, A. Costille, K. Dohlen, C. Dominik, D. Fantinel, P. Feautrier, M. Feldt, T. Fusco, P. Gigan, J. H. Girard, L. Gluck, C. Gry, T. Henning, M. Janson, M. Langlois, F. Madec, Y. Magnard, D. Maurel, D. Mawet, M. R. Meyer, J. Milli, O. Moeller-Nilsson, D. Mouillet, A. Pavlov, D. Perret, P. Pujet, S. P. Quanz, S. Rochat, G. Rousset, A. Roux, B. Salasnich, G. Salter, J.-F. Sauvage, H. M. Schmid, A. Sevin, C. Soenke, E. Stadler, M. Turatto, S. Udry, F. Vakili, Z. Wahhaj and F. Wildi, *First light of the VLT planet finder SPHERE - IV. Physical and chemical properties of the planets around HR8799*, A&A, **2016**.

- C. A. Gomez Gonzalez, O. Wertz, O. Absil, V. Christiaens, D. Defrère, D. Mawet, J. Milli, P.-A. Absil, M. Van Droogenbroeck, F. Cantalloube, P.M. Hinz, A.J. Skemer, M. Karlsson and J. Surdej, *VIP: Vortex Image Processing Package for High-contrast Direct Imaging*, APJAJ, **submitted**.

- Bonnefoy M. (**in prep**) - (publication on GJ504 b using SPHERE)

- Samland M. (**in prep**) - (publication on Eri51 b using SPHERE)

Conference proceedings

- Herscovici-Schiller O., Mugnier L. M., Sauvage J. F., Le Duigou J. M., Cantalloube F., *Analytical expression of a long exposure coronagraphic point spread function. Application to the estimation of quasi-static aberrations in the presence of residual turbulence with COFFEE*, SPIE, **2016**.
- Thiébaut E., Denis L., Mugnier L. M., Ferrari A., Mary D., Langlois M., Cantalloube F., Devaney N., *Fast and robust exo-planet detection in multi-spectral, multi-temporal data*, SPIE, **2016**.

Conferences

Given talks

- *The MEDUSAE approach: performance on ideal and realistic simulated data.* 1st International Vortex Workshop, CalTech, Pasadena, USA (August 2016)
- *Image processing to detect and characterize exoplanets in high contrast images: ANDROMEDA.* AO data processing tools, LAM, Marseille, France (May 2015)
- *Image reconstruction from high contrast SPHERE data.* Journées Scientifiques Onera, JSO, Onera Châtillon, France (January 2015)
- *Inverse problems applied to the detection and characterization of exoplanets by imaging.* Elbereth 2014, Conférence des doctorants en astrophysique d'Ile de France, IAP, Paris, France (December 2014)
- *Image processing for the detection and characterization of exoplanets: context and methods.* Elbereth 2013, Conférence des doctorants en astrophysique d'Ile de France, IAP, Paris, France (November 2013)
- *Image processing for the detection and characterization of exoplanets: the ANDROMEDA method.* RJP 2013, Rencontre des Jeunes Physicien-ne-s, CNAM, Paris, France (November 2013)

Posters

- *ANDROMEDA on-sky validation: Towards automatic and homogeneous companion detection.* In the spirit of Lyot, Montréal, Canada (July 2015)
- *MEDUSAE: Multispectral Exoplanet Detection Using Simultaneous Aberration Estimation.* In the spirit of Lyot, Montréal, Canada (July 2015)
- *Image processing methods to detect and characterize exoplanets.* Santander summer school, Heidelberg Center for Latin America, Santiago, Chile (November 2014)
- *Beta-Pictoris b as seen by ANDROMEDA.* Thirty Years of Beta Pictoris - IAP, Paris, France (September 2014)
- *Image processing methods to detect and characterize exoplanets based on Bayesian inverse problems solving.* Sagan summer workshop, Imaging Planets and Disks, CalTEch, Pasadena, USA (July 2014)
- *Bayesian inverse problems solving to directly detect and characterize exoplanets.* SF2A 2014, Société Française d'Astronomie et d'Astrophysique, Université Paris 7, France (June 2014)

Seminars

- *Image processing methods based on inverse problem solving, to detect and characterize exoplanets.* Université de Liège, Liège, Belgium (April 2015 and September 2015)
- *ANDROMEDA: Image processing based on inverse problemes to detect and characterize exoplanets.* Royal Observatory Edinburgh, Edinburgh, Scotland (March 2015)
- *Image processing to detect and characterize exoplanets from ground-based telescope.* Max Planck Institute for Astronomy, Heidelberg, Germany (November 2015)
- *Inverse problems applied to the detection and characterization of exoplanets from high contrast images.* Centre de Recherche Astrophysique de Lyon, Lyon, France (December 2015)

Bibliography

Absil, O., Milli, J., Mawet, D., Lagrange, A.-M., Girard, J., Chauvin, G., Boccaletti, A., Delacroix, C., and Surdej, J. (2013). Searching for companions down to 2 AU from β Pictoris using the L'-band AGPM coronagraph on VLT/NACO. *Astron. & Astrophys.*, 559:L12.

Aime, C. and Soummer, R. (2004). The Usefulness and Limits of Coronagraphy in the Presence of Pinned Speckles. *Astrophys. J. Letter.*, 612:L85–L88.

Amara, A. and Quanz, S. P. (2012). PYNPOINT: an image processing package for finding exoplanets. *Mon. Not. R. astr. Soc.*, 427:948–955.

Antichi, J., Dohlen, K., Gratton, R. G., Mesa, D., Claudi, R. U., Giro, E., Boccaletti, A., Mouillet, D., Puget, P., and Beuzit, J.-L. (2009). BIGRE: A Low Cross-Talk Integral Field Unit Tailored for Extrasolar Planets Imaging Spectroscopy. *Astrophys. J.*, 695:1042–1057.

Antichi, J., Gratton, R. G., Claudi, R. U., Giro, E., Mesa, D., Desidera, S., Scuderi, S., Bruno, P., Turatto, M., Cascone, E., De Caprio, V., Beuzit, J.-L., Puget, P., and Dohlen, K. (2008). Sphere ifs optical concept description and design overview.

Artigau, É., Biller, B. A., Wahhaj, Z., Hartung, M., Hayward, T. L., Close, L. M., Chun, M. R., Liu, M. C., Trancho, G., Rigaut, F., Toomey, D. W., and Ftaclas, C. (2008). NICI: combining coronagraphy, ADI, and SDI. In *Ground-based and Airborne Instrumentation for Astronomy II*, volume 7014 of *Proc. SPIE*, page 70141Z.

Babcock, H. W. (1953). The Possibility of Compensating Astronomical Seeing. *Pub. Astron. Soc. Pacific.*, 65:229.

Backer, D. C., Kulkarni, S. R., Heiles, C., Davis, M. M., and Goss, W. M. (1982). A millisecond pulsar. *Nature*, 300:615–618.

Baldwin, J. E., Haniff, C. A., Mackay, C. D., and Warner, P. J. (1986). Closure phase in high-resolution optical imaging. *Nature*, 320:595–597.

Baraffe, I., Chabrier, G., Barman, T. S., Allard, F., and Hauschildt, P. H. (2003). Evolutionary models for cool brown dwarfs and extrasolar giant planets. The case of HD 209458. *Astron. & Astrophys.*, 402:701–712.

Barman, T. S., Konopacky, Q. M., Macintosh, B., and Marois, C. (2015). Simultaneous Detection of Water, Methane, and Carbon Monoxide in the Atmosphere of Exoplanet HR8799b. *Astrophys. J.*, 804:61.

Barman, T. S., Macintosh, B., Konopacky, Q. M., and Marois, C. (2011). Clouds and Chemistry in the Atmosphere of Extrasolar Planet HR8799b. *Astrophys. J.*, 733:65.

Baudino, J.-L., Bézard, B., Boccaletti, A., Bonnefoy, M., Lagrange, A.-M., and Galicher, R. (2015). Interpreting the photometry and spectroscopy of directly imaged planets: a new atmospheric model applied to β Pictoris b and SPHERE observations. *Astron. & Astrophys.*, 582:A83.

Baudoz, P., Boccaletti, A., Rabbia, Y., and Gay, J. (2005). Stellar Coronagraphy: Study and Test of a Hybrid Interfero-Coronagraph. *Pub. Astron. Soc. Pacific.*, 117:1004–1011.

Baudoz, P., Dorn, R. J., Lizon, J.-L., Fusco, T., Dohlen, K., Charton, J., Beuzit, J.-L., Puget, P., Mouillet, D., Felt, M., Wildi, F., Barrufolo, A., Kasper, M., and Hubin, N. (2010). The differential tip-tilt sensor of sphere.

Baudoz, P., Galicher, R., Baudrand, J., and Boccaletti, A. (2008). Theory and laboratory tests of the multi-stage phase mask coronagraph. In *Adaptive Optics Systems*, volume 7015 of *Proc. SPIE*, page 70156C.

Beers, T. C., Flynn, K., and Gebhardt, K. (1990). Measures of location and scale for velocities in clusters of galaxies - A robust approach. *Astron. J.*, 100:32–46.

Benisty, M., Juhasz, A., Boccaletti, A., Avenhaus, H., Milli, J., Thalmann, C., Dominik, C., Pinilla, P., Buenzli, E., Pohl, A., Beuzit, J.-L., Birnstiel, T., de Boer, J., Bonnefoy, M., Chauvin, G., Christiaens, V., Garufi, A., Grady, C., Henning, T., Huelamo, N., Isella, A., Langlois, M., Ménard, F., Mouillet, D., Olofsson, J., Pantin, E., Pinte, C., and Pueyo, L. (2015). Asymmetric features in the protoplanetary disk MWC 758. *Astron. & Astrophys.*, 578:L6.

Beuzit, J.-L., Feldt, M., Dohlen, K., Mouillet, D., Puget, P., Wildi, F., Abe, L., Antichi, J., Baruffolo, A., Baudoz, P., Boccaletti, A., Carbillet, M., Charton, J., Claudi, R., Downing, M., Fabron, C., Feautrier, P., Fedrigo, E., Fusco, T., Gach, J.-L., Gratton, R., Henning, T., Hubin, N., Joos, F., Kasper, M., Langlois, M., Lenzen, R., Moutou, C., Pavlov, A., Petit, C., Pragt, J., Rabou, P., Rigal, F., Roelfsema, R., Rousset, G., Saisse, M., Schmid, H.-M., Stadler, E., Thalmann, C., Turatto, M., Udry, S., Vakili, F., and Waters, R. (2008). SPHERE: a 'Planet Finder' instrument for the VLT. In *Ground-based and Airborne Instrumentation for Astronomy II*, volume 7014 of *Proc. SPIE*, page 701418.

Boccaletti, A., Thalmann, C., Lagrange, A.-M., Janson, M., Augereau, J.-C., Schneider, G., Milli, J., Grady, C., Debes, J., Langlois, M., Mouillet, D., Henning, T., Dominik, C., Maire, A.-L., Beuzit, J.-L., Carson, J., Dohlen, K., Engler, N., Feldt, M., Fusco, T., Ginski, C., Girard, J. H., Hines, D., Kasper, M., Mawet, D., Ménard, F., Meyer, M. R., Moutou, C., Olofsson, J., Rodigas, T., Sauvage, J.-F., Schlieder, J., Schmid, H. M., Turatto, M., Udry, S., Vakili, F., Vigan, A., Wahhaj, Z., and Wisniewski, J. (2015). Fast-moving features in the debris disk around AU Microscopii. *Nature*, 526:230–232.

Bonavita, M., Chauvin, G., Desidera, S., Gratton, R., Janson, M., Beuzit, J. L., Kasper, M., and Mordasini, C. (2012). MESS (multi-purpose exoplanet simulation system). A Monte Carlo tool for the statistical analysis and prediction of exoplanet search results. *Astron. & Astrophys.*, 537:A67.

Bond, I., Abe, F., Dodd, R., Hearnshaw, J., Honda, M., Jugaku, J., Kilmartin, P., Marles, A., Masuda, K., Matsubara, Y., Muraki, Y., Nakamura, T., Nankivell, G., Noda, S., Noguchi, C., Ohnishi, K., Rattenbury, N., Reid, M., Saito, T., Sato, H., Sekiguchi, M., Skuljan, J., Sullivan, D., Sumi, T., Takeuti, M., Watase, Y., Wilkinson, S., Yamada, R., Yanagisawa, T., and Yock, P. (2001). Real-time difference imaging analysis of moa galactic bulge observations during 2000. *Monthly Notices of the Royal Astronomical Society*, 327(3):868–880.

Bongard, S., Soulez, F., Thiébaut, É., and Pecontal, É. (2011). 3D deconvolution of hyper-spectral astronomical data. *Mon. Not. R. astr. Soc.*, 418:258–270.

Bonnefoy, M., Marleau, G.-D., Galicher, R., Beust, H., Lagrange, A.-M., Baudino, J.-L., Chauvin, G., Borgniet, S., Meunier, N., Rameau, J., Boccaletti, A., Cumming, A., Helling, C., Homeier, D., Allard, F., and Delorme, P. (2014). Physical and orbital properties of β Pictoris b. *Astron. & Astrophys.*, 567:L9.

Bonnefoy, M., Zurlo, A., Baudino, J. L., Lucas, P., Mesa, D., Maire, A.-L., Vigan, A., Galicher, R., Homeier, D., Marocco, F., Gratton, R., Chauvin, G., Allard, F., Desidera, S., Kasper, M., Moutou, C., Lagrange, A.-M., Antichi, J., Baruffolo, A., Baudrand, J., Beuzit, J.-L., Boccaletti, A., Cantalloube, F., Carbillet, M., Charton, J., Claudi, R. U., Costille, A., Dohlen, K., Dominik, C., Fantinel, D., Feautrier, P., Feldt, M., Fusco, T., Gigan, P., Girard, J. H., Gluck, L., Gry, C., Henning, T., Janson, M., Langlois, M., Madec, F., Magnard, Y., Maurel, D., Mawet, D., Meyer, M. R., Milli, J., Moeller-Nilsson, O., Mouillet, D., Pavlov, A., Perret, D., Pujet, P., Quanz, S. P., Rochat, S., Rousset, G., Roux, A., Salasnich, B., Salter, G., Sauvage, J.-F., Schmid, H. M., Sevin, A., Soenke, C., Stadler, E., Turatto, M., Udry, S., Vakili, F., Wahhaj, Z., and Wildi, F. (2016). First light of the VLT planet finder SPHERE. IV. Physical and chemical properties of the planets around HR8799. *Astron. & Astrophys.*, 587:A58.

Booth, M., Jordán, A., Casassus, S., Hales, A. S., Dent, W. R. F., Faramaz, V., Matrà, L., Barkats, D., Brahm, R., and Cuadra, J. (2016). Resolving the Planetesimal Belt of HR 8799 with ALMA. *Mon. Not. R. astr. Soc.*.

Borgniet, S., Meunier, N., and Lagrange, A.-M. (2015). Using the Sun to estimate Earth-like planets detection capabilities. V. Parameterizing the impact of solar activity components on radial velocities. *Astron. & Astrophys.*, 581:A133.

Borysow, A., Champion, J. P., Jørgensen, U. G., and Wenger, C. (2003). Preliminary CH_4 Line List Data for Stellar Atmospheres. In Hubeny, I., Mihalas, D., and Werner, K., editors, *Stellar Atmosphere Modeling*, volume 288 of *Astronomical Society of the Pacific Conference Series*, page 352.

Boss, A. P. (2002). Evolution of the Solar Nebula. V. Disk Instabilities with Varied Thermodynamics. *Astrophys. J.*, 576:462–472.

Bouchy, F., Moutou, C., Queloz, D., and CoRoT Exoplanet Science Team (2009). Radial velocity follow-up for confirmation and characterization of transiting exoplanets. In Pont, F., Sasselov, D., and Holman, M. J., editors, *Transiting Planets*, volume 253 of *IAU Symposium*, pages 129–139.

Bowler, B. P., Liu, M. C., Dupuy, T. J., and Cushing, M. C. (2010). Near-infrared Spectroscopy of the Extrasolar Planet HR 8799 b. *Astrophys. J.*, 723:850–868.

Brandt, T. D., McElwain, M. W., Turner, E. L., Mede, K., Spiegel, D. S., Kuzuhara, M., Schlieder, J. E., Wisniewski, J. P., Abe, L., Biller, B., Brandner, W., Carson, J., Currie, T., Egner, S., Feldt, M., Golota, T., Goto, M., Grady, C. A., Guyon, O., Hashimoto, J., Hayano, Y., Hayashi, M., Hayashi, S., Henning, T., Hodapp, K. W., Inutsuka, S., Ishii, M., Iye, M., Janson, M., Kandori, R., Knapp, G. R., Kudo, T., Kusakabe, N., Kwon, J., Matsuo, T., Miyama, S., Morino, J.-I., Moro-Martín, A., Nishimura, T., Pyo, T.-S., Serabyn, E., Suto, H., Suzuki, R., Takami, M., Takato, N., Terada, H., Thalmann, C., Tomono, D., Watanabe, M., Yamada, T., Takami, H., Usuda, T., and Tamura, M. (2014). A Statistical Analysis of SEEDS and Other High-contrast Exoplanet Surveys: Massive Planets or Low-mass Brown Dwarfs? *Astrophys. J.*, 794:159.

Burke, D. and Devaney, N. (2010). Enhanced faint companion photometry and astrometry using wavelength diversity. *Journal of the Optical Society of America A*, 27(27):A246.

Cady, E., Baranec, C., Beichman, C., Brenner, D., Burruss, R., Crepp, J., Dekany, R., Hale, D., Hillenbrand, L., Hinkley, S., Ligon, E. R., Lockhart, T., Oppenheimer, B., Parry, I., Pueyo, L., Rice, E., Roberts, L. C., Roberts, J., Shao, M., Sivaramakrishnan, A., Soummer, R., Tang, H., Truong, T., Vasisht, G., Vescelus, F., Wallace, J. K., Zhai, C., and Zimmerman, N. (2013). Electric field conjugation with the project 1640 coronagraph. In *Techniques and Instrumentation for Detection of Exoplanets VI*, volume 8864 of *Proc. SPIE*, page 88640K.

Cagigal, M. P. and Canales, V. E. (2000). Generalized Fried parameter after adaptive optics partial wave-front compensation. *Journal of the Optical Society of America A*, 17:903–910.

Cantalloube, F., Mouillet, D., Mugnier, L. M., Milli, J., Absil, O., Gomez Gonzalez, C. A., Chauvin, G., Beuzit, J.-L., and Cornia, A. (2015). Direct exoplanet detection and characterization using the ANDROMEDA method: Performance on VLT/NaCo data. *Astron. & Astrophys.*, 582:A89.

Carbillet, M., Boccaletti, A., Thalmann, C., Fusco, T., Vigan, A., Smith, I., Mouillet, D., Dohlen, K., Bendjoya, P., and Ferrari, A. (2008). The Software Package SPHERE: a CAOS-based numerical tool for end-to-end simulations of SPHERE/VLT. In *Adaptive Optics Systems*, volume 7015 of *Proc. SPIE*, page 70156Z.

Carlotti, A., Kasdin, N. J., Vanderbei, R. J., and Delorme, J.-R. (2012). Optimized shaped pupil masks for pupil with obscuration. In *Space Telescopes and Instrumentation 2012: Optical, Infrared, and Millimeter Wave*, volume 8442 of *Proc. SPIE*, page 844254.

Cassan, A., Kubas, D., Beaulieu, J.-P., Dominik, M., Horne, K., Greenhill, J., Wambsganss, J., Menzies, J., Williams, A., Jørgensen, U. G., Udalski, A., Bennett, D. P., Albrow, M. D., Batista, V., Brillant, S., Caldwell, J. A. R., Cole, A., Coutures, C., Cook, K. H., Dieters, S., Prester, D. D., Donatowicz, J., Fouqué, P., Hill, K., Kains, N., Kane, S., Marquette, J.-B., Martin, R., Pollard, K. R., Sahu, K. C., Vinter, C., Warren, D., Watson, B., Zub, M., Sumi, T., Szymański, M. K., Kubiak, M., Poleski, R., Soszynski, I., Ulaczyk, K., Pietrzyński, G., and Wyrzykowski, Ł. (2012). One or more bound planets per Milky Way star from microlensing observations. *Nature*, 481:167–169.

Cassan, A. and Ranc, C. (2016). Interferometric observation of microlensing events. *Mon. Not. R. astr. Soc.*, 458:2074–2079.

Charbonneau, D., Brown, T. M., Latham, D. W., and Mayor, M. (2000). Detection of Planetary Transits Across a Sun-like Star. *Astrophys. J. Letter.*, 529:L45–L48.

Chauvin, G., Lagrange, A.-M., Beust, H., Bonnefoy, M., Boccaletti, A., Apai, D., Allard, F., Ehrenreich, D., Girard, J. H. V., Mouillet, D., and Rouan, D. (2012). Orbital characterization of the β Pictoris b giant planet. *Astron. & Astrophys.*, 542:A41.

Chauvin, G., Lagrange, A.-M., Dumas, C., Zuckerman, B., Mouillet, D., Song, I., Beuzit, J.-L., and Lowrance, P. (2004). A giant planet candidate near a young brown dwarf. Direct VLT/NACO observations using IR wavefront sensing. *Astron. & Astrophys.*, 425:L29–L32.

Chauvin, G., Vigan, A., Bonnefoy, M., Desidera, S., Bonavita, M., Mesa, D., Boccaletti, A., Buenzli, E., Carson, J., Delorme, P., Hagelberg, J., Montagnier, G., Mordasini, C., Quanz, S. P., Segransan, D., Thalmann, C., Beuzit, J.-L., Biller, B., Covino, E., Feldt, M., Girard, J., Gratton, R., Henning, T., Kasper, M., Lagrange, A.-M., Messina, S., Meyer, M., Mouillet, D., Moutou, C., Reggiani, M., Schlieder, J. E., and Zurlo, A. (2015). The VLT/NaCo large program to probe the occurrence of exoplanets and brown dwarfs at wide orbits. II. Survey description, results, and performances. *Astron. & Astrophys.*, 573:A127.

Choquet, E., Perrin, M. D., Chen, C., Golimowski, D. A., Debes, J. H., Schneider, G., Pueyo, L., Hines, D. C., Wolff, S., Mittal, T., Moro-Martin, A., Mawet, D., Milli, J., Brendan Hagan, J., Rajan, A., Moerchen, M., N'Diaye, M., Aguilar, J., and Soummer, R. (2015). ALICE: Analysis of New Debris Disk Images. In *American Astronomical Society Meeting Abstracts*, volume 225 of *American Astronomical Society Meeting Abstracts*, page 349.20.

Claudi, R. U., Turatto, M., Gratton, R. G., Antichi, J., Bonavita, M., Bruno, P., Cascone, E., De Caprio, V., Desidera, S., Giro, E., Mesa, D., Scuderi, S., Dohlen, K., Beuzit, J. L., and Puget, P. (2008). SPHERE IFS: the spectro differential imager of the VLT for exoplanets search. In *Society of Photo-Optical Instrumentation Engineers (SPIE) Conference Series*, volume 7014 of *Society of Photo-Optical Instrumentation Engineers (SPIE) Conference Series*.

Close, L. M., Males, J. R., Kopon, D. A., Gasho, V., Follette, K. B., Hinz, P., Morzinski, K., Uomoto, A., Hare, T., Riccardi, A., Esposito, S., Puglisi, A., Pinna, E., Busoni, L., Arcidiacono, C., Xompero, M., Briguglio, R., Quiros-Pacheco, F., and Argomedo, J. (2012). First closed-loop visible AO test results for the advanced adaptive secondary AO system for the Magellan Telescope: MagAO's performance and status. In *Adaptive Optics Systems III*, volume 8447 of *Proc. SPIE*, page 84470X.

Conan, J.-M. (1994). *Étude de la correction partielle en optique adaptative.* PhD thesis, Ph. D. thesis, Université Paris XI Orsay, (1994).

Conan, J.-M., Mugnier, L. M., Fusco, T., Michau, V., and Rousset, G. (1998). Myopic deconvolution of adaptive optics images by use of object and point spread function power spectra. 37(21):4614–4622.

Cornia, A. (2010). *High-contrast differential image processing for extrasolar planet detection.* PhD thesis, Université Paris Diderot - Paris 7.

Cornia, A., Mugnier, L. M., Mouillet, D., Vigan, A., Eggenberger, A., Rousset, G., Boccaletti, A., Carbillet, M., Dohlen, K., Fusco, T., Carson, J., and Montagnier, G. (2010). Optimal method for exoplanet detection by spectral and angular differential imaging. In *Adaptive Optics Systems II*, volume 7736 of *Proc. SPIE*, pages 77361E–77361E–12.

Crepp, J. R. and Johnson, J. A. (2010). Combining High-Contrast Imaging with Doppler Radial Velocity: a Survey of Subgiant Stars that Exhibit Long-term Linear Trends. In *American Astronomical Society Meeting Abstracts #215*, volume 42 of *Bulletin of the American Astronomical Society*, page 289.

Currie, T., Burrows, A., Itoh, Y., Matsumura, S., Fukagawa, M., Apai, D., Madhusudhan, N., Hinz, P. M., Rodigas, T. J., Kasper, M., Pyo, T.-S., and Ogino, S. (2011). A Combined Subaru/VLT/MMT 1-5 μm Study of Planets Orbiting HR 8799: Implications for Atmospheric Properties, Masses, and Formation. *Astrophys. J.*, 729:128.

Currie, T., Fukagawa, M., Thalmann, C., Matsumura, S., and Plavchan, P. (2012a). Direct Detection and Orbital Analysis of the Exoplanets HR 8799 bcd from Archival 2005 Keck/NIRC2 Data. *Astrophys. J. Letter.*, 755:L34.

Currie, T., Fukagawa, M., Thalmann, C., Matsumura, S., and Plavchan, P. (2012b). Direct Detection and Orbital Analysis of the Exoplanets HR 8799 bcd from Archival 2005 Keck/NIRC2 Data. *Astrophys. J. Letter.*, 755:L34.

De Rosa, R. J., Nielsen, E. L., Blunt, S. C., Graham, J. R., Konopacky, Q. M., Marois, C., Pueyo, L., Rameau, J., Ryan, D. M., Wang, J. J., Bailey, V., Chontos, A., Fabrycky, D. C., Follette, K. B., Macintosh, B., Marchis, F., Ammons, S. M., Arriaga, P., Chilcote, J. K., Cotten, T. H., Doyon, R., Duchêne, G., Esposito, T. M., Fitzgerald, M. P., Gerard, B., Goodsell, S. J., Greenbaum, A. Z., Hibon, P., Ingraham, P., Johnson-Groh, M., Kalas, P. G., Lafrenière, D., Maire, J., Metchev, S., Millar-Blanchaer, M. A., Morzinski, K. M., Oppenheimer, R., Patel, R. I., Patience, J. L., Perrin, M. D., Rajan, A., Rantakyrö, F. T., Ruffio, J.-B., Schneider, A. C., Sivaramakrishnan, A., Song, I., Tran, D., Vasisht, G., Ward-Duong, K., and Wolff, S. G. (2015). Astrometric Confirmation and Preliminary Orbital Parameters of the Young Exoplanet 51 Eridani b with the Gemini Planet Imager. *Astrophys. J. Letter.*, 814:L3.

Dekany, R., Roberts, J., Burruss, R., Bouchez, A., Truong, T., Baranec, C., Guiwits, S., Hale, D., Angione, J., Trinh, T., Zolkower, J., Shelton, J. C., Palmer, D., Henning, J., Croner, E., Troy, M., McKenna, D., Tesch, J., Hildebrandt, S., and Milburn, J. (2013). PALM-3000: Exoplanet Adaptive Optics for the 5 m Hale Telescope. *Astrophys. J.*, 776:130.

Delorme, P., Gagné, J., Malo, L., Reylé, C., Artigau, E., Albert, L., Forveille, T., Delfosse, X., Allard, F., and Homeier, D. (2012). CFBDSIR2149-0403: a 4-7 Jupiter-mass free-floating planet in the young moving group AB Doradus? *Astron. & Astrophys.*, 548:A26.

Denis, L., Ferrari, A., Mary, D., Mugnier, L., and Thiébaut, E. (2016). Fast and robust detection of a known pattern in an image. *EUSIPCO*.

Dohlen, K., Langlois, M., Saisse, M., Hill, L., Origne, A., Jacquet, M., Fabron, C., Blanc, J.-C., Llored, M., Carle, M., Moutou, C., Vigan, A., Boccaletti, A., Carbillet, M., Mouillet, D., and Beuzit, J.-L. (2008). The infra-red dual imaging and spectrograph for sphere: design and performance.

Dohlen, K., Madec, F., N'Diaye, M., Paul, B., Fusco, T., Jolivet, A., Luo, D., Yatcheva, L., Sauvage, J.-F., Mugnier, L., and Ferrari, M. (2013). Lab demonstration of the Zernike phase mask near-coronagraph quasi static aberrations sensor, ZELDA. In Esposito, S. and Fini, L., editors, *Proceedings of the Third AO4ELT Conference*, page 86.

Dou, J., Ren, D., Zhao, G., Zhang, X., Chen, R., and Zhu, Y. (2015). A High-contrast Imaging Algorithm: Optimized Image Rotation and Subtraction. *Astrophys. J.*, 802:12.

Eggenberger, A., Cornia, A., Mugnier, L. M., Mouillet, D., Chauvin, G., Boccaletti, A., and Rousset, G. (2010). Testing the ANDROMEDA method for exoplanet detection on VLT/ NACO data. In *In the Spirit of Lyot 2010*.

Esposito, S., Mesa, D., Skemer, A., Arcidiacono, C., Claudi, R. U., Desidera, S., Gratton, R., Mannucci, F., Marzari, F., Masciadri, E., Close, L., Hinz, P., Kulesa, C., McCarthy, D., Males, J., Agapito, G., Argomedo, J., Boutsia, K., Briguglio, R., Brusa, G., Busoni, L., Cresci, G., Fini, L., Fontana, A., Guerra, J. C., Hill, J. M., Miller, D., Paris, D., Pinna, E., Puglisi, A., Quiros-Pacheco, F., Riccardi, A., Stefanini, P., Testa, V., Xompero, M., and Woodward, C. (2013). LBT observations of the HR 8799 planetary system. First detection of HR 8799e in H band. *Astron. & Astrophys.*, 549:A52.

Esposito, S., Riccardi, A., Fini, L., Puglisi, A. T., Pinna, E., Xompero, M., Briguglio, R., Quirós-Pacheco, F., Stefanini, P., Guerra, J. C., Busoni, L., Tozzi, A., Pieralli, F., Agapito, G., Brusa-Zappellini, G., Demers, R., Brynnel, J., Arcidiacono, C., and Salinari, P. (2010). First light AO (FLAO) system for LBT: final integration, acceptance test in Europe, and preliminary on-sky commissioning results. In *Adaptive Optics Systems II*, volume 7736 of *Proc. SPIE*, page 773609.

Fitzgerald, M. P. and Graham, J. R. (2006). Speckle Statistics in Adaptively Corrected Images. *Astrophys. J.*, 637:541–547.

Fusco, T. (2000). *Correction partielle et anisoplanétisme en optique adaptative : Traitements a posteriori et optique adaptative multiconjuguée.* PhD thesis, Université de Nice Sophia-Antipolis.

Fusco, T., Beuzit, J.-L., Sauvage, J.-F., Mouillet, D., Kasper, M., Petit, C., Dohlen, K., Costille, A., Girard, J.-H., Suarez, M., Soenke, C., Milli, J., Vigan, A., Barrufolo, A., Salasnich, B., Zins, G., Perret, D., Baudoz, P., and Wildi, F. (2016). SPHERE on-sky results: final performance, lesson learned, and possible upgrades. In *Extreme Adaptive Optics Systems I*, Proc. SPIE.

Fusco, T., Rousset, G., Sauvage, J.-F., Petit, C., Beuzit, J.-L., Dohlen, K., Mouillet, D., Charton, J., Nicolle, M., Kasper, M., Baudoz, P., and Puget, P. (2006). High-order adaptive optics requirements for direct detection of extrasolar planets: Application to the SPHERE instrument. *Optics Express*, 14:7515.

Fusco, T., Sauvage, J.-F., Petit, C., Costille, A., Dohlen, K., Mouillet, D., Beuzit, J.-L., Kasper, M., Suarez, M., Soenke, C., Fedrigo, E., Downing, M., Baudoz, P., Sevin, A., Perret, D., Barrufolo, A., Salasnich, B., Puget, P., Feautrier, F., Rochat, S., Moulin, T., DeboulbÃ©, A., Hugot, E., Vigan, A., Mawet, D., Girard, J., and Hubin, N. (2014). Final performance and lesson-learned of saxo, the vlt-sphere extreme ao: from early design to on-sky results.

Galicher, R., Lagrance, A. M., Mesa, D., Janson, M., Chauvin, G., Biller, B., Cantalloube, F., Vigan, A., Langlois, M., and Gratton, R. (2015). Blind tests on SPHERE data: ADI and SDI pipelines. In *In the Spirit of Lyot 2015*.

Galicher, R. and Marois, C. (2011). Astrometry and photometry in high contrast imaging. In *Second International Conference on Adaptive Optics for Extremely Large Telescopes. Online at <A href="http://ao4elt2.lesia.obspm.fr">http://ao4elt2.lesia.obspm.fr</A>, id.P25*, page P25.

Garden, R. P. (1994). Mircam: a portable mid-infrared camera for broadband imaging.

Garrel, V., Guyon, O., and Baudoz, P. (2012). A Highly Efficient Lucky Imaging Algorithm: Image Synthesis Based on Fourier Amplitude Selection. *Pub. Astron. Soc. Pacific.*, 124:861–867.

Gendron, E. (1995). *Optimisation de la commande modale en optique adaptative : application á l'astronomie*. PhD thesis, Ph. D. thesis, Université Paris VII Diderot, (1995).

Gomez Gonzalez, C. A., Absil, O., Absil, P.-A., Van Droogenbroeck, M., Mawet, D., and Surdej, J. (2016a). Low-rank plus sparse decomposition for exoplanet detection in direct-imaging ADI sequences. The LLSG algorithm. *Astron. & Astrophys.*, 589:A54.

Gomez Gonzalez, C. A., Wertz, O., Absil, O., Christiaens, V., Defrére, D., Mawet, D., Milli, J., Absil, P.-A., Van Droogenbroeck, M., Hinz, P., and Surdej, J. (2016b). Vortex Image Processing package for high-contrast direct imaging. Application to HR8799 L-band vortex LBTI-LMIRCam data. *Astrophys. J.*.

Gonsalves, R. A. (1982). Phase retrieval and diversity in adaptive optics. *Optical Engineering*, 21:829–832.

Goodman, J. (1975). Statistical properties of laser speckle patterns. In *Laser Speckle and Related Phenomena*, volume 9 of *Topics in Applied Physics*, pages 9–75. Springer Berlin Heidelberg.

Greco, J. P. and Brandt, T. D. (2016). The Measurement, Treatment, and Impact of Spectral Covariance and Bayesian Priors in Integral-field Spectroscopy of Exoplanets. *Astrophys. J.*, 833:134.

Guyon, O. (2003). Phase-induced amplitude apodization of telescope pupils for extrasolar terrestrial planet imaging. *Astron. & Astrophys.*, 404:379–387.

Guyon, O. (2004). Imaging faint sources within a speckle halo with synchronous interferometric speckle subtraction. *The Astrophysical Journal*, 615(1):562.

Guyon, O. (2005). Limits of Adaptive Optics for High-Contrast Imaging. *Astrophys. J.*, 629:592–614.

Guyon, O., Martinache, F., Garrel, V., Vogt, F., Yokochi, K., and Yoshikawa, T. (2010). The Subaru coronagraphic extreme AO (SCExAO) system: wavefront control and detection of exoplanets with coherent light modulation in the focal plane. In *Adaptive Optics Systems II*, volume 7736 of *Proc. SPIE*, page 773624.

Guyon, O., Matsuo, T., and Angel, R. (2009). Coronagraphic Low-Order Wave-Front Sensor: Principle and Application to a Phase-Induced Amplitude Coronagraph. *Astrophys. J.*, 693:75–84.

Guyon, O., Pluzhnik, E. A., Galicher, R., Martinache, F., Ridgway, S. T., and Woodruff, R. A. (2005). Exoplanet Imaging with a Phase-induced Amplitude Apodization Coronagraph. I. Principle. *Astrophys. J.*, 622:744–758.

Guyon, O., Pluzhnik, E. A., Kuchner, M. J., Collins, B., and Ridgway, S. T. (2006). Theoretical Limits on Extrasolar Terrestrial Planet Detection with Coronagraphs. *Astrophys. J. Supp. Ser.*, 167:81–99.

Hayano, Y., Takami, H., Guyon, O., Oya, S., Hattori, M., Saito, Y., Watanabe, M., Murakami, N., Minowa, Y., Ito, M., Colley, S., Eldred, M., Golota, T., Dinkins, M., Kashikawa, N., and Iye, M. (2008). Current status of the laser guide star adaptive optics system for subaru telescope.

Hercovisci, O., Mugnier, L., Sauvage, J.-F., Cantalloube, F., and Le Duigou, J.-M. (2016). Analytical expression of a long exposure coronagraphic point spread function and application to the estimation of quasi-static aberrations in the presence of residual turbulence with COFFEE. In *Adaptive Optics Systems II*, Proc. SPIE.

Herriot, G., Morris, S., Anthony, A., Derdall, D., Duncan, D., Dunn, J., Ebbers, A. W., Fletcher, J. M., Hardy, T., Leckie, B., Mirza, A., Morbey, C. L., Pfleger, M., Roberts, S., Shott, P., Smith, M., Saddlemyer, L. K., Sebesta, J., Szeto, K., Wooff, R., Windels, W., and Veran, J.-P. (2000). Progress on Altair: the Gemini North adaptive optics system. In Wizinowich, P. L., editor, *Adaptive Optical Systems Technology*, volume 4007 of *Proc. SPIE*, pages 115–125.

Hewish, A., Bell, S. J., Pilkington, J. D. H., Scott, P. F., and Collins, R. A. (1968). Observation of a Rapidly Pulsating Radio Source. *Nature*, 217:709–713.

Hinkley, S., Oppenheimer, B. R., Soummer, R., Sivaramakrishnan, A., Roberts, Jr., L. C., Kuhn, J., Makidon, R. B., Perrin, M. D., Lloyd, J. P., Kratter, K., and Brenner, D. (2007). Temporal Evolution of Coronagraphic Dynamic Range and Constraints on Companions to Vega. *Astrophys. J.*, 654:633–640.

Hinkley, S., Oppenheimer, B. R., Zimmerman, N., Brenner, D., Parry, I. R., Crepp, J. R., Vasisht, G., Ligon, E., King, D., Soummer, R., Sivaramakrishnan, A., Beichman, C., Shao, M., Roberts, L. C., Bouchez, A., Dekany, R., Pueyo, L., Roberts, J. E., Lockhart, T., Zhai, C., Shelton, C., and Burruss, R. (2011). A New High Contrast Imaging Program at Palomar Observatory. *Pub. Astron. Soc. Pacific.*, 123:74–86.

Hoaglin, D. C., Mosteller, F., and Tukey, J. W. (1983). *Understanding robust and exploratory data anlysis.*

Hodapp, K. W., Jensen, J. B., Irwin, E. M., Yamada, H., Chung, R., Fletcher, K., Robertson, L., Hora, J. L., Simons, D. A., Mays, W., Nolan, R., Bec, M., Merrill, M., and Fowler, A. M. (2003). The Gemini Near-Infrared Imager (NIRI). *Pub. Astron. Soc. Pacific.*, 115:1388–1406.

Holman, M. J., Fabrycky, D. C., Ragozzine, D., Ford, E. B., Steffen, J. H., Welsh, W. F., Lissauer, J. J., Latham, D. W., Marcy, G. W., Walkowicz, L. M., Batalha, N. M., Jenkins, J. M., Rowe, J. F., Cochran, W. D., Fressin, F., Torres, G., Buchhave, L. A., Sasselov, D. D., Borucki, W. J., Koch, D. G., Basri, G., Brown, T. M., Caldwell, D. A., Charbonneau, D., Dunham, E. W., Gautier, T. N., Geary, J. C., Gilliland, R. L., Haas, M. R., Howell, S. B., Ciardi, D. R., Endl, M., Fischer, D., Fürész, G., Hartman, J. D., Isaacson, H., Johnson, J. A., MacQueen, P. J., Moorhead, A. V., Morehead, R. C., and Orosz, J. A. (2010). Kepler-9: A System of Multiple Planets Transiting a Sun-Like Star, Confirmed by Timing Variations. *Science*, 330:51.

Hulse, R. A. and Taylor, J. H. (1975). Discovery of a pulsar in a binary system. *Astrophys. J. Letter.*, 195:L51–L53.

Ingraham, P., Marley, M. S., Saumon, D., Marois, C., Macintosh, B., Barman, T., Bauman, B., Burrows, A., Chilcote, J. K., De Rosa, R. J., Dillon, D., Doyon, R., Dunn, J., Erikson, D., Fitzgerald, M. P., Gavel, D., Goodsell, S. J., Graham, J. R., Hartung, M., Hibon, P., Kalas, P. G., Konopacky, Q., Larkin, J. A., Maire, J., Marchis, F., McBride, J., Millar-Blanchaer, M., Morzinski, K. M., Norton, A., Oppenheimer, R., Palmer, D. W., Patience, J., Perrin, M. D., Poyneer, L. A., Pueyo, L., Rantakyrö, F., Sadakuni, N., Saddlemyer, L., Savransky, D., Soummer, R., Sivaramakrishnan, A., Song, I., Thomas, S., Wallace, J. K., Wiktorowicz, S. J., and Wolff, S. G. (2014). Gemini Planet Imager Spectroscopy of the HR 8799 Planets c and d. *Astrophys. J. Letter.*, 794:L15.

Janson, M., Brandt, T. D., Kuzuhara, M., Spiegel, D. S., Thalmann, C., Currie, T., Bonnefoy, M., Zimmerman, N., Sorahana, S., Kotani, T., Schlieder, J., Hashimoto, J., Kudo, T., Kusakabe, N., Abe, L., Brandner, W., Carson, J. C., Egner, S., Feldt, M., Goto, M., Grady, C. A., Guyon, O.,

Hayano, Y., Hayashi, M., Hayashi, S., Henning, T., Hodapp, K. W., Ishii, M., Iye, M., Kandori, R., Knapp, G. R., Kwon, J., Matsuo, T., McElwain, M. W., Mede, K., Miyama, S., Morino, J.-I., Moro-Martín, A., Nakagawa, T., Nishimura, T., Pyo, T.-S., Serabyn, E., Suenaga, T., Suto, H., Suzuki, R., Takahashi, Y., Takami, M., Takato, N., Terada, H., Tomono, D., Turner, E. L., Watanabe, M., Wisniewski, J., Yamada, T., Takami, H., Usuda, T., and Tamura, M. (2013). Direct Imaging Detection of Methane in the Atmosphere of GJ 504 b. *Astrophys. J. Letter.*, 778:L4.

Jolissaint, L., Véran, J.-P., and Conan, R. (2006). Analytical modeling of adaptive optics: foundations of the phase spatial power spectrum approach. *Journal of the Optical Society of America A*, 23:382–394.

Jovanovic, N., Martinache, F., Guyon, O., Clergeon, C., Singh, G., Kudo, T., Garrel, V., Newman, K., Doughty, D., Lozi, J., Males, J., Minowa, Y., Hayano, Y., Takato, N., Morino, J., Kuhn, J., Serabyn, E., Norris, B., Tuthill, P., Schworer, G., Stewart, P., Close, L., Huby, E., Perrin, G., Lacour, S., Gauchet, L., Vievard, S., Murakami, N., Oshiyama, F., Baba, N., Matsuo, T., Nishikawa, J., Tamura, M., Lai, O., Marchis, F., Duchene, G., Kotani, T., and Woillez, J. (2015). The Subaru Coronagraphic Extreme Adaptive Optics System: Enabling High-Contrast Imaging on Solar-System Scales. *Pub. Astron. Soc. Pacific.*, 127:890–910.

Kasdin, N. J., Vanderbei, R. J., Spergel, D. N., and Littman, M. G. (2003). Optimal shaped pupil coronagraphs for extrasolar planet finding. In Schultz, A. B., editor, *High-Contrast Imaging for Exo-Planet Detection.*, volume 4860 of *Proc. SPIE*, pages 240–250.

Kenworthy, M. A., Codona, J. L., Hinz, P. M., Angel, J. R. P., Heinze, A., and Sivanandam, S. (2007). First On-Sky High-Contrast Imaging with an Apodizing Phase Plate. *Astrophys. J.*, 660:762–769.

Konacki, M., Torres, G., Jha, S., and Sasselov, D. D. (2003). An extrasolar planet that transits the disk of its parent star. *Nature*, 421:507–509.

Kopon, D., Close, L. M., Males, J., Gasho, V., and Follette, K. (2010). The Magellan Adaptive Secondary VisAO Camera: diffraction-limited broadband visible imaging and 20mas fiber array IFU. In *Adaptive Optics Systems II*, volume 7736 of *Proc. SPIE*, page 77362V.

Kuhn, J. R., Potter, D., and Parise, B. (2001). Imaging Polarimetric Observations of a New Circumstellar Disk System. *Astrophys. J. Letter.*, 553:L189–L191.

Kuzuhara, M., Tamura, M., Kudo, T., Janson, M., Kandori, R., Brandt, T. D., Thalmann, C., Spiegel, D., Biller, B., Carson, J., Hori, Y., Suzuki, R., Burrows, A., Henning, T., Turner, E. L., McElwain, M. W., Moro-Martín, A., Suenaga, T., Takahashi, Y. H., Kwon, J., Lucas, P., Abe, L., Brandner, W., Egner, S., Feldt, M., Fujiwara, H., Goto, M., Grady, C. A., Guyon, O., Hashimoto, J., Hayano, Y., Hayashi, M., Hayashi, S. S., Hodapp, K. W., Ishii, M., Iye, M., Knapp, G. R., Matsuo, T., Mayama, S., Miyama, S., Morino, J.-I., Nishikawa, J., Nishimura, T., Kotani, T., Kusakabe, N., Pyo, T.-S., Serabyn, E., Suto, H., Takami, M., Takato, N., Terada, H., Tomono, D., Watanabe, M., Wisniewski, J. P., Yamada, T., Takami, H., and Usuda, T. (2013). Direct Imaging of a Cold Jovian Exoplanet in Orbit around the Sun-like Star GJ 504. *Astrophys. J.*, 774:11.

Labeyrie, A. (1970). Attainment of Diffraction Limited Resolution in Large Telescopes by Fourier Analysing Speckle Patterns in Star Images. *Astron. & Astrophys.*, 6:85.

Lafrenière, D., Marois, C., Doyon, R., Nadeau, D., and Artigau, É. (2007). A New Algorithm for Point-Spread Function Subtraction in High-Contrast Imaging: A Demonstration with Angular Differential Imaging. *Astrophys. J.*, 660:770–780.

Lagrange, A.-M., Boccaletti, A., Milli, J., Chauvin, G., Bonnefoy, M., Mouillet, D., Augereau, J. C., Girard, J. H., Lacour, S., and Apai, D. (2012). The position of β Pictoris b position relative to the debris disk. *Astron. & Astrophys.*, 542:A40.

Lagrange, A.-M., Bonnefoy, M., Chauvin, G., Apai, D., Ehrenreich, D., Boccaletti, A., Gratadour, D., Rouan, D., Mouillet, D., Lacour, S., and Kasper, M. (2010). A Giant Planet Imaged in the Disk of the Young Star β Pictoris. *Science*, 329:57.

Lagrange, A.-M., Gratadour, D., Chauvin, G., Fusco, T., Ehrenreich, D., Mouillet, D., Rousset, G., Rouan, D., Allard, F., Gendron, É., Charton, J., Mugnier, L., Rabou, P., Montri, J., and Lacombe, F. (2009). A probable giant planet imaged in the β Pictoris disk. VLT/NaCo deep L'-band imaging. *Astron. & Astrophys.*, 493:L21–L25.

Langlois, M., Dohlen, K., Augereau, J.-C., Mouillet, D., Boccaletti, A., and Schmid, H.-M. (2010). High contrast imaging with IRDIS near infrared polarimeter. In *Society of Photo-Optical Instrumentation Engineers (SPIE) Conference Series*, volume 7735 of *Society of Photo-Optical Instrumentation Engineers (SPIE) Conference Series*.

Lattanzi, M. G. and Sozzetti, A. (2010). Gaia and the Astrometry of Giant Planets. In Coudé du Foresto, V., Gelino, D. M., and Ribas, I., editors, *Pathways Towards Habitable Planets*, volume 430 of *Astronomical Society of the Pacific Conference Series*, page 253.

Law, N. M., Mackay, C. D., and Baldwin, J. E. (2006). Lucky imaging: high angular resolution imaging in the visible from the ground. *Astron. & Astrophys.*, 446:739–745.

Le Bouquin, J.-B. and Absil, O. (2012). On the sensitivity of closure phases to faint companions in optical long baseline interferometry. *Astron. & Astrophys.*, 541:A89.

Leisenring, J. M., Skrutskie, M. F., Hinz, P. M., Skemer, A., Bailey, V., Eisner, J., Garnavich, P., Hoffmann, W. F., Jones, T., Kenworthy, M., Kuzmenko, P., Meyer, M., Nelson, M., Rodigas, T. J., Wilson, J. C., and Vaitheeswaran, V. (2012). On-sky operations and performance of LMIRcam at the Large Binocular Telescope. In *Ground-based and Airborne Instrumentation for Astronomy IV*, volume 8446 of *Proc. SPIE*, page 84464F.

Lena, P., Rouan, D., Lebrun, F., Mignard, F., and Pelat, D. (2012). *Observational Astrophysics*. Springer International Publishing.

Lenzen, R., Close, L., Brandner, W., Biller, B., and Hartung, M. (2004). A novel simultaneous differential imager for the direct imaging of giant planets. In A. F. M. Moorwood & M. Iye, editor, *Society of Photo-Optical Instrumentation Engineers (SPIE) Conference Series*, volume 5492 of *Society of Photo-Optical Instrumentation Engineers (SPIE) Conference Series*, pages 970–977.

Lenzen, R., Hartung, M., Brandner, W., Finger, G., Hubin, N. N., Lacombe, F., Lagrange, A.-M., Lehnert, M. D., Moorwood, A. F. M., and Mouillet, D. (2003). NAOS-CONICA first on sky results in a variety of observing modes. In Iye, M. and Moorwood, A. F. M., editors, *Instrument Design and Performance for Optical/Infrared Ground-based Telescopes*, volume 4841 of *Proc. SPIE*, pages 944–952.

Lyot, B. (1939). The study of the solar corona and prominences without eclipses (George Darwin Lecture, 1939). *Mon. Not. R. astr. Soc.*, 99:580.

Macintosh, B. (2013). The Gemini Planet Imager Exoplanet Survey. NASA OSS Proposal.

Macintosh, B., Graham, J. R., Barman, T., De Rosa, R. J., Konopacky, Q., Marley, M. S., Marois, C., Nielsen, E. L., Pueyo, L., Rajan, A., Rameau, J., Saumon, D., Wang, J. J., Patience, J., Ammons, M., Arriaga, P., Artigau, E., Beckwith, S., Brewster, J., Bruzzone, S., Bulger, J., Burningham, B., Burrows, A. S., Chen, C., Chiang, E., Chilcote, J. K., Dawson, R. I., Dong, R., Doyon, R., Draper, Z. H., Duchêne, G., Esposito, T. M., Fabrycky, D., Fitzgerald, M. P., Follette, K. B., Fortney, J. J., Gerard, B., Goodsell, S., Greenbaum, A. Z., Hibon, P., Hinkley, S., Cotten, T. H., Hung, L.-W., Ingraham, P., Johnson-Groh, M., Kalas, P., Lafreniere, D., Larkin, J. E., Lee, J., Line, M., Long, D., Maire, J., Marchis, F., Matthews, B. C., Max, C. E., Metchev, S., Millar-Blanchaer, M. A.,

Mittal, T., Morley, C. V., Morzinski, K. M., Murray-Clay, R., Oppenheimer, R., Palmer, D. W., Patel, R., Perrin, M. D., Poyneer, L. A., Rafikov, R. R., Rantakyrö, F. T., Rice, E. L., Rojo, P., Rudy, A. R., Ruffio, J.-B., Ruiz, M. T., Sadakuni, N., Saddlemyer, L., Salama, M., Savransky, D., Schneider, A. C., Sivaramakrishnan, A., Song, I., Soummer, R., Thomas, S., Vasisht, G., Wallace, J. K., Ward-Duong, K., Wiktorowicz, S. J., Wolff, S. G., and Zuckerman, B. (2015). Discovery and spectroscopy of the young jovian planet 51 Eri b with the Gemini Planet Imager. *Science*, 350:64–67.

Macintosh, B. A., Graham, J. R., Palmer, D. W., Doyon, R., Dunn, J., Gavel, D. T., Larkin, J., Oppenheimer, B., Saddlemyer, L., Sivaramakrishnan, A., Wallace, J. K., Bauman, B., Erickson, D. A., Marois, C., Poyneer, L. A., and Soummer, R. (2008). The Gemini Planet Imager: from science to design to construction. In *Adaptive Optics Systems*, volume 7015 of *Proc. SPIE*, page 701518.

Madhusudhan, N., Freedman, R., and Tennyson, J. (2013). The Importance of Accurate Atomic and Molecular Line-lists for Characterizing Exoplanetary Atmospheres. In *American Astronomical Society Meeting Abstracts*, volume 222 of *American Astronomical Society Meeting Abstracts*, page 301.02.

Marchis, F., Nielsen, E. L., Blunt, S., Rameau, J., Barman, T., De Rosa, R. J., Konopacky, Q., Marley, M. S., Marois, C., Pueyo, L., Rajan, A., Wang, J. J., Macintosh, B., and Graham, J. R. (2015). Discovery and follow-up of 51 Eri b, a directly-imaged Jupiter-like exoplanet and status of the GPIES campaign. In *AAS/Division for Planetary Sciences Meeting Abstracts*, volume 47 of *AAS/Division for Planetary Sciences Meeting Abstracts*, page 501.01.

Markwardt, C. B. (2009). Non-linear Least-squares Fitting in IDL with MPFIT. In Bohlender, D. A., Durand, D., and Dowler, P., editors, *Astronomical Data Analysis Software and Systems XVIII*, volume 411 of *Astronomical Society of the Pacific Conference Series*, page 251.

Marley, M. S., Fortney, J. J., Hubickyj, O., Bodenheimer, P., and Lissauer, J. J. (2007). On the Luminosity of Young Jupiters. *Astrophys. J.*, 655:541–549.

Marois, C., Correia, C., Véran, J.-P., and Currie, T. (2014). TLOCI: A Fully Loaded Speckle Killing Machine. In Booth, M., Matthews, B. C., and Graham, J. R., editors, *IAU Symposium*, volume 299 of *IAU Symposium*, pages 48–49.

Marois, C., Doyon, R., Nadeau, D., Racine, R., Riopel, M., Vallée, P., and Lafrenière, D. (2005a). TRIDENT: An Infrared Differential Imaging Camera Optimized for the Detection of Methanated Substellar Companions. *Pub. Astron. Soc. Pacific.*, 117:745–756.

Marois, C., Doyon, R., Racine, R., and Nadeau, D. (2000). Efficient Speckle Noise Attenuation in Faint Companion Imaging. *Pub. Astron. Soc. Pacific.*, 112:91–96.

Marois, C., Doyon, R., Racine, R., Nadeau, D., Lafreniere, D., Vallee, P., Riopel, M., and Macintosh, B. (2005b). Direct Exoplanet Imaging around Sun-like Stars: Beating the Speckle Noise with Innovative Imaging Techniques. *J. R. astr. Soc. Canada*, 99:130.

Marois, C., Lafrenière, D., Doyon, R., Macintosh, B., and Nadeau, D. (2006). Angular Differential Imaging: A Powerful High-Contrast Imaging Technique. *Astrophys. J.*, 641:556–564.

Marois, C., Lafrenière, D., Macintosh, B., and Doyon, R. (2008a). Confidence Level and Sensitivity Limits in High-Contrast Imaging. *Astrophys. J.*, 673:647–656.

Marois, C., Macintosh, B., Barman, T., Zuckerman, B., Song, I., Patience, J., Lafrenière, D., and Doyon, R. (2008b). Direct Imaging of Multiple Planets Orbiting the Star HR 8799. *Science*, 322:1348.

Marois, C., Macintosh, B., and Véran, J.-P. (2010a). Exoplanet imaging with LOCI processing: photometry and astrometry with the new SOSIE pipeline. In *Adaptive Optics Systems II*, volume 7736 of *Proc. SPIE*, page 77361J.

Marois, C., Zuckerman, B., Konopacky, Q. M., Macintosh, B., and Barman, T. (2010b). Images of a fourth planet orbiting HR 8799. *Nature*, 468:1080–1083.

Matthews, B., Kennedy, G., Sibthorpe, B., Booth, M., Wyatt, M., Broekhoven-Fiene, H., Macintosh, B., and Marois, C. (2014). Resolved Imaging of the HR 8799 Debris Disk with Herschel. *Astrophys. J.*, 780:97.

Mawet, D., Absil, O., Delacroix, C., Girard, J. H., Milli, J., O'Neal, J., Baudoz, P., Boccaletti, A., Bourget, P., Christiaens, V., Forsberg, P., Gonte, F., Habraken, S., Hanot, C., Karlsson, M., Kasper, M., Lizon, J.-L., Muzic, K., Olivier, R., Peña, E., Slusarenko, N., Tacconi-Garman, L. E., and Surdej, J. (2013). L'-band AGPM vector vortex coronagraph's first light on VLT/NACO. Discovery of a late-type companion at two beamwidths from an F0V star. *Astron. & Astrophys.*, 552:L13.

Mawet, D., Milli, J., Wahhaj, Z., Pelat, D., Absil, O., Delacroix, C., Boccaletti, A., Kasper, M., Kenworthy, M., Marois, C., Mennesson, B., and Pueyo, L. (2014). Fundamental Limitations of High Contrast Imaging Set by Small Sample Statistics. *Astrophys. J.*, 792:97.

Mawet, D., Pueyo, L., Lawson, P., Mugnier, L., Traub, W., Boccaletti, A., Trauger, J. T., Gladysz, S., Serabyn, E., Milli, J., Belikov, R., Kasper, M., Baudoz, P., Macintosh, B., Marois, C., Oppenheimer, B., Barrett, H., Beuzit, J.-L., Devaney, N., Girard, J., Guyon, O., Krist, J., Mennesson, B., Mouillet, D., Murakami, N., Poyneer, L., Savransky, D., Vérinaud, C., and Wallace, J. K. (2012). Review of small-angle coronagraphic techniques in the wake of ground-based second-generation adaptive optics systems. In *Space Telescopes and Instrumentation 2012: Optical, Infrared, and Millimeter Wave*, volume 8442 of *Proc. SPIE*, page 844204.

Mawet, D., Riaud, P., Absil, O., and Surdej, J. (2005). Annular Groove Phase Mask Coronagraph. *Astrophys. J.*, 633:1191–1200.

Mayor, M. and Queloz, D. (1995). A Jupiter-mass companion to a solar-type star. *Nature*, 378:355–359.

McLean, I. S. and Chaffee, F. H. (2000). Instrumentation for the Keck Observatory. In Iye, M. and Moorwood, A. F., editors, *Optical and IR Telescope Instrumentation and Detectors*, volume 4008 of *Proc. SPIE*, pages 2–7.

Meimon, S., Fusco, T., and Mugnier, L. M. (2010). LIFT: a focal-plane wavefront sensor for real-time low-order sensing on faint sources. *Optics Letters*, 35:3036.

Mesa, D., Gratton, R., Zurlo, A., Vigan, A., Claudi, R. U., Alberi, M., Antichi, J., Baruffolo, A., Beuzit, J.-L., Boccaletti, A., Bonnefoy, M., Costille, A., Desidera, S., Dohlen, K., Fantinel, D., Feldt, M., Fusco, T., Giro, E., Henning, T., Kasper, M., Langlois, M., Maire, A.-L., Martinez, P., Moeller-Nilsson, O., Mouillet, D., Moutou, C., Pavlov, A., Puget, P., Salasnich, B., Sauvage, J.-F., Sissa, E., Turatto, M., Udry, S., Vakili, F., Waters, R., and Wildi, F. (2015). Performance of the VLT Planet Finder SPHERE. II. Data analysis and results for IFS in laboratory. *Astron. & Astrophys.*, 576:A121.

Milli, J., Baner, T., Mouillet, D., Mawet, D., Girard, J. G., Vigan, A., Boccaletti, A., Kasper, M., Wahhaj, Z., Lagrange, A. M., Beuzit, J. L., Fusco, T., Sauvage, J. F., and Gallicher, R. (2016). Speckle lifetime in XAO coronagraphic images: temporal evolution of SPHERE coronagraphic images. In *Society of Photo-Optical Instrumentation Engineers (SPIE) Conference Series*, Society of Photo-Optical Instrumentation Engineers (SPIE) Conference Series.

Milli, J., Lagrange, A.-M., Mawet, D., Absil, O., Augereau, J.-C., Mouillet, D., Boccaletti, A., Girard, J. H., and Chauvin, G. (2014). Very deep images of the innermost regions of the β Pictoris debris disc at L'. *Astron. & Astrophys.*, 566:A91.

Morton, T. D., Bryson, S. T., Coughlin, J. L., Rowe, J. F., Ravichandran, G., Petigura, E. A., Haas, M. R., and Batalha, N. M. (2016). False Positive Probabilities for all Kepler Objects of Interest: 1284 Newly Validated Planets and 428 Likely False Positives. *Astrophys. J.*, 822:86.

Morzinski, K. M., Close, L. M., Males, J. R., Kopon, D., Hinz, P. M., Esposito, S., Riccardi, A., Puglisi, A., Pinna, E., Briguglio, R., Xompero, M., Quirós-Pacheco, F., Bailey, V., Follette, K. B., Rodigas, T. J., Wu, Y.-L., Arcidiacono, C., Argomedo, J., Busoni, L., Hare, T., Uomoto, A., and Weinberger, A. (2014). MagAO: Status and on-sky performance of the Magellan adaptive optics system. In *Adaptive Optics Systems IV*, volume 9148 of *Proc. SPIE*, page 914804.

Mouillet, D., Larwood, J. D., Papaloizou, J. C. B., and Lagrange, A. M. (1997). A planet on an inclined orbit as an explanation of the warp in the Beta Pictoris disc. *Mon. Not. R. astr. Soc.*, 292:896.

Mourya, R., Denis, L., Becker, J.-M., and Thiébaut, E. (2015a). Augmented lagrangian without alternating directions: Practical algorithms for inverse problems in imaging. In *Image Processing (ICIP), 2015 IEEE International Conference on*, pages 1205–1209. IEEE.

Mourya, R., Denis, L., Becker, J.-M., and Thiébaut, E. (2015b). A blind deblurring and image decomposition approach for astronomical image restoration. In *Signal Processing Conference (EUSIPCO), 2015 23rd European*, pages 1636–1640. IEEE.

Mugnier, L. (2012). From data to object: the inverse problem. In Léna, P., Rouan, D., Lebrun, F., Mignard, F., and Pelat, D., editors, *Observational Astrophysics*, chapter 9, section 6, pages 575–596. Springer.

Mugnier, L. and Le Besnerais, G. (2001). Problèmes inverses en imagerie optique à travers la turbulence. In Idier, J., editor, *Approche bayésienne pour les problèmes inverses*, chapter 10, pages 241–270. Hermes, Paris.

Mugnier, L. M., Conan, J.-M., Fusco, T., and Michau, V. (1998). Joint maximum a posteriori estimation of object and PSF for turbulence-degraded images. In Mohammad-Djafari, A., editor, *Bayesian Inference for Inverse Problems*, volume 3459 of *Proc. SPIE*, pages 50–61.

Mugnier, L. M., Cornia, A., Sauvage, J.-F., Rousset, G., Fusco, T., and Védrenne, N. (2009). Optimal method for exoplanet detection by angular differential imaging. *Journal of the Optical Society of America A*, 26:1326.

Mugnier, L. M., Fusco, T., and Conan, J.-M. (2004). MISTRAL: a myopic edge-preserving image restoration method, with application to astronomical adaptive-optics-corrected long-exposure images. *Journal of the Optical Society of America A*, 21:1841–1854.

Mugnier, L. M., Robert, C., Conan, J.-M., Michau, V., and Salem, S. (2001). Myopic deconvolution from wavefront sensing. *Journal of the Optical Society of America A*, 18:862–872.

Muterspaugh, M. W., Lane, B. F., Kulkarni, S. R., Konacki, M., Burke, B. F., Colavita, M. M., Shao, M., Hartkopf, W. I., Boss, A. P., and Williamson, M. (2010). The Phases Differential Astrometry Data Archive. V. Candidate Substellar Companions to Binary Systems. *Astron. J.*, 140:1657–1671.

Nakamura, O., Kawata, S., and Minami, S. (1988). Optical microscope tomography. II. Nonnegative constraint by a gradient-projection method. *Journal of the Optical Society of America A*, 5:554–561.

Narayan, R. and Nityananda, R. (1986). Maximum entropy image restoration in astronomy. *Ann. Rev. of Astron. & Astrophys.*, 24:127–170.

N'Diaye, M., Dohlen, K., Fusco, T., and Paul, B. (2013). Calibration of quasi-static aberrations in exoplanet direct-imaging instruments with a Zernike phase-mask sensor. *Astron. & Astrophys.*, 555:A94.

N'Diaye, M., Vigan, A., Dohlen, K., Sauvage, J.-F., Caillat, A., Costille, A., Girard, J. H. V., Beuzit, J.-L., Fusco, T., Blanchard, P., Le Merrer, J., Le Mignant, D., Madec, F., Moreaux, G., Mouillet, D., Puget, P., and Zins, G. (2016). Calibration of quasi-static aberrations in exoplanet direct-imaging instruments with a Zernike phase-mask sensor. II. Concept validation with ZELDA on VLT/SPHERE. *ArXiv e-prints*.

Nisenson, P. and Papaliolios, C. (2001). Detection of Earth-like Planets Using Apodized Telescopes. *Astrophys. J. Letter.*, 548:L201–L205.

Oppenheimer, B. R., Baranec, C., Beichman, C., Brenner, D., Burruss, R., Cady, E., Crepp, J. R., Dekany, R., Fergus, R., Hale, D., Hillenbrand, L., Hinkley, S., Hogg, D. W., King, D., Ligon, E. R., Lockhart, T., Nilsson, R., Parry, I. R., Pueyo, L., Rice, E., Roberts, J. E., Roberts, Jr., L. C., Shao, M., Sivaramakrishnan, A., Soummer, R., Truong, T., Vasisht, G., Veicht, A., Vescelus, F., Wallace, J. K., Zhai, C., and Zimmerman, N. (2013). Reconnaissance of the HR 8799 Exosolar System. I. Near-infrared Spectroscopy. *Astrophys. J.*, 768:24.

Paczynski, B. (1986). Gravitational microlensing at large optical depth. *Astrophys. J.*, 301:503–516.

Paul, B., Sauvage, J.-F., Mugnier, L. M., Dohlen, K., Petit, C., Fusco, T., Mouillet, D., Beuzit, J.-L., and Ferrari, M. (2014). Compensation of high-order quasi-static aberrations on SPHERE with the coronagraphic phase diversity (COFFEE). *Astron. & Astrophys.*, 572:A32.

Perrot, C., Boccaletti, A., Pantin, E., Augereau, J., Lagrange, A., Galicher, R., Maire, A., Mazoyer, J., Milli, J., Rousset, G., Gratton, R., Bonnefoy, M., Brandner, W., Buenzli, E., Langlois, M., Lannier, J., Mesa, D., Peretti, S., Salter, G., Sissa, E., Chauvin, G., Desidera, S., Feldt, M., Vigan, A., Di Folco, E., Dutrey, A., Péricaud, J., Baudoz, P., Benisty, M., De Boer, J., Garufi, A., Girard, J. H., Menard, F., Olofsson, J., Quanz, S. P., Mouillet, D., Christiaens, V., Casassus, S., Beuzit, J.-L., Blanchard, P., Carle, M., Fusco, T., Giro, E., Hubin, N., Maurel, D., Moeller-Nilsson, O., Sevin, A., and Weber, L. (2016). Discovery of concentric broken rings at sub-arcsec separations in the HD 141569A gas-rich, debris disk with VLT/SPHERE. *ArXiv e-prints*.

Perryman, M. (2011). *The Exoplanet Handbook*.

Perryman, M., Hartman, J., Bakos, G. Á., and Lindegren, L. (2014). Astrometric Exoplanet Detection with Gaia. *Astrophys. J.*, 797:14.

Peters-Limbach, M. A., Groff, T. D., Kasdin, N. J., Driscoll, D., Galvin, M., Foster, A., Carr, M. A., LeClerc, D., Fagan, R., McElwain, M. W., Knapp, G., Brandt, T., Janson, M., Guyon, O., Jovanovic, N., Martinache, F., Hayashi, M., and Takato, N. (2013). The optical design of CHARIS: an exoplanet IFS for the Subaru telescope. In *Techniques and Instrumentation for Detection of Exoplanets VI*, volume 8864 of *Proc. SPIE*, page 88641N.

Petit, C., Fusco, T., Charton, J., Mouillet, D., Rabou, P., Buey, T., Rousset, G., Sauvage, J.-F., Baudoz, P., Gigan, P., Kasper, M., Fedrigo, E., Hubin, N., Feautrier, P., Beuzit, J.-L., and Puget, P. (2008). The sphere xao system: design and performance.

Petit, C., Sauvage, J.-F., Fusco, T., Sevin, A., Suarez, M., Costille, A., Vigan, A., Soenke, C., Perret, D., Rochat, S., Barrufolo, A., Salasnich, B., Beuzit, J.-L., Dohlen, K., Mouillet, D., Puget, P., Wildi, F., Kasper, M., Conan, J.-M., Kulcsár, C., and Raynaud, H.-F. (2014). SPHERE eXtreme AO control scheme: final performance assessment and on sky validation of the first auto-tuned LQG based operational system. In *Adaptive Optics Systems IV*, volume 9148 of *Proc. SPIE*, page 91480O.

Pollack, J. B., Hubickyj, O., Bodenheimer, P., Lissauer, J. J., Podolak, M., and Greenzweig, Y. (1996). Formation of the Giant Planets by Concurrent Accretion of Solids and Gas. *Icarus*, 124:62–85.

Poyneer, L. A. and Macintosh, B. (2004). Spatially filtered wave-front sensor for high-order adaptive optics. *Journal of the Optical Society of America A*, 21:810–819.

Press, W. H., Teukolsky, S. A., Vetterling, W. T., and Flannery, B. P. (2007). *Numerical Recipes, The Art of Scientific Computing*, pages 818 – 920. Cambridge University Press, The Edinburgh Building, Cambridge CB2 8RU, UK, 3rd edition.

Pueyo, L. (2016). Detection and Characterization of Exoplanets using Projections on Karhunen Loeve Eigenimages: Forward Modeling. *Astrophys. J.*, 824:117.

Pueyo, L., Crepp, J. R., Vasisht, G., Brenner, D., Oppenheimer, B. R., Zimmerman, N., Hinkley, S., Parry, I., Beichman, C., Hillenbrand, L., Roberts, L. C., Dekany, R., Shao, M., Burruss, R., Bouchez, A., Roberts, J., and Soummer, R. (2012). Application of a Damped Locally Optimized Combination of Images Method to the Spectral Characterization of Faint Companions Using an Integral Field Spectrograph. *Astrophys. J. Supp. Ser.*, 199:6.

Pueyo, L. and Kasdin, N. J. (2007). Polychromatic Compensation of Propagated Aberrations for High-Contrast Imaging. *Astrophys. J.*, 666:609–625.

Pueyo, L. and Norman, C. (2013). High-contrast Imaging with an Arbitrary Aperture: Active Compensation of Aperture Discontinuities. *Astrophys. J.*, 769:102.

Racine, R., Walker, G. A. H., Nadeau, D., Doyon, R., and Marois, C. (1999). Speckle Noise and the Detection of Faint Companions. *Pub. Astron. Soc. Pacific.*, 111:587–594.

Ragazzoni, R. and Farinato, J. (1999). Sensitivity of a pyramidic Wave Front sensor in closed loop Adaptive Optics. *Astron. & Astrophys.*, 350:L23–L26.

Rameau, J., Chauvin, G., Lagrange, A.-M., Boccaletti, A., Quanz, S. P., Bonnefoy, M., Girard, J. H., Delorme, P., Desidera, S., Klahr, H., Mordasini, C., Dumas, C., and Bonavita, M. (2013). Discovery of a Probable 4-5 Jupiter-mass Exoplanet to HD 95086 by Direct Imaging. *Astrophys. J. Letter.*, 772:L15.

Rameau, J., Chauvin, G., Lagrange, A.-M., Maire, A.-L., Boccaletti, A., and Bonnefoy, M. (2015). Detection limits with spectral differential imaging data. *Astron. & Astrophys.*, 581:A80.

Rameau, J., Chauvin, G., Lagrange, A.-M., Thébault, P., Milli, J., Girard, J. H., and Bonnefoy, M. (2012). High-contrast imaging of the close environment of HD 142527. VLT/NaCo adaptive optics thermal and angular differential imaging. *Astron. & Astrophys.*, 546:A24.

Ranc, C., Cassan, A., Albrow, M. D., Kubas, D., Bond, I. A., Batista, V., Beaulieu, J.-P., Bennett, D. P., Dominik, M., Dong, S., Fouqué, P., Gould, A., Greenhill, J., Jørgensen, U. G., Kains, N., Menzies, J., Sumi, T., Bachelet, E., Coutures, C., Dieters, S., Dominis Prester, D., Donatowicz, J., Gaudi, B. S., Han, C., Hundertmark, M., Horne, K., Kane, S. R., Lee, C.-U., Marquette, J.-B., Park, B.-G., Pollard, K. R., Sahu, K. C., Street, R., Tsapras, Y., Wambsganss, J., Williams, A., Zub, M., Abe, F., Fukui, A., Itow, Y., Masuda, K., Matsubara, Y., Muraki, Y., Ohnishi, K., Rattenbury, N., Saito, T., Sullivan, D. J., Sweatman, W. L., Tristram, P. J., Yock, P. C. M., and Yonehara, A. (2015). MOA-2007-BLG-197: Exploring the brown dwarf desert. *Astron. & Astrophys.*, 580:A125.

Ren, D., Dou, J., Zhang, X., and Zhu, Y. (2012). Speckle noise subtraction and suppression with adaptive optics coronagraphic imaging. *The Astrophysical Journal*, 753(2):99.

Roddier, F. (1981). The effects of atmospheric turbulence in optical astronomy. *Progress in optics. Volume 19. Amsterdam, North-Holland Publishing Co., 1981, p. 281-376.*, 19:281–376.

Roddier, F. (1988). Curvature sensing and compensation: a new concept in adaptive optics. *Adaptive Optics*, 27:1223–1225.

Roddier, F. and Roddier, C. (1997). Stellar Coronograph with Phase Mask. *Pub. Astron. Soc. Pacific.*, 109:815–820.

Rodigas, T. J., Weinberger, A., Mamajek, E. E., Males, J. R., Close, L. M., Morzinski, K., Hinz, P. M., and Kaib, N. (2015). Direct Exoplanet Detection with Binary Differential Imaging. *Astrophys. J.*, 811:157.

Roelfsema, R., Schmid, H. M., Pragt, J., Gisler, D., Waters, R., Bazzon, A., Baruffolo, A., Beuzit, J.-L., Boccaletti, A., Charton, J., Cumani, C., Dohlen, K., Downing, M., Elswijk, E., Feldt, M., Groothuis, C., de Haan, M., Hanenburg, H., Hubin, N., Joos, F., Kasper, M., Keller, C., Kragt, J., Lizon, J.-L., Mouillet, D., Pavlov, A., Rigal, F., Rochat, S., Salasnich, B., Steiner, P., Thalmann, C., Venema, L., and Wildi, F. (2010). The zimpol high-contrast imaging polarimeter for sphere: design, manufacturing, and testing.

Rouan, D., Riaud, P., Boccaletti, A., Clénet, Y., and Labeyrie, A. (2000). The Four-Quadrant Phase-Mask Coronagraph. I. Principle. *Pub. Astron. Soc. Pacific.*, 112:1479–1486.

Rousset, G., Fontanella, J. C., Kern, P., Gigan, P., and Rigaut, F. (1990). First diffraction-limited astronomical images with adaptive optics. *Astron. & Astrophys.*, 230:L29–L32.

Rousset, G., Lacombe, F., Puget, P., Hubin, N. N., Gendron, E., Fusco, T., Arsenault, R., Charton, J., Feautrier, P., Gigan, P., Kern, P. Y., Lagrange, A.-M., Madec, P.-Y., Mouillet, D., Rabaud, D., Rabou, P., Stadler, E., and Zins, G. (2003). NAOS, the first AO system of the VLT: on-sky performance. In Wizinowich, P. L. and Bonaccini, D., editors, *Adaptive Optical System Technologies II*, volume 4839 of *Proc. SPIE*, pages 140–149.

Santerne, A., Díaz, R. F., Moutou, C., Bouchy, F., Hébrard, G., Almenara, J.-M., Bonomo, A. S., Deleuil, M., and Santos, N. C. (2012). SOPHIE velocimetry of Kepler transit candidates. VII. A false-positive rate of 35% for Kepler close-in giant candidates. *Astron. & Astrophys.*, 545:A76.

Saumon, D. and Marley, M. S. (2008). The Evolution of L and T Dwarfs in Color-Magnitude Diagrams. *Astrophys. J.*, 689:1327–1344.

Sauvage, J.-F., Mugnier, L., Fusco, T., and Rousset, G. (2006). Post processing of differential images for direct extrasolar planet detection from the ground. In *Society of Photo-Optical Instrumentation Engineers (SPIE) Conference Series*, volume 6272 of *Proc. SPIE*, page 62722B.

Sauvage, J.-F., Mugnier, L., Paul, B., and Villecroze, R. (2012). Coronagraphic phase diversity: a simple focal plane sensor for high-contrast imaging. *Optics Letters*, 37:4808.

Sauvage, J.-F., Mugnier, L. M., Rousset, G., and Fusco, T. (2010). Analytical expression of long-exposure adaptive-optics-corrected coronagraphic image First application to exoplanet detection. *Journal of the Optical Society of America A*, 27(27):A157.

Savransky, D. (2015). Sequential Covariance Calculation for Exoplanet Image Processing. *Astrophys. J.*, 800:100.

Shack, R. B. and Platt, B. C. (1971). Production and use of a lenticular Hartmann Screen. *J. Opt. Soc. Am.*, 61:656.

Singh, G., Martinache, F., Baudoz, P., Guyon, O., Matsuo, T., Jovanovic, N., and Clergeon, C. (2014). Lyot-based Low Order Wavefront Sensor for Phase-mask Coronagraphs: Principle, Simulations and Laboratory Experiments. *Pub. Astron. Soc. Pacific.*, 126:586–594.

Sivanandam, S., Hinz, P. M., Heinze, A. N., Freed, M., and Breuninger, A. H. (2006). Clio: a 3-5 micron AO planet-finding camera. In *Society of Photo-Optical Instrumentation Engineers (SPIE) Conference Series*, volume 6269 of *Proc. SPIE*, page 62690U.

Skemer, A. J., Hinz, P., Esposito, S., Skrutskie, M. F., Defrère, D., Bailey, V., Leisenring, J., Apai, D., Biller, B., Bonnefoy, M., Brandner, W., Buenzli, E., Close, L., Crepp, J., De Rosa, R. J., Desidera, S., Eisner, J., Fortney, J., Henning, T., Hofmann, K.-H., Kopytova, T., Maire, A.-L., Males, J. R., Millan-Gabet, R., Morzinski, K., Oza, A., Patience, J., Rajan, A., Rieke, G., Schertl, D., Schlieder, J., Su, K., Vaz, A., Ward-Duong, K., Weigelt, G., Woodward, C. E., and Zimmerman, N. (2014). High contrast imaging at the LBT: the LEECH exoplanet imaging survey. In *Adaptive Optics Systems IV*, volume 9148 of *Proc. SPIE*, page 91480L.

Skemer, A. J., Hinz, P. M., Esposito, S., Burrows, A., Leisenring, J., Skrutskie, M., Desidera, S., Mesa, D., Arcidiacono, C., Mannucci, F., Rodigas, T. J., Close, L., McCarthy, D., Kulesa, C., Agapito, G., Apai, D., Argomedo, J., Bailey, V., Boutsia, K., Briguglio, R., Brusa, G., Busoni, L., Claudi, R., Eisner, J., Fini, L., Follette, K. B., Garnavich, P., Gratton, R., Guerra, J. C., Hill, J. M., Hoffmann, W. F., Jones, T., Krejny, M., Males, J., Masciadri, E., Meyer, M. R., Miller, D. L., Morzinski, K., Nelson, M., Pinna, E., Puglisi, A., Quanz, S. P., Quiros-Pacheco, F., Riccardi, A., Stefanini, P., Vaitheeswaran, V., Wilson, J. C., and Xompero, M. (2012). First Light LBT AO Images of HR 8799 bcde at 1.6 and 3.3 μm: New Discrepancies between Young Planets and Old Brown Dwarfs. *Astrophys. J.*, 753:14.

Skemer, A. J., Morley, C. V., Zimmerman, N. T., Skrutskie, M. F., Leisenring, J., Buenzli, E., Bonnefoy, M., Bailey, V., Hinz, P., Defrére, D., Esposito, S., Apai, D., Biller, B., Brandner, W., Close, L., Crepp, J. R., De Rosa, R. J., Desidera, S., Eisner, J., Fortney, J., Freedman, R., Henning, T., Hofmann, K.-H., Kopytova, T., Lupu, R., Maire, A.-L., Males, J. R., Marley, M., Morzinski, K., Oza, A., Patience, J., Rajan, A., Rieke, G., Schertl, D., Schlieder, J., Stone, J., Su, K., Vaz, A., Visscher, C., Ward-Duong, K., Weigelt, G., and Woodward, C. E. (2016). The LEECH Exoplanet Imaging Survey: Characterization of the Coldest Directly Imaged Exoplanet, GJ 504 b, and Evidence for Superstellar Metallicity. *Astrophys. J.*, 817:166.

Skrutskie, M. F., Jones, T., Hinz, P., Garnavich, P., Wilson, J., Nelson, M., Solheid, E., Durney, O., Hoffmann, W., Vaitheeswaran, V., McMahon, T., Leisenring, J., and Wong, A. (2010). The Large Binocular Telescope mid-infrared camera (LMIRcam): final design and status. In *Ground-based and Airborne Instrumentation for Astronomy III*, volume 7735 of *Proc. SPIE*, page 77353H.

Smith, I., Ferrari, A., and Carbillet, M. (2009). Detection of a moving source in speckle noise. application to exoplanet detection. *Signal Processing, IEEE Transactions on*, 57(3):904–915.

Soummer, R., Dohlen, K., and Aime, C. (2003). Achromatic dual-zone phase mask stellar coronagraph. *Astron. & Astrophys.*, 403:369–381.

Soummer, R., Ferrari, A., Aime, C., and Jolissaint, L. (2007a). Speckle Noise and Dynamic Range in Coronagraphic Images. *Astrophys. J.*, 669:642–656.

Soummer, R., Pueyo, L., and Larkin, J. (2012). Detection and Characterization of Exoplanets and Disks Using Projections on Karhunen-Loève Eigenimages. *Astrophys. J. Letter.*, 755:L28.

Soummer, R., Pueyo, L., Sivaramakrishnan, A., and Vanderbei, R. J. (2007b). Fast computation of Lyot-style coronagraph propagation. *Optics Express*, 15:15935.

Soummer, R., Sivaramakrishnan, A., Pueyo, L., Macintosh, B., and Oppenheimer, B. R. (2011). Apodized Pupil Lyot Coronagraphs for Arbitrary Apertures. III. Quasi-achromatic Solutions. *Astrophys. J.*, 729:144.

Sparks, W. B. and Ford, H. C. (2002). Imaging Spectroscopy for Extrasolar Planet Detection. *Astrophys. J.*, 578:543–564.

Spergel, D. and Kasdin, J. (2001). A Shaped Pupil Coronagraph: A Simpler Path towards TPF. In *American Astronomical Society Meeting Abstracts*, volume 33 of *Bulletin of the American Astronomical Society*, page 1431.

Struve, O. (1952). Proposal for a project of high-precision stellar radial velocity work. *The Observatory*, 72:199–200.

Su, K. Y. L., Rieke, G. H., Stapelfeldt, K. R., Malhotra, R., Bryden, G., Smith, P. S., Misselt, K. A., Moro-Martin, A., and Williams, J. P. (2009). The Debris Disk Around HR 8799. *Astrophys. J.*, 705:314–327.

Sumi, T., Kamiya, K., Bennett, D. P., Bond, I. A., Abe, F., Botzler, C. S., Fukui, A., Furusawa, K., Hearnshaw, J. B., Itow, Y., Kilmartin, P. M., Korpela, A., Lin, W., Ling, C. H., Masuda, K., Matsubara, Y., Miyake, N., Motomura, M., Muraki, Y., Nagaya, M., Nakamura, S., Ohnishi, K., Okumura, T., Perrott, Y. C., Rattenbury, N., Saito, T., Sako, T., Sullivan, D. J., Sweatman, W. L., Tristram, P. J., Udalski, A., Szymański, M. K., Kubiak, M., Pietrzyński, G., Poleski, R., Soszyński, I., Wyrzykowski, Ł., Ulaczyk, K., and Microlensing Observations in Astrophysics (MOA) Collaboration (2011). Unbound or distant planetary mass population detected by gravitational microlensing. *Nature*, 473:349–352.

Suzuki, R., Kudo, T., Hashimoto, J., Carson, J., Egner, S., Goto, M., Hattori, M., Hayano, Y., Hodapp, K., Ito, M., Iye, M., Jacobson, S., Kandori, R., Kusakabe, N., Kuzuhara, M., Matsuo, T., Mcelwain, M., Morino, J.-I., Oya, S., Saito, Y., Shelton, R., Stahlberger, V., Suto, H., Takami, H., Thalmann, C., Watanabe, M., Yamada, H., and Tamura, M. (2010). Performance characterization of the hiciao instrument for the subaru telescope.

Tamura, M. (2009). Subaru Strategic Exploration of Exoplanets and Disks with HiCIAO/AO188 (SEEDS). In Usuda, T., Tamura, M., and Ishii, M., editors, *American Institute of Physics Conference Series*, volume 1158 of *American Institute of Physics Conference Series*, pages 11–16.

Thatte, N., Abuter, R., Tecza, M., Nielsen, E. L., Clarke, F. J., and Close, L. M. (2007). Very high contrast integral field spectroscopy of AB Doradus C: 9-mag contrast at 0.2arcsec without a coronagraph using spectral deconvolution. *Mon. Not. R. astr. Soc.*, 378:1229–1236.

Thiebaut, E. (2002). Optimization issues in blind deconvolution algorithms. In Starck, J.-L. and Murtagh, F. D., editors, *Astronomical Data Analysis II*, volume 4847 of *Proc. SPIE*, pages 174–183.

Thiébaut, E. and Conan, J.-M. (1995). Strict a priori constraints for maximum-likelihood blind deconvolution. *Journal of the Optical Society of America A*, 12:485–492.

Thiebaut, E., Denis, L., Mugnier, L.-M., Ferrari, A., Mary, D., Langlois, M., Cantalloube, F., and Devaney, N. (2016). Fast and robust exo-planet detection in multi-spectral, multi-temporal data. In *Extreme AO*, Proc. SPIE.

Thiébaut, E. and Mugnier, L. (2006). Maximum a posteriori planet detection and characterization with a nulling interferometer. In *IAUC 200, Direct Imaging of Exoplanets: Science & Techniques*. October 2005, Nice, France.

Tokovinin, A. and Kornilov, V. (2007). Accurate seeing measurements with MASS and DIMM. *Mon. Not. R. astr. Soc.*, 381:1179–1189.

Vernin, J. and Roddier, F. (1973). Experimental determination of two-dimensional spatiotemporal power spectra of stellar light scintillation. Evidence for a multilayer structure of the air turbulence in the upper troposphere. *Journal of the Optical Society of America (1917-1983)*, 63:270–273.

Vigan, A., Langlois, M., Dohlen, K., Zurlo, A., Moutou, C., Costille, A., Gry, C., Madec, F., Le Mignant, D., Gluck, L., and Sauvage, J.-F. (2014). Sphere/irdis: final performance assessment of the dual-band imaging and long slit spectroscopy modes.

Vigan, A., Langlois, M., Moutou, C., and Dohlen, K. (2008). Long slit spectroscopy for exoplanet characterization in sphere.

Vigan, A., Moutou, C., Langlois, M., Allard, F., Boccaletti, A., Carbillet, M., Mouillet, D., and Smith, I. (2010). Photometric characterization of exoplanets using angular and spectral differential imaging. *Mon. Not. R. astr. Soc.*, 407:71–82.

Vigan, A., Patience, J., Marois, C., Bonavita, M., De Rosa, R. J., Macintosh, B., Song, I., Doyon, R., Zuckerman, B., Lafrenière, D., and Barman, T. (2012). The International Deep Planet Survey. I. The frequency of wide-orbit massive planets around A-stars. *Astron. & Astrophys.*, 544:A9.

Wahhaj, Z., Cieza, L. A., Mawet, D., Yang, B., Canovas, H., de Boer, J., Casassus, S., Ménard, F., Schreiber, M. R., Liu, M. C., Biller, B. A., Nielsen, E. L., and Hayward, T. L. (2015). Improving signal-to-noise in the direct imaging of exoplanets and circumstellar disks with MLOCI. *Astron. & Astrophys.*, 581:A24.

Wilson, R. W. (2002). SLODAR: measuring optical turbulence altitude with a Shack-Hartmann wavefront sensor. *Mon. Not. R. astr. Soc.*, 337:103–108.

Wizinowich, P., Acton, D. S., Shelton, C., Stomski, P., Gathright, J., Ho, K., Lupton, W., Tsubota, K., Lai, O., Max, C., Brase, J., An, J., Avicola, K., Olivier, S., Gavel, D., Macintosh, B., Ghez, A., and Larkin, J. (2000). First Light Adaptive Optics Images from the Keck II Telescope: A New Era of High Angular Resolution Imagery. *Pub. Astron. Soc. Pacific.*, 112:315–319.

Wolszczan, A. and Frail, D. A. (1992). A planetary system around the millisecond pulsar PSR1257 + 12. *Nature*, 355:145–147.

Ygouf, M. (2012). *Nouvelle méthode de traitement d'images multispectrales fondée sur un modèle d'instrument pour le haut-contrast : Application á la détection d'exoplanètes.* PhD thesis, Université de Grenoble.

Ygouf, M., Mugnier, L., Sauvage, J.-F., Fusco, T., Mouillet, D., and Beuzit, J.-L. (2010). Approximate analytical expression for AO-corrected coronagraphic imaging in preparation of exoplanet signal extraction. In Boissier, S., Heydari-Malayeri, M., Samadi, R., and Valls-Gabaud, D., editors, *SF2A-2010: Proceedings of the Annual meeting of the French Society of Astronomy and Astrophysics*, page 97.

Ygouf, M., Mugnier, L. M., Mouillet, D., Fusco, T., and Beuzit, J.-L. (2013). Simultaneous exoplanet detection and instrument aberration retrieval in multispectral coronagraphic imaging. *Astron. & Astrophys.*, 551:A138.

Zuckerman, B., Song, I., Bessell, M. S., and Webb, R. A. (2001). The β Pictoris Moving Group. *Astrophys. J. Letter.*, 562:L87–L90.

Zurlo, A., Vigan, A., Galicher, R., Maire, A.-L., Mesa, D., Gratton, R., Chauvin, G., Kasper, M., Moutou, C., Bonnefoy, M., Desidera, S., Abe, L., Apai, D., Baruffolo, A., Baudoz, P., Baudrand, J., Beuzit, J.-L., Blancard, P., Boccaletti, A., Cantalloube, F., Carle, M., Cascone, E., Charton, J., Claudi, R. U., Costille, A., de Caprio, V., Dohlen, K., Dominik, C., Fantinel, D., Feautrier, P., Feldt, M., Fusco, T., Gigan, P., Girard, J. H., Gisler, D., Gluck, L., Gry, C., Henning, T., Hugot, E., Janson, M., Jaquet, M., Lagrange, A.-M., Langlois, M., Llored, M., Madec, F., Magnard, Y., Martinez, P., Maurel, D., Mawet, D., Meyer, M. R., Milli, J., Moeller-Nilsson, O., Mouillet, D., Origné, A., Pavlov, A., Petit, C., Puget, P., Quanz, S. P., Rabou, P., Ramos, J., Rousset, G., Roux, A., Salasnich, B., Salter, G., Sauvage, J.-F., Schmid, H. M., Soenke, C., Stadler, E., Suarez, M., Turatto, M., Udry, S., Vakili, F., Wahhaj, Z., Wildi, F., and Antichi, J. (2016). First light of the VLT planet finder SPHERE. III. New spectrophotometry and astrometry of the HR 8799 exoplanetary system. *Astron. & Astrophys.*, 587:A57.

Contents

General introduction **10**

1 Exoplanet imaging with high contrast instruments **12**
1.1 Studying exoplanets . . . 13
1.1.1 Indirect methods of detecting and studying exoplanets . . . 14
1.1.1.1 Pulsar timing . . . 14
Accessible astrophysical parameters . . . 15
Fundamental limitations and biases . . . 15
1.1.1.2 Radial velocity . . . 15
Astrophysical parameters accessible with this method . . . 15
Fundamental limitations and main detection biases . . . 16
False alarms . . . 16
Technical challenges . . . 16
Main instruments dedicated to RV . . . 16
1.1.1.3 Planetary transit . . . 17
Accessible astrophysical parameters . . . 17
Fundamental limitations and main detection biases . . . 18
False alarms . . . 18
Main instruments dedicated to transit . . . 18
1.1.1.4 Gravitational micro-lensing . . . 18
Accessible astrophysical parameters . . . 19
Fundamental limitations and main observational biases . . . 19
1.1.1.5 Summary of the indirect observational methods for exoplanets . . . 19
1.1.2 Direct imaging for exoplanet study . . . 19
1.1.2.1 Astrophysical context enabling direct imaging . . . 20
First detection of an exoplanet by direct imaging . . . 20
Companions detected by direct imaging today . . . 21
1.1.2.2 Derived astrophysical parameters . . . 21
Obtaining information about the orbital properties of the stellar system 21
Obtaining the mass of the detected companion . . . 21
Constraining the estimations by probing different wavelengths . . . 22
Deriving exoplanet atmospheric spectra . . . 22
Obtaining constrains on the presence of exoplanets . . . 22
1.1.2.3 Major results obtained thanks to DI . . . 22
1.1.2.4 False positives in direct imaging . . . 23
Observational noise . . . 23
Instrumental noise . . . 23
Processing and human noise . . . 24
1.2 High contrast imaging with ground-based telescopes . . . 25
1.2.1 Adaptive optics systems . . . 26
1.2.1.1 Characterizing the turbulence strength . . . 26
Seeing and Fried parameter . . . 26

Cn^2 profile . . . 26
Coherence time . . . 26
1.2.1.2 Adaptive optics system . . . 26
Wavefront sensing . . . 26
Extreme AO . . . 27
Main limitations of the AO concept . . . 27
1.2.1.3 Characterizing the post-AO images . . . 28
Residual phase variance . . . 28
Strehl ratio . . . 28
Power spectral density . . . 29
Residual phase structure function . . . 29
1.2.1.4 Limitations of an AO system . . . 29
1.2.2 High contrast for exoplanet imaging: Coronagraphy . . . 30
1.2.2.1 Focal plane mask coronagraphs (FPM) . . . 31
The classical Lyot coronagraph . . . 31
Phase focal mask coronagraphs . . . 32
1.2.2.2 Pupil apodizers . . . 32
Amplitude apodization . . . 32
Phase apodization . . . 32
1.2.2.3 Hybrid coronagraph . . . 33
1.2.2.4 Measuring and correcting for low-order aberrations to center the coronagraph . . . 33
1.2.2.5 Current limitations and future designs of coronagraph . . . 33
1.2.3 The speckle noise limitation . . . 34
1.2.4 Dedicated instruments to high contrast exoplanet imaging . . . 34
1.2.4.1 Current instrument . . . 34
1.2.4.2 Previous generation of high contrast instruments: the example of VLT/NaCo 35
The adaptive optics module NAOS . . . 35
The infrared camera CONICA . . . 35
Observation modes available . . . 35
Spectral bands available for exoplanet imaging . . . 35
Coronagraphic masks available . . . 35
1.2.4.3 Recent generation of high-contrast instruments: the example of VLT/SPHERE 36
SAXO: the extreme adaptive optics module . . . 36
Coronagraphic masks and pupil apodization . . . 37
IRDIS: the different observing modes . . . 37
IFS: the different observing modes . . . 37
Major results obtained with SPHERE . . . 38
1.3 Image processing for exoplanet observation . . . 39
1.3.1 Image restoration: inverse problems . . . 39
Forward problem . . . 39
Inverse problem . . . 40
Ill-posed problem . . . 40
Inversion process . . . 40
1.3.1.1 Deterministic approach . . . 40
1.3.1.2 Stochastic approach . . . 40
1.3.1.3 Regularization . . . 41
1.3.1.4 Model of noise . . . 41
1.3.1.5 Example of image deconvolution with MAP . . . 41
Positivity constraint . . . 42
L2 spatial regularization on the object . . . 42
L1L2 spatial regularization on the object . . . 42

L^p spatial regularization on the object . . . 42
1.3.2 Current image processing for exoplanet imaging . . . 43
1.3.2.1 Exploitation of the temporal diversity: ADI . . . 43
Classical ADI . . . 44
Locally optimized combination of images, LOCI . . . 44
Principal component analysis, PCA . . . 45
1.3.2.2 Exploitation of the spectral diversity: SDI and SSDI . . . 46
1.3.2.3 Other information exploited . . . 47
Polarimetric differential imaging, PDI . . . 47
Reference differential imaging, RDI . . . 47
Coherence differential imaging, CDI . . . 48
Binary differential imaging, BDI . . . 48

Summary in French of the introduction chapter **50**
Détection par imagerie directe . . . 51
Spectro-photométrie par imagerie directe . . . 51
Astrométrie par imagerie directe . . . 51
Diversité temporelle grâce au suivi de pupille . . . 52
Diversité spectrale grâce à l'imagerie multispectrale . . . 52

I ANDROMEDA: Exploitation of the temporal diversity in the images. 54

2 The ANDROMEDA approach and initial status 56
2.1 ANDROMEDA's principle . . . 57
2.1.1 Theoretical concept . . . 57
2.1.1.1 Differential images: Accommodating the noise distribution and appearance of a planet signature . . . 57
2.1.1.2 Maximum likelihood estimation (MLE) of the planetary signals' parameters . . . 58
2.1.2 Practical solutions . . . 59
2.1.2.1 Differential images: image couple selection . . . 59
2.1.2.2 Differential images: image couple flux scaling . . . 61
2.1.2.3 Building the model of a potential companion signature . . . 61
2.1.2.4 Estimation of the noise variance to compute the likelihood . . . 63
2.1.3 Inversion method . . . 63
2.1.3.1 Maximizing the likelihood . . . 64
2.1.3.2 Estimating the flux a of the companion . . . 64
2.1.3.3 Estimating the uncertainty $\sigma(a)$ on the flux map . . . 64
2.1.3.4 Estimating the initial position r_0 of the companion . . . 65
2.1.3.5 Link between the likelihood and the SNR . . . 65
2.1.3.6 Positivity constraint on the estimated flux . . . 65
2.1.3.7 Conclusion on ANDROMEDA's principle . . . 66
2.2 Previous work on the ANDROMEDA method . . . 67
2.2.1 Description of the simulated data used to test the method . . . 67
2.2.2 Theoretical study of the potential sources of errors . . . 68
Errors due to a bad centering of the images . . . 68
Errors due the smearing of the companion . . . 68
Errors due to the level of photon noise in the images . . . 68
Errors due to the level of speckle noise residuals . . . 68
2.2.3 Optimal set of user-parameters derived from simulated data application . . . 69
Size of the reference PSF window N_{PSF} . . . 69
Minimum separation constraint for the ADI δ_{min} . . . 69

Thickness of the annuli in which the minimum separation constraint applies d_r . . . 69
Optimization method used for the ADI subtraction . . . 69
Optimization to subtraction area ratio R_A . . . 69
Type of variance for the likelihood computation . . . 69
Precision of the subpixel shift to build the planet signature model . . . 70
Positivity constraint . . . 70
Conclusion & summary . . . 70
2.3 Application of ANDROMEDA on real data as it is . . . 73
2.3.1 Description of the real data used to apply ANDROMEDA . . . 73
Target star properties . . . 73
Observation conditions . . . 73
Data reduction: science frames . . . 73
Data reduction: reference PSF . . . 73
Data reduction: parallactic angles . . . 73
Summary of the data-set properties . . . 74
Introduction of synthetic companions . . . 74
2.3.2 Output provided by ANDROMEDA . . . 74
2.3.3 Detected problems affecting ANDROMEDA's capabilities on real data . . . 76
2.3.4 Conclusion on ANDROMEDA's original capabilities . . . 77

3 ANDROMEDA: making it operational to process real data 79
3.1 Stages required to make ANDROMEDA operational . . . 80
3.1.1 Removing the low spatial frequencies in the reduced images . . . 80
3.1.1.1 Implementation of a high-pass Fourier filtering . . . 80
3.1.1.2 High-pass filtered images . . . 81
3.1.1.3 Energy loss of the companion signal induced by the pre-filtering . . . 81
3.1.1.4 Consequences on ANDROMEDA's principle . . . 83
3.1.1.5 Consequences on the computation of the scaling factor γ . . . 84
3.1.1.6 Consequences on ANDROMEDA's output . . . 84
Shape of the planetary pattern in the SNR map . . . 84
Consequences on the SNR map . . . 85
3.1.2 Correcting for the radial dependency of the SNR statistics . . . 87
3.1.2.1 Inconsistency between the model of noise and the real noise distribution in the differential images . . . 88
Qualitative explanations on the origins of the noise model discrepancy . 88
Whiteness of the noise in the differential images . . . 88
Consequences on the SNR map output by ANDROMEDA . . . 90
Solutions to account for the noise model discrepancy . . . 90
3.1.2.2 Implementation of a normalization procedure for the SNR map . . . 90
Normalizing the SNR map by its own radial standard deviation profile . 90
Smoothing the normalization profile . . . 91
Effect of the smoothing amount on the normalized SNR map . . . 92
3.1.2.3 Corresponding detection limits estimated with ANDROMEDA . . . 94
Implementing the small sample statistics . . . 94
Discussion on the notion of detection limit . . . 95
3.1.2.4 Distribution of the residuals in the normalized SNR map . . . 96
3.1.2.5 Conclusion on ANDROMEDA's post-processing . . . 97
3.1.3 Conclusion on ANDROMEDA in its operational state . . . 97
3.2 Exploring variations on building the differential images . . . 97
3.2.1 Description of the data to illustrate this part . . . 98
3.2.2 Interpretation of the scaling factor γ after pre-filtering the images . . . 98
3.2.3 Refining the ADI process included in ANDROMEDA . . . 102

Robust optimization . . . 102
Non-linear subtraction . . . 102
Proposed solution . . . 103
3.2.3.1 Algorithm to perform a robust affine fit . . . 103
3.2.3.2 Practical implementation of the robust affine fit in ANDROMEDA . . 103
3.2.4 Test of the robust affine fit in real differential images . . . 104
3.2.4.1 Impact of the robust affine fit on the SNR map . . . 106
3.2.4.2 Conclusion: which differential imaging optimization for which case . . 109
3.2.5 Adapting the model of the planetary signature in the differential images . . . 109
Taking into account the scaling factor in the planetary signature model 109
Without taking into account the scaling factor in the planetary signature model . . . 110
Impact on the ANDROMEDA performance on real data . . . 110
Impact on the ANDROMEDA SNR maps . . . 110
3.3 Automatic companion extraction, properties and reliability criteria . . . 112
3.3.1 Detection and astrometry . . . 112
Automatic detection . . . 112
Subpixel position estimation . . . 113
Estimation of the detection SNR . . . 113
Estimation of the 3-σ error on the position estimation . . . 113
3.3.2 Photometry . . . 114
Contrast estimation . . . 114
Estimation of the 3-σ error on the contrast estimation . . . 114
3.3.3 Sorting out artifacts from probable true detections . . . 115
3.3.4 Estimation of the detection limit . . . 116
3.3.5 Ergonomics of the detection module . . . 116
Detection map . . . 116
Subimages of the detections . . . 117
Detection limit . . . 117
Results file . . . 117

4 Sensitivity to user-defined parameters and final contrast performance 119
4.1 Test case: VLT/NaCo data in H-band . . . 119
4.1.1 Target star: data set TYC-8979-1683-1 . . . 120
4.1.2 Reference case: user-parameters setting . . . 120
4.1.3 Reference case: Results with ANDROMEDA . . . 121
4.2 Sensitivity to the user-defined parameters . . . 121
4.2.1 Pre-filtering of the reduced images . . . 122
Expected results: . . . 122
Obtained results: . . . 122
Conclusion: . . . 123
4.2.2 Building the differential images via ADI . . . 124
4.2.2.1 Minimum angular separation, δ_{min} . . . 124
Expected results: . . . 124
Obtained results: . . . 125
Conclusion: . . . 126
4.2.2.2 Annuli width, d_r . . . 127
Expected results: . . . 127
Obtained results: . . . 127
Conclusion: . . . 128
4.2.2.3 Optimization to subtraction areas ratio, R_A . . . 128
Expected results: . . . 128
Obtained results: . . . 129

Conclusion: . . . 129
4.2.3 Building the model of the differential images . . . 130
4.2.3.1 Size of the input reference PSF, N_{PSF} . . . 131
Expected results: . . . 131
Obtained results: . . . 131
Conclusion: . . . 132
4.2.3.2 Precision of the PSF subpixel shift, PSF_{shift} . . . 132
Expected results: . . . 133
Obtained results: . . . 133
Conclusion: . . . 133
4.2.4 Post-normalization of the SNR map . . . 134
Expected results: . . . 134
Obtained results: . . . 134
Conclusion: . . . 135
4.3 Discussion on the threshold set for the detection . . . 137
4.4 Performance of the ANDROMEDA method . . . 138
Detection capabilities . . . 139
Separation estimation . . . 139
Position angle estimation . . . 140
Contrast estimation . . . 140
Estimation of the detection limit . . . 141

5 ANDROMEDA: Comparison with other methods 143
5.1 Dataset: The SPHERE-IRDIS blind test . . . 144
5.1.1 Description of the provided dataset . . . 144
5.1.2 Synthetic companions injected . . . 144
5.1.3 Description of the provided images . . . 145
5.2 Short description of the other algorithms used . . . 145
5.2.1 Radial ADI, r-ADI . . . 146
Procedure . . . 146
Detection . . . 147
Characterization . . . 147
Errorbar estimation . . . 147
Detection limit retrieval . . . 147
Similarities with ANDROMEDA . . . 147
5.2.2 Upgraded T-LOCI . . . 148
Procedure . . . 148
Detection . . . 148
Characterization . . . 148
Errorbar estimation . . . 149
Detection limit retrieval . . . 149
Similarities with ANDROMEDA . . . 149
5.2.3 Classical PCA, c-PCA . . . 149
Procedure . . . 149
Detection . . . 149
Characterization . . . 149
Errorbar estimation . . . 150
Detection limit retrieval . . . 150
Similarities with ANDROMEDA . . . 150
5.2.4 ANDROMEDA . . . 150
5.3 Comparison criteria . . . 151
5.3.1 Detection capabilities . . . 152
Contrast weighting function $\mathscr{C}(a)$: . . . 152

Separation weighting function $\mathscr{S}(r)$: . . . 152
5.3.2 Characterization capabilities . . . 153
Astrometry: . . . 153
Photometry: . . . 153
Astrometry and photometry including uncertainties . . . 154
5.3.3 Practical aspects . . . 155
5.3.4 Ranking metric used for this study . . . 155
5.4 Results obtained and comparison . . . 155
5.4.1 Final images obtained by the pipelines . . . 156
5.4.2 Detected planetary companions . . . 157
5.4.3 Results of the characterization by the pipelines . . . 157
5.4.3.1 Astrometry retrieved with the pipelines . . . 158
Separation to the star: . . . 158
Position angle: . . . 158
5.4.3.2 Photometry retrieved with the pipelines . . . 159
5.4.3.3 Detection limits provided by each pipeline . . . 160
5.4.4 Processing time for each pipeline . . . 160
5.4.5 Practical aspects . . . 161
Objectiveness of the detections . . . 162
Number of user-defined parameters to obtain the final image . . . 162
Number of steps to obtain the different characterization information . . . 162
5.4.6 Conclusion on the different pipelines performance . . . 162

6 ANDROMEDA: Applications on various experimental data 164
6.1 Response of ANDROMEDA to the different narrow band filters offered by SPHERE-IRDIS . . . 166
6.1.1 The planetary companion GJ504 b . . . 166
6.1.2 Properties of the GJ504 IRDIS images . . . 167
6.1.3 User-parameters to run ANDROMEDA on the GJ504 IRDIS images . . . 167
6.1.4 Results from ANDROMEDA applied to the GJ504 SPHERE-IRDIS images . . . 168
6.1.4.1 SNR maps of GJ504 for the different wavelengths of observation . . . 168
6.1.4.2 Detection limits for the different wavelengths of observation . . . 168
6.2 Response of ANDROMEDA to different observing conditions . . . 169
6.2.1 Observation conditions of the star GJ504 at different epochs . . . 170
6.2.2 User-parameters set to process the images of GJ504 at different epochs . . . 170
6.2.3 Results from the application of ANDROMEDA on the GJ504 images at different epochs . . . 170
6.2.3.1 SNR maps of GJ504 for the two different observation conditions . . . 170
6.2.3.2 Detection limits of GJ504 for the two different observation conditions 171
6.3 Investigating for a difficult source: the case of 51Eri b in H-band . . . 173
6.3.1 The planetary companion 51Eri b . . . 173
6.3.2 Observation conditions of the star 51Eri by SPHERE-IRDIS in H-band . . . 174
6.3.3 ANDROMEDA user-parameters to process the SPHERE-IRDIS 51Eri data . . . 174
6.3.4 Results of ANDROMEDA applied to the SPHERE-IRDIS images of 51Eri . . . 174
6.4 SDI+ADI process of SPHERE-IRDIS data in DBI mode, by ANDROMEDA . . . 175
6.4.1 The case of a companion showing an absorption band: 51Eri images in H2H3 bands . . . 176
6.4.2 The case of the planetary system HR8799 in H2H3 bands . . . 177
6.4.2.1 The planetary system around HR8799 . . . 178
6.4.2.2 HR8799 SPHERE-IRDIS data description . . . 178
6.4.2.3 ANDROMEDA user-parameters to process HR8799 SPHERE-IRDIS images . . . 178

6.4.2.4 HR8799 data processed in SADI using ANDROMEDA: results and discussion . . . 179
6.5 Processing SPHERE-IFS data with ANDROMEDA . . . 182
6.5.1 Multispectral cubes properties and user-parameters set for ANDROMEDA . . 182
6.5.2 Collapsing the images to obtain the detection . . . 182
6.5.3 Multi-channel detection and channelwise spectrum estimation . . . 184
Detection . . . 184
Characterization . . . 184
Overlap of the spectra . . . 186
Detection limits . . . 187
6.5.4 Using SADI to increase the detectability and sensitivity . . . 188
Choosing the channels to be spectrally subtracted . . . 188
Detection . . . 188
Characterization . . . 188
Overlap of the spectra . . . 188
Detection limits . . . 190
6.5.5 Preliminary spectra retrieved by ANDROMEDA . . . 191
Reducing the computing time by parallelizing the ML search: . . . 194
Including the potential temporal variation of the companion PSF: . . . 194
Modifying the angular differential images construction: . . . 194
Adaptation to DBI data: . . . 195
Finding the optimal frame correlation: . . . 195
Frame selection: . . . 196
Implementing an evolutionary model of the speckle field: . . . 196
Robust detection criterion: . . . 196
Modifying the model of noise: . . . 196
Probing extended sources: . . . 196

Summary in French of the first part **198**

II MEDUSAE: Exploitation of the spectral diversity in the images. **203**

7 The MEDUSAE approach and initial status **205**
7.1 The MEDUSAE approach: image model and inversion . . . 206
7.1.1 Model of the multispectral images . . . 206
7.1.1.1 Model of the speckle field: $f_\lambda^* \times h_\lambda^c$ . . . 206
Short exposure expression: . . . 208
Long exposure expression: . . . 208
Multispectral adaptation: . . . 208
Main difficulty arising from the use of this model: . . . 209
Other models explored: . . . 209
7.1.1.2 Model of the circumstellar objects image: $o_\lambda * h_\lambda^{nc}$ . . . 209
7.1.1.3 Model of the noise: n_λ . . . 210
7.1.2 Inversion criterion . . . 210
7.1.3 Methods to estimate the three unknowns . . . 210
7.1.3.1 Star flux f_λ^* . . . 210
7.1.3.2 Upstream aberration map δ_{up} using phase retrieval (for a given object) 211
7.1.3.3 Object map o_λ using a non-myopic deconvolution (for a given upstream *opd*) . . . 211
7.1.4 Minimization algorithm used for the phase retrieval in MEDUSAE . . . 212
7.1.5 Inversion scheme to run MEDUSAE . . . 212
Initialization stage: . . . 212

Inversion core: . . . 213
7.2 Main hypothesis used in MEDUSAE . . . 213
7.3 Previous work on the MEDUSAE method . . . 214
7.3.1 Simulated data to validate the MEDUSAE concept . . . 214
Method used to produce the multispectral cube . . . 214
Numerical values used to produce the data set . . . 215
Injected planetary companions . . . 215
7.3.2 Tests and conclusion from the inverse crime MEDUSAE application . . . 215
Number of spectral channels . . . 216
Distance between the spectral channels . . . 216
Starting point for the upstream phase . . . 216
Sensitivity to the downstream aberration map given in input . . . 216
Sensitivity to the star flux estimation . . . 216
Sensitivity to the chosen spatial regularization for the object estimation 216

8 Refining the MEDUSAE strategy on inverse crime 219
8.1 Simulated data and analysis criteria . . . 219
8.1.1 Simulated data used for tests . . . 219
8.1.2 Analysis criteria . . . 221
General inversion efficiency: . . . 221
Estimated star spectrum $\hat{f}^*_\lambda$: . . . 221
Estimated object map $\hat{o}_\lambda$: . . . 222
Estimated upstream aberration map $\hat{\delta}_{up}$: . . . 222
8.2 Inversion scheme: revisiting the strategy . . . 222
8.2.1 Multispectral phase retrieval for a known object . . . 223
8.2.2 Initialization procedure . . . 224
8.2.2.1 The four equivalent phase maps . . . 225
8.2.2.2 Alternated estimation of the object and the aberration map . . . 226
8.2.2.3 Object spatial regularization during the initialization . . . 226
8.2.2.4 Wavelengths used for the initialization . . . 227
8.2.2.5 Summary of the new initialization procedure . . . 227
8.2.3 MEDUSAE core . . . 228
8.2.3.1 MEDUSAE core: Object regularization . . . 229
8.3 Corruption due to intense planetary signals . . . 230
8.4 Sensitivity to the inputs required by MEDUSAE . . . 231
8.4.1 Error on the downstream aberration map δ_{down} . . . 231
8.4.2 Error on the residual phase structure function $D_{\phi_{res}}$ . . . 234

9 Towards application on real data: tests on realistic simulated data 237
9.1 Simulation of realistic multispectral high contrast images . . . 238
9.1.1 Short exposure realistic coronagraphic PSF . . . 238
9.1.2 SPHERE-IFS data characteristics . . . 239
Pixel scale and sampling of the images . . . 239
Channel number and wavelengths . . . 239
Pupils of the set up . . . 239
APLC coronagraph characteristics . . . 239
Multispectral adaptation . . . 240
9.1.3 Chosen characteristics of the images . . . 240
Static aberrations, ϕ_{up} and ϕ_{do} . . . 240
Turbulence residuals . . . 240
Building the multispectral coronagraphic PSF cube . . . 240
Adding planetary signals to the star images . . . 241
Noise propagation in the set up . . . 241

9.1.4 Generation of a representative $D_{\phi_{res}}$ . . . 241
9.1.5 Resulting realistic simulated images . . . 242
Spatial structures of the simulated images . . . 243
Spectral behavior of the simulated images . . . 244
9.2 Application of MEDUSAE on the realistic simulated data . . . 244
9.2.1 First application: Reference case . . . 244
9.2.2 Estimating the speckle field only . . . 247
9.2.2.1 Choice of the weight map . . . 247
9.2.2.2 With a flat pupil as in the model . . . 250
9.2.2.3 Spectral diversity: YH vs YJ modes . . . 250
9.2.3 Estimating the object map with MEDUSAE . . . 252
9.3 Perspectives for the MEDUSAE methods . . . 255
Dealing with the knowledge of $D_{\phi_{res}}$ . . . 255
Dealing with the knowledge of ϕ_{down} . . . 256
Finding a correct starting point for ϕ_{up} . . . 256
Modifying the spatial regularization for the object deconvolution . . . 256
Optimizing the computing time . . . 256
Implementing further knowledge: spectral information on the star . . . 257
Implementing further knowledge: spectral information on the object . . . 257

Summary in French of the second part **258**

General conclusion **262**

General conclusion in French **264**

Appendix **265**

A Publication on the ANDROMEDA pipeline applied on VLT/NaCo data **265**

B User Manual for the ANDROMEDA pipeline **285**

C Analytical models of long exposure coronographic PSF **304**
C.1 Notations and hypothesis: . . . 304
C.1.1 Notations for the coronagraph setup: . . . 304
Amplitude: . . . 304
Aberrations: . . . 304
C.1.2 Definition of the residual turbulence phase structure function: . . . 305
C.1.3 Definition of convolution, inter-correlation and auto-correlation: . . . 305
Convolution: . . . 305
Auto-correlation: . . . 305
Inter-correlation: . . . 305
C.2 Ideal coronagraph (Sauvage et al., 2010) . . . 305
C.2.1 Difference between the two models . . . 305
C.3 Almost perfect coronagraph (Ygouf, 2012) . . . 305
C.4 The Fourier coronagraph (Hercovisci et al., 2016) . . . 306
C.4.1 Special case of Eq. C.20: without coronagraph . . . 308
C.4.2 Special case of Eq. C.20: without turbulence . . . 308

D Preliminary results: Application of MEDUSAE on in-lab data **309**
D.1 Description of the in-lab data . . . 309
D.2 Results from MEDUSAE applied on in-lab data . . . 309
D.2.1 Different couples of ϕ_{down} and $D_{\phi_{res}}$ input . . . 309
D.2.1.1 Input upstream phase ϕ_{down}: . . . 309

D.2.1.2 Input residual phase structure function $D_{\phi_{res}}$: 310
D.2.1.3 Other parameters used to run MEDUSAE: 310
Weight maps 311
Wavelengths 311
Object regularization 311
D.2.1.4 Results of the MEDUSAE application on the in-lab data 312
D.2.2 Results of further tests for the MEDUSAE application on the in-lab data . . . 312
D.2.3 Conclusions on preliminary tests on the in-lab data 315

E List of communications **317**

Bibliographic references **319**